

**THE FLUID DYNAMICS OF HEART DEVELOPMENT: THE EFFECT OF
MORPHOLOGY ON FLOW AT SEVERAL STAGES**

Nicholas A. Battista

A dissertation submitted to the faculty at the University of North Carolina at Chapel Hill in partial fulfillment of the requirements for the degree of Doctor of Philosophy in the Department of Mathematics in the College of Arts and Sciences.

Chapel Hill
2017

Approved by:

Laura A. Miller

M. Gregory Forest

Boyce E. Griffith

Daphne Klotsa

Jiandong Liu

© 2017
Nicholas A. Battista
ALL RIGHTS RESERVED

ABSTRACT

Nicholas A. Battista: The Fluid Dynamics of Heart Development: The
effect of morphology on flow at several stages
(Under the direction of Laura A. Miller)

Proper cardiogenesis requires a delicate balance between genetic and environmental (epigenetic) signals, and mechanical forces. While many cellular biologists and geneticists have extensively studied heart morphogenesis using various experimental techniques, only a few scientists have begun using mathematical modeling as a tool for studying cardiogenic events. Hemodynamic processes, such as vortex formation, are important in the generation of shear at the endothelial surface layer and strains at the epithelial layer, which aid in proper morphology and functionality. The purpose of this thesis is to study the underlying fluid dynamics in various stages on heart development, in particular, the morphogenic stages when the heart is a linear heart tube as well as during the onset of ventricular trabeculation.

Previous mathematical models of the linear heart tube stage have focused on mechanisms of valveless pumping, whether dynamic suction pumping (impedance pumping) or peristalsis; however, they all have neglected hematocrit. The impact of blood cells was examined by fluid-structure interaction simulations, via the immersed boundary method. Moreover, electrophysiology models were incorporated into an immersed boundary framework, and bifurcations within the morphospace were studied that give rise to a spectrum of pumping regimes, with peristaltic-like waves of contraction and impedance pumping at the extremes. Lastly, effects of resonant pumping, damping, and boundary inertial effects (added mass) were studied for dynamic suction pumping.

The other stage of heart development considered here is during the onset of ventricular trabeculation. This occurs after the heart has undergone the cardiac looping stage and now is a multi-chambered pumping system with primitive endocardial cushions, which act as precursors to valve leaflets. Trabeculation introduces complex morphology onto the inner lining of the endocardium in the ventricle. This transition of a smooth endocardium to one with complex geometry, may have

significant effect on the intracardial fluid dynamics and stress distribution within embryonic hearts. Previous studies have not included these geometric perturbations along the ventricular endocardium. The role of trabeculae on intracardial (and intertrabecular) flows was studied using two different mathematical models implemented within an immersed boundary framework. It is shown that the trabecular geometry and number density have a significant effect on such flows.

Furthermore this thesis also focused attention to the creation of software for scientists and engineers to perform fluid-structure interaction simulations at an accelerated rate, in user-friendly environments for beginner programmers, e.g., MATLAB or Python 3.5. The software, *IB2d*, performs fully coupled fluid-structure interaction problems using Charles Peskin's immersed boundary method. *IB2d* is capable of running a vast range of biomechanics models and contains multiple options for constructing material properties of the fiber structure, advection-diffusion of a chemical gradient, muscle mechanics models, Boussinesq approximations, and artificial forcing to drive boundaries with a preferred motion. The software currently contains over 50 examples, ranging from rubber-bands oscillating to flow past a cylinder to a simple aneurysm model to falling spheres in a chemical gradient to jellyfish locomotion to a heart tube pumping coupled with electrophysiology, muscle, and calcium dynamics models.

To my mother, sister, Grandma Yoshi, and Grandma and Grandpa
Handley.

ACKNOWLEDGEMENTS

I cannot put into words how eternally grateful I am for the guidance and support from my thesis advisor, Dr. Laura Miller. Her highly fluid advising style has allowed myself, as well as all of her students, to grow into the scientists we are today. From my beginnings at UNC, with virtually no biology background, to leaving UNC with immense appreciation and awe of biology and medicine, I would like to thank Laura for first introducing me to that world. I cannot express how thankful I am for her patience and willingness to work with me and train me to think, both mathematically and biologically, and mold me into becoming a better scientist. Furthermore, I would like to thank her for helping me conquer my fear of being in the ocean, e.g., being eaten by a shark(s), by planning the scuba diving adventures her lab. Thank you for convincing me to get open water and advanced scuba certified and for taking the training courses with me.

On that note, I would like to thank all of Laura's lab members, current, former and associated, in alphabetical order, Austin Baird, Terry Campbell, Christy Hamlet, Alex Hoover, Shannon Jones, Shilpa Khatri, Andrea Lane, Grace McLaughlin, Jennifer Prairie, Julia Samson, Arvind Santhanakrishnan, Michael Senter, Christopher Strickland, Anne Talkington, and Lindsay Waldrop. In particular I would like to especially thank Julia Samson, for our setting up our weekly lab lunches and coffee breaks, teaching me a lot about biology, and being a great lab buddy. May our practical joke war(s) live on in infamy.

I would also like to thank all of my former undergraduate research assistants, in alphabetical order, Michelle Corea, John Cruickshank, Patrick McCarthy, James Norton, Andrea Lane, Leigh Percy, and Samuel Worth. They have all helped me learn how to become a more effective research mentor and added a lot of fun to my graduate school experience. I would like to thank Michelle Corea for her ideas in designing a temperature regulation system for our layer formation (horizontal convection) experiments and lugging hundreds of pounds of ice around campus with me. Furthermore, I would like to especially thank Andrea Lane, to whom I had the pleasure of mentoring for almost 3.5 years. Thanks for working with me on a lot of the crazy research ideas and introducing me to

the intricacies of fancy macaroni and cheese based dishes.

I am indebted to Nobuyo Maeda, who admitted me into the Integrative Vascular Biology training program at UNC-CH, and thereby granting me support on the NIH T32 HL069768-14 grant, as well as Christopher Mack, who later took over the training program. My participation in that program helped me learn a tremendous amount of cellular biology, the way cell biologists and geneticist think, and how to be an effective science communicator. Trying to explain my mathematical models and computational techniques to scientists well outside of my field was a truly rewarding experience. I would also like to thank the fellow trainees in my cohort, particularly Leigh Ann Samsa, Christopher Givens, and Sarah Shelton, for their constructive input, questions, and general conversations about science.

I would also like to thank my entire thesis committee: Boyce Griffith, Daphne Klotsa, Jiandong Liu, and M. Gregory Forest. I would like to thank Boyce for all his expert insights into numerical techniques and algorithm implementation and for his suggestions, Daphne Klotsa for her unending positivity and always asking seemingly innocuous questions that always eventual lead me to a much deeper understanding of the science at hand, Jiandong Liu for introducing me to the beauty of various stages of heart development and motivating a lot of the questions that we sought to answer in this thesis, and Greg Forest for his mathematical and scientific expertise and his continual support and guidance throughout my, and all of my fellow colleague's, entire graduate school tenures. I would also like to thank William Kier for training me to be capable of viewing biomechanics problems through, both, a mathematical and biological lens.

I would also like to specifically thank Laurie Straube in the Mathematics Student Support Office for always being so motivating, encouraging, and selflessly going above and beyond for all of us students on a daily basis.

I am also thankful for having had the opportunity to participate in the Emerging Leaders in Science and Society program (ELISS), designed and directed by Melanie Roberts, and co-directed by Renske Erion, through the American Association for the Advancement of Science (AAAS). I met many remarkable individuals and had the chance to work in the spirit of science policy with them. In particular I would like to specifically thank members of the "Triangle Group" to which I was apart of, Kasia Grzebyk, Shaili Jha, John Wachen, Andrew George, Brian Langross, Joyell Arscott, and Justin Lana.

I would also like to thank my friends, who helped keep me grounded and added excitement and fun during this whole graduate school process. In particular I would like to thank, in alphabetical order, the following people, Michael Abel, Manuchehr (Nuch) Aminian, Holly Arrowood, Austin Baird, Tim Bald, Aaron Barrett, Kevin Bates, Bob and Kim Booth, Namdi Brandon, Curtis Byrd, Kathleen Carroll, Amanda Casella, Agathe Ceppe, Caitlin Hult, Shanda Kamien, Chris Lawrence, Jae Ho (Mike) Lee, Brian and Katrina Lelli, Vlad Levering, Michael Malahe, Gilberto Martinez, Tesfaye Mohammed, Quentin Robinson, Julia Samson, Nick and Megan Sereni, Jackie Stone, Ben Vadala-Roth, and Tim Wessler. I would like to especially thank Austin Baird, Namdi Brandon, and Bob Booth for all the nerdy (and non-nerdy) lunches, fun weekends, and capers, Kathleen Carroll, who really encouraged and supported me during my last year of graduate school and added in lots of adventures, and Chris Lawrence for being my first weight training partner since I left RIT and for his advice, counsel, and divulging all the secrets of strength training.

Moverover, I would like to thank Dr. Anthony Harkin for first introducing me to the joys of applied mathematics, scientific computing, and spectral theory early in my undergraduate education. I would also like to thank Dr. David Ross, for all of the mathematics, physics, and overall science he has taught (and continues to teach) me, but more so, for being such an incredible mentor since the time I have left RIT.

Furthermore, I would like to especially thank my mother, Carol Battista, and my sister, Christina Battista, for all their love, support, and encouragement they always have given me. Without them, I would not be the person I am today, nor would I have accomplished a fraction of what I have. I do not think it is common for a brother and sister to begin a Ph.D. program at the same time, for the same degree, at schools only 30 miles apart, but I am truly thankful that Chris and I were granted that opportunity. Her love and support has meant the most to me.

TABLE OF CONTENTS

LIST OF FIGURES	xiii
LIST OF TABLES	xxix
CHAPTER 1: INTRODUCTION	1
CHAPTER 2: CARDIOGENESIS	5
2.1 Heart Morphology	5
2.2 Experimental Studies on Mechanical Forces and Heart Morphogenesis	17
2.3 Zebrafish used as a model organism for cardiogenesis	24
2.4 Mathematical Models in Heart Morphogenesis	26
2.4.1 Linear Heart Tube Modeling	28
2.4.2 Cardiac Looping and Chamber Formation Models	39
2.4.3 Cardiac Valve Development	53
CHAPTER 3: MATHEMATICAL METHODS	60
3.1 Conservation of mass, momentum, and the Navier-Stokes equations - oh my!	60
3.1.1 Intuitive derivation of the Navier-Stokes Equations	61
3.1.2 Navier-Stokes Equations	68
3.1.3 Vorticity Formulation	69
3.1.4 Mathematical derivation of the Navier-Stokes Equations	71
3.2 Non-dimensional quantities of interest	78
3.2.1 Example: Damped Harmonic Oscillator	79
3.2.2 The Reynolds Number and Different Fluid Regimes	81
3.2.3 The Womersley Number	86
3.3 The Immersed Boundary Method (IB)	88
3.3.1 Introduction to IB	90

3.3.2	IBM Framework	92
3.3.3	<i>IB2d</i> Work Flow	111
3.3.4	Selected <i>IB2d</i> Examples	115
3.3.5	<i>IB2d</i> Data Analysis Package	128
3.3.6	<i>IB2d</i> Code Validation	131
3.3.7	Discussion and Conclusion Regarding <i>IB2d</i>	135
3.3.8	Boyce Griffith's IBAMR	137
CHAPTER 4: FLOW THROUGH HEART TUBES		141
4.0.1	Goals of heart tube with blood cells model	145
4.0.2	Goals of the electro-mechanical model	146
4.0.3	Goals of the resonant pumping model	146
4.1	Heart Tube Blood Cells	146
4.1.1	Model Geometry	147
4.1.2	Results	153
4.1.3	Discussion and Conclusions	159
4.2	Electro-dynamical Pumping	160
4.2.1	Computational Model	161
4.2.2	Results of the electro-dynamical model	166
4.2.3	Discussion and Conclusion of Electro-dynamic Model	171
4.3	Resonant Pumping	172
4.3.1	Computational Model	172
4.3.2	Results of Resonant Studies	174
4.3.3	Discussion and Conclusion for DSPs Pumping at Resonance	187
CHAPTER 5: FLOW THROUGH EMBRYONIC CARDIAC TRABECULAE		189
5.1	Trabeculation Introduction	189
5.1.1	Goals of cavity model	192
5.1.2	Goals of two-chamber model	193
5.2	Trabeculated Cavity Model	193
5.2.1	Computational Model	193

5.2.2	Experimental Validation of the Numerical Model	200
5.2.3	Trabeculated Ventricular Cavity Results	201
5.2.4	Trabeculated Cavity Conclusions	206
5.3	Two Chamber - Trabeculated Ventricle Model	211
5.3.1	Computational Model	212
5.3.2	Prescribed Motion of the Two-Chambered Heart	217
5.3.3	Two-Chamber Heart Results	220
5.3.4	Two-Chamber Heart Conclusions	233
CHAPTER 6: DISCUSSION AND CONCLUSIONS		236
6.1	Quick Review of Thesis Topics	236
6.1.1	<i>IB2d</i> Discussion and Conclusion	236
6.1.2	Linear Heart Tube Models Discussion and Conclusions	237
6.1.3	Trabeculation Models Discussion and Conclusions	240
6.1.4	Future Work	242
APPENDIX A: IMMERSED BOUNDARY DISCRETIZATION APPENDICES 243		
A.1	Discretizing the Navier-Stokes Equations	243
A.2	Discretizing the Fourth Derivatives of the Non-Invariant Beam Model	244
A.3	Discretizing the Normal Derivatives on the Boundary	245
A.4	Discretizing the FitzHugh-Nagumo Equations	246
A.5	Discretizing the Advection-Diffusion Equation	247
A.5.1	Advection-Diffusion Example	248
APPENDIX B: <i>IB2D</i> EXTRAS		253
APPENDIX C: NUMERICAL METHODS FOR COMPUTATIONAL FLUID DY-		
NAMICS (CFD)		256
C.1	Projection Methods	256
C.1.1	Projection Methods Example	257
C.2	Spectral Methods via Fast Fourier Transform (FFT)	259
C.2.1	Spectral Methods (FFT) Example	262

C.3	Lattice Boltzmann Methods	264
C.3.1	Lattice Boltzmann Example	268
REFERENCES	270

LIST OF FIGURES

2.1	A comparison of early developmental landmarks between different species. Chick embryo stages are described according to the Hamburger-Hamilton (HH) scale, zebrafish stages are measured in hpf (hours post fertilization), mouse stages are marked as postconception days (E), and human stages are developmental days.	6
2.2	Snapshots of the contractile wave propagating through the endothelium in the linear tube of an embryonic zebrafish heart at 28 hpf. The contractile wave is outlined in blue. These images are courtesy of Leigh Ann Samsa.	7
2.3	Snapshot taken of an embryonic zebrafish heart's endothelium at 42 hpf illustrating the looping process' morphogenetic changes from a linear heart tube. Image courtesy of Leigh Ann Samsa.	8
2.4	Frontal view of the embryonic mouse heart during day 9 (approximate human age is 25 days) and cartoon schematic. When the heart tube elongates and begins to loop, blood flows into the sinus venosus, then into the primitive atria, the ventricles and bulbus arteriosus before entering the visceral arch vessels. We note that mammalian hearts are four chambered (two atria and two ventricles), while fish hearts are two chambered (one atria and one ventricle) [1]. SEM images courtesy of Dr. Kathleen K. Sulik. Diagram redrawn from [2].	9
2.5	Images illustrating the development and morphology of endocardial cushions. (a) shows a cartoon depiction of the zebrafish embryonic heart at 36 hpf of the pinching to create the atrioventricular canal and endocardial cushion formation. (b) gives the associated <i>in vivo</i> image of (a). (c) illustrates the zebrafish heart at 60 hpf with the endocardial cushions highlighted in green with green arrows. (a) and (b) were adapted from [3] and (c) from [4].	11
2.6	Images from Liu et al. 2010 [5] and Samsa et al. 2016 [6], taken by utilizing two cardiomyocyte specific lines, <i>Tg(cmlc2:GFP)</i> and <i>Tg(cmlc2:ras-GFP)</i> , which express GFP or membrane-bound GFP in all differentiated cardiomyocytes and confocal optical imaging of the ventricle, respectively. (1) Shows the onset of trabeculation in the 72 hpf zebrafish heart. The arrow indicates the beginning of a primitive trabeculae. Note that it is located directly across from the atrioventricular canal, implicating that higher regions of mechanical forces undergo trabeculation first. (2) The continued trabeculation process undergoing in the zebrafish heart at 80 hpf, where more trabeculae are present. (3) Shows a similar image to (1) but using a different imaging method.	12
2.7	(1) Endocardial cells are smooth and polygonal in shape before trabeculation occurs. (2) During the onset of trabeculation, endocardial cells become elongated and become slightly more depressed than surrounding endocardial cells. (3) Endocardial cells (E) invaginate the cardiac jelly (CJ) and extend toward the myocardium (M). (4) A primitive trabeculae is formed (illustrated by the white arrow) once the endocardial cells protrude into the myocardium. SEM images taken from Icardo et al. 1987 [7].	13
2.8	Illustrating the exponential increase in cardiac output during development in avian (chick) embryos, as seen from a variety of studies. Image modified from Kowalski et al. 2014 [8].	15

2.9	A summary of morphogenetic landmarks in zebrafish cardiogenesis. In (a), the linear heart tube begins to develop around 19 hpf, (b) illustrates the continued development of a linear heart tube from once being a cardiac disc and the zebrafish's first heart beat around 22 hpf. Shortly thereafter, within a few hours the presence of hemacrit is seen. At 28 hpf, (c), the linear heart tube has settled into its final stage before undergoing cardiac looping around 36 hpf (d). As the heart loops, the chamber begins to balloon, forming into their more mature shape. Also, the atrioventricular canal develops and endocardial cushions form within that canal by 48 hpf, as depicted in (e). At this stage, the now two-chambered heart begins to pump in a fashion reminiscent to its adult counterpart. In (f), the first signs of ventricular trabeculation become apparent at approximately 72 hpf. Image modified from Bakkers et. al. [9].	16
2.10	A summary of morphogenetic landmarks of human heart morphogenesis, given in weeks. Figure is adapted from [10].	17
2.11	An image illustrating the mechanical forces, i.e., shear stress and pressure forces, from the fluid onto the endocardial wall. Image taken from Lindsey et al. 2014 [11].	18
2.12	The figure illustrates three different experimental placements of a $50\mu m$ bead in a 37 hpf embryonic zebrafish heart <i>in vivo</i> . (1) The bead is placed near the sinus venosus, without obstructing the inflow to the looping heart. Valve and chamber development occur normally, without malfunction. (2) The bead is placed obstructing the sinus venosus (the atrial inflow tract). (3) The bead is positioned obstructing the bulbus arteriosus (ventricular outflow tract). In cases (2) and (3), normal blood flow does not occur and neither valvulogenesis, proper cardiac looping, nor chamber ballooning initiates. Image taken from [12].	19
2.13	A ventral view of a normal heart tube (1), the elongation and narrowing of the tubular heart when the SPL is removed (2), and self-restoration of the tubular diameter, thought to be due to tensile forces. Images taken from Nerukar et al 2006 [13].	21
2.14	Data collected from a study from ErbB2 zebrafish mutants by Liu et al. 2010 [5]. (1) These mutants experience a decrease in fractional shortening. It seen that as embryogenesis progresses, fractional shortening further decreases. (2) Their hearts also undergo bradycardia, where the heart beat also progressively decreases during development. (3) and (4) are optical mappings of cardiac conduction in their ventricle at 10 dpf. More prevalent ventricular conduction regions can seen in wild type mutants (3) compared to their ErbB2 mutant counterparts (4). It is also evident in (3) and (4) that the wild type ventricle is more massive than the mutant's.	22
2.15	Evolution of the activation pattern of HH stage 16 to HH stage 36 hearts in chicken embryos. Initially all electrical activation propagates as base-to-apex signals, which lasts until around HH stage 27 embryonic chicken hearts. Next a shift to 2 locations of ventricular activation occurs, one at the base, showing immature activation foci, and another at the apex, the location of mature activation foci. This type of 2-foci activation persists until HH stage 36, when there is full maturity in activation patterns. Images adapted from Reckova et al. 2003 [14].	23
2.16	Illustrating optical clarity at two stages of heart morphogenesis, the linear heart tube stage (1) and (2), and chamber formation (3) and (4). (1) shows the zebrafish embryo 24 hpf, while in (2) a light microscope is used to visualize the optical clarity of the heart tube, which is outlined in blue. Blood cells at this stage are spherical. (3) shows the still transparency of the zebrafish at 48 hpf. In (4) a light microscope is used to affirm that two distinct chambers have formed, pumping more elliptical erythrocytes. These images are courtesy of Leigh Ann Samsa, School of Pathology at UNC-CH.	25

2.17	Schematic diagram of dynamic suction pumping adapted from Santhanakrishnan et al. 2011 [15]. (A) Illustrates the tube at initially at rest, while (B) shows the asymmetric location of a single actuation point undergoing contraction. (C) That contraction creates a bidirectional wave traveling down the tube and in (D) one side of that wave reflects off the left end of the tube, since that end is closer to the actuation point. In (E) both the reflected wave and last portion of the initial bidirectional wave are traveling in the same direction. Finally in (F) there is reflection of that wave, while presumably another contraction on of the actuation will occur.	29
2.18	Model geometry as adapted from [16]. Their geometry, although $3D$, is axisymmetric. The model is at rest in (a), and under one contraction in (b). The inlet and outlets are held rigid for proper wave reflection, and the tube is elastic, allowing passive traveling waves from the actuating.	30
2.19	Results taken from [16] regarding the dynamic suction pumping mechanism, i.e., location of the actuation site, occlusion amplitude, and duty cycle %. (a) Shows the dependence of flow rate on the location of the actuation site. As the location moves to the center of the tube, flow rate decreases. Their data is confirmed against experiments performed by Hickerson et al. 2005 [17, 18]. (b) Illustrates the flow rate dependence on the pinching occlusion, in an almost linear relationship. As occlusion increase, as does flow rate. In (c) they explore flow rate's dependence on duty cycle % and see good agreement with experimental work done by Hickerson et al. 2005. [17, 18]	31
2.20	Plot adapted from [16] illustrating the non-linear relationship between flow rate and frequency for dynamic suction pumps.	31
2.21	Geometry of the linear heart tube geometry. In (a), the tubular geometry with endocardial cushions is shown in its resting state, while (b) illustrates the difference between the deformation geometry (dashed lines) and rest state (solid lines). As a wave passes by, the cushions thicken and deform. Figure adapted from Taber et al. 2007 [19].	32
2.22	Results depicted differences in pressure and flow waveforms for both simulations with and without endocardial cushions in the heart tube. (a) and (c) show the pressure and flow waveforms respectively for a simulation without endocardial cushions. It is clear in (c) that a flow waveform for peristalsis can be seen. (b) and (d) illustrate the transition to pulsatile pressure and flow profiles once endocardial cushions are included. Figures adapted from [19].	33
2.23	Geometry of the closed racetrack. Flexible regions are indicated by the dotted portions, while rigid parts are shown by solid lines. The pumping mechanisms, peristalsis or dynamic suction pumping, are implemented along the flexible portion. Figure adapted from [20, 21].	34
2.24	Simulation results illustrating average velocities for peristalsis and dynamic suction pumping as a function of Womersley number, while showing effects of varying tube diameter in each case. (A) Results for peristalsis, while (B) illustrates the results for dynamic suction pumping. For Wo in the biologically relevant range, $Wo \approx 0.1$, only peristalsis initiates significant flow, with velocities in the order of $\sim 0.01cm/s$, where as dynamic suction pumping at the same scale gives velocities <i>at least</i> two orders of magnitude smaller. Figure adapted from [20].	35
2.25	Geometry of the flexible region of the racetrack. The springs depict muscles that generate the contraction, once the action potential signal propagates to its location. The muscle then contracts according to $\mathbf{F}_{electro}$. Figure adapted from [22].	35
2.26	A comparison of the dimensionless spatially-averaged flow velocities measured across the cross-section of the top of the tube for dimensionless time. The solid line represents the neuro-mechanical pump, the dashed line is peristaltic pumping, and the dotted line is impedance pumping. Figure adapted from [22].	36

2.27	A comparison of the dimensionless spatially-averaged and temporally-averaged flow velocities measured across the cross-section of the top of the tube for different Wo . The solid line represents the neuro-mechanical pump, the dashed line is peristaltic pumping, and the dotted line is impedance pumping. Figure adapted from [22].	37
2.28	Geometry of the racetrack with a shorter length flexible region and wider cross-section, when compared to Figure 2.23. Figure adapted from Waldrop et al. 2015 [23].	38
2.29	Data illustrating the non-linear behavior of these peristalsis assumptions. These figure show speed vs. a parameter in the model. The figure on the left shows a non-linear relationship between speed and Wo , where U_{avg} is given by black circles, U_{max} by white diamonds, and U_{peak} as white, inverted triangles. The middle figure shows how speed changes by varying the compression ratio (occlusion). The figure on the right shows the fluid speed against the speed of the contraction wave. The dotted line gives the speed for the constant, non-dimensional compressive wave speed. The figure was adapted from [23].	38
2.30	Data showing the non-linear behavior of peristalsis when wave speed is decoupled from initiation frequency of the compressive wave. In grey are when wave speed and frequency are linearly proportional; in black, when wave speed is held constant and frequency is varied. U_{avg} are circles, U_{max} are diamonds, and U_{peak} are inverted triangles. The figure was adapted from [23].	39
2.31	Ramasubramanian et al. 2008's 2D and 3D model geometries. In (a) the model for the primitive atria is shown, with its associated cross section, while (b) illustrates the full 3D geometry for the heart tube to undergo c-looping. A ventral view as well as side view is given. The models in (a) and (b) are used to explore varying degrees of contraction of the primitive atria to exert forces which may be responsible for ventral bending. The geometry depicted in (c) is a 2D cross-sectional model for studying cardiac rotation when perturbations may arise during cardiac looping, here the removal of the SPL. (HT = heart tube, CT= outflow tract, TA = top atrial region, BA = bottom atrial region, DM = dorsal mesocardium, FG = foregut wall, MY = myocardium, CJ = cardiac jelly, and SPL = splanchnopleure). Adapted from [24].	41
2.32	Three-dimensional finite element model for cardiac looping without the SPL. The base geometry with before mechanical loading is shown in (a), and in (b) the effects of mechanical loading can be seen to cause the heart tube to deform and ventrally bend. This is in good agreement with experimental data exploring ventral bending. The model depicted in (c) explores asymmetric contraction between each side of the heart tube, with contraction nonexistent on the right side. They found that the amount of ventral bending is decreased as compared to the situation in (b). Furthermore in (d) they show the case when contraction is turned off on both sides, giving rise to even less bending than (c). Adapted from [24].	42
2.33	A 2D model of a cross-sectional area of the heart tube with myocardial and cardiac jelly layers fixed to the dorsal mesocardium is seen in (b),(b'), and (b''). Progressive time points within the simulation are shown, with the associated experimental data at the same time points in (a),(a'), and (a''). In (a) and (b) show the chick stage-11 heart with the SPL in contact with the myocardium. The same heart is shown in (a') and (b') but 20 minutes post-SPL removal. In each case an immediate loss of rotation can be seen. However, 6 hours later in both cases the heart shows reversal back to being fully rotated, as signaling a return to normal development. Figure adapted from [24].	42

2.34	(A) and (B) show experimental images for when the left OV is removed immediately after removal and 12 hrs. later. Similarly (C) and (D) show analogous images, but for right OV removal, as does (E) and (F) but for when both OV are removed. (G) and (H) show images of removing the portion of the heart tube itself above the primitive atria. The black lines illustrate the cuts where each component was surgically removed. (A') and (B') illustrate the complementary simulations to the images in (A) and (B). Similarly (C') and (D') are associated simulations for (C) and (D), (E') and (F') are models of (E) and (F), and finally (G') and (H') illustrate the simulations performed for heart tube removal at similar time points of (G) and (H). In all cases the simulations model predicts the same qualitative behavior as the experiments. Figure adapted from [25].	44
2.35	(A) illustrates how the rotation angle is defined, that is, as the angle between the the long axis of the elliptical lumen and the dorsal-ventral axis, all within a cross-section of the heart tube. The components are labeled as MY, as the myocardium, DM, as the dorsal mesocardium, and CJ, as the cardiac jelly. (B) compares the experimental rotation angle against the hearts at HH stages 10 to 12. The model supports the experimental data, and both show an increase in rotation angle as heart development progresses. Adapted from Shi et al. 2014, [25].	45
2.36	A comparison of the strain within various components of chick hearts at HH stages 10 to 12 from experimental data to the simulated model. LHT, RHT, and VHT stand for the right, left, and ventral sides of the heart tube. LOV and ROV describe the left and right omphalomesenteric veins and LAIP and RAIP are the left and right sides of the anterior intestinal portal. Figure adapted from Shi et al. 2014, [25].	45
2.37	Geometry used in the mathematical model as well as physical model, adapted from [26]. The velocity, U , at the inflow is held constant during the simulations and experiments as is the channel width, d . The chamber depth, C , and cushion heigh, V , are varied.	47
2.38	Simulations without cardiac cushions in which the Reynolds number is varied, showing that the regime for vortex formation happens around $Re \sim \mathcal{O}(10)$. Adapted from [26].	47
2.39	A comparison of a numerical simulation and physical model experiment for $Re = 50$. Both show the formation of a large intracardial vortex and are in qualitative agreement. Adpated from [26].	48
2.40	Model geometry, where the atrial wall moves in a prescribed manner, allowing the ventricle to fill, via its wall being flexible, and then ventricular contract occurs due to the elastic deformations of its wall wanting to return to its equilibrium rest state. Adapted from Miller et al. 2011 [27].	49
2.41	Data from parameter sweeps on the endocardial cushion heights, (A) and (B), and varying ventricular wall stiffness, (C) and (D). In (A) and (B), varying the cushion height from 0 to $15\mu m$ increases the normal force acting on the chamber walls more than fivefold. In (C) and (D) varying the ventricle wall stiffness also increases the force necessary for ventricular filling. Adapted from Miller et al. 2011, [27].	50
2.42	$Tg(fli1a:EGFP)$ embryos were used to obtain biologically relevant endocardium geometries in the computational mode and perform <i>in vivo</i> PIV experiment, in concert with green fluorescent protein (GFP). This can be seen in Figure(2.42)-(a),(b), and (c), where (a) shows the tubular embryonic heart between 20-30 hpf, (b) illustrates the heart structure between 40-50 hpf, and (c) shows the distinct two chamber geometry around 110-120 hpf. The corresponding model geometries can be found in (a'), (b'), and (c') respectively. A denotes the atria and V stands for the ventricle. Adapted from [28].	51

2.43	(a) illustrates the use of transgenic $Tg(fli1a:EGFP)y1$ embryos for a clear visual delineation of the endocardial layer for constructed the computational model and (b) shows the use of $Tg(gata1:dsRedsd2)$ transgenic zebrafish to visualize hematocrit for accurate PIV and particle tracking. A denotes the atrium, V, the ventricle, and B, the bulbus arteriosus. In (c), a comparison between time averaged flow velocities through a cross section of the AV canal is shown between experimental PIV data and the computationally modeled data. Images and data taken from [28].	52
2.44	(a),(b), and (c) show the wall shear stress within the AV canal for zebrafish hearts between 20-30 hpf, 40-50 hpf, and 110-120 hpf over the course of one heart beat, as predicted by the computational model. (d) gives the averaged predicted shear stress at each stage of development in the AV canal. (e) illustrates the averaged pressure gradients within the AV canal for varying phases of heart morphogenesis, given by the computational model. Figures adapted from [28].	53
2.45	The tubular geometry used to study valve leaflet formation can be seen in Figure 2.45, adapted from [29]. Although shown in 3D, the model investigated was a 2D construction, where hemodynamic forces will act both tangentially (shear stress) and normal (pressure) to the endocardial cushions.	54
2.46	The steady-state flow profiles, illustrated via streamline analysis, are shown for $Re = 4.2$, (a), and $Re = 71.0$, (b). It is seen that the size of eddies is sensitive to Re , where smaller eddies are observed in the smaller Re case, (a), while larger vortices form after the flow passes the cushions in (b), corresponding to a higher Re . Figure adapted from [29]. . . .	54
2.47	Shear stress and pressure profiles corresponding to simulations for $Re = 4.2$, (a), and $Re = 71.0$, (b). It is clear that in the higher Re case, (b), the cushions undergo more shear stress than in the lower Re case. However, in both cases the pressure exerted on the cushions remains relatively static. Furthermore, the maximum shear is located at the center of the cushion. Adapted from Biechler et al. 2010, [29].	55
2.48	In (a), a cross-section of the AV canal geometry is shown, with endocardial cushions protruding into the canal. The flow is specified going left to right, i.e., from the atrium to ventricle. (b) illustrates the colormap of the modeled growth rate parameter, $a(r)$ in a 2D cushion cross-section. Figure adapted from [30].	56
2.49	Figure illustrating the iterative approach in decoupling the fluid component from the solid mechanics portion of the fluid-solid-mechanics model. In step 1, the fluid model is solved and then in step 2 the hemodynamic forces, shear and pressure, are transferred to the solid mechanics finite element model. In step 3, the solid model equations are solved and hence the valve deforms. Finally in step 4, the fluid mesh is updated, and all preceding steps are repeated. Adapted from [30].	57
2.50	In (a) a plot of the area ratio vs. simulation time is shown. There are four cases illustrated-shear only, pressure only, no external loads, and full external loads (both pressure and shear). It is clear that for the area ratio, there is good agreement between pressure and the full external load cases, while the shear only case and no external load case are also consistent. In (b), deformations from each configuration (shear only, pressure only, and full external loading) are shown. It is evident that the cushion begins to elongate under these hemodynamic forces in the direction of flow. Figure adapted from [30].	57
2.51	In (a) there is good qualitative agreement between the shear only and full external load cases, while there is agreement between the pressure and no external load cases, showing that shearing has a greater effect on migration of the top center point. (b) further illustrates that orientation angle has greater dependence on shear than pressure from simulation images. These figures are adapted from [30].	58
3.1	Pressure gradients acting on a fluid parcel.	64

3.2	Shear-stress acting on fluid parcel near a boundary.	65
3.3	Cartoon depictions for the vorticity of fluid parcels. Vorticity is a measure of the <i>local</i> rotation of a fluid blob, not of the global continuum, as illustrated in these examples. The three examples include rigid body-like rotation ($v\omega r$), parallel shear flow, and irrotational vortical flow ($v\alpha\frac{1}{r}$). Row 2 of the table shows the <i>global</i> velocity field in each case, while row 3 depicts the <i>absolute</i> velocities around a fluid parcel at specific locations, specified by the red dot, in the velocity field. Row 4 shows the <i>local relative</i> velocities around the same fluid blobs. In the cases of rigid body-like rotation and parallel shear flow there is nonzero vorticity, while in the case of irrotational vortical, there is no vorticity.	70
3.4	Initial domain, \mathcal{W} , at $t = 0$ being mapped by \mathcal{X} into $\mathcal{X}(\mathcal{W}, t)$ at $t > 0$	71
3.5	Flow past a fixed cylinder at different Reynolds Numbers, illustrating different regimes in the fluid flow. In these examples, the characteristic length is given by the diameter of the cylinder and velocity is given by the inflow velocity. For $Re < 5$, flow is unseparated and moves around the cylinder. For $5 < Re < 15$ symmetric vortices begin to form on the trailing edge of the cylinder. Once $40 < Re < 150$, vortices sheets begin to be shed off the cylinder. For $150 < Re < 3 \times 10^5$, the vortex sheets transition to turbulent vortical flow. At Re higher than that, the laminar boundary layer undergoes a transition to turbulent and the wake behind the cylinder becomes more narrow and more disorganized. For high enough Re ($\sim 3,500,000$) there is a transition back to a turbulent vortex sheet. Image courtesy of Thermopedia.com	85
3.6	Organ systems for various species of organisms, plotted to show where they fall on the axis given by a characteristic length scale, the vertical axis, and Re , shown on the horizontal axis. The embryonic human heart is shown as $Re \sim 0.05$ with characteristic length of $D \sim 2.5 \times 10^{-4}$	86
3.7	Velocity profiles at $t = 0$ are shown for varying Wo . For small Wo , <i>Poiseuille</i> flow is obtained, while for large values of Wo , the velocity profile becomes flat. This figure is adapted from [31].	89
3.8	A visual guide to the standard steps in Peskin's immersed boundary method. (a) The elastic deformation forces are computed from the current configuration of the immersed structure. (b) Those deformation forces are spread to neighboring fluid grid points, via Eq.(3.74). (c) The fluid velocity is updated everywhere in the domain using Eqs.(3.72) and (3.73). (d) The immersed boundary is moved at the local fluid velocity by Eq.(3.75). Note that the deformation force vectors in (b) and velocity vectors in (c) are not parallel, as the fluid already may have some underlying non-zero velocity field, which gets perturbed due to the presence of the deformation forces.	94
3.9	Illustrating the key points of various fiber models implemented in <i>IB2D</i> . (a) Two nodes connected by a virtual spring held at the resting-length of the spring (top) and a rendering of the longitudinal forces induced when the spring is stretched (bottom). (b) A torsional spring connecting three adjacent Lagrangian nodes at its equilibrium configuration, e.g. angle θ (left) and an illustration of the force experienced by the middle node, \mathbf{X}_M , when the system is not at its lowest energy state (right). (c) A massless and massive point, \mathbf{X} and \mathbf{Y} respectively, connected by a stiff virtual spring. Incoming flow moves the massless point to a new position, which exerts a pulling-like effect on the massive point. The massive point will move depending on a coupled constitutive equation. (d) Incoming flow permeates a porous boundary. The amount of flow that moves through the body depends on the permeability of the membrane; all flow through the boundary is normal to the body itself.	97
3.10	Example force-velocity and length-tension curves illustrating the respective relationships that the <i>FV-LT</i> model is trying to capture.	104

3.11	Schematic diagram of the 3-Element Hill model of muscle contraction, containing a contractile element, series element, and parallel element modeling actin and myosin cross-bridges, tendons, and connective tissues, respectively.	105
3.12	A depiction of exerting an arbitrary force onto the background fluid grid to obtain the desirable flow profile. The fluid grid is given by the rectangular grid with the selected grid points to enforce the penalty-force highlighted and circled in green and orange. The penalty force is applied to the fluid lattice points in green if the flow profiles do not match at those selected nodes. A cartoon rendering of the resulting flow is illustrated as the blue arrows.	109
3.13	Descriptions of selections in <i>input2d</i> . This file controls what inputs get passed to the main <i>IB</i> driver method.	112
3.14	Input format for the <i>.vertex</i> file	113
3.15	Input format for a <i>.spring</i> file	113
3.16	Input format for a <i>.beam</i> (torsional spring) file	113
3.17	Input format for a <i>.target</i> file	113
3.18	Input format for a <i>.mass</i> file	114
3.19	Input format for a <i>.porous</i> file	114
3.20	(a) Order of porous stencil IDs. (b) An example of how the stencil IDs are defined using the porous structure from Figure 3.9d.	114
3.21	Input format for a <i>.muscle</i> (FV-LT muscle) file	115
3.22	Input format for a <i>.tracer</i> file	115
3.23	A comparison of a porous rubberband (left) and a non-porous rubberband (right) done in a single simulation. The colormap is of the fluid pressure. It is clear that both rubberbands start stretched from their equilibrium position, but end at a circle; however, the porous rubberband does not conserve the same volume, as fluid flows through it as the simulation progresses.	116
3.24	The flexible beam shown at various times during the simulation. The colormap is of the magnitude of velocity and is depicted along with the background fluid velocity vectors. .	117
3.25	"The Date" example shows target points moving around the computational domain by interpolating positions between three states which spell out certain phrases. The background color map is vorticity.	118
3.26	3 spheres of different masses, with each sphere composed of uniform mass points, under the influence of gravity with a pulsatile flow competing against gravity upwards. The sphere on the left is the lightest and sphere on the right is the heaviest. In the left case, the pulsatile flow dominates, while on the right gravity dominates, and in the middle, the pulsatile flow and gravitational forces are approximately equivalent. The colormap depicts magnitude of velocity.	119
3.27	Simulation of the Rayleigh-Taylor Instability using the Boussinesq Approximation. A heavier fluid (red) sits above a lighter fluid (blue). Note a more sophisticated advection-diffusion solver will give rise to higher resolution of the instability fronts.	121

3.28	Simulation of a falling sphere through a fluid with a background salinity stratification. A spherical mass is released in the lighter salinity background (red) that sits above a heavier background salinity (blue) and the mass falls due to gravity.	122
3.29	A comparison of two idealized anguilliform swimmers moving forward due to continually changes in the preferred curvature of the configuration. One has a stroke frequency of $f = 0.25s^{-1}$ and the other, $f = 0.5s^{-1}$. The colormap illustrates vorticity.	123
3.30	The two phases, in which, the preferred curvature was interpolated between to cause forward swimming.	124
3.31	A comparison of the distances swam by both swimmers as a function of the number of strokes.	125
3.32	An idealized swimmer moving forward and turning due to the asynchronous muscle activation. The colormap illustrates vorticity.	125
3.33	A linear heart tube, which pumps when an action potential travels down the tube, once enough free calcium binds to muscle filaments, to induce muscle contraction. The colormap illustrates a background concentration gradient.	126
3.34	All the data (Lagrangian positions, Eulerian data, and Lagrangian force data) imported in the data analysis software.	129
3.35	Simulation images taken from a channel with a parabolic flow condition at varying times. The parabolic flow is enforced by an external forcing condition on the Eulerian grid in the section outline in purple and shaded in red, while the vertical lines correspond to the cross-sections of the tube where the velocity data will be analyzed.	130
3.36	Data shown from three different time points during the simulation for velocities across four different cross-sections of the tube. As time increases, the velocity profile becomes more fully developed.	131
3.37	A cross-section of an insect wing moving laterally from left to right in a prescribed manner for $Re = 128$. The background colormap depicts vorticity and the vector field is the fluid velocity.	132
3.38	Non-dimensional lift (3.38a) and drag (3.38b) forces vs non-dimensional time for a cross-section of an insect wing moving laterally at $Re = 128$	133
3.39	A convergence study of the relative error of the lift and drag force, between each simulation and the highly resolved simulation using IBAMR with 1024×1024 resolution on the fluid grid. We note that the horizontal axis is the spatial step size, dx , where $dx = 1/N$, and $N = \{32, 64, 96, 128, 256, 512, 768, 1024\}$	133
3.40	Comparison of <i>IB2d</i> simulation snapshots and PIV experimental data for a wing moving laterally across the domain for $Re = \{1, 10, 100\}$. The figures show the magnitude of velocity, background velocity field, and streamlines.	135
3.41	Illustrations of AMR Meshing. Note that Figure 3.41a illustrates an improperly nested hierarchical structure, since the lower resolved Level 0 cells are directly adjacent to the higher resolved Level 2 cells. Figure 3.41b shows a properly nested hierarchical structure. Images adapted from [32].	138
3.42	An interface between a coarse grid and localised refined grid. Ghost cells are located at the coarse-fine interface in this two-dimensional locally refined grid. Ghost cells are indicated in gray and valid cells are indicated in black. Figure adapted from [32].	139

3.43	An example of AMR from a simulation with a two chambered heart containing a trabeculated ventricle. It is clear that near the immersed structure there is the highest level of refinement.	139
4.1	Figure adapted from Grosskurth <i>et al.</i> [33] illustrating the evolution of hearts from the valveless heart tubes in the open circulatory systems of tunicates to the adult multi-chambered-valvular of vertebrates.	142
4.2	Figure illustrating the phylogenetic relationship and general heart structure of the Chordate subphyla. Cephalochordates, like amphioxus, have a series of four peristaltic vessels that serve as a pump, while tunicates have a single-chamber pump, which is composed of a single layer of myocardium (red) surrounded by stiff pericardial layer (pink). The earliest vertebrates, e.g., lampreys, have at least a two-chambered myocardium composed of a layer of cardiac myocardial cells (red), an endocardial cellular layer (yellow), valves that separate distinct chambers, and a surrounding pericardium (pink). Figure adapted from [34].	143
4.3	Schematic diagram illustrating dynamic suction pumping [15]. (A) The flexible tube is at rest. (B) Active contraction of the tube in a non-central location along the tube. (C) Contraction induces an elastic passive bidirectional wave to propagate along the tube. (D) Wave reflects off rigid portion of the tube on side nearest to contraction point. (E) The reflected wave travels down the tube. (F) The waves reflect off the rigid section at the far side of the tube. Notice the the reflected wave amplitude is smaller than the reflected wave off the other end.	144
4.4	The embryonic heart tube of a Zebrafish 30 hpf courtesy of [35]. Spherical blood cells are seen within the tubular heart. The heart tube is roughly 5 blood cells thick in diameter.	145
4.5	(a) illustrates the racetrack geometry, which is held rigid except for the bottom of the tube which is flexible. It also includes flexible blood cells, here illustrating the initial position for a volume fraction of 15%. (b) depicts the geometrical features of the racetrack.	148
4.6	Interpolation phases for the traveling contraction wave along the bottom portion of the racetrack geometry. From Phase 1 (straight red tube) to Phase 2, the tube gets pinched on the left side. From Phase 2 to Phase 3, the occlusive pinch travels down the tube at speed c . From Phase 3, the pinch is released and goes back to the straight tube (in red).	150
4.7	A comparison of simulations with different Womersley Number, $Wo = \{0.2, 2.0, 6.0, 10.0, 20.0\}$, but same amount of blood cells, $VF = 15\%$. The images were taken after at 11.5, 22.5, 33.5, and 44.5 heartbeats during the simulations. In the case of $Wo = 0.2$ and $Wo = 2.0$, there is no visual transport for the mock blood cells; however, there is clear transport when $Wo \geq 6.0$. Moreover, in the cases when $Wo \geq 6.0$, the hematocrit begins to clump together, rather than move uniformly throughout the tube.	154
4.8	A comparison of the spatially averaged velocity vs. time over the course of the simulation, for five cases with uniform hematocrit ($VF = 15\%$), but varying Womersley Number, $Wo = \{0.2, 2, 6, 10, 20\}$. The average velocity was spatially computed across a cross-section in the center of the top of the tube. As Wo increases the amplitude of oscillations in average velocity also increases. In the biologically relevant case, $Wo = 0.2$, there are slight oscillations; however, bulk net flow is insignificant.	155
4.9	A comparison of the spatially averaged velocity vs. time over the course of the simulation, for varying hematocrit, $VF = \{5\%, 15\%, 25\%\}$, for three different Womersley Numbers, $Wo = 0.2$ [(4.9a), (4.9c)], $Wo = 2.0$ (4.9d), and $Wo = 6.0$ [(4.9b), (4.9e)]. The average velocity was spatially computed across a cross-section in the center of the top of the tube. [(4.9a), (4.9b)] illustrate how similar the waveforms are for varying volume fractions for Wo , 0.2 and 6.0, respectively. [(4.9c), (4.9d), (4.9e)] give the average velocities, in diameters/heartbeat, over the course of the simulation, in heartbeats.	156

4.10	4.10a shows the spatially- and temporally-averaged velocity for each simulation vs. Womersley Number for a hematocrit range of $[0\%, 25\%]$. 4.10b shows the spatially- and temporally-averaged magnitude of velocity vs. Wo for a hematocrit range of $[0\%, 25\%]$.	156
4.11	A comparison of simulations for two different Womersley Numbers, $Wo = \{0.2, 2.0\}$, but same hematocrit, $VF = 15\%$. The images were taken after at 1.5, 2.5, 3.5, and 4.5 heartbeats during the simulations. It is clear that there is significant mixing of the blood cells with peristalsis, as the colored sections begin to mix	157
4.12	A comparison of the spatially averaged velocity vs. time over the course of the simulation, for hematocrit, $VF = 15\%$, for three different Womersley Numbers, $Wo = 0.2, 2, 20$ is shown in (4.12a). The spatially-averaged velocity was computed across a cross-section in the center of the top of the tube, given in diameters/heartbeat. (4.12b) and (4.12c) give the spatially-averaged velocities for $Wo = 0.2$ and $Wo = 20$, respectively, for three volume fractions, $VF = 5\%, 15\%, 25\%$	158
4.13	Computational geometry for the electro-mechanical pumping model. The racetrack is held stiff (black), except for the bottom straight-tube portion, which is flexible (red). There is a stiff pericardium model surrounding the flexible region (blue).	161
4.14	Schematic of electrodynamical pumping. (1) The tube at rest; the springs connecting the top and bottom of the tube are the muscles. (2) The pacemaker initiates an action potential, in which the tube will contract based on the magnitude of the signal (3)-(4) The action potential propagates along the tube, inducing contraction.	164
4.15	Schematic of electrodynamical pumping. (1) The tube at rest; the springs connecting the top and bottom of the tube are the muscles. (2) The pacemaker initiates an action potential, in which the tube will contract based on the magnitude of the signal (3)-(4) The action potential propagates along the tube, inducing contraction.	165
4.16	Different traveling wave propagation properties arising out of the FitzHugh-Nagumo equations for varying diffusivities, $\mathbb{D} = \{0.1, 1.0, 10.0, 100.0\}$	166
4.17	The non-dimensional spatially-averaged velocity computed across a cross-section of the top of the race-track geometry vs non-dimensional time for $\mathbb{D} = 0.1$, e.g., the ‘dynamic suction pumping’ regime, for $Wo = \{0.1, 1.0, 10.0\}$. The zoomed in portion illustrates the resulting wave-form and the high frequency oscillations that result from this pumping regime.	167
4.18	The non-dimensional spatially-averaged velocity computed across a cross-section of the top of the race-track geometry vs non-dimensional time for $\mathbb{D} = 100.0$, e.g., the ‘peristaltic’ regime, for $Wo = \{0.1, 1.0, 10.0\}$. The zoomed in portion illustrates the resulting wave-form.	168
4.19	A comparison of non-dimensional spatially-averaged velocity computed across a cross-section at the top of the racetrack vs non-dimensional time in the simulation for varying diffusive coefficients, $\mathbb{D} = \{0.1, 1.0, 10.0, 100.0\}$. The two plots compare different Wo , e.g., (a) $Wo = 0.1$ and (b) $Wo = 10$	169
4.20	A plot of non-dimensional spatially-averaged velocity computed across a cross-section at the top of the racetrack vs the non-dimensional stretching and bending stiffness coefficients for pumping in the ‘dynamic suction pumping’ regime, for a variety of diffusivities, $\mathbb{D} = \{0.1, 0.25, 0.5, 0.75, 1.0\}$	170
4.21	A comparison of the spatially- and temporally-averaged non-dimensional velocities computed across a cross-section of the racetrack vs. Wo for varying diffusivities, $\mathbb{D} = \{0.1, 1.0, 10.0, 100.0\}$	170
4.22	Flow chart illustrating the flow of this section.	172

4.23	Computational geometry for the resonance studies. The straight section (dotted red) is flexible, while the branched vessels (black) are held nearly rigid. The springs connecting the top and bottom of a subset of the flexible section are the mock muscles which induce the impedance pumping behavior.	173
4.24	Dextran was injected at the posterior end of the heart while the heart pumped in the branchail direction (A) and dextran injected at the anterior end of the heart, while the heart pumped in the visceral direction. The dextran helps visualize the morphology of the heart and the branching vessels, motivation our computational geometry in Figure 4.23. The scale bar in B at the bottom left is 10 mm. This figure and description was adapted from [36].	173
4.25	Illustrating the 1 st and 2 nd vibrational mode waveforms. The waveforms are in blue, while the solid black represents rigid sections along the straight portion, and the dotted black line resembles the tube's equilibrium position.	175
4.26	Free vibration studies for two situations, where each case corresponds to a different vibration mode, 1 st (left) and 2 nd (right), for the same flexible geometry. However, in each case, there are two simulation snapshots shown corresponding to two different viscosities, i.e., $\mu = 1.0 \frac{kg}{m \cdot s}$ (blue) and $\mu = 3.5 \frac{kg}{m \cdot s}$ (pink). It is clear that the 1 st and 2 nd mode have differing resonant frequencies.	176
4.27	Plots showing the displacement from equilibrium of the peaks of the first and second modes of vibration during the free vibration tests. It is clear that for some viscosities the system is over-, under-, and critically-damped.	177
4.28	Numerically found resonant frequencies in both the first and second vibrational modes for a flexible tube immersed in a fluid. A free vibration test was performed in each viscosity and vibrational mode.	178
4.29	Illustrating the pumping dynamics and the resulting passive elastic waves for the first (a) and second (b) mode resonances for varying snapshots from a single period, T , of dynamic suction pumping. The orange bar represents the active region of actuation. The blue coloring of the tube (at 50% of a period) show that the vibrational mode waveform shows up during the pumping.	179
4.30	Illustrating the passive elastic waves arising from pumping the tube at a frequency of $f_m = 0.9Hz$ and viscosity, $\mu = 1.75 \frac{kg}{m \cdot s}$. The orange bar represents the region of active contraction. The blue coloring of the tube represents where the first and second mode waveforms are visible during one period of dynamic suction pumping.	180
4.31	Snapshots from simulations pumping at varying frequencies, qualitatively showing bulk flow properties via the movement of passive tracers in the flow. The tube was pumped at the first and second vibrational mode resonance frequencies, $f = 0.28Hz$ and $f = 2.03Hz$, respectively, as well as two other frequencies in the between those values, $f = \{0.55, 1.1\}Hz$	182
4.32	Snapshots comparing qualitative bulk flow for two simulations pumping at the same frequency $f = 0.28Hz$ (first mode resonance), but two different viscosities $\mu = \{0.07, 1.75\} \frac{kg}{m \cdot s}$. There appears to be more bulk from in the case with $\mu = 1.75 \frac{kg}{m \cdot s}$	183
4.33	Snapshots from simulations with viscosity $\mu = 0.07 \frac{kg}{m \cdot s}$ and at frequencies $f = \{0.28, 0.55\}Hz$, illustrating the waveforms of the passive elastic waves. In each case there is a strong interaction of the tube walls during each dynamic suction pump.	184

4.34	Snapshots from simulations with viscosity $\mu = 0.07 \frac{kg}{m \cdot s}$ and at frequencies $f = \{0.28, 0.55\} Hz$, illustrating the waveforms of the passive elastic waves. In each case there is a strong interaction of the tube walls during each dynamic suction pump.	186
4.35	Snapshots from simulations with differing amounts of added mass to the boundary, while pumping at the same frequency ($f = 0.28 Hz$) and viscosity ($\mu = 1.75 \frac{kg}{m \cdot s}$).	187
5.1	Cartoon renditions of the geometries considered for motivation for the computational models in Section 5.2 and Section 5.3. (a) is the trabeculated ventricular cavity model and (b) is the two-chamber model with a trabeculated ventricle.	192
5.2	5.2a is a snapshot of an embryonic zebrafish's ventricle at 96 hpf right using spinning disk confocal microscopy. The snapshot was taken right before its systolic phase. The protrusions into the ventricular chamber are trabeculation. Image from Tg(cmlc2:dsRed)s879; Tg(flk1:mcherry)s843 embryos expressing fluorescent proteins that label the myocardium and endocardium, respectively [5]. Figure 5.2b illustrates the idea for our computational model geometry found in Figure 5.2c, that is, blood flows from the atrio-ventricular canal into the ventricle and then proceeds into the bulbus arteriosus. The computational model geometry is a flattened out rendition of 5.2b. The following geometric parameters, a_V and b_V , the semi-major and semi-minor axis of the elliptical chamber, h_T and r_T , the height and radii of the trabeculae, and w_{AV} and w_{SV} , the widths of the AV canal and sinus venosus respectively.	194
5.3	A cartoon depiction of the two parabolic inflow conditions within the model geometry. .	196
5.4	(a) The PIV physical model geometry, which was 3D printed and placed into a flow tank. (b) the PIV setup, which includes a flow tank, containing the 3D model, with a laser shining orthogonally to the direction of flow, and camera oriented downwards vertically capturing the motion of the neutrally buoyant glass beads.	199
5.5	Comparison between PIV (left) and simulations (right) of the fluid velocity field (top) and streamlines (bottom). The fluid dynamics qualitatively match in this high Re range.	201
5.6	Streamline analysis performed for the case of steady flow into the trabeculated ventricle of a zebrafish at 96 hpf for varying Re and trabeculae heights.	203
5.7	Streamline analysis performed for the case of pulsatile flow into the trabeculated ventricle of a zebrafish at 96 hpf for $Re = 0.1$ and varying trabeculae heights.	205
5.8	Streamline analysis performed for the case of pulsatile flow into the trabeculated ventricle of a zebrafish at 96 hpf for $Re = 1.0$ and varying trabeculae heights.	207
5.9	Streamline analysis performed for the case of pulsatile flow into the trabeculated ventricle of a zebrafish at 96 hpf for $Re = 10.0$ and varying trabeculae heights.	208
5.10	Streamline analysis performed for the case of pulsatile flow into the trabeculated ventricle of a zebrafish at 96 hpf for $Re = 100$ and varying trabeculae heights.	209
5.12	5.12a and 5.12b are snapshots of an embryonic zebrafish's ventricle at 96 hpf right using spinning disk confocal microscopy. The snapshots were taken right before systole and diastole, respectively. The protrusions into the ventricular chamber are trabeculae and blood cells are fluorescing red [5].	212

5.11	5.11a and 5.11b are snapshots of an embryonic zebrafish's ventricle at 96 hpf right using spinning disk confocal microscopy. The snapshots were taken right before its diastolic and systolic phase, respectively. The protrusions into the ventricular chamber are trabeculae. Dashed lines show the minor and major axes. Images are from Tg(cmlc2:dsRed)s879; Tg(flk1:mcherry)s843 embryos expressing fluorescent proteins that label the myocardium and endocardium, respectively [5]. 5.11c and 5.11d illustrate the computational geometry right before diastole and systole, respectively. The computational geometry, as shown in 5.11e, includes the two chambers, the atria (bottom chamber) and ventricle (top chamber), the atrioventricular canal connecting the chambers, and the bulbus arteriosus and sinus venosus, which all have endocardial cushions, which can occlude cardiac flow, as well as flexible blood cells.	213
5.13	5.13a and 5.13b illustrate the maximum distance for the height and width (in pixels) respectively, in the atria and ventricle of a 4 <i>dpf</i> embryonic zebrafish heart from [5]. . .	216
5.14	We describe four phases of each heart cycle. Note that the position at the beginning of each phase is shown. Phase 1: the ventricle rests after contraction and the atrium rests after expansion. The AV canal goes from fully occluded to 10% occlusion. Phase 2: The diastolic phase when the ventricle expands while the atria contracts. Phase 3: the ventricle rests after expansion and the atrium rests after contraction. The AV canal becomes fully occluded state. Phase 4: The systolic phase, when the ventricle contracts and the atria expands.	218
5.15	Vorticity analysis performed for the case of biologically sized trabeculae and varying Wo at different time points during one heart cycle.	222
5.16	223
5.17	(a) Illustrating the indexing of trabeculae (b) Plot illustrating the average magnitude of the force on chosen trabeculae over the course of one heart cycle for $Wo = 0.8$, the biologically relevant case. (c) Plot showing the average magnitude of the tangential and normal forces at each time, for chosen trabeculae, during one heart cycle for $Wo = 0.8$. (d) A plot illustrating the average magnitude of force at each time-step for Wo ranging from 0.5 (half the biologically relevant case) to 12.0.	226
5.18	Streamline analysis for $Wo = \{0.5, 1.0, 4.0\}$ and trabecular heights from half to twice the biologically relevant size. The analysis was performed within the ventricle immediately after diastole finishes and when the ventricle stops expanding.	227
5.19	Magnitude of velocity colormaps, corresponding to simulations of varying Wo for biologically relevant trabeculae height. The images were taken immediately after diastole, when the ventricle stops expanding.	228
5.20	The total magnitude of force (top row), magnitude of the normal force to the boundary (middle row), and magnitude of the tangential force to the boundary (bottom) for different trabeculae heights at the biologically relevant Wo , $Wo = 0.8$. It is clear that while the tangential and normal force magnitudes differ, the main contributor to total force on the boundary is the normal component. The largest force are felt by the trabeculae on the left most side of the ventricle. As the trabeculae height increases, the most force is still felt on the same trabeculae, but with reduced magnitude.	229
5.21	Streamline analysis for $Wo = \{0.5, 1.0, 4.0\}$ and hematocrit of $VF = \{5\%, 15\%, 25\%\}$. The analysis was performed within the ventricle immediately after diastole finishes and the ventricle ceases its expansion.	230

5.22	The total magnitude of force (top row), magnitude of the normal force to the boundary (middle row), and magnitude of the tangential force to the boundary (bottom) for different volume fractions at the biologically relevant Wo , $Wo = 0.8$. It is clear that while the tangential and normal force magnitudes differ, the main contributor to total force on the boundary is the normal component. Moreover, the blood cells do not appear to affect the magnitude of the force on the boundary in any case.	231
5.23	5.23a and 5.23b illustrate the average fluid vorticity on the left and right side of the ventricle, respectively, immediately after diastole, as a function of Wo . It is clear there is a non-linear relationship between the spatially-averaged vorticity and biological scale, given by Wo	232
5.24	Plots of the spatially-averaged magnitude of vorticity for $Wo = \{0.5, 0.8, 1.5, 8.0\}$ for $VF = \{0\%, 5\%, 15\%, 25\%\}$. The vertical dotted line indicates when diastole ends. For every case of Wo , the higher the hematocrit, the more spatially-averaged vorticity magnitude is induced.	233
A.1	Steady circular velocity field.	249
A.2	Illustrated is an initial concentration advecting and diffusing in a circle around the computational domain for various diffusive coefficients, D	250
A.3	Illustrated is an initial concentration advecting and diffusing in a circle around the computational domain $D = 1e - 6$ using the split upwind and split Lax-Wendroff method.	251
B.1	Example of statistics pertaining to visitors to the GitHub site for <i>IB2d</i> from October 19, 2016 to November 1, 2016. We note this was before the release of the <i>IB2d</i> paper [37].	253
B.2	Punch card from GitHub user-statistics illustrating when I did commits to my GitHub repositories [38]. It is clear that between the hours of 3am and 8am, I tended to sleep, as no code was committed during that time. Moreover, I seemed to reserve Saturday nights for playing music with friends, or at least not committing code.	254
B.3	A collage of a fraction of the simulations that can be run upon immediate download of the open source <i>IB2d</i> software.	255
C.1	Snapshots from the simulation using a projection method to model cavity flow. The background colormap is of the magnitude of velocity and the vector field illustrates the fluid's velocity field.	259
C.2	Snapshots from the simulation using a spectral method (FFT) to solve the incompressible, Navier-Stokes equations in the vorticity formulation. The background colormap is of vorticity.	263
C.3	Snapshots from the same simulation of nested vortices using a spectral method (FFT) to solve the incompressible, Navier-Stokes equations in the vorticity formulation. These images illustrate the magnitude of velocity and the background velocity field.	264
C.4	Figure illustrating the possible streaming directions, $\{\mathbf{e}_i\}$ for the D2Q9 Lattice Boltzmann model.	265
C.5	Figure illustrating the idea of streaming by showing color correlated particle probability functions, f_i , before the streaming process and post-streaming, f_i^*	266

C.6	Illustration of bounce-back boundary conditions. The pre-streaming step there are microscopic velocities set on the boundary and then they are reversed during the streaming step	268
C.7	Snapshots from a Lattice Boltzmann simulation of flow around 3 cylinders. The background colormap is vorticity. It is clear that vortex shedding occurs.	269

LIST OF TABLES

4.1	Geometric parameters used in the numerical experiments. d is the diameter of the tube, R_1 and r_o give the outer radius (or distance from the centerline) of the tube, R_2 and r_i give the inner radius (or distance from the centerline) for the tube, L is the length of the flexible section for DSP and contractile wave section for peristalsis, L_A is the length of straight tube before the actuation section for DSP, L_S is the size of the actuation section for DSP, and r_C is the radii of a blood cell.	147
4.2	Table of temporal parameters for the prescribed peristaltic wave. T is the non-dimensional period. T_1 and T_3 gives the non-dimensional period for the initial pinching and release of the tube. T_3 gives the non-dimensional translation time of the peristaltic wave.	150
4.3	Table of mechanical parameters used in the computational model. Note that \tilde{k}_{sbtwn} gives the stiffness coefficient of the actuating springs in the DSP model, while it describes the stiffness coefficients of springs connecting the outer and inner layer of the top of the tube in the peristalsis model. \tilde{k}_{stube} is the stretching stiffness between adjacent points along the tube while \tilde{k}_{sbtwn} gives the stretching stiffness between opposite points along a cross-section of the tube. \tilde{k}_{target} is the tethering stiffness of target points, \tilde{k}_{beam} gives the bending stiffness between adjacent points along the tube, and \tilde{k}_{scell} gives the stretching stiffness between points making up the blood cells.	153
4.4	Table of the parameters associated with the fluid and the immersed boundary fiber models.	162
4.5	Table of the parameters associated with the FitzHugh-Nagumo electrophysiology model.	163
4.6	Table of the parameters associated with the fluid and the immersed boundary fiber models for the resonance studies.	174
5.1	Table of non-dimensional geometric parameters used in the numerical model. The height of trabeculae, h_T , were varied for numerical experiments.	195
5.2	Inflow boundary conditions for both simulations, one pertaining to parabolic steady inflow and the other corresponding to a parabolic pulsatile inflow. The parameters used for the boundary conditions are f , the non-dimensional frequency, which is matched to the zebrafish heart at 96 <i>hpf</i> , and V_{in} , the maximum inflow velocity.	197
5.3	Table of dimensionless geometric parameters used in the numerical model. The non-dimensionalization was done by dividing by V_{aexp} . The height of trabeculae, h_T , were varied for numerical experiments.	214
5.4	The morphological parameters in physical units as computed from the kinematic analysis.	217
5.5	Average percentage and duration of each phase during the heart cycle obtained from kinematic analysis.	217
5.6	Table of polynomial coefficients for the interpolating function, $g_j(t)$	219
5.7	Table of temporal parameters used in the interpolating function, $g_j(t)$	219

CHAPTER 1

Introduction

Hold on to your butts.

-John "Ray" Arnold (Jurassic Park)

Congenital heart disease (CHD) is the most common birth defect in humans and results from deficient cardiac development. Roughly 1% of people are born with CHD in the United States, which equates to more than 35,000 babies being born annually with cardiovascular abnormalities [39, 40]. Unfortunately, many congenital heart defects show few signs and symptoms; and in some cases, they are not diagnosed until later in childhood or even as an adult.

There is a wide range of heart defects; some are simple defects that show no mild symptoms, while some are complex with severe, life-threatening symptoms. Congenital heart defects range from abnormalities in the morphological structure of the heart itself, from holes in a heart chamber to irregular, dysfunctional size, to defective valves separating adjacent chambers, to arteries and veins, which carry blood to and from the heart, and other various other cardiomyopathies [41]. Each of these deficiencies effect how oxygen, nutrients, and metabolic wastes are properly transported throughout the body. Moreover since the heart is the first functioning organ in the embryo, any defects in the it may have detrimental affects on the organogenesis of other bodily systems [42].

In some cases, children who were born with CHD do not require treatment, while others with severe symptoms and complications may require treatment or surgery. A treatment for CHD depends of the type and severity of the defect, as well as, the patients age, size, and general health [39]. Roughly 0.3% of all live births require either catheter-based or surgical intervention within their first year of life [43]. Fortunately many people with CHD are able to survive to adulthood and live

active, productive lives.

Cardiogenesis involves a dynamic interaction of genetic and environmental (epigenetic) factors. It is a precise coordination of a multitude of processes, such as cellular proliferation, migration, differentiation, and integrated morphogenetic interactions. Hence it is unfortunately susceptible to many anomalies and pathologies, like CHD [44]. A vast array of cardiogenic research has focused on genetic aspects, with unsurmountable success; however, experiments have also highlighted the underlying importance of the hemodynamics governing proper morphogenesis of the heart [12]. Understanding the interplay between the mechanical forces arising from blood flow and biological sensory and regulatory networks may lead to invaluable insight about how cardiovascular defects arise and possible remedies to irregularities and perturbations in cardiac morphogenesis [45, 46, 47, 48, 12, 49, 19, 26, 15, 50].

Embryogenesis involves a seemingly uncountable amount of biological processes; however, most all can be grouped into three sub-groups [47, 48] - *growth*, *remodeling*, and *morphogenesis*. Clearly these processes must be coupled in nature and, by definition, but is useful to describe them separately since they each describe different culminations of embryogenic processes.

Growth can be described as the increase or decrease of volume in cardiovascular tissues. This change in volume can arise from hyperplasia (adjustments in the number density of cells), hypertrophy (variations in cell geometry, i.e., size), or modifications in the amount of extracellular matrix. During cardiogenesis, essentially all growth is due to hyperplasia, but interestingly enough after birth, growth is attributed to hypertrophy. These changes in cell density, geometry, and amount of extracellular matrix are thought to not only have global importance in cardiac growth, but have profound regional effects via the introduction of stresses and forces that may be important to overall heart function as well as cardiogenesis [48].

Remodeling of cellular types occurs tightly along side growth of the cardiovascular system. As the heart develops from a primitive myocardial heart tube composed mostly of epithelial cells to a multi-chambered valvular pumping system in vertebrates, cells from the initial myocardium differentiate to the usual form of myocardium (muscle cells), where actin and myosin combine to

form sacromeres, and along with myofibrils, to constitute a vast network of highly oriented muscle cells in a mature heart [51].

Lastly *morphogenesis* characterizes the dramatic changes in organ morphology during embryogenesis. For example, in cardiogenesis, the heart undergoes dramatic changes in shape, not only to form a mature heart, but also for utility and function. For example, in various animal models, it has been documented that the embryonic heart begins pumping much before oxygen, nutrients, metabolic waste transport are seemingly necessary in the circulatory system [52]. However, during the various phases of heart morphogenesis, it is clear that a precise choreography of events (hemodynamics and genetic-chemical-mechanical signaling) must take place, with no irregularities, for proper heart development and function. Any slight perturbation in any of the complex cardiogenic phases could lead to a morphological defect, of which could be detrimental to the embryo or potentially fatal in an unspecified time after birth.

Thus far scientists have constructed extensive *in vitro* models to study the effect of hemodynamic shear stress on endocardial cells to induce local epigenetic signaling changes [12, 35, 53]. It is well known that that mechanical forces have an important role for inducing changes within biological regulatory networks and pathways within these endocardial cells; however, it is difficult to extrapolate the information gained from an *in vitro* model to predict physiological situations *in vivo*, due to limitations in imaging resolution and surgical technology [54]. Hence it could be fruitful to create biological relevant and verified fluid-structure morphological models in developing a better understanding of what role hemodynamic forces undertake in cardiogenesis.

By a continued focus on discovering and studying previously unidentified genes, epigenetic signals, and biological regulatory networks as a whole, as well as an exciting opportunity to study the recent spotlight, that is, the importance of hemodynamics and mechanical forces on cardiogenesis, may all-together lead to a better understanding of the causes of CHD, i.e., which mutations and irregular flow patterns may lead to morphological abnormalities and suppression of the cardiac conduction system [51]. Integrating all these parameters could possibly advance medical technology in the development of novel therapies for heart disease in children and adults, including the creation of

artificial valves, vessels, and even whole hearts, or transplants, or even possible sophisticated *in vivo* therapies when heart morphogenesis is actually taking place.

In this thesis we explore the role fluid dynamics performs in various phases of heart morphogenesis, specifically focusing on the effects of hematocrit and trabeculation on the underlying hemodynamics. In Chapter 2 we discuss vertebrate heart morphology and function in humans and our model organism, zebrafish (*Danio rerio*), and compare their respective morphogenic timelines and geometric differences and conservation between the two. Furthermore we will discuss previous mathematical modeling work that has been done in various stages of cardiogenesis. In Chapter 3 we introduce the governing equations of fluid dynamics, e.g., the *Navier-Stokes* equations, and explain the numerical method we use to solve our fluid-structure interaction models' equations, e.g., the *Immersed Boundary Method*. In Chapter 4, we discuss various pumping mechanisms in linear heart tubes. In Chapter 5, we investigate the role of trabeculation during morphogenesis and study their effect on intracardial fluid flows.

CHAPTER 2

Cardiogenesis

Throw me the idol; I'll throw you the whip!

- Satipo (Raiders of the Lost Ark)

In this chapter we will review the various phases of vertebrate heart development, from its humble beginnings as a mere linear heart tube to its adult counterpart as a multi-chambered valvular system, which pumps blood efficiently throughout the entire cardiovascular system. During cardiogenesis the developing heart undergoes a series of complicated morphological changes that are thought to arise from a balanced and well-coordinated interaction of hemodynamic forces, robust genetic regulatory and signaling networks, and all the intracellular and intercellular processes that couple them.

For the remainder of the chapter, we will explore the various phases of heart morphology in vertebrates, why mechanical forces are believed to have significant roles in proper cardiac development through both previous experimental, as well as some mathematical modeling achievements, and why we choose the zebrafish, *Danio rerio*, to be our model organism for studying cardiogenesis.

2.1 Heart Morphology

Heart morphology is seemingly well conserved throughout the vertebrate kingdom [35, 55, 56], even though embryogenesis takes place on different time scales, i.e., humans are born roughly nine months post fertilization, while zebrafish embryos hatch and begin swimming after approximately five days post fertilization [12]. In both cases similar heart morphogenetic steps occur, but on widely varied time-scales. While the process of heart formation in zebrafish only takes roughly five days before the heart matures into a morphological form reminiscent of its adult counterpart [57], the same process takes roughly two months in human cardiogenesis [10]. In this section we will discuss

the various phases of cardiac morphogenesis in vertebrates, while also comparing time-scales of heart development between zebrafish and humans.

	Chick	Zebrafish	Mouse	Human
Developmental landmarks	HH	hpf	E	Days
Formation of single heart tube	7–9	19	8	22
First myocardial contractions	7–10	22	8.5	23
Heart looping	11–13	33	8.5	24
First blood flow through heart	10	26–28	9.5	24

Figure 2.1: A comparison of early developmental landmarks between different species. Chick embryo stages are described according to the Hamburger-Hamilton (HH) scale, zebrafish stages are measured in hpf (hours post fertilization), mouse stages are marked as postconception days (E), and human stages are developmental days.

The heart begins to form as the precardiac mesoderm forms into a linear tube, which is only a few cells thick and consists of three layers- a thin-layer of endocardium, a relatively thick gelatinous middle layer of extracellular matrix, called cardiac jelly, and a thin outer layer of myocardium [58, 59, 19]. Shortly after the heart-tube forms, the first heart beats occur. In humans this happens at approximately between 22 and 23 days post fertiliation (dpf), while in zebrafish the formation of the heart-tube and initiation of heart beat occurs within 19 hours post fertilization (hpf) and 22 hpf respectively [60]. A comparison of early developmental landmarks for four different vertebrate species is found in Figure 2.1, adapted from Furst [61]. Chick embryo stages are described according to the Hamburger-Hamilton (HH) scale [62], zebrafish stages are measured in hours post fertilization (hpf), mouse stages are marked as postconception days (E), and human stages are given by developmental days.

All subsequent steps in heart morphogenesis may now be potentially affected by myocardial function [53], hence if bradycardia or tachycardia occur, e.g., abnormal decreasing or increasing of the heart rate, respectively, the result could be detrimental in the resulting organogenesis of the heart or other organs. At this stage, a zebrafish’s heart rate is approximately 90 contractions per minute shortly after circulation begins [56].

The linear heart tube contracts rhythmically to push blood via waves of contraction running

down the tube, seemingly in a slow peristaltic manner [63, 64, 48, 60], inducing unidirectional flow in the throughout the embryonic cardiovascular system. The wave of contraction can be seen running from the venous to arterial end of the heart tube.

Some scientists claim that this wave of contraction is due to elastic, passive waves traveling down along the endocardium [65], suggesting the embryonic heart pumps via dynamic suction pumping, i.e., impedance pumping. However, whether there is a well-coordinated active contractile wave traveling down the myocardium (peristalsis) or a single point of actuation that initiates a bidirectional wave that reflects causing a net flow induced by passive traveling waves along the endocardium (dynamic suction pumping), it is clear that this wave of contraction induces flow within the embryonic heart.



Figure 2.2: Snapshots of the contractile wave propagating through the endothelium in the linear tube of an embryonic zebrafish heart at 28 hpf. The contractile wave is outlined in blue. These images are courtesy of Leigh Ann Samsa.

Initially blood is absent of erythrocytes, nutrients, and metabolic wastes (in zebrafish younger than ~ 24 hpf) ; however, the hemodynamic forces arising from the primitive embryonic blood are seen to have significant roles in morphogenesis [12]. In zebrafish, within a few hours of the initiation of the first heart beat, blood cells are seen being transported around the cardiovascular system.

Throughout the linear heart tube stage, which lasts between days 22 and 23 post fertilization in human embryos and between hours 19 to roughly 30 post fertilization in zebrafish, the heart rate steadily increases. The increase in heart rate is coupled with an increase in cavity volume to complement the ever increasing and demanding blood transport rates at this phase. As a result of higher flow rates, higher pressures are necessary to propagate the higher quantities of blood, which also aid in driving expansion and remodeling of the system [19, 60]. Thereby the heart undergoes

it's first instance of asymmetry and begins the complicated cardiac looping stage. This occurs in humans around 23 dpf [60] and in zebrafish around 30 hpf [56]. In parallel during this process, the vascular network grows and expands to serve the metabolic needs of the rapidly developing embryo.

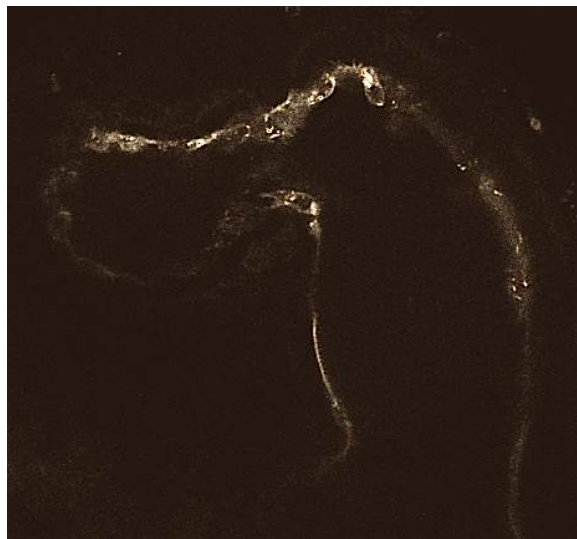


Figure 2.3: Snapshot taken of an embryonic zebrafish heart's endothelium at 42 hpf illustrating the looping process' morphogenetic changes from a linear heart tube. Image courtesy of Leigh Ann Samsa.

Once the heart-tube begins to loop to the embryo's right side, the embryonic zebrafish heart is pumping at approximately 140 beats per minute. The direction of the looping tubular heart is a commonality among all of vertebrate heart morphology and evolution, beginning with cyclostomes [56]. This must be a perfectly coordinated phase, as even the slightest perturbations in looping morphology can lead to serious physiological defects [66]. During this phase, the once linear tube is undergoes precise choreography of bending and twisting.

Even though looping is such a crucial phase in heart morphogenesis, our understanding of the process remains relatively poorly understood [46, 67]. This is not to say that scientists have dismissed studying this phase, on the contrary, it has received a great deal of focus and several hypothesis have been proposed for the mechanisms that govern looping. Unfortunately, none of the proposed mechanisms are consistent with the experimental data gained. It has been experimentally observed that the dorsal mesocardium, which attaches the heart to the embryo, has a significant role in looping.

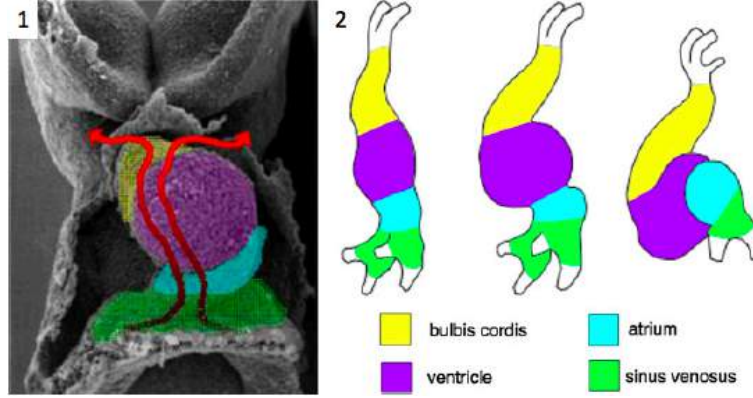


Figure 2.4: Frontal view of the embryonic mouse heart during day 9 (approximate human age is 25 days) and cartoon schematic. When the heart tube elongates and begins to loop, blood flows into the sinus venosus, then into the primitive atria, the ventricles and bulbus arteriosus before entering the visceral arch vessels. We note that mammalian hearts are four chambered (two atria and two ventricles), while fish hearts are two chambered (one atria and one ventricle) [1]. SEM images courtesy of Dr. Kathleen K. Sulik. Diagram redrawn from [2].

The dorsal mesocardium is a very stiff structure, and thereby because the heart tube is attached longitudinally, as the linear heart tube undergoes bending and twisting, the dorsal mesocardium must bend and twist in unison [68].

Therefore all of the proposed mechanisms for looping, describe an intricate relationship between the heart tube, dorsal mesocardium, and physiological constraints on the dynamics. One candidate presumes that when pressure rises in the heart tube, it causes the cardiac jelly to swell and expand the cardiac tube. The heart tube is then forced to bend because of the stiff structure of the dorsal mesocardium. Another possible mechanism has suggested that because the dorsal mesocardium is initially under residual tension when it tears as the ventricle pulls away from the embryo, the remnants of the dorsal mesocardium shorten and force the tubular heart to bend. Another proposal hypothesizes that circumferential microfilaments contract and the endothelial cells undergo circumferential shortening as well, forcing longitudinal extension of the tube, because of incompressibility constraints. Then because the heart tube is attached along the stiff dorsal mesocardium, the dorsal mesocardium restricts the expansion and forces the tube to bend [46, 48, 69]. Other hypothesis suggest that looping occurs from forces arising from adjacent organs pushing against the tubular heart [12]. Although physical models have shown that on their own, each of these proposed mechanisms are limited in the amount of bending that can be induced [46, 70], it is possible that a combination

of these candidates along with other mechanical or bio-chemical processes contribute to looping.

During looping chamber septation also begins [64], demarcated by narrow rings of tissue at their junction [56]. Furthermore *chamber ballooning* begins to occur when the cardiac jelly regresses in the primitive ventricle so that ventricular outgrowth can proceed. A similar process takes place in the atrial chamber. The secondary myocardium from the outer curvature of the primary heart tube is responsible for initiating the ballooning phase, as it begins to expand and dilate to assist in shaping the chambers [71, 72]. These primitive chambers resemble a simple balloon with a smooth inner surface [55].

By around 48 hpf, the zebrafish heart has developed into a two-chambered pumping system, separated by the atrioventricular canal. It performs at a heart rate of around 200 – 215 beats per minute, with flow velocities around 0.3 cm/s [57]. At this state the ventricle to bodyweight ratio is approximately 11%. The heart is lined with endocardium, separated from the myocardium by a layer of cardiac jelly in the atrium and bulbus arteriosus. The myocardium is still only about one cell thick in each segment of the heart, except the ventricle, which has 2-3 cell layers. There is still no evidence of valve leaflets at this stage, although each component of the heart can be identified by a constriction between the segments [59]. Instead the atrioventricular canal contains endocardial cushions, which are the precursors to cardiac valve leaflets.

Also at this stage, the pumping mechanics in the zebrafish embryonic heart resemble that of its adult counterpart. Even though, the heart is not geometrically scalable to its adult heart, as other morphological changes in topology have yet to take place, the embryonic heart undergoes similar pumping behavior. First the atria fills with embryonic blood, contracts, and blood is forced through the atrioventricular canal and into the ventricle, where it expands to fill and quickly contracts to push blood through the bulbus arteriosus and out through the developing embryo. Each chamber has begun to beat as a synchronous unit, inducing more pulsatile flow, rather than the previously described peristaltic-like flow profile.

This pulsatile flow profile becomes more pronounced during the onset of compressible endocardial

cushions, which form as mounds of gelatinous tissue matrix that are secreted by cells in the myocardium [29]. These cushions begin as constrictions near the ends of the heart tube and function as primitive valves during late stages of the linear heart tube, and early stages of cardiac looping, chamber formation, and the multi-chambered pumping heart. As the heart loops, it becomes less efficient at preventing retrograde flow, causing the need for some kind of valvular system, to which the cushions undertake. When a wave of contraction passes the cushions, they appear to pinch off the lumen to prevent back-flow, and hence are thought to be essential for proper cardiogenesis. Moreover, significant forward blood flow and pulsatile pumping only become possible only when the endocardial cushions appear, and hence it is speculated that pulsatile flow is required for normal development of the vascular system.

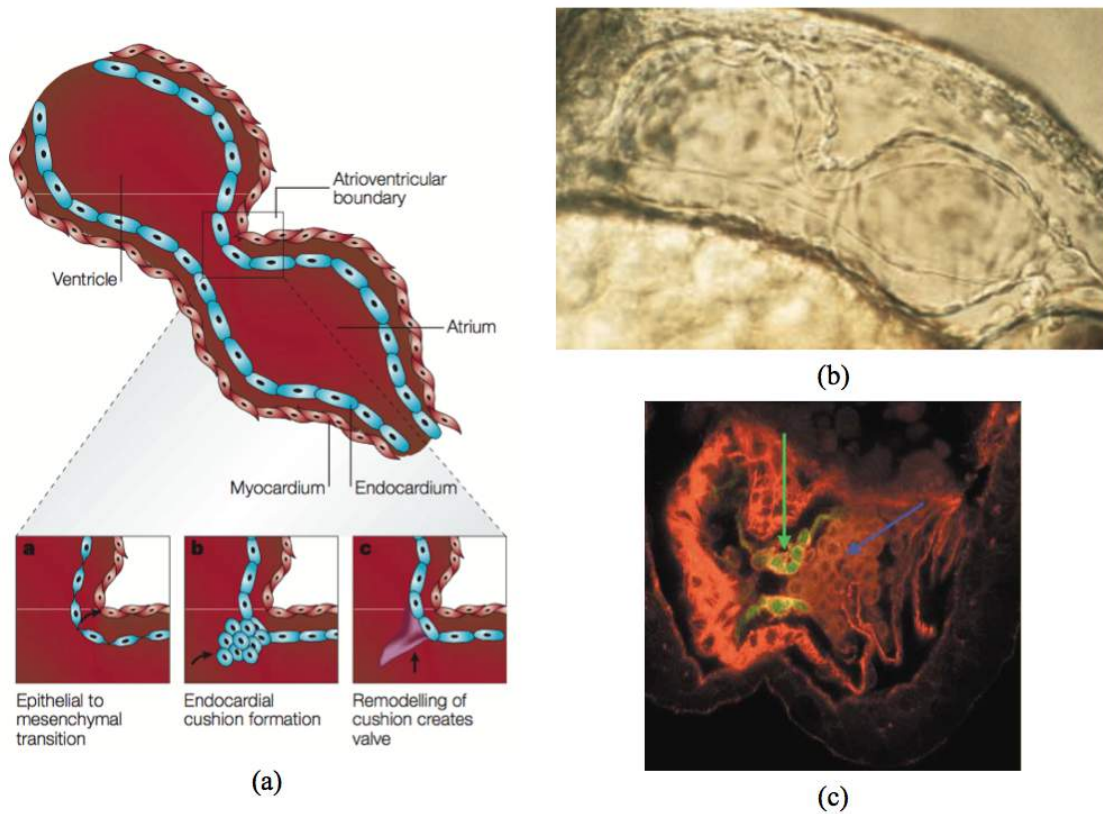


Figure 2.5: Images illustrating the development and morphology of endocardial cushions. (a) shows a cartoon depiction of the zebrafish embryonic heart at 36 hpf of the pinching to create the atrioventricular canal and endocardial cushion formation. (b) gives the associated *in vivo* image of (a). (c) illustrates the zebrafish heart at 60 hpf with the endocardial cushions highlighted in green with green arrows. (a) and (b) were adapted from [3] and (c) from [4].

An illustration of endocardial cushion development and morphology are shown in Figure 2.5,

which was adapted from [3, 4]. (a) shows a cartoon depiction of the zebrafish embryonic heart at 36 hpf of the pinching to create the atrioventricular canal and endocardial cushion formation. (b) gives the associated *in vivo* image of (a). (c) illustrates the zebrafish heart at 60 hpf with the endocardial cushions highlighted in green with green arrows.

The endocardial cushions appear to have evolved as an elegant solution to aid in proper heart morphogenesis. The endocardial cushions will not form without myocardial function and hence blood flow [53]. Since the cushions help induce more unidirectional pulsatile flow, there is an increase in both hemodynamic pressure, flow rates, mass flux, and hence cavity volume. This in turn benefits the growing embryo, as it demands ever increasing flow of blood and nutrients. However, fully developed valve leaflets would not be appropriate at this stage, as mature valves would obstruct other morphogenetic processes, i.e., cardiac looping and its predecessors, due to their stiff nature as being connective tissue [19]. Later these cushions will remodel into fully functional valvular leaflets [4].

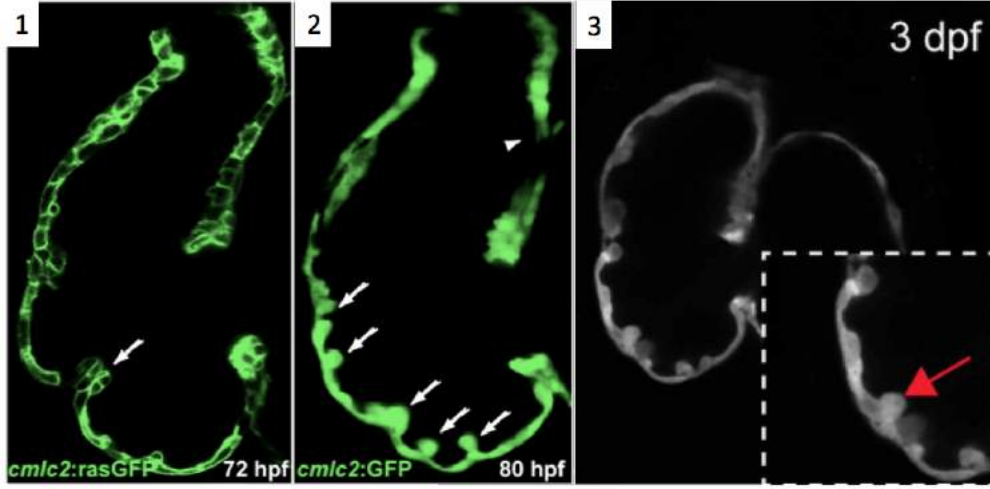


Figure 2.6: Images from Liu et al. 2010 [5] and Samsa et al. 2016 [6], taken by utilizing two cardiomyocyte specific lines, $Tg(cmlc2:GFP)$ and $Tg(cmlc2:ras-GFP)$, which express GFP or membrane-bound GFP in all differentiated cardiomyocytes and confocal optical imaging of the ventricle, respectively. (1) Shows the onset of trabeculation in the 72 hpf zebrafish heart. The arrow indicates the beginning of a primitive trabeculae. Note that it is located directly across from the atrioventricular canal, implicating that higher regions of mechanical forces undergo trabeculation first. (2) The continued trabeculation process undergoing in the zebrafish heart at 80 hpf, where more trabeculae are present. (3) Shows a similar image to (1) but using a different imaging method.

While the multi-chambered heart's hemodynamics at this stage are mitigated by the endocardial cushions, other morphological processes are occurring within the developing cardiovascular system,

specifically to both assist and drive heart morphogenesis. Around 72 hpf in zebrafish, cardiomyocytes proliferate and protrude into the lumen from specific locations along the ventricular outer curvature, roughly opposite the atrioventricular canal. This is seen in Figure 2.6. These protrusions, called *trabeculae*, appear to be an expression of three interrelated events- formation of endocardial outgrowths that eventually invade the myocardium, development of large of intercellular regions between myocytes, and a decrease in cardiac jelly thickness [7]. This process occurs roughly between 5 and 6 weeks in human embryogenesis [10].

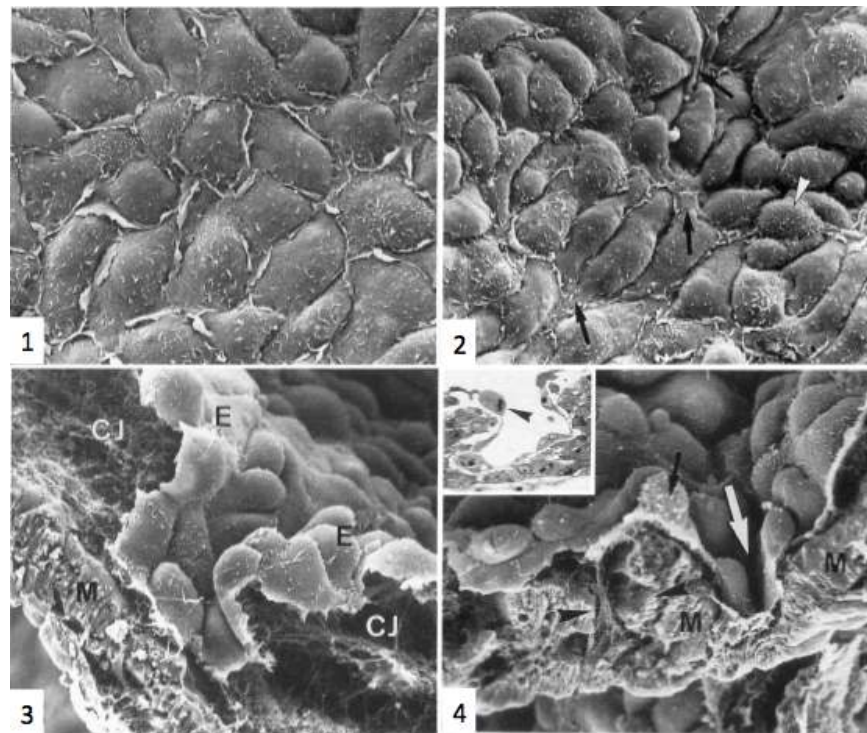


Figure 2.7: (1) Endocardial cells are smooth and polygonal in shape before trabeculation occurs. (2) During the onset of trabeculation, endocardial cells become elongated and become slightly more depressed than surrounding endocardial cells. (3) Endocardial cells (E) invaginate the cardiac jelly (CJ) and extend toward the myocardium (M). (4) A primitive trabeculae is formed (illustrated by the white arrow) once the endocardial cells protrude into the myocardium. SEM images taken from Icardo et al. 1987 [7].

Prior to trabeculation, the endocardial ventricular cells are smooth and polygonal in shape. However, at the onset of trabeculation several endocardial cells become elongated, where a few extend cellular projections. Moreover these cells appear slightly more depressed than the surrounding endocardial cells. The depressions progressively become more deep and wide, where endocardial cells

invaginate the cardiac jelly, and extend toward the basal surface of the myocardium. Eventually myocardial cells separate due to the potent endocardial cell invasion, and definitive trabeculae are formed. Hence trabeculae are composed of both a myocardial and endocardium component [7]. This process can be seen in Figure 2.7.

Hemodynamic forces may contribute to the site selection for trabeculae, where the initial location reflects a peak site of normal mechanical loading. Lumenal ridges continue to appear and propagate along the outer curvature in a radial pattern and eventually mature into thick bundles around 96 hpf. The thick bundles will detach from the ventricular wall and create elaborate networks within the ventricle, and by about 4 dpf the inner surface of a zebrafish ventricle has an impressive trabeculated morphology [55, 44].

The presence of trabeculae also lead to an increase in ventricular mass during the continued process of chamber formation [58], and moreover ventricular wall and compact layer increased to 3 – 4 cellular layers thick [73]. Their structure, although initially may resemble finger-like projections, quickly becomes more geometrically complex and appears as a sponge-like structure.

Now that the interior of the ventricle is no longer smooth and open, it is clear that the hemodynamics within it will be drastically different. Trabeculae are believed to play various roles on blood flow, such as to provide sufficient pumping function during growth, to allow for nutrition of the embryonic myocardium before coronary vascularization, to separate blood currents in the pre-septated heart [74], increase intramyocardial blood flow [53], and not enable the heart to have stagnated flow regions.

Furthermore trabeculae (as well as endocardial cushions) are themselves particularly sensitive to changes in intracardiac hemodynamic shear stress [52]. This becomes crucial when considering that trabeculae may help assist in mechanotransduction for biological signaling, which may still play a vital role in heart morphogenesis at this stage. Another hypothesis is that trabeculation helps regulate and distribute shear stress over the ventricular endocardium; however, some studies believe that the presence of trabeculation develop a more uniform transmural stress distribution [53].

Trabeculation is not confined to solely the ventricular chamber of the heart. Atrial trabeculation, in fact, occurs along the luminal side of the atrial wall; however, this process occurs much later than in the onset of trabeculation in the ventricle.

During the complex formation of trabeculation, endocardial cushions undergo a transformation into valve leaflets. It is believed that both hemodynamic shear stress, genetic factors, and overall myocardial function may help shape and regulate this development [53, 29]. The atrioventricular cushions elongate, fuse, and thin into fibrous leaflets. These leaflets, once constructed, are exceptionally powerful mechanisms for preventing regurgitation of blood from the ventricle back into the arterial chamber. By 102 hpf, the leaflets in the embryonic heart are similar to the adult [75]. Flow rates are approximately 0.4 cm/s and the zebrafish heart beats at around 255 beats per minute [57].

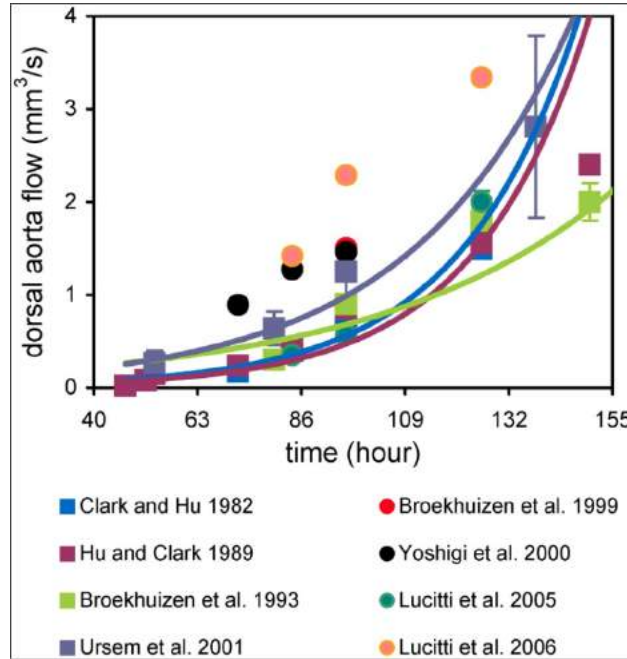


Figure 2.8: Illustrating the exponential increase in cardiac output during development in avian (chick) embryos, as seen from a variety of studies. Image modified from Kowalski et al. 2014 [8].

As the heart grows, the relative mass of the heart decreases with the increase in size and complexity of the embryo. This relationship is seen among many vertebrate species where the heart becomes a progressively smaller percent of the total mass [73]. Recall when embryogenesis first initiates, the heart comprises a vast bulk of the overall mass. Furthermore throughout cardiogenesis, cardiac

output increases exponentially, see Figure 2.8.

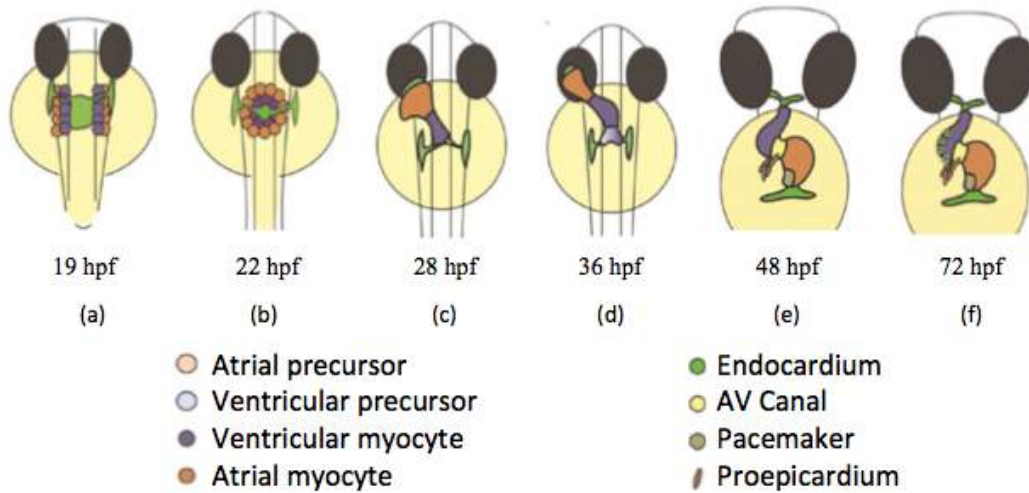


Figure 2.9: A summary of morphogenetic landmarks in zebrafish cardiogenesis. In (a), the linear heart tube begins to develop around 19 hpf, (b) illustrates the continued development of a linear heart tube from once being a cardiac disc and the zebrafish’s first heart heart around 22 hpf. Shortly thereafter, within a few hours the presence of hemacrit is seen. At 28 hpf, (c), the linear heart tube has settled into its final stage before undergoing cardiac looping around 36 hpf (d). As the heart loops, the chamber begins to balloon, forming into their more mature shape. Also, the atrioventricular canal develops and endocardial cushions form within that canal by 48 hpf, as depicted in (e). At this stage, the now two-chambered heart begins to pump in a fashion reminiscent to its adult counterpart. In (f), the first signs of ventricular trabeculation become apparent at approximately 72 hpf. Image modified from Bakkers et. al. [9].

Figure 2.9, modified from [9], summarizes the morphogenetic landmark events in zebrafish cardiogenesis discussed above. In (a), the linear heart tube begins to develop around 19 hpf, (b) illustrates the continued development of a linear heart tube from once being a cardiac disc and the zebrafish’s first heart heart around 22 hpf. Shortly thereafter, within a few hours the presence of hemacrit is seen. At 28 hpf, (c), the linear heart tube has settled into its final stage before undergoing cardiac looping around 36 hpf (d). As the heart loops, the chamber begins to balloon, forming into their more mature shape. Meanwhile the atrioventricular canal develops and endocardial cushions form within that canal by 48 hpf, as depicted in (e). At this stage, the now two-chambered heart begins to pump in a fashion reminiscent to its adult counterpart. In (f), the first signs of ventricular trabeculation become apparent at approximately 72 hpf. Moving forward trabeculation becomes heavily pronounced. The corresponding stages of human heart development are shown in

Figure 2.10, where similar morphogenetic stages occur but on different time-scales. Furthermore, the adult zebrafish (fish) heart has fewer chambers than that of a mature human (mammalian) heart.

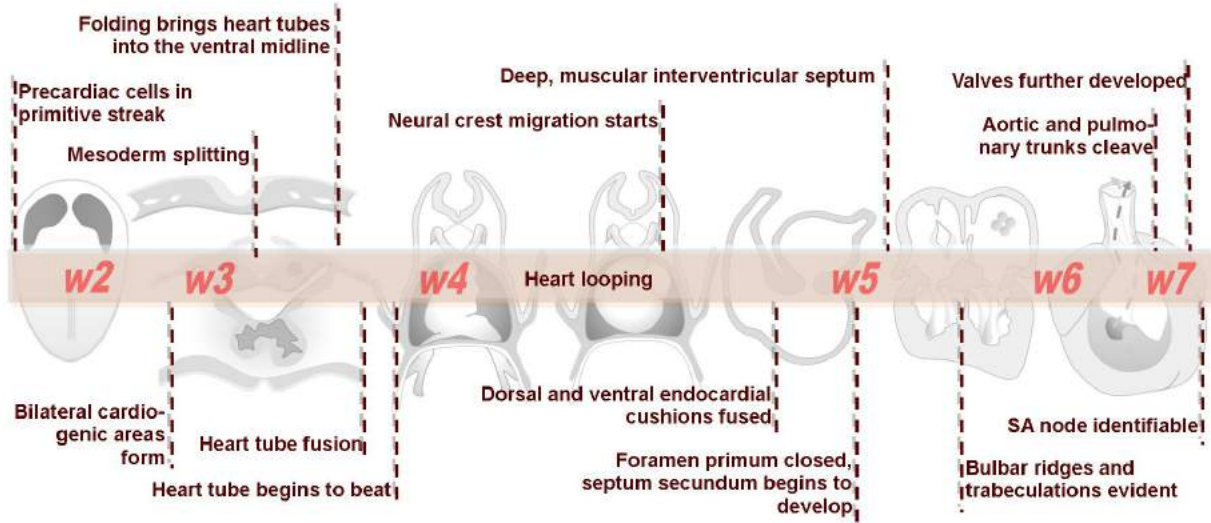


Figure 2.10: A summary of morphogenetic landmarks of human heart morphogenesis, given in weeks. Figure is adapted from [10].

After these stages the cardiovascular system continues to develop with the formation and remodeling of aortic arch arteries and other vascular components [76], the maturation of the cardiac valvular system, progressing the endocardial cushions to valve leaflets, atrial trabeculation, and overall systematic growth of the heart. This thesis, however, will focus on the former stages of heart development, which were discussed above.

2.2 Experimental Studies on Mechanical Forces and Heart Morphogenesis

The notion that mechanical forces are essential for proper cardiogenesis is not a recent idea. It was first proposed by Thoma in 1893 [77] and Chapman in 1918 [78] when they surgically dissected the hearts of chicken embryos during embryogenesis, and observed that the resulting circulatory system did not develop properly. Moreover, the absence of erythrocytes when the embryonic heart begins beating in the linear heart tube stage, supports the belief that the early developing heart does not pump for oxygen or nutrient transport for the embryo. This naturally leads to an interpretation that the embryonic heart performs to aid in the growth, shape, and morphogenesis of the heart and circulatory system [79].

Furthermore from zebrafish studies, it has been shown that a complete lack of hematocrit in mutant specimens does not affect their developing vasculature and can be raised to adulthood [80, 63, 15]. Although these mutants die earlier than their non-mutant counterparts, it is clear that these organisms were able to develop normally by using some other process, such as diffusion of oxygen, nutrients, metabolic wastes, and hormones. These erythrocyte-deprived zebrafish mutants die around 7 dpf, indicating that proper heart function and nutrient delivery is essential for cardiac morphology only significantly later than 4.5 dpf [12].

Many scientists have proposed that hemodynamic forces help regulate and drive organogenesis in developing embryos [81, 82, 83, 84, 85, 86, 12, 26, 54, 15, 87, 8, 11]. Such forces, e.g., shear stresses and pressure forces, may be key components of a large biochemical regulatory network, see Figure 2.11. The hemodynamic forces act on endothelial cells, where the mechanical stimuli is then transmitted to the interior of the endothelial cells via intracellular signalling pathways (mechanotransduction). The biochemical signal is then propagated throughout a pipeline of epigenetic signaling mechanisms, which may lead to a regulation of gene expression, cellular differentiation, proliferation, and migration, and angiogenesis [88]. *Epigenetics* refers to the study of heritable changes in gene expression and phenotype that occur without any changes in the DNA sequence.

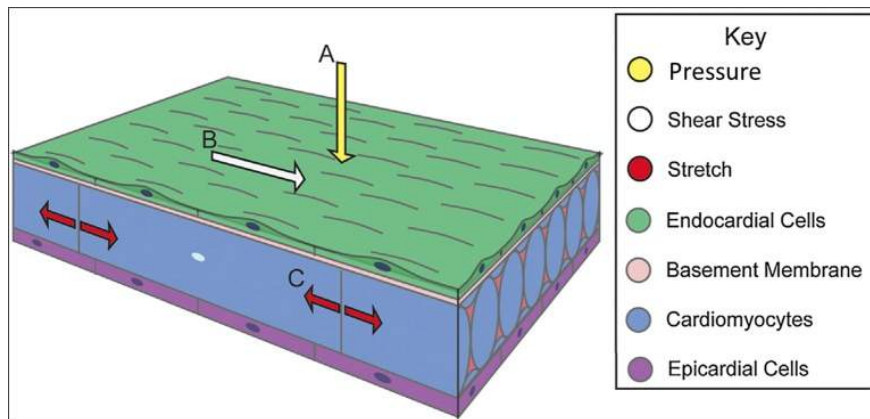


Figure 2.11: An image illustrating the mechanical forces, i.e., shear stress and pressure forces, from the fluid onto the endocardial wall. Image taken from Lindsey et al. 2014 [11].

In vitro studies have discovered that endothelial cells can detect shear stresses as low as 1 dyn/cm^2

resulting in up or down regulation of gene expressions [63]. Embryonic zebrafish hearts beyond 36 hpf are known to admit shear stresses on the order of $\sim 8 - 15 \text{ dyn/cm}^2$. Shear stresses in this range can cause cytoskeletal rearrangement [12].

However, mechanotransduction has only been successfully studied in conjunction with blood vessels, which morphologically remodel over time and either widen or regress in order to adapt to the amount of the flow they carry. Vessels do this by sensing shear stress in order to remodel and change size as heart rates and blood volume increases. Shear stress initiates a chain of cytoskeletal rearrangements that help them realign in flow. Namely in laminar flow, genes that promote proliferation and inflammatory responses are downregulated, while in more turbulent flow the opposite situation occurs where proliferation is upregulated [54].

During cardiogenesis there is an exceptional number of molecular mechanisms that have been implicated in conferring mechanosensitivity of endothelial cells [15, 89]. This indicates of the complexity of the cellular response to hemodynamic forces. Moreover it is unclear how much information *in vitro* can be accurately extrapolated to *in vivo* data.

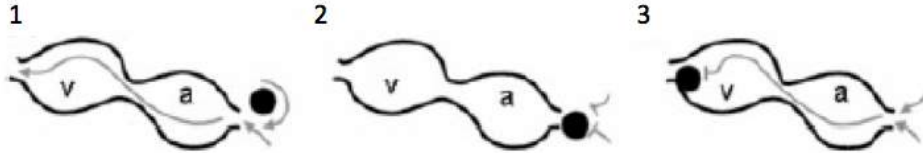


Figure 2.12: The figure illustrates three different experimental placements of a $50\mu\text{m}$ bead in a 37 hpf embryonic zebrafish heart *in vivo*. (1) The bead is placed near the sinus venosus, without obstructing the inflow to the looping heart. Valve and chamber development occur normally, without malfunction. (2) The bead is placed obstructing the sinus venosus (the atrial inflow tract). (3) The bead is positioned obstructing the bulbus arteriosus (ventricular outflow tract). In cases (2) and (3), normal blood flow does not occur and neither valvulogenesis, proper cardiac looping, nor chamber ballooning initiates. Image taken from [12].

Hove et al. 20003 [12] manipulated hemodynamics within developing zebrafish hearts at 37 hpf. They used a 50 micrometer bead to obstruct blood flow through the looping heart either at the atrial inflow region or in the ventricular outflow tract. Furthermore they also performed a control experiment, where a $50\mu\text{m}$ bead was placed near the sinus venosus without obstructing the flow to illustrate their *in vivo* surgical procedure did not hinder cardiogenesis. The geometries can be seen

in Figure 2.12.

In case (1) of Figure 2.12, normal, functional valves and chambers develop. However, in both cases (2) and (3) neither valvulogenesis, proper cardiac looping, nor chamber ballooning occurs, and detrimental heart abnormalities arise. Peristaltic-like (myocardial) contractions persist even though hemodynamics are obstructed. Ultimately, the heart will not develop correctly, as can be seen by ECG when comparing wave forms from a obstructed zebrafish’s adult counterpart to a wild type zebrafish.

A similar study by Stekelenburg-de Vos et al. 2008 [90] modified the hemodynamics in a HH stage 17 chicken embryo (~ 60 hpf in zebrafish) by obstructing the venous inflow tract. They investigated the effect of venous clipping over a 5 hour period, measuring heart rate, peak systolic velocity, time-averaged velocity, peak and mean blood flow, peak acceleration, and stroke volume. All hemodynamic parameters decreased acutely initially; however, only heart rate, time-averaged velocity, and mean blood flow recovered near baseline levels. This study helps to begin bridging the gap between quantitative and qualitative in embryonic hemodynamics, which may provide further insight into any morphological abnormalities or heart dysfunction caused by irregular blood flow.

Moreover, a study by Gruber and Epstein [43] found that improper blood flow may lead to hypoplastic left heart syndrome (HLHS), in which the ventricle is too small or absent during the remainder of cardiogenesis. HLHS occurs in approximately 1 in every 4000 births. They also suggest that HLHS may occur only secondary to perturbations in blood flow, rather than as the primary genetic or developmental defect in the ventricle.

An investigation into mechanical loading during cardiac looping phase in chick embryos, by Nerukar et al. [13], found the heart has the ability to respond and adapt to perturbations in normal morphogenetic mechanisms. They removed the splanchnopleure (SPL) in chick hearts, thereby reducing compression and longitudinal forces on the heart tube. Remarkably, the heart stiffened nearly four-fold in response to the decreased loading. They hypothesize that the increased stiffness is due to cytoskeletal reorganization and contraction, which is not usually a large contributing

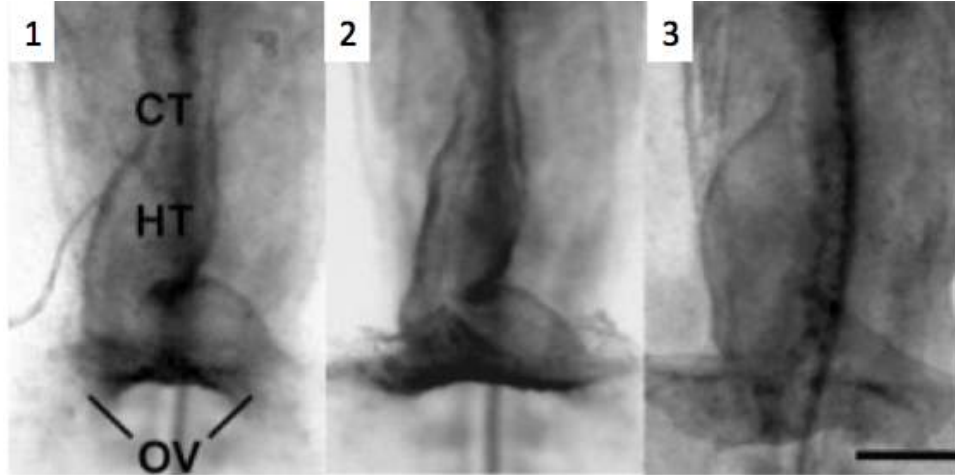


Figure 2.13: A ventral view of a normal heart tube (1), the elongation and narrowing of the tubular heart when the SPL is removed (2), and self-restoration of the tubular diameter, thought to be due to tensile forces. Images taken from Nerukar et al 2006 [13].

stressor in cardiac looping. Moreover, they suggest myocardial cells actively contract in response to decreased loads. Figure 2.13 shows a ventral view of a normal heart tube (1), the elongation and narrowing of the tubular heart when the SPL is removed (2), and self-restoration of the tubular diameter, thought to be due to tensile forces.

Cyclic strains and stretching forces during the cardiac cycle help shape the overall architecture of the trabeculated ventricle. Furthermore it initiates myogenesis in the cellular components of primitive trabeculae [91]. Since trabeculation first occurs near peak stress sites in the ventricle, altering blood flow may directly produce structural and morphological abnormalities in cardiogenesis. Previous work focusing on hemodynamic unloading in an embryonic heart has resulted in disorganized trabeculation and arrested growth of trabeculae [92, 55, 53]. This could be one of the main contributing factors for embryos experiencing hypotrabeclated ventricles. On the other hand, embryos with a hypertrabeclated ventricle also experience impaired cardiac function [55]. Such abnormalities can result in congenital heart defects, and in some cases are detrimental to an embryo or infant, usually stemming from defective diastolic function.

Even subtle defects in trabeculation, spawned from slight modifications in hemodynamics, may magnify over time. In concert with Neuregulin signaling levels and other genetic signals, which also are governed by a complex system of mechanotransduction, trabeculation deformities will

further deviate heart morphogenesis, and more importantly cardiac function, from normal healthy cardiogenesis.

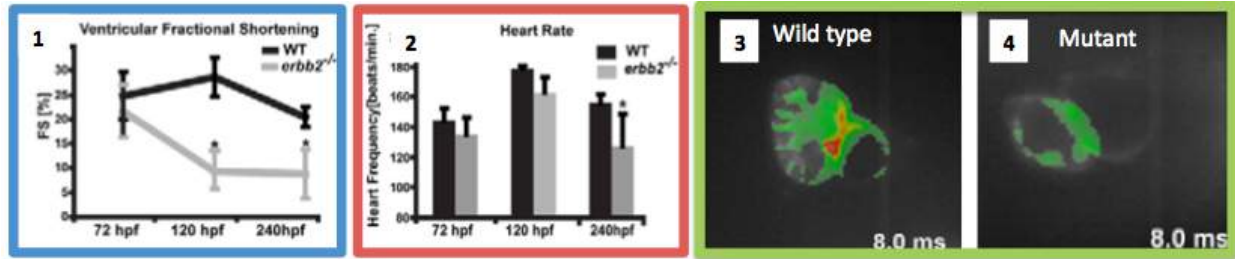


Figure 2.14: Data collected from a study from ErbB2 zebrafish mutants by Liu et al. 2010 [5]. (1) These mutants experience a decrease in fractional shortening. It seen that as embryogenesis progresses, fractional shortening further decreases. (2) Their hearts also undergo bradycardia, where the heart beat also progressively decreases during development. (3) and (4) are optical mappings of cardiac conduction in their ventricle at 10 dpf. More prevalent ventricular conduction regions can seen in wild type mutants (3) compared to their ErbB2 mutant counterparts (4). It is also evident in (3) and (4) that the wild type ventricle is more massive than the mutant's.

Liu et al. 2010 [5] showed that in ErbB2 zebrafish mutants that their lack of trabeculae leads to severe physiological defects. These mutants experienced bradycardia, decreased fractional shortening, and impaired cardiac conduction. Their data can be seen in Figure 2.14. Due to a decreased heart rate, these mutant embryonic hearts suffer from more mechanical defects because of the disrupted hemodynamics, and moreover these ErbB2 mutants die around 12 dpf. Their results directly illustrate that trabeculae enhance cardiac contractility, which may be a result of the mutant hearts failing to increase cell mass like what happens normally during trabeculation, and intraventricular conduction directly.

Furthermore a study by Reckova et al. 2003 [14] found that in chicken embryonic hearts, maturation of the ventricular conduction cells depends on hemodynamic forces. They found that increased loading accelerated the conversion from an immature to mature pattern of ventricular activation, while decreased load delayed the conversion. Moreover, mapping of the endocardial surface showed that trabeculae accounted for the last observations of immature activation patterns, i.e., base-to-apex activation. Without proper maturation of such myocardial cells, these hearts may later exhibit ventricular conduction and hence contractile defects, such as arrhythmias, abnormal fractional shortening, or even ventricular fibrillation.

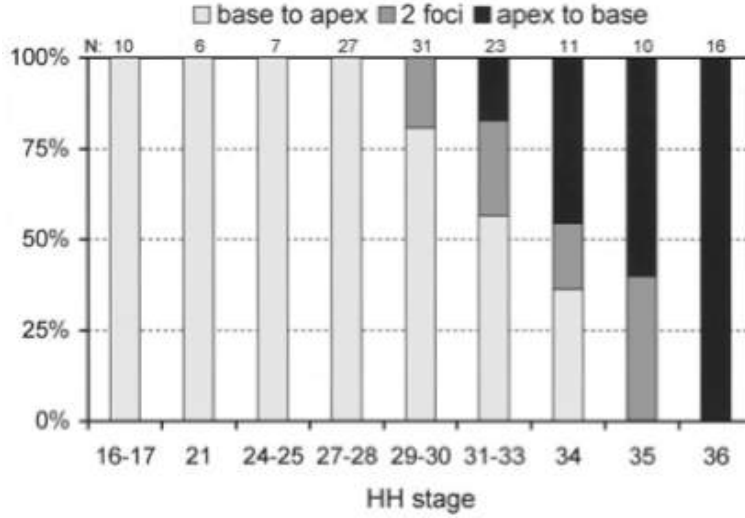


Figure 2.15: Evolution of the activation pattern of HH stage 16 to HH stage 36 hearts in chicken embryos. Initially all electrical activation propagates as base-to-apex signals, which lasts until around HH stage 27 embryonic chicken hearts. Next a shift to 2 locations of ventricular activation occurs, one at the base, showing immature activation foci, and another at the apex, the location of mature activation foci. This type of 2-foci activation persists until HH stage 36, when there is full maturity in activation patterns. Images adapted from Reckova et al. 2003 [14].

Figure 2.15 illustrates activation pattern evolution from HH stage 16 to HH stage 36 hearts in chicken embryos. Initially all electrical activation propagates as base-to-apex signals, which lasts until around HH stage 27 embryonic chicken hearts. Next a shift to 2 locations of ventricular activation occurs, one at the base, showing immature activation foci, and another at the apex, the location of mature activation foci. This type of 2-foci activation persists until HH stage 36, when there is full maturity in activation patterns.

By the same token, proper myocardial function is essential in endocardial cushion development. In a study by Bartman et al. 2004 [53] an inhibitor of myofibril function was administered in embryonic zebrafish hearts, whose effects did not directly inhibit blood flow. Even though blood flow ceased in all embryos, they witnessed a majority of them still being able to form endocardial rings and cushions by 48 hpf. This suggests that endocardial cushions may not need blood flow to initiate; however, that does not dissociate blood from being a contributing factor in cushion formation. Myocardial contractions generate circumferential stress on the heart chamber walls, which is resisted by the very viscous embryonic blood within the heart. The blood then applies a force

onto the endothelial lining of the heart, the heart wall applies an equal and opposite force onto the fluid causing it to move, and finally shear stresses on the heart's surface are generated [93].

It is evident that there is a complex and strong relationship between intracardial hemodynamics, genetic regulatory networks, and cardiac conduction. The electrophysiology and hemodynamics of the embryonic heart are clearly coupled since electrical impulses trigger the contraction of myocardial cells which then drive blood flow. To complicate matters even more, fluid shear stress is known to increase the conduction velocities of action potentials within the myocardium, illustrating how the fluid dynamics, in turn, can also affect the electrophysiology of the embryonic heart [14]. Furthermore, Tucker et al. 1988 [94] confirmed that hemodynamics are directly involved in proper pacemaker and cardiac conduction tissue formation.

Hence altering, the hemodynamics, will modify the cardiac conduction system, which will then cause abnormal contractile behavior, and in turn cause irregular intracardiac hemodynamics. The cycle can then perpetuate itself, and thus magnify any defects themselves during the remainder of embryogenesis.

2.3 Zebrafish used as a model organism for cardiogenesis

In vitro experiments, while essential and useful in progressive research among a vast array of important scientific endeavors, unfortunately cannot be used with complete certainty to describe what happens in an organism *in vivo* [54]. For example, *in vitro* studies have shown that endothelial cells are sensitive to mechanical stimuli like shear stress and pressure forces, resulting in either up or down regulation of gene expression, [12, 29, 35, 51]; however, it remains unclear how accurate these results can be extrapolated to circumstances *in vivo*.

In vivo experiments are necessary, usually in parallel with *in vitro* experiments, in studying heart morphogenesis. Naturally, the next question becomes what organism to consider for such investigations. Many scientists have performed instrumental experiments, in which progress the understanding of cardiogenesis, using many different animal species. Cardiogenetic vertebrate animal models have traditionally been either mice, chickens, frogs, or zebrafish, while some invertebrates

such as sea squirts have been used for studying linear heart tube dynamics [21, 22, 95].

Heart development remains relatively conserved between all vertebrates, but in particular, mice, chicken, zebrafish, and human cardiogenesis is conserved. We choose zebrafish, *Danio rerio*, as our model organism in studying heart morphogenesis. Zebrafish have genetic complexity to that of mammals. However, whereas avian and mammalian hearts are four-chambered, fish hearts have only two-chambers.

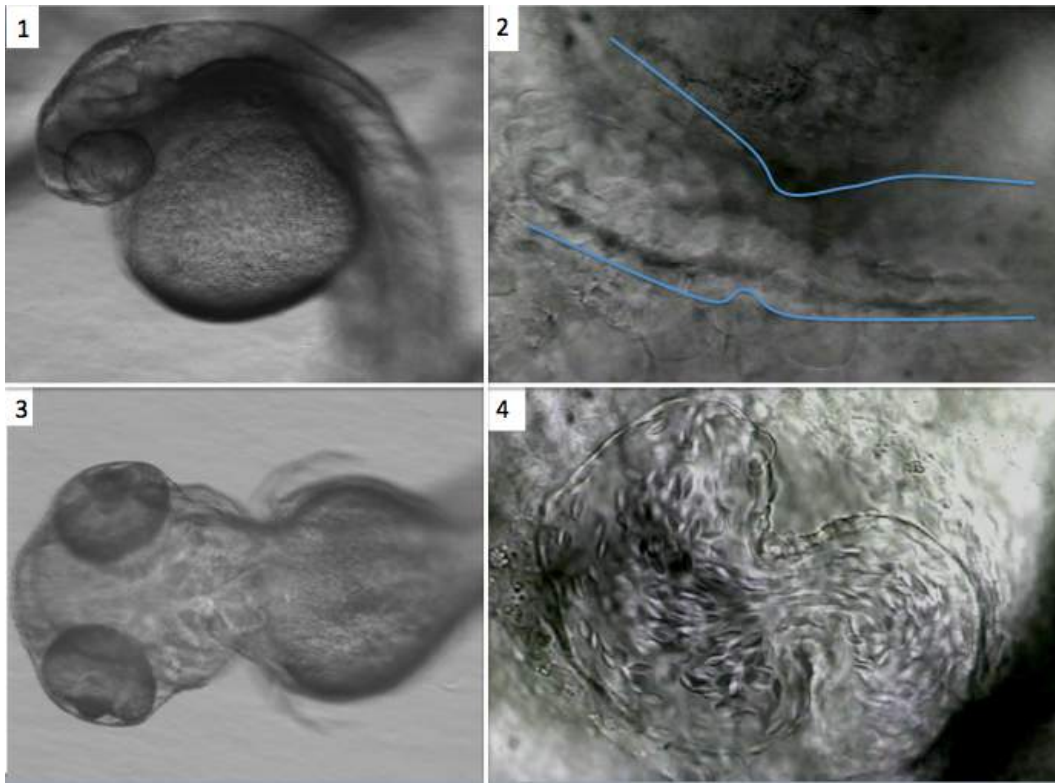


Figure 2.16: Illustrating optical clarity at two stages of heart morphogenesis, the linear heart tube stage (1) and (2), and chamber formation (3) and (4). (1) shows the zebrafish embryo 24 hpf, while in (2) a light microscope is used to visualize the optical clarity of the heart tube, which is outlined in blue. Blood cells at this stage are spherical. (3) shows the still transparency of the zebrafish at 48 hpf. In (4) a light microscope is used to affirm that two distinct chambers have formed, pumping more elliptical erythrocytes. These images are courtesy of Leigh Ann Samsa, School of Pathology at UNC-CH.

Zebrafish embryos are transparent, which make them an ideal candidate for imaging *in vivo* [63, 44]. This can be seen in Figure 2.16. It is evident from images taken at two drastically different stages in heart development (the linear heart tube phase at 24 hpf, and the stage proceeding the

majority of cardiac looping, at approximately 48 hpf), the zebrafish embryo as a whole is still transparent and allows for high resolution *in vivo* imaging with only a light microscope.

Another aspect that makes zebrafish an ideal candidate for *in vivo* studies is there vast scale of mutants [44, 96] and ease of selective gene knockdown [57]. Furthermore due of their small size and ease of genetic manipulations, large-scale mutagenesis screens are also possible [57, 75]. Contrary to other common vertebrate cardiogenesis model organisms, zebrafish mutants can survive with severe heart defects until later stages of heart development [63]. It is believed that a low metabolism and their small size attribute to their hearts, although functional, not being essential in the early developmental stages. This allows for longer analysis of mutants with compromised or no cardiac function, whereas frog, mouse, or chick models die [44].

2.4 Mathematical Models in Heart Morphogenesis

Unfortunately, animal models, including zebrafish, can only be exploited experimentally, until the lingering limitations of technology prevail. Even though imaging techniques and genetic manipulation are extremely powerful tools in studying cardiogenic events, at this junction they cannot be used to to fully predict all possible ailments and deformities that may arise in heart development [97, 98]. Subtle irregularities may not be resolved and a complete understanding for the remainder of the morphogenic process is not possible. Moreover, where experiments can take months of planning, funding, preparation, approval, and time to carry out, mathematical models may be able to to accurately and swiftly prognosticate heart morphogenic events.

Mathematical models have been used successfully to describe various systems in biology and medicine. Some examples include cellular blebbing [99, 100, 101, 102], sperm motility and detachment [103, 104, 105], blood clotting [106, 107, 108], design of antibodies [109], chromosome dynamics [110], cellular signaling and drug design [111, 112], and cancer progression and treatment [113, 114, 115]. In fact, it has been argued that computational and quantitative biology is paramount to the quest of understanding biology and life [116]. It is not surprising that mathematical and computational modeling has latched itself into virtually every subfield of biology.

Studying cardiac dynamics and blood flow is not a new subfield of science. It dates back until roughly 130 AD, when the Roman physician Galen palpated the pulse and disproved that arteries and veins carried air throughout the body. Quite comically, in hindsight, Galen believed that the venous and arterial systems were exclusive, and that the heart mainly produced heat, while the arteries cooled the heart, acting as the regulator of body temperature [117]. In the 17th century, the English physician, William Harvey, made a fundamental breakthrough when he fully described the circulation of blood throughout the body. Upon doing so, he was the first to understand the role of the heart in circulation using both qualitative and quantitative metrics, although in a very primitive sense [118].

It was not until the late 18th century, when a more quantitative description of cardiac dynamics began to unravel, started with Stephen Hales. He was the first to measure arterial pressure in animals and correlate a loss of pressure to a loss of blood volume in 1733 [119]. In 1840, Jean-Leonard Marie Pouseuille studied pipe and channel flow, and unearthed an underlying relationship between flow rate, pressure gradients, and the diameter of a pipe or channel. About forty years later Osborne Reynolds discovered a dynamical transition from laminar flow to turbulent flow in a pipe based on certain parameters of the system [120]. Otto Frank, in 1903, uncovered the relationship to ventricular filling and contraction [121]. Roughly fifty years later in 1955, John Womersley uncovered a mathematical relationship between pressure, pulsatile flow, and effects of viscosity [122].

Since the 1950s, the scientific community has placed considerable focus on fleshing out an accurate quantitative description of cardiac dynamics. With ever-increasing computational power, this goal has become more tractable and realistic; however, there is much work to left to do. There are also many avenues scientists take to studying cardiovascular dynamics. Some models use $1D$ geometries and couple sophisticated vessel wall and viscoelastic constitutive models to study flow through arterial networks, and can successful match *ex vivo* data [123]. However, other studies focus on moving flexible boundaries, immersed within a fluid, to accurately model pumping heart chambers and leaflets.

The first time fully coupled fluid-structure interaction models could be simulated was with the invent of Peskin's immersed boundary method in the 1970s [124, 125]. Since then many fluid-structure numerical methods, most based off of the immersed boundary method, have been designed and

implemented to study various problems in biological fluid dynamics. There have also been many efficient improvements of the immersed boundary method, such as parallelization [126], adaptive mesh refinement [32, 127], higher order versions of the method [128, 129, 130], or a hybrid finite difference and finite element immersed boundary method [131].

Furthermore, mathematical modeling in embryogenesis, specifically in heart morphogenesis, has only relatively recently been placed in the spotlight. For the remainder of this section, we will briefly review previous mathematical models for various phases in the vein of cardiogenesis.

2.4.1 Linear Heart Tube Modeling

Much of heart morphogenic modeling has focused on the linear heart tube stage [20, 22, 19, 16, 35, 95]. It is clear there is a large discrepancy whether the embryonic heart pumps via peristaltic contractions of the myocardial walls aligning the heart tube or dynamic suction pumping (impedance pumping), where a single actuation point is contracted on the heart tube [20, 16, 65].

Peristalsis is known to be efficient at pumping over a large parameter space, i.e., Reynolds number (Re). In many biological applications, like the ureters and gastrointestinal tract [132], and medical devices, the traveling actuation wave almost fully occludes the tube, pushing the fluid and/or other contents further along. Because of the incompressible nature of fluid in these cases, the fluid must proceed further along the tract. The velocity of the fluid and its contents are being pushed roughly on par with the speed of contractile wave, forming a linear relationship between frequency and volumetric flow rates [133].

On the other hand, dynamic suction pumping has recently gathered a lot of interest among the engineering community due to its elegance [65, 16]. Only a single actuation point is necessary to induce flow, if the contraction point is in an elastic portion, located asymmetrically between two stiff ends of a tube. A single contraction forces a bidirectional passive wave to travel down both ends of the tube. Depending on where such single impedance point is fixed, one wave will reach an end of the tube before the other, reflecting back. The reflected wave then travels in the same direction as the other half of the bidirectional wave, thereby creating bulk unidirectional flow for a brief time. While those

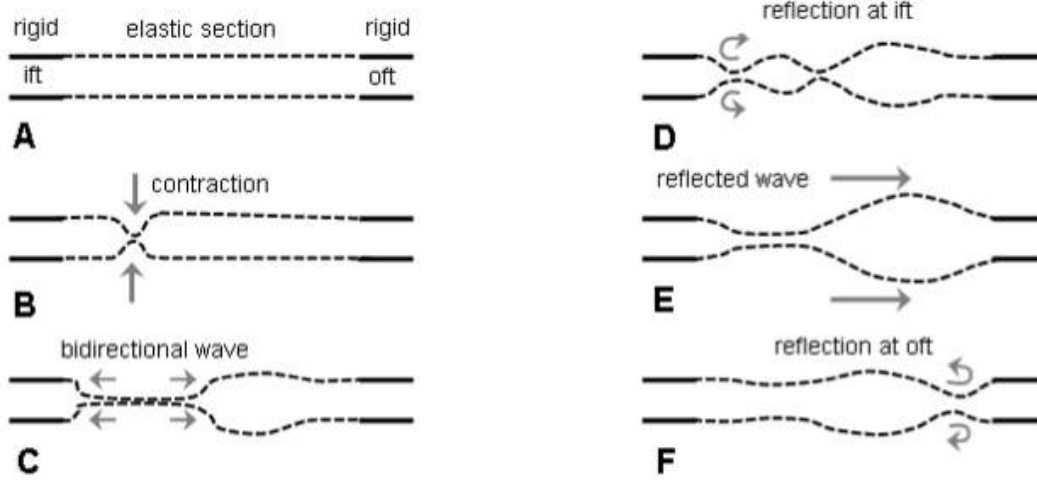


Figure 2.17: Schematic diagram of dynamic suction pumping adapted from Santhanakrishnan et al. 2011 [15]. (A) Illustrates the tube at initially at rest, while (B) shows the asymmetric location of a single actuation point undergoing contraction. (C) That contraction creates a bidirectional wave traveling down the tube and in (D) one side of that wave reflects off the left end of the tube, since that end is closer to the actuation point. In (E) both the reflected wave and last portion of the initial bidirectional wave are traveling in the same direction. Finally in (F) there is reflection of that wave, while presumably another contraction on of the actuation will occur.

waves will reflect back, their magnitude will have largely decreased, and presumably another contraction of the actuation point will have taken place, overpowering the reflected wave's momentum. Thus there is interference between the passive waves created by the impedance pumping and the reflected wave, hopefully creating bulk flow within the tube. This can be seen in Figure 2.17, adapted from [15].

Dynamic suction pump exhibits a nonlinear relationship between frequency and volumetric flow rate. Moreover, the direction of unidirectional pumping is dependent upon many parameters, such as frequency and actuation site location.

Studies by Avrahami et. al 2008 [16] Avrahami et al 2008 studied the resonance properties of dynamic suction pumping in compliant tubes. They examined a wide range of parameters such as actuation location, frequency, pinching occlusion, and duty cycle, which is the ratio of pinching duration to time period. Their work discerns frequencies, pinching amplitude, and duty cycle % for optimal flow rates as well as location of pincher along the tube to get desired flow directions and rates [16].

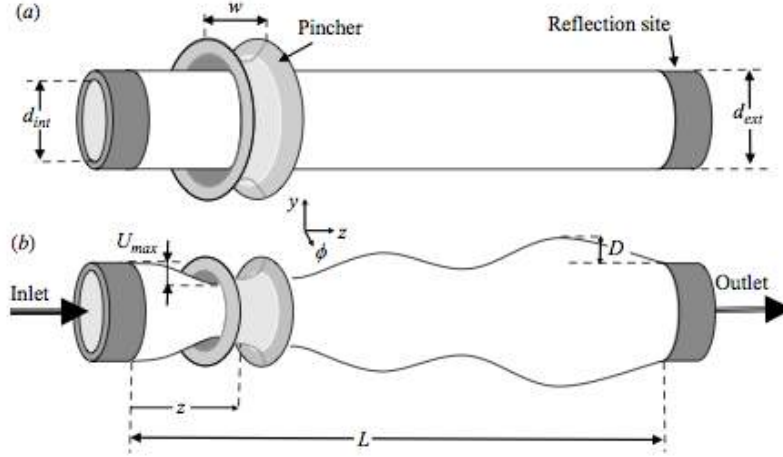


Figure 2.18: Model geometry as adapted from [16]. Their geometry, although $3D$, is axisymmetric. The model is at rest in (a), and under one contraction in (b). The inlet and outlets are held rigid for proper wave reflection, and the tube is elastic, allowing passive traveling waves from the actuating.

Their geometry is seen in Figure 2.18, as adapted from [16]. Their geometry, although $3D$, is axisymmetric. The model is at rest in (a), and under one contraction in (b). The inlet and outlets are held rigid for proper wave reflection, and the tube is elastic, allowing passive traveling waves from the actuating. Simulations of their model were performed using a finite element scheme within the ADINA commercial software package. The software was able to incorporate contact of the pincher with the flexible wall, elasticity dynamics of the tube, and the fluid-structure interaction at the interface, as well as the dynamics of the fluid.

Their results regarding the dynamic suction pumping mechanism, i.e., location of the actuation site, occlusion amplitude, and duty cycle % can be found in Figure(2.19). (a) Shows the dependence of flow rate on the location of the actuation site. As the location moves to the center of the tube, flow rate decreases. Their data is confirmed against experiments performed by Hickerson et al. 2005, [17, 18]. (b) Illustrates the flow rate dependence on the pinching occlusion, in an almost linear relationship. As occlusion increase, as does flow rate. In (c) they explore flow rate's dependence on duty cycle % and see good agreement with experimental work done by Hickerson et al. 2005.

Results adapted from [16] regarding the dependency of flow rate on frequency. It is clear there is a nonlinear relationship between frequency and flow rates, as expected from dynamic suction pumping.

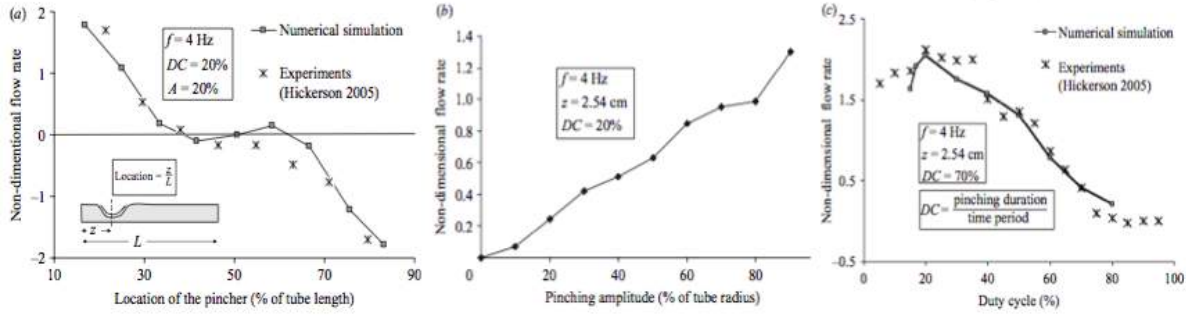


Figure 2.19: Results taken from [16] regarding the dynamic suction pumping mechanism, i.e., location of the actuation site, occlusion amplitude, and duty cycle %. (a) Shows the dependence of flow rate on the location of the actuation site. As the location moves to the center of the tube, flow rate decreases. Their data is confirmed against experiments performed by Hickerson et al. 2005 [17, 18]. (b) Illustrates the flow rate dependence on the pinching occlusion, in an almost linear relationship. As occlusion increase, as does flow rate. In (c) they explore flow rate's dependence on duty cycle % and see good agreement with experimental work done by Hickerson et al. 2005. [17, 18]

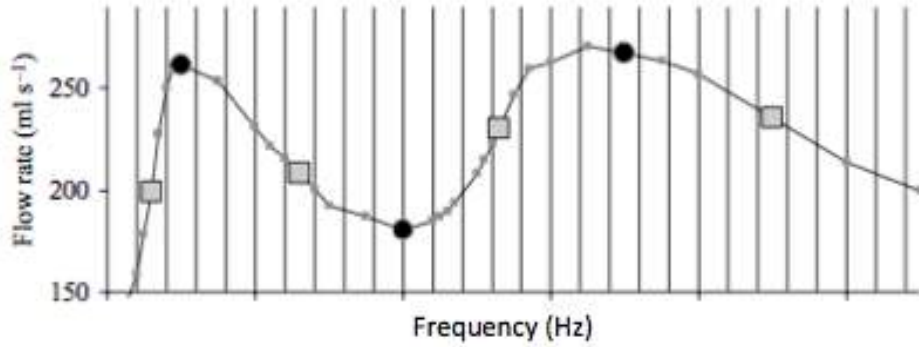


Figure 2.20: Plot adapted from [16] illustrating the non-linear relationship between flow rate and frequency for dynamic suction pumps.

Unfortunately these results do not extend into the range of Reynolds number, Re , or Womersley number, Wo , for linear heart tubes. These results *may* be useful for the investigation of the embryonic heart being pumped via dynamic suction pumping; however, they are not conclusive that at this stage in development the embryonic heart would be able to effectively drive blood at those scales. These considerations were studied by Baird et al. 2014 [20], which is discussed below.

Studies by Taber et. al 2007 [19] Taber et al. 2007 [19] considered what could cause a transition from peristaltic to pulsatile flow within a heart tube. They discovered that the presence of bumps within a channel, i.e., modeling endocardial cushions, were enough to induce such transition.

Their model results were also in good agreement for various pressure and flow parameters with experimental data.

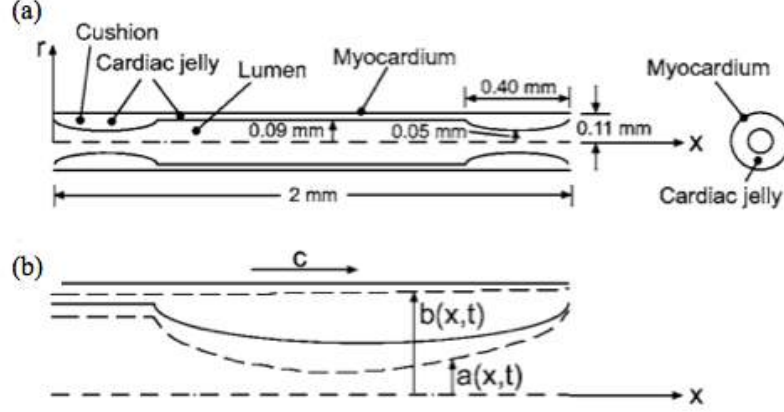


Figure 2.21: Geometry of the linear heart tube geometry. In (a), the tubular geometry with endocardial cushions is shown in its resting state, while (b) illustrates the difference between the deformation geometry (dashed lines) and rest state (solid lines). As a wave passes by, the cushions thicken and deform. Figure adapted from Taber et al. 2007 [19].

Their model geometry can be seen in Figure 2.21, adapted from [19]. In (a), the tubular geometry with endocardial cushions is shown in its resting state, while (b) illustrates the difference between the deformation geometry (dashed lines) and rest state (solid lines). As a wave passes by, the cushions thicken and deform. Their model was simulated using a finite element implementation within the Comsol Multiphysics v3.2a software package [134].

From performing simulations with and without the endocardial cushions, they discovered that the presence of the cushions induces a transition from peristaltic flow to pulsatile flow by comparing pressure waveforms and flow profiles in the outflow tract, after the cushions, in each case. These contrasts can be discerned in Figure 2.22, from [19].

In Figure 2.22-(a) and (c) show the pressure and flow waveforms respectively for a simulation without endocardial cushions. It is clear in (c) that a flow waveform for peristalsis can be seen. (b) and (d) illustrate the transition to pulsatile pressure and flow profiles once endocardial cushions are included.

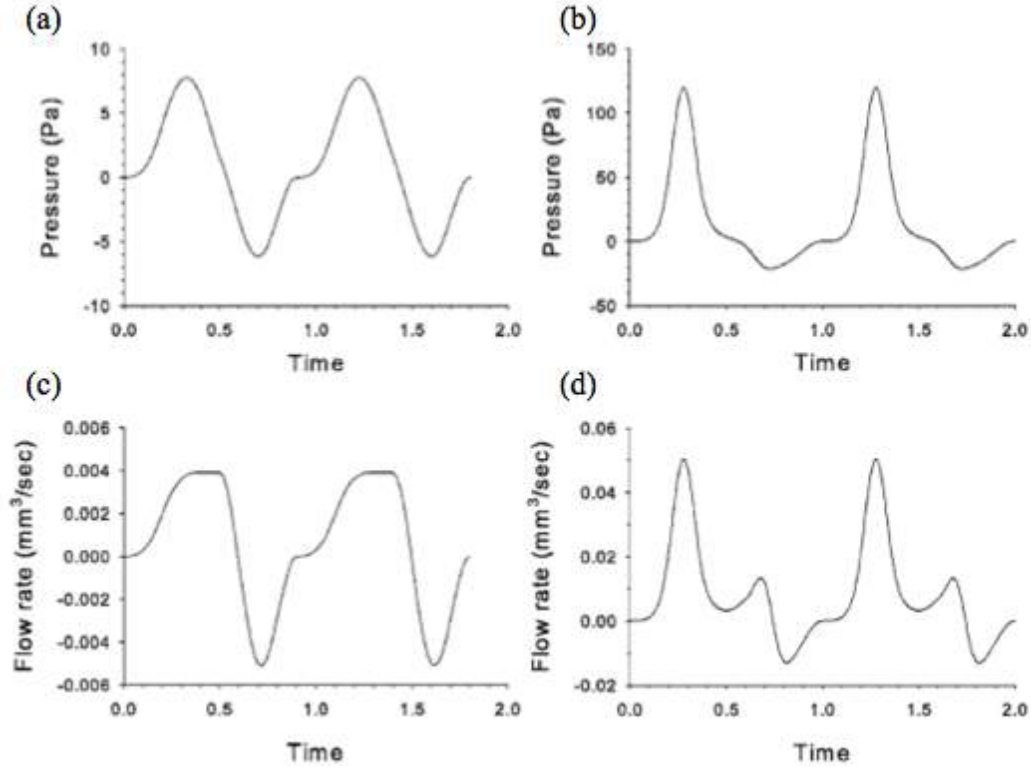


Figure 2.22: Results depicted differences in pressure and flow waveforms for both simulations with and without endocardial cushions in the heart tube. (a) and (c) show the pressure and flow waveforms respectively for a simulation without endocardial cushions. It is clear in (c) that a flow waveform for peristalsis can be seen. (b) and (d) illustrate the transition to pulsatile pressure and flow profiles once endocardial cushions are included. Figures adapted from [19].

Studies by Baird et al. 2014 [20] Baird et al. 2014 [20, 21] studied the flow generation due to peristalsis and dynamic suction pumping for a wide range of *Womersley number*, Wo , and diameter to length ratios of the flexible portion of the tube [20, 21]. They found that the diameter to length ratio has a pronounced effect on volumetric flow rates as well as direction in dynamic suction pumping. This effect was not significant in peristalsis since flow rates are determined by the speed of the contraction wave. However, variations in Wo , performed by varying viscosity, illustrate at what scales peristalsis and dynamic suction pumping effectively pump fluid. They found that impedance pumping did not generate significant bulk flow for $Wo < 1$.

Baird et al. 2014 used a racetrack geometry, as depicted in Figure 2.23 adapted from [20, 21]. Both pumping mechanisms were implemented on this same geometry, with peristalsis enforced along most of the flexible portion on the bottom of the racetrack, while the dynamic suction pumping

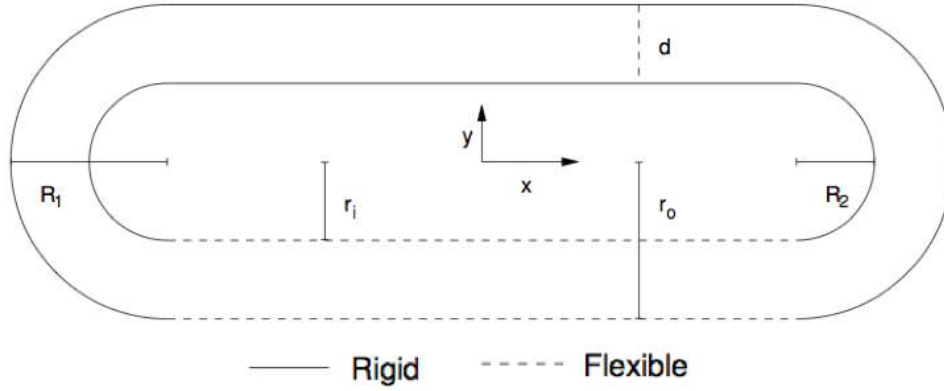


Figure 2.23: Geometry of the closed racetrack. Flexible regions are indicated by the dotted portions, while rigid parts are shown by solid lines. The pumping mechanisms, peristalsis or dynamic suction pumping, are implemented along the flexible portion. Figure adapted from [20, 21].

actuation was induced in a small portion along the flexible region away from its center.

The tube is itself was immersed in an incompressible fluid and the fully coupled fluid-structure interaction model is simulated using the immersed boundary method. To perform each respective pumping mechanism, the deformations of the tube (for both the traveling contractile wave for peristalsis or single actuating contraction in impedance pumping) were implementing in a prescribed fashion using tethering target points to the immersed structure. As the tube is compressed, deformation forces act on the fluid, driving it to move, while also inducing a complementary force back onto the immersed boundary.

Their simulation results can be seen in Figure 2.24, adapted from [20]. Their results illustrate average velocities for peristalsis and dynamic suction pumping as a function of Womersley number, while also showing effects of varying tube diameter in each case. (A) shows the results for peristalsis, while (B) illustrates the results for dynamic suction pumping. For Wo in the biologically relevant range, $Wo \approx 0.1$, only peristalsis initiates significant flow.

Studies by Baird et al. 2015 [22] Baird et al. 2015 [22] developed a new neuro-mechanical model of pumping in valveless, tubular hearts, inspired by the tunicate, *Ciona savignyi*. The model incorporated the FitzHugh-Nagumo equations to model the propagation of an action potential that induces myocardial contraction. They compared fluid flows generated using this neuro-mechanical

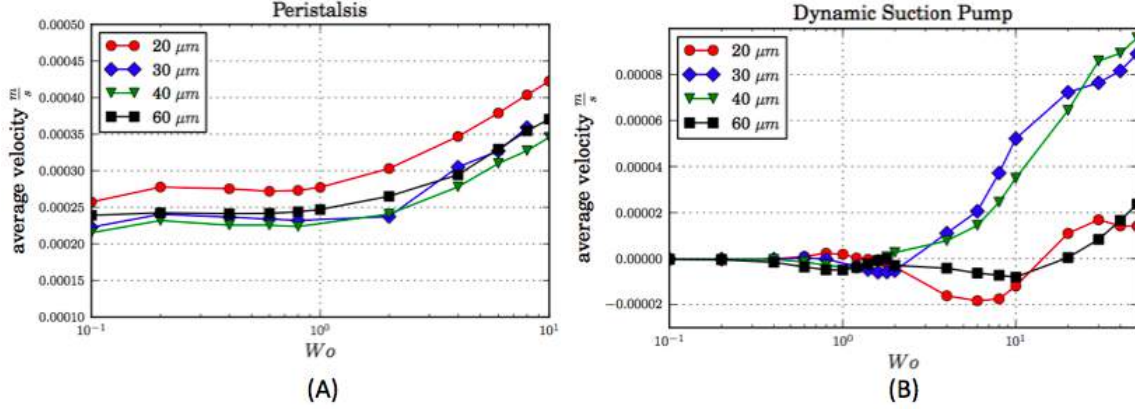


Figure 2.24: Simulation results illustrating average velocities for peristalsis and dynamic suction pumping as a function of Womersley number, while showing effects of varying tube diameter in each case. (A) Results for peristalsis, while (B) illustrates the results for dynamic suction pumping. For Wo in the biologically relevant range, $Wo \approx 0.1$, only peristalsis initiates significant flow, with velocities in the order of $\sim 0.01 \text{ cm/s}$, where as dynamic suction pumping at the same scale gives velocities *at least* two orders of magnitude smaller. Figure adapted from [20].

pumping model to prescribed peristalsis and prescribed impedance pumping, as in [20], across a parameter space relevant to the *Ciona savignyi*. They discovered that the neuro-mechanical pumping mechanism and peristalsis are able to reproduce the strong flows observed in the tunicate heart; however, only the neuro-mechanical model was able to produce flow patterns that have been reported with valveless, tubular hearts [65]. The neuro-mechanical pumping model was able to generate a bidirectional wave of contraction, which was reported in [65], to which traditional peristalsis, as in Baird et al. 2014 [20], does not.

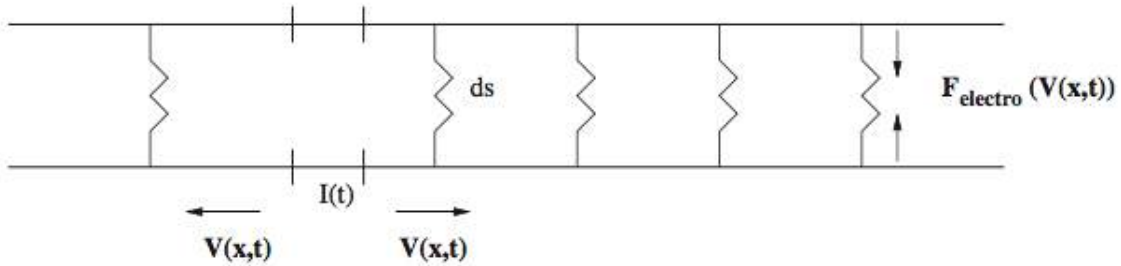


Figure 2.25: Geometry of the flexible region of the racetrack. The springs depict muscles that generate the contraction, once the action potential signal propagates to its location. The muscle then contracts according to F_{electro} . Figure adapted from [22].

The same racetrack geometry that was used in [20] was used in here, e.g., Figure 2.23. However, for the neuro-mechanical model. the flexible tube had additional properties, that included the

myocardial muscles that contract upon initiation by an action potential. This model was studied using the immersed boundary method coupled to the FitzHugh-Nagumo equations.

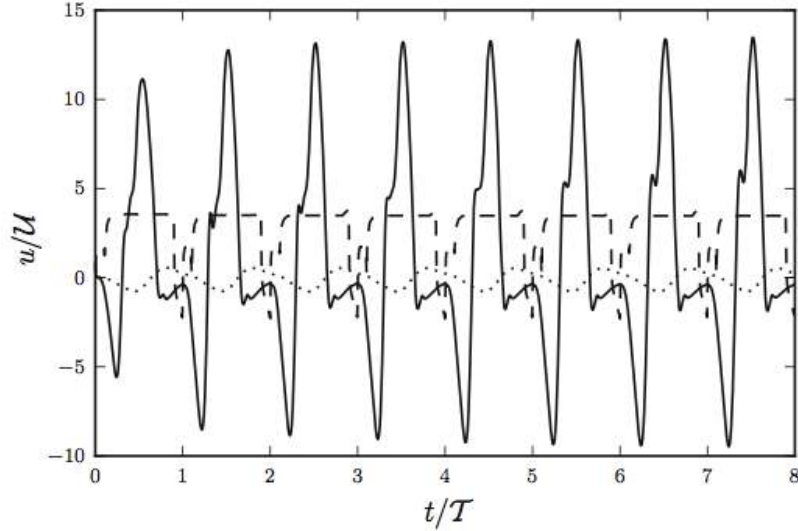


Figure 2.26: A comparison of the dimensionless spatially-averaged flow velocities measured across the cross-section of the top of the tube for dimensionless time. The solid line represents the neuro-mechanical pump, the dashed line is peristaltic pumping, and the dotted line is impedance pumping. Figure adapted from [22].

For biologically relevant parameter regimes, given by $Wo \approx 1$, in the *Ciona savignyi*, a comparison of the dimensionless spatially-averaged flow velocities measured across the cross-section of the top of the tube for dimensionless time is found in Figure 2.26. The solid line represents the neuro-mechanical pump, the dashed line is peristaltic pumping, and the dotted line is impedance pumping.

Neuro-mechanical pumping achieves higher maximum and lower minimum flow velocities than both impedance pumping and peristalsis. Peristaltic pumping produces strong positive flows with little back flow, and the flow rapidly approaches a constant velocity during translation of the contraction site, while flow produced by neuro-mechanical pumping is more transient and unstable. It does not reach steady flow velocity during the translation of the traveling wave down the tube, unlike peristalsis. This can be seen in Figure 2.26.

Neuro-mechanical pumping has higher bulk flow rates than impedance pumping; however, bulk flow rates are still greater in peristalsis than neuro-mechanical pumping. These properties remain consistent for a wide range of Wo , including the biologically relevant range. This data is seen in Figure 2.27.

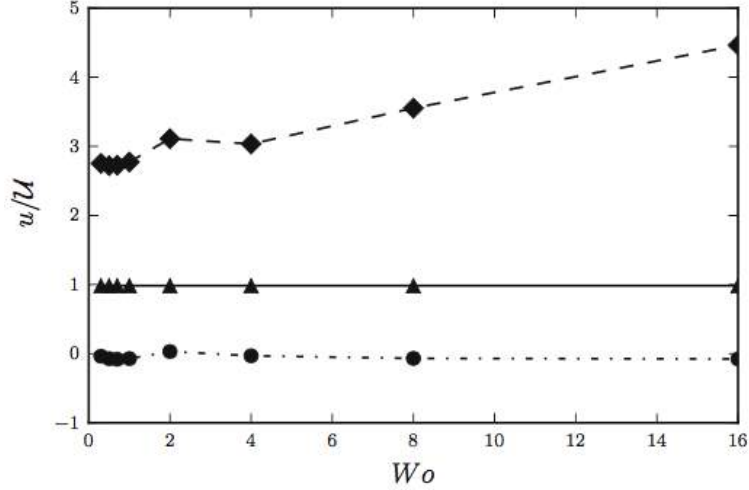


Figure 2.27: A comparison of the dimensionless spatially-averaged and temporally-averaged flow velocities measured across the cross-section of the top of the tube for different Wo . The solid line represents the neuro-mechanical pump, the dashed line is peristaltic pumping, and the dotted line is impedance pumping. Figure adapted from [22].

Studies by Waldrop et al. 2015 [23] Waldrop et al. 2015 [23] investigated perturbations upon the traditional assumptions of peristalsis, by studying large-amplitude, short-wave length peristalsis, rather than small-amplitude, long-wave peristalsis. They focused on the relationships between fluid flow, compression frequency, compression wave speed, and tube occlusion, to seek out inconsistencies with the traditional peristalsis flow properties. They discovered that bulk flow speeds produced by these new assumptions on peristalsis are greater than the speeds of the compression wave, fluid flow is pulsatile in nature, and flow speeds have a non-linear relationship with compression frequency, when the compression wave speed is held constant. These properties make peristalsis a viable candidate for the pumping mechanism in embryonic hearts, when compared to observations in [65].

This model used a similar model to that in Baird et al. 2014 [20]; however, with a short length flexible region and wider tubular cross-section. This can be seen in Figure 2.28. Similarly the peristaltic contraction was prescribed in this model.

Data from Figure 2.29 gives a non-linear relationship between fluid flow speed and Wo , which is uncharacteristic of traditional long-wave, short-amplitude peristalsis. The dotted line gives the speed for the constant, non-dimensional compressive wave speed. Note that fluid flows are greater than contraction speed, in this case. This is also not a characteristic of traditional peristalsis. Furthermore, they illustrate the sensitivity of peristalsis to perturbations of compressive ratio (occlusion) and

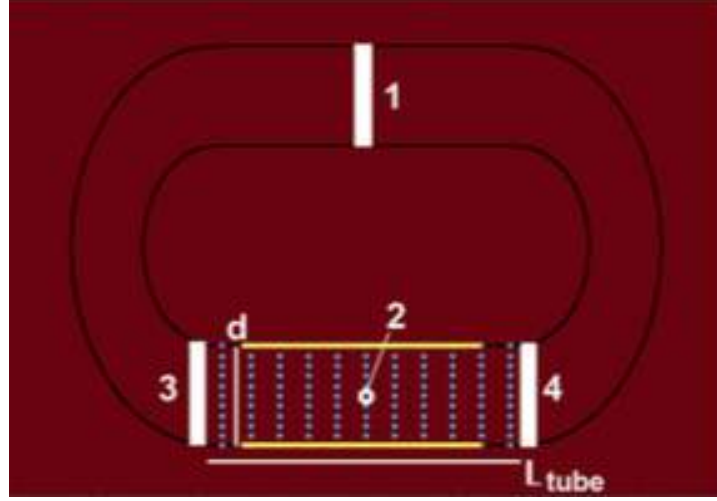


Figure 2.28: Geometry of the racetrack with a shorter length flexible region and wider cross-section, when compared to Figure 2.23. Figure adapted from Waldrop et al. 2015 [23].

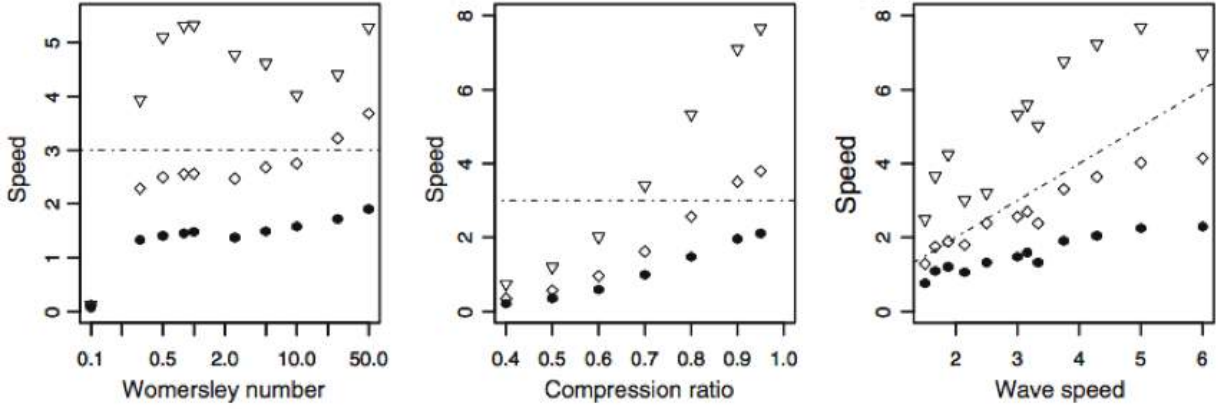


Figure 2.29: Data illustrating the non-linear behavior of these peristalsis assumptions. These figure show speed vs. a parameter in the model. The figure on the left shows a non-linear relationship between speed and Wo , where U_{avg} is given by black circles, U_{max} by white diamonds, and U_{peak} as white, inverted triangles. The middle figure shows how speed changes by varying the compression ratio (occlusion). The figure on the right shows the fluid speed against the speed of the contraction wave. The dotted line gives the speed for the constant, non-dimensional compressive wave speed. The figure was adapted from [23].

wave speed.

Moreover, Waldrop et al. 2015 found that when wave speed is decoupled from initiation frequency of the peristaltic wave, there is a clear non-linear relationship between flow speed and frequency. This is shown in Figure 2.30. This new peristalsis data is consistent with qualitative data from [65]; however [65] claims that those observations could only be consistent with dynamic suction pumping.

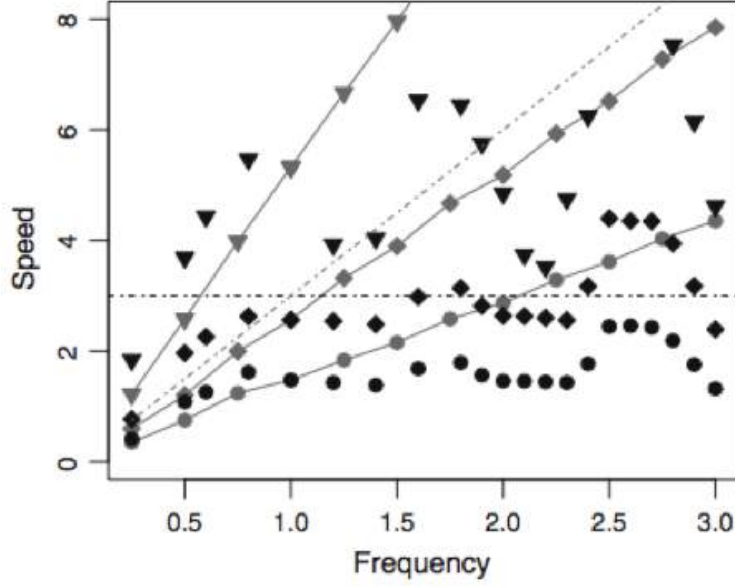


Figure 2.30: Data showing the non-linear behavior of peristalsis when wave speed is decoupled from initiation frequency of the compressive wave. In grey are when wave speed and frequency are linearly proportional; in black, when wave speed is held constant and frequency is varied. U_{avg} are circles, U_{max} are diamonds, and U_{peak} are inverted triangles. The figure was adapted from [23].

2.4.2 Cardiac Looping and Chamber Formation Models

Due to its inherent complicated dynamics, most cardiac looping phase mathematical models have been limited in their robustness. Many of the models focus their efforts on capturing very specific behavior, rather than the full developmental progression of linear heart tube to a multi-chambered valvular pumping system [24, 27, 26, 28, 25].

Ramasubramanian et al. 2008 [24] focused on the first stage of cardiac looping, *c-looping*, when the heart tube bends ventrally and twists dextrally to become c-shaped. Their model explores the mechanisms responsible for the torsional components that aid to c-looping. Furthermore Shi et. al 2014 studies differential myocardial hypertrophic growth as the main driving force for ventral bending and regional growth, cytoskeletal contraction in the primitive atria, and compressive loads exerted by the splanchnopleuric membrane to drive rightward torsion [25].

Moreover, Lee et al. 2013 [28] studied the hemodynamics in embryonic zebrafish at 20-30 hpf, 40-50 hpf, and 110-120 hpf. In each case they were interested in computing the time-averaged shear

stress and pressure gradients near the AV canal. They used *Tg(fli1a:EGFP)* transgenic zebrafish embryos to delineate and reconstruct the endocardium for model geometries and validated their flow profiles against particle image velocimetry experiments.

On the other hand Santhanakrishnan et al. 2009 [26] investigated flow within primitive heart chambers for various primitive chamber and endocardial cushion geometries. Miller 2011 [27] focused on ventricular filling in primitive chambers of the heart, for various heart membrane properties and chamber and cushion geometries. These models, although do not give the full mechanistic progression of heart tube to chamber ballooning, can be used in reflecting upon necessary developmental parameters, scales, and events for proper cardiogenesis.

Ramasubramanian et al. 2008 [24] and Shi et al. 2014 [25]. Ramasubramanian et al. 2008 [24] and Shi et al. 2014 [25] investigated the first stage of cardiac looping, called *c-looping*, where the heart tube bends ventrally and twists dextrally to become c-shaped. Their focus was to determine the mechanisms responsible for driving and regulating c-looping. Their data supports experimental evidence indicating that c-looping is driven primarily by forces exerted on the embryonic heart by the splanchnopleure (SPL) and primitive atria. Furthermore their model suggests that slight perturbations in the stress distribution of the heart can generate an adaptive feedback mechanism that restores normal looping.

Ramasubramanian et al. 2008's 2D and 3D model geometries can be seen in Figure 2.31. In (a) the model for the primitive atria is shown, with its associated cross section, while (b) illustrates the full 3D geometry for the heart tube to undergo c-looping. A ventral view as well as side view is given. The models in (a) and (b) are used to explore varying degrees of contraction of the primitive atria to exert forces which may be responsible for ventral bending when the SPL is removed. The geometry depicted in (c) is a 2D cross-sectional model for cardiac rotation. This geometry is used to study effects of SPL removal in attempting to understand the embryonic heart's ability to self-correct for small perturbations in cardiac looping. These figures were adapted from [24].

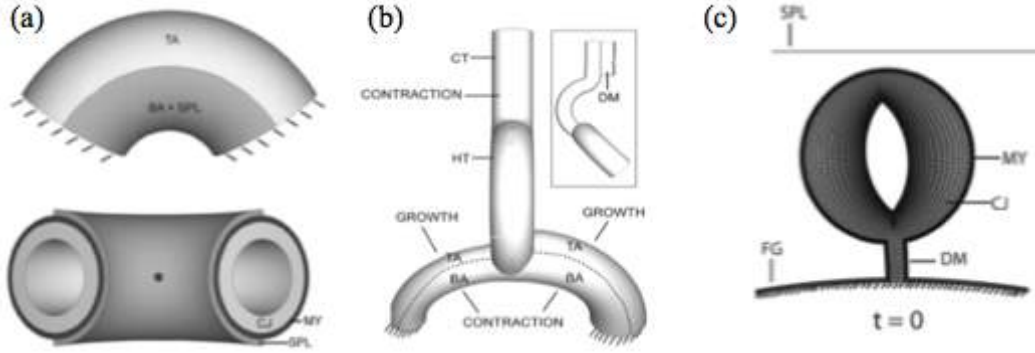


Figure 2.31: Ramasubramanian et al. 2008's 2D and 3D model geometries. In (a) the model for the primitive atria is shown, with its associated cross section, while (b) illustrates the full 3D geometry for the heart tube to undergo c-looping. A ventral view as well as side view is given. The models in (a) and (b) are used to explore varying degrees of contraction of the primitive atria to exert forces which may be responsible for ventral bending. The geometry depicted in (c) is a 2D cross-sectional model for studying cardiac rotation when perturbations may arise during cardiac looping, here the removal of the SPL. (HT = heart tube, CT= outflow tract, TA = top atrial region, BA = bottom atrial region, DM = dorsal mesocardium, FG = foregut wall, MY = myocardium, CJ = cardiac jelly, and SPL = splanchnopleure). Adapted from [24].

In all cases the geometry was used in a finite element model for cardiac looping, analyzed with the ABAQUS (version 6.4) software. The tissues in the model were taken as pseudo-elastic and are slightly compressible. Growth and cytoskeletal contraction were implemented by a subroutine called *User MATERIAL*, in which time-dependent variables were used to incorporate mechanical feedback mechanisms. However, this model, although rigorous, does not include the effects of the underlying hemodynamics in this stage of the heart morphogenesis, which may play in an important role.

Some results of various morphogenic loads for their 3D finite element model of c-looping, without the splanchnopleure, are seen in Figure 2.32, as adapted from [24]. The base geometry with before mechanical loading is shown in (a), and in (b) the effects of mechanical loading can be seen to cause the heart tube to deform and ventrally bend. This is in good agreement with experimental data exploring ventral bending. The model depicted in (c) explores asymmetric contraction between each side of the heart tube, with contraction nonexistent on the right side. [24] found that the amount of ventral bending is decreased as compared to the situation in (b). Furthermore in (d) they show the case when contraction is turned off on both sides, giving rise to even less bending than (c).

To study specific mechanical effects of SPL removal, [24] constructed a 2D model of a cross-

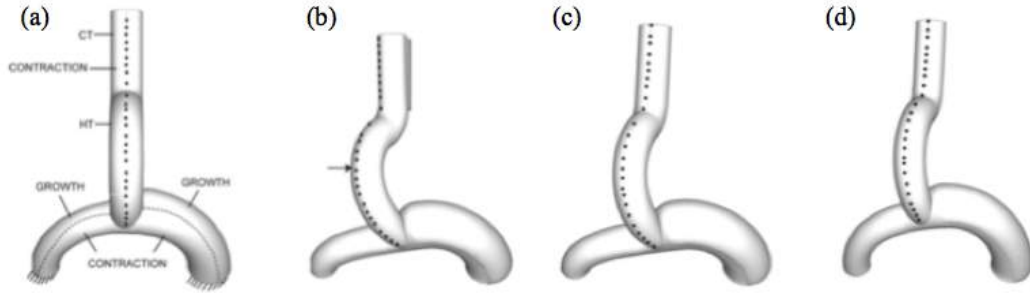


Figure 2.32: Three-dimensional finite element model for cardiac looping without the SPL. The base geometry with before mechanical loading is shown in (a), and in (b) the effects of mechanical loading can be seen to cause the heart tube to deform and ventrally bend. This is in good agreement with experimental data exploring ventral bending. The model depicted in (c) explores asymmetric contraction between each side of the heart tube, with contraction nonexistent on the right side. They found that the amount of ventral bending is decreased as compared to the situation in (b). Furthermore in (d) they show the case when contraction is turned off on both sides, giving rise to even less bending than (c). Adapted from [24].

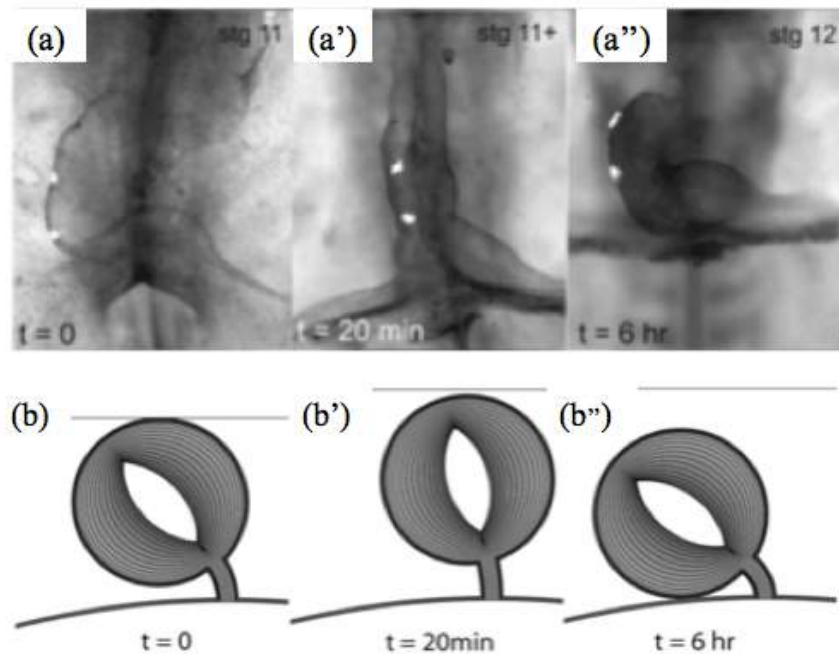


Figure 2.33: A 2D model of a cross-sectional area of the heart tube with myocardial and cardiac jelly layers fixed to the dorsal mesocardium is seen in (b),(b'), and (b''). Progressive time points within the simulation are shown, with the associated experimental data at the same time points in (a),(a'), and (a''). In (a) and (b) show the chick stage-11 heart with the SPL in contact with the myocardium. The same heart is shown in (a') and (b') but 20 minutes post-SPL removal. In each case an immediate loss of rotation can be seen. However, 6 hours later in both cases the heart shows reversal back to being fully rotated, as signaling a return to normal development. Figure adapted from [24].

sectional area of the heart tube with myocardial and cardiac jelly layers fixed to the dorsal mesocardium. Progressive time points within the simulation are shown in Figure 2.33-(b),(b'), and (b''), with the associated experimental data at the same time points in (a),(a'), and (a''), as adapted from [24]. In (a) and (b) show the chick stage-11 heart with the SPL in contact with the myocardium. The same heart is shown in (a') and (b') but 20 minutes post-SPL removal. In each case an immediate loss of rotation can be seen. However, 6 hours later in both cases the heart shows reversal back to being fully rotated, as signaling a return to normal development.

Their model seems to capture qualitatively most of the dynamics that occur to do SPL removal. However, since their model is purely a mechanical loading model without incorporating the underlying hemodynamics, it is unclear how effective this mechanism will be once one includes the relevant pulsatile blood dynamics.

Furthermore Shi et al. 2014, [25], extended the investigations of [24] by studying the effects of removing omphalomesenteric veins, OV's, as well as the heart tube using the same computational model. The omphalomesenteric veins empty into the sinus venosus.

Figure 2.34 illustrates the qualitative similarities between experiments and simulation for remove the OV's and heart tube. (A) and (B) show experimental images for when the left OV is removed immediately after removal and 12 hrs. later. Similarly (C) and (D) show analogous images, but for right OV removal, as does (E) and (F) but for when both OV are removed. (G) and (H) show images of removing the portion of the heart tube itself above the primitive atria. The black lines illustrate the cuts where each component was surgically removed. (A') and (B') illustrate the complementary simulations to the images in (A) and (B). Similarly (C') and (D') are associated simulations for (C) and (D), (E') and (F') are models of (E) and (F), and finally (G') and (H') illustrate the simulations performed for heart tube removal at similar time points of (G) and (H). In all cases the simulations model predicts the same qualitative behavior as the experiments. The figure is adapted from [25].

They also quantified rotation angles of the heart tube during c-looping in chick hearts from HH Stage 10 to 12 in both experiments and simulations, Figure 2.35, adapted from [25]. (A) illustrates

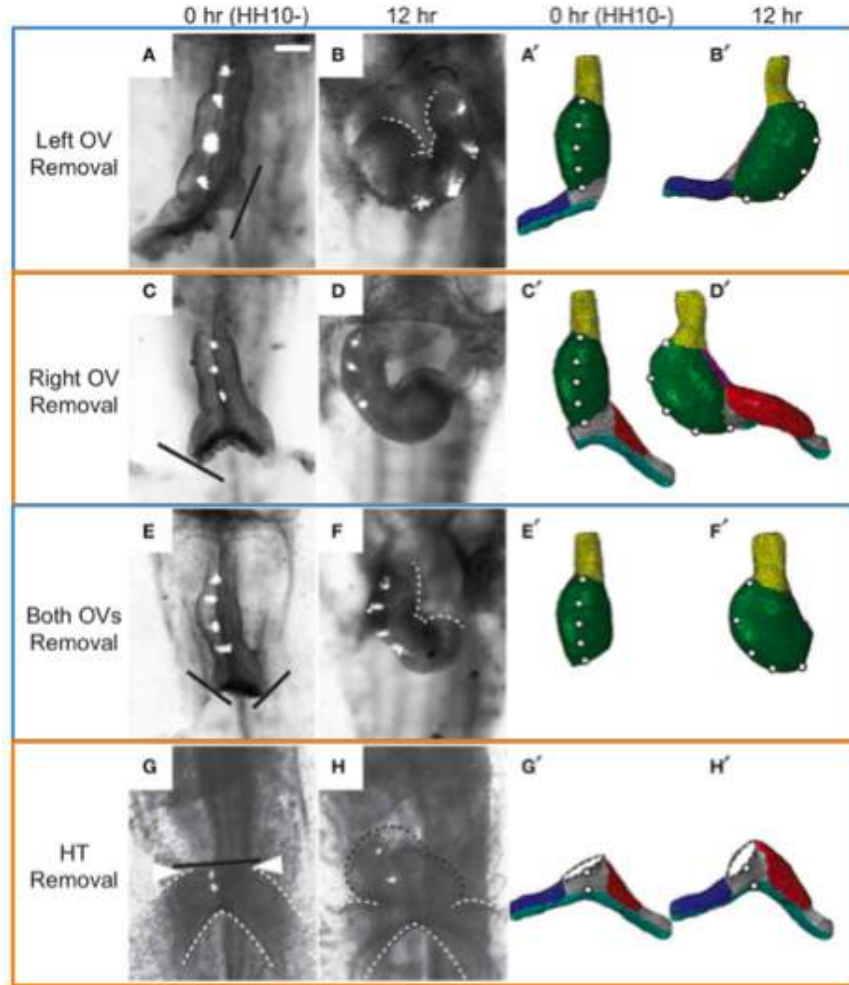


Figure 2.34: (A) and (B) show experimental images for when the left OV is removed immediately after removal and 12 hrs. later. Similarly (C) and (D) show analogous images, but for right OV removal, as does (E) and (F) but for when both OV are removed. (G) and (H) show images of removing the portion of the heart tube itself above the primitive atria. The black lines illustrate the cuts where each component was surgically removed. (A') and (B') illustrate the complementary simulations to the images in (A) and (B). Similarly (C') and (D') are associated simulations for (C) and (D), (E') and (F') are models of (E) and (F), and finally (G') and (H') illustrate the simulations performed for heart tube removal at similar time points of (G) and (H). In all cases the simulations model predicts the same qualitative behavior as the experiments. Figure adapted from [25].

how the rotation angle is defined, that is, as the angle between the the long axis of the elliptical lumen and the dorsal-ventral axis, all within a cross-section of the heart tube. The components are labeled as MY, as the myocardium, DM, as the dorsal mesocardium, and CJ, as the cardiac jelly. (B) compares the experimental rotation angle against the hearts at HH stages 10 to 12. The model supports the experimental data, and both show an increase in rotation angle as heart development progresses.

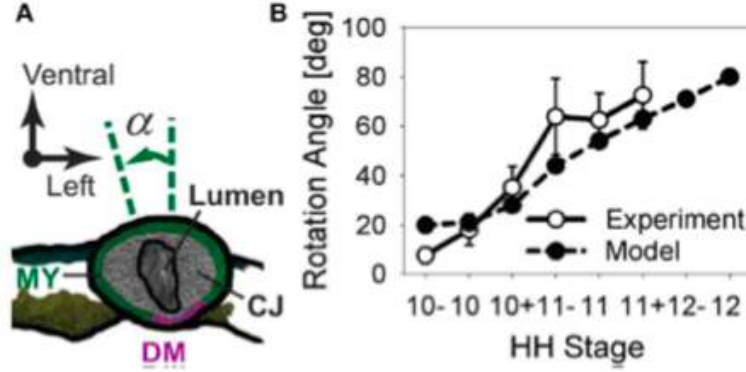


Figure 2.35: (A) illustrates how the rotation angle is defined, that is, as the angle between the the long axis of the elliptical lumen and the dorsal-ventral axis, all within a cross-section of the heart tube. The components are labeled as MY, as the myocardium, DM, as the dorsal mesocardium, and CJ, as the cardiac jelly. (B) compares the experimental rotation angle against the hearts at HH stages 10 to 12. The model supports the experimental data, and both show an increase in rotation angle as heart development progresses. Adapted from Shi et al. 2014, [25].

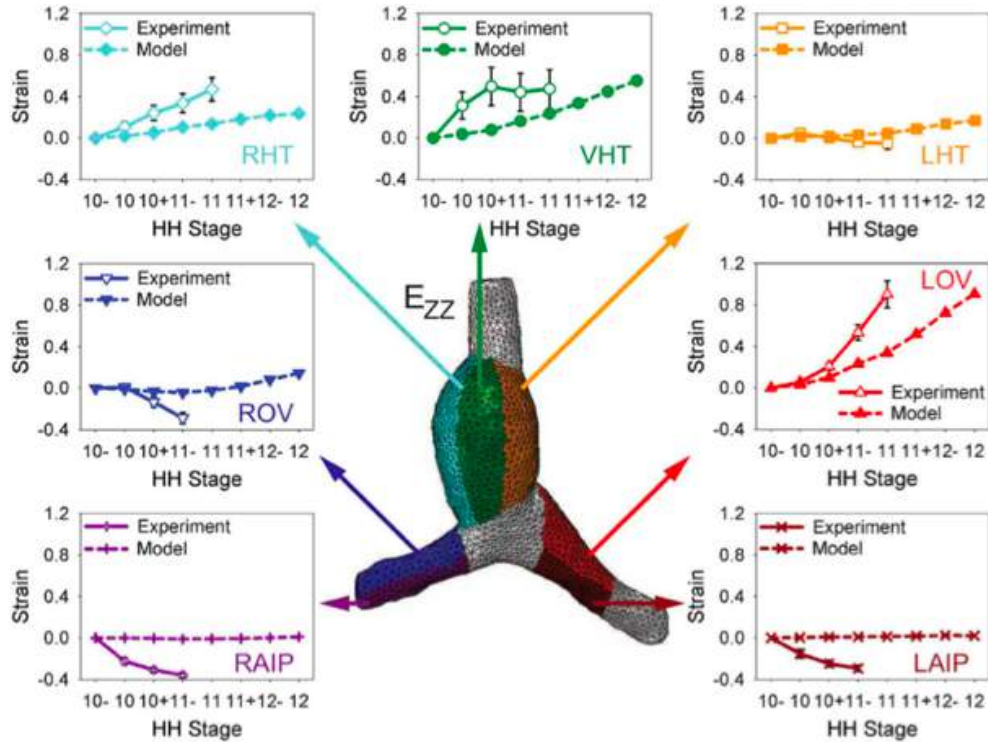


Figure 2.36: A comparison of the strain within various components of chick hearts at HH stages 10 to 12 from experimental data to the simulated model. LHT, RHT, and VHT stand for the right, left, and ventral sides of the heart tube. LOV and ROV describe the left and right omphalomesenteric veins and LAIP and RAIP are the left and right sides of the anterior intestinal portal. Figure adapted from Shi et al. 2014, [25].

Moreover, Shi et al. 2014 also compared the strain within various components of chick hearts at HH stages 10 to 12 in experiments and simulations, shown in Figure(2.36), adapted from [25]. In each case there is decent agreement between models and experiments, showing similar trends. LHT, RHT, and VHT stand for the right, left, and ventral sides of the heart tube. LOV and ROV describe the left and right omphalomesenteric veins and LAIP and RAIP are the left and right sides of the anterior intestinal portal.

Their work suggests that ventral bending and and rightward torsion are driven by differential hypertrophic growth and myocardial forces and regional growth, cytoskeletal contraction of the OVs (primitive atria), and compressive loads by the SPL respectively. They also speculate that several other mechanisms contribute to c-looping but only in secondary effects, but may play central roles when looping is perturbed [25].

Santhanakrishnan et al. 2009 [26] Santhanakrishnan et al. 2009 [26] explored flow within chambers on the embryonic heart. They performed numerical investigations and validated them with flow visualization experiments on equivalently scaled physical models. Their models included various cardiac chambers and cardiac cushions geometries and studied the flow within the chambers for Reynolds numbers ranging from 0.01 to 1000. They found that intracardial vortex formation occurred for Reynolds numbers on the order of 1-10; however, the transition to vortical flow was highly sensitive to chamber and cushion geometry.

The geometry for the physical model and mathematical model is found in Figure 2.37, adapted from [26]. The velocity, U , at the inflow is held constant during the simulations and experiments as is the channel width, d . The chamber depth, C , and cushion height, V , are varied as geometric parameters. Moreover, the Reynolds number was varied by either changing the fluid viscosity (simulation) or fluid composition (physical experiments). The mathematical model simulations were performed using the immersed boundary method using a tethered boundary formulation to keep the heart tube structure fixed in place. The physical experiments were performed using a propeller driven flow tank based on the design by Vogel and LaBarbera 1978, [135], utilizing a variable speed

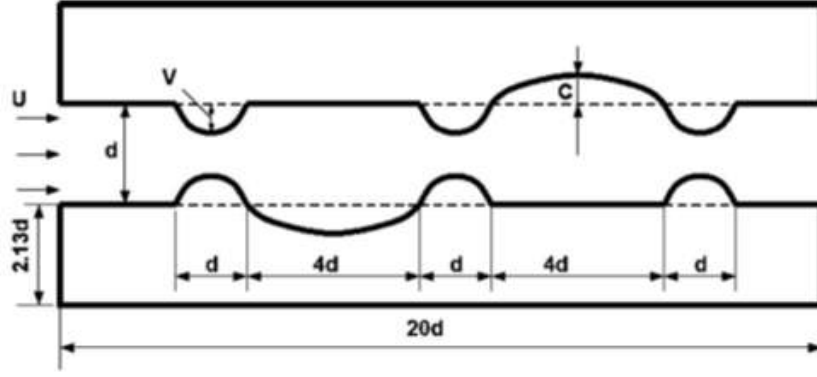


Figure 2.37: Geometry used in the mathematical model as well as physical model, adapted from [26]. The velocity, U , at the inflow is held constant during the simulations and experiments as is the channel width, d . The chamber depth, C , and cushion height, V , are varied.

pump.

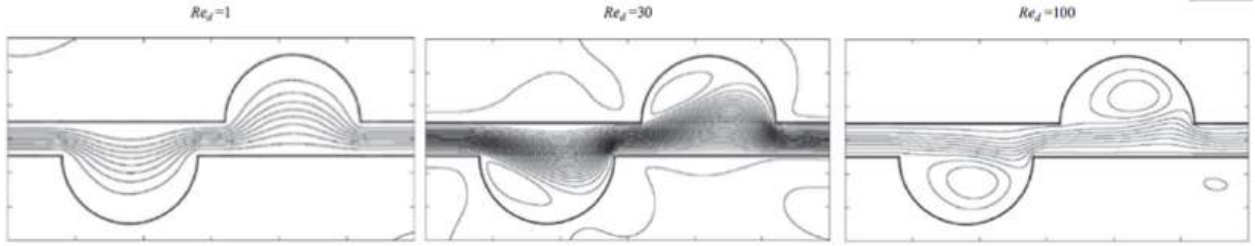


Figure 2.38: Simulations without cardiac cushions in which the Reynolds number is varied, showing that the regime for vortex formation happens around $Re \sim \mathcal{O}(10)$. Adapted from [26].

From varying the Reynolds numbers in both simulations and physical experiments, vortex formation occurred for Re between 1 and 10, depending on the chamber and cushion geometries. The embryonic heart at this stage is on the order of $\mathcal{O}(0.01 - 0.1)$. For Reynolds numbers on the order of the biological relevant case, there is no flow separation and hence no closed vortices appear. For Re above this range, a new regime occurs where flow separation is evident and vortices form. This can be seen in Figure 2.38, adapted from [26].

To validate these numerical results, the data was compared to that of the physical models. An example comparison is shown in Figure 2.39, in which a simulation and physical experiment are compared for $Re = 50$. In both cases the dynamics appear qualitatively equivalent.

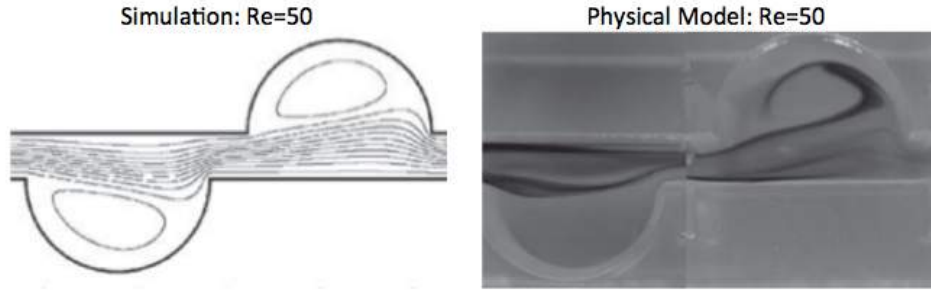


Figure 2.39: A comparison of a numerical simulation and physical model experiment for $Re = 50$. Both show the formation of a large intracardial vortex and are in qualitative agreement. Adapted from [26].

Santhanakrishnan et al. 2009 discovered that vortex formation is highly sensitive to heart morphology and Re in the model. Moreover, it implies that the morphology of the embryonic heart is important to the underlying hemodynamics, which is also thought to help regulate and drive cardiogenesis itself. These results also illustrate the importance of modeling each phase of heart development, as incremental perturbations to the geometry (growth), can have large bifurcations in the hemodynamics there within.

Miller et al. 2011 [27] Miller et al. 2011 investigated the spatial distribution of normal forces exerted on the heart's endothelial layer by the underlying hemodynamics during chamber ballooning. They studied these effects in regards to cushion formation and cardiac wall stiffness. As one may expect, the normal forces acting on the endothelial layer, increased during atrial contraction since the ventricular walls must be stretched during filling. Moreover, endocardial cushion height and heart wall stiffness both dramatically increase the force necessary to both fill and contract the ventricle.

The geometry used in [27] is very similar to the geometry from [26]; however, rather than the boundaries being fixed, they move during the simulation, allowing the atria to contract, in a prescribed fashion. The fluid then fills the ventricle, which is composed of a flexible membrane. The ventricle contracts due to elastic deformation forces wanting to return it to its equilibrium state. The immersed boundary method is employed to solve the full fluid-structure interaction equations, via a tethered target-point and virtual spring force implementation. In their study, they varied the

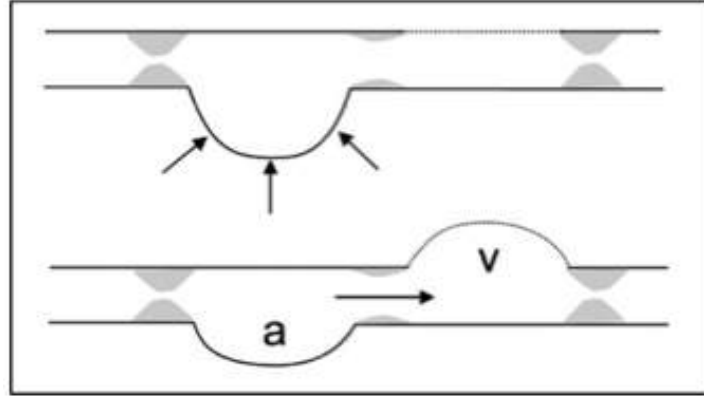


Figure 2.40: Model geometry, where the atrial wall moves in a prescribed manner, allowing the ventricle to fill, via its wall being flexible, and then ventricular contract occurs due to the elastic deformations of its wall wanting to return to its equilibrium rest state. Adapted from Miller et al. 2011 [27].

wall stiffnesses via changing the stiffness parameters as well as the cushion heights.

Parameter sweeps were performed for a constant stiffness and varying endocardial cushion heights, as well as the other case for, a constant cardiac cushion height but varying ventricular wall stiffnesses. These results can be seen in Figure 2.41, which is adapted from [27]. When varying the cushion height, they discover that the maximum normal force acting on the heart wall increases more than fivefold for an increase of cushion height from 0 to $15\mu m$. This is illustrated in (A) and (B). On the other hand, when holding the cushion height constant, at $15\mu m$, and varying the wall stiffness, they find that the force required to fill the ventricle also increases. Figure adapted from [27].

This work further illustrates the importance of modeling each phase of heart development to gain insight into the biological mechanisms within cardiogenesis. Furthermore, it shows that it is imperative to model these stages of heart morphogenesis using a moving boundary approach to be able to adequately capture critical dynamics.

Lee et al. 2013 [28] Lee et al. 2013 investigated the time-varying and spatial varying wall shear stress in the AV canal of embryonic zebrafish hearts. They found through a combination of computational modeling and PIV validation that both intracardial velocities and heart rates increase

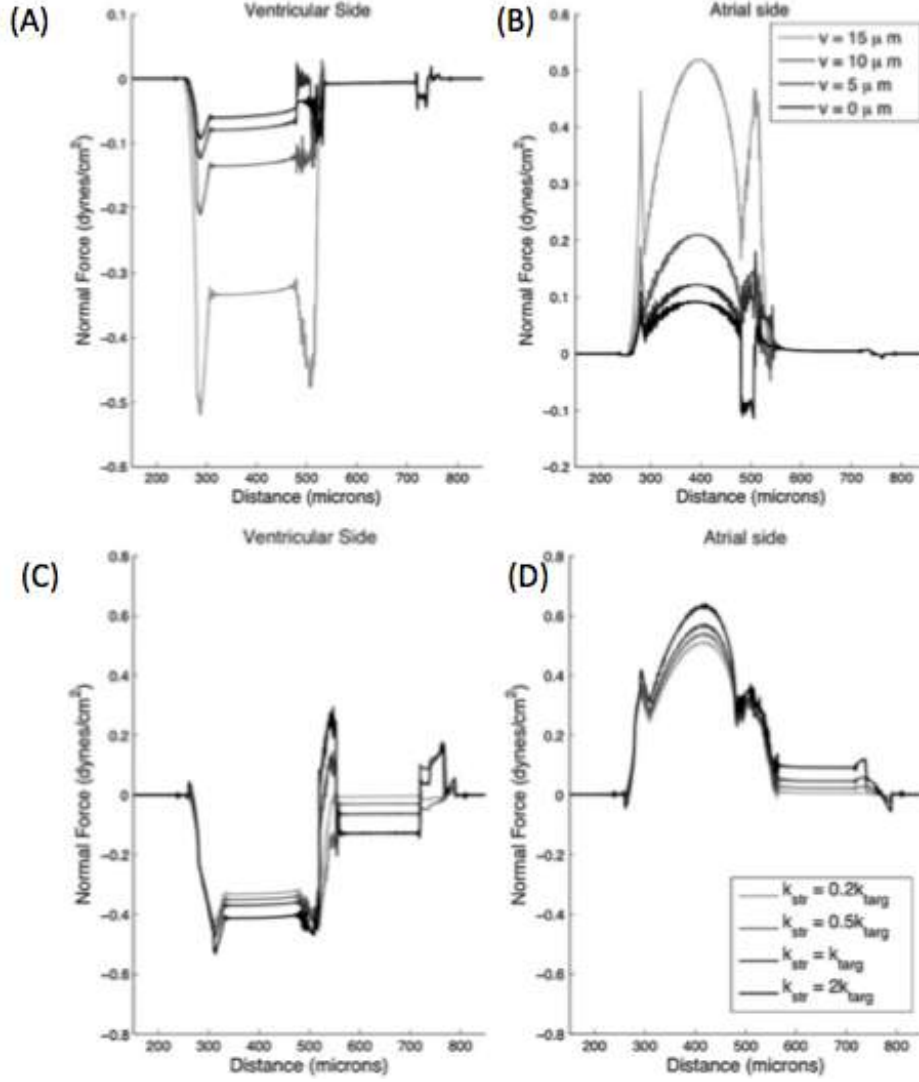


Figure 2.41: Data from parameter sweeps on the endocardial cushion heights, (A) and (B), and varying ventricular wall stiffness, (C) and (D). In (A) and (B), varying the cushion height from 0 to $15\mu\text{m}$ increases the normal force acting on the chamber walls more than fivefold. In (C) and (D) varying the ventricle wall stiffness also increases the force necessary for ventricular filling. Adapted from Miller et al. 2011, [27].

as morphogenesis progresses, as well that atrial systole decreases in duration from earlier to later stages of development. Furthermore their simulations predict an increase in wall shear stress (WSS) and pressure gradients across the AV canal for later stages in development, with a complementary decrease in bidirectional flow due to the maturation of the cardiac valvular system [28].

Tg(fli1a:EGFP) embryos were used to obtain biologically relevant endocardium geometries in the computational mode and perform *in vivo* PIV experiment, in concert with green fluorescent protein

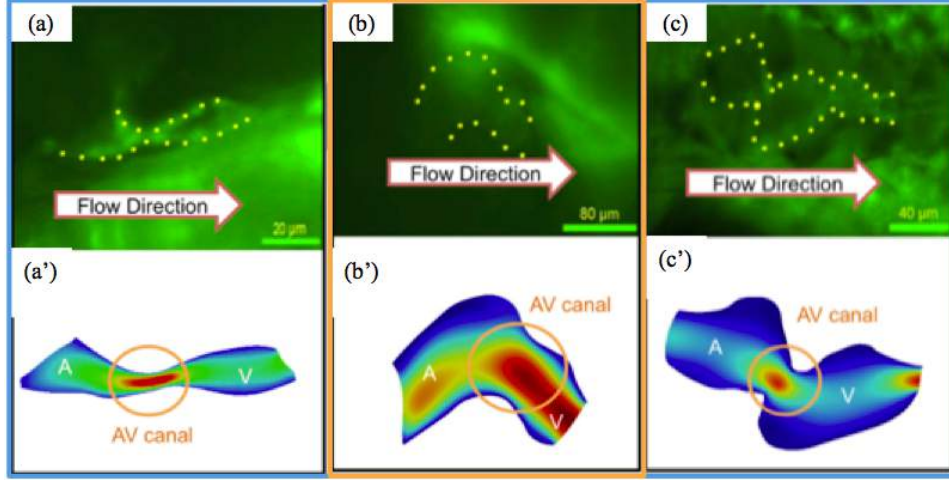


Figure 2.42: *Tg(fli1a:EGFP)* embryos were used to obtain biologically relevant endocardium geometries in the computational mode and perform *in vivo* PIV experiment, in concert with green fluorescent protein (GFP). This can be seen in Figure(2.42)-(a),(b), and (c), where (a) shows the tubular embryonic heart between 20-30 hpf, (b) illustrates the heart structure between 40-50 hpf, and (c) shows the distinct two chamber geometry around 110-120 hpf. The corresponding model geometries can be found in (a'), (b'), and (c') respectively. A denotes the atria and V stands for the ventricle. Adapted from [28].

(GFP). This can be seen in Figure(2.42)-(a),(b), and (c), where (a) shows the tubular embryonic heart between 20-30 hpf, (b) illustrates the heart structure between 40-50 hpf, and (c) shows the distinct two chamber geometry around 110-120 hpf. The corresponding model geometries can be found in (a'), (b'), and (c') respectively. A denotes the atria and V stands for the ventricle. This figure is adapted from [28]. Note that each simulation image depicts the magnitude of velocity after atrial contraction; however, the scale bars in each simulation are different.

The simulations were performed using an in house code developed at UCLA, using a 2D finite element model for the heart walls, assuming a Newtonian incompressible fluid there-within, in a Lagrangian-Eulerian framework. The wall motions were prescribed, using data collected from Lagrangian tracked images of experimental data. To validate their simulations, PIV experiments were performed in each stage, focusing on averaged flow velocities in the AV canal during atrial contraction.

A comparison between experimental PIV data and the computational model is seen in Figure 2.43-(c). In (c) time averaged flow velocities across a cross section of the AV canal were corroborated for 30 hpf, 70 hpf, and 120 hpf embryonic zebrafish hearts. There is decent agreement between

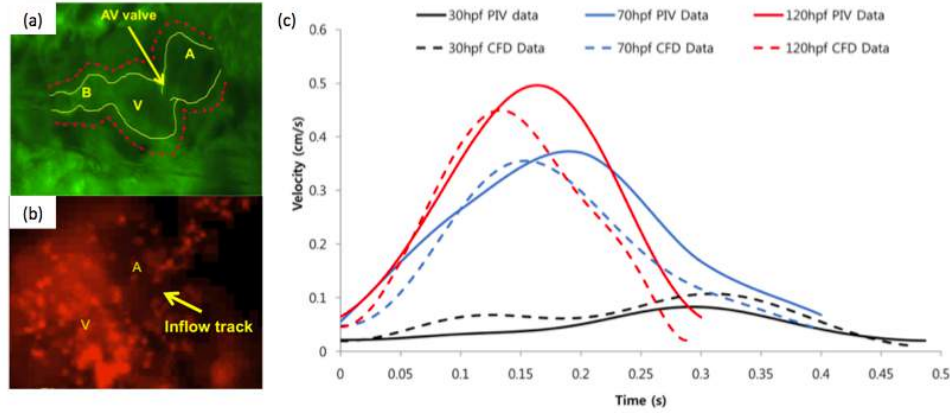


Figure 2.43: (a) illustrates the use of transgenic *Tg(fli1a:EGFP)y1* embryos for a clear visual delineation of the endocardial layer for constructed the computational model and (b) shows the use of *Tg(gata1:dsRedsd2)* transgenic zebrafish to visualize hematocrit for accurate PIV and particle tracking. A denotes the atrium, V, the ventricle, and B, the bulbus arteriosus. In (c), a comparison between time averaged flow velocities through a cross section of the AV canal is shown between experimental PIV data and the computationally modeled data. Images and data taken from [28].

modeled and experimental data. (a) illustrates the use of transgenic *Tg(fli1a:EGFP)y1* embryos for a clear visual delineation of the endocardial layer for constructed the computational model and (b) shows the use of *Tg(gata1:dsRedsd2)* transgenic zebrafish to visualize hematocrit for accurate PIV and particle tracking. A denotes the atrium, V, the ventricle, and B, the bulbus arteriosus. Figure adapted from Lee et al. 2013, [28].

Figure 2.44 gives a plot of the endocardial shear stress within the AV canal are shown for zebrafish hearts between 20-30 hpf, 40-50 hpf, and 110-120 hpf in (a),(b), and (c) respectively, over the course of one heart beat. In each case there are two peaks, one illustrating the time of maximum atrial contraction and other for the period of maximum ventricular contraction. As the heart progresses, the shear stress increases in the AV canal, with a fivefold increase between 20-30 hpf and 40-50 hpf, and another threefold increase between 40-50 hpf and 110-120 hpf. This results are better quantified in (d), which shows the averaged predicted shear stress at each stage of development in the AV canal. (e) illustrates the averaged pressure gradients within the AV canal for varying phases of heart morphogenesis, as predicted by the computational model. Figures adapted from [28].

The 2D moving domain computational fluid dynamics model implemented by Lee et al. 2013 pro-

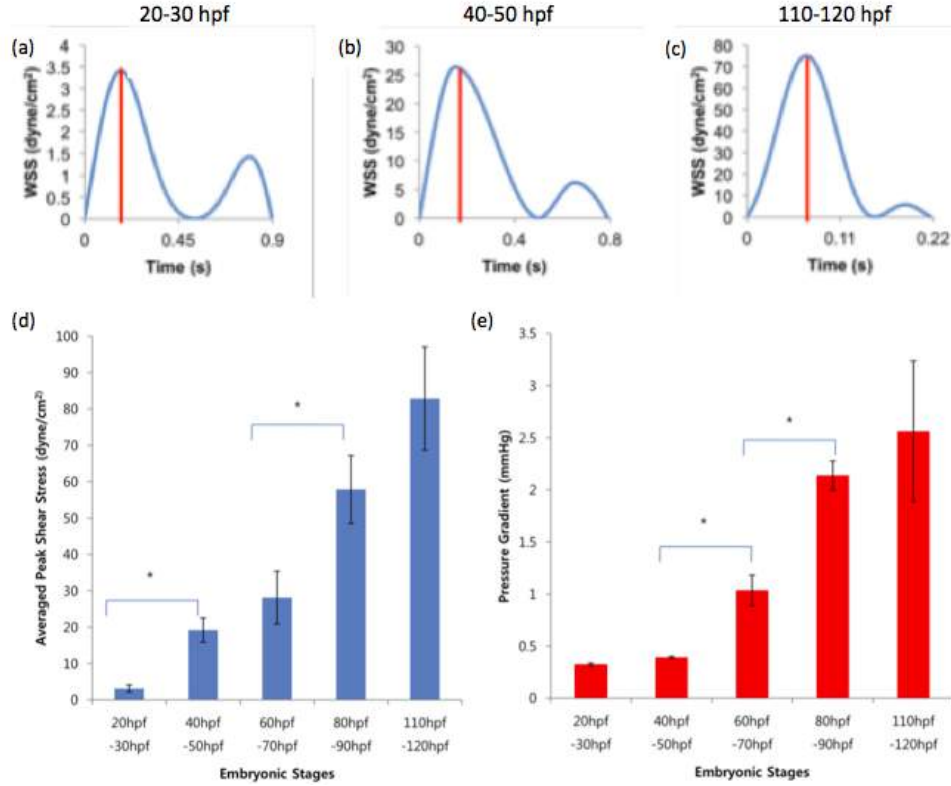


Figure 2.44: (a),(b), and (c) show the wall shear stress within the AV canal for zebrafish hearts between 20-30 hpf, 40-50 hpf, and 110-120 hpf over the course of one heart beat, as predicted by the computational model. (d) gives the averaged predicted shear stress at each stage of development in the AV canal. (e) illustrates the averaged pressure gradients within the AV canal for varying phases of heart morphogenesis, given by the computational model. Figures adapted from [28].

vides an insightful link between hemodynamics and cardiac morphogenesis in various phases of heart development. The accuracy of the model geometry reflecting the biological morphology is limited only by the clarity and resolution of the imaging techniques used in parallel with transgenic zebrafish embryos. However, their model does not capture trabeculation morphologies within the developing ventricle that are hypothesized to have an important role in regulating the intracardial hemodynamics.

2.4.3 Cardiac Valve Development

Since valvular defects are the most common cardiac defects, quantifying the mechanisms of valve development is crucial to understanding how to possibly treat such disorders [29]. Hence there have been various mathematical models to study cardiac valve development, namely effects of endocardial cushions on the underlying hemodynamics and vice versa [29], and even transformation from cushions to a more leaflet morphology [30]. When endocardial cushions beginning forming

in the AV canal, the underlying hemodynamics exert shear stresses and pressure on the primitive cushions, that contribute to remodeling the mounds into valve leaflets.

Biechler et al. 2010 [29] Biechler et al. 2010 [29] devised a tubular geometry with a cushion-like projection to study the shear stresses exerted on the endocardial cushions for a developing chick heart. Upon doing so, they uncovered flow patterns and resulting forces, shear stresses and pressure, have comparable orders of magnitude, and in unison may produce a vortical flow that aids in cushion-to-leaflet transformation.

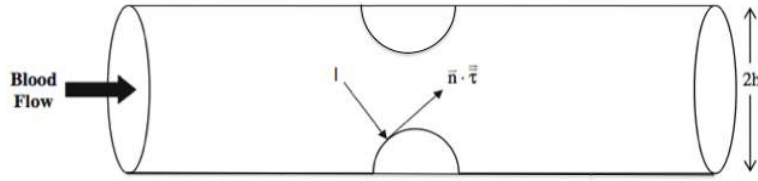


Figure 2.45: The tubular geometry used to study valve leaflet formation can be seen in Figure 2.45, adapted from [29]. Although shown in 3D, the model investigated was a 2D construction, where hemodynamic forces will act both tangentially (shear stress) and normal (pressure) to the endocardial cushions.

The tubular geometry used to study valve leaflet formation can be seen in Figure(2.45), adapted from [29]. Although shown in 3D, the model investigated was a 2D construction, where hemodynamic forces will act both tangentially (shear stress) and normal (pressure) to the endocardial cushions. The model equations describing the 2D incompressible Newtonian steady-state flow through the geometry were solved in COMSOL Multiphysics 3.4 [134].

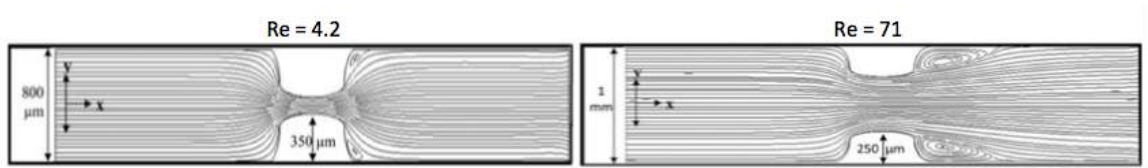


Figure 2.46: The steady-state flow profiles, illustrated via streamline analysis, are shown for $Re = 4.2$, (a), and $Re = 71.0$, (b). It is seen that the size of eddies is sensitive to Re , where smaller eddies are observed in the smaller Re case, (a), while larger vortices form after the flow passes the cushions in (b), corresponding to a higher Re . Figure adapted from [29].

The steady-state flow profiles, illustrated via streamline analysis, can be found in Figure 2.46, adapted from [29]. Two simulations are shown, one for $Re = 4.2$, (a), and $Re = 71.0$, (b). It is seen that the size of eddies is sensitive to Re , where smaller eddies are observed in the smaller Re case, (a), while larger vortices form after the flow passes the cushions in (b), corresponding to a higher Re .

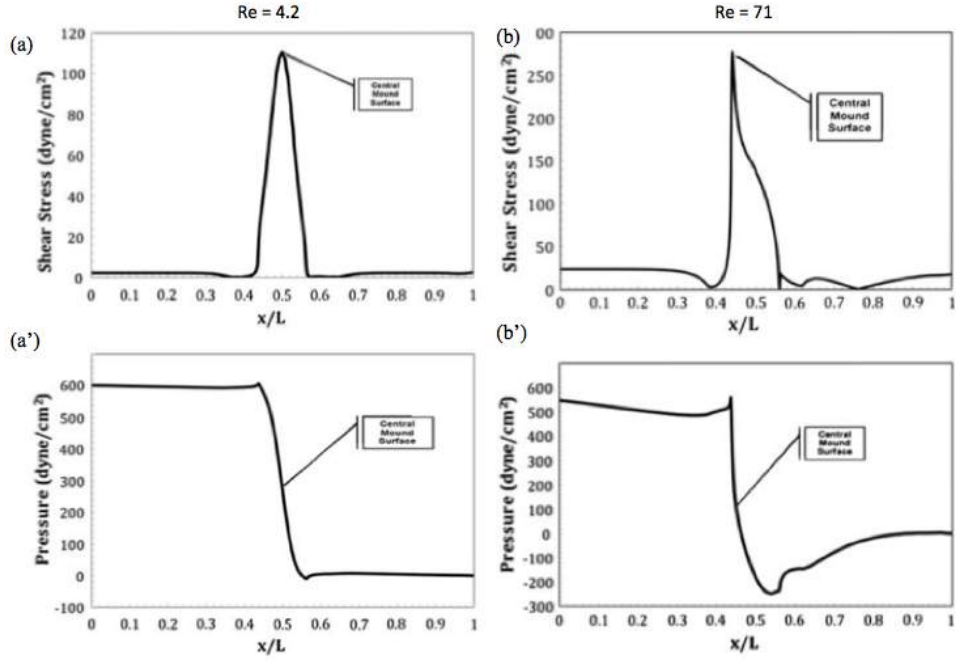


Figure 2.47: Shear stress and pressure profiles corresponding to simulations for $Re = 4.2$, (a), and $Re = 71.0$, (b). It is clear that in the higher Re case, (b), the cushions undergo more shear stress than in the lower Re case. However, in both cases the pressure exerted on the cushions remains relatively static. Furthermore, the maximum shear is located at the center of the cushion. Adapted from Biechler et al. 2010, [29].

For each simulation shear stress and pressure were computed over the cushions. Some results are found in Figure 2.47, corresponding to $Re = 4.2$, (a), and $Re = 71.0$, (b). It is clear that in the higher Re case, (b), the cushions undergo more shear stress than in the lower Re case. However, in both cases the pressure exerted on the cushions remains relatively static. Furthermore, the maximum shear is located at the center of the cushion. Adapted from Biechler et al. 2010, [29].

Unfortunately the paper does not discuss, which simulations are biologically relevant, or why downstream vortex formation would influence and be critical for progression from endocardial cushions to valve leaflets. However, a better understanding of shear stress and pressure distributions

on the cushions can help formulate better hypothesis about such progression.

Buskohl et al. 2012 [30] Buskohl et al. 2012 [30] modeled the progression from endocardial cushions to valve leaflets via exerting hemodynamic forces on the cushions integrated with evolution equations that regulate the growth and remodeling aspects in the model. They discovered that the pressure distribution on the AV cushion was sufficient to induce cushion-elongation in the direction of flow to remodel the cushions to leaflets. Moreover, they found that shearing minimally altered tissue volume, but assisting in remodeling of the tissue near the endothelial surface.

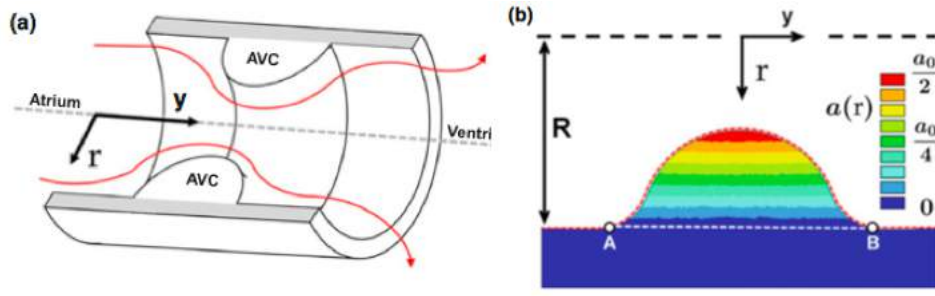


Figure 2.48: In (a), a cross-section of the AV canal geometry is shown, with endocardial cushions protruding into the canal. The flow is specified going left to right, i.e., from the atrium to ventricle. (b) illustrates the colormap of the modeled growth rate parameter, $a(r)$ in a 2D cushion cross-section. Figure adapted from [30].

The computational model geometry is found in Figure 2.48, adapted from [30]. In (a), a cross-section of the AV canal geometry is shown, with endocardial cushions protruding into the canal. The flow is specified going left to right, i.e., from the atrium to ventricle. (b) illustrates the colormap of the modeled growth rate parameter, $a(r)$ in a 2D cushion cross-section.

The simulations were performed by an iterative approach that attempts to decouple the hemodynamics forces with growth and remodeling in a solid finite element model. First the pressure and velocity profiles were updated from the pure fluids problem. The induced shear stress and pressure forces were then transferred to the solid finite element model to simulate the appropriate elastic and inelastic deformations. After a user-specified time of inelastic deformation, the fluid mesh was updated, and the fluid model was again simulated in the revised AV geometry, and all steps repeated.

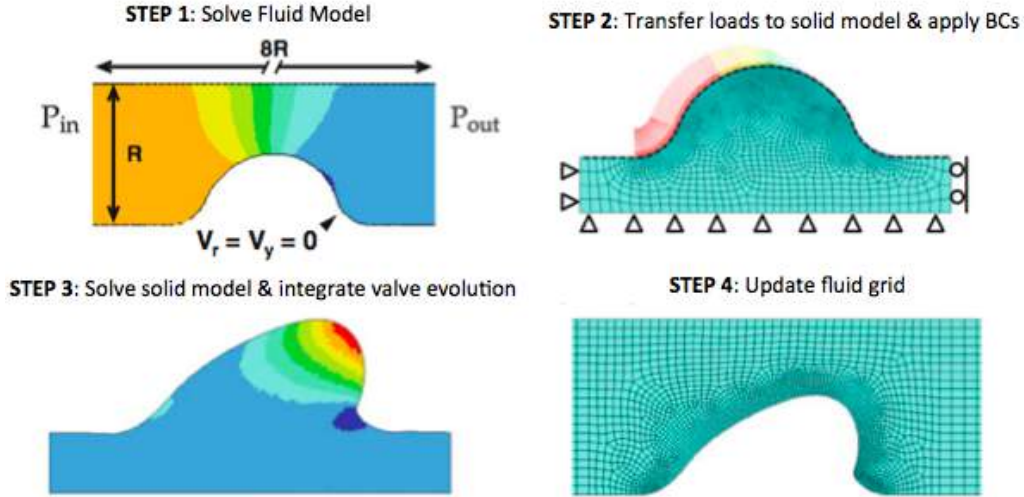


Figure 2.49: Figure illustrating the iterative approach in decoupling the fluid component from the solid mechanics portion of the fluid-solid-mechanics model. In step 1, the fluid model is solved and then in step 2 the hemodynamic forces, shear and pressure, are transferred to the solid mechanics finite element model. In step 3, the solid model equations are solved and hence the valve deforms. Finally in step 4, the fluid mesh is updated, and all preceding steps are repeated. Adapted from [30].

These ideas are depicted in Figure 2.49, taken from [30].

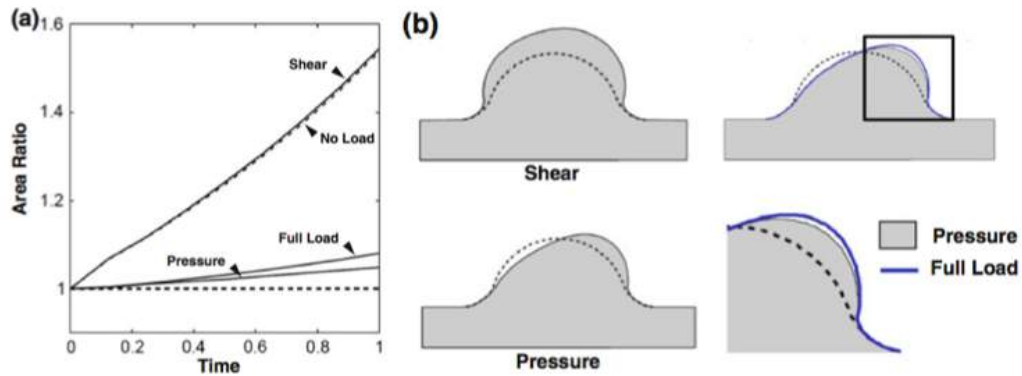


Figure 2.50: In (a) a plot of the area ratio vs. simulation time is shown. There are four cases illustrated- shear only, pressure only, no external loads, and full external loads (both pressure and shear). It is clear that for the area ratio, there is good agreement between pressure and the full external load cases, while the shear only case and no external load case are also consistent. In (b), deformations from each configuration (shear only, pressure only, and full external loading) are shown. It is evident that the cushion begins to elongate under these hemodynamic forces in the direction of flow. Figure adapted from [30].

From the fluid-solid model, it was seen that pressure modulates volume deformations, while shearing regulates remodeling. In Figure 2.50-(a), a plot of the area ratio vs. simulation time is shown. There are four cases illustrated- shear only, pressure only, no external loads, and full external

loads (both pressure and shear). It is clear that for the area ratio, there is good agreement between pressure and the full external load cases, while the shear only case and no external load case are also consistent. In (b), deformations from each configuration (shear only, pressure only, and full external loading) are shown. It is evident that the cushion begins to elongate under these hemodynamic forces in the direction of flow. Figure adapted from [30].

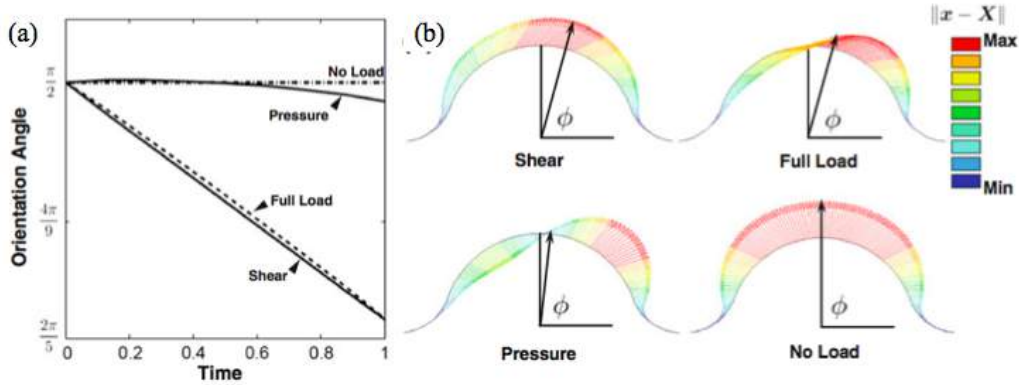


Figure 2.51: In (a) there is good qualitative agreement between the shear only and full external load cases, while there is agreement between the pressure and no external load cases, showing that shearing has a greater effect on migration of the top center point. (b) further illustrates that orientation angle has greater dependence on shear than pressure from simulation images. These figures are adapted from [30].

On the other hand, the orientation angles of the top center point of the cushion is coordinated by the shear stress, rather than the pressure forces. This is clear from Figure 2.51-(a). There is good qualitative agreement between the shear only and full external load cases, while there is agreement between the pressure and no external load cases, showing that shearing has a greater effect on migration of the top center point. (b) further illustrates that orientation angle has greater dependence on shear than pressure from simulation images. These figures are adapted from [30].

Buskohl et al. 2012's data strongly suggests that pressure is responsible for cushion growth and remodeling, while shearing may play a significant role in surface remodeling on the cushions. Moreover, their model also predicted that mechanical aspects of valvulogenesis may be self-propagating, since the newly transformed elongated cushion shape only promoted further elongation to a leaflet morphology. In the AV canal, these hemodynamic forces may be the key regulators in the progression

of endocardial cushions to leaflets; however, they may not be the only components in modeling the remodeling and growth in other valves of the heart [30].

CHAPTER 3

Mathematical Methods

We're not going to use magic?

- Ron Weasley (HP and the Order of the Phoenix)

In this chapter, we will introduce the fundamental equations of fluid dynamics, namely the *Navier-Stokes* equations, their non-dimensionalization, dimensionless numbers of interest that are used to quantify different biological scales, vorticity and streamlines, and our fiber model's material properties, e.g., elasticity and/or rigidity, equations.

Furthermore due to the complicated nonlinear form of the Navier-Stokes equations, and inherent difficulty attached to coupling elastic interactions, we must use numerical methods to solve our model system. In the remainder of this chapter we will discuss the numerical scheme we employ to solve the fully coupled fluid-structure interaction, *the immersed boundary method*.

3.1 Conservation of mass, momentum, and the Navier-Stokes equations - oh my!

In this section we will introduce and derive the governing equations of fluid dynamics, the Navier-Stokes equations, via conservation of momentum and mass. We will do this in two different ways. First, we will derive the Navier-Stokes equations using an intuitive approach. We will begin by motivating the different forces, e.g., force densities, that may act on a parcel of fluid, and upon doing so will lead us to the governing equations. Secondly, we will use derive the equations by considering the conservation of mass and momentum for a continuum and then directly apply the transport theorem. We will also briefly address conservation of angular momentum.

3.1.1 Intuitive derivation of the Navier-Stokes Equations

In this subsection we will introduce the basic idea of a fluid and derive the governing equations of fluid dynamics using an intuitive approach. As we will see, the Navier-Stokes equations include an equation giving the conservation of momentum of the fluid and an equation giving the conservation of mass of a fluid.

Intuitive derivation momentum equation The story of the motion of fluids has no clear place beginning. We first begin with the initial goal of defining what we mean by a fluid. As compared to solids, a fluid cannot maintain its shape under any amount of shear stress for any amount of time. That is to say, forces parallel to the surface of the fluid will affect its overall shape and behavior. The way to think about a fluid is as a continuum of particles, whether they are gas particles, liquid particles, or even plasma elements. One then tries to understand the overall flow of the continuum rather than the single trajectories of any one particle. If you have had the pleasure of being well-versed in electromagnetism, you could think of a fluid like a current, in that you do not study a current with discrete moving charges but rather as a whole.

Therefore asking oneself, what it means to have a single quantity of fluid is a vague and esoterically silly question. Instead we begin quantifying fluid dynamics with the next closest idea, a single cubic blob, or parcel, of fluid. We first wish to describe the forces that can act upon this fluid blob. To simplify this even more, let's assume the fluid is *incompressible*. This allows us to believe that this fluid parcel has a constant material density. The incompressible condition states that

$$\nabla \cdot \mathbf{v} = 0, \tag{3.1}$$

where \mathbf{v} is the velocity of the fluid. The mass of the fluid blob is the density of the fluid, ρ , multiplied by the volume of the blob, δV . Hence the mass is $\rho(\delta V)$.

The next natural question to ask is what forces are acting, or can act, on the fluid blob? On each face of the blob, the most primitive forces would be a normal force onto the fluid parcel, i.e., pressure, and a force tangent to the face due to the *viscosity* of the fluid, i.e., shear. Both pressure

and shear stress are “internal fluid forces”, in which exist due to the nature of continuum mechanics. For example, even if the fluid is at rest, e.g., the fluid velocity is zero everywhere, these forces still exist and must be used to compute the equilibrium state the system is in.

Moreover, there are external forces that can act of the fluid. These forces may come from a background physical field, e.g., electromagnetic forces or gravity, or may be due to moving immersed structures, whether elastic or inelastic, in which can exert a force onto the fluid. We note that the latter is the case we consider for our biological fluid-structure interaction models. Furthermore, in our considerations, the immersed structure is deformable under the presence of fluid forces, via non-zero fluid velocities, and these elastic deformations cause the structure to want to return to a lower energy state, and hence the structure exerts a force back onto the fluid.

Naturally, since we have we have multiple forces acting on the fluid parcel, and because we are not at the subatomic physical regime nor are we assuming our fluids will be traveling near relativistic velocities, we can use the familiar form of conversation of momentum, i.e., Newton’s 2nd Law, to quantify our system,

$$(\rho\delta V) \frac{D\mathbf{v}}{Dt} = \sum_i \mathbf{F}_i = \mathbf{F}_{pressure} + \mathbf{F}_{shear} + \mathbf{F}_{ext} \quad (3.2)$$

The only unfamiliar character in (3.2) is writing the acceleration operator as $\frac{D}{Dt}$ rather than the traditional $\frac{d}{dt}$. Typo? Nope! This is one of the very subtle, but fundamental points in fluid mechanics. We found the acceleration for this fluid blob at one particular point in time, *not* the entire fluid itself! We have no way of knowing what the acceleration of the fluid is anywhere else besides at this particular point in time. Luckily we can easily remedy this.

Note that if the velocity of the blob is $v(x, y, z, t)$, the velocity of the same blob at a time Δt later will be $v(x + \Delta x, y + \Delta y, z + \Delta z, t + \Delta t)$, where

$$\Delta x = v_x \Delta t, \quad \Delta y = v_y \Delta t, \quad \Delta z = v_z \Delta t.$$

Hence to first order we get the following approximation,

$$v(x + \Delta x, y + \Delta y, z + \Delta z, t + \Delta t) = v(x, y, z, t) + \frac{\partial \mathbf{v}}{\partial x} v_x \Delta t + \frac{\partial \mathbf{v}}{\partial y} v_y \Delta t + \frac{\partial \mathbf{v}}{\partial z} v_z \Delta t + \frac{\partial \mathbf{v}}{\partial t} \Delta t.$$

Therefore from the above we find the acceleration to be

$$\frac{D\mathbf{v}}{Dt} = \frac{\Delta\mathbf{v}}{\Delta t} = \frac{v(x + \Delta x, y + \Delta y, z + \Delta z, t + \Delta t) - v(x, y, z, t)}{\Delta t} = \frac{\partial\mathbf{v}}{\partial x}v_x + \frac{\partial\mathbf{v}}{\partial y}v_y + \frac{\partial\mathbf{v}}{\partial z}v_z + \frac{\partial\mathbf{v}}{\partial t}.$$

Because this is exactly the definition of partial derivative from elementary Calculus, pushing this into a more sophisticated mathematical language we find that

$$\frac{D\mathbf{v}}{Dt} = (\mathbf{v} \cdot \nabla)\mathbf{v} + \frac{\partial\mathbf{v}}{\partial t}. \quad (3.3)$$

Traditionally the operator $\frac{D}{Dt}$ is called the *material derivative*. The material derivative in our case describes the evolution of a particular fluid blob that moves along a certain trajectory, as it flows alongside the rest of the fluid. To describe the overall velocity field of the fluid, we need (3.3) to connect the evolution of our particular fluid blob to the overall evolution of the entire fluid.

Therefore we can finally put together a skeletal version of the Navier-Stokes equations,

$$(\rho\delta V) \left[\frac{\partial\mathbf{v}}{\partial t} + (\mathbf{v} \cdot \nabla)\mathbf{v} \right] = \sum_i \mathbf{F}_i = \mathbf{F}_{pressure} + \mathbf{F}_{shear} + \mathbf{F}_{ext} \quad (3.4)$$

As a quick aside, it is interesting to note that the fluid may experience an acceleration even under constant velocity. We consider the case when $\frac{\partial\mathbf{v}}{\partial t} = 0$. Hence the only term left from the material derivative is $(\mathbf{v} \cdot \nabla)\mathbf{v}$. It is not obvious how this term describes the acceleration of fluid, but imagine what would be one of the fascinating flows to witness- water flowing in a circle with constant velocity. Even though the velocity at a given point in the flow is constant, the velocity of a particular blob in the flow points in a different direction any short time later. This of course can be summarized in introductory physics as centripetal acceleration.

We will now motivate the derivation of each of these forces in (3.4).

Normal Forces: Pressure

First we consider a force normal to the fluid parcel's body. Recall that pressure $P = \frac{force}{area}$, i.e., to get the normal force, one will need to multiply the pressure by the area considered. Now consider the pressure on the left wall of the blob at x . We find it to be $pdydz$. The pressure on the face

at an infinitesimal distance Δx further we get $-\left(p + \frac{\partial p}{\partial x} dx\right) dydz$. Hence the net pressure in the x direction is:

$$p_{netx} = p dydz - \left(p + \frac{\partial p}{\partial x} dx\right) dydz = -\frac{\partial p}{\partial x} dydz.$$

Hence looking at the pressure on the remaining faces of the cube lead us to get that the force due to pressure per unit volume is $-\nabla p$, or the pressure force itself is $-(\delta V)\nabla p$. This idea is illustrated in Figure(3.1).

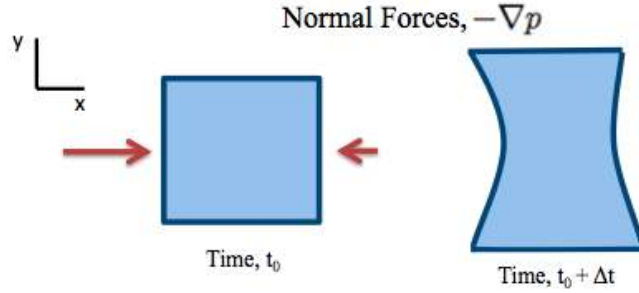


Figure 3.1: Pressure gradients acting on a fluid parcel.

Therefore plugging this term into the conversation of momentum, e.g., (3.4), we obtain

$$(\rho \delta V) \left[\frac{\partial \mathbf{v}}{\partial t} + (\mathbf{v} \cdot \nabla) \mathbf{v} \right] = -(\delta V) \nabla p + \mathbf{F}_{shear} + \mathbf{F}_{ext} \quad (3.5)$$

Tangential Forces: Shear-Stress

To understand tangential forces on the fluid parcel, it is imperative to that get a clear idea of what viscosity is, and moreover, what shear-stress is. As a child, have you ever played a game with someone tries to push you over, but the catch is that you are only allowed to stand still and pray your feet and the ground bonded to form some kind of stable alliance? If your friend (or foe) has any common sense, they will try to push you over somewhere around the head, since that will create the more torque and instability then if they tried to push you over by the knee. Unfortunately, any push by them is going to slightly perturb your stand-still behavior, but we shall only consider a force induced at the very top of our head.

In a very crude nutshell, this is the idea of a shear-stress. The viscosity of a fluid can be thought to be the resistance of the fluid to perturb its original state due to this applied tangential force. The analogy makes more sense when we consider what has been discovered experimentally of fluids against a boundary. At the boundary of a flow, like a wall, it's been seen that the fluid velocity on the boundary is zero. So if you think of a single fluid blob "standing" against the boundary, the very bottom of the fluid blob has velocity zero. However, this does not mean that the top of the fluid blob has zero velocity. The top of the fluid blob will have some velocity due to the deformations induced by the shear stresses acting on the top of the blob. The blob will look as though it is being stretched in the direction of the shearing. This is illustrated in Figure(3.2).

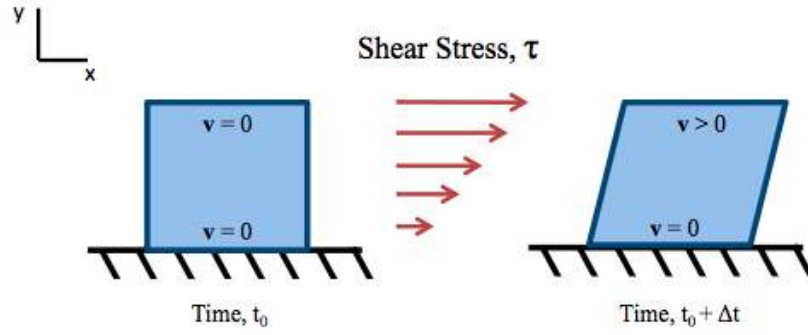


Figure 3.2: Shear-stress acting on fluid parcel near a boundary.

If we try to quantify the shear-stress on the fluid blob in the above picture, we note that shear-stress is defined as a force per unit area. Say the fluid blob in the above diagram has a density of ρ , the shear-stress, τ , is

$$\tau = \rho\nu \frac{\partial v_x}{\partial y}, \quad (3.6)$$

where $\frac{\partial v_x}{\partial y}$ describes the change in the x component of velocity with respect to the coordinate y and ν is a parameter called the *kinematic viscosity*. We now note that if the blob was not against the boundary but in the middle of the flow, the blob would still experience shear-stress, and if the flow is not unidirectional, there will be shear-stresses in the y direction as well. In 2 dimensions, the shear-stress on a fluid blob is

$$\tau_{xy} = \rho\nu \left(\frac{\partial v_x}{\partial y} + \frac{\partial v_y}{\partial x} \right). \quad (3.7)$$

Note in 3 dimensions, the quantitative definition of shear-stress follows analogously.

This shear-stress term gives rise to the tangential force term in the conversation of momentum

equation. We can write this force as,

$$\mathbf{F}_{\text{tangential}} = \mathbf{F}_{\text{shear}} = \left(\frac{\partial \tau_{ij}}{\partial x_j} \right) (\rho \delta V) = \frac{\partial}{\partial x_j} \left[\rho \nu \left(\frac{\partial v_i}{\partial x_j} + \frac{\partial v_j}{\partial x_i} \right) \right] (\delta V), \quad (3.8)$$

for $i, j = \{x, y, z\}$.

We can mathematically massage the force term due to the shear-stress to get a more compact form because we assume the fluid is incompressible. Note that the incompressibility condition gives

$$\frac{\partial u_x}{\partial x} + \frac{\partial u_y}{\partial y} + \frac{\partial u_z}{\partial z} = 0.$$

Using this fact we see that

$$\frac{\partial}{\partial x_j} \left[\left(\frac{\partial v_i}{\partial x_j} + \frac{\partial v_j}{\partial x_i} \right) \right] = \left[\frac{\partial^2 u_x}{\partial y^2} + \frac{\partial^2 u_x}{\partial z^2} \right] \hat{i} + \left[\frac{\partial^2 u_y}{\partial x^2} + \frac{\partial^2 u_y}{\partial z^2} \right] \hat{j} + \left[\frac{\partial^2 u_z}{\partial x^2} + \frac{\partial^2 u_z}{\partial y^2} \right] \hat{k}.$$

Hence we get that

$$\left(\frac{\partial \tau_{ij}}{\partial x_j} \right) = \nabla^2 \mathbf{v} = \Delta \mathbf{v}.$$

Therefore our statement about the conversation of momentum of a fluid is now,

$$(\rho \delta V) \left[\frac{\partial \mathbf{v}}{\partial t} + (\mathbf{v} \cdot \nabla) \mathbf{v} \right] = -\nabla p (\delta V) + \mu (\delta V) \Delta \mathbf{v} + \mathbf{F}_{\text{ext}}, \quad (3.9)$$

where $\mu = \frac{\nu}{\rho}$ and is called the *dynamic viscosity*. The differences between *kinematic* and *dynamic* are subtle, but important. Dynamic viscosity describes the tangential force per unit area *required* to move one plane with respect to another tangential plane at a unit velocity while maintaining a unit distance apart in the fluid. On the other hand, kinematic viscosity is the ratio of dynamic viscosity to the fluid density, ρ , and no force is involved.

External Forces:

There can be different kinds of external forces being applied to the fluid. We will break these external forces down into two types, forces induced by conservative fields and fluid-structure interaction forces.

Now suppose there are external body forces acting on the cubic blob through a background field, e.g., electromagnetic or gravitational forces. These forces can be spatially dependent forces. Regardless of these forces's identity, we will define their potential per unit mass that generalizes their contributions, and call it ϕ . (Here we assuming under the rug that these forces are conservative). From field theory we note that from a potential field, we can define a force as $F = -\nabla\phi$.

Furthermore we can also have forces arising from fluid-structure interaction terms, e.g., a deformed elastic structure immersed in a fluid that wishes to return to it's lower energy state. We will call these forces \mathbf{F}_{body} for now.

Therefore the from Newton's 2nd Law, we find that force on the parcel is

$$(\rho\delta V) \frac{D\mathbf{v}}{Dt} = -(\delta V)\nabla p + \mu(\delta V)\Delta\mathbf{v} - (\rho\delta V)\nabla\phi + (\rho\delta V)\mathbf{F}_{body}, \quad (3.10)$$

Dividing by the volume of the parcel, δV , and spatially- and time-dependent density, ρ , we get that the acceleration on the cubic blob will be

$$\frac{D\mathbf{v}}{Dt} = \frac{\partial\mathbf{v}}{\partial t} + (\mathbf{v} \cdot \nabla)\mathbf{v} = -\frac{1}{\rho}\nabla p + \nu\Delta\mathbf{v} - \nabla\phi + \mathbf{f}_{body}. \quad (3.11)$$

We will discuss the fluid-structure interaction terms when we introduce the immersed boundary method in Section()

Conservation of Mass Beyond conversation of momentum, physical systems also need to conserve mass. This can be summarized by the simple analogy of water flowing through a hose.

Now since you're a human, you've probably dreamt about being a fireman at some point in your life, if not, you know how much fun it is to spray stuff with a hose. Imagine if you take a hose, turn it on and decide to spray your driveway with it. You begin to think about the conservation of mass because, hey you're a scientist after-all. You know generally this type of conservation of mass can be summed up as, "what goes out, must come in." Hence the fluid coming out of the end of the hose can be written as

$$\int_S (\rho\mathbf{v}) \cdot d\mathbf{A} = \int_V (\nabla \cdot (\rho\mathbf{v})) d\Omega,$$

using the Divergence Theorem. We then note that this flow of the fluid can cause a change in density, so we have,

$$\frac{\partial}{\partial t} \int_V \rho \, d\Omega = \int_V \frac{\partial \rho}{\partial t} \, d\Omega.$$

Hence putting these together, we find the continuity equation for mass in fluid dynamics can be written as,

$$\int_V \left[\nabla \cdot (\rho \mathbf{v}) \right] \, d\Omega = - \int_V \frac{\partial \rho}{\partial t} \, d\Omega,$$

or more explicitly as

$$\frac{\partial \rho}{\partial t} + \nabla \cdot (\rho \mathbf{v}) = 0, \quad (3.12)$$

or

$$\frac{\partial \rho}{\partial t} + \rho \nabla \cdot \mathbf{v} + \mathbf{v} \cdot \nabla \rho = 0. \quad (3.13)$$

We note that since we have focused our discussion incompressible fluids, we assume the fluid is incompressible, that is, the density of a fluid parcel is constant that moves with the flow velocity. Hence our statement about the conservation of mass in fluids becomes

$$\nabla \cdot \mathbf{v} = 0. \quad (3.14)$$

3.1.2 Navier-Stokes Equations

From our derivations above, we found the governing equations of fluid dynamics given in (3.11) and (3.13). For the remainder of our studies we will consider only the *incompressible* Navier-Stokes equations and external forces arising only from interactions with an immersed boundary, e.g., $\phi = 0$. Hence the version of the Navier-Stokes equations we concern ourselves with are

$$\frac{\partial \mathbf{v}}{\partial t} + (\mathbf{v} \cdot \nabla) \mathbf{v} = -\frac{1}{\rho} \nabla p + \nu \Delta \mathbf{v} + \mathbf{f}_{body} \quad (3.15)$$

$$\nabla \cdot \mathbf{v} = 0. \quad (3.16)$$

3.1.3 Vorticity Formulation

Recall our statement of the conservation of momentum for a fluid (3.13),

$$\frac{D\mathbf{v}}{Dt} = \frac{\partial\mathbf{v}}{\partial t} + (\mathbf{v} \cdot \nabla)\mathbf{v} = -\frac{1}{\rho}\nabla p + \nu\Delta\mathbf{v} - \nabla\phi + \mathbf{f}_{body}.$$

Without loss of generality, suppose that there are no external forces acting on the fluid, i.e., $\mathbf{f}_{body} = 0$ and $\nabla\phi = 0$. We recall the following identity from vector calculus,

$$(\mathbf{F} \cdot \nabla)\mathbf{F} = (\nabla \times \mathbf{F}) \times \mathbf{F} + \frac{1}{2}\nabla(\mathbf{F} \cdot \mathbf{F}).$$

Substituting the above identity into the conservation of momentum equation gives us,

$$\frac{\partial\mathbf{v}}{\partial t} + (\nabla \times \mathbf{v}) \times \mathbf{v} + \frac{1}{2}\nabla(\mathbf{v} \cdot \mathbf{v}) = -\frac{1}{\rho}\nabla p + \nu\Delta\mathbf{v}. \quad (3.17)$$

We define a new quantity called the vorticity,

$$\omega = \nabla \times \mathbf{v}. \quad (3.18)$$

It is tempting to think that ω describes the global rotation of the fluid, but this is misleading. Although many flows can be characterized by local regions of intense rotation, such as smoke rings, whirlpools, tornadoes, or even the red spot on jupiter, some flows have no global rotation, but do have vorticity. Vorticity describes the *local* spinning of a fluid near a fixed point, as seen by an observer in the Eulerian framework. Examples of velocity field, where there is and is not vorticity are illustrated in Figure(3.3).

The three examples in Figure(3.3) include rigid body-like rotation (ϖr), parallel shear flow, and irrotational vortical flow ($\varpi \alpha \frac{1}{r}$). Row 2 of the table shows the *global* velocity field in each case, while row 3 depicts the *absolute* velocities around a fluid parcel at specific locations, specified by the red dot, in the velocity field. Row 4 shows the *local relative* velocities around the same fluid blobs. In the cases of rigid body-like rotation and parallel shear flow there is nonzero vorticity, while in the case of irrotational vortical, there is no vorticity.

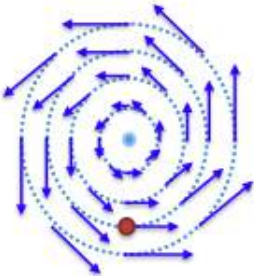
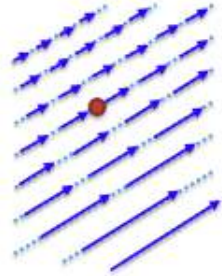
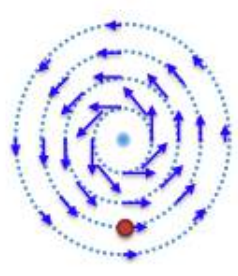


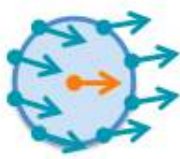
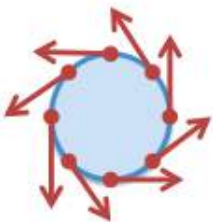
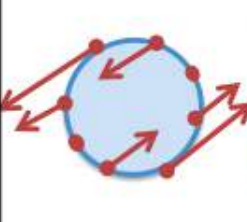
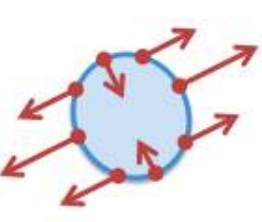
Example Fluid Flows	Rigid Body-like Rotation ($v \propto r$)	Parallel Shear Flow	Irrotational Vortex ($v \propto 1/r$)
Corresponding Velocity Fields			
Absolute velocities about highlighted point			
Relative velocities (magnified) about highlighted point			
Vorticity?	$\omega \neq 0$	$\omega \neq 0$	$\omega = 0$

Figure 3.3: Cartoon depictions for the vorticity of fluid parcels. Vorticity is a measure of the *local* rotation of a fluid blob, not of the global continuum, as illustrated in these examples. The three examples include rigid body-like rotation ($v \propto r$), parallel shear flow, and irrotational vortical flow ($v \propto 1/r$). Row 2 of the table shows the *global* velocity field in each case, while row 3 depicts the *absolute* velocities around a fluid parcel at specific locations, specified by the red dot, in the velocity field. Row 4 shows the *local relative* velocities around the same fluid blobs. In the cases of rigid body-like rotation and parallel shear flow there is nonzero vorticity, while in the case of irrotational vortical, there is no vorticity.

Substituting the definition of vorticity into (3.17), we obtain

$$\frac{\partial \mathbf{v}}{\partial t} + \omega \times \mathbf{v} + \frac{1}{2} \nabla(v^2) = -\frac{1}{\rho} \nabla p + \nu \Delta \mathbf{v}.$$

Now taking the curl of the above equation we get an equation for the evolution of the vorticity,

$$\frac{\partial \omega}{\partial t} + \nabla \times (\omega \times \mathbf{v}) = \nu \Delta \omega, \quad (3.19)$$

since $\nabla \times (\Delta \mathbf{v}) = \Delta(\nabla \times \mathbf{v}) = \Delta \omega$.

Furthermore we note that the pressure terms drop out because the force from pressure acts perpendicular to the surface of the fluid blobs and not parallel to it, i.e., $\nabla \times (\nabla \psi) = 0$ for any vector field ψ

We also note that in the case, where shear-stress and all external forces are absent, that **if** $\omega = 0$ everywhere at any particular point in time, then $\omega = 0$ for any time in the future. Hence we would call the fluid *irrotational* in this case, having $\omega = \nabla \times \mathbf{v} = 0$.

3.1.4 Mathematical derivation of the Navier-Stokes Equations

In this subsection we will introduce the governing equations of fluid dynamics using a more mathematical approach. We will begin with the statement and proof of the transport theorem. Next for each equation, momentum and mass, we will start with a statement of conservation of momentum or mass of a continuum, and apply the transport theorem. As we will see, the Navier-Stokes equations include an equation stating the conservation of momentum of the fluid and an equation giving the conservation of mass of a fluid.

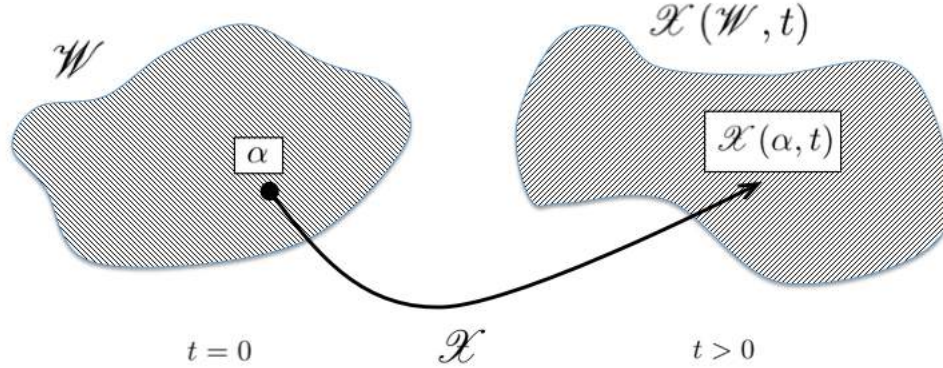


Figure 3.4: Initial domain, \mathcal{W} , at $t = 0$ being mapped by \mathcal{X} into $\mathcal{X}(\mathcal{W}, t)$ at $t > 0$

Transport Theorem Consider a continuum, e.g., a domain of fluid, \mathcal{W} . This domain at time $t = 0$ is shown in Figure 3.4. Overtime this domain is thought to change shape, but not topology. Consider a particle trajectory from α to a point later in time, $\mathcal{X}(\alpha, t)$ for $t > 0$. Hence we consider the change of shape as the continuous map, \mathcal{X} , i.e., $\mathcal{W} \rightarrow \mathcal{X}(\mathcal{W}, t)$. Writing out the particle trajectory explicitly, we have

$$\begin{cases} \frac{d\mathcal{X}}{dt} = \mathbf{v}(\mathcal{X}(\alpha, t), t) \\ \mathcal{X}(\alpha, 0) = \alpha. \end{cases} \quad (3.20)$$

The map \mathbf{v} we consider to be the velocity of the changing continuum, e.g., the fluid velocity. We will now introduce the Transport Theorem.

Theorem 1. *The **Transport Theorem** states that for any function of \mathbf{x} and t , we have*

$$\frac{d}{dt} \int_{W_t} f(\mathbf{x}, t) dV = \int_{W_t} \left(\frac{\partial f}{\partial t} \right) dV - \oint_{\partial W_t} (\mathbf{v} \cdot \hat{n}) f(\mathbf{x}, t) dA = \int_{W_t} \left(\frac{\partial f}{\partial t} + \nabla \cdot (\mathbf{v} f) \right) dV$$

Note that the above theorem is a higher dimensional case of differentiating under an integral sign, i.e., the *Leibniz integral rule*. If $f(\mathbf{x}, t) = f(x, t)$ and $W_t = [a(t), b(t)]$, then the following is true

$$\frac{d}{dt} \int_{a(t)}^{b(t)} f(x, t) dx = f(b(t), t) b'(t) - f(a(t), t) a'(t) + \int_{a(t)}^{b(t)} \frac{\partial}{\partial t} f(x, t) dx,$$

and can be proved using the Fundamental Theorem of Calculus. We will now prove the result for the Transport Theorem.

Proof. To begin this proof, we consider a material volume, $W(t)$, which contains moving fluid blobs. The volume is then bounded by its surface, $\partial W(t)$. We first consider the volume integration of a quantity ϕ , e.g.,

$$\int_{W(t)} \phi(\mathbf{x}, t) dV,$$

and consider that quantity sometime later, at $t + dt$,

$$\int_{W(t+dt)} \phi(\mathbf{x}, t + dt) dV.$$

Using Taylor Series, we see that this can be written as

$$\int_{W(t+dt)} \phi(\mathbf{x}, t + dt) dV = \int_{W(t+dt)} \left[\phi(\mathbf{x}, t) + \frac{\partial \phi}{\partial t} dt + \mathcal{O}(dt^2) \right] dV. \quad (3.21)$$

Note however that as $W(t)$ changes the shape, the surface $\partial W(t)$ will also change. The Volume

change in $W(t)$ corresponds the surface element

$$\text{surface element due to changing volume} = \phi \mathbf{v} \cdot \hat{n} dS dt,$$

where \mathbf{v} is the underlying velocity vector field and \hat{n} is the normal vector to the surface. The volume change's influence of quantity ϕ from $W(t)$ to $W(t + dt)$ can then be decomposed into

$$\int_{W(t+dt)} \phi(\mathbf{x}, t + dt) dV = \int_{W(t)} \phi(\mathbf{x}, t + dt) dV + \int_{\partial W(t)} \phi(\mathbf{x}, t + dt) \mathbf{v} \cdot \hat{n} dV dt.$$

Using (3.21) we have

$$\begin{aligned} \int_{W(t+dt)} \phi(\mathbf{x}, t + dt) dV &= \int_{W(t)} \left[\phi(\mathbf{x}, t) + \frac{\partial \phi}{\partial t} dt + \mathcal{O}(dt^2) \right] dV + \\ &\quad \int_{\partial W(t)} \left[\phi(\mathbf{x}, t) + \frac{\partial \phi}{\partial t} dt + \mathcal{O}(dt^2) \right] \mathbf{v} \cdot \hat{n} dV dt \end{aligned} \quad (3.22)$$

$$\begin{aligned} &= \int_{W(t)} \phi(\mathbf{x}, t) dV + \left[\int_{W(t)} \frac{\partial \phi}{\partial t} dV + \int_{\partial W(t)} \phi(\mathbf{v}, t) (\mathbf{v} \cdot \hat{n}) dS \right] dt + \mathcal{O}(dt^2). \end{aligned} \quad (3.23)$$

Rearranging the terms in (3.23), we obtain

$$\int_{W(t+dt)} \phi(\mathbf{x}, t + dt) dV - \int_{W(t)} \phi(\mathbf{x}, t) dV = \left[\int_{W(t)} \frac{\partial \phi}{\partial t} dV + \int_{\partial W(t)} \phi(\mathbf{v}, t) (\mathbf{v} \cdot \hat{n}) dS \right] dt + \mathcal{O}(dt^2). \quad (3.24)$$

Next by imploring the divergence theorem on the surface integral and dividing by the infinitesimal dt , we get

$$\frac{\int_{W(t+dt)} \phi(\mathbf{x}, t + dt) dV - \int_{W(t)} \phi(\mathbf{x}, t) dV}{dt} = \int_{W(t)} \left[\frac{\partial \phi}{\partial t} + \nabla \cdot (\mathbf{v} \phi) \right] dV + \mathcal{O}(dt). \quad (3.25)$$

Finally taking the limit as $dt \rightarrow 0$, we obtain the desired result

$$\frac{d}{dt} \int_{W(t)} \phi(\mathbf{x}, t) dV = \int_{W(t)} \left[\frac{\partial \phi}{\partial t} + \nabla \cdot (\mathbf{v} \phi) \right] dV. \quad (3.26)$$

□

We will now use Theorem 1 to derive the governing equations of fluid dynamics.

Mathematical formulation of mass equation For a control volume, we can find its mass by integrating the density over such a volume, i.e.,

$$\text{mass} = \int_{\mathcal{X}(W,t)} \rho(\mathbf{x}, t) d\mathbf{x}.$$

From conservation of mass, it is understood that mass is neither created nor destroyed, hence we have

$$\frac{d}{dt}(\text{mass}) = \frac{d}{dt} \int_{\mathcal{X}(W,t)} \rho(\mathbf{x}, t) d\mathbf{x} = 0.$$

We can now apply the Transport Theorem to obtain

$$\frac{d}{dt} \int_{\mathcal{X}(W,t)} \rho(\mathbf{x}, t) d\mathbf{x} = \int_{\mathcal{X}(W,t)} \left[\frac{\partial \rho}{\partial t} + \nabla \cdot (\mathbf{v} \rho) \right] d\mathbf{x} = 0.$$

Note the following property. For all open sets Ω , if $\int_{\Omega} g(\mathbf{x}) d\mathbf{x} = 0$, then $g(\mathbf{x}) = 0$.

Using the above property, this implies that

$$\frac{\partial \rho}{\partial t} + \nabla \cdot (\mathbf{v} \rho) = 0. \quad (3.27)$$

(3.27) is the general statement of the conservation of mass for a fluid. No assumptions have been made about the fluid at this junction, e.g., we have not said if it is incompressible, viscoelastic, etc. However, for our modeling, we will only consider an incompressible fluid, that is, we are assuming the fluid density is constant. This gives us:

$$\frac{\partial \rho}{\partial t} + \rho \nabla \cdot \mathbf{v} + \mathbf{v} \cdot \nabla \rho = \rho \nabla \cdot \mathbf{v} = 0,$$

since $\frac{\partial \rho}{\partial t} = 0$ and $\nabla \rho = 0$. Hence we have that

$$\nabla \cdot \mathbf{v} = 0. \quad (3.28)$$

(3.28) is the incompressibility condition. We note that this implies the fluid velocity is divergence-free. That is, there are no sources or sinks within the continuum.

Mathematical formulation of momentum equation Here we will perform the same steps as we did to find the incompressibility condition. First we compute the momentum in our control volume,

$$\text{momentum in control volume} = \int_{\mathcal{X}(W,t)} \rho \mathbf{v}(\mathbf{x}, t) d\mathbf{x}.$$

Next we will essentially take the time derivative of the above statement; however, conservation of momentum dictates the rate of change of momentum is balanced by the forces acting on the control volume and not nullity. Hence we have the following statement

$$\frac{d}{dt} \int_{\mathcal{X}(W,t)} \rho \mathbf{v}(\mathbf{x}, t) d\mathbf{x} = \int_{\partial \mathcal{X}(W,t)} \text{"forces (stresses) acting on the surface of control volume"} dS.$$

If we define σ to be a stress tensor, where each component has the units of a force per unit area, we can rewrite the above as

$$\frac{d}{dt} \int_{\mathcal{X}(W,t)} \rho \mathbf{v}(\mathbf{x}, t) d\mathbf{x} = \int_{\partial \mathcal{X}(W,t)} \sigma \cdot \hat{n} dS.$$

Application of the divergence theorem, gives

$$\frac{d}{dt} \int_{\mathcal{X}(W,t)} \rho \mathbf{v}(\mathbf{x}, t) d\mathbf{x} = \int_{\mathcal{X}(W,t)} (\nabla \cdot \sigma) d\mathbf{x}.$$

We will discuss the stress tensor, σ , in a moment. Now we apply the Transport Theorem onto the LHS of the above equation to get

$$\frac{d}{dt} \int_{\mathcal{X}(W,t)} \rho \mathbf{v}(\mathbf{x}, t) d\mathbf{x} = \int_{\mathcal{X}(W,t)} \rho \left[\frac{\partial \mathbf{v}}{\partial t} + \mathbf{v} \cdot \nabla \mathbf{v} \right] d\mathbf{x}.$$

To see this we will consider the i^{th} component and apply the Transport Theorem.

Proof.

$$\begin{aligned}
\left[\frac{d}{dt} \int_{\mathcal{X}(W,t)} \rho \mathbf{v}(\mathbf{x}, t) d\mathbf{x} \right]_i &= \int_{\mathcal{X}(W,t)} \left[\frac{\partial}{\partial t} (\rho u_i) + \nabla \cdot (\mathbf{v} \rho u_i) \right] d\mathbf{x} \\
&= \int_{\mathcal{X}(W,t)} \left[u_i \frac{\partial \rho}{\partial t} + \rho \frac{\partial u_i}{\partial t} + u_i \nabla \cdot (\rho \mathbf{u}) + \rho \mathbf{u} \cdot \nabla u_i \right] d\mathbf{x} \\
&= \int_{\mathcal{X}(W,t)} \left[\rho \frac{\partial u_i}{\partial t} + \rho \mathbf{u} \cdot \nabla u_i \right] d\mathbf{x}.
\end{aligned}$$

The last equality holds true from (3.27), the general statement of the conservation of mass of a fluid.

Hence going back from component to vector form, we have

$$\frac{d}{dt} \int_{\mathcal{X}(W,t)} \rho \mathbf{v}(\mathbf{x}, t) d\mathbf{x} = \int_{\mathcal{X}(W,t)} \rho \left[\frac{\partial \mathbf{v}}{\partial t} + \mathbf{v} \cdot \nabla \mathbf{v} \right] d\mathbf{x}.$$

□

Now our general statement for the conservation of momentum for a fluid currently is in the form of

$$\int_{\mathcal{X}(W,t)} \rho \left[\frac{\partial \mathbf{u}}{\partial t} + \mathbf{u} \cdot \nabla \mathbf{u} \right] d\mathbf{x} = \int_{\mathcal{X}(W,t)} (\nabla \cdot \sigma) d\mathbf{x}.$$

Note that we are only considering forces from the fluid acting upon the fluid. That is, we are not considering external body forces. We will now briefly focus our attention on the stress tensor, σ .

The stress tensor, σ , is traditionally written in the following form,

$$\sigma = \begin{pmatrix} \sigma_{xx} & \tau_{xy} & \tau_{xz} \\ \tau_{yx} & \sigma_{yy} & \tau_{yz} \\ \tau_{zx} & \tau_{zy} & \sigma_{zz} \end{pmatrix},$$

where the diagonal entries, $\{\sigma_{ii}\}$, describe pressure stresses and the off diagonal terms, $\{\tau_{jk}\}$ with $j \neq k$, describe the shear-stresses. Intuitively the pressure and shearing stresses are separated into two components,

$$\sigma = -pI + \tau, \tag{3.29}$$

where p is the pressure, I is the identity matrix, and τ contains the shear-stress terms. If you imagine an infinitesimal square sub-domain of the control volume, then each component of τ , $\{\tau_{jk}\}$, gives the shear-stress on face j in direction k . Furthermore, we have $\tau_{jk} = \tau_{kj}$ by symmetry arising from the conservation of angular momentum.

Hence we now have the following statement regarding the conservation of momentum of a fluid,

$$\int_{\mathcal{X}(W,t)} \rho \left[\frac{\partial \mathbf{u}}{\partial t} + \mathbf{u} \cdot \nabla \mathbf{u} \right] d\mathbf{x} = \int_{\mathcal{X}(W,t)} (\nabla \cdot (-pI + \tau)) d\mathbf{x},$$

and therefore we get

$$\rho \left[\frac{\partial \mathbf{u}}{\partial t} + \mathbf{u} \cdot \nabla \mathbf{u} \right] = \nabla \cdot (-pI + \tau),$$

and then simplifying

$$\rho \left[\frac{\partial \mathbf{u}}{\partial t} + \mathbf{u} \cdot \nabla \mathbf{u} \right] = -\nabla p + \nabla \cdot \tau. \quad (3.30)$$

Eq.(3.30) is the general statement regarding the conservation of momentum of a fluid and can be thought of as a general Navier-Stokes equation. No assumptions about whether the fluid is incompressible, viscoelastic, etc. were made. However, we will now assume the fluid is *Newtonian* and incompressible for the remainder of our studies.

A *Newtonian* fluid models a fluid in which its shearing is linearly proportional the gradient of velocity, i.e., all local viscous stresses are linearly proportional to the local strain-rates (deformations) within the fluid. This can be written as

$$\tau = \mu [\nabla \mathbf{u} + (\nabla \mathbf{u})^T], \quad (3.31)$$

where μ is a proportionality constant. Note that μ is also the dynamic viscosity of the fluid. If we define the components of \mathbf{u} as $\mathbf{u} = (u, v, w)$, then can write τ as

$$\tau = \mu \begin{bmatrix} 2\frac{\partial u}{\partial x} & \frac{\partial u}{\partial y} + \frac{\partial v}{\partial x} & \frac{\partial u}{\partial z} + \frac{\partial w}{\partial x} \\ \frac{\partial u}{\partial y} + \frac{\partial v}{\partial x} & 2\frac{\partial v}{\partial y} & \frac{\partial v}{\partial z} + \frac{\partial w}{\partial y} \\ \frac{\partial u}{\partial z} + \frac{\partial w}{\partial x} & \frac{\partial v}{\partial z} + \frac{\partial w}{\partial y} & 2\frac{\partial w}{\partial z} \end{bmatrix}. \quad (3.32)$$

Finally we compute $\nabla \cdot \tau$, by first considering only the 1st component, i.e.,

$$\begin{aligned}
\frac{1}{\mu}(\nabla \cdot \tau)_1 &= \frac{\partial}{\partial x} \left(2 \frac{\partial u}{\partial x} \right) + \frac{\partial}{\partial x} \left(\frac{\partial u}{\partial y} + \frac{\partial v}{\partial x} \right) + \frac{\partial}{\partial x} \left(\frac{\partial u}{\partial z} + \frac{\partial w}{\partial x} \right) \\
&= 2u_{xx} + u_{yy} + v_{xy} + u_{zz} + w_{xz} \\
&= (u_{xx} + u_{yy} + u_{zz}) + (u_{xx} + v_{xy} + w_{xz}) \\
&= \Delta u + \frac{\partial}{\partial x}(\nabla \cdot \mathbf{u}) \\
&= \Delta u.
\end{aligned}$$

Note that $\nabla \cdot \mathbf{u} = 0$ by assuming the fluid is incompressible. Now if we had done this for the other components, we will find that

$$\nabla \cdot \tau = \mu \Delta \mathbf{u}. \quad (3.33)$$

Hence we find the incompressible, Navier-Stokes equations,

$$\rho \left[\frac{\partial \mathbf{u}}{\partial t} + \mathbf{u} \cdot \nabla \mathbf{u} \right] = -\nabla p + \mu \Delta \mathbf{u} \quad (3.34)$$

$$\nabla \cdot \mathbf{u} = 0. \quad (3.35)$$

From these derivations it is clear we have made two modeling assumptions about the fluid, namely that the fluid is

1. Incompressible, e.g., the fluid has constant density
2. Newtonian, e.g., stress is linearly proportional to the shear rate.

If we wished to model the fluid with other properties, such as viscoelasticity, we would have to revisit (3.27) and (3.30) and make appropriate assumptions.

3.2 Non-dimensional quantities of interest

In this section we will discuss two non-dimensional quantities, the Reynolds Number, Re , and the Womersley Number, Wo . Non-dimensional quantities are very important in mathematical modeling as they allow to study a system's dynamical evolution, bifurcations, and overall properties at scales that are more accessible to manage in laboratory physical models or computationally.

Let's look at a quick example using *damped harmonic oscillators*.

3.2.1 Example: Damped Harmonic Oscillator

The equations of motion for a damped harmonic oscillator is the following,

$$m\ddot{x} + b\dot{x} + kx = 0, \quad (3.36)$$

where x is the displacement from the mass' equilibrium position, k is the spring stiffness coefficient, and b is the damping coefficient. We note in this example there are no external forces present, since the equation is *homogeneous*.

To non-dimensionalize this system, we take

$$x = x_c \mathfrak{X} \quad \text{and} \quad t = t_c \tau,$$

where x_c and t_c hold the units of length and time respectively, while \mathfrak{X} and τ are the non-dimensional quantities. Substituting these definitions into (3.36), we obtain

$$\frac{mx_c}{t_c^2} \ddot{\mathfrak{X}} + \frac{bx_c}{t_c} \dot{\mathfrak{X}} + kx_c \mathfrak{X} = 0. \quad (3.37)$$

Next we divide the equation by the leading coefficients on the second-order term,

$$\ddot{\mathfrak{X}} + t_c \frac{b}{m} \dot{\mathfrak{X}} + t_c^2 \frac{k}{m} \mathfrak{X} = 0. \quad (3.38)$$

We now make the choice to normalize the coefficient on the linear term, \mathfrak{X} , hence we let

$$t_c = \sqrt{\frac{m}{k}}. \quad (3.39)$$

The governing system now becomes,

$$\ddot{\mathfrak{X}} + \frac{b}{\sqrt{mk}} \dot{\mathfrak{X}} + \mathfrak{X} = 0. \quad (3.40)$$

Finally, we call the remaining coefficient on the first-order term,

$$2\zeta = \frac{b}{\sqrt{mk}}. \quad (3.41)$$

The reason for the factor of 2 is purely aesthetic and arbitrary; it will later allow us to parameterize solutions in terms of ζ solely. Hence the non-dimensional form of the damped harmonic oscillator is,

$$\ddot{\mathfrak{X}} + 2\zeta\dot{\mathfrak{X}} + \mathfrak{X} = 0, \quad (3.42)$$

where we have made the assumptions that $\zeta = \frac{b}{2\sqrt{mk}}$ and $t_c = \sqrt{\frac{m}{k}}$.

To solve (3.42), we make the ansatz that we will have solutions of the form

$$\mathfrak{X} = e^{\lambda t},$$

since it is a second-order, linear, constant-coefficient ordinary differential equation. Substituting this ansatz into (3.42), we find

$$e^{\lambda t}(\lambda^2 + 2\zeta\lambda + 1) = 0,$$

and then solving for λ , we obtain

$$\lambda = -\zeta \pm \sqrt{\zeta^2 - 1} \quad (3.43)$$

We now have the following three possible branches:

1. *Overdamped*: $\zeta > 1$ We now have two distinct *eigenvalues* of our differential operator, giving us the following transient solution,

$$\mathfrak{X}(t) = c_1 e^{\tau\sqrt{\zeta^2-1}} + c_2 e^{-\tau\sqrt{\zeta^2-1}}.$$

2. *Critically damped*: $\zeta = 1$ We now only have *one* distinct eigenvalue of our differential operator.

Hence at this stage, we have one transient solution, $\mathfrak{X}_1(t) = c_3 e^{-\tau}$. However, we will also have a resonant eigenfunction, $\mathfrak{X}_2(t) = c_4 \tau e^{-\tau}$. Therefore our transient solution for this critically

damped case is

$$\mathfrak{X}(t) = (c_3 + \tau c_4)e^{-\tau}.$$

3. *Under damped*: $\zeta < 1$ We have two distinct eigenvalues of our differential operator; however, they are both complex with nonzero imaginary part. This is not an issue as our transient solutions can be written as

$$\mathfrak{X}(t) = \tilde{c}_5 e^{-(\tau + \sqrt{1-\zeta^2})} + \tilde{c}_6 e^{-(\tau - \sqrt{1-\zeta^2})},$$

or equivalently, using some algebraic sorcery,

$$\mathfrak{X}(t) = e^{-\tau} \left[c_5 \cos(\tau \sqrt{1-\zeta^2}) + c_6 \sin(\tau \sqrt{1-\zeta^2}) \right].$$

Hence we found there are *three* regimes for the damped harmonic oscillator system - overdamped, underdamped, and critically damped. Moreover, we were able to discern when such bifurcation would occur by using non-dimensionalization, giving rise to a natural non-dimensionalization quantity, ζ , we can quantify the transient solution regimes by. We note that the quantity, ζ is sometimes referred to as the *damping ratio*, which is heavily used by the engineering community to model decaying oscillations in a system after undergoing a perturbation.

We will now introduce two non-dimensional quantities used to model the hemodynamics in heart morphogenesis.

3.2.2 The Reynolds Number and Different Fluid Regimes

Quite possibly, the most heavily used metric for quantifying different fluid regimes is given by the non-dimensionalization parameter the *Reynolds Number*, Re . We will briefly give its derivation, via non-dimensionalizing the Navier-Stokes equations (3.11). For our purposes in this section, we will assume there is no external body force, i.e., $\mathbf{f}_{ext} = 0$ and $-\nabla\phi = \mathbf{f}_{body} = 0$, exerted on the fluid. Therefore we start with the following traditional form of the Navier-Stokes equation,

$$\frac{\partial \mathbf{v}}{\partial t} + (\mathbf{v} \cdot \nabla) \mathbf{v} = -\frac{1}{\rho} \nabla p + \frac{\mu}{\rho} \Delta \mathbf{v}. \quad (3.44)$$

Next we assume the following non-dimensionalization,

$$\mathbf{x} = L\tilde{\mathbf{x}} \quad \mathbf{v} = U\tilde{\mathbf{v}} \quad t = \frac{L}{U}\tilde{t} \quad p = \rho U^2 \tilde{p}, \quad (3.45)$$

where L and U are characteristic length scale and characteristic velocity of the system. We note that the choice of L and U are heavily dependent upon the geometry of the problem and are important to specify, as different people may choose these quantities differently. Hence it is important to be consistent and also declare how they are chosen.

Before substituting these non-dimensional definitions, we must also non-dimensionalize the differential operators. Consider the following spatial variable's non-dimensionalize as described above, $x = L\tilde{x}$, e.g., $\mathbf{x} = (\mathbf{x}, \mathbf{y}, \mathbf{z}) = \mathbf{L}(\tilde{\mathbf{x}}, \tilde{\mathbf{y}}, \tilde{\mathbf{z}})$. Hence

$$x = L\tilde{x} \Rightarrow dx = Ld\tilde{x},$$

and therefore

$$\frac{d\tilde{x}}{dx} = \frac{1}{L}.$$

Hence the dimensionless operator becomes

$$\frac{d}{dx} = \frac{d\tilde{x}}{dx} \frac{d}{d\tilde{x}} = \frac{1}{L} \frac{d}{d\tilde{x}}. \quad (3.46)$$

Using (3.46), we can the following non-dimensional forms of the gradient operator, ∇ , and Laplacian operator, Δ , analogously,

$$\nabla = \frac{1}{L} \tilde{\nabla} \quad (3.47)$$

$$\Delta = \frac{1}{L^2} \tilde{\Delta}. \quad (3.48)$$

Furthermore, the time differential operator, $\frac{\partial}{\partial t}$, gets non-dimensionalized similarly to (3.46), i.e.,

$$\frac{\partial}{\partial t} = \frac{L}{U} \frac{\partial}{\partial \tilde{t}}. \quad (3.49)$$

Substituting (3.45), (3.47), (3.48), and (3.49) into (3.44) we obtain,

$$\frac{U^2}{L} \frac{\partial \tilde{\mathbf{v}}}{\partial \tilde{t}} + (\tilde{\mathbf{v}} \cdot \tilde{\nabla}) \tilde{\mathbf{v}} = -\frac{\rho U^2}{\rho} \tilde{\nabla} \tilde{p} + \frac{\mu U}{\rho L^2} \tilde{\Delta} \tilde{\mathbf{v}}. \quad (3.50)$$

Dividing both sides by the coefficient on the material derivative, gives

$$\frac{\partial \tilde{\mathbf{v}}}{\partial \tilde{t}} + (\tilde{\mathbf{v}} \cdot \tilde{\nabla}) \tilde{\mathbf{v}} = -\tilde{\nabla} \tilde{p} + \frac{\mu}{\rho U L} \tilde{\Delta} \tilde{\mathbf{v}}. \quad (3.51)$$

Note that there is only one unique parameter ratio left, i.e., $\frac{\mu}{\rho U L}$. This quantity is the reciprocal of the *Reynolds Number*, e.g.,

$$Re = \frac{\rho U L}{\mu}, \quad (3.52)$$

and finally the traditional Navier-Stokes equations can be written,

$$\frac{\partial \tilde{\mathbf{v}}}{\partial \tilde{t}} + (\tilde{\mathbf{v}} \cdot \tilde{\nabla}) \tilde{\mathbf{v}} = -\tilde{\nabla} \tilde{p} + \frac{1}{Re} \tilde{\Delta} \tilde{\mathbf{v}} \quad (3.53)$$

We note that Re was first introduced by George Stokes in 1851, but it was later popularized by Osborne Reynolds 30 years later. It has since been historically known by Reynolds contribution, rather than Stokes [136]. The Re describes the ratio of inertial forces to viscous forces. If inertial forces dominate, $Re \gg 1$; however if viscous forces dominate, $Re \ll 1$, and if they are comparable, i.e., $O(0.01) \leq Re \leq O(100)$, we say this is the *intermediate* Re range. Furthermore if viscous forces dominate to the extent that virtually $Re = 0$, we call this the *Stokes* regime and it is time independent.s

Once transformed into the non-dimensional Navier-Stokes form, it is clear that once characteristic length scales, characteristic velocity scales, and fluid properties, i.e., density and dynamic viscosity, are selected, the problem is now set at a particular Re . Hence in the broad sense all incompressible flows with the same Re will be comparable. We note this also assumes that the fluid is *Newtonian*, i.e., meaning that the shear rate is not linearly proportional to the shear stress exerted on the fluid.

From (3.53), we see that in the limit as $Re \rightarrow \infty$, the fluid becomes *inviscid*, meaning that the viscous terms are negligible. Looking at the form of Re , this can be equated to either the viscosity going to zero or velocity going to zero, since we expect the characteristic length not to infinite, nor

the density of fluid to be infinite. Furthermore neglecting the viscous term in (3.53), gives rise to the governing equation of inviscid flow known as the *Euler equation*,

$$\frac{\partial \tilde{\mathbf{v}}}{\partial t} + (\tilde{\mathbf{v}} \cdot \tilde{\nabla}) \tilde{\mathbf{v}} = -\tilde{\nabla} \tilde{p}. \quad (3.54)$$

Also, (3.54) does an adequate job modeling inviscid flow fields; however, viscous forces must be considered when modeling fluid flow near a boundary. This is because of the presence of *boundary layers*, which form for even the modest amount of viscosity, like in air. Moreover, in turbulent flows, such as those synonymous with high Re , energy dissipation takes place through the fluid's viscosity on the microscales, and hence must be considered.

Example: Flow Past A Cylinder One of the most standard examples illustrating different fluid regimes, quantified by Re , is the problem of flow past a cylinder. Imagine a fixed cylinder in a flow tank, undergoing flow moving left to right. The inflow velocity is given by V , the diameter of the cylinder, d , and the fluid is homogeneous, i.e., constant density and viscosity. Re for this problem is defined by such parameters.

One can modify the Re in this system experimentally by keeping the fluid static and by changing the inflow velocity, or in numerical simulations by changing the dynamic viscosity. We note that in principle you could change any of the parameters to change Re but by only changing the dynamic viscosity in numerical simulations keeps the Strouhal Number constant for the system. Ideally in laboratory experiments, one would try to keep the Strouhal Number constant when varying Re but it is more difficult to change properties of the fluid in many cases. The Strouhal Number, St , which is also a non-dimensional quantity, is given by

$$St = \frac{fL}{U}, \quad (3.55)$$

and describes systems with oscillating flow, hence the frequency parameter, f , in its definition. Lastly we note that f is usually associated with a frequency of shedding vortices in many systems.

For $Re < 5$, flow is unseparated and moves around the cylinder. For $5 < Re < 15$ symmetric vortices begin to form on the trailing edge of the cylinder. Once $40 < Re < 150$, vortices sheets begin to be shed off the cylinder. For $150 < Re < 3 \times 10^5$, the vortex sheets transition to turbulent

vortical flow. At Re higher than 350,000, the laminar boundary layer undergoes a transition to turbulent and the wake behind the cylinder becomes more narrow and more disorganized. For high enough Re ($\sim 3,500,000$) there is a transition back to a turbulent vortex sheet. These regimes are illustrated in Figure(3.5), which is adapted from Thermopedia.com.

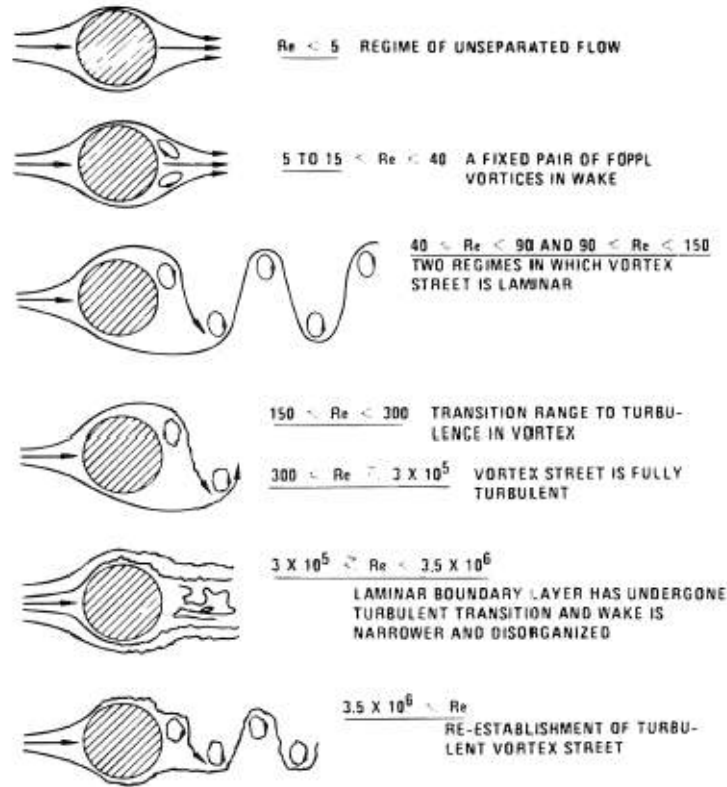


Figure 3.5: Flow past a fixed cylinder at different Reynolds Numbers, illustrating different regimes in the fluid flow. In these examples, the characteristic length is given by the diameter of the cylinder and velocity is given by the inflow velocity. For $Re < 5$, flow is unseparated and moves around the cylinder. For $5 < Re < 15$ symmetric vortices begin to form on the trailing edge of the cylinder. Once $40 < Re < 150$, vortices sheets begin to be shed off the cylinder. For $150 < Re < 3 \times 10^5$, the vortex sheets transition to turbulent vortical flow. At Re higher than that, the laminar boundary layer undergoes a transition to turbulent and the wake behind the cylinder becomes more narrow and more disorganized. For high enough Re ($\sim 3,500,000$) there is a transition back to a turbulent vortex sheet. Image courtesy of Thermopedia.com

We briefly mention a quote that arose when the late great German physicist Werner Heisenberg was asked what he would ever ask a deity. "When I meet God, I am going to ask him two questions: Why relativity? And why turbulence? I really believe he will have an answer for the first." Although this quote is also attributed to Horace Lamb [137].

However, although many biological systems do in fact live in the regime of turbulent fluid flows

or at least $Re > 1000$, e.g., aortic blood flow, swimming and flying in large fish and birds, etc., many interesting biological organisms operate at lower and modest Re ranges. For example some of the tiniest insects, e.g., thrips, fly at $Re \sim 10$; some jellyfish swim at $Re \sim 100$, e.g., Aurelia (moon jellyfish). For our considerations of the hemodynamics involved in heart morphogenesis, the Re can fall between $Re \sim [0.01, 100]$. It should be noted that these Re are also for specified characteristic length and velocity scales. For various organ systems of differing species, their Re and characteristic length scales, D , can be seen in Figure(3.6), which is adapted from [21].

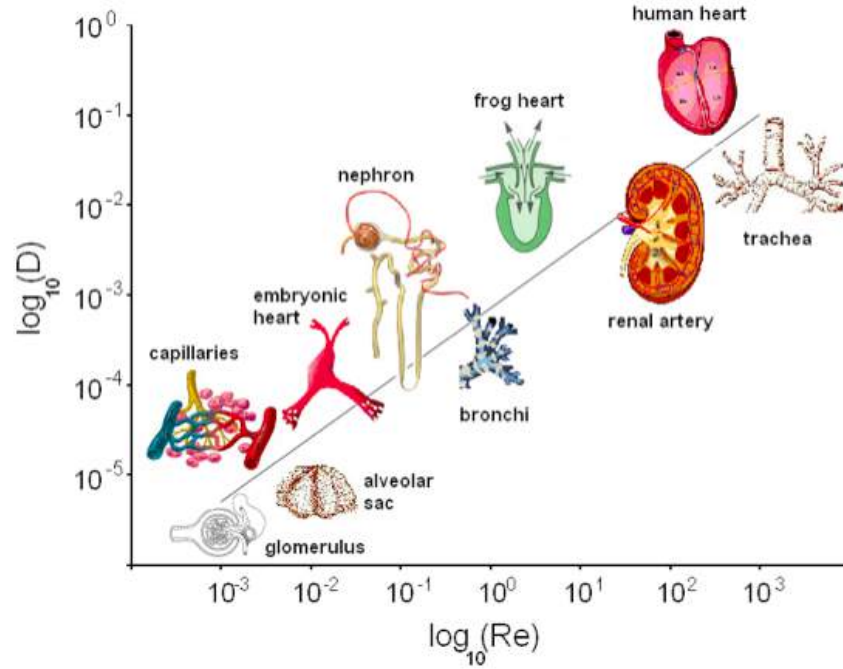


Figure 3.6: Organ systems for various species of organisms, plotted to show where they fall on the axis given by a characteristic length scale, the vertical axis, and Re , shown on the horizontal axis. The embryonic human heart is shown as $Re \sim 0.05$ with characteristic length of $D \sim 2.5 \times 10^{-4}$.

3.2.3 The Womersley Number

Besides the *Reynolds Number* and *Strouhal Number*, there are other useful nondimensional parameters in biological fluid dynamics, one being the *Womersley Number*. The Womersley Number, Wo , is a “close cousin” of Re , with the difference being that Wo describes the ratio of *pulsatile* inertial forces to viscous forces.

To derive Wo , we begin by considering the Navier-Stokes equations in a rigid tube in cylindrical coordinates. To simplify matters more, we consider axisymmetric flow, where $\mathbf{v} = u\hat{\mathbf{e}}_{\mathbf{r}} + v\hat{\mathbf{e}}_{\mathbf{z}}$.

Eq.(3.44) then becomes

$$\frac{\partial u}{\partial t} + u \frac{\partial u}{\partial r} + v \frac{\partial u}{\partial z} = -\frac{1}{\rho} \frac{\partial p}{\partial r} + \frac{\mu}{\rho} \left[\frac{1}{r} \frac{\partial}{\partial r} \left(r \frac{\partial u}{\partial r} \right) - \frac{u}{r^2} + \frac{\partial^2 u}{\partial z^2} \right] \quad (3.56)$$

$$\frac{\partial v}{\partial t} + u \frac{\partial v}{\partial r} + v \frac{\partial v}{\partial z} = -\frac{1}{\rho} \frac{\partial p}{\partial z} + \frac{\mu}{\rho} \left[\frac{1}{r} \frac{\partial}{\partial r} \left(r \frac{\partial v}{\partial r} \right) + \frac{\partial^2 v}{\partial z^2} \right], \quad (3.57)$$

with the incompressibility condition (3.14) becoming

$$\nabla \cdot \mathbf{v} = \frac{1}{r} \frac{\partial}{\partial r} (ru) + \frac{\partial v}{\partial z} = 0. \quad (3.58)$$

Now we assume zero radial flow, i.e., $u = 0$. Substituting this into (3.58), (3.56), and (3.57), we find the system of equations simplifies to

$$\frac{\partial v}{\partial z} = 0 \quad (\text{incompressibility}) \quad (3.59)$$

$$\frac{\partial p}{\partial r} = 0 \quad (\text{radial comp. of Navier-Stokes}) \quad (3.60)$$

$$\frac{\partial v}{\partial t} = -\frac{1}{\rho} \frac{\partial p}{\partial z} + \frac{\mu}{\rho} \left[\frac{1}{r} \frac{\partial}{\partial r} \left(r \frac{\partial v}{\partial r} \right) + \frac{\partial^2 v}{\partial z^2} \right] \quad (z \text{ axis comp. of Navier-Stokes}). \quad (3.61)$$

Next we consider harmonic solutions for the pressure and velocity, i.e.,

$$p = p_0 + p(z)e^{i\omega t} \quad \text{and} \quad v = v(r)e^{i\omega t}, \quad (3.62)$$

where p_0 is constant. Substituting (3.62) into (3.59), (3.60), and (3.61), we obtain

$$\frac{\partial v}{\partial z} = 0 \quad (3.63)$$

$$i\omega v(r)e^{i\omega t} = -\frac{1}{\rho} \frac{\partial p}{\partial z} e^{i\omega t} + \frac{\mu}{\rho} \frac{1}{r} \frac{\partial}{\partial r} \left(r \frac{\partial v}{\partial r} \right) e^{i\omega t}. \quad (3.64)$$

Now we will begin the non-dimensionalization procedure. We define

$$r = L_r \tilde{r} \quad z = L_z \tilde{z} \quad t = \bar{\omega} \tilde{t} \quad p = P \tilde{p} \quad u = U \tilde{u}, \quad (3.65)$$

as the non-dimensional parameters, where L_r , L_z , $\bar{\omega}$, P , and U are the characteristic radial length scale, longitudinal length scale, angular frequency, pressure, and velocity respectively. Substituting

these definitions into (3.63) and (3.64), we find

$$\frac{\partial \tilde{v}}{\partial \tilde{z}} = 0 \quad (3.66)$$

$$i\tilde{v} = -\frac{P}{\rho\bar{\omega}U} \frac{\partial \tilde{p}}{\partial \tilde{z}} + \frac{\mu}{L_r^2 \rho \omega} \frac{1}{\tilde{r}} \frac{\partial}{\partial \tilde{r}} \left(\tilde{r} \frac{\partial \tilde{v}}{\partial \tilde{r}} \right) \quad (3.67)$$

We define the *Womersley Number*, Wo , as the square root of the coefficient on the viscous term, e.g.,

$$Wo^2 = L_r^2 \frac{\rho \omega}{\mu}, \quad (3.68)$$

where L_r , ρ , ω , and μ are the characteristic length, density, pulsation angular frequency, and dynamic viscosity. Eq.(3.67) now becomes,

$$i\tilde{v} = -\frac{P}{\rho\bar{\omega}U} \frac{\partial \tilde{p}}{\partial \tilde{z}} + \frac{1}{Wo^2} \frac{1}{\tilde{r}} \frac{\partial}{\partial \tilde{r}} \left(\tilde{r} \frac{\partial \tilde{v}}{\partial \tilde{r}} \right). \quad (3.69)$$

Eq.(3.69) has an analytic solution given in terms of Bessel functions of order zero [122], i.e.,

$$\tilde{v} = i \frac{P}{\rho\bar{\omega}U} \frac{\partial \tilde{p}}{\partial \tilde{z}} \left(1 - \frac{J_0(\tilde{r}Wo)}{J_0(Wo)} \right). \quad (3.70)$$

Like Re , varying Wo can drastically change fluid regimes. Unsteady effects are significant for $Wo > 1$ and are negligible for $Wo < 1$. Furthermore, Wo can be related to Re by careful selection of characteristic velocity, i.e., if it is chosen to correspond to the oscillating structure, $U = \omega L_r$. Hence we find that $Wo \approx Re$ in this case[20].

For this example of tubular flow, velocity profiles at $t = 0$ are shown for varying Wo in Figure(3.7). For small Wo , *Poiseuille* flow is obtained, while for large values of Wo , the velocity profile becomes flat. This figure is adapted from [31].

3.3 The Immersed Boundary Method (IB)

In this section we will present an introduction to the numerical that we use to solve the coupled fluid-structure interaction problem (FSI) called the immersed boundary method. We will begin by giving a general overview of the immersed boundary method and then an in-depth description of the software, *IB2d* [37]. Finally we will give an overview of IBAMR, which is Boyce Griffith's open source

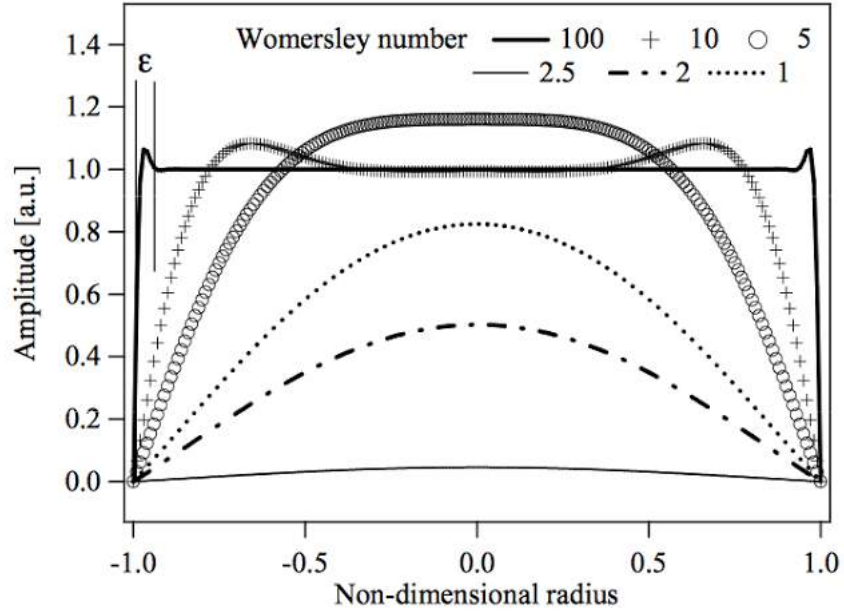


Figure 3.7: Velocity profiles at $t = 0$ are shown for varying Wo . For small Wo , *Poiseuille* flow is obtained, while for large values of Wo , the velocity profile becomes flat. This figure is adapted from [31].

immersed boundary code, which is an adaptive and distributed-memory parallel implementation of IB [138].

The development of fluid-structure interaction (FSI) software involves trade-offs between ease of use, generality, performance, and cost. Typically there are large learning curves when using low-level software to model the interaction of an elastic structure immersed in a uniform density fluid. Many existing codes are not publicly available, and the commercial software that exists usually requires expensive licenses and may not be as robust or allow the necessary flexibility that in house codes can provide. We present an open source immersed boundary software package, *IB2d*, with full implementations in both MATLAB and Python, that is capable of running a vast range of biomechanics models and is accessible to scientists who have experience in high-level programming environments. *IB2d* contains numerous options for constructing material properties of the fiber structure, as well as the advection-diffusion of a chemical gradient, muscle mechanics models, electrophysiology, and artificial forcing to drive boundaries with a preferred motion.

3.3.1 Introduction to IB

Fully coupled fluid-structure interaction problems is a rapidly growing discipline across all the sciences, ranging from engineering to biology [139]. Fully coupled FSI is different from models in which the motion or bending of a structure is prescribed. The action of the aortic valve is a good example of fully coupled FSI, since the motion of the valve is governed by the motion of the fluid, and in turn, the valve alters the underlying blood flow. Note that in a fully coupled simulation, the movement of the valve would not be prescribed.

The immersed boundary (*IB*) framework was first published in 1972 to study blood flow around valve leaflets of the heart by Charles Peskin [124]. It has been applied to a plethora of biomechanics problems which involve the interaction of a flexible structure immersed in a viscous, incompressible fluid. The method has been successfully applied to study fluid dynamics in a variety of biological settings within the intermediate Reynolds number range, defined here as $0.01 < Re < 1000$, where

$$Re = \frac{\rho LV}{\mu}. \quad (3.71)$$

μ and ρ are the dynamic viscosity and density of the fluid, respectively, and L and V are a characteristic length and velocity of the problem. Some of these applications include cardiovascular dynamics [125, 32], aquatic locomotion [140, 141], insect flight [142, 143, 144], muscle-fluid-structure interactions [145, 146, 147], and plant biomechanics [148].

The strength of this method is that it can be used to model fully coupled fluid-structure interaction problems involving complicated time-dependent geometries using a regular fixed Cartesian discretization of the fluid domain, while the elastic fibers describing the structure are discretized on a Lagrangian mesh. The fluid and elastic fibers constitute a coupled system in which the structure moves at the local fluid velocity and the structure applies a singular force to the fluid.

Beyond fully-coupled fluid-structure interaction models, many scientists have successfully coupled other constitutive equations within the *IB* framework [149, 150, 145, 151, 152, 153, 22, 95]. For example, in [150], Fogelson and Guy modeled platelets suspended in an incompressible fluid to study blood clotting and included chemical reaction equations modeling the mechanisms for binding-unbinding, platelet stimulus-response, and chemistry on the platelets surfaces. Moreover, in [145], Tytell *et al.* incorporated calcium dynamics, which governed the muscle contraction dynamics that

were responsible for force generation in a swimming lamprey.

Many implementations of the immersed boundary method (*IBM*) exist in compiled programming languages, including a few open source and freely available packages, e.g., IBIS [154] and IBAMR [138]. IBIS is *IB* software written in FORTRAN that includes its own graphical user interface, *ibisview*, to visualize the simulations. IBAMR is an adaptive and parallelized implementation of the *IBM* in *C++*, with extensions to a hybrid implementation of *IB* which uses a finite element discretization of the immersed structure [131]. It depends on many open source libraries, including PETSc [155], SAMRAI [156], libMesh [157], and OpenMPI [158] which make it robust and very efficient to run but at the cost of a steep learning curve for anyone inexperienced at high performance computing. Moreover installation of IBAMR is non-trivial, as it requires installing the above open source libraries and coupling them with the IBAMR framework. Furthermore, without multi-processor computational resources available, IBAMR cannot run at its full potential.

IBAMR was developed for highly resolved computational grids and specifically designed to include adaptive mesh refinement (AMR) capabilities. AMR allows for more computational speedup; it dynamically adapts the computational grid for higher resolution near regions of interest, e.g., boundaries and regions of vorticity above a user-prescribed threshold, while solving at lower resolution in other areas. Because of IBAMR's AMR and parallelization capabilities, it can be used for 3D applications unlike previous open source *IB* software, such as IBIS, which was strictly developed for 2D applications.

IBIS AND IBAMR, having been written in lower level programming languages, e.g., FORTRAN and *C++* respectively, require familiarity with these languages. For students and scientists from disciplines that are not typically trained in rigorous programming, these languages are often inaccessible and necessitate a steep learning curve.

Recently there have been a few open source 2D *IB* codes available on GitHub, such as matIB [159] and pyIBM [160], which are a MATLAB and Python 3.5 implementation, respectively. Charlie Peskin also has a MATLAB 2D *IB* implementation available on his website [161]. All these implementations use the standard immersed boundary framework [162] but do not include a breadth of fiber models or examples and are not as robust or efficient in comparison to their 3D counterparts, such as IBAMR. However, implementations in these high-level programming languages offer many powerful advantages, perhaps foremost being that they are more readable and familiar to a broad audience of

scientists and engineers.

In this thesis, we present *IBM* software called *IB2d* with full implementations in both MATLAB [163] and Python 3.5 [164] that is capable of modeling a broad array of problems in biomechanics including (but not limited to) locomotion, physiological processes, and plant biomechanics. Even for skilled programmers, *IB2d* represents a nice option for preliminary tests of new models. For example, one may add new muscle models to the software quite easily for testing before attempting an implementation in a more challenging software framework such as IBAMR.

IB2d is an extension of the preliminary code found in [146]. It extends the capabilities of this code by introducing a full implementation in Python, numerous additions in functionality, such as more fiber-structure modelling options, advection-diffusion, electrophysiology models, and artificial forcing, as well as visualization output and data analysis options. The package also contains 50+ examples, which illustrate the breadth of the software.

3.3.2 IBM Framework

IB2d models fluid motion in two dimensions using the Navier-Stokes equations in Eulerian form, given as

$$\rho \left(\frac{\partial \mathbf{u}(\mathbf{x}, t)}{\partial t} + \mathbf{u}(\mathbf{x}, t) \cdot \nabla \mathbf{u}(\mathbf{x}, t) \right) = -\nabla p(\mathbf{x}, t) + \mu \Delta \mathbf{u}(\mathbf{x}, t) + \mathbf{f}(\mathbf{x}, t) \quad (3.72)$$

$$\nabla \cdot \mathbf{u}(\mathbf{x}, t) = 0, \quad (3.73)$$

where $\mathbf{u}(\mathbf{x}, t) = (u(\mathbf{x}, t), v(\mathbf{x}, t))$ is the fluid velocity, $p(\mathbf{x}, t)$ is the pressure, and $\mathbf{f}(\mathbf{x}, t)$ is the force per unit volume (area in $2D$) applied to the fluid by the immersed boundary. The independent variables are the position, $\mathbf{x} = (x, y)$, and time, t . Eq.(3.72) is equivalent to the conservation of momentum for a fluid, while Eq.(3.73) is the condition mandating that the fluid is incompressible. *IB2d* also assumes a periodic and square fluid domain. Future implementations will incorporate non-square domains as well as the inclusion of a projection method solver to enforce Dirichlet and Neumann boundary conditions [165, 166].

The interaction equations between the fluid and the immersed structure are given by

$$\mathbf{f}(\mathbf{x}, t) = \int \mathbf{F}(r, t) \delta(\mathbf{x} - \mathbf{X}(r, t)) dr \quad (3.74)$$

$$\mathbf{U}(\mathbf{X}(r, t), t) = \frac{\partial \mathbf{X}(r, t)}{\partial t} = \int \mathbf{u}(\mathbf{x}, t) \delta(\mathbf{x} - \mathbf{X}(r, t)) d\mathbf{x}, \quad (3.75)$$

where $\mathbf{X}(r, t)$ gives the Cartesian coordinates at time t of the material point labeled by Lagrangian parameter r , $\mathbf{F}(r, t)$ is the force per unit area imposed onto the fluid by elastic deformations in the immersed structure as a function of the Lagrangian position, r , and time, t . The force density, $\mathbf{F}(r, t)$, is a functional of the current immersed boundary's configuration. Moreover, we write the force density as

$$\mathbf{F}(r, t) = \mathbb{F}(\mathbf{X}(\mathbf{r}, \mathbf{t}), \mathbf{t}), \quad (3.76)$$

where $\mathbb{F}(\mathbf{X}, \mathbf{t})$ is a combination of all the fiber components modeling the desired material properties of the immersed structure. The fiber models implemented in *IB2d* are described in subsequent sections.

Eq.(3.74) applies a force from the immersed boundary to the fluid through a delta-kernel integral transformation. Eq.(3.75) sets the velocity of the boundary equal to the local fluid velocity, to satisfy the no-slip condition.

Upon discretizing Eqs.(3.74) and (3.75), regularized delta functions, δ_h , are implemented,

$$\delta_h(\mathbf{x}) = \frac{1}{h^2} \phi\left(\frac{x}{h}\right) \phi\left(\frac{y}{h}\right), \quad (3.77)$$

where h is the fluid grid width and

$$\phi(r) = \begin{cases} \frac{1}{4} (1 + \cos(\frac{\pi r}{2})) & |r| \leq 2 \\ 0 & \text{otherwise} \end{cases}, \quad (3.78)$$

where r is the distance from the Lagrangian node. This regularized delta function has compact support. Other compactly supported discrete delta functions may be easily incorporated into the code as well. More details on regularized delta functions and their discretizations may be found in [162, 167].

The coupled equations (3.72-3.75) are solved using the algorithm described in Peskin's *IB* review paper [162] with periodic boundary conditions imposed on both the fluid and immersed boundary. Details on the discretization used in *IB2d* are found in A.1.

The standard numerical algorithm for immersed boundary [162], illustrated in Figure 3.8, is as

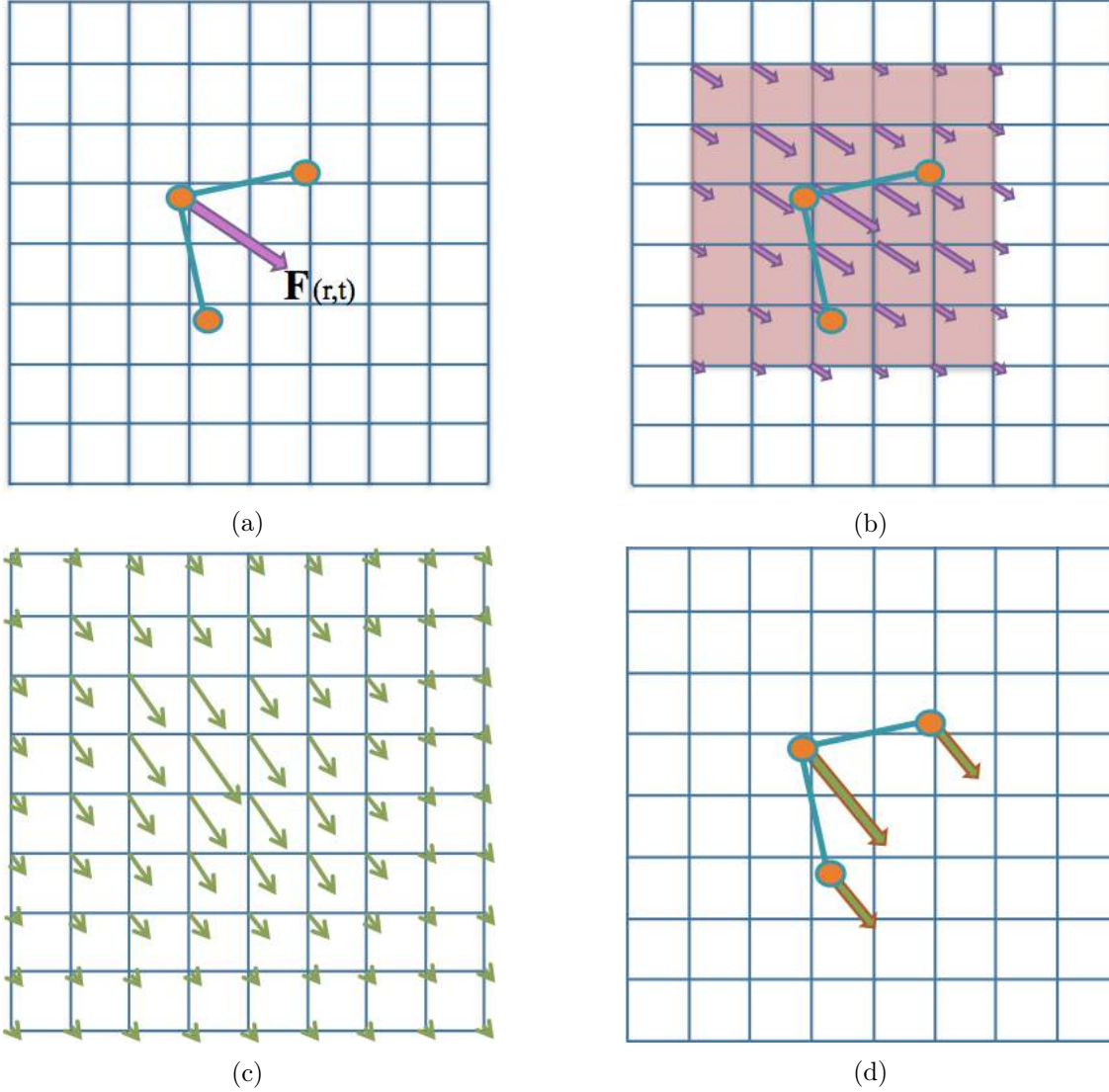


Figure 3.8: A visual guide to the standard steps in Peskin's immersed boundary method. (a) The elastic deformation forces are computed from the current configuration of the immersed structure. (b) Those deformation forces are spread to neighboring fluid grid points, via Eq.(3.74). (c) The fluid velocity is updated everywhere in the domain using Eqs.(3.72) and (3.73). (d) The immersed boundary is moved at the local fluid velocity by Eq.(3.75). Note that the deformation force vectors in (b) and velocity vectors in (c) are not parallel, as the fluid already may have some underlying non-zero velocity field, which gets perturbed due to the presence of the deformation forces.

follows:

- Step 1:* Compute the force density $\mathbf{F}^n(r, t)$ on the immersed boundary from the current boundary deformations, \mathbf{X}^n , where n indicates the n^{th} time-step.
- Step 2:* Use Eq.(3.74) to spread these deformation forces from the Lagrangian nodes to the fluid lattice points nearby.
- Step 3:* Solve the Navier-Stokes equations, Eqs.(3.72) and (3.73), on the Eulerian domain. E.g., update \mathbf{u}^{n+1} and p^{n+1} from \mathbf{u}^n and \mathbf{f}^n . Note: since we are enforcing periodic boundary conditions on the computational domain, the Fast Fourier Transform (FFT) [168, 169] is used to solve for these updated quantities at an accelerated rate.
- Step 4:* Update the fiber model positions, \mathbf{X}^{n+1} , using the local fluid velocities, \mathbf{U}^{n+1} , using \mathbf{u}^{n+1} and Eq.(3.75). E.g., move the immersed structure at the local fluid velocities thereby enforcing *no slip* boundary conditions.

Fiber Models Implemented in *IB2d* In this section, all current fiber models implemented in *IB2d* are described. Various fiber models give the immersed boundary certain desirable material properties relevant to many scientific applications. Currently the following types of fiber models are available:

1. Springs (Hookean or Non-Hookean and/or Damped)
2. Torsional Springs
3. Non-invariant Beams
4. Target Points
5. Mass Points (with or without gravity)
6. Porosity
7. Muscle-Fluid-Structure Models
8. User-defined Force Model

Once the deformation energy has been calculated in the algorithm, e.g., in Step 3,

$$E(\mathbf{X}(r, t), t) = \sum_{k=0}^M E_k(\mathbf{X}_{k,1}, \mathbf{X}_{k,2}, \dots, \mathbf{X}_{k,M}), \quad (3.79)$$

the corresponding elastic forces can be computed via derivatives of the elastic energy, where the elastic deformation force at point c of fiber model k is calculated as

$$\mathbb{F}_{\mathbf{k},\mathbf{c}}(\mathbf{X}(\mathbf{r}, \mathbf{t}), \mathbf{t}) = -\frac{\partial \mathbf{E}(\mathbf{X}(\mathbf{r}, \mathbf{t}), \mathbf{t})}{\partial \mathbf{X}_{\mathbf{k},\mathbf{c}}}. \quad (3.80)$$

Note that \mathbf{X} contains the coordinates of all immersed boundary points, M is the number of fiber structures in the system, M is the number of immersed boundary points in fiber structure, and the negative sign is chosen to drive the system towards a minimal energy state. Furthermore we note that (3.79) is a combination of the deformation energies from all respective fiber models, which are described below.

Springs

Resistance to stretching between successive Lagrangian points can be achieved by modeling the connections with Hookean (or Non-Hookean) springs of resting length R_L and spring stiffness k_S . If the virtual spring displacement is below or beyond R_L , the model will drive the system back towards a lower energy state. The elastic potential energy for a Hookean spring is given by

$$E_{spring} = \frac{1}{2} k_S (||\mathbf{X}_{SL} - \mathbf{X}_M|| - R_L)^2, \quad (3.81)$$

where \mathbf{X}_M and \mathbf{X}_{SL} are master and slave node coordinates respectively. The corresponding deformation forces is given by differentiation of the elastic energy as in Eq.(3.80)

$$F_{spring} = k_S \left(1 - \frac{R_L}{||\mathbf{X}_{SL} - \mathbf{X}_M||} \right) \cdot \begin{pmatrix} x_{SL} - x_M \\ y_{SL} - y_M \end{pmatrix}. \quad (3.82)$$

This fiber model is illustrated in Figure 3.9a. Note that the above calculation computes the forces

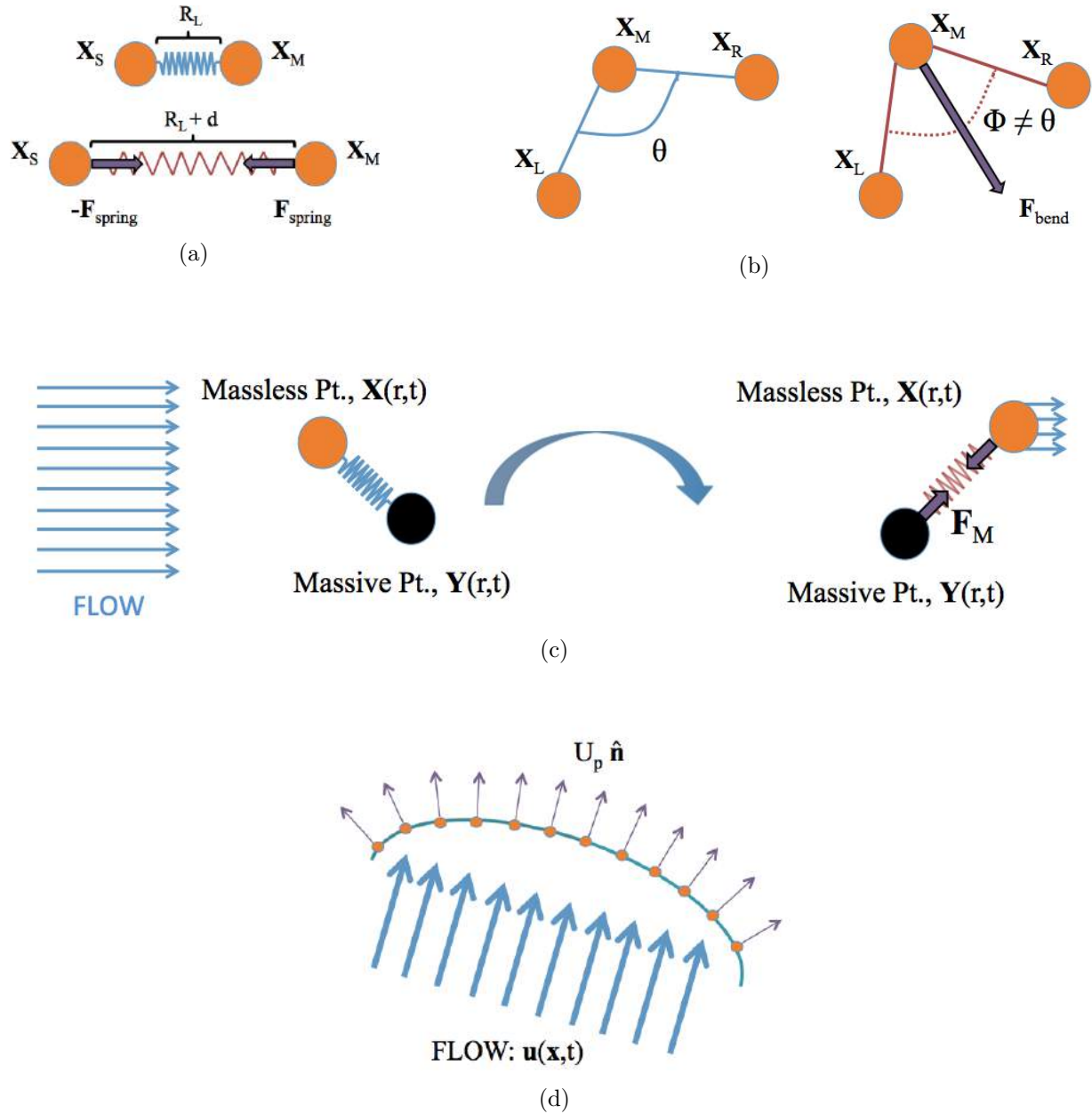


Figure 3.9: Illustrating the key points of various fiber models implemented in *IB2D*. (a) Two nodes connected by a virtual spring held at the resting-length of the spring (top) and a rendering of the longitudinal forces induced when the spring is stretched (bottom). (b) A torsional spring connecting three adjacent Lagrangian nodes at its equilibrium configuration, e.g. angle θ (left) and an illustration of the force experienced by the middle node, \mathbf{X}_M , when the system is not at its lowest energy state (right). (c) A massless and massive point, \mathbf{X} and \mathbf{Y} respectively, connected by a stiff virtual spring. Incoming flow moves the massless point to a new position, which exerts a pulling-like effect on the massive point. The massive point will move depending on a coupled constitutive equation. (d) Incoming flow permeates a porous boundary. The amount of flow that moves through the body depends on the permeability of the membrane; all flow through the boundary is normal to the body itself.

acting on the master node; a change in sign gives the forces acting onto the slave node. Two nodes are connected by a virtual spring shown when the spring is at resting-length (top). A rendering of the longitudinal forces induced when the spring is stretched is also depicted (bottom).

Furthermore, *IB2d* also implements nonlinear springs that assume the nonlinear extension of Eq.(3.81), i.e.

$$E_{spring} = \frac{1}{2}k_S (||\mathbf{X}_{SL} - \mathbf{X}_M|| - R_L)^{\beta+1}, \quad (3.83)$$

where $\beta \in \mathbb{Z}^+$. The corresponding force onto the master node is then given by

$$F_{spring} = \frac{\beta+1}{2} k_S \left(1 - \frac{R_L}{||\mathbf{X}_{SL} - \mathbf{X}_M||} \right)^{\beta} \cdot \begin{pmatrix} x_{SL} - x_M \\ y_{SL} - y_M \end{pmatrix}. \quad (3.84)$$

Moreover, one may also choose to use damped springs, which assumes a frictional damping force that is proportional to the velocity of the oscillation. We note that these take a similar form to the linear spring case, but with an additional term modeling the damping, i.e.,

$$F_{d.spring} = k_S \left(1 - \frac{R_L}{||\mathbf{X}_{SL} - \mathbf{X}_M||} \right) \cdot \begin{pmatrix} x_{SL} - x_M \\ y_{SL} - y_M \end{pmatrix} + b_S \frac{d}{dt} ||\mathbf{X}_{SL} - \mathbf{X}_M||, \quad (3.85)$$

where b_S is the damping coefficient.

Torsional Springs

Resistance to bending between three successive Lagrangian points is modeled using a torsional spring connecting the three nodes. The model assumes a desired angle θ , a prescribed ‘curvature’ between the three Lagrangian points, with corresponding bending stiffness k_B . Hence the bending energy is given as

$$E_{bend} = \frac{1}{2}k_B (\hat{z} \cdot (\mathbf{X}_R - \mathbf{X}_M) \times (\mathbf{X}_M - \mathbf{X}_L) - C)^2, \quad (3.86)$$

where $\mathbf{X}_R, \mathbf{X}_L$, and \mathbf{X}_M are right, left, and master Lagrangian nodal coordinates, and $C = d_{LM}d_{MR}\sin\theta$. Note that C is not the standard definition of curvature, but a curvature defined at the desired angle θ and distances between links, d_{LM} and d_{MR} . This is only accurate for small

changes in amplitude or radii and higher order accurate curvature models will be implemented in future releases.

The penalty force is designed to drive any deviations in the angle between these links back towards a lower energy state, i.e., θ . The corresponding bending force is given by

$$\mathbf{F}_{bend_L} = -k_B \left((x_R - x_M)(y_M - y_L) - (y_R - y_M)(x_M - x_L) - C \right) \cdot \begin{pmatrix} (y_R - y_M) \\ -(x_R - x_M) \end{pmatrix} \quad (3.87)$$

$$\mathbf{F}_{bend_M} = k_B \left((x_R - x_M)(y_M - y_L) - (y_R - y_M)(x_M - x_L) - C \right) \cdot \begin{pmatrix} (y_M - y_L) + (y_R - y_M) \\ -(x_R - x_M) - (x_M - x_L) \end{pmatrix} \quad (3.88)$$

$$\mathbf{F}_{bend_R} = k_B \left((x_R - x_M)(y_M - y_L) - (y_R - y_M)(x_M - x_L) - C \right) \cdot \begin{pmatrix} (y_M - y_L) \\ (x_M - x_L) \end{pmatrix} \quad (3.89)$$

An illustration of 2D torsional springs is shown in Figure 3.9b, where a torsional spring connects three adjacent Lagrangian nodes \mathbf{X}_L , \mathbf{X}_M , and \mathbf{X}_R at their equilibrium configuration with angle θ (left). The force is experienced by the middle node, \mathbf{X}_M , when the system is not at its lowest energy state (right), driving it back to its preferred configuration.

In this configuration, torsional deformation forces can only occur on immersed boundary points on the interior or the fiber structure, not the endpoints.

Non-invariant Beams

Another way to model the resistance bending between three successive Lagrangian points is using a non-invariant beam connecting the three successive nodes. The model assumes a prescribed ‘curvature’ (in both x and y components) between the three Lagrangian points, with corresponding bending stiffness k_{NIB} . The corresponding bending deformation forces are modeled as

$$\mathbf{F}_{beam} = k_{NIB} \frac{\partial^4}{\partial s^4} (\mathbf{X}(s, t) - \mathbf{X}_b(s)), \quad (3.90)$$

where $\mathbf{X}(s, t)$ is the current Lagrangian configuration at time t , e.g., the mapping of the Lagrangian points s to the underlying Cartesian grid, and $\mathbf{X}(s)$ is the preferred configuration of the fiber model. More details about this fiber model can be found in [162, 170, 171] and the discretization is discussed in Appendix A.2. This model is denoted as non-invariant beams since these beams are non-invariant under rotations.

Similarly to the torsional spring model, non-invariant beam deformation forces can only occur on immersed boundary points on the interior or the fiber structure, not the endpoints.

Target Points

Target points can be used to prescribe a preferred position or motion of the Lagrangian points. In this formulation, each Lagrangian point is associated with a *virtual* or target point. The boundary point is connected to its virtual target point via a stiff spring, i.e., a spring with zero resting length. Essentially the virtual point mandates where the target point should be. The deformation energy is given similarly to Eq.(3.81),

$$E_T(\mathbf{X}_M) = \frac{1}{2} k_T \left\| \mathbf{X}_M - \mathbf{X}_M^T \right\|^2, \quad (3.91)$$

where k_T is the target point stiffness and \mathbf{X}_M and \mathbf{X}_M^T are the coordinates of the physical Lagrangian point and virtual target point, respectively. Hence the corresponding deformation forces are given as

$$\mathbf{F}_T = -\frac{\partial E_T}{\partial \mathbf{x}_M} = -k_T \begin{pmatrix} x_M - x_M^T \\ y_M - y_M^T \end{pmatrix}. \quad (3.92)$$

Note that in both cases, it is standard for k_T to be very large in order to hold the Lagrangian points nearly rigid or move them in a prescribed manner based on updating the positions of the virtual nodes. Many scientists have used this formulation to prescribe motion in a variety of contexts [143, 172].

Massive Points

Artificial mass can be modeled on the fiber structure using an approach that is similar to target points. $\mathbf{Y}(r, t)$ gives the Cartesian coordinates of the *massive* points, with associated mass density $M(r)$. These points do not interact with the fluid directly and can be thought to be a virtual point. $\mathbf{X}(r, t)$ give the Cartesian coordinates of the Lagrangian boundary points which are massless and interact with the fluid. Recall that the boundary points also move at the local fluid velocity, and exert elastic deformation forces to the local fluid grid. If the massive points deviate from the Lagrangian boundary points, a restoring force will drive them back together.

The equations modeling this system are

$$\mathbf{F}_M = k_M(\mathbf{Y}(r, t) - \mathbf{X}(r, t)) \quad (3.93)$$

$$M(r) \frac{\partial^2 \mathbf{Y}(r, t)}{\partial t^2} = -\mathbf{F}_M - M(r)g\hat{e}_2, \quad (3.94)$$

where k_M is a stiffness coefficient with $k_M \gg 1$, and g is the acceleration due to gravity in direction \hat{e}_2 .

Note that the coupling is very similar to the target point formulation with the distinct difference that, rather than the movement of the massive points being prescribed, it is based on a constitutive equation, Eq.(3.94). Furthermore, gravity does not have to be applied in Eq.(3.94); rather, the system can be modeled by purely artificial mass alone without the influence of gravity.

A simple rendering of the massive point fiber model is depicted in Figure 3.9c. The Lagrangian boundary point and massive point, with Cartesian coordinates \mathbf{X} and \mathbf{Y} , are shown respectively, connected by a stiff virtual spring. Background fluid flow potential moves the massless point to a new position which exerts a pulling-like effect on the massive point. The massive point will move depending on the coupled constitutive equation given in Eq.(3.94).

Porosity

An interpretation of Darcy's Law is used to make the immersed structure permeable to fluid. In other words, the porous structure allows fluid to flow through it. Darcy's Law is a phenomenologically derived constitutive equation, which states the velocity of the fluid flowing through a porous medium is proportional to a pressure gradient of the two sides of the medium. This relation can be written as

$$U_p = -\frac{\kappa_p[p]}{\mu\sigma}, \quad (3.95)$$

where $U_p\hat{n}$ is the porous slip velocity and κ_p is the membrane permeability, μ is the fluid's dynamic viscosity, σ is the structure's thickness, $[p]$ is the pressure gradient across the boundary, and \hat{n} is a unit vector normal to the structure. However, the pressure jump may be simplified by first integrating across Eq.(3.72) to eliminate the singular forcing term and obtain jump conditions for the normal and tangential fluid stresses across the boundary, which can be simplified to reduce the pressure jump to

$$[p] = \frac{\mathbf{F} \cdot \hat{n}}{\|\mathbf{X}_r\|}, \quad (3.96)$$

as in [173],[174]. Hence the porous slip velocity is found to be

$$U_p = -\frac{\alpha\mathbf{F} \cdot \hat{n}}{\|\mathbf{X}_r\|}, \quad (3.97)$$

where $\alpha = \frac{\kappa_p}{\mu a}$ is the porous slip parameter and \mathbf{X}_r is the position of the porous Lagrangian structure. As stated in [173], since κ_p can be easily obtained from experiments, α can be easily found as well.

Once the Darcy porous slip velocity, e.g. Eq.(3.97), is found, Eq.(3.75) must be adjusted to account for the porosity

$$\mathbf{U}(\mathbf{X}(r, t), t) = -U_p\hat{n} + \int \mathbf{u}(\mathbf{x}, t)\delta(\mathbf{x} - \mathbf{X}(r, t))d\mathbf{x}. \quad (3.98)$$

This formulation was first described in [175] and the discretization used to find the normal vectors in *IB2d* can be found in A.3. An illustration of porosity is shown in Figure 3.9d, where incoming

fluid flow permeates a porous boundary. The amount of flow that moves through the body depends on the permeability parameter, α , associated with the membrane. All flow through the boundary is normal to the body itself.

Muscle-Fluid-Structure Models: FV-LT Model

The simple muscle model described in [146] has been incorporated into *IB2d*. This muscle model attempts to model both a force-velocity (FV) and length-tension (LT) relationship in muscle without coupling in the underlying cellular processes like calcium signaling, myosin cross-bridge attachment and detachment, or filament compliance.

The force a muscle can generate depends on the speed of muscle contraction; e.g., the faster a muscle shortens, the less force it generates. Traditionally a Hill model is used to describe this relationship and takes the following form [176, 177],

$$V_F = \frac{b(F_{max} - F)}{F + a}, \quad (3.99)$$

where V_F is the muscle fiber's shortening velocity, F is the force generated by the fiber, and F_{max} is the maximum load at zero contractile velocity. Parameters a and b can be determined experimentally and are related to the internal thermodynamics of the muscle. An example force-velocity curve is shown in Figure 3.10a.

The force a muscle fiber can generate is also known to be a function of its length. Initially when the thick filaments begin to bind to the thin filaments, the resulting force increases as the muscle shortens. However, if the muscle is contracted too far, there are fewer myosin heads to attach to the actin filaments, and the resulting force exerted is smaller. Hence the maximal muscle tension is generated between the two extremes, i.e., when the myosin heads are within reach of the thin filaments. An example length-tension curve is shown in Figure 3.10b where actin and myosin binding is depicted at varying muscle lengths. A simple model of a length-tension relationship is described in [178],

$$F_I = F_{IO} \exp \left[- \left(\frac{Q-1}{SK} \right)^2 \right], \quad (3.100)$$

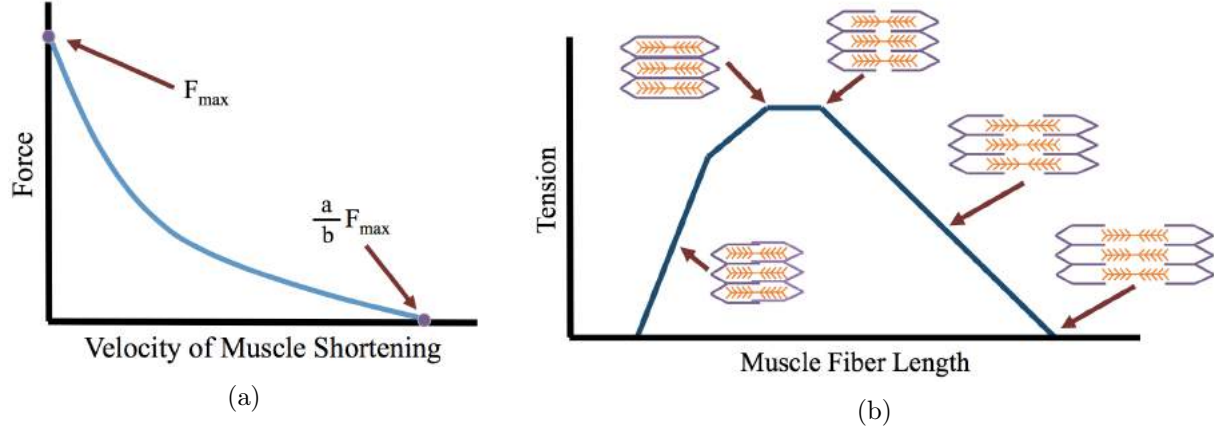


Figure 3.10: Example force-velocity and length-tension curves illustrating the respective relationships that the FV - LT model is trying to capture.

where $Q = \frac{L_F}{L_{FO}}$ is the ratio of the length of the muscle fibers to their length when they generate their maximum tension, F_I is the maximum isometric tension at a given fiber length L_F , F_{IO} is the maximum isometric force exerted at the optimum length of the muscle fibers, and SK is a parameter specific for each muscle. Note that these parameters can be determined experimentally.

An easy way to combine Eqs.(3.99) and (3.100) is to take the product of their normalized versions, as in [179, 146]. The resulting model is given by

$$F_{muscle}(L_F, V_F) = a_f \tilde{F}_{max} F_1(L_F) F_2(V_F), \quad (3.101)$$

where a_f is the activation strength of the muscle and \tilde{F}_{max} is the normalized maximum isometric force generated at the full activation of the muscle fibers at their optimum lengths, and $F_1(L_F)$ and $F_2(V_F)$ are normalized versions of Eqs.(3.99) and (3.100), given by

$$F_1(L_F) = \exp \left[- \left(\frac{L_F/L_{FO} - 1}{SK} \right)^2 \right], \quad (3.102)$$

$$F_2(V_F) = \frac{1}{F_{max}} \left[\frac{bF_{max} - aV_F}{b + V_F} \right]. \quad (3.103)$$

Muscle-Fluid-Structure Models: 3-Element Hill Model

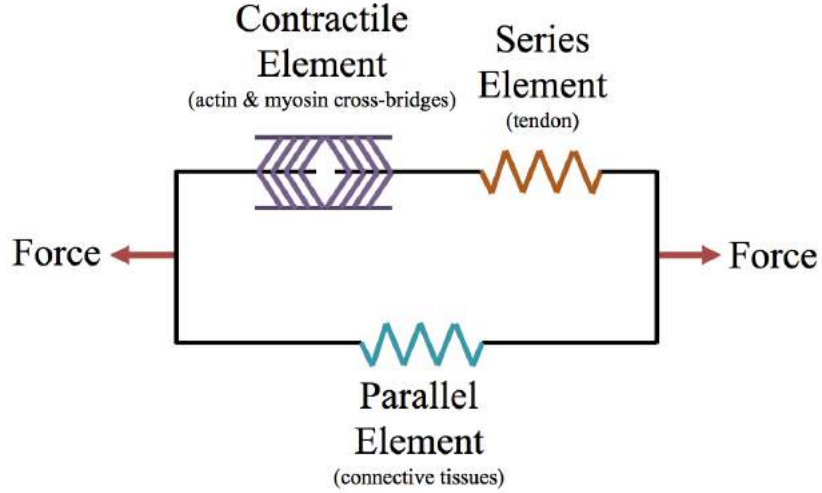


Figure 3.11: Schematic diagram of the 3-Element Hill model of muscle contraction, containing a contractile element, series element, and parallel element modeling actin and myosin cross-bridges, tendons, and connective tissues, respectively.

The 3-Element Hill model of muscle activation describes sustained muscle contraction by modeling the actin and myosin cross-bridges, muscle tendon, and connective tissues for a muscle. The model has a contractile element which models the force generated by the actin and myosin cross-bridges at the sarcomere level, and two non-linear spring elements, one in parallel and one in series with the contractile element. The series element models the muscle tendon, i.e., the intrinsic elasticity of the myofilaments, and has a soft tissue response and provides energy storing mechanism. The parallel element takes care of the passive behavior when the muscle is stretched, representing connective tissues with a soft tissue-like behavior. Furthermore, the contractile element is fully extensible when inactive but capable of shortening when activated [176, 177]. The 3-elements are depicted in Figure 3.11.

The net force-length properties of a muscle are a result of both the active (contractile element and series element) and passive (parallel element) components' force-length characteristics. If F_{CE} , F_{SE} , and F_{PE} represent the force produced by the contractile, series, and parallel elements respectively, their relations satisfy

$$F_{tot} = F_{SE} + F_{PE} \quad (3.104)$$

$$F_{CE} = F_{SE}, \quad (3.105)$$

where F_{tot} is the total force produced by muscle contraction. Furthermore the relations for muscle shortening are

$$L_{tot} = L_{CE} + L_{SE} = L_{PE}, \quad (3.106)$$

where L_{tot} is the total length of the muscle. Since the overall muscle length is conserved, if the series element is stretched, the contractile element must contract an equal amount.

As mentioned previously, to model the force produced from the series and parallel elements, we use non-linear springs, e.g.,

$$F_{SE} = k_{SE} (L - L_{CE})^n \quad (3.107)$$

$$F_{PE} = k_{PE} (L - L_{PE_R})^n, \quad (3.108)$$

where k_{SE} and k_{PE} are the spring stiffnesses for the series and parallel elements respectively, and L_{PE_R} is the resting-length of parallel element's non-linear spring. Note that the series element's spring has zero resting-length as it's length depends solely on the length of the contractile element. n is an integer assumed to be greater than or equal to 2. There are many ways to represent these elements; these are only one possible choice.

The contractile element assumes the length-tension and force-velocity relationship of muscle. For this reason, Eq.(3.101) is one possible choice for modeling its force generation, e.g.,

$$F_{CE} = a_f \tilde{F}_{max} F_1(L_{CE}) F_2(V_{CE}), \quad (3.109)$$

where L_{CE} is the length of the muscle fibers and V_{CE} is the contraction speed of the muscle fibers being represented in the contractile element. Another possible choice is described in [147].

User-defined Force Model

IB2d also allows the option for the user to define their own force model. The user has control in how they define their model as well as what Lagrangian points are involved, as many items are passed into the model automatically, such as the current and previous position of the Lagrangian points, current time, time-step, etc, and also includes the functionality for the user to read in appropriately

chosen data for parameters, etc.

Incorporated Models In this section, we will describe inclusions within the current *IB2d* software that are in addition to the fiber and material property models. Currently the following capabilities have been added to the framework:

1. Tracer particles
2. Concentration gradients of a chemical (advection-diffusion)
3. Background flow profiles (artificial forcing)
4. Basic electrophysiology frameworks
5. Boussinesq Approximation

These models are incorporated either by additional forcing terms in Eq. (3.72) (background flow profiles), a constitutive equation that depends on $u(\mathbf{x}, t)$ without affecting the fluid momentum itself (tracers and concentration gradients), or by coupling into a specific fiber model (electrophysiology).

Tracers

Tracers are neutrally buoyant particles that move at the local fluid velocity. They have no impact on the fluid motion themselves, but rather “go with the flow.” If a tracer’s position is given by \mathbf{X}_{tr} , their equation of motion is solely given by

$$\frac{d\mathbf{X}_{tr}}{dt} = u_{tr}(\mathbf{x}, t), \quad (3.110)$$

where $u_{tr}(\mathbf{x}, t)$ is the background fluid velocity interpolated to the tracer particle. Tracers are useful to observe the fluid motion during a simulation. The tracers move in the simulation by harnessing the discrete delta functions to interpolate the velocity of the exact position of the tracer.

Concentration Gradients

Similar to tracers, concentration gradients can be used to observe the motion of the underlying fluid; however, this model also incorporates diffusion. Rather than observing individual particles advect and diffuse, a concentration gradient is given as a continuum, c , which then gets spread out by an advection-diffusion constitutive equation,

$$\frac{\partial c}{\partial t} + \mathbf{u}(\mathbf{x}, t) \cdot \nabla c = D \Delta c, \quad (3.111)$$

where D is the diffusivity coefficient. We note that D is a constant in this formulation, there are no sources or sinks, and that \mathbf{u} is, of course, assumed to be incompressible. The details of the numerical solver are found in A.5.

We also include functionality for incorporating the Boussinesq approximation to couple the advection-diffusion equation to forces [180, 181].

Background Flow Profiles (Artificial Forcing)

Although the computational domain is assumed to have periodic boundaries, one can induce a desired background flow profile by artificially adding a force onto the fluid, realized as an additional forcing term on Eq.(3.72).

Essentially, the additional force will be a penalty-type term, which exerts a force onto a desired subset of the fluid grid, if the fluid velocity does not match the desired flow profile. Such a forcing term can take the form

$$\mathbf{F}_{arb} = k_{arb} (\mathbf{u}(\mathbf{x}, t) - \mathbf{u}_{flow}(\mathbf{x}, t)), \quad (3.112)$$

where k_{arb} is the penalty-strength coefficient, and $\mathbf{u}_{flow}(\mathbf{x}, t)$ is the desired background flow profile as in [26, 172], where it was used to create parabolic inflow into a channel along the x -direction, i.e.,

$$\mathbf{u}_{flow}(\mathbf{x}, t) = \begin{pmatrix} U_{max} \left(1 - \left(\frac{0.5-x}{d/2} \right)^2 \right) \\ 0 \end{pmatrix}. \quad (3.113)$$

We note this idea has also been used when a preferred mode of active force is desired [182, 183, 184].

This idea is illustrated in Figure 3.12, where the fluid grid is given by a rectangular grid with

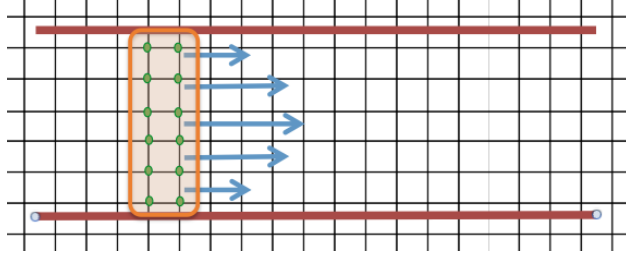


Figure 3.12: A depiction of exerting an arbitrary force onto the background fluid grid to obtain the desirable flow profile. The fluid grid is given by the rectangular grid with the selected grid points to enforce the penalty-force highlighted and circled in green and orange. The penalty force is applied to the fluid lattice points in green if the flow profiles do not match at those selected nodes. A cartoon rendering of the resulting flow is illustrated as the blue arrows.

the selected grid points to enforce the penalty-force highlighted and circled in green and orange, respectively. The penalty force is applied to those green fluid lattice points if the flow profiles do not match at those selected nodes. An example rendering of the resulting flow is illustrated as the blue arrows, if the desired flow profile is parabolic. Note that this addition of momentum (energy) into the system is not an issue, because of the assumed periodic boundary conditions.

Electrophysiology

A basic model of action potential propagation is incorporated using the FitzHugh-Nagumo equations (FHN) to model the system. FHN is a reduced order model of the Hodgkin-Huxley equations, which were the first equations to describe the propagation of an electrical signal along excitable cells. FHN has been incorporated into fluid-structure interaction models before [22]. The governing equations are given as

$$\frac{\partial v}{\partial t} = \mathbb{D}\nabla^2 v + v(v - v_a)(v - 1) - w - \mathbb{I}(t) \quad (3.114)$$

$$\frac{\partial w}{\partial t} = \epsilon(v - \gamma w), \quad (3.115)$$

where $v(x, t)$ is the membrane potential, $w(x, t)$ is the blocking mechanism, \mathbb{D} is the diffusion rate of the membrane potential, v_a is the threshold potential, γ is the resetting rate, ϵ is the blocking strength parameter, and $\mathbb{I}(t)$ is an applied current, e.g., an initial stimulus potentially from pacemaker signal activation. Note that v is the action potential and that w can be thought to model a sodium

blocking channel.

Once the membrane potential is found, it must be interpolated to the Lagrangian grid. Action potential propagation can only then be used to activate pumping or initiate motion to which induces deformations of the structure to model desired biological or physical phenomena. Coupling the action potential to the generation of force can be done in many different ways for various applications, such as for cardiac contraction [185, 22, 95] or locomotion [186, 187, 145].

Boussinesq Approximation

The Boussinesq approximation is incorporated into *IB2d* to model fluctuations in the dynamics of both a concentration gradient (background field) and the momentum equation. The Boussinesq approximation can be thought of as an approximation to a variable density field, where the essence is that any differences in inertia are negligible, but gravity is strong enough to make the specific weight appreciably different between two fluids.

In general the approximation ignores density differences, except where they are multiplied by a gravitational acceleration field, \mathbf{g} . It assumes that density variables have no effect on the fluid flow field, only that they give rise to buoyancy forces. By using the Boussinesq approximation, one bypasses the issue of having to solve the fully compressible Navier-Stokes equations for certain applications.

The extra forcing term on the incompressible Navier-Stokes equations (3.72)-(3.73) are of the form

$$\mathbf{f}_{Bouss} = \alpha_B \rho \mathbf{g} C, \quad (3.116)$$

where α_B is the expansion coefficient, e.g., thermal expansion, etc., ρ is the density of the fluid, \mathbf{g} is the gravitational field, and C is the background concentration. When implementing the Boussinesq approximation, the Navier-Stokes equations then take the form,

$$\rho \left(\frac{\partial \mathbf{u}(\mathbf{x}, t)}{\partial t} + \mathbf{u}(\mathbf{x}, t) \cdot \nabla \mathbf{u}(\mathbf{x}, t) \right) = -\nabla p(\mathbf{x}, t) + \mu \Delta \mathbf{u}(\mathbf{x}, t) + \mathbf{f}(\mathbf{x}, t) + \alpha_B \rho \mathbf{g} C \quad (3.117)$$

$$\nabla \cdot \mathbf{u}(\mathbf{x}, t) = 0. \quad (3.118)$$

We note that these models have been incorporating into immersed boundary frameworks before, see [188, 138, 189].

3.3.3 *IB2d* Work Flow

We will now briefly describe the typical work flow for using the *IB2d* software. Both MATLAB and Python have their own respective directories which in turn contain two folders: "Examples" and "IBM_Blackbox". The Examples folder contains all currently implemented simulation examples including the necessary input files to run each simulation, with each example organized in its own folder. The IBM_Blackbox folder contains all methods for solving the fluid-structure interaction problems. The software is set up such that the user will not have to change the underlying mechanics of the immersed boundary method unless they wish to make additions to the algorithm, e.g., implementing more fiber models, etc.

Vectorized functions were used in solving the Navier-Stokes equations, i.e., updating the fluid velocities, and throughout *IB2d* when appropriate. At this time *IB2d* uses only built-in MATLAB functions for the MATLAB implementation and the Python 3 implementation uses the standard python library, as well as, packages numpy, matplotlib, numba, and pandas in its implementation.

Inside an example sub-directory, there are multiple files. Two files that must be in every example are *input2d* and *main2d*. *input2d* is the file where the user chooses all parameters required for a simulation, i.e., the fluid parameters, temporal information, grid parameters, fiber model construction, how to save the data, etc. *main2d* will read in this file and then read in the corresponding input files associated with the choices selected in *input2d*. A graphical description of *input2d* is given in Figure 3.13.

After setting desired parameters and selecting the necessary flags in *input2d*, assuming the user has the appropriate associated input files corresponding to those selections the simulation is started by calling the *main2d* script. This script reads in all the information from *input2d* and passes it to the *IBM_Driver* script. Once the simulation finishes, a visualization folder, viz_IB2d, will have all the Lagrangian structure and dynamical data from the simulation in .vtk format [190]. .vtk files can be visualized using Paraview [191] or VisIt [192].

Each fiber model has an associated input file type, with the first line being the number of total


```

1 ***** INPUT2d FILE: *****
2 ***** DO NOT SWAP ROWS OR ELSE THERE WILL BE ERRORS! *****
3 ***** KEEP SPACES BETWEEN '='s! *****
4
5 % FLUID PARAMETER VALUES %
6 mu = 0.1 % Dynamic Viscosity (N*s/m^2)
7 rho = 1 % Density (kg/m^2)
8
9 % TEMPORAL INFORMATION %
10 Tfinal = 0.4 % Final time of simulation (s)
11 dt = 2.5e-6 % Time-step (s)
12
13 % GRID PARAMETERS / INFORMATION %
14 Nx = 128 % # of Eulerian Grid Pts. in x-Direction (MUST BE EVEN!!!)
15 Ny = 128 % # of Eulerian Grid Pts. in y-Direction (MUST BE EVEN!!!)
16 Lx = 1.0 % Length of Eulerian Grid in x-Direction (m)
17 Ly = 1.0 % Length of Eulerian Grid in y-Direction (m)
18 supp = 4 % Choose dirac-delta support (KEEP IT EVEN!!!)
19
20 % LAGRANGIAN STRUCTURE MODEL INFORMATION %
21 springs = 0 % 0 (for no) or 1 (for yes)
22 update_springs = 0 % 0 (for no) or 1 (for yes)
23 target_pts = 1 % 0 (for no) or 1 (for yes)
24 update_target = 1 % 0 (for no) or 1 (for yes)
25 beams = 0 % 0 (for no) or 1 (for yes)
26 update_beams = 0 % 0 (for no) or 1 (for yes)
27 FV_LT_muscle = 0 % 0 (for no) or 1 (for yes) % Force-Velocity & Length-Tension Model
28 3_element_muscle = 0 % 0 (for no) or 1 (for yes) % Hill 3-Element Model w/ FV-LT Model
29 arb_ext_force = 0 % 0 (for no) or 1 (for yes)
30 tracers = 0 % 0 (for no) or 1 (for yes)
31 mass_pts = 0 % 0 (for no) or 1 (for yes)
32 gravity = 0 % 0 (for no) or 1 (for yes) %PLEASE CHECK GRAVITY VECTOR BELOW
33 x_gravity_vec_comp = 0 % x-Component of Gravity Vector
34 y_gravity_vec_comp = -1 % y-Component of Gravity Vector
35 porous_media = 0 % 0 (for no) or 1 (for yes)
36 concentration = 0 % 0 (for no) or 1 (for yes)
37 electro_phys = 0 % 0 (for no) or 1 (for yes)
38
39
40 % PRINTING INFORMATION
41 print_Dump = 1000 % How often to print (PLOT) to screen
42 plot_Matlab = 0 % Plot in Matlab? (1=YES, 0=NO)
43 plot_LagPts = 1 % Plot Lagrangian Points ONLY in Matlab
44 plot_Velocity = 1 % Plot Lagrangian Points + VELOCITY FIELD in Matlab
45 plot_Vorticity = 1 % Plot Lagrangian Points + VORTICITY colormap in Matlab
46 plot_MagVelocity = 1 % Plot Lagrangian Points + MAGNITUDE OF VELOCITY colormap in Matlab
47 plot_Pressure = 1 % Plot Lagrangian Points + PRESSURE colormap in Matlab
48
49 % LAGRANGIAN STRUCTURE NAME %
50 string_name = dear_KC % String name for simulation (NO QUOTATIONS ARE NECESSARY!!!)
51

```

Fluid parameter values

Time-stepping information

Grid parameters
(size and resolution)

Lagrangian fiber model
selection
(where to declare what type
of fibers and other model
attributes are to be
implemented)

How data is to be saved

Lagrangian structure name

Figure 3.13: Descriptions of selections in *input2d*. This file controls what inputs get passed to the main *IB* driver method.

fiber points associated with that type. If the immersed structure is called “struct”, the possible file types are as follows

- **struct.vertex**: A list of all the (X, Y) initial coordinates of the Lagrangian points

1	N_{Lag}	
2	x-Vertices	y-Vertices
\vdots	\vdots	\vdots

Figure 3.14: Input format for the .vertex file

- **struct.spring**: A list of the master and slave nodes for each linear spring along with their associated spring stiffness, resting-length, and degree of non-linearity. Note that if using only Hookean springs, the degree of non-linearity can be omitted and *IB2d* will automatically assume linear springs.

1	$N_{springs}$				
2	Lag. ID _{master}	Lag. ID _{slave}	Spring Stiffness, k_{spr}	Resting Length, R_L	Deg. of Nonlinearity, β
\vdots	\vdots	\vdots	\vdots	\vdots	\vdots

Figure 3.15: Input format for a .spring file

- **struct.beam**: A list of the left, middle, and right Lagrangian indices associated with each torsional spring (beam) and their associated beam stiffness and curvature.

1	N_{beams}				
2	Lag. ID _L	Lag. ID _M	Lag. ID _R	Beam Stiffness, k_b	Curvature, C
\vdots	\vdots	\vdots	\vdots	\vdots	\vdots

Figure 3.16: Input format for a .beam (torsional spring) file

- **struct.target**: A list of all target point indices with their associated target point stiffness.

1	N_{target}	
2	Lag. ID	Target Pt. Stiffness, k_T
\vdots	\vdots	\vdots

Figure 3.17: Input format for a .target file

- **struct.mass**: A list of all Lagrangian mass point indices along with their associated mass-spring stiffness and mass.

1	N_{mass}			
2	Lag. ID	Mass Pt.	Stiffness, k_M	Mass (kg)
\vdots	\vdots		\vdots	\vdots

Figure 3.18: Input format for a .mass file

- **struct.porous:** A list of all porous Lagrangian points, along with their associated porosity coefficient, α , and their Stencil ID.

1	N_{porous}			
2	Lag. ID	Porosity Coefficient, α	Stencil ID	
\vdots	\vdots	\vdots	\vdots	

Figure 3.19: Input format for a .porous file

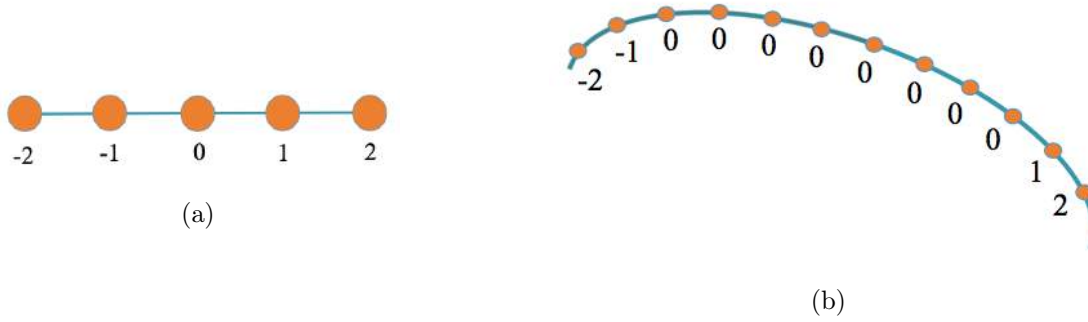


Figure 3.20: (a) Order of porous stencil IDs. (b) An example of how the stencil IDs are defined using the porous structure from Figure 3.9d.

Note: the stencil ID is an integer between $\{-2, -1, 0, 1, 2\}$, which declares which points around the node of interest will be used in the derivative calculations. For porosity, you need a minimum of 4 nodes surrounding the porous node. This idea is illustrated in Figure 3.20, which shows how a group of 5 porous stencil IDs would be labeled and an example of how they would be labeled in practice for a toy example.

- **struct.muscle:** A list of all *FV-LT* muscle master and slave node Lagrangian indices, along with their associated muscle length in which the fibers generate their maximum tension (L_{FO}), *SK*-parameter, thermodynamic parameters, a and b , respectively, and the muscle's maximum load at zero contractile velocity (F_{max}).

1	$N_{FV-LT}^{muscles}$								
2	Lag.	ID _{Master}	Lag.	ID _{Slave}	L_{FO}	SK	a	b	F_{max}
\vdots	\vdots	\vdots	\vdots	\vdots	\vdots	\vdots	\vdots	\vdots	\vdots

Figure 3.21: Input format for a .muscle (FV-LT muscle) file

- **struct.tracer:** A list of all tracer particles' initial coordinates, (X, Y) .

1	$N_{tracers}$	
2	x-Vertices	y-Vertices
\vdots	\vdots	\vdots

Figure 3.22: Input format for a .tracer file

- **struct.user_force:** The user has the functionality to define this input file appropriately as they desire. It is our hope that they would treat this like the previous fiber model input files.

These file formats are consistent with those necessary to run simulations in IBAMR, making this software an appropriate learning and analysis tool before scaling up to larger and more highly resolved simulations.

3.3.4 Selected *IB2d* Examples

In this section we will present some examples which show some of the software's functionality. The software currently contains over 50 examples built-in; we will choose some that highlight specific features of the software.

- The Rubber-band
- The Flexible Beam
- The "Date"
- Falling Spheres under Gravity vs. Pulsatile Flow
- Idealized Swimmer
- HeartTube with Electrophysiology and Calcium Dynamics

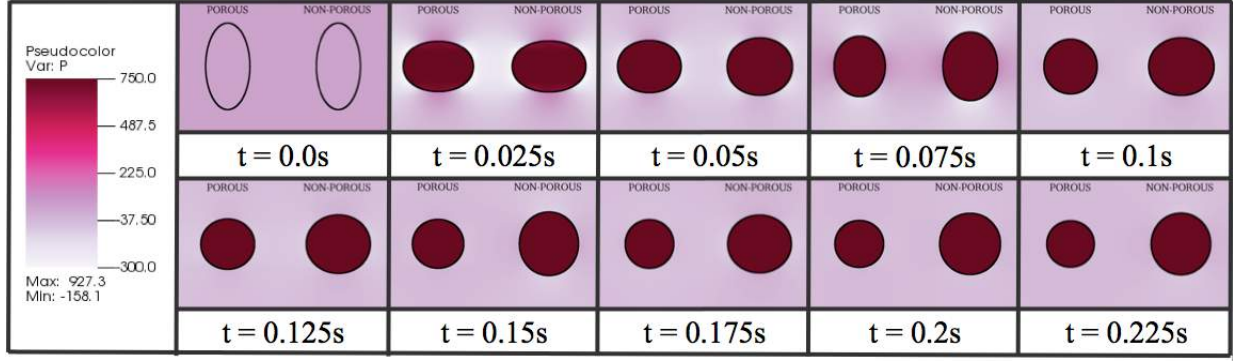


Figure 3.23: A comparison of a porous rubberband (left) and a non-porous rubberband (right) done in a single simulation. The colormap is of the fluid pressure. It is clear that both rubberbands start stretched from their equilibrium position, but end at a circle; however, the porous rubberband does not conserve the same volume, as fluid flows through it as the simulation progresses.

The Rubber-band The rubber-band is one of the quintessential problems in FSI. The band is composed of springs between adjacent nodes, all with a preferred resting length of zero and constant spring stiffness. We will model two such rubber-bands with equivalently perturbed initial states, but the rubber-band on the left will be porous at each Lagrangian node to show how fluctuations cause it to lose volume over time. In summary, the fiber models used are:

- Linear Springs
- Porosity (non-traditional rubber-band)

The simulation starts with the rubber band stretched into an elliptical shape with a fixed volume of fluid trapped within the elastic band. The resting lengths were chosen to be zero, as to drive the rubber bands toward their lowest energy state, which minimizes length for a given internal area, i.e., a circle. As the band moves toward this equilibrium position, it will contract and expand periodically across the semi-major and semi-minor directions of the axis. In the case of the porous rubber-band, it will also shrink in size. Simulation images are shown in Figure 3.23.

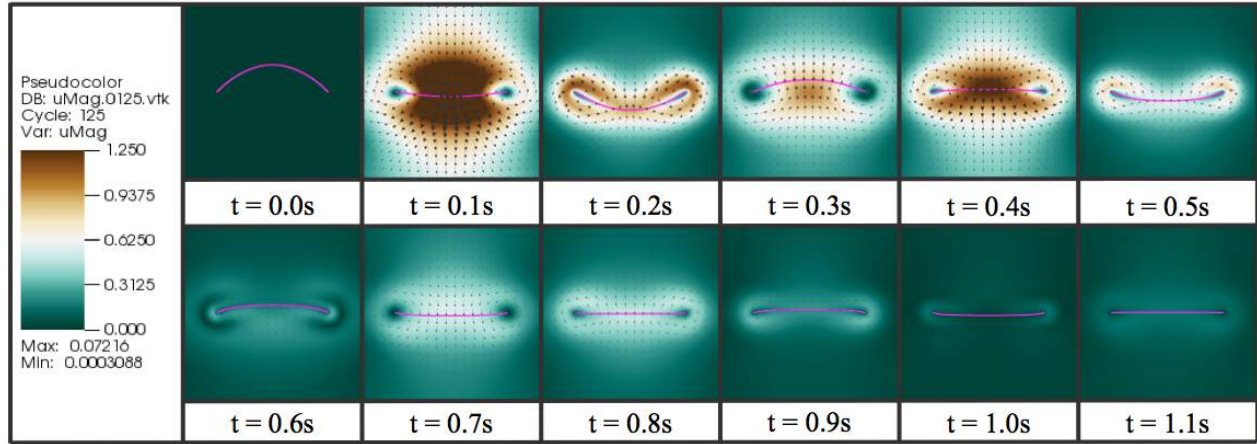


Figure 3.24: The flexible beam shown at various times during the simulation. The colormap is of the magnitude of velocity and is depicted along with the background fluid velocity vectors.

The Flexible Beam The flexible beam is another standard problem in FSI. It includes a “beam” composed of adjacent torsional springs between three successive nodes and tethered to two fixed points at the ends of the beam, modeled using target points. The torsional springs all have a preferred ‘curvature’ of zero, making any perturbation in the geometry move towards a straight line. The fiber models implemented are:

- Torsional Springs
- Target Points (fixed)

The simulation starts with the beam having been perturbed from its equilibrium position by an ellipsoidal arc. Since the preferred torsional spring ‘curvature’ is zero, the torsional springs will move the system towards an equilibrium where they all line up. Since the ends of the beam are fixed horizontally from each other, the lowest energy state of the system will be when the beam forms a horizontal line between the two end points. Time-slices from the simulation are illustrated in Figure 3.24.

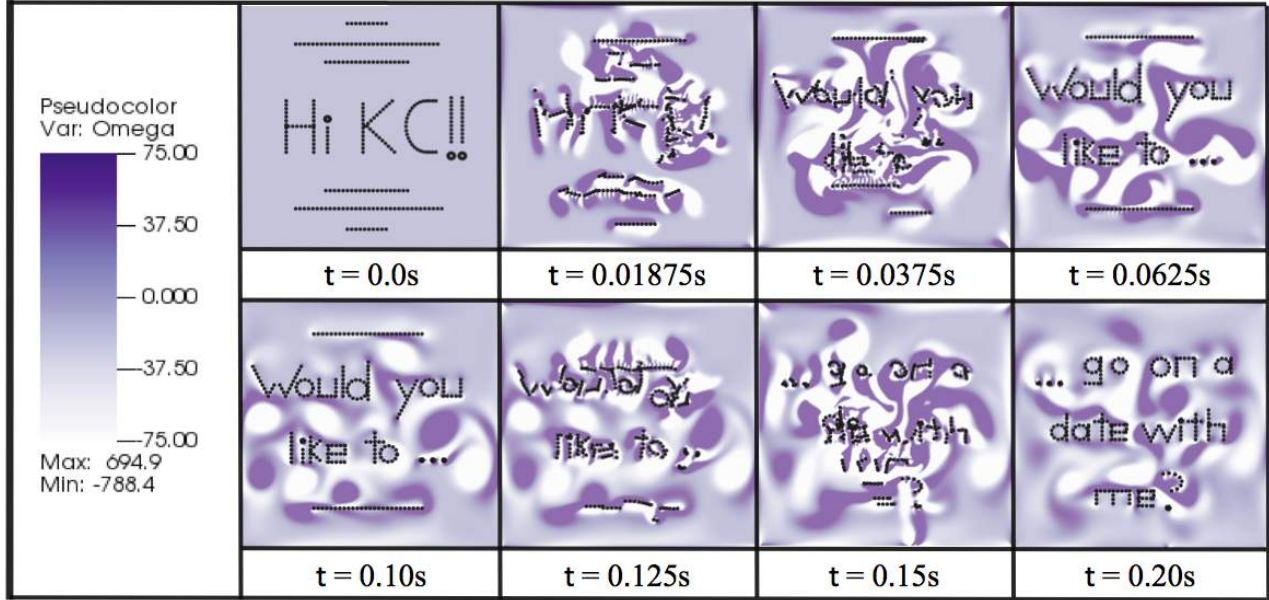


Figure 3.25: “The Date” example shows target points moving around the computational domain by interpolating positions between three states which spell out certain phrases. The background color map is vorticity.

The “Date” The “Date” illustrates the software’s ability to update target point positions. Every Lagrangian point in this simulation is modeled as a target point and is given a specific location. As the simulation progresses, Lagrangian point positions are moved to new prescribed positions via an interpolation function, implemented within *update_target_point_positions*. The fiber models used are:

- Target Points (with dynamically updating positions)

The simulation starts in a configuration that spells out “Hi KC!!” enclosed within a square of Lagrangian points with a few other lines of Lagrangian points in decor. As the simulation progresses, those Lagrangian points are interpolated to their next prescribed configuration, spelling “Would you like to...”. Finally, they move to their final configuration, spelling “... go on a date with me?” Snapshots of the simulation are illustrated in Figure 3.25.

As stated before, the script *update_target_point_positions* was used to dynamically update the position of the target points. Furthermore, within this script, one could also change any of the target point parameters, i.e., target point tethering stiffnesses or position.

Similarly, other scripts can be used to dynamically update parameters of springs and/or torsional

springs as a simulation progresses, e.g., ‘*update_springs*’ and ‘*update_beams*’. In the case of springs, one can update the spring stiffnesses, resting-lengths, or even non-linearity properties (see *Example_HeartTube*), and in the case of torsional springs one can update their torsional spring stiffness or preferred ‘curvature’ (See *Example_Jellyfish*). The stiffnesses, resting-lengths, curvatures, etc., can be spatially or time-dependent and appropriately set in the ‘*update_springs*’ or ‘*update_beams*’ scripts.

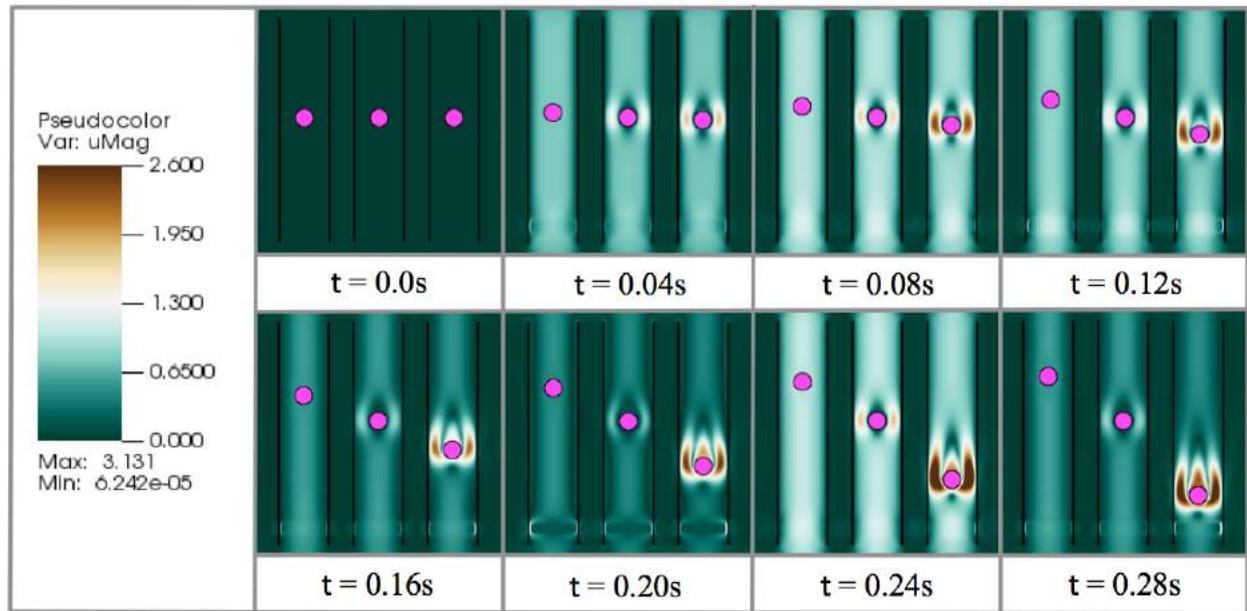


Figure 3.26: 3 spheres of different masses, with each sphere composed of uniform mass points, under the influence of gravity with a pulsatile flow competing against gravity upwards. The sphere on the left is the lightest and sphere on the right is the heaviest. In the left case, the pulsatile flow dominates, while on the right gravity dominates, and in the middle, the pulsatile flow and gravitational forces are approximately equivalent. The colormap depicts magnitude of velocity.

Falling Spheres under Gravity vs. Pulsatile Flow This example simulates a competition between spheres falling under gravity and upward flow, which acts to help the spheres resist gravity. There are three vertical channels composed of fixed target points. In each channel there is also a sphere, composed of stiff springs and stiff torsional beams between each adjacent Lagrangian node. Each point on the sphere has an associated mass with gravity pointed in the downward vertical direction. There is also a net prescribed flow upwards, arising from an artificial force directly applied onto the Eulerian (fluid) grid. The fiber models and functionality used are:

- Linear Springs
- Torsional Springs
- Target Points (fixed)
- Massive Points
- Artificial Forcing on the Fluid Grid

The simulation begins with three spheres of different masses. Each sphere is itself composed of individual uniform mass points; however, the individual mass points differ from sphere to sphere. Gravity is acting on the masses to pull them downward while upward flow is providing a force in the opposite direction. In one case, the flow dominates, in another gravity is balanced by the imposed flow, and in the other case, gravity is dominant. This is illustrated in Figure 3.26.

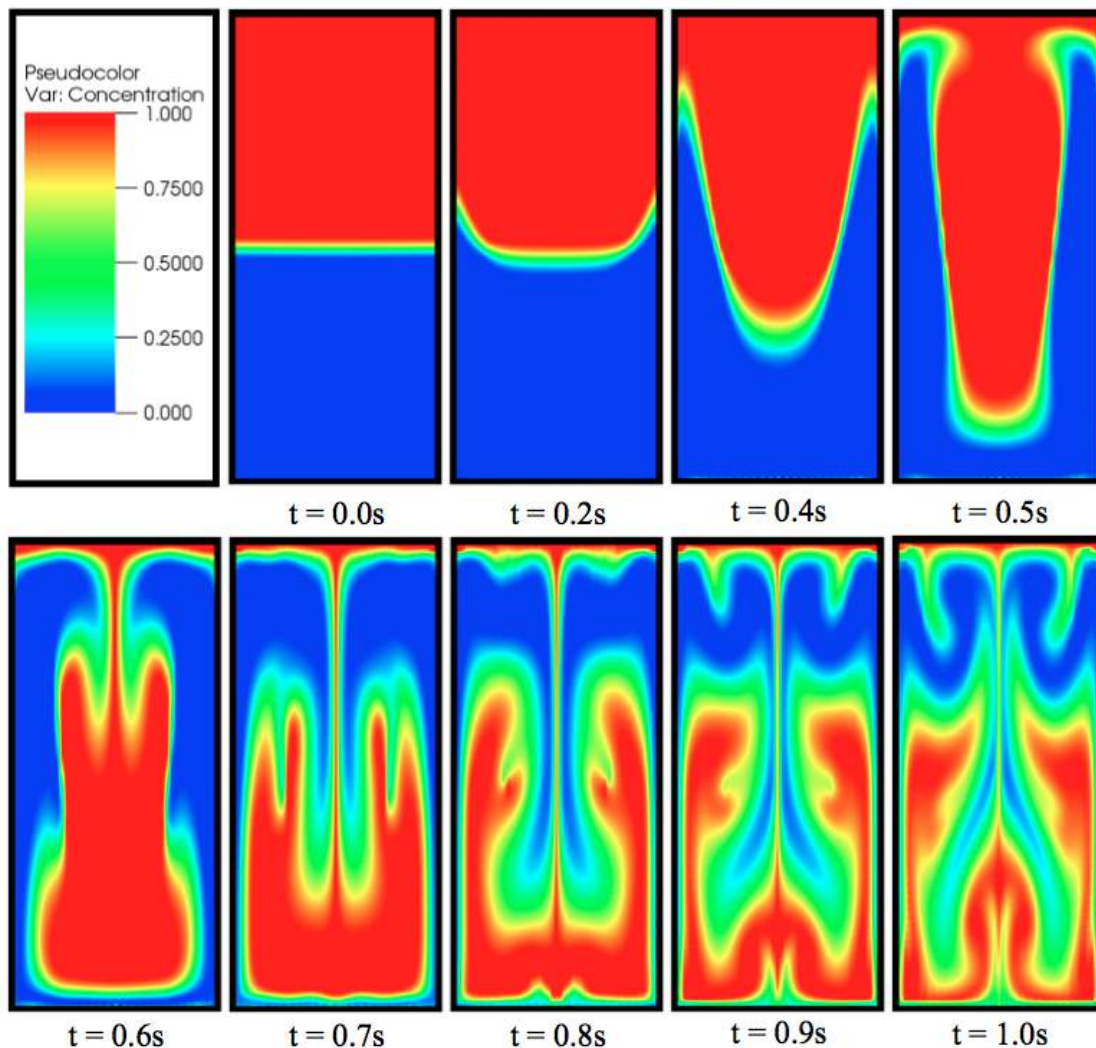


Figure 3.27: Simulation of the Rayleigh-Taylor Instability using the Boussinesq Approximation. A heavier fluid (red) sits above a lighter fluid (blue). Note a more sophisticated advection-diffusion solver will give rise to higher resolution of the instability fronts.

Rayleigh-Taylor Instability This example uses the Boussinesq Approximation to model the Rayleigh-Taylor Instability. The instability manifests itself at the interface between two fluids of different densities when the lighter fluid begins pushing the heavier fluid. The model itself only uses target points to bounday the fluids in a rectangular domain, concentration gradients, and the Boussinesq approximation frameworks. Hence the fiber models and functionality used are:

- Target Points (fixed)
- Background Concentration (advection-diffusion)

- Boussinesq Approximation (with gravity flag)

The simulation begins when a heavier fluid (red) is placed over a lighter fluid (blue) with a linear change in concentration at the interface. The lighter fluid begins pushing itself upwards while the heavier fluid falls downward, resulting in the instability. The dynamics can be seen in Figure 3.27. Note a more sophisticated advection-diffusion solver will give rise to higher resolution of the instability fronts. Operator splitting methods [193] and flux limiters [194] are currently being implemented.

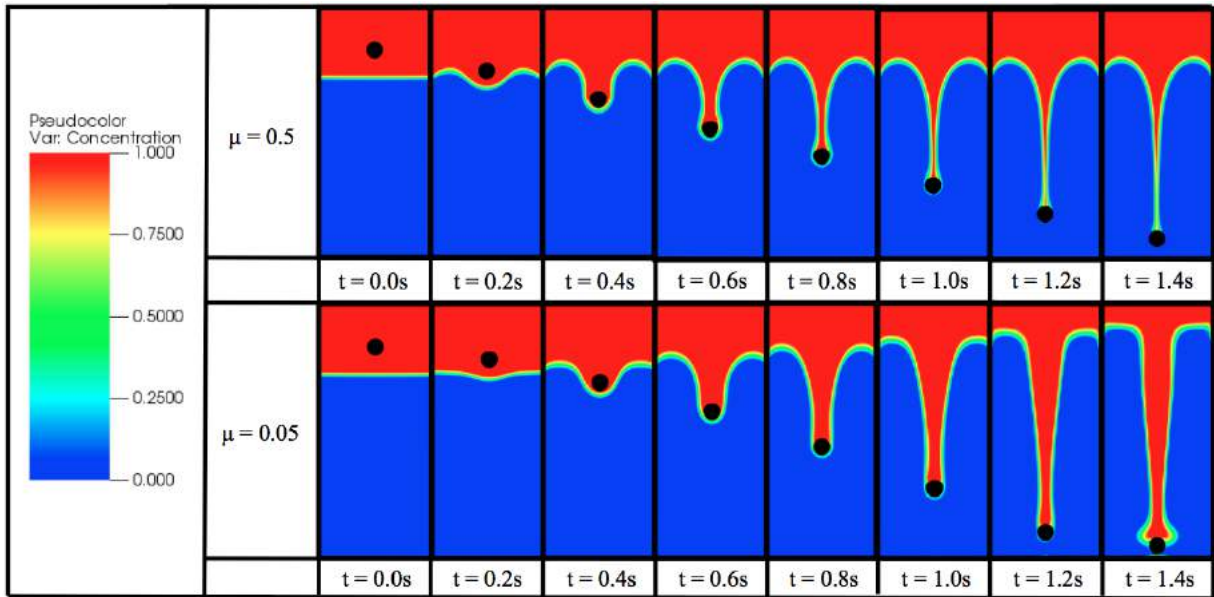


Figure 3.28: Simulation of a falling sphere through a fluid with a background salinity stratification. A spherical mass is released in the lighter salinity background (red) that sits above a heavier background salinity (blue) and the mass falls due to gravity.

Falling Sphere with Boussinesq Approximation This example uses massive points to model a sphere that is released in a lighter salinity background and then falls into the heavier salinity portion. The sphere is composed of massive points along the boundary, springs connecting adjacent Lagrangian points and the associated Lagrangian point across the sphere, and beams around adjacent points on the sphere. The domain itself is composed of target points. Hence the fiber models and functionality used are:

- Springs (linear)

- Beams (torsional springs)
- Target Points (fixed)
- Massive Points (w/ gravity)
- Background Concentration (advection-diffusion)
- Boussinesq Approximation (with gravity flag)

When the sphere begins falling, it sphere entrains some of the lighter salinity concentration around, carrying the lighter fluid downward. Two cases are compared corresponding to different ambient fluid viscosities. The sphere in the less viscous fluid falls faster than the higher viscosity case, and it also entrains more of the lighter salinity concentration.

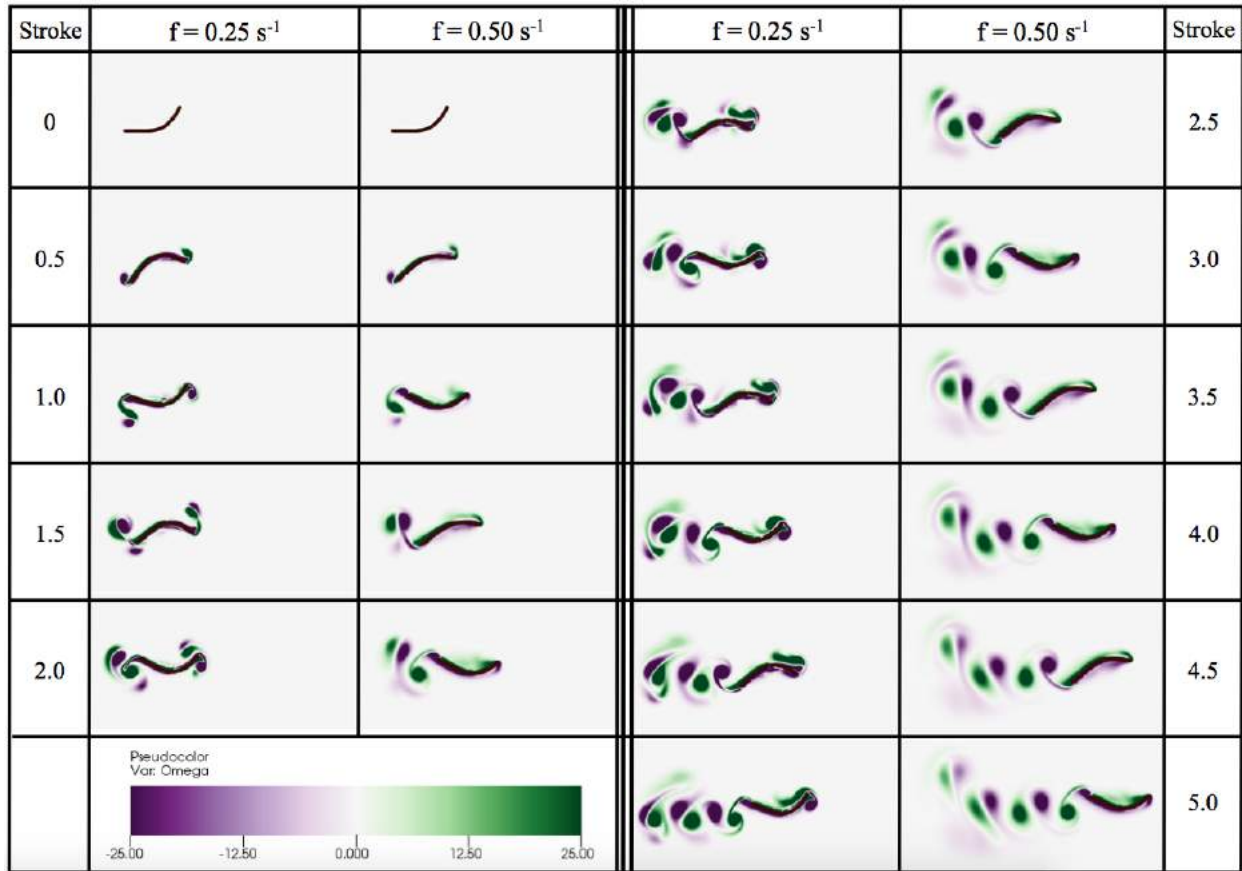


Figure 3.29: A comparison of two idealized anguilliform swimmers moving forward due to continually changes in the preferred curvature of the configuration. One has a stroke frequency of $f = 0.25 \text{ s}^{-1}$ and the other, $f = 0.5 \text{ s}^{-1}$. The colormap illustrates vorticity.

Idealized Anguilliform Swimmer This example uses non-invariant beams and dynamically updates the preferred beam curvature through the ‘*update_nonInv_Beams*’ script to move forward. The model also uses linear springs to connect successive Lagrangian points and all successive Lagrangian points are connected by non-invariant beams. The following fiber models were used:

- Linear Springs
- Non-Invariant Beams

The motion is completely induced by changing the preferred curvature. Within the ‘*update_nonInv_Beams*’, the curvature is changed by interpolating through two different configurative phases of the swimmer, more specifically their associated curvatures of each phase. The swimming motion is illustrating in Figure 3.29. Those phases are shown below,

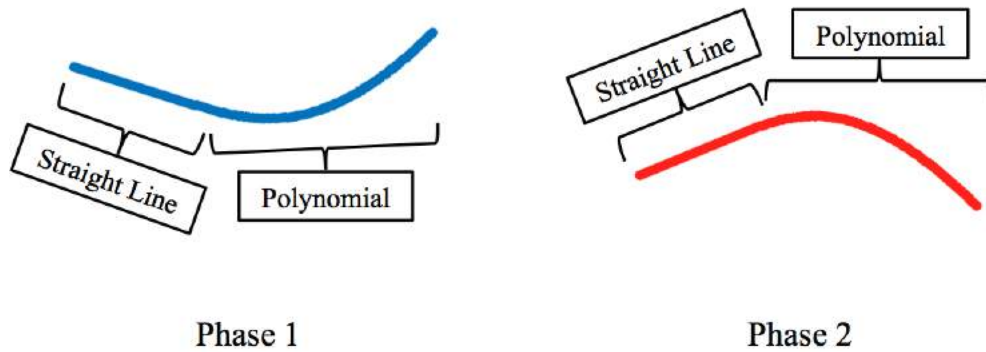


Figure 3.30: The two phases, in which, the preferred curvature was interpolated between to cause forward swimming.

Using the Data Analysis package in *IB2d*, which is described in Section 3.3.5, a comparison of distances swam by each swimmer as a function of the number of strokes is shown. The swimmer with the slower stroke frequency performs better.

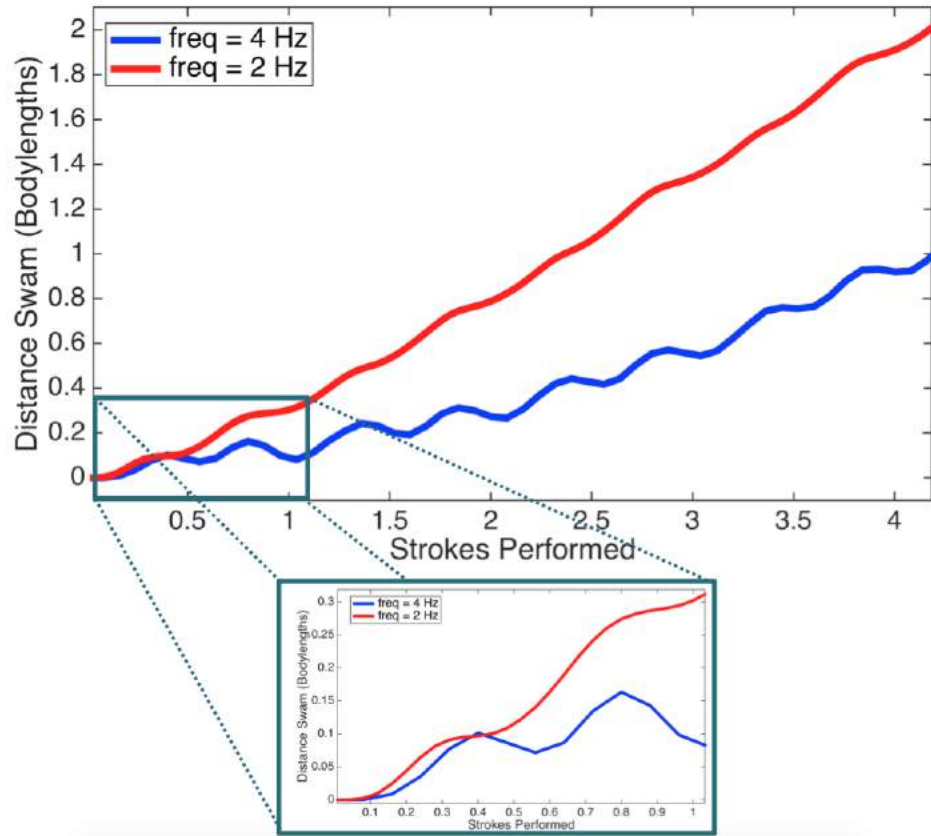


Figure 3.31: A comparison of the distances swam by both swimmers as a function of the number of strokes.

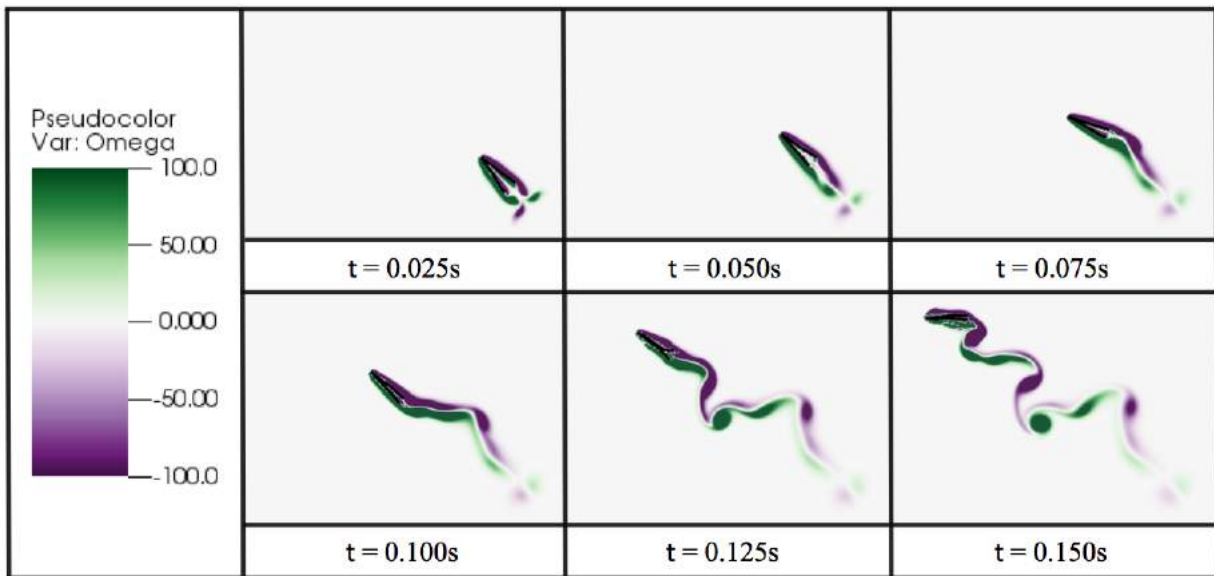


Figure 3.32: An idealized swimmer moving forward and turning due to the asynchronous muscle activation. The colormap illustrates vorticity.

Idealized Muscle Swimmer This example uses the 3-element Hill muscle model to cause an idealized swimmer, shaped like a V , to move forward and turn. There are stiff linear springs and stiff torsional springs connecting all adjacent Lagrangian points. Only 3 muscles connect one leg of the V to the other, and are equally spaced at intervals $3L/10$, $2L/5$, and $9L/10$ down the leg of the swimmer, where L is the length of each leg. The fiber models used are:

- Linear and Non-Linear Springs
- Torsional Springs
- 3-Element Hill Model

The simulation begins with the swimmer in a V -shaped starting position at rest. Throughout the simulation the muscles fire out of phase, causing the swimmer to move forward and turn. The swimming behavior is shown in Figure 3.32.

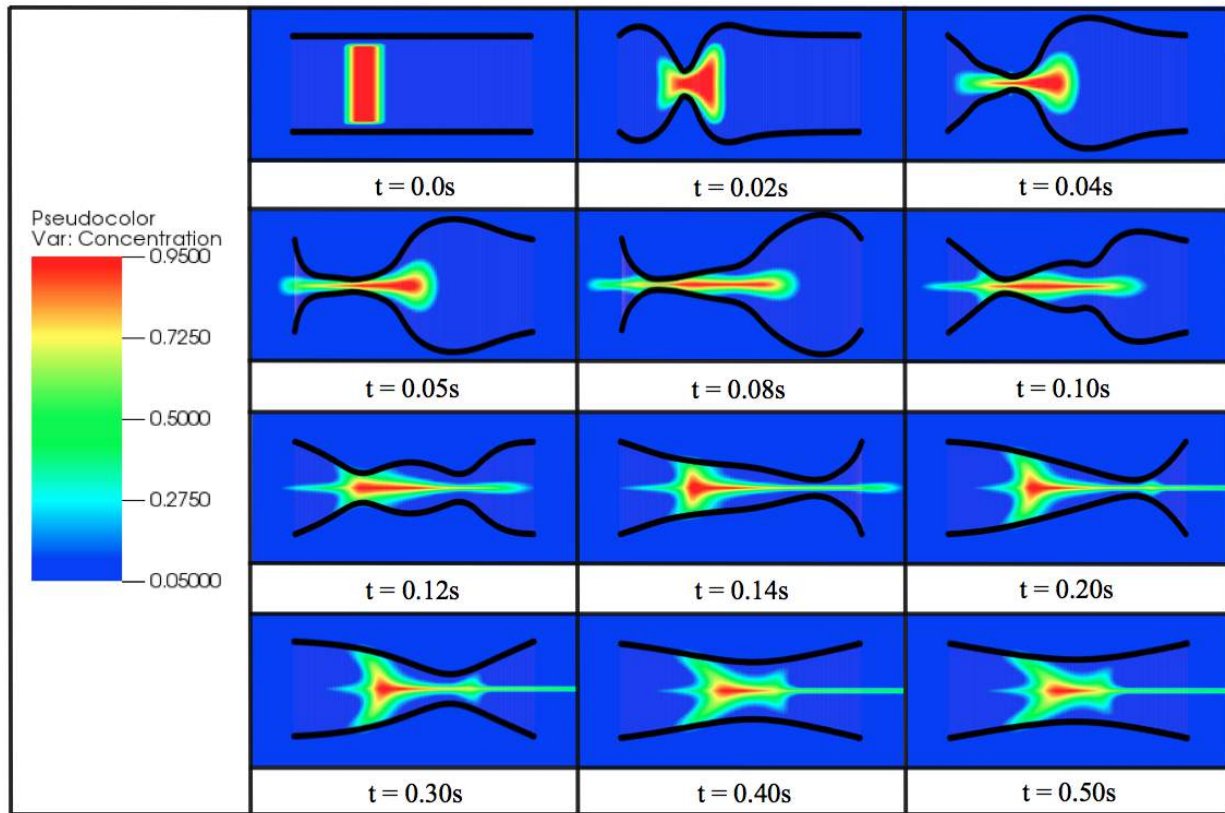


Figure 3.33: A linear heart tube, which pumps when an action potential travels down the tube, once enough free calcium binds to muscle filaments, to induce muscle contraction. The colormap illustrates a background concentration gradient.

HeartTube with Electrophysiology and Calcium Dynamics This example models a linear heart tube, in which pumps via a traveling action potential that induces muscle contraction to occlude the flexible tube. The propagation of the action potential is governed by the FitzHugh-Nagumo equations, as in Eqs.(3.114) and (3.114). This model also accounts for free calcium ions binding and release to induce the action potential signal.

The rate of calcium binding to, and release from, the actin filaments and the sarcoplasmic reticulum is modeled using the law of mass action, such as in [186, 187],

$$\frac{dCa}{dt} = \begin{cases} (k_4Ca_f - k_3Ca)(1 - Ca_f) + k_1(C - Ca - Ca_f) & \text{STIMULUS ON} \\ (k_4Ca_f - k_3Ca)(1 - Ca_f) + k_2Ca(C - S - Ca - Ca_f) & \text{STIMULUS OFF} \end{cases} \quad (3.119)$$

$$\frac{dCa_f}{dt} = -(k_4Ca_f - k_3Ca)(1 - Ca_f), \quad (3.120)$$

where Ca_f is a the ratio of calcium-bound filament sites to total number of filament sites, Ca is the ratio of free calcium ions to total number of filament sites, C is the ratio of total number of calcium ions to total number of filament sites, S is the ratio of total number of sarcoplasmic reticulum binding sites to total number of filament sites, and $\{k_1, k_2, k_3, k_4\}$ are rate constants for binding and release of Ca^{2+} .

Force generation is modeled using the following non-linear spring-like formulation,

$$F_{gen} = k_{HT} [v(x, t)]^4, \quad (3.121)$$

where k_{HT} is a stiffness parameter and $v(x, t)$ is the magnitude of the action potential.

The heart tube itself is composed of linear springs and torsional springs between adjacent Lagrangian points along the top and the bottom of the tube and the ends of the tube are held nearly fixed using target points.

The fiber models and functionality used are:

- Linear Springs
- Torsional Springs

- Target Points (fixed)
- Background Concentration (advection-diffusion)
- Electrophysiology (via FitzHugh-Nagumo)

Movement in the simulation begins when the threshold of free Ca^{2+} ions have binded to the actin filaments has been exceeding, giving rise to an activation signal that propagates an action potential down the hearttube. As the action potential propagates, it induces muscle contraction to contract the flexible tube. The tube then relaxes as the action potential passes. Snapshots of the simulation are shown in Figure 3.33. Note that this example was modeled after the computational model in [22], with the addition of the calcium dynamics.

3.3.5 *IB2d* Data Analysis Package

IB2d also includes a data analysis package, which converts the data (*.vtk*) files back into useful data structures in MATLAB or Python. Once imported, the data can then be manipulated appropriately.

The data is imported using three different functions:

1. *give_Lag_Positions()*: gives all the Lagrangian positions at a specific time-step
2. *import_Eulerian_Data()*: gives all the Eulerian grid data at a specific time-step
3. *import_Lagrangian_Force_Data()*: gives the force data on the Lagrangian structure at a specific time-step

Descriptions of all the data imported can be see in Figure 3.34.

```

% Imports immersed boundary positions %
[xLag,yLag] = give_Lag_Positions(pathViz,numSim);

% Imports (x,y) grid values and ALL EULERIAN DATA %
%
%           DEFINITIONS
%           x: x-grid           y: y-grid
%           Omega: vorticity     P: pressure
%           uMag: mag. of velocity
%           uX: mag. of x-Velocity   uY: mag. of y-Velocity
%           U: x-directed velocity   V: y-directed velocity
%           Fx: x-directed Force     Fy: y-directed Force
%
% Note: U(j,i): j-corresponds to y-index, i to the x-index
%
[x,y,Omega,P,uMag,uX,uY,U,V,Fx,Fy] = import_Eulerian_Data(pathViz,numSim);

% Imports Lagrangian Pt. FORCE (magnitude) DATA %
%
%           DEFINITIONS
%
%           fX_Lag: forces in x-direction on boundary
%           fY_Lag: forces in y-direction on boundary
%           fLagMag: magnitude of force at boundary
%           fLagNorm: magnitude of NORMAL force at boundary
%           fLagTan: magnitude of TANGENT force at boundary
%
[fX_Lag,fY_Lag,fLagMag,fLagNorm,fLagTan] = import_Lagrangian_Force_Data(pathForce,numSim);

```

Figure 3.34: All the data (Lagrangian positions, Eulerian data, and Lagrangian force data) imported in the data analysis software.

An example is contained within the code that analyzes data from a parabolic channel flow example that computes the magnitude of the velocity across multiple cross-sections of the channel. This simulation uses the following fiber model and functionality:

- Target Points (fixed)
- Artificial Forcing on Fluid Grid

Simulation images are shown in Figure 3.35, which illustrate the magnitude of velocity in the channel, and data from the simulation is given in Figure 3.36.

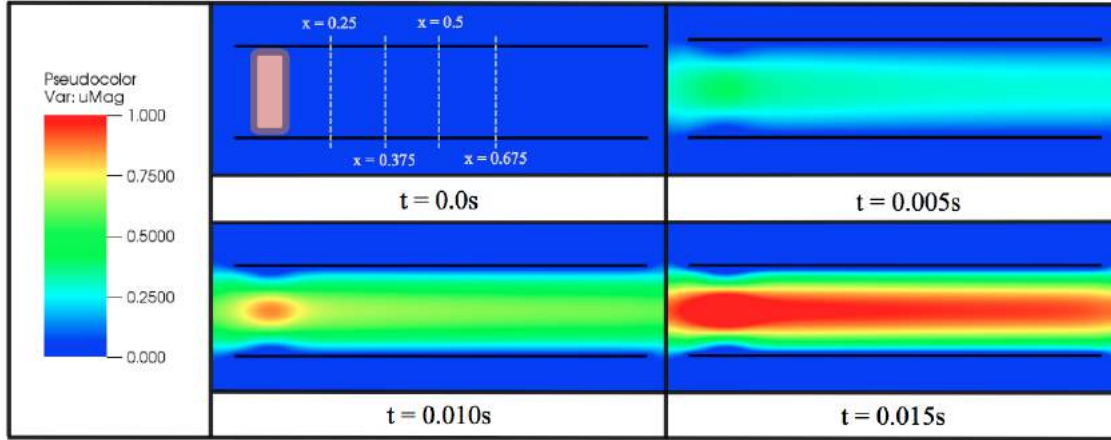


Figure 3.35: Simulation images taken from a channel with a parabolic flow condition at varying times. The parabolic flow is enforced by an external forcing condition on the Eulerian grid in the section outline in purple and shaded in red, while the vertical lines correspond to the cross-sections of the tube where the velocity data will be analyzed.

It is clear from Figure 3.36 that as the simulation progresses the velocity profile within a cross-section of the tube fully develops. The data plotted was taken along the dashed-vertical lines from Figure 3.35.

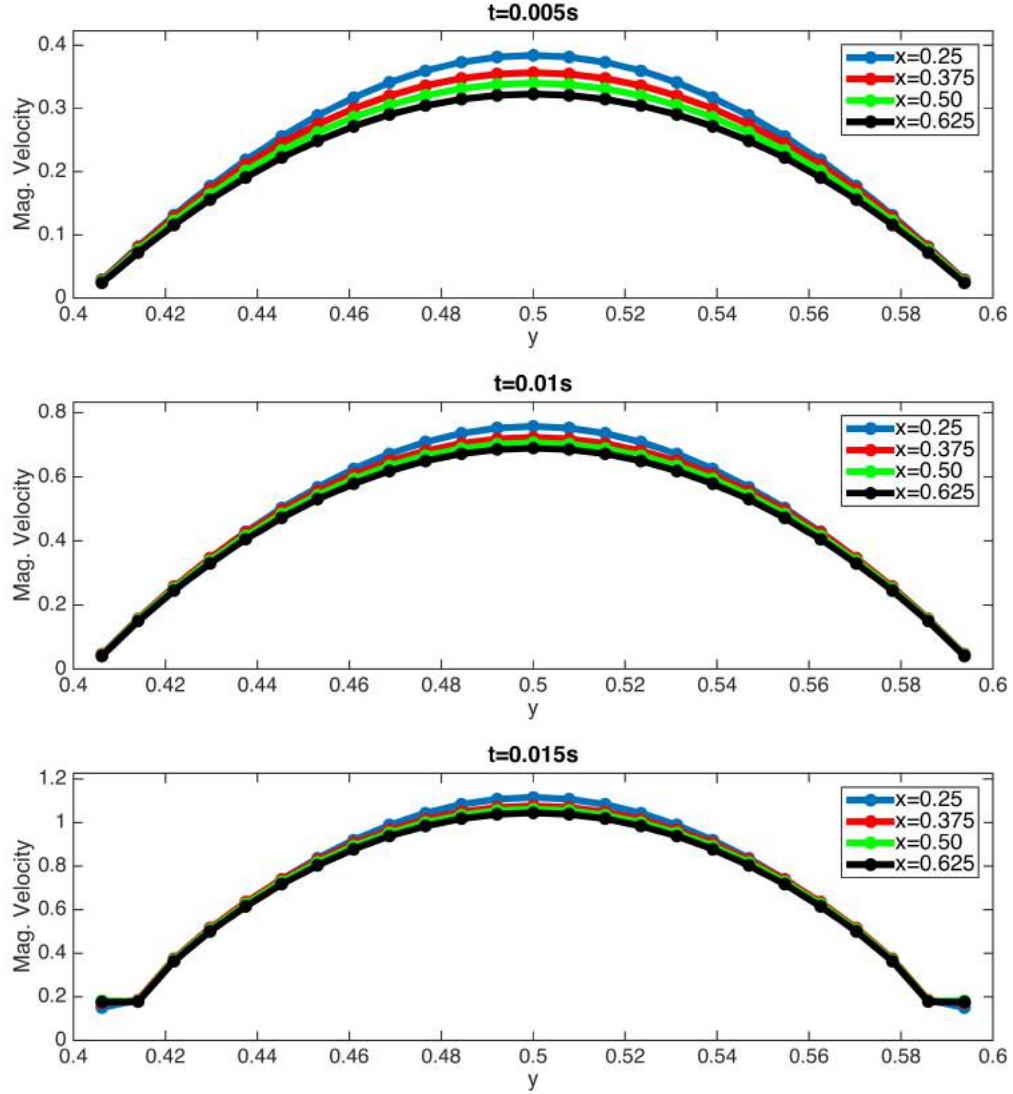


Figure 3.36: Data shown from three different time points during the simulation for velocities across four different cross-sections of the tube. As time increases, the velocity profile becomes more fully developed.

3.3.6 IB2d Code Validation

In this section we present a validation of the code, both in the form of a convergence study for a particular example, as well as in the form of a comparison to experimental data.

Consider the example of a cross-sectional piece of an insect wing moving laterally across the domain at a 45 degree angle of attack at $Re = 128$. The insect wing's motion is governed by updating

the target point positions, as in the example in Section 3.3.4. Snapshots from the simulation are shown in Figure 3.37.

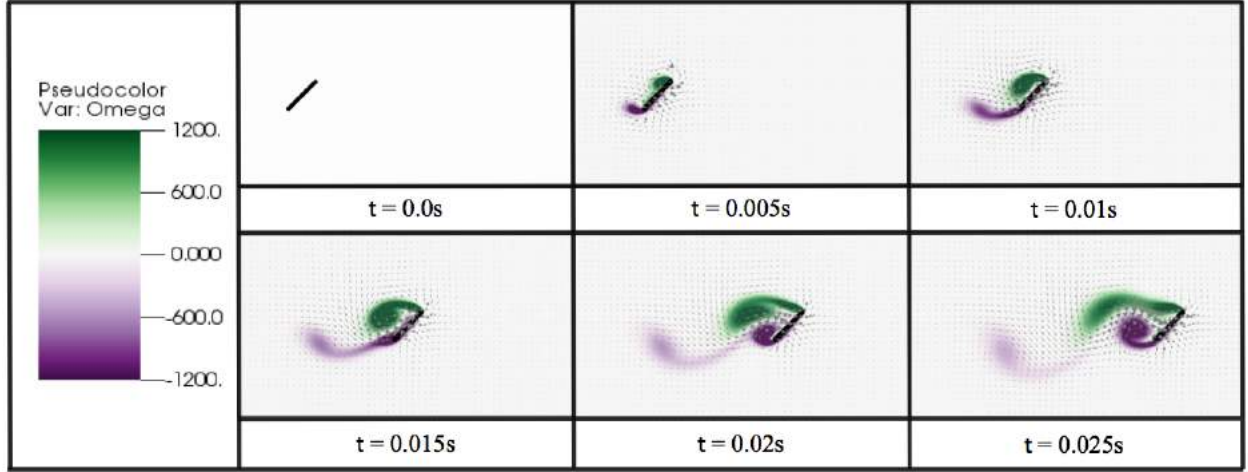


Figure 3.37: A cross-section of an insect wing moving laterally from left to right in a prescribed manner for $Re = 128$. The background colormap depicts vorticity and the vector field is the fluid velocity.

Convergence Study In this section, we perform a convergence study focusing on the forces in the x - and y -directions, respectively referred to as drag and lift, which act on the immersed structure (wing). We ran the simulations for different grid resolutions of the fluid domain (and complementary Lagrangian spacing in the immersed structure) with $Re = 128$ at equivalent time-step, dt , and uniform material properties of the wing. The fluid grid resolutions studied were $\{32 \times 32, 64 \times 64, 96 \times 96, 128 \times 128, 256 \times 256, 512 \times 512, 768 \times 768, 1024 \times 1024\}$. The forces over time are plotted below in Figure 3.38.

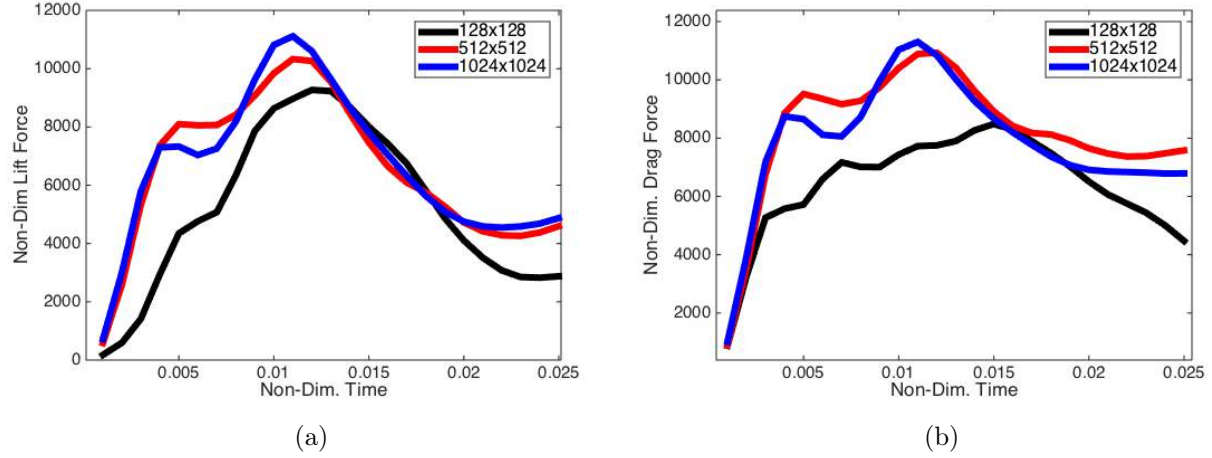


Figure 3.38: Non-dimensional lift (3.38a) and drag (3.38b) forces vs non-dimensional time for a cross-section of an insect wing moving laterally at $Re = 128$.

The mean lift and drag forces were calculated over the wing at $t = 0.025s$ for each simulation, and then the relative error was computed between each simulation and a highly resolved case using IBAMR with 1024x1024 fluid grid resolution.

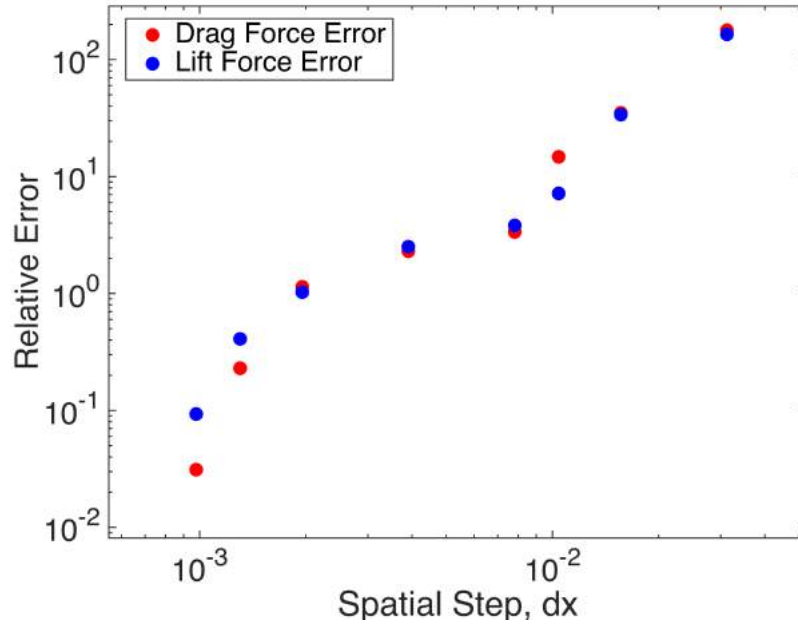


Figure 3.39: A convergence study of the relative error of the lift and drag force, between each simulation and the highly resolved simulation using IBAMR with 1024x1024 resolution on the fluid grid. We note that the horizontal axis is the spatial step size, dx , where $dx = 1/N$, and $N = \{32, 64, 96, 128, 256, 512, 768, 1024\}$.

Applying a best fit line to the data produces the relative error convergence rates

$$\text{Relative Error}_{\text{Drag}} \sim 281838.29 (dx)^{2.16} \quad (3.122)$$

$$\text{Relative Error}_{\text{Lift}} \sim 67920.36 (dx)^{1.83}. \quad (3.123)$$

For $Re \ll 1$ or $Re \gg 1$, e.g., $Re \lesssim 0.01$ or $Re \gtrsim 1000$, we expect less accuracy from our software in its current implementation. More sophisticated fluid solvers could be implemented to help remedy this issues in these fluid regimes. Moreover, enforcing no-slip boundary conditions on the Lagrangian structure to higher-order, i.e., 2^{nd} order or higher, as in [127, 128], will further increase the accuracy. Currently, *IB2d* only enforces the no-slip condition to 1^{st} order.

Experimental Validation In this section we compare simulation results from *IB2d* to experimental data for a cross-section of an insect wing moving laterally across the domain for three orders of magnitude of Re . The experimental data was obtained using particle image velocimetry (PIV) [195], using a dynamically-scaled flapping robot, e.g., Robofly. [196, 197]. The simulations were run on a 1024x1024 grid.

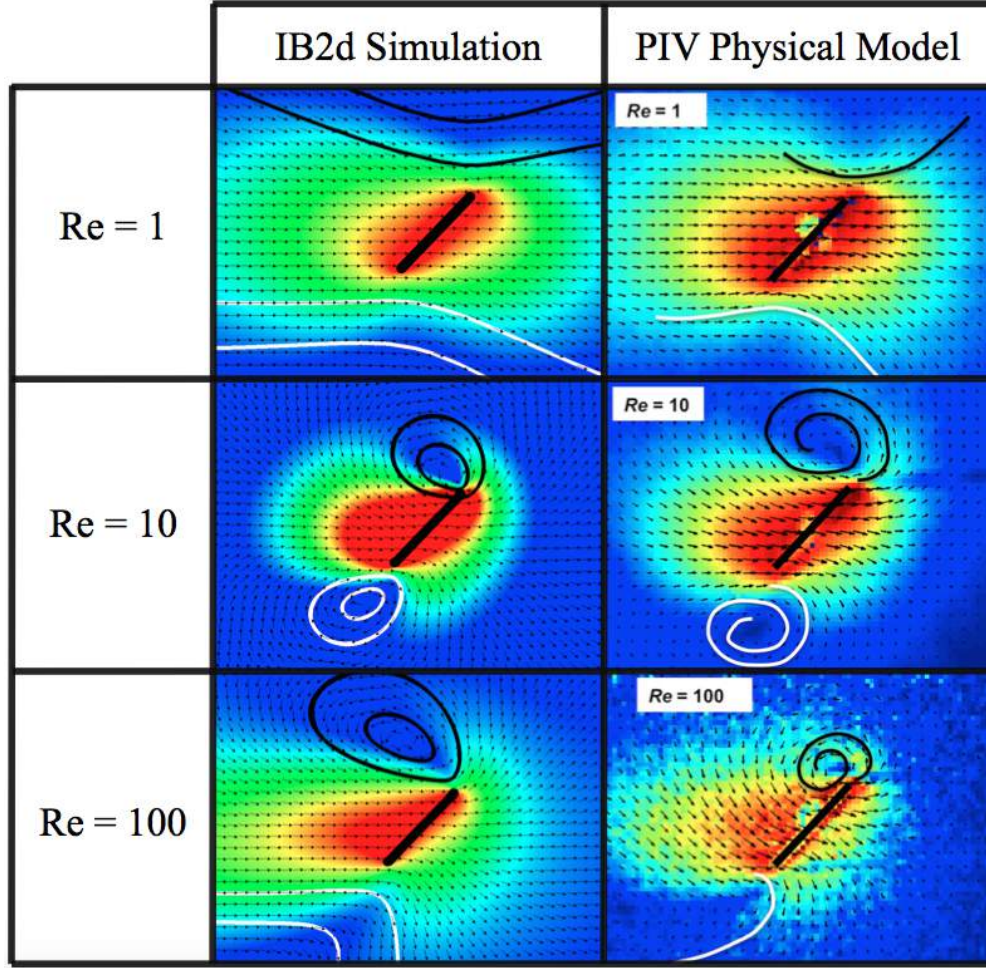


Figure 3.40: Comparison of *IB2d* simulation snapshots and PIV experimental data for a wing moving laterally across the domain for $Re = \{1, 10, 100\}$. The figures show the magnitude of velocity, background velocity field, and streamlines.

Figure 3.40 shows a comparison of snapshots taken from *IB2d* and the PIV physical model over a range of Re . The basic flow structures are reproduced in all cases.

3.3.7 Discussion and Conclusion Regarding *IB2d*

IB2d is immersed boundary software with full implementations in both MATLAB and Python 3.5. It offers a vast array of fiber model options for constructing the immersed structure and has functionality for advection-diffusion, artificial forcing, muscle mechanics, and electrophysiology. Furthermore, having been written in high-level programming languages, it allows one to implement new fiber models and functionality easily and at an accelerated rate.

High-level programming languages also come with a few drawbacks. Grid sizes should not be implemented beyond a 512×512 resolution due to computational costs. If higher resolution is

required, we suggest moving to IBAMR. Additionally unlike IBAMR, *IB2d* was strictly designed for $2D$ applications. While full $3D$ simulations are often desired, some applications may only require fluids with two-dimensions [145, 198, 199, 200, 95]. *IB2d* was written in $2D$ to make it more readable and to lend itself for easier modification, particularly as a first step in trying to implement a new model.

The format of *IB2d* was designed to mirror the input file formats used in IBAMR, and as such can be used as a stepping stone to using IBAMR. Neither *IB2d* nor IBAMR include functionality for compressible fluids, non-Newtonian fluids, or variable density fluid applications at this time, but there are plans to incorporate them in the future.

At this time *IB2d* does not include a turbulence model for large Re simulations. IBAMR is capable of direct numerical simulations as it supports implicit large eddy simulation (LES) turbulence modeling. For other kinds of turbulence models, one is directed to use other software packages such as OpenFOAM by OpenCFD LTD [201], which is capable of FSI applications and is open source. Commercial software, such as COMSOL [134] and ANSYS Fluent [202] can model FSI as well. OpenFOAM, COMSOL, and Fluent allow easier entry into FSI through well developed GUIs and manuals. However, licenses for COMSOL and Fluent are both expensive when not being used for academic teaching purposes. It is also difficult to implement or modify numerical approaches in COMSOL or Fluent, and there would be a steep learning curve for OpenFOAM.

Note that there are other methods for simulating fluid-structure interactions in addition to Peskin's immersed boundary method. Some examples include immersed interface methods [203, 204], sharp interface methods [205, 206], the blob projection method [207], and level set methods [208, 209]. These methods have the benefit that they can capture high resolution of flow near interface when desired. For further information and broader perspective on immersed boundary methods see [210]. However, the authors are not aware of any open source implementations at this time, and thus they require a large entry time for research and development - especially in the case for $3D$, adaptive, or parallelized applications. The mathematical work for compressible, non-Newtonian, and variable density fluids applications may be limited at this time as well. Furthermore, most sharp interface approaches have been limited to thin structures (e.g., elastic membranes) or rigid bodies.

For teaching FSI applications, or fast implementations of new fiber models, numerical models and approaches, or varying fluid solvers, *IB2d* is an ideal environment.

3.3.8 Boyce Griffith's IBAMR

For many of the models presented in this dissertation, they were studied using the IBAMR framework, that is, the immersed boundary method with adaptive mesh refinement [127, 32]. It was developed by Boyce Griffith and is available as open source software [211]. Before the release of IBAMR, other authors had explored the immersed boundary method with adaptive mesh refinement [212, 213]; however, IBAMR was based off of a formally second-order accurate implementation of IB, and is itself *formally* second-order accurate [32].

As opposed to *IB2d*, IBAMR is capable of both *2D* and *3D* applications; however, it currently does not offer as many options for fiber models as *IB2d*, such as porosity or muscle models. It does, however, offer a highly efficient way to solve Eqs. (3.72-3.75) and allow for highly resolved solutions via adaptive mesh refinement. The AMR is used in regions to resolve the Eulerian fluid grid near the immersed boundary as well as near regions of vorticity, that are higher than a user desired threshold. Furthermore it is a parallelized implementation of IB. AMR and Parallelization made it an optimal IB code, especially for *3D*.

Adaptive Mesh Refinement (AMR) The basic idea of AMR is to boost the solving speed of your numerical method by only highly resolving regions of the domain that require higher resolution. That is, in regions away from the immersed structure or where not a lot of dynamics, the domain will stay less resolved. The grid resolution is updated every specified number of time-steps, as not to bog down the computational efficiency by continually changing the grid. IBAMR uses SAMRAI for AMR [156]. An illustration of AMR meshes are found in Figure 3.41.

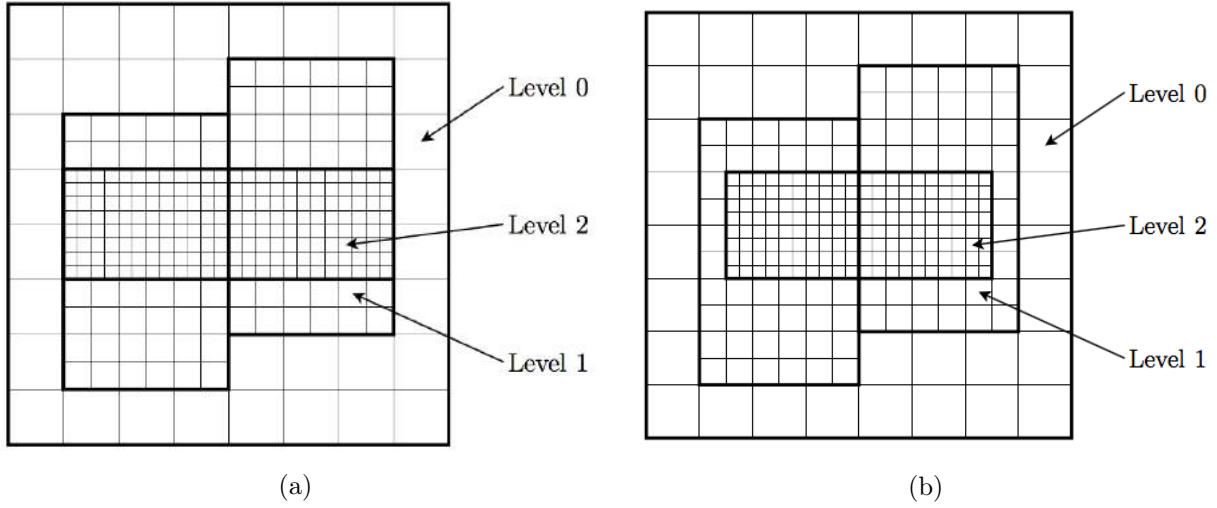


Figure 3.41: Illustrations of AMR Meshing. Note that Figure 3.41a illustrates an improperly nested hierarchical structure, since the lower resolved Level 0 cells are directly adjacent to the higher resolved Level 2 cells. Figure 3.41b shows a properly nested hierarchical structure. Images adapted from [32].

Figure 3.41 illustrates the difference properly and improperly nested hierarchical patch levels. Figure 3.41a illustrates an improperly nested hierarchical structure, since the lower resolved Level 0 cells are directly adjacent to the higher resolved Level 2 cells. Figure 3.41b shows a properly nested hierarchical structure.

The coarse and locally refined grid data are interpolated between grids. Multiple levels of refinement (> 2) are possible, making the composite interpolation between all the grid levels non-trivial. Ghost cells are used to improve the accuracy and ease of the interpolation, as seen in Figure 3.42, adapted from [32]. The composite grid interpolation (averaging) operator, discrete divergence operator, and discrete gradient operators all make use ghost cells as to be able to compute such operators using standard uniform grid implementations [32].

Such interpolation schemes at the coarse-fine interface are not truly second-order accurate; however, away from the interfaces solutions still maintain that level of accuracy. It is well known that reducing the order of accuracy on lower dimensional interfaces within the computational domain does not alter the global accuracy of the the solution and IBAMR has seen second-order convergence rates for sufficiently smooth problems [32, 127].

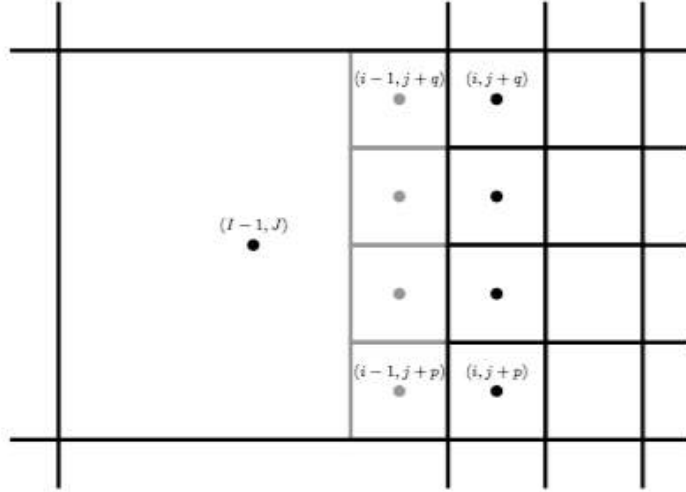


Figure 3.42: An interface between a coarse grid and localised refined grid. Ghost cells are located at the coarse-fine interface in this two-dimensional locally refined grid. Ghost cells are indicated in gray and valid cells are indicated in black. Figure adapted from [32].

An example of an AMR mesh from a simulation from Section 5.3 is shown in Figure 3.43.

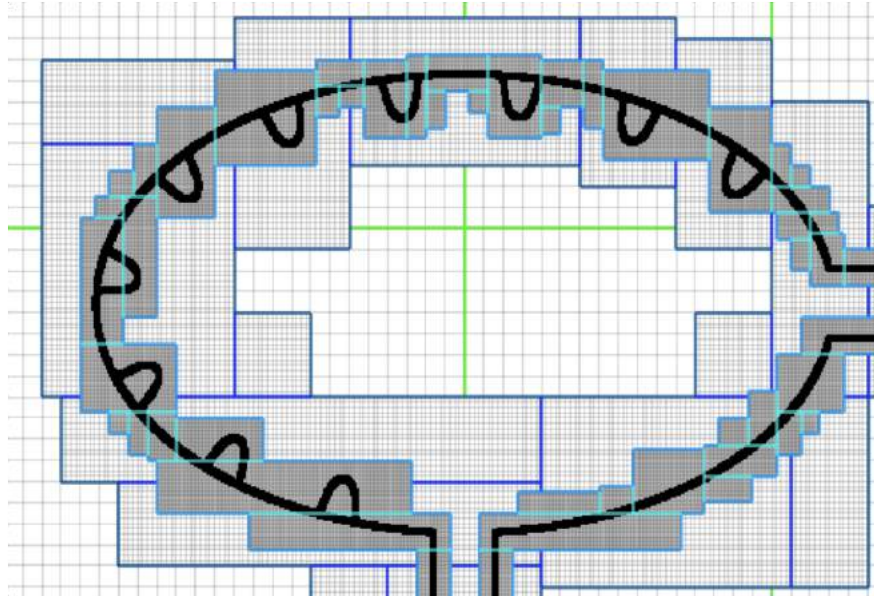


Figure 3.43: An example of AMR from a simulation with a two chambered heart containing a trabeculated ventricle. It is clear that near the immersed structure there is the highest level of refinement.

The only difference in the main algorithm of IB is that every specified number of steps, the Eulerian grid may get regridded depending on the movement of the immersed boundary, or vorticity values. The skeleton of the algorithm is listed below.

Step 1: Find the force density, \mathbf{F}^n on the immersed boundary, from the current boundary configuration, \mathbf{X}^n .

Step 2: Use Eq.(3.74) to spread this boundary force from the curvilinear mesh to nearby fluid lattice points.

Step 3: Solve the Navier-Stokes equations, Eqs.(3.72) and (3.73), on the Eulerian domain. In doing so, we are updating \mathbf{u}^{n+1} and p^{n+1} from \mathbf{u}^n and \mathbf{f}^n . Note: because of the periodic boundary conditions on our computational domain, we can easily use the Fast Fourier Transform (FFT) [168, 169], to solve for these updates at an accelerated rate.

Step 4: 4*a.* Update the material positions, \mathbf{X}^{n+1} , using the local fluid velocities, \mathbf{U}^{n+1} , using \mathbf{u}^{n+1} and Eq.(3.75).

4*b.* Refine Eulerian grid in areas of the domain that contain an immersed structure or where the vorticity exceeds a predetermined threshold, if on a selected time-step for AMR.

CHAPTER 4

Flow Through Heart Tubes

*Many common household items mimic
the properties of human body parts.
Like cantaloupe melons, pudding.*

-Professor Bunsen Jude (Bones)

Various kinds of hearts are found throughout the animal kingdom [214, 215, 216]. As previously discussed in Chapter 2, linear heart tubes are the first stage of vertebrate heart development. However, many other organisms, e.g., invertebrates, also have valveless, tubular hearts [217]. We begin our discussion of heart tubes looking at the evolution of hearts in the animal kingdom.

Figure 4.1 shows the evolution of hearts from tunicates to humans. Tunicates have an open circulatory system from infancy through adulthood, in which blood is pushed through out the organism by a valvless-tubular heart [214, 36]. Next on the evolutionary chain is the amphioxus. The amphioxus heart is a rostrocaudally extended tube from its infancy through adulthood [218]. Similar to the tunicate heart, an amphioxus heart consists only of a monolayer of myocardial cells. Furthermore its heart has no chambers, valves, endocardium, epicardium, or other differentiated features of vertebrate hearts. Still, the amphioxus is regarded as the closest living invertebrate relative to vertebrates [219]. The amphioxus appears fish-like.

Furthermore, Figure 4.1 illustrates the bifurcation to multi-chambered hearts in a vertebrate - the lamprey. Lampreys are jawless fishes that are a very ancient lineage of vertebrates [220]. The lamprey is considered to have four heart chambers, which are the sinus venosus, atrium, ventricle, and conus arteriosus [221]. This is similar as to the zebrafish heart, which contains four chambers - the sinus venosus, atrium, ventricle, and bulbus arteriosus. Lamprey hearts also are valvular pumping systems, containing valve leaflets between chambers [222]. An evolutionary depiction of

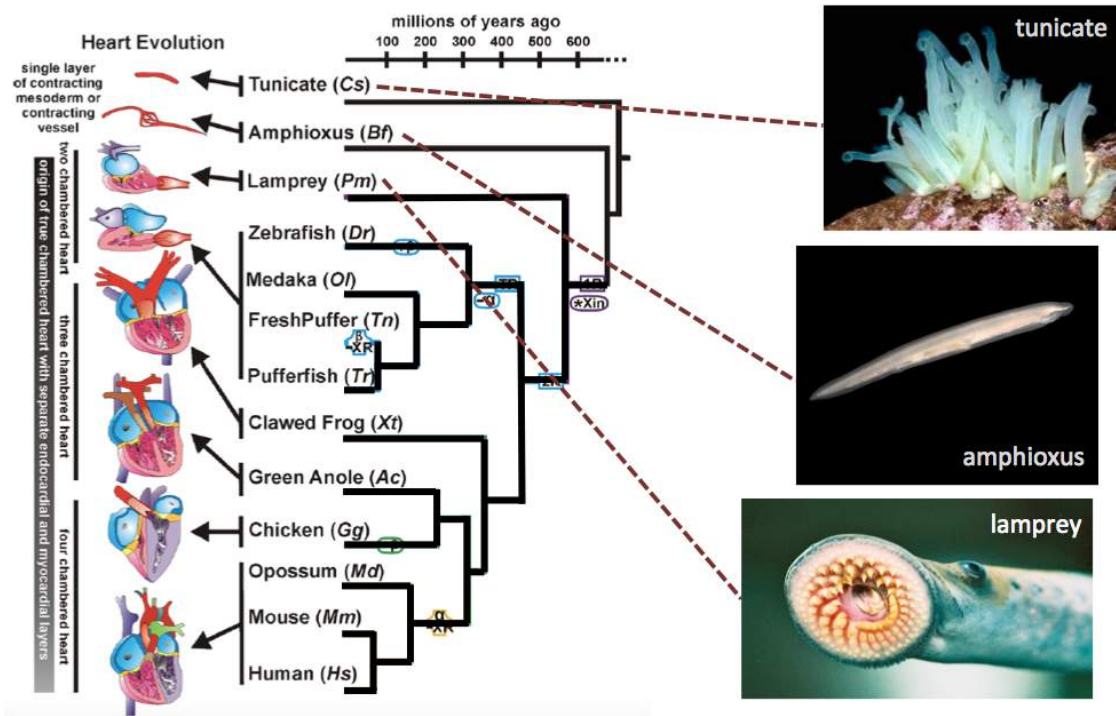


Figure 4.1: Figure adapted from Grosskurth *et al.* [33] illustrating the evolution of hearts from the valveless heart tubes in the open circulatory systems of tunicates to the adult multi-chambered-valvular of vertebrates.

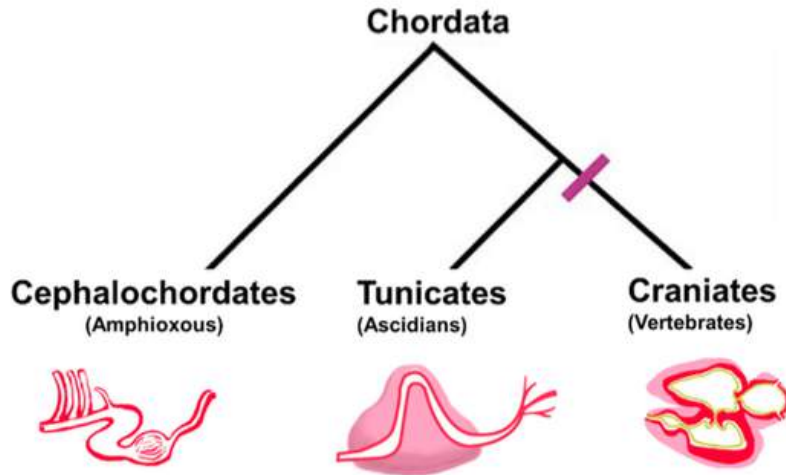


Figure 4.2: Figure illustrating the phylogenetic relationship and general heart structure of the Chordate subphyla. Cephalochordates, like amphioxus, have a series of four peristaltic vessels that serve as a pump, while tunicates have a single-chamber pump, which is composed of a single layer of myocardium (red) surrounded by stiff pericardial layer (pink). The earliest vertebrates, e.g., lampreys, have at least a two-chambered myocardium composed of a layer of cardiac myocardial cells (red), an endocardial cellular layer (yellow), valves that separate distinct chambers, and a surrounding pericardium (pink). Figure adapted from [34].

heart morphology is illustrated in Figure 4.2, which was adapted from [34].

However, as discussed, the vertebrate embryonic heart is a valveless tube, similar to those in various invertebrates, such as urochordates and cephalochordates [223, 224], making invertebrates like sea squirts a possible model for heart development [225]. Historically, the pumping mechanism in these hearts has been described as peristalsis [223, 15]. More recently, dynamic suction pumping (DSP) has been proposed as a novel cardiac pumping mechanism for the vertebrate embryonic heart by Kenner *et. al.* in 2000 [226], and was later declared the main pumping mechanism in vertebrate embryonic hearts by Fourhar *et. al.* in 2004 [65]. Debate over which is the actual pumping mechanism of the embryonic heart continues today, with the possibility that the mechanism may vary between species or may be some hybrid of both mechanisms [23, 227].

The Liebau pump, a dynamic suction pump, was first described in 1954 [228], and was studied as a novel way to pump water. It has not been until the past 20 years that scientists started looking at the pump as a valveless pumping mechanism in many biological systems and biomedical applications, including microelectromechanical systems (MEMs) and micro-fluidic devices. Direct applications of such pumps include tissue engineering, implantable micro electrodes, and drug delivery

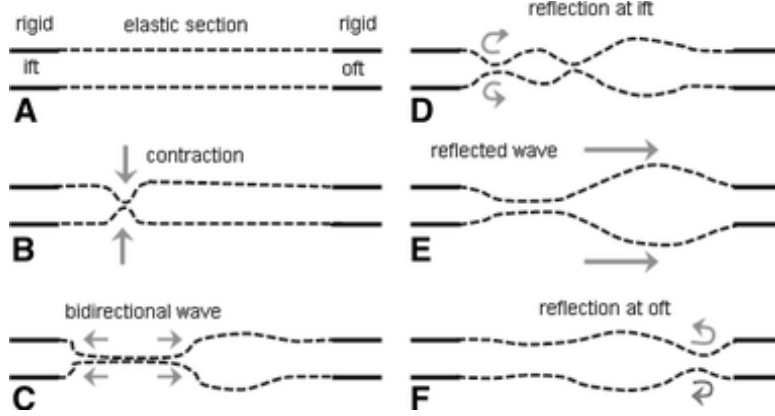


Figure 4.3: Schematic diagram illustrating dynamic suction pumping [15]. (A) The flexible tube is at rest. (B) Active contraction of the tube in a non-central location along the tube. (C) Contraction induces an elastic passive bidirectional wave to propagate along the tube. (D) Wave reflects off rigid portion of the tube on side nearest to contraction point. (E) The reflected wave travels down the tube. (F) The waves reflect off the rigid section at the far side of the tube. Notice the the reflected wave amplitude is smaller than the reflected wave off the other end.

[133, 229, 230, 228].

With extensive industrial applications, dynamic suction pumping has proven to be a suitable means of transport for fluids and other materials in a valveless system, for scales of $Wo > 1$ [20]. DSP can be most simply described by an isolated region of actuation, located asymmetrically along a flexible tube with stiffer ends. Flexibility of the tube is required to allow passive elastic traveling waves, which augment bulk transport throughout the system. The rigid ends of the tube cause the elastic waves to reflect and continue to propagate in the opposite direction, which when coupled with an asymmetric actuation point, can promote unidirectional flow. DSP is illustrated in Figure 4.3.

Due to a coupling between the system's geometry, material properties of the tube wall, and pumping mechanics, there is a complex, nonlinear relationship between volumetric flow rate and pumping frequency [20, 231, 17]. Analytic models of DSP have been developed to address this relationship [232, 233, 234, 235, 231, 236]. Most models use simplifications such as the inviscid assumption, long wave approximation, small contraction amplitude, one-dimensional flow. Furthermore, no analytical model has described flow reversals, which can occur with changes in the pumping frequency. Relaxing many of these assumptions, physical experiments have been performed to better understand DSP [17, 18, 231, 228], as well as *in silico* investigations [237, 238, 16, 20, 21]. Most of these experimental and computational studies focus on the 'high' Wo regime ($Wo \gg 1$), besides studies by Baird *et al.* [20, 21].

Although the size of the blood cells during the tubular heart stage is on the same order of magnitude as the tube itself, previous work with numerical, analytical, and physical have not considered their presence. Given their size ($d \approx 4 \mu m$) and volume fraction (hematocrit) that ranges from 0-40%, it is likely that the blood cells are having some effect on the flow. When the first coordinated myocardial contractions begin to drive blood flow, the embryonic blood lacks blood cells. However, as the heart tube stage progresses, the hematocrit (the volume fraction of blood cells) becomes present, as seen in Figure 4.4, and increases linearly during development [239]. Hematocrit may play a role in the distribution of forces along the endothelial lining that contribute to the shaping and growth of the heart.

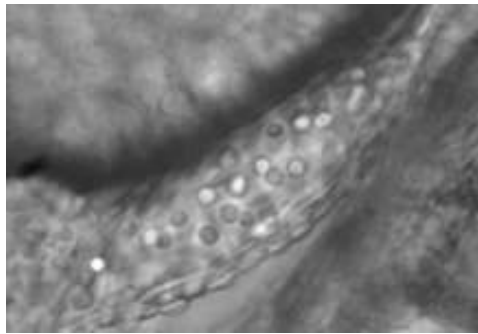


Figure 4.4: The embryonic heart tube of a Zebrafish 30 hpf courtesy of [35]. Spherical blood cells are seen within the tubular heart. The heart tube is roughly 5 blood cells thick in diameter.

In this chapter we will investigate three phenomena pertaining to valveless, tubular hearts. First we explore differences in bulk transport of mock blood cells when comparing dynamic suction pumping to peristalsis. Next we explore a more biologically inspired pumping mechanism coupling the electrophysiology to the initiation and contractile properties of the pumping behavior itself. Last, we explore resonance properties of dynamic suction pumping.

4.0.1 Goals of heart tube with blood cells model

We seek to explore the performance DSP and peristalsis when blood cells are added to the flow. In particular, a central goal is to quantify the relationship between the magnitude of flow and the hematocrit in tubular hearts over a range of Womersley Numbers, Wo . While the vertebrate tubular heart is on the order of tens of microns ($Wo < 1$) [20], the tubular hearts of many invertebrates span from the tens to hundreds of microns ($Wo < 1$), e.g., sea squirts, to salps hearts on the order of millimeters ($Wo > 1$) [223]. These ranges of Wo naturally lend themselves to numerical study

via the immersed boundary method. The particular geometry for the computational models will be based upon experimental data from zebrafish, *Danio rerio*, embryonic tubular hearts. This data was also presented in [240].

4.0.2 Goals of the electro-mechanical model

Upon exploring the electro-mechanical model, we have coupled the propagation of action potentials to muscle contraction and hence the overall pumping behavior. Upon comparison to the previous model, the electro-mechanical model does not have any prescribed motion, but rather the dynamics are coupled to the electrophysiology model and model of muscle force generation. We focus on perturbing a diffusive parameter in the electrophysiology model, e.g., the FitzHugh-Nagumo equations, to investigate the bifurcation in action potential propagation. This bifurcation is able to capture a variety of pumping regimes, e.g., both dynamic suction pumping and peristalsis.

4.0.3 Goals of the resonant pumping model

To further explore the properties of dynamic suction pumping, we investigate the resonant properties of elastic tubes influence bulk flow properties in dynamic suction pumping. Upon doing so, we also study how the addition of mass to the boundary, e.g., increasing boundary inertia, affects the pumping wave-forms and bulk flow rates. We also explore these effects when the elastic tube is over-, under-, and critically-damped.

4.1 Heart Tube Blood Cells

In this section we compare the performance of DSP to peristalsis when blood cells are added to the flow. Our central focus is to quantify the relationship between the magnitude of the bulk fluid transport and the hematocrit in tubular hearts over a wide range of Womersley Numbers, Wo . While the vertebrate tubular heart is on the order of tens of microns ($Wo < 1$) [20], the tubular hearts of many invertebrates span from the tens to hundreds of microns ($Wo < 1$), e.g., sea squirts, to salps hearts on the order of millimeters ($Wo > 1$) [223]. These ranges of Wo naturally lend themselves to numerical study via the immersed boundary method. We will also study this phenomena for non-biologically relevant Wo , ($2 \leq Wo \leq 30$) The particular geometric and physical parameter values for the computational models will be based upon experimental data from zebrafish, *Danio rerio*, embryonic tubular hearts.

Parameter	Value
d	1
$R_1 = r_o$	3.75
$R_2 = r_i$	2.75
L	7.5
L_A	0.9375
L_S	0.75
r_C	0.1

Table 4.1: Geometric parameters used in the numerical experiments. d is the diameter of the tube, R_1 and r_o give the outer radius (or distance from the centerline) of the tube, R_2 and r_i give the inner radius (or distance from the centerline) for the tube, L is the length of the flexible section for DSP and contractile wave section for peristalsis, L_A is the length of straight tube before the actuation section for DSP, L_S is the size of the actuation section for DSP, and r_C is the radii of a blood cell.

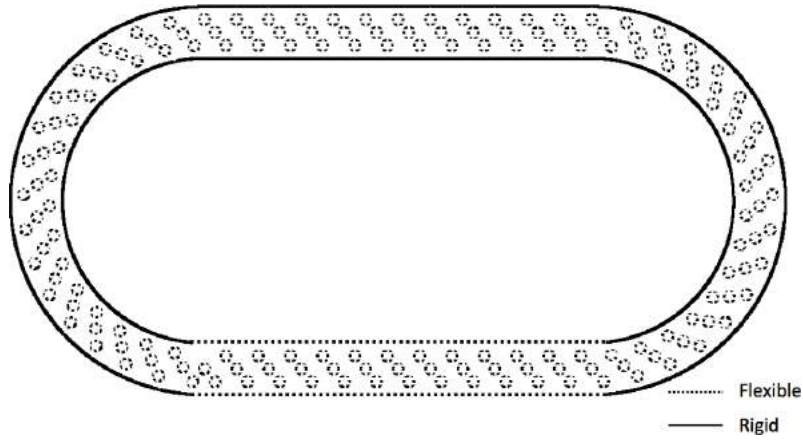
4.1.1 Model Geometry

We numerically model a $2D$ closed racetrack where the walls of the tube are modeled as $1D$ fibers. The closed tube is composed of two straight portions, of equal length, connected by two half circles, of equal inner and equal outer radii. The tube, or racetrack, has uniform diameter throughout. The geometry of the racetrack is given in Figure 4.5.

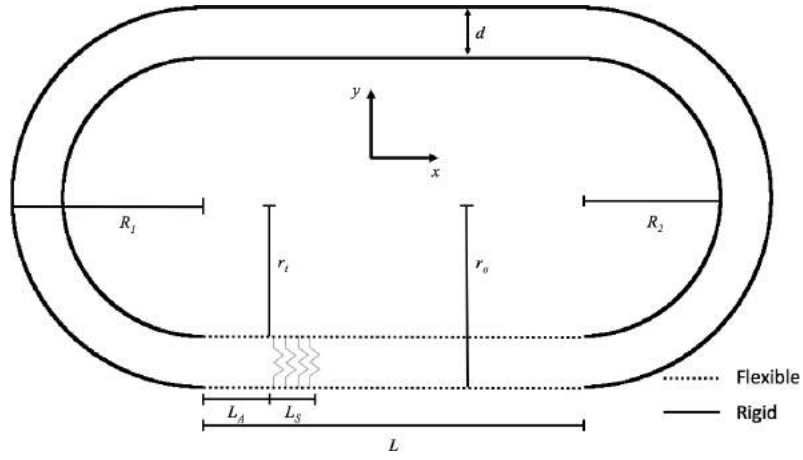
This study goes beyond previous work [20, 21, 238] through the addition of deformable blood cells, composed of springs connecting adjacent and opposite side Lagrangian nodes. The blood cells are modeled circular, in agreement with *in vivo* imaging illustrating their spherical geometry in embryonic blood [35], rather than biconcave [241].

All of the mock blood cells in our simulations have the same radii. The diameter of the blood cells was set to $d/5$ [63]. The flexible cells were modeled via attaching springs between adjacent Lagrangian points for each cell, i.e. beams and target points are not used. The geometry of the heart tube with mock blood cells is illustrated in Figure 4.5a with all parameter values listed in Table4.1. It is important to note that everywhere within our rectangular domain, the fluid has *constant* density ρ and viscosity μ , even within our elastic structures.

DSP Model In the DSP model, the straight portion on the bottom of the racetrack geometry is flexible, e.g., is composed of beams and springs and is not tethered to target points. All other sides of the tube are held nearly rigid in a fixed position using target points, as well as springs and beams. There are also springs attached over a finite actuation region from the inner to outer boundary in



(a)



(b)

Figure 4.5: (a) illustrates the racetrack geometry, which is held rigid except for the bottom of the tube which is flexible. It also includes flexible blood cells, here illustrating the initial position for a volume fraction of 15%. (b) depicts the geometrical features of the racetrack.

the bottom elastic section of the tube. These springs are used to actuate the tube, modeling DSP. We model the action of "muscles" with linear springs, whose resting lengths change in time. These springs are attached between the inner and outer Lagrangian boundaries of the heart-tube.

Resistance to stretching is included in the tethered portion of the tube and in the sections with preferred motion to reduce high frequency oscillations in the boundary. Small bending resistance is added to the simulations to 1) better approximate heart tubes that have some resistance to bending, 2) reduce high frequency oscillations in the tethered portion of the tube, 3) smooth the transition from the flexible portion of the tube to the tethered portion, e.g. smooth the connection points, and 4) eliminate any kinks in the elastic section of the tube.

Rather than attaching these muscles between all points within this region, we choose a region that is 10% of the length of the flat portion, $L_S = L/10$, which is also translated a distance of $L_A = L/8$ along the tube from the beginning of the flat portion from the left. This model was selected since traditional DSP only assumes an off-center region of active contraction. The resting lengths of these springs were changed according to

$$R_L(s, t) = d \left(1 - \frac{8.5}{10} \left| \sin(2.3\pi t) \right| \right) \quad (4.1)$$

Peristalsis Model A prescribed motion of the actuation region along the bottom straight portion of the tube is used to drive peristalsis. To permit volume conservation in the closed racetrack, the top straight section of the racetrack is modeled using springs and beams and is allowed to expand. The reasons for using both springs and beams, which allow for stretching and bending respectively, here are the same as in the dynamic suction pumping model.

The rest of the racetrack geometry composed of target points is held nearly rigid, similarly to Section 4.1.1. There are also springs connecting the outer and inner layer of the top of the tube for additional support. The peristaltic wave of contraction is prescribed by interpolating between multiple positions as described below.

Phase 1 is defined by the position of the relaxed, straight tube. Phase 2 is defined as a fully pinched tube at the initial position of contraction. Phase 3 is defined as a full pinched tube at the end of the peristaltic wave. The initial contraction (pinching) of the tube was prescribed by interpolating between Phase 1 and Phase 2. Similarly, the contractile release was performed by interpolating back

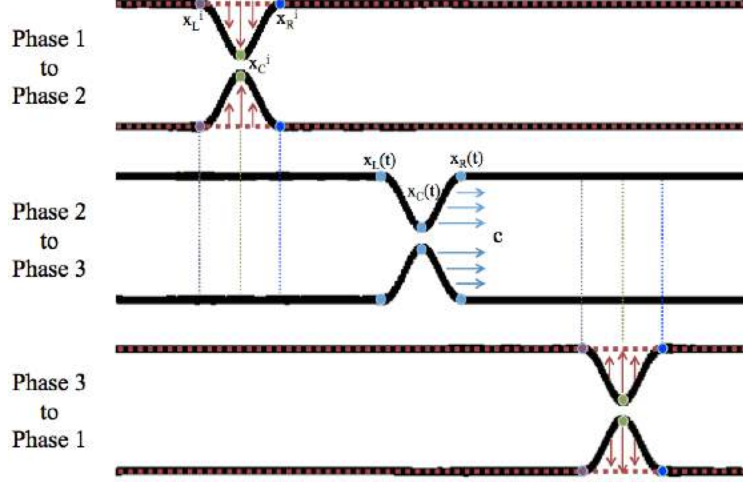


Figure 4.6: Interpolation phases for the traveling contraction wave along the bottom portion of the racetrack geometry. From Phase 1 (straight red tube) to Phase 2, the tube gets pinched on the left side. From Phase 2 to Phase 3, the occlusive pinch travels down the tube at speed c . From Phase 3, the pinch is released and goes back to the straight tube (in red).

Parameter	Time
T	0.435
T_1	$0.025 \times T$
T_2	$0.95 \times T$
T_3	$0.025 \times T$

Table 4.2: Table of temporal parameters for the prescribed peristaltic wave. T is the non-dimensional period. T_1 and T_3 gives the non-dimensional period for the initial pinching and release of the tube. T_3 gives the non-dimensional translation time of the peristaltic wave.

between Phase 3 and Phase 1. This is illustrated in Figure 4.6. The traveling wave of contraction was performed by translating the pinch along the length of the contractile section of the tube.

The motion motion of the actual immersed boundary is driven by changing the position of the target points, which are tethered to each immersed boundary point along the racetrack. The times of each phase (contraction, translation, and relaxation) are seen in Table 4.2, where T is the period of one complete peristaltic wave. The following function was used to induce the traveling peristaltic wave between Phases 2 and 3,

$$X_{target} = \begin{cases} \pm \tilde{A}(x - x_L(t))^2(x_R(t) - x)^2 \exp - \frac{(x - x_C(t))^2}{(0.5w)^2} - R_{o/i}, & x \in [x_L(t), x_R(t)] \\ 0 & \text{elsewhere} \end{cases}, \quad (4.2)$$

and

$$\begin{aligned}
x_L(t) &= x_L^i + c(t - T_1), \\
x_C(t) &= x_C^i + c(t - T_1), \\
x_R(t) &= x_R^i + c(t - T_1), \\
c &= -\frac{2x_C^i}{T_2}, \\
\tilde{A} &= 850.0,
\end{aligned}$$

where x_L^i, x_C^i , and x_R^i are the left-most, center, and right-most points associated with the first pinch. These points are illustrated in Figure 4.6. The parameters c and \tilde{A} are the wave speed and amplitude, respectively. $\pm\tilde{A}$ and $R_{o/i}$ correspond to the bottom and the top wall of the tube, respectively.

Determining Biologically Relevant Parameter Values To determine the lower range of Wo within the heart tube, we take characteristic values for zebrafish embryonic hearts between 26 and 30 hpf and match our non-dimensionless model parameters accordingly. The characteristic frequency, f_{zf} was measured *in vivo*, and the characteristic length, L_{zf} , was taken as the diameter of the heart tube. The Wo was then calculated as

$$Wo = L_{zf} \sqrt{\frac{2\pi \cdot f_{zf} \cdot \rho_{zf}}{\mu_{zf}}} = 0.15, \quad (4.3)$$

where $f_{zf} = 2.2 \text{ s}^{-1}$ [57], $\rho_{zf} = 1025 \text{ kg/m}^3$ [15], $\mu_{zf} = 0.0015 \text{ kg/(m} \cdot \text{s)}$ [242, 243], and $L_{zf} = 0.05 \text{ mm}$ [20]. The occlusion ratio is assumed to be $occ = 0.85$ [63]. We take the characteristic velocity to be $V_{pump} = f_{zf} \cdot occ \cdot \frac{L_{zf}}{2} = 0.047 \text{ mm/s}$. The dimensionless frequency may then be calculated as

$$\tilde{f} = \frac{L_{zf}}{V_{pump}} \cdot f_{zf} = 2.3. \quad (4.4)$$

For the mathematical model, the parameters values were chosen to keep the dimensionless frequency fixed at $f_{sim} = 2.3$, and hence we get the dimensionless pumping velocity of $V_{sim} = f_{sim} \cdot occ \cdot \frac{d}{2} = 0.978$.

The Wo was varied by changing the dynamic viscosity, μ . For the simulations, the Wo_{sim} is calculated using a characteristic length of d , the width of the tube, and dimensionless density of $\rho = 1000$. The simulations were performed for $Wo_{sim} = \{0.2, 0.4, 0.6, 0.8, 0.9, 1.0, 1.5, 2, \dots, 9, 10, 15, 20, 30\}$. Note that the higher end of these values describe a fully inertial regime which may be outside of what is found in nature. The stiffness of the target tethering points were chosen to minimize the deformations of the boundary, i.e, to keep it rigid, and were directly correlated to Wo . The motivation for the wide range of Wo considered is that we want to compare parameter values relevant to other types of tubular hearts, such as salps, tunicates, and insects. We also want to compare our results to the Wo range considered in most previous DSP studies, (typically $Wo > 1$). The other mechanical parameters were chosen to allow deformation and reexpansion of the heart tube on relevant timescales. Our parameter choices are given in Table 4.3, where they have been non-dimensionalized, using the following relations for springs (and target points) and beams, respectively,

$$\tilde{k}_{spring/target} = \frac{k_{spring/target}}{\rho * d * V_{sim}^2} \quad (4.5)$$

$$\tilde{k}_{beam} = \frac{k_{beam}}{\rho * V_{sim}^2 * d^3}. \quad (4.6)$$

Note that:

- The top portion of the tube in the peristaltic cases is allowed to be flexible to conserve volume (e.g. this section expands with the tube compresses). This is not necessary in the case of dynamic suction pumping because the lower portion of the tube is flexible and can expand to conserve volume.
- In the case of peristalsis, the entire motion of the boundary is moved with a preferred motion (with the exception of the top which simply expands to conserve volume). In this set up, the elastic forces only serve to minimize deviations from that preferred motion and to reduce high frequency oscillations. As long as the actual motion is sufficiently close to the preferred motion, the parameters chosen do not alter the results.
- In the case of DSP, the stretching stiffness of the bottom, untethered portion of the tube, is a primary factor that influences the average velocity. We selected this value to give reasonable

Mechanical Parameters	Symbol	DSP Value	Peristalsis Value
Stretching Stiffness of the Tube	\tilde{k}_{stube}	1.3e7	3.3e6
Stretching Stiffness of Springs Across Tube	\tilde{k}_{sbtwn}	2.3e3	6.5e2
Stretching Stiffness of Target Points	\tilde{k}_{target}	1.3e5	1.3e5
Bending Coefficient of the Tube	\tilde{k}_{beam}	3.3e2	3.3e10
Stretching Stiffness of Blood Cells	\tilde{k}_{scell}	2.8e5	2.8e5

Table 4.3: Table of mechanical parameters used in the computational model. Note that \tilde{k}_{sbtwn} gives the stiffness coefficient of the actuating springs in the DSP model, while it describes the stiffness coefficients of springs connecting the outer and inner layer of the top of the tube in the peristalsis model. \tilde{k}_{stube} is the stretching stiffness between adjacent points along the tube while \tilde{k}_{sbtwn} gives the stretching stiffness between opposite points along a cross-section of the tube. \tilde{k}_{target} is the tethering stiffness of target points, \tilde{k}_{beam} gives the bending stiffness between adjacent points along the tube, and \tilde{k}_{scell} gives the stretching stiffness between points making up the blood cells.

bulk flow at higher Wo . In future studies, we will characterize how this stiffness affects average flow.

All of the reported values have been non-dimensionalized according to Eqs. (4.5), (4.5). The viscosity may be used to change the Wo without affecting the dimensionless stiffnesses. In other words, viscosity can be used to vary the Wo without significantly effecting the dynamics of the structure. Note that the Wo considered fall within the range of many biological pumps, see [15].

4.1.2 Results

In this study, we present simulations of dynamic suction pumping and peristalsis within a closed racetrack containing flexible blood cells of varying volume fractions but uniform geometry. The simulations were run for a range of Womersley Number, $Wo \in [0.1, 30]$, and hematocrit, $VF = \{0\%, 5\%, 10\%, 15\%, 20\%, 25\%\}$. Examples of the locations of the blood cells and boundaries at different points in time are seen in Figure 4.7.

DSP Results Figure 4.7 shows snapshots from simulations of DSP at five different Womersley numbers, $Wo = \{0.2, 2.0, 6.0, 10.0, 20.0\}$, where volume fraction is held constant at $VF = 15\%$. The images were taken after at 11.5, 22.5, 33.5, and 44.5 heartbeats. In the cases of $Wo = 0.2$ thru $Wo = 2.0$, there is no significant net transport for the mock blood cells as evidenced by the negligible movement of the blood cells (note the color coding of blood cells in each quadrant). There is, however, clear transport when $Wo \geq 6.0$. Moreover, in the cases when $Wo \geq 6.0$, the blood cells begin to clump together, rather than move uniformly throughout the tube.

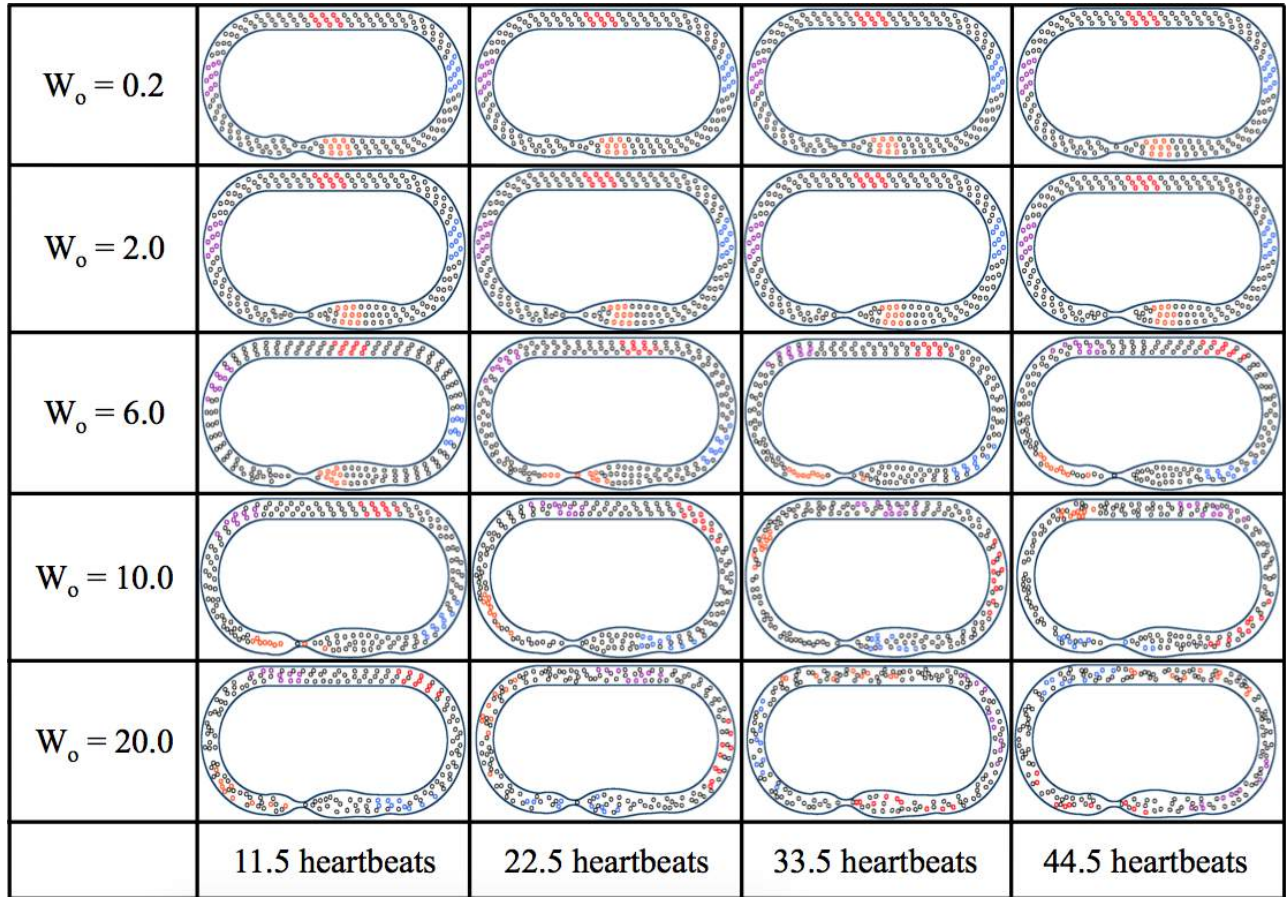


Figure 4.7: A comparison of simulations with different Womersley Number, $Wo = \{0.2, 2.0, 6.0, 10.0, 20.0\}$, but same amount of blood cells, $VF = 15\%$. The images were taken after at 11.5, 22.5, 33.5, and 44.5 heartbeats during the simulations. In the case of $Wo = 0.2$ and $Wo = 2.0$, there is no visual transport for the mock blood cells; however, there is clear transport when $Wo \geq 6.0$. Moreover, in the cases when $Wo \geq 6.0$, the hematocrit begins to clump together, rather than move uniformly throughout the tube.

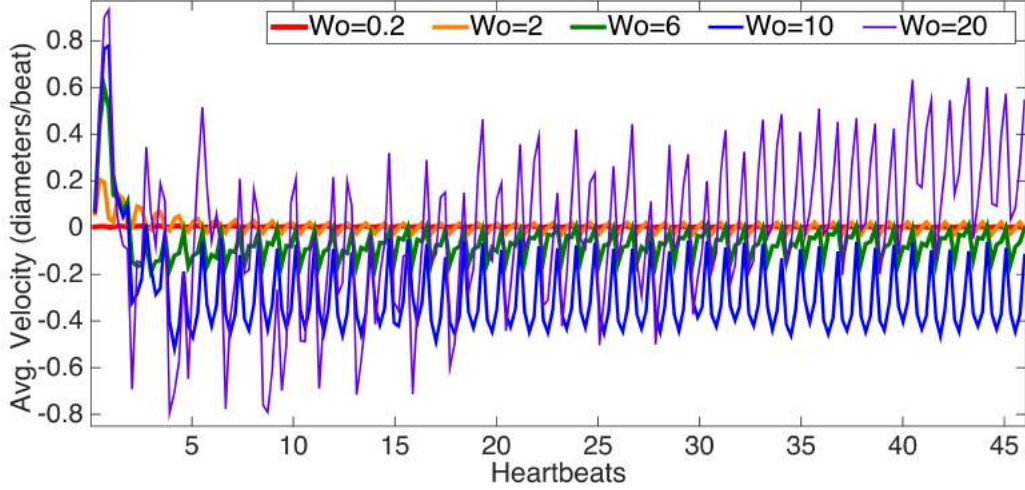


Figure 4.8: A comparison of the spatially averaged velocity vs. time over the course of the simulation, for five cases with uniform hematocrit ($VF = 15\%$), but varying Womersley Number, $Wo = \{0.2, 2, 6, 10, 20\}$. The average velocity was spatially computed across a cross-section in the center of the top of the tube. As Wo increases the amplitude of oscillations in average velocity also increases. In the biologically relevant case, $Wo = 0.2$, there are slight oscillations; however, bulk net flow is insignificant.

Keeping the volume fraction constant, we compared the spatially-averaged velocity across a cross-section in the center of the top of the tube, for three different Womersley Numbers, $Wo \in \{0.2, 2.0, 6.0, 10.0, 20.0\}$. Note that deformations of this section of the tube are negligible such that the average velocity is directly proportional to the volumetric flow rate. Figure 4.8 illustrates this for the case of $VF = 15\%$. From the figure, it is evident that the lower Wo case induces less net flow than the other two higher Wo cases. However, we can also deduce that the direction of flow is a non-linear function of Wo . Note that for $Wo = 10.0$, flow is moving in the opposite direction to that of the $Wo = 20.0$ case.

This study has considered two orders of magnitude in Wo . Given that Wo scales like the square root of the Re , note that our study spans four orders of magnitude in Re . For the range of Wo considered, higher volume fractions result only in flow in the negative direction. It would be interesting to see if this is the case for all Wo . Future studies will consider a larger and more detailed range of Wo to better resolve the changes in flow direction.

Moreover, an example comparison of the spatially-averaged velocity vs. time for three different volume fractions, $VF = \{5\%, 15\%, 25\%\}$, for three specific Womersley numbers, $Wo = \{0.2, 2.0, 6.0\}$, are shown in Figure 4.9. Figures[(4.9a),(4.9b)] show the similarity of the waveforms illustrating little

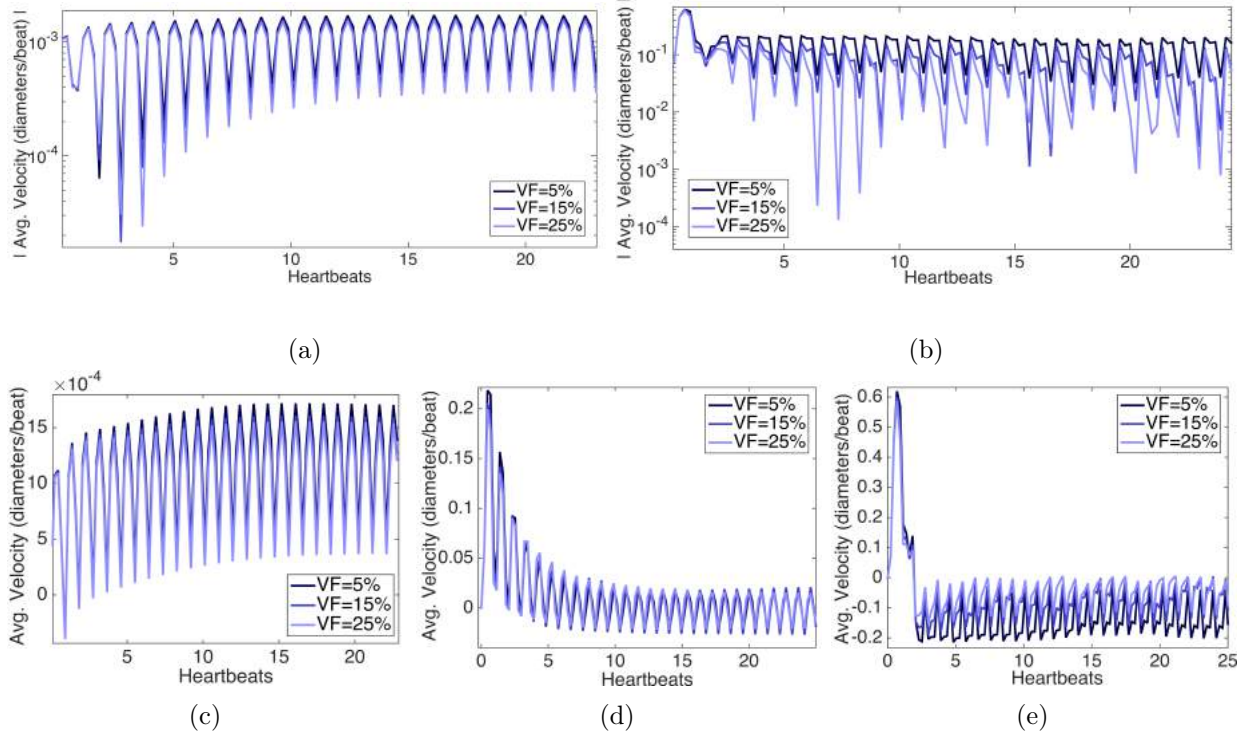


Figure 4.9: A comparison of the spatially averaged velocity vs. time over the course of the simulation, for varying hematocrit, $VF = \{5\%, 15\%, 25\%\}$, for three different Womersley Numbers, $Wo = 0.2$ [(4.9a), (4.9c)], $Wo = 2.0$ (4.9d), and $Wo = 6.0$ [(4.9b), (4.9e)]. The average velocity was spatially computed across a cross-section in the center of the top of the tube. [(4.9a), (4.9b)] illustrate how similar the waveforms are for varying volume fractions for Wo , 0.2 and 6.0, respectively. [(4.9c), (4.9d), (4.9e)] give the average velocities, in diameters/heartbeat, over the course of the simulation, in heartbeats.

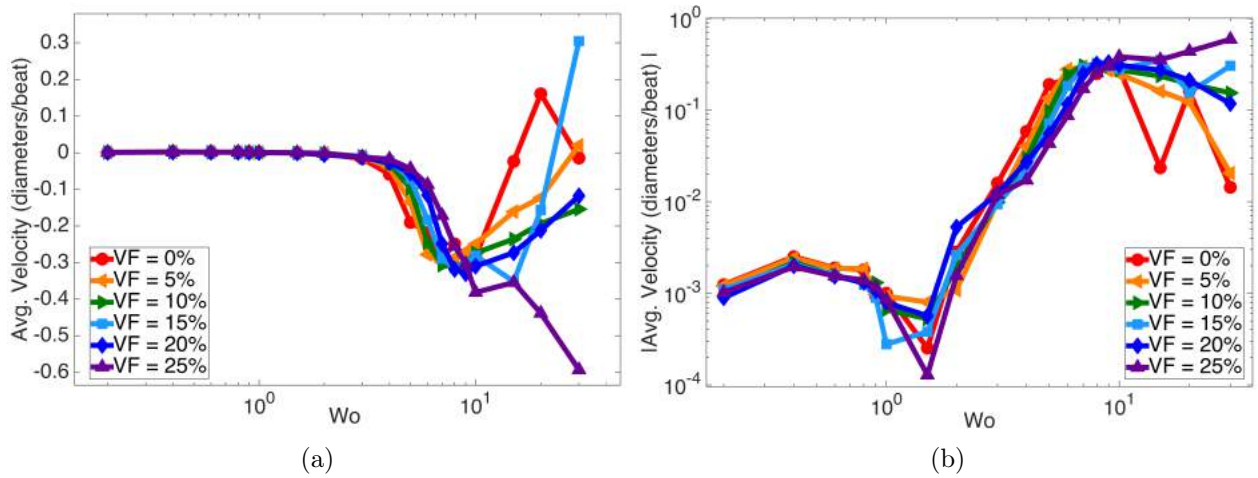


Figure 4.10: 4.10a shows the spatially- and temporally-averaged velocity for each simulation vs. Womersley Number for a hematocrit range of $[0\%, 25\%]$. 4.10b shows the spatially- and temporally-averaged magnitude of velocity vs. Wo for a hematocrit range of $[0\%, 25\%]$.

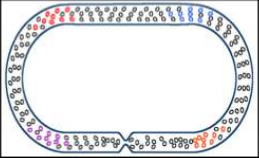
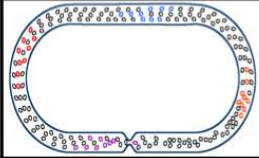
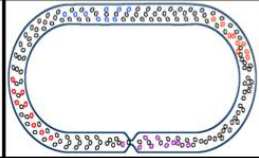
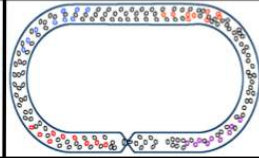
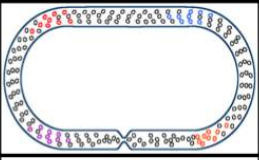

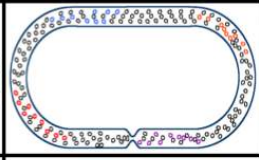
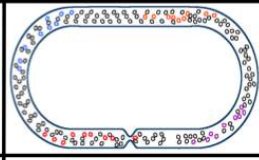
$W_o = 0.2$				
$W_o = 2.0$				
	1.5 heartbeats	2.5 heartbeats	3.5 heartbeats	4.5 heartbeats

Figure 4.11: A comparison of simulations for two different Womersley Numbers, $Wo = \{0.2, 2.0\}$, but same hematocrit, $VF = 15\%$. The images were taken after at 1.5, 2.5, 3.5, and 4.5 heartbeats during the simulations. It is clear that there is significant mixing of the blood cells with peristalsis, as the colored sections begin to mix

effect of blood cells on bulk flow patterns, for all three Wo . [(4.9c),(4.9d),(4.9e)] give the spatially averaged velocities (in diameters/heartbeat) vs. time over the course of the simulation. Time is given in number of heartbeats. In the $Wo = 0.2$ case, the average velocities asymptotically increase until they reach a periodic cycle. It is clear the maximal flow rates in both the $Wo = 0.2$ and $Wo = 2.0$ cases are multiple orders of magnitude below one diameter/heartbeat. These are well below the experimentally observed velocity of ~ 0.9 diameters/heartbeat recorded in zebrafish [65].

To quantify the effect of blood cells further, spatially- and temporally-averaged velocities for various Wo and hematocrits were compared. This is illustrated in Figure 4.10. From Figure 4.10a, it is clear that flow rates are a non-linear function of Wo . The case with zero hematocrit is in agreement with previous results reported in [20]. Moreover, the addition of hematocrit does not significantly perturb flow rates for $Wo \lesssim 10$, as seen in Figure 4.10b, except for the case where $Wo = 1.5$. In the case of $Wo = 1.5$, the addition of hematocrit affects flow rates; however, absolute bulk flow rates are minimal over the range of Wo considered. Furthermore, for $Wo \gtrsim 10$, the addition of hematocrit affects flow rates in a non-linear fashion.

Peristalsis Results Figure(4.11) shows snapshots from simulations for two different Womersley numbers, $Wo = \{0.2, 2.0\}$, where hematocrit is held constant at $VF = 15\%$. The images were taken after 1.5, 2.5, 3.5, and 4.5 heart beats during the simulations. It is clear from both simulations that there is significant bulk flow throughout the tube. Moreover, significant mixing is observed in both

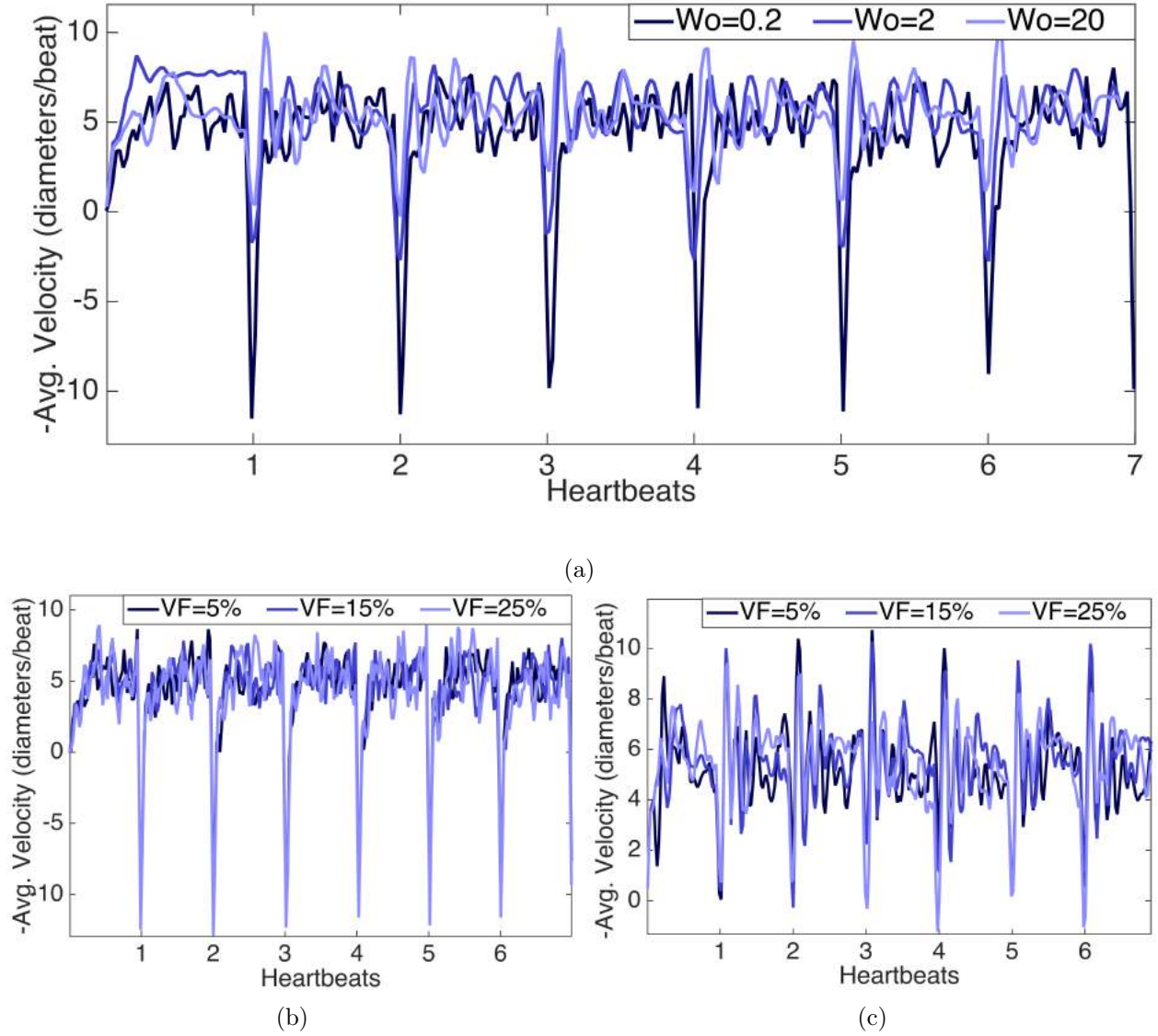


Figure 4.12: A comparison of the spatially averaged velocity vs. time over the course of the simulation, for hematocrit, $VF = 15\%$, for three different Womersley Numbers, $Wo = 0.2, 2, 20$ is shown in (4.12a). The spatially-averaged velocity was computed across a cross-section in the center of the top of the tube, given in diameters/heartbeat. (4.12b) and (4.12c) give the spatially-averaged velocities for $Wo = 0.2$ and $Wo = 20$, respectively, for three volume fractions, $VF = 5\%, 15\%, 25\%$.

cases. Note that although the top portion of the racetrack is elastic, it has a relatively high bending rigidity. The top of the tube expands just enough to compensate for the volume of the bottom of the tube that is lost due to the presence of the peristaltic wave.

The volume fraction was kept constant, at $VF = 15\%$, in Figure(4.12a) to explore the effect of scaling on bulk flow for $Wo = 0.2, 2.0, 20.0$. The spatially-averaged velocity across the top of the tube, given in diameters/heartbeat, is similar between all three cases of Wo . Furthermore the direction of flow is consistent in all cases, with bulk flow moving counterclockwise around the tube, with a sharp decrease in velocity, showing flow going in the opposite direction, at the end of each heartbeat.

Figures(4.12b) and (4.12c) illustrate the effect of varying hematocrit for simulations with $Wo = 0.2$ and $Wo = 20$, respectively. In both cases the waveforms look similar, suggesting the addition of blood cells does not significantly affect bulk flow rates. However, we note that the sharp decrease in velocity at the end of the heartbeat is more pronounced in the $Wo = 0.2$ case, than in the $Wo = 20$ case.

4.1.3 Discussion and Conclusions

In this section, two-dimensional immersed boundary simulations were used to model dynamic suction pumping and peristalsis for a single actuation frequency over a range of Womersley numbers and hematocrits relevant to valveless, tubular hearts. When strong net flow was generated in the tube at higher Wo , blood cells clumped together, and did not flow uniformly throughout the tube. The spatially- and temporally- averaged velocities across a cross-section along the top of the tube showed a non-linear relationship between net flow rates and Wo for DSP. The effect of hematocrit on the net flow rate was significant for $Wo \gtrsim 10$ and was nonlinear. In particular, the varying levels of hematocrit changed the direction of flow for DSP for Wo on the order of 10. The addition of blood cells did not enhance the weak net flows produced for $Wo < 1$. These results highlight the complex dynamics governing dynamic suction pumping.

For DSP at low Wo and for the range of tube material properties considered here, the fluid is nearly-reversible. This reversibility may explain in part why there is little net flow in the tube for the case of DSP (a reversible motion) at $VF = 0$. This result is in agreement with [20, 21]. Previous studies have shown enhanced fluid transport and animal locomotion in non-Newtonian fluids at low Re and Wo [244]. Since the addition of blood cells in a Newtonian fluid makes the bulk fluid

effectively non-Newtonian, it is possible that the addition of blood cells could make the flow in tubular hearts irreversible. For the parameters considered here, any such effect was negligible.

For the case of peristalsis, flow was consistently driven around the racetrack for all Wo and for all hematocrits. Similar to DSP, the addition of hematocrit did not significantly change net flow rates at low Wo . Unlike the case of DSP, the addition of hematocrit also did not significantly alter the velocity waveform or the net flow at higher Wo .

Although the bulk transport of fluid was not significantly changed, the addition of blood cells may affect the shear stresses experienced by the cardiac cells and the amount of mixing within the heart tube. The peristalsis simulations show enhanced mixing as compared to that of DSP at the same Wo and VF . Furthermore for $Wo = 0.2, 2$, peristalsis was able achieve similar levels of blood cell mixing an order of magnitude faster than the DSP simulation at $Wo = 20$. These results are important when considering the role that fluid mixing and shear stress may play in cardiogenesis.

Experimental evidence has shown blood flow, and more specifically hemodynamic forces, are essential for proper heart morphogenesis [12]. Furthermore, it is evident that there is a strongly coupled relationship between the underlying hemodynamics, cardiac electrophysiology, and activation of some genetic regulatory networks. For example, hemodynamics is thought to regulate the development of the pacemakers and the conduction of action potentials in the heart [94, 14]. Since there is direct feedback between the underlying electrophysiology and the flow induced by muscle contraction, changes in traveling action potentials will affect the hemodynamic forces felt at the endothelial layer, e.g., shear stress and pressure. These changes may then result in changes in gene expression via epigenetic signaling mechanisms, e.g., mechanotransduction. However, the exact pipelines that contribute to mechanotransduction are not completely understood [245].

4.2 Electro-dynamical Pumping

In this section we explore a model coupling electrophysiology, muscle-force production, and flow induction using a computational electro-dynamical model. The propagation of action potentials are coupled to muscular contraction and hence the overall pumping dynamics. Upon comparison to the previous model, the electro-dynamical model does not use prescribed motion, but rather the pumping dynamics are fully coupled to an electrophysiology model. We will perturb the diffusion parameter in the electrophysiology model to investigate the bifurcation in dynamics of action potential propagation. This bifurcation is able to two different pumping regimes, i.e., dynamic suction pumping as well as

peristalsis. The electrophysiology model is governed by the FitzHugh-Nagumo equations.

4.2.1 Computational Model

We numerically model a $2D$ closed racetrack where the walls of the tube are modeled as $1D$ fibers. The closed tube is composed of two straight portions, of equal length, connected by two half circles, of equal inner and equal outer radii. The tube, or racetrack, has uniform diameter throughout. This is similar to the model geometry as in Figure 4.5; however, the material properties are slightly different and we do not include mock blood cells in this model. Moreover, unlike Figure 4.5, we include the presence of an idealized stiff pericardium surrounding the flexible region of the heart tube.

The tunicate heart consists of a myocardium which is surrounded by a stiff pericardium [246, 95], which provides structural support to the myocardium. Muscle fibers spiral around the heart tube itself, and action potentials propagate to induce myocardial contraction. These action potentials have been previously measured [223]. Myocardial contractions may begin at either end of the heart tube, allowing the propagation of the action potential to occur in either direction [247]. However, we will not concern ourselves with flow reversals in this model. Although the tunicate heart tube has different material properties and physiological properties than the vertebrate embryonic heart, it still is an interesting model for vertebrate heart morphogenesis [225]. However, the conduction properties, e.g., velocities, of action potentials are much more uniform in tunicates than mammalian hearts [248].

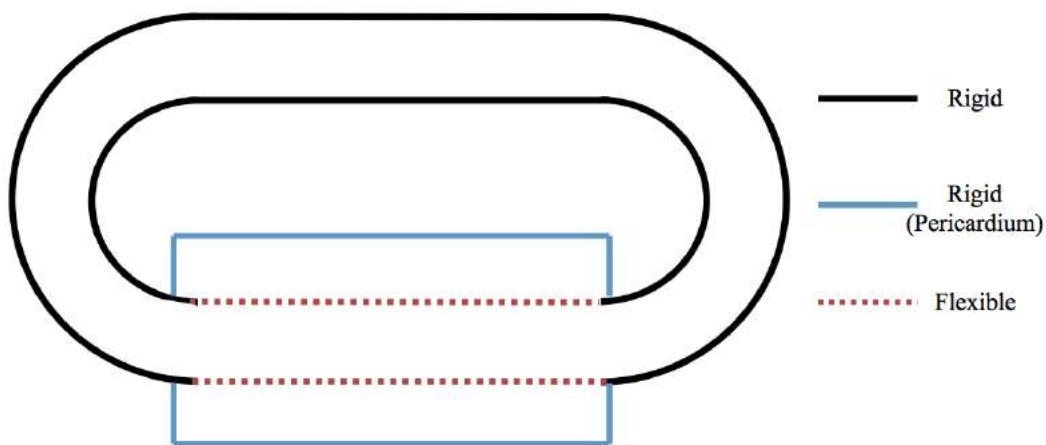


Figure 4.13: Computational geometry for the electro-mechanical pumping model. The racetrack is held stiff (black), except for the bottom straight-tube portion, which is flexible (red). There is a stiff pericardium model surrounding the flexible region (blue).

The computational model we investigate is seen in Figure 4.13. Linear springs and beams connect adjacent Lagrangian points in the flexible region of the racetrack geometry. All other Lagrangian points of the boundary are modeled using target points, to hold the stiff portions of the racetrack and pericardium region as rigid as possible. The parameters used in the model are found in Table 4.4 below.

Parameter	Value
Length/Width of comp. domain (m)	5.0×10^{-4}
Diameter of tube $[d]$ (m)	3.5×10^{-5}
Outer Radius $[R_o]$ (m)	1×10^{-5}
Inner Radius $[R_i]$ (m)	$d - R_o$
Length of Straight Tube (m)	5.0×10^{-4}
Eulerian Resolution $[dx]$ (m)	8.33×10^{-7}
Lagrangian Resolution $[ds]$ (m)	4.17×10^{-7}
Density of fluid $(\rho) \left[\frac{kg}{m^3} \right]$	1025
Viscosity of fluid $(\mu) \left[\frac{kg}{ms} \right]$	<i>varied</i>
Stretching stiffness of the boundary $(k_{spr}) \left[\frac{kg}{s^2} \right]$	3.24×10^5
Stretching stiffness of target points $(k_{target}) [Nm^2]$	3.24×10^5
Bending coefficient of boundary $(k_{beam}) \left[\frac{kg}{s^2} \right]$	3.24×10^5

Table 4.4: Table of the parameters associated with the fluid and the immersed boundary fiber models.

Instead of prescribing contraction, we develop a model for the underlying electrophysiology of the heart, i.e., traveling action potentials arising from a single pacemaker region, to couple to myocardial contraction and hence intracardiac fluid flow. The model of action potential propagation is given by the FitzHugh-Nagumo equations, as in Section 3.3.4 and [249, 22], and below,

$$\frac{\partial v}{\partial t} = \mathbb{D} \nabla^2 v + v(v - v_a)(v - 1) - w - \mathbb{I}(t) \quad (4.7)$$

$$\frac{\partial w}{\partial t} = \epsilon(v - \gamma w), \quad (4.8)$$

where $v(x, t)$ is the membrane potential, $w(x, t)$ is the blocking mechanism, \mathbb{D} is the diffusion

rate of the membrane potential, v_a is the threshold potential, γ is the resetting rate, ϵ is the blocking strength parameter, and $\mathbb{I}(t)$ is an applied current, e.g., an initial stimulus potentially from pacemaker signal activation. Note that v is the action potential and that w can be thought to model a sodium blocking channel. We note that the FitzHugh-Nagumo equations (4.7)-(4.8) are a reduced order model of the Hodgkin-Huxley equations, which were the first quantitative model to describe the propagation of an electrical signal across excitable cells [250]. The parameters used in the electrophysiology model are found in Table 4.5.

Parameter	Value
Threshold potential [v_a]	0.1
Strength of blocking [ϵ]	0.1
Diffusive coefficient [\mathbb{D}]	0.1 – 200
Resetting rate [γ]	0.5
Current injection [\mathbb{I}]	0.5
Frequency [f] (Hz)	1.0

Table 4.5: Table of the parameters associated with the FitzHugh-Nagumo electrophysiology model.

Next we need to interpolate the information from the electrophysiology model to the fluid-structure interaction solver, i.e., immersed boundary method. Time is scaled in order to match the dynamics of the generated action potentials to the desired active wave of contraction and is given by:

$$dt_f = \frac{dt\mathbb{F}}{\mathbb{T}}, \quad (4.9)$$

where dt is the time-step associated with the fluid solver, \mathbb{F} is a non-dimensional scaling parameter, and \mathbb{T} is the desired pumping period. The spatial location, x , in (4.7)-(4.8) is also scaled to match the dynamics of the active wave of contraction on the tube. When the propagating action potential reaches one of the muscles along the tube, the associated spring stiffness of said muscle model is given by

$$k_e(x, t) = k_m(v^4(x, t)). \quad (4.10)$$

The simplified muscle model is given by a dynamic spring stiffness coefficient, given by $k_e(x, t)$,

which is a non-linear function of the traveling action potential, $v(x, t)$. This idea was adapted from Baird *et al.* [21, 22]. The force generated by the springs that connect the bottom and top of the elastic tube can then be computed. These forces represents muscular contraction. The value of k_m is tuned to produce the amount of contraction observed in Ciona hearts, as in [21, 22].



Figure 4.14: Schematic of electrodynamical pumping. (1) The tube at rest; the springs connecting the top and bottom of the tube are the muscles. (2) The pacemaker initiates an action potential, in which the tube will contract based on the magnitude of the signal (3)-(4) The action potential propagates along the tube, inducing contraction.

The idea for electro-dynamic pumping can be seen in Figure 4.14, which is a schematic for electro-dynamical pumping behavior. First the tube is at rest until a pacemaker initiates a potential signal, which contracts the tube in one singular region. Next the action potential propagates along the tube inducing contraction. Once the action potential passes outside a region on the tube, that location no longer has active contraction, but can return to its resting position.

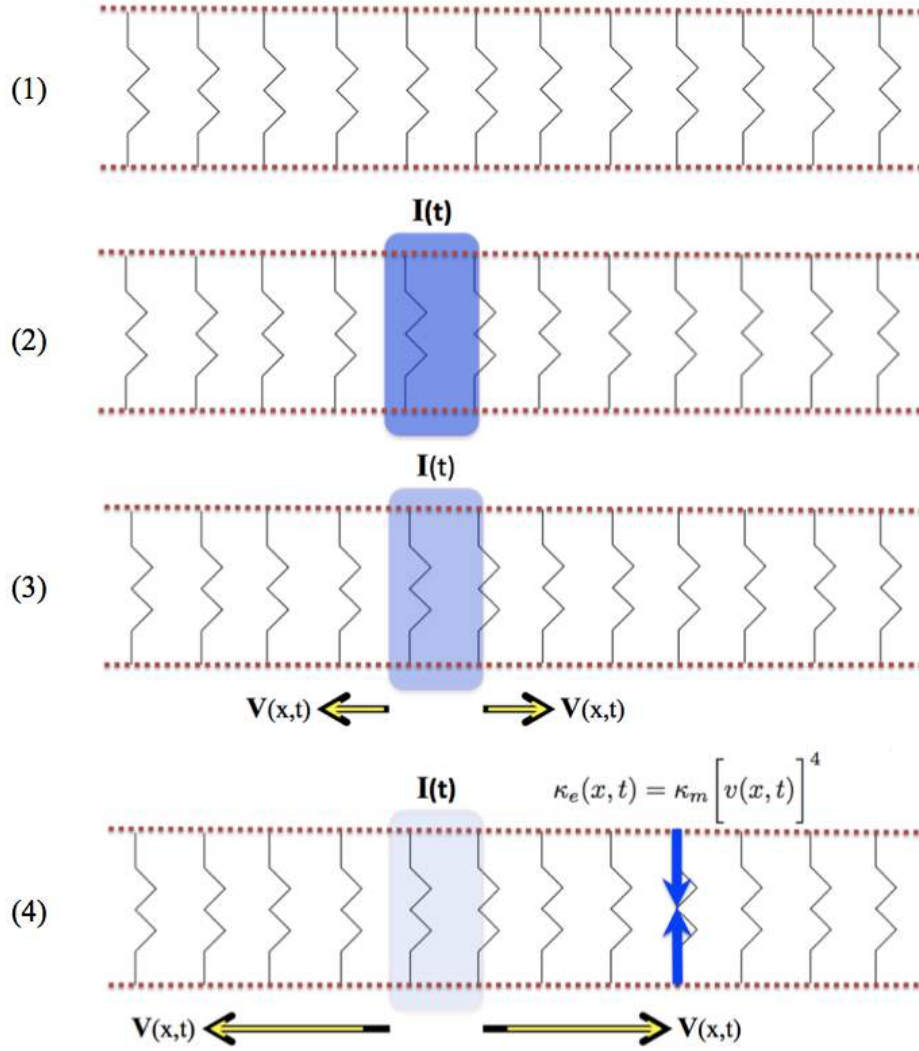


Figure 4.15: Schematic of electrodynamical pumping. (1) The tube at rest; the springs connecting the top and bottom of the tube are the muscles. (2) The pacemaker initiates an action potential, in which the tube will contract based on the magnitude of the signal (3)-(4) The action potential propagates along the tube, inducing contraction.

Furthermore the main electrophysiology idea behind the model is illustrated in Figure 4.15. In diagram 1 the flexible tube is at rest. Next 2 depicts a pacemaker initiating an input signal (current). Then that voltage (action potential) travels down the tube, while the input signal dissipates. Once the action potential reaches a muscle fiber, the tube contracts based on a non-linear relationship between spring stiffness and the magnitude of the action potential (voltage).

4.2.2 Results of the electro-dynamical model

In this study, we conducted numerical experiments of the electro-dynamic pumping model, which encompassed fully coupled electrophysiology to pumping behavior for a heart tube, modeling as a closed racetrack geometry. We investigated various diffusivities, \mathbb{D} , which give rise to different pumping regimes, e.g., either a ‘dynamic suction pumping-esque’ or ‘peristaltic-like’ pumping regime. Furthermore, we explored these regimes for over 3 orders of magnitude in Wo .

Results of the FitzHugh-Nagumo Model Here we present the varying action potential dynamics given via the FitzHugh-Nagumo equation, which models the electrophysiology. We explored this model for a variety of diffusive coefficients, $\mathbb{D} = \{0.1, 1.0, 10.0, 100.0\}$.

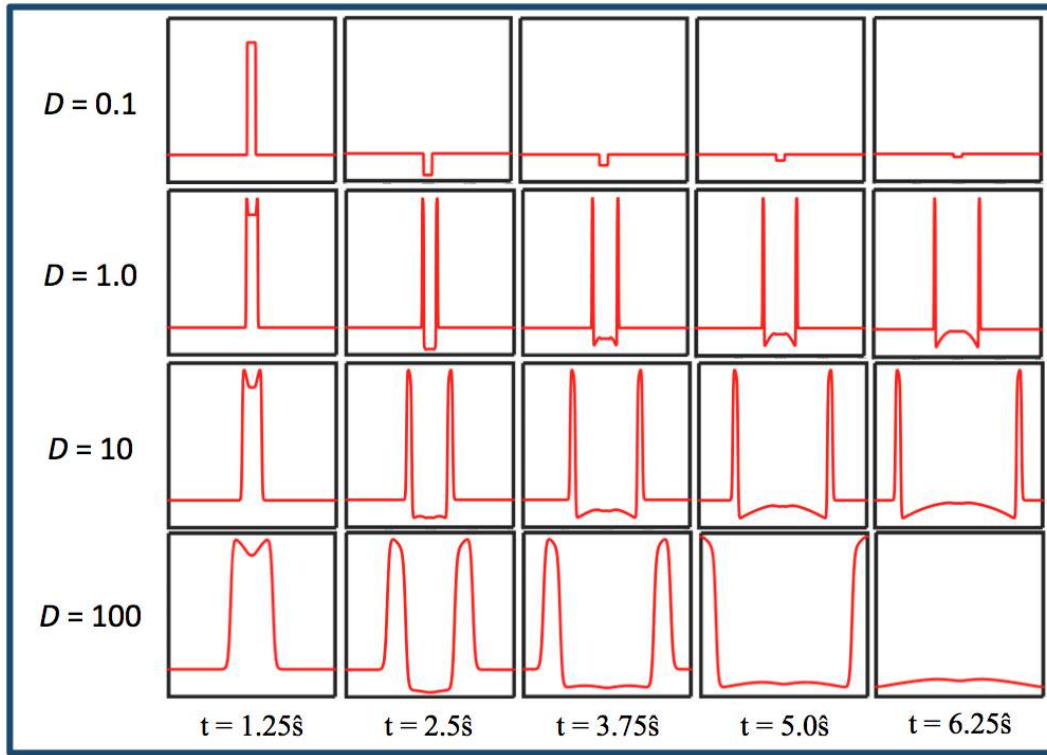


Figure 4.16: Different traveling wave propagation properties arising out of the FitzHugh-Nagumo equations for varying diffusivities, $\mathbb{D} = \{0.1, 1.0, 10.0, 100.0\}$.

Figure 4.16 illustrates the kinds of traveling action potentials that arise out of the electrophysiology model. It is clear that the $\mathbb{D} = 0.1$ case resembles a signal that could be reminiscent of that of dynamic suction pumping, whereas \mathbb{D} gives rise to a propagating action potential that could model a more peristaltic-like contraction. It is clear that as diffusivity increases, the waves propagate

outwards, and with greater wave-speed. Furthermore, the wave-form itself gets wider.

Results of the electro-dynamical heart tube model In this section we present the results describing how bulk flow rates are affected by varying the diffusivity, to capture different pumping behaviors for a variety of Wo .

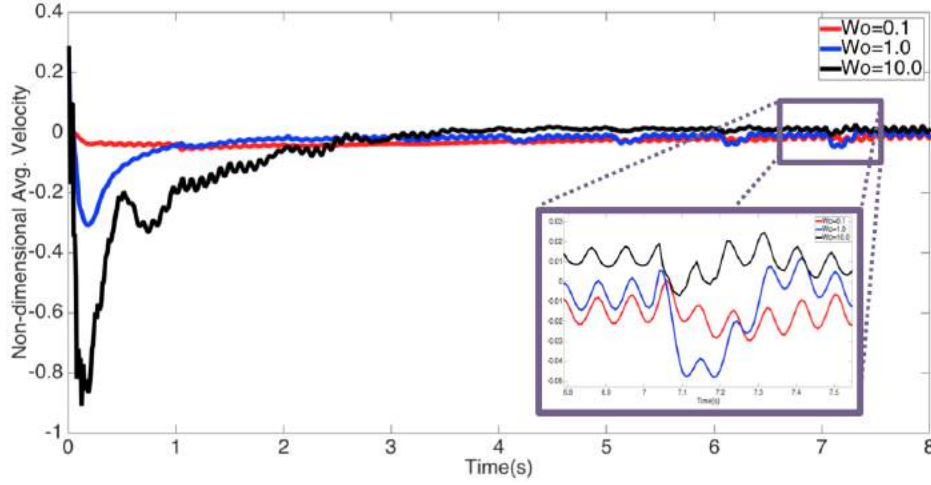


Figure 4.17: The non-dimensional spatially-averaged velocity computed across a cross-section of the top of the race-track geometry vs non-dimensional time for $\mathbb{D} = 0.1$, e.g., the ‘dynamic suction pumping’ regime, for $Wo = \{0.1, 1.0, 10.0\}$. The zoomed in portion illustrates the resulting wave-form and the high frequency oscillations that result from this pumping regime.

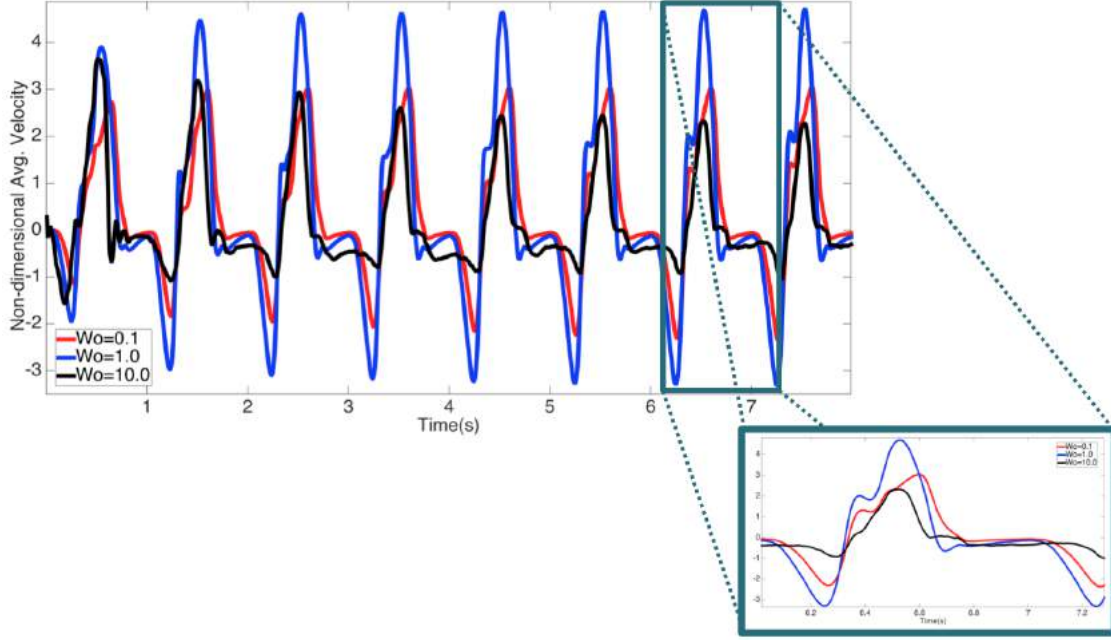
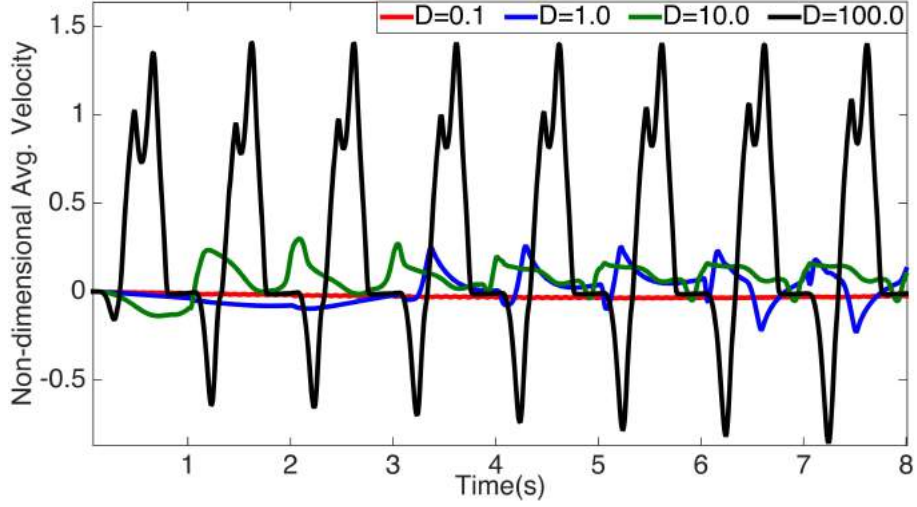


Figure 4.18: The non-dimensional spatially-averaged velocity computed across a cross-section of the top of the race-track geometry vs non-dimensional time for $\mathbb{D} = 100.0$, e.g., the ‘peristaltic’ regime, for $Wo = \{0.1, 1.0, 10.0\}$. The zoomed in portion illustrates the resulting wave-form.

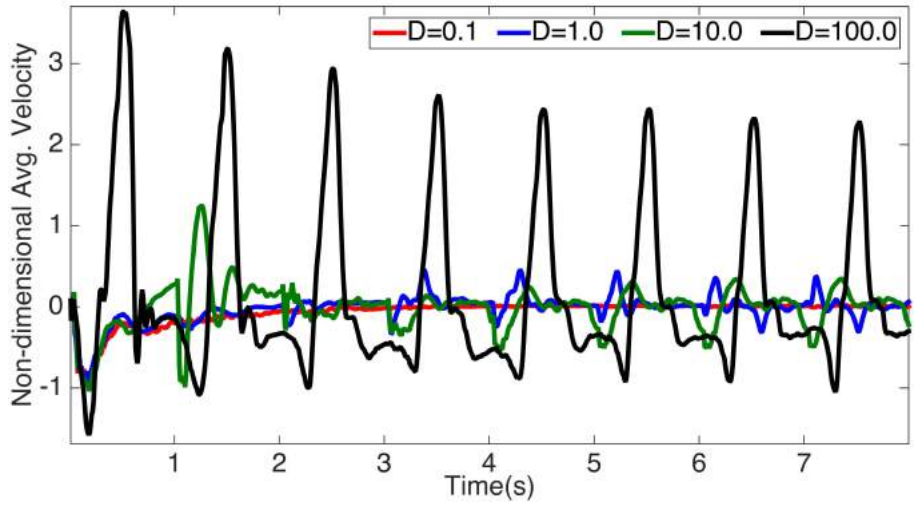
Figures 4.17 and 4.18 illustrate the non-dimensional spatially-averaged velocity computed across a cross-section of the top of the race-track geometry vs non-dimensional time for $\mathbb{D} = 0.1$ (Figure 4.17) and $\mathbb{D} = 100.0$ (Figure 4.18). It is clear that when $\mathbb{D} = 0.1$ there is not significant bulk flow produced regardless of Wo , unlike the case when $\mathbb{D} = 100.0$, where significant bulk flow is produced over all $Wo = \{0.1, 10, 10\}$. It is also clear that the wave-form produced for $\mathbb{D} = 0.1$ undergoes many more high frequency oscillations as compared to the case for $\mathbb{D} = 100$.

Comparing corresponding Wo pumping mechanisms for a variety of $\mathbb{D} = \{0.1, 1.0, 10.0, 100.0\}$ are shown in Figure 4.19, where Figure 4.19a compares pumping regimes for $Wo = 0.1$ and Figure 4.19b for $Wo = 10$. It is clear that in both cases that the most bulk flow is produced when $\mathbb{D} = 100$, and some flow is produced in the cases of $\mathbb{D} = \{1, 10\}$. There is still backflow in the $\mathbb{D} = 100$ case and less overall backflow in the $\mathbb{D} = 10$ case.

Furthermore, the wave-form in the $\mathbb{D} = 100$ case is different between the $Wo = 0.1$ and $Wo = 10$ cases. There is a single peak for the case when $Wo = 10$ and a dual peaks for $Wo = 0.1$ for the forward flow; however, in the backflow, the situation is reversed, where a dual-peak is observed for $Wo = 10$ and a single peak for $Wo = 0.1$.



(a)



(b)

Figure 4.19: A comparison of non-dimensional spatially-averaged velocity computed across a cross-section at the top of the racetrack vs non-dimensional time in the simulation for varying diffusive coefficients, $\mathbb{D} = \{0.1, 1.0, 10.0, 100.0\}$. The two plots compare different Wo , e.g., (a) $Wo = 0.1$ and (b) $Wo = 10$.

In attempt to maximize bulk flow for the dynamic suction pumping-esque regime, the stretching-stiffness and bending stiffness coefficients of the tube were varied. The results are shown in Figure 4.20. It is clear that as the stiffness is varied there is a non-linear relationships between flow speed (spatially- and temporally-averaged non-dimensional velocity across a cross-section of the racetrack)

and stiffness. However, not a considerable amount of more bulk flow was produced from increasing these stiffness coefficients.

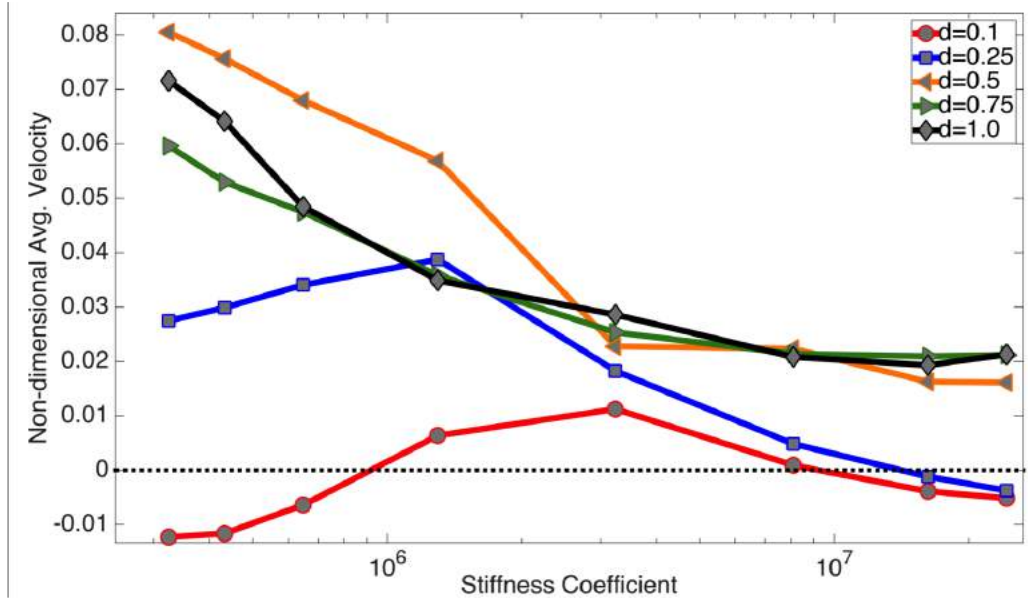


Figure 4.20: A plot of non-dimensional spatially-averaged velocity computed across a cross-section at the top of the racetrack vs the non-dimensional stretching and bending stiffness coefficients for pumping in the ‘dynamic suction pumping’ regime, for a variety of diffusivities, $\mathbb{D} = \{0.1, 0.25, 0.5, 0.75, 1.0\}$.

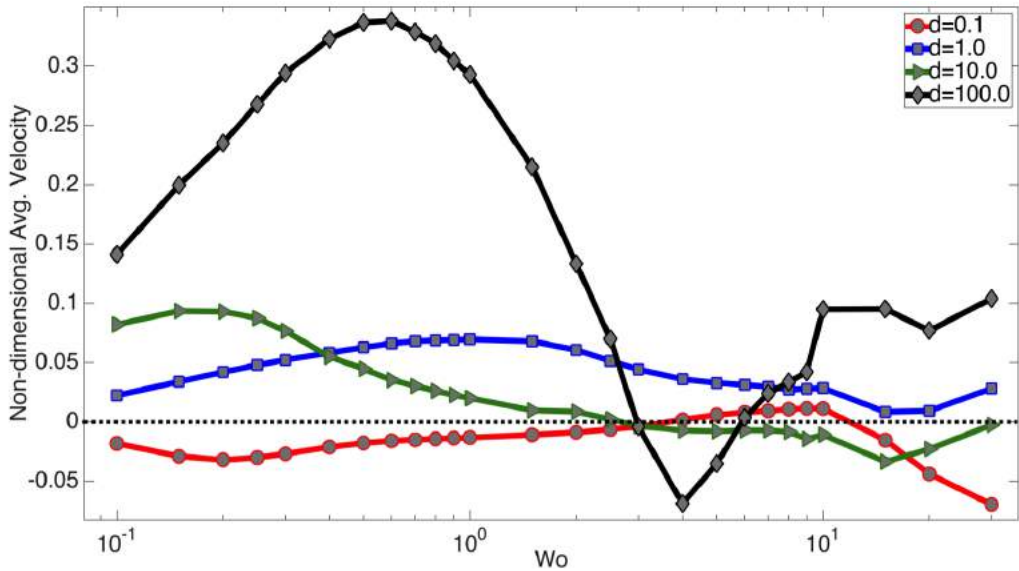


Figure 4.21: A comparison of the spatially- and temporally-averaged non-dimensional velocities computed across a cross-section of the racetrack vs. Wo for varying diffusivities, $\mathbb{D} = \{0.1, 1.0, 10.0, 100.0\}$.

Lastly we compared the spatially- and temporally-averaged non-dimensional velocities across a

cross-section of the racetrack against Wo for a variety of \mathbb{D} . The results are shown in Figure 4.21. It is clear there is a non-linear relationship in average velocity and scale arising from this model of pumping in every pumping regime, given by \mathbb{D} . Furthermore, the highest bulk flow rates were seen in the case of $\mathbb{D} = 100$ for $Wo \sim 0.8$, which correspond to the Wo around that of tunicate tubular hearts [20, 21].

4.2.3 Discussion and Conclusion of Electro-dynamic Model

This 2D model coupled the propagation of action potentials, given via the FitzHugh-Nagumo equations, to the force generation and myocardial contraction, given through a non-linear spring-like muscle model, to induce pumping behavior in a flexible tube, where the fully coupled fluid-structure interaction model was solved using the immersed boundary method. This model was first described in [22]. We explored the effect of perturbing a diffusive coefficient in the electrophysiology model to capture different pumping regimes.

It was clear that by varying this diffusive term, \mathbb{D} , the model was able to recreate a spectrum of pumping mechanisms, ranging from one that in which the action potential remained localized and did not diffuse, i.e., a dynamic suction pumping-esque behavior, and one where the action potential diffused along the heart tube in as a more traveling wave, e.g., peristaltic-like active wave of contraction. Our model showed that when \mathbb{D} was in the more peristaltic-like regime, i.e., $\mathbb{D} \sim 100$, more bulk flow was produced in the racetrack geometry, as compared to more negligible amounts from the dynamic suction pumping-esque regime, $\mathbb{D} \sim 0.1$. This result was consistent for the range of Wo considered.

Moreover, in all cases considered, there was a non-linear relationship between average flow rate, scale (Wo), and diffusivity (pumping behavior). More bulk flow was produced on average (both spatially and temporally), with a maximum around $Wo \sim 0.8$ than for higher Wo , up to $Wo = 30$, in the peristaltic-like regime. However, perturbing the material properties of the tube could potentially affect bulk flow rates across all pumping regimes, given by \mathbb{D} . Our focus was limited to perturbing the stretching and bending stiffnesses of the tube specifically within the dynamic suction pumping-esque regime, $\mathbb{D} \sim [0.1, 1]$. Furthermore, our study only considered increasing the stiffnesses and not decreasing them. For the regime and material properties considered, we found a non-linear relationship between flow rates and stiffness.

As blood flow and the resulting hemodynamic forces are essential for proper heart development

[12], it is important that the pumping model capture as much biology as possible. Each pumping regime considered here, via the specified model of action potential propagation, will give rise to a different force distribution along the endothelial lining of the heart and hence possibly change epigenetic signal that gets transmitted through mechanotransduction [251, 252]. Furthermore the flow profiles resulting from each pumping mechanism would be different. These differences in the flow patterns itself could impact the way morphogens advect and diffuse during embryogenesis [253, 254]. A preliminary simulation of an underlying concentration gradient was modeling using this electrophysiology-FSI model in Section 3.3.4, and there are many interesting biological questions to explore.

4.3 Resonant Pumping

In this section we investigate resonant properties elastic tubes, specifically interested in deciphering how pumping via dynamic suction pumping near resonant frequencies may induce more bulk flow. Furthermore we also investigate how the addition of mass, which changes the effective damping if all other parameters are held constant, affects overall bulk flow rates in such pumping systems. We will first determine resonant frequencies for the first and second modes of vibration. Next we explore pumping near such resonant modes. Lastly, we add mass to the boundary and investigate pumping when the tube is over-,under-, and critically-damped. Previous studies have looked at resonant properties of impedance pumping [16], but have not considered a massive boundary, nor did they use the *IB* formulation for investigating the phenomena.

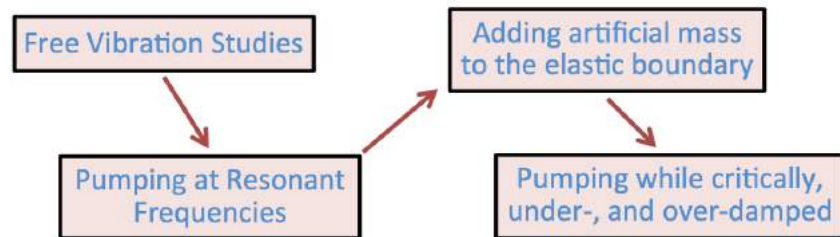


Figure 4.22: Flow chart illustrating the flow of this section.

4.3.1 Computational Model

We numerically model a $2D$ open-branched geometry, where the walls of the tube are modeled as $1D$ fibers. The straight section of the tube is flexible with uniform bending and stretching stiffnesses; however, the branched ends are held nearly rigid. The computational geometry is illustrated in

Figure 4.23. This geometry was motivated by branching vessels in tunicate embryonic hearts, see Figure 4.24, which was adapted from [36].

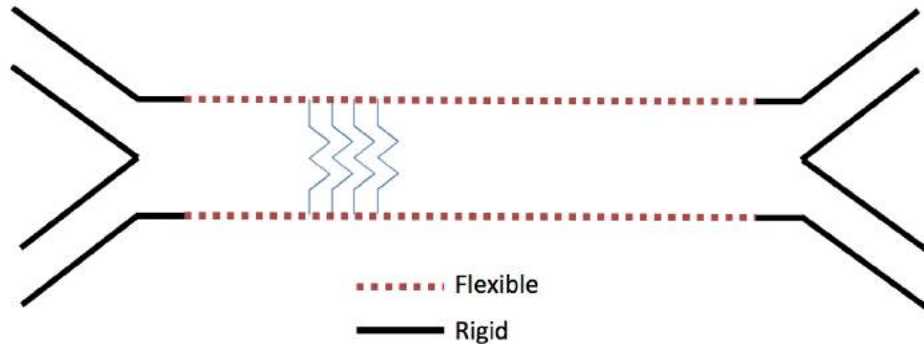


Figure 4.23: Computational geometry for the resonance studies. The straight section (dotted red) is flexible, while the branched vessels (black) are held nearly rigid. The springs connecting the top and bottom of a subset of the flexible section are the mock muscles which induce the impedance pumping behavior.

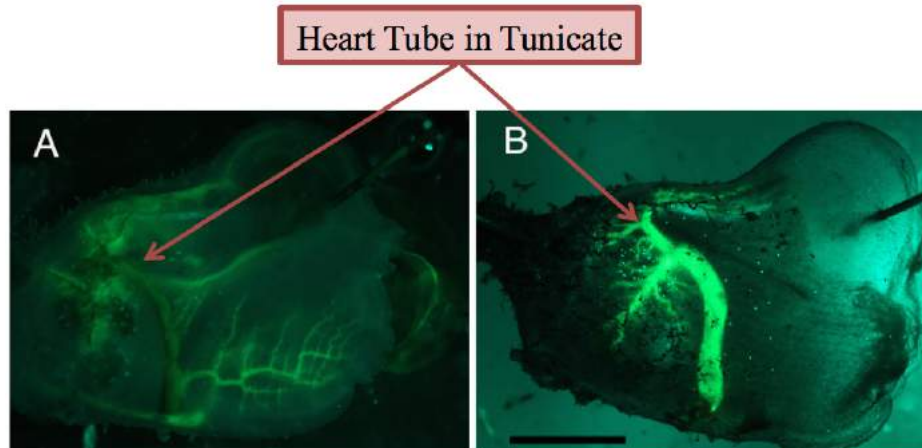


Figure 4.24: Dextran was injected at the posterior end of the heart while the heart pumped in the branchail direction (A) and dextran injected at the anterior end of the heart, while the heart pumped in the visceral direction. The dextran helps visualize the morphology of the heart and the branching vessels, motivation our computational geometry in Figure 4.23. The scale bar in B at the bottom left is 10 mm. This figure and description was adapted from [36].

The computational model we investigate is seen in Figure 4.23. The flexible region is composed of linear springs and beams connecting adjacent Lagrangian points. All other Lagrangian points of the boundary are modeled using target points, to hold the branching vessels nearly rigid. The parameters used in the model are found in Table 4.6. Also, no slip boundary conditions are enforced on all sides of the computational domain. This is to reduce the amount of flow artifacts from periodic

boundary conditions for the open branched tube geometry.

Parameter	Value
Length/Width of comp. domain (m)	1.0
Diameter of tube $[d]$ (m)	0.1
Length of Flexible Portion of Straight Tube (m)	0.4
Length of Rigid Portion on Each End of Straight Tube (m)	0.125
Angle Between Branched Vessels (radians)	$\frac{\pi}{6}$
Width of Branched Vessels (m)	0.05
Width of Actuator Region (m)	0.04
Distance to where Actuator Region begins (from left flexible region) (m)	0.085
Eulerian Resolution $[dx]$ (m)	1.95×10^{-3}
Lagrangian Resolution $[ds]$ (m)	9.77×10^{-4}
Density of fluid $(\rho) \left[\frac{kg}{m^3} \right]$	1000
Viscosity of fluid $(\mu) \left[\frac{kg}{ms} \right]$	<i>varied</i>
Frequency of Impedance Pump (s^{-1})	<i>varied</i>
Stretching stiffness of the boundary $(k_{spr}) \left[\frac{kg}{s^2} \right]$	2.05×10^3
Stretching stiffness of target points $(k_{target}) [Nm^2]$	2.05×10^3
Bending coefficient of boundary $(k_{beam}) \left[\frac{kg}{s^2} \right]$	5.38×10^8
Mass of Massive Points (kg)	<i>varied</i>

Table 4.6: Table of the parameters associated with the fluid and the immersed boundary fiber models for the resonance studies.

4.3.2 Results of Resonant Studies

Using this model we first calculated the resonant frequencies of the first and second modes of vibrations for the a flexible tube with material properties described in Table 4.6. After computing those frequencies we then investigated pumping performance near such resonant frequencies. Finally we added damping to the system by modeling the flexible region with massive points and explored the role damping has on bulk transport when pumping near resonance.

Free Vibration Studies We started by conducting free vibration studies to determine resonant frequencies for a variety of fluid viscosities. The tube was pulled from its equilibrium position (preferred configuration), e.g., straight geometry, as in a way that geometrically resembles the first or second mode of vibration. The first and second modes of vibration waveforms are illustrated in Figure 4.25. The tube is then released and is free to oscillate and/or return to its equilibrium position.

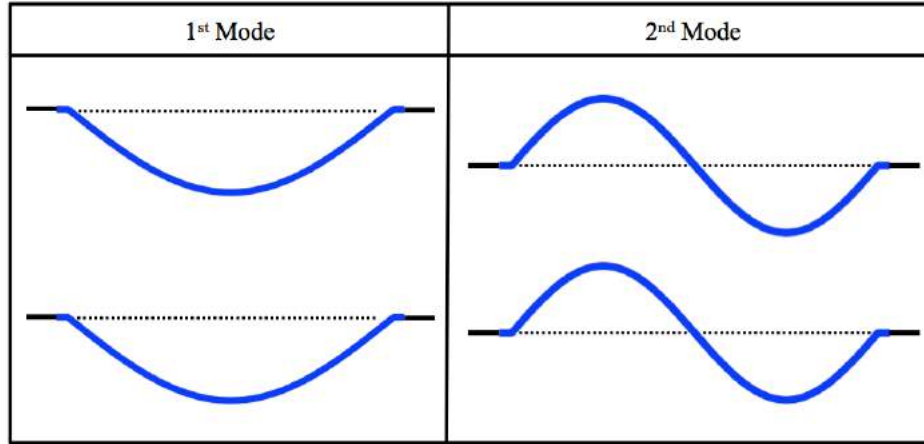


Figure 4.25: Illustrating the 1st and 2nd vibrational mode waveforms. The waveforms are in blue, while the solid black represents rigid sections along the straight portion, and the dotted black line resembles the tube's equilibrium position.

Figure 4.26 shows the oscillatory dynamics for two different vibration studies, corresponding to differing vibrational modes and viscosities. It is clear that in both the first and second mode, with the material properties of the tube described in Table 4.6, that for a viscosity of $\mu = 1.0 \frac{kg}{m \cdot s}$ (blue), the tube is under-damped, while for a viscosity of $\mu = 3.5 \frac{kg}{m \cdot s}$ (pink), the tube appears either critically- or over-damped. Note that for the two different vibration modes, a different resonant frequency emerges, with that of the 1st mode being almost an order of magnitude less than that of the 2nd mode. We comment that the third mode could have been investigated as well, but we forewent to include that in this study.

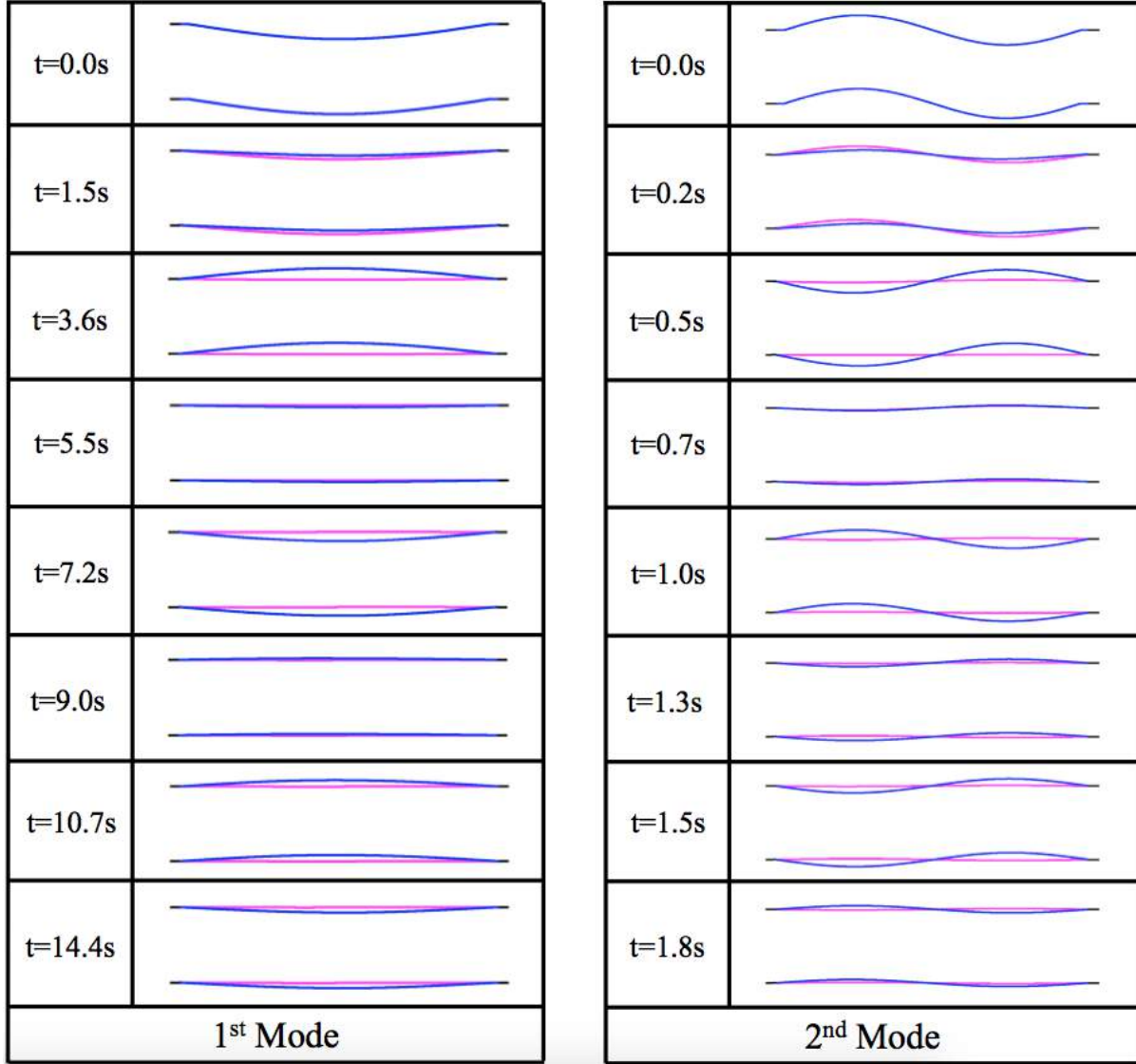


Figure 4.26: Free vibration studies for two situations, where each case corresponds to a different vibration mode, 1st (left) and 2nd (right), for the same flexible geometry. However, in each case, there are two simulation snapshots shown corresponding to two different viscosities, i.e., $\mu = 1.0 \frac{kg}{m \cdot s}$ (blue) and $\mu = 3.5 \frac{kg}{m \cdot s}$ (pink). It is clear that the 1st and 2nd mode have differing resonant frequencies.

Finally we can perform similar free vibration tests for a range of viscosities for both the first and second modes of vibration. A figure illustrating the oscillations associated with varying viscosities for the first and second mode is shown in Figure 4.27. This plot shows the displacement from equilibrium of the peaks in the first and second mode. It is evident that for some viscosities the system is over-, under-, or critically-damped. The resonant frequencies we found in our study are shown in Figure 4.28. Over the range of viscosities considered, e.g., $\sim [6 \times 10^{-3}, 40]$, the resonant

frequency for the first mode is approximately found to be constant around $f_{Res_1} \sim 0.28s^{-1}$. The resonant frequency of the second mode slightly decreases as viscosity increases.

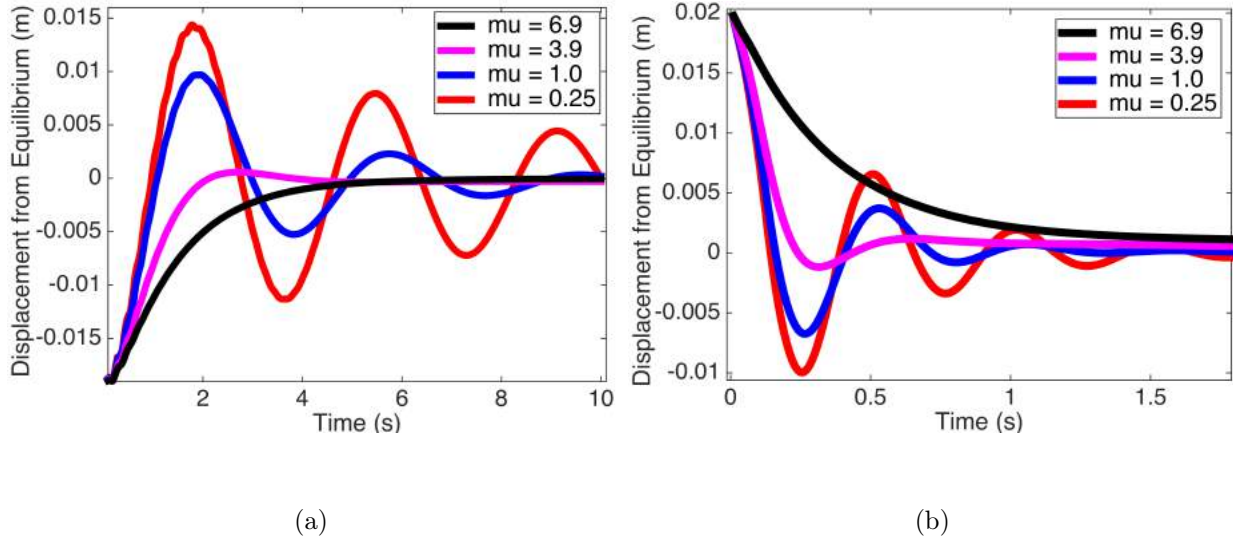


Figure 4.27: Plots showing the displacement from equilibrium of the peaks of the first and second modes of vibration during the free vibration tests. It is clear that for some viscosities the system is over-, under-, and critically-damped.

Although while changing the viscosity of the fluid, will change the Womersley Number, Wo , we find over this range of viscosities, the resonant frequencies do not differ significantly. Because of this, it will be possible to compare simulations with differing Wo , but similar resonant frequencies, to see how much the resonance properties of the tube affect the resulting bulk flows rates. We will now explore pumping these tubes near and away from the first and second vibrational mode's resonances to investigate such effects.

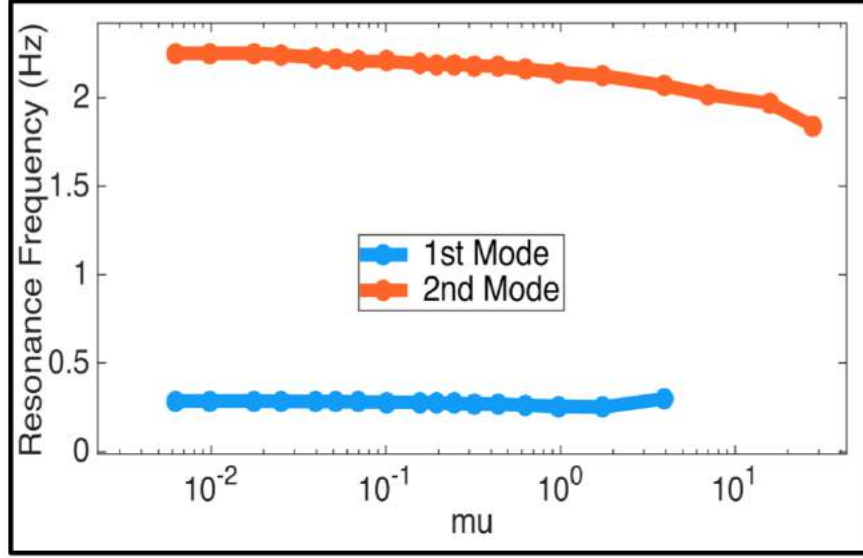
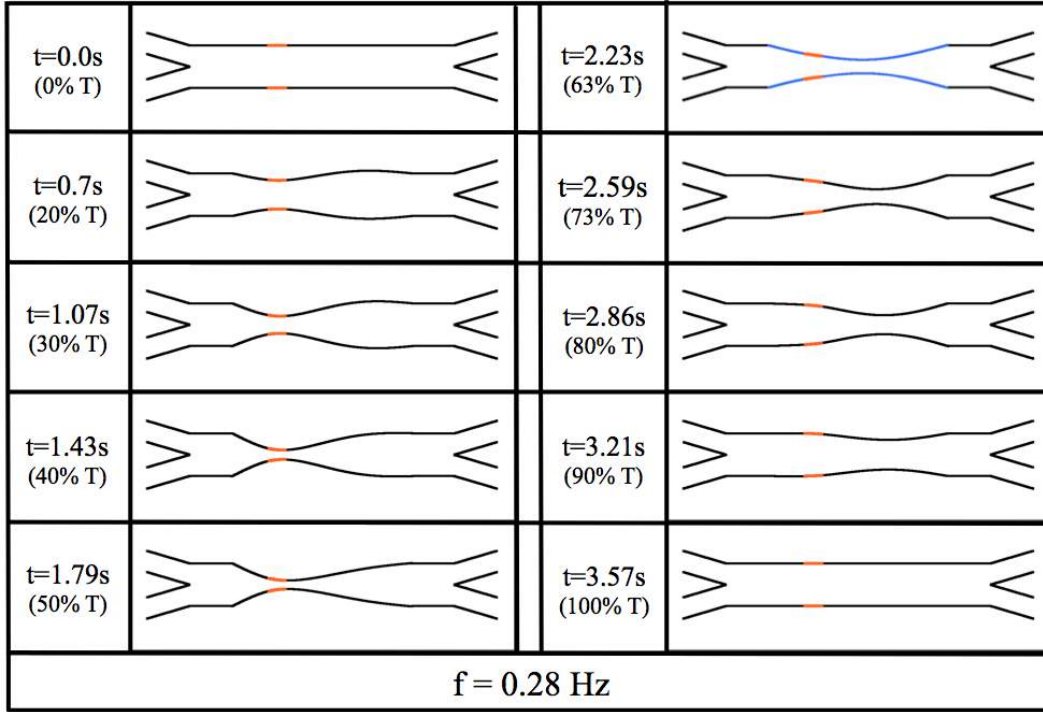


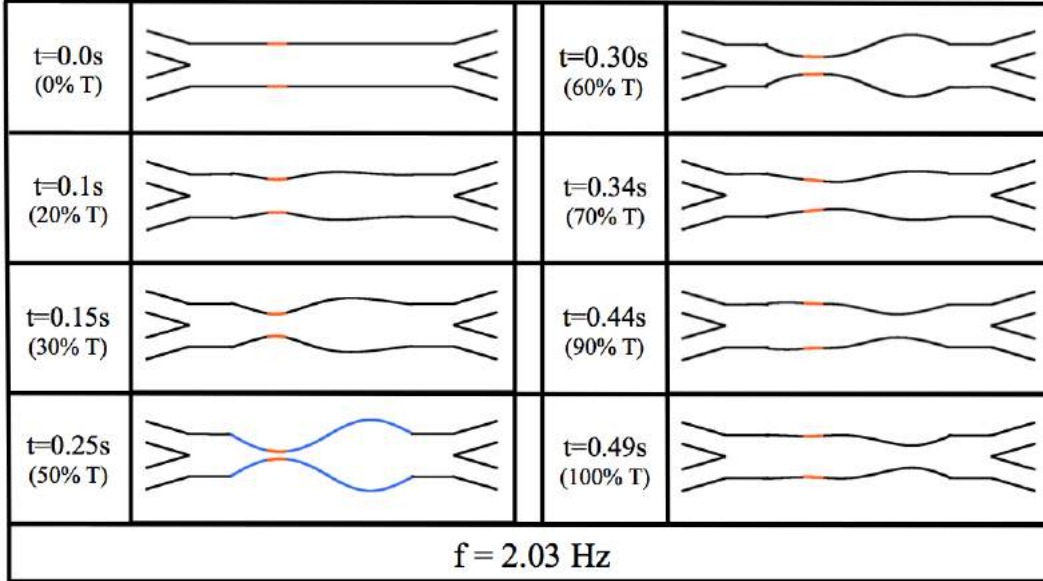
Figure 4.28: Numerically found resonant frequencies in both the first and second vibrational modes for a flexible tube immersed in a fluid. A free vibration test was performed in each viscosity and vibrational mode.

Pumping Near the 1st and 2nd Mode Resonances We begin by pumping the branched tube at the first and second vibrational mode's resonances, as well as, a frequency in the middle, to observe the passive elastic waveforms, which result from dynamic suction pumping. We ran these simulations for a viscosity of $\mu = 1.75 \frac{kg}{m \cdot s}$ and $f_{1st} = 0.28Hz$, $f_{2nd} = 2.03Hz$, and $f_m = 0.9Hz$, where f_{1st} and f_{2nd} are the first and second mode resonances, respectively, and f_m is some arbitrary frequency chosen between those resonance frequencies.

First, we observed the passive elastic waveforms arising from pumping at the first and second mode resonances. Snapshots of the pumping tube for the first and second mode resonances are found in Figures 4.29a and 4.29b, respectively. The orange bar gives the active region of actuation along the tube, while the blue coloring on the tube at 50% of one dynamic suction pumping period, T , illustrate that presence of the respective mode's waveform arising from pumping at that mode's resonance.



(a)



(b)

Figure 4.29: Illustrating the pumping dynamics and the resulting passive elastic waves for the first (a) and second (b) mode resonances for varying snapshots from a single period, T , of dynamic suction pumping. The orange bar represents the active region of actuation. The blue coloring of the tube (at 50% of a period) show that the vibrational mode waveform shows up during the pumping.

It is clear that the resulting passive elastic waves are vastly different when pumping at either the first or second vibrational mode's resonant frequencies. A simulation of a tube being pumped at a frequency between those resonance frequencies, but the same viscosity, is shown in Figure 4.30. Comparing the passive elastic waveforms from Figure 4.30 to 4.29, it is evident that the passive elastic waveforms are different. However, the case of $f_m = 0.9Hz$ has both the first and second mode waveforms arising during the course of one period of dynamic suction pumping, as shown by the blue coloring of the flexible tube in Figure 4.30.

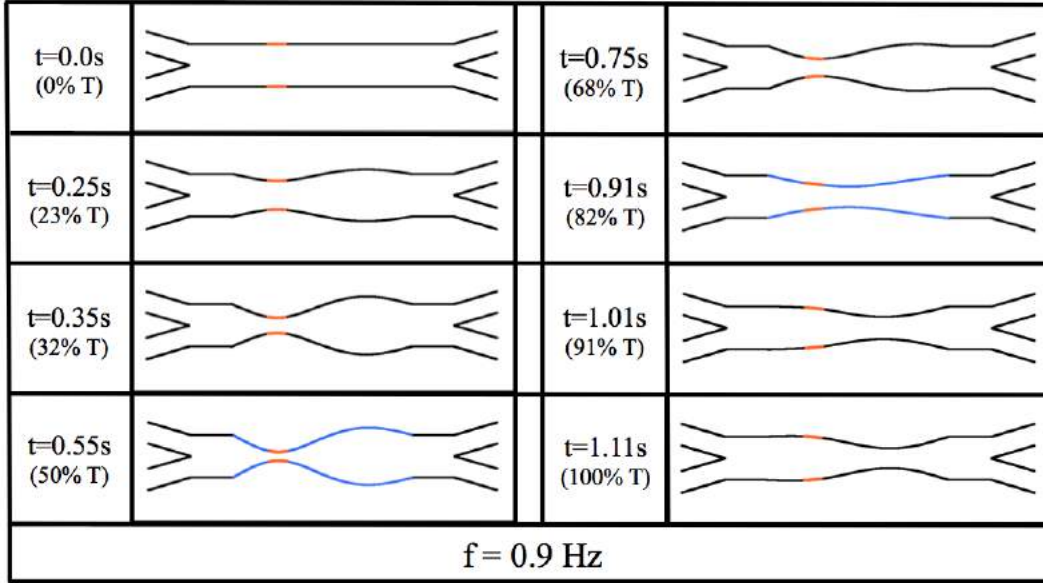


Figure 4.30: Illustrating the passive elastic waves arising from pumping the tube at a frequency of $f_m = 0.9Hz$ and viscosity, $\mu = 1.75 \frac{kg}{m \cdot s}$. The orange bar represents the region of active contraction. The blue coloring of the tube represents where the first and second mode waveforms are visible during one period of dynamic suction pumping.

Next we performed a frequency sweep for the case of $mu = 1.75 \frac{kg}{m \cdot s}$. Figure 4.31 shows snapshots of a few select simulations. The pink dots represent passive tracers in the flow that move at the local fluid velocities, but have no effect on the flow itself. From qualitative observations it is clear that there is a non-linear relationship between frequency and flow, and hence also Wo . Moreover the select cases illustrate that more bulk flow is going towards the right hand side of the computational domain. The cases of $f = 0.28Hz$ (the 1st mode resonance) and $f = 0.55Hz$ seemed to produce the most bulk flow, followed by the case with $f = 2.03Hz$ (the 2nd mode resonance), while the case with $f = 1.1Hz$ produced the least bulk flow. Note that the backscattering of the passive tracers on the

right side of the branched vessels is because of the no slip boundary conditions enforced on the walls of the computational domain.

Although Figure 4.31 compares flow behavior at corresponding pumping points throughout the simulation, it is important to note that since each case is being pumped at a different frequency, the total amount of bulk transport will be different at a particular time. For example, in the case of $f = 0.28Hz$, which seemingly produced the most bulk flow after 5.5 dynamic suction pumps, in that same amount of time it took to achieve those 5.5 pumps, the case for $f = 2.03Hz$ will have almost completed 40 complete pumps.

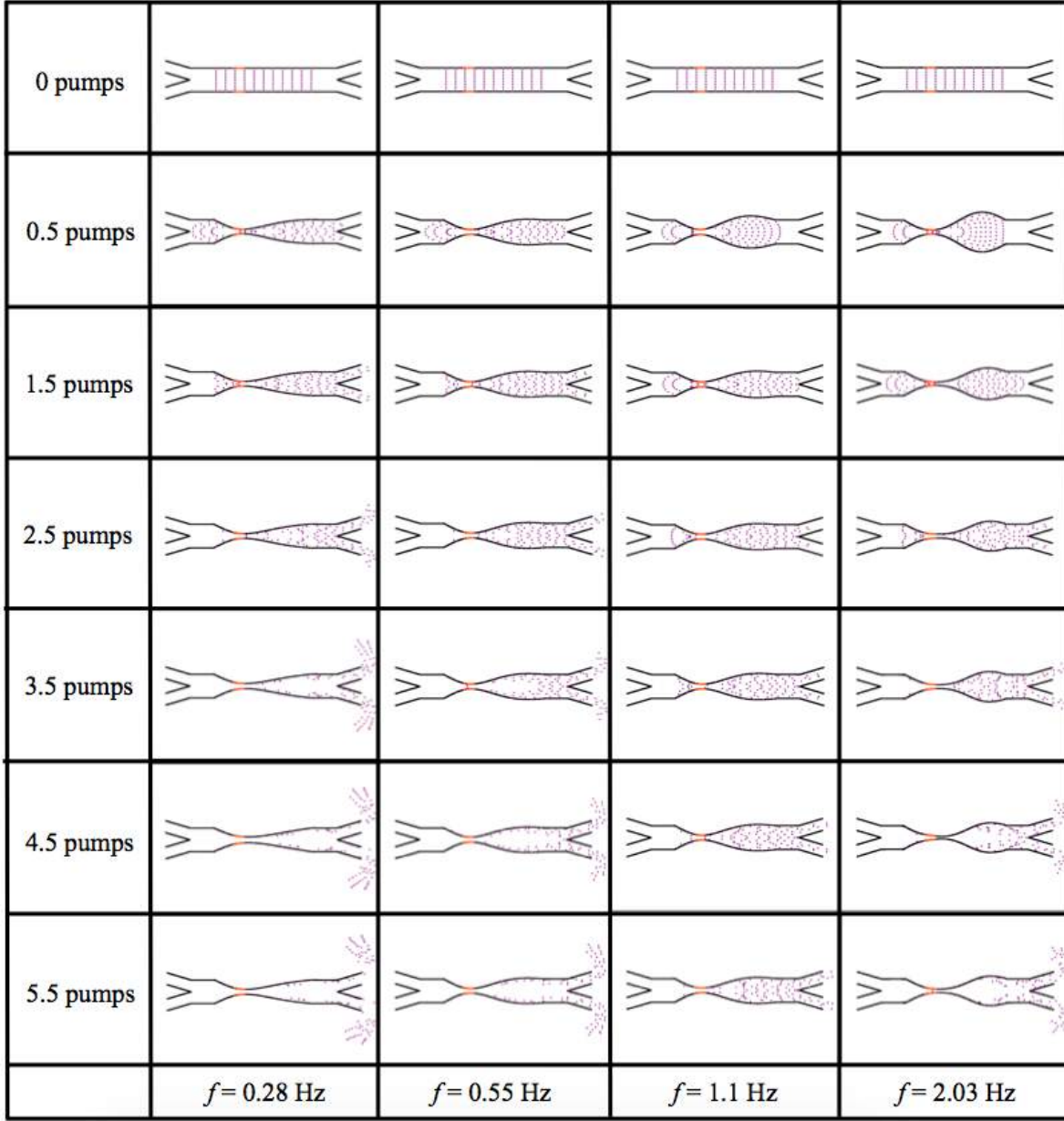


Figure 4.31: Snapshots from simulations pumping at varying frequencies, qualitatively showing bulk flow properties via the movement of passive tracers in the flow. The tube was pumped at the first and second vibrational mode resonance frequencies, $f = 0.28 \text{ Hz}$ and $f = 2.03 \text{ Hz}$, respectively, as well as two other frequencies in between those values, $f = \{0.55, 1.1\} \text{ Hz}$.

We can now compare the bulk flow dynamics for the case of $f = 0.28 \text{ Hz}$ for $\mu = \{0.07, 1.75\} \frac{\text{kg}}{\text{m} \cdot \text{s}}$, as the resonant frequency remains approximately equal as shown in Figure 4.28. The snapshot illustrated in Figure 4.32 compares the two cases after 3.75 dynamic suction pumps as well as one later image from 10.5 impedance pumps for the case of $\mu = 1.75 \frac{\text{kg}}{\text{m} \cdot \text{s}}$. There appears to be more bulk

flow per pump of the passive tracers in the case of lower viscosity case, $\mu = 0.07 \frac{kg}{m \cdot s}$. Furthermore, from this observation, inconjunction with observations from Figure 4.31, we see there is a complex non-linear relationship between flow rates, viscosity, and frequency.

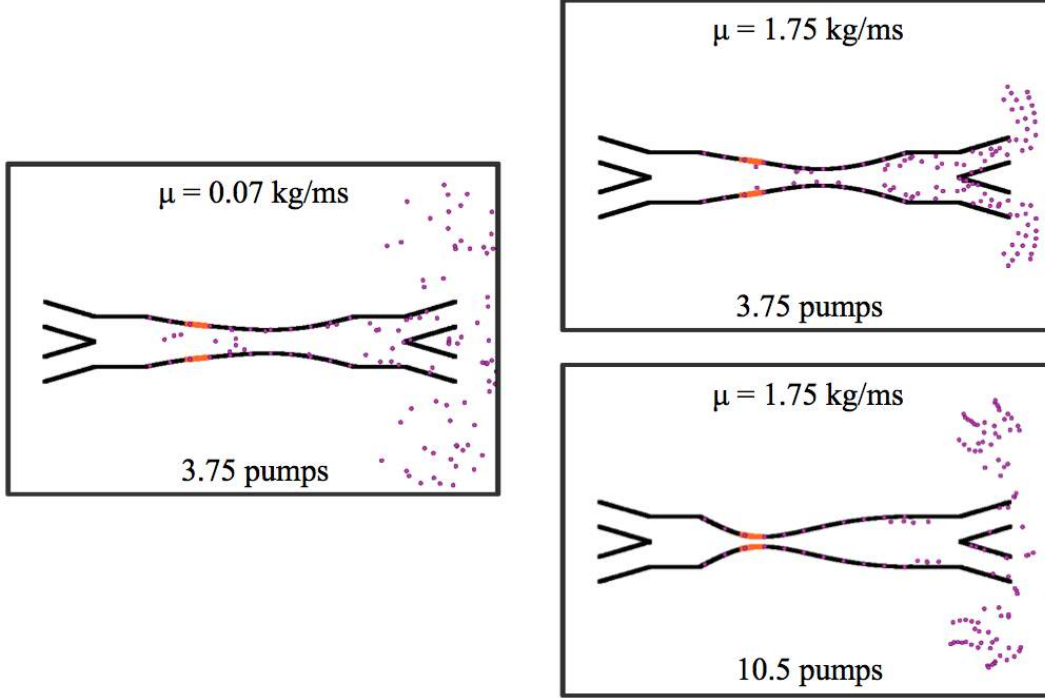


Figure 4.32: Snapshots comparing qualitative bulk flow for two simulations pumping at the same frequency $f = 0.28Hz$ (first mode resonance), but two different viscosities $\mu = \{0.07, 1.75\} \frac{kg}{m \cdot s}$. There appears to be more bulk from in the case with $\mu = 1.75 \frac{kg}{m \cdot s}$.

We will now investigate the effect of adding mass to the flexible boundary, using the massive point fiber model of immersed boundary, as described in Section 3.3.2.

Effects of Damping While Pumping Near Resonance We begin this study by quickly recalling that each of our studies in the previous section used a dynamic viscosity of $\mu = 1.75 \frac{kg}{m \cdot s}$. Here we begin by showing snapshots from simulations with lower viscosity, $\mu = 0.07 \frac{kg}{m \cdot s}$ and pumping at the first mode's vibrational resonant frequency $f = 0.55Hz$, which showed good bulk flow in Figure 4.31. Snapshots from this simulation are shown in Figure 4.33.

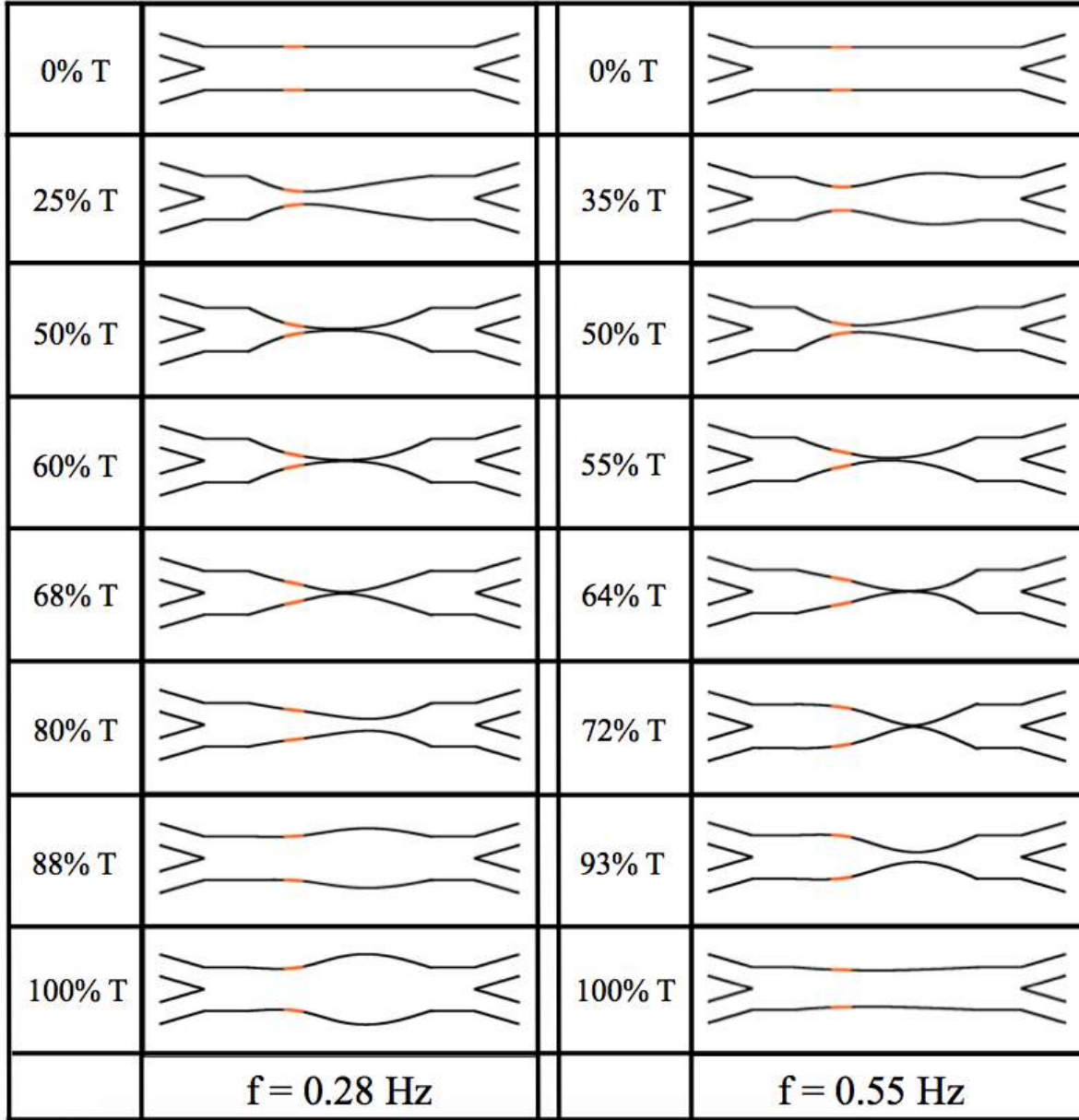


Figure 4.33: Snapshots from simulations with viscosity $\mu = 0.07 \frac{kg}{m \cdot s}$ and at frequencies $f = \{0.28, 0.55\} Hz$, illustrating the waveforms of the passive elastic waves. In each case there is a strong interaction of the tube walls during each dynamic suction pump.

From Figure 4.33 we observe that, in the case of $f = 0.28 Hz$, the tube oscillates more (i.e., at snapshots 88%T and 100%T) than the case with viscosity $\mu = 1.75 \frac{kg}{m \cdot s}$ in Figure 4.26. Furthermore, another qualitative difference is that there is almost full occlusion for $\mu = 0.07 \frac{kg}{m \cdot s}$ in Figure 4.33. Moreover, this occlusion causes an highly oscillatory interaction between the top and bottom of the tube walls for a fraction of the entire pumping cycle.

We now add massive points to the boundary. The hypothesis is that the added mass will add extra inertia to the boundary. This could potentially introduce new dynamics to the passive elastic waveforms, which could affect bulk flow rates, for better or worse. Note that adding additional mass will lower the effective damping. Recall the damping of a spring, as described in Section 3.2.1,

$$\zeta = \frac{b}{2\sqrt{mk}}, \quad (4.11)$$

where b is the damping coefficient which is proportional to viscosity, k is the spring stiffness, and m is the effective mass. The effective mass is a sum of the boundary layer plus the boundary mass. Hence adding mass decreases damping ratio, and we note that when the damping ratio is less than one, the system will be under-damped.

We first illustrate the change in the passive elastic waves during pumping due to added mass on the boundary. Each mass point is set at $2.0kg$ with a mass stiffness coefficient of $5 \times 10^7 \frac{kg}{s^2}$, while pumping at the first mode resonance. It is clear that the added mass had an impact on the waveforms of the passive elastic waves, essentially decreasing the amplitude of oscillation, while simultaneously adding in extra inertia. However, the resulting passive elastic waves still briefly took on the waveform associated with the first mode's waveform. This behavior is illustrated in Figure 4.34.

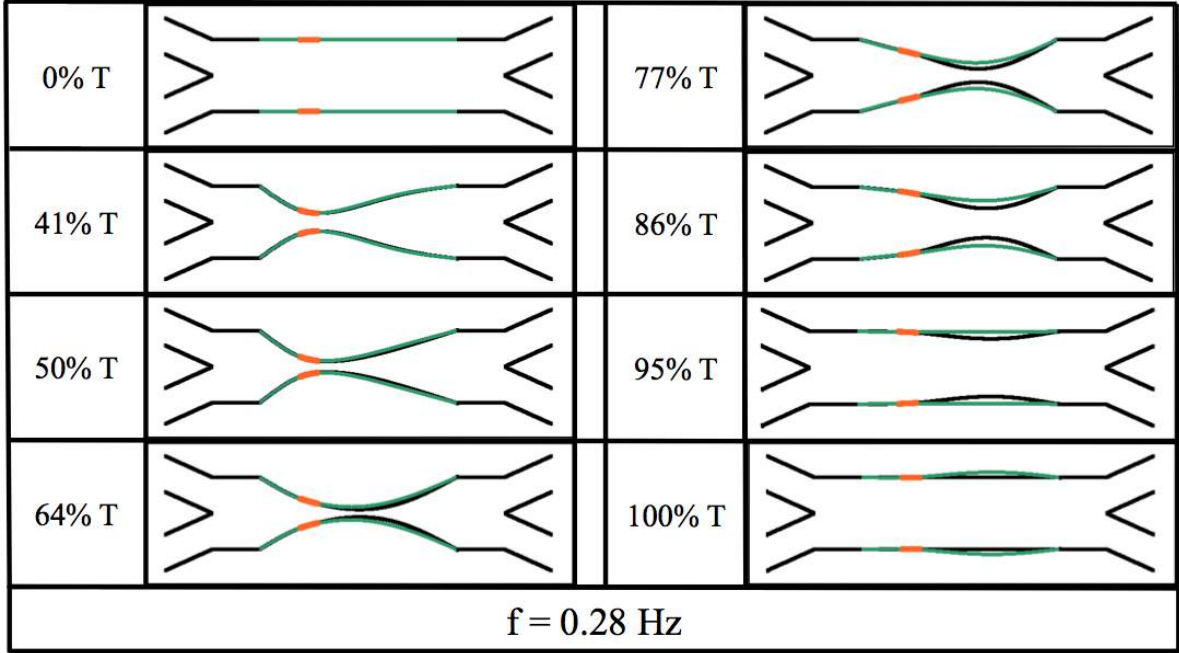


Figure 4.34: Snapshots from simulations with viscosity $\mu = 0.07 \frac{kg}{m \cdot s}$ and at frequencies $f = \{0.28, 0.55\} Hz$, illustrating the waveforms of the passive elastic waves. In each case there is a strong interaction of the tube walls during each dynamic suction pump.

Next we can compare bulk flow rates between three cases - one case with no mass added and two cases with added masses of $m = 0.2$ and $2.0kg$. A simple qualitative comparison is shown in Figure 4.35, which uses passive tracers to illustrate the bulk flow for subsequent pumping cycles. All cases pumped at a frequency of $f = 0.28Hz$ (the resonant frequency of the 1st vibrational mode) and viscosity of $\mu = 1.75 \frac{kg}{m \cdot s}$. Note that both added mass cases use an associated mass tethering stiffness of $5 \times 10^7 \frac{kg}{s^2}$. Both cases of added mass qualitatively produced more bulk flow than the case without mass; however, the case with $m = 0.2kg$ seems to have produced more bulk flow than the case of $m = 2.0kg$. Hence there appears to be a complex non-linear relationship between added mass to the boundary and performance of dynamic suction pumps.

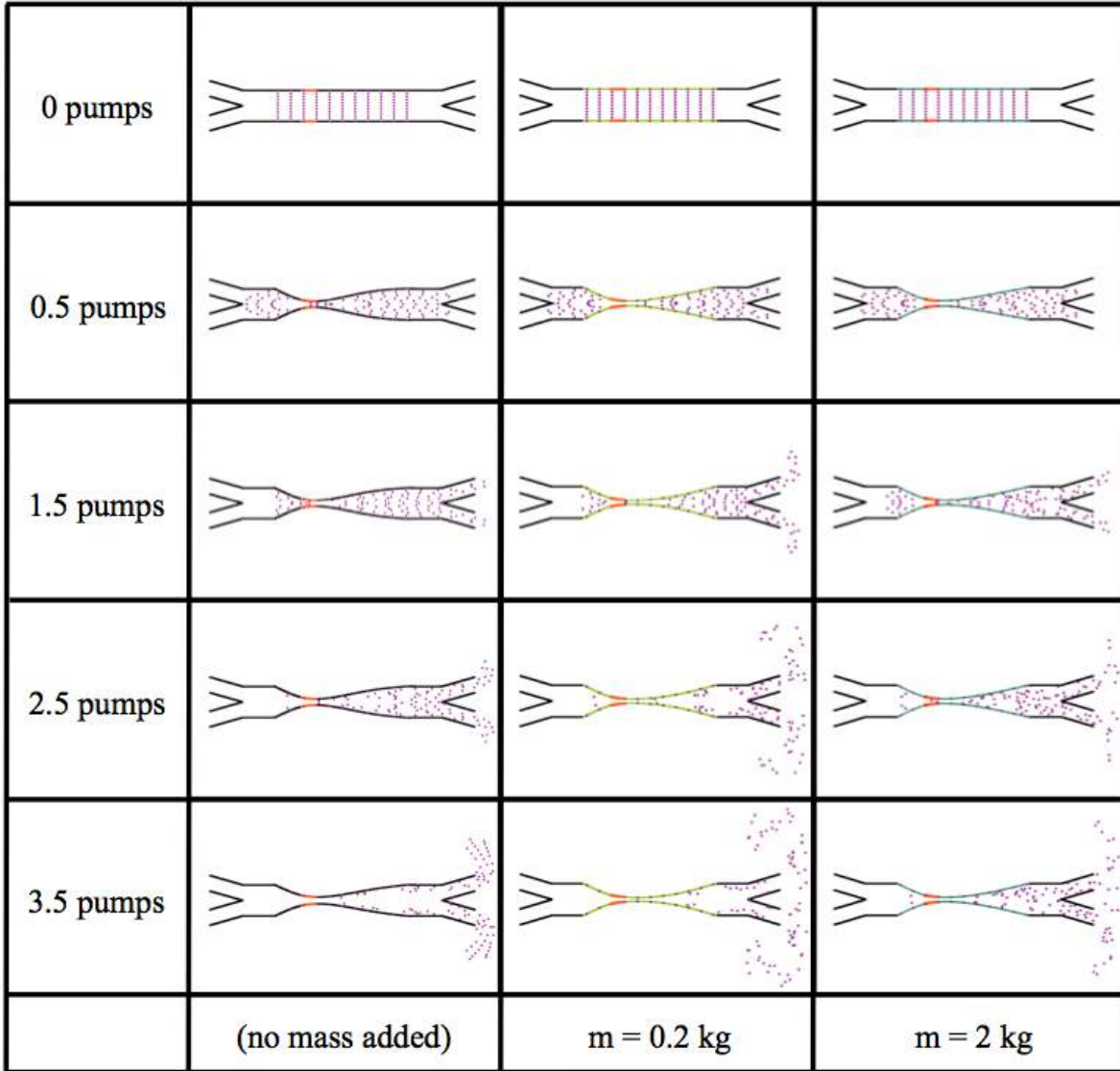


Figure 4.35: Snapshots from simulations with differing amounts of added mass to the boundary, while pumping at the same frequency ($f = 0.28Hz$) and viscosity ($\mu = 1.75 \frac{kg}{m \cdot s}$).

4.3.3 Discussion and Conclusion for DSPs Pumping at Resonance

The preliminary simulations performed here illustrate that exploring the resonance properties of dynamic suction pumping leads to interesting behavior. We first found that over a large regime of viscosities, that the resonance properties of a flexible tube, with material properties given in Table 4.6, show little dependence on viscosity for the first vibrational mode's resonant frequency, while the second mode's resonant frequency depended slightly on viscosity. Using this information allows once to directly compare simulations with the same resonance properties, while varying viscosity (and hence Wo).

Next we showed that while pumping at the first and second mode resonant frequencies that the resulting passive elastic waves from impedance pumping take on that mode's associated vibrational waveform. This remained consistent even in the case of adding mass to the boundaries. Furthermore we saw a non-linear relationship between bulk flow and frequency. Moreover, we witnessed that pumping near resonant frequencies seems to produce more bulk flow, although pumping at the second mode's resonance frequency did not qualitatively produce more bulk than pumping at a frequency near the first mode's.

Lastly adding mass to the boundary had a significant effect on the resulting passive elastic waveforms from dynamic suction pumping. We saw that the effect of mass looked to decrease the amplitude of oscillation, but add extra oscillatory behavior by added inertial effects on the boundary, and hence had an impact on bulk flow rates. For the simulations performed, we qualitatively showed that adding mass to the boundary had a non-linear effect on bulk flow. The added mass has an effect to lower the over-all damping of the system, which seems to significantly contribute to bulk flow rates in dynamic suction pumping.

Although dynamic suction pumping is an easy to prescribe pumping mechanism, the relationships between all parameters of the system (frequency, material properties, viscosity, e.g., scale) and bulk flow rates are very complex in nature. More work can be done in trying to understand the details of these very intricate, non-linear relationships.

CHAPTER 5

Flow Through Embryonic Cardiac Trabeculae

Micro changes in air density, my ass.

-Ripley (Alien)

5.1 Trabeculation Introduction

Fluid dynamics is important to organogenesis in many systems. The advection and diffusion of morphogens as well as the hemodynamic forces generated are known to regulate morphogenesis [255]. Forces such as shear stress and pressure may be key components that activate developmental regulatory networks [49]. These mechanical forces act on the cardiac cells, where the mechanical stimuli is then transmitted to the interior of the cell via intracellular signalling pathways, i.e., mechanotransduction [256]. In terms of mixing, the magnitude, direction, and pulsatile behavior of flow near the endothelial layer may influence receptor-ligand bond formation [257] and enhance the mixing of chemical morphogens. Advection-driven chemical gradients act as epigenetic signals driving morphogenesis in ciliary-driven flows [258, 259], and it is possible that flow-driven gradients near the endothelial surface layer also play a role in cardiogenesis and vasculogenesis.

The notion that flow is essential for proper vertebrate cardiogenesis is not a recent idea. It was first investigated by Thoma in 1893 and Chapman in 1918 when chicken hearts were surgically dissected during embryogenesis, and their resulting circulatory systems did not develop properly [78, 77]. Moreover, the absence of erythrocytes at the initiation of the first heart beat and for a period of time later, supports the belief that the early developing heart does not pump for nutrient transport. These results suggest that the function of the embryonic heart is to aid in its own growth as well as that of the circulatory system [79].

Later experiments show that obstructing flow in the venous inflow tract of developing hearts *in vivo* results in problems in proper chamber and valve morphogenesis [43, 12, 90]. For example,

Gruber *et al.* [43] found that irregular blood flow can lead to hypoplastic left heart syndrome (HLHS), where the ventricle is too small or absent during the remainder of cardiogenesis. Hove *et al.* [12] observed that when inflow and outflow tracts are obstructed in 37 hpf zebrafish, regular waves of myocardial contractions continue to persist and neither valvulogenesis, cardiac looping, nor chamber ballooning occur. Similarly, de-Vos *et al.* [90] performed a similar experiment in chicken embryos at a similar stage of development, e.g., HH-stage 17 [62, 260], whereby the venous inflow tract was obstructed temporarily. They noticed that all hemodynamic parameters decreased initially, i.e., heart rate, peak systolic velocity, time-averaged velocity, peak and mean volumetric flow, and stroke volume. Only the heart rate, time-averaged velocity, and mean volumetric flow recovered near baseline levels.

Trabeculae are particularly sensitive to changes in intracardiac hemodynamics [52]. They fail to form in the absence of blood flow [261, 262, 89], and moreover require an endocardium to form [55, 263]. Trabeculae are bundles of muscle that protrude from the interior walls of the ventricles of the heart. The sensitivity of the trabeculae under varying mechanical loads is important when considering they may serve as important structures in which cellular mechanotransduction occurs. Trabeculation may also help regulate and distribute shear stress over the ventricular endocardium, enhance mixing, and modify chemical morphogen gradients. Furthermore, the presence of trabeculation may contribute to a more uniform transmural stress distribution over the cardiac wall [57]. Even subtle trabeculation defects spawning from slight modifications in hemodynamics may magnify over time. As the mechanical force distribution changes due to the absence of normal trabeculae, Neuregulin signalling, along with other genetic signals, are disrupted, leading to further deviations from healthy cardiogenesis. For example, zebrafish embryos that are deficient in the key Neuregulin co-receptor ErbB2 display severe cardiovascular defects including bradycardia, decreased fractional shortening, and impaired cardiac conduction [5]. Disrupted shear distributions in the ventricle leads to immature myocardial activation patterns, which perpetuate ventricular conduction and contractile deficiencies, i.e., arrhythmia, abnormal fractional shortening, and possibly ventricular fibrillation [14].

The fluid dynamics of heart development, particularly at the stage when the trabeculae form, is complex due to the balance of inertial and viscous forces. The Reynolds number, Re is a dimensionless number that describes the ratio of inertial to viscous forces in the fluid and is given as $Re = (\rho UL)/\mu$. In cardiac applications, μ is the viscosity of the blood, ρ is the density of the blood, U is the

characteristic velocity (often chosen as the average or peak flow rate), and L is the characteristic length (often chosen as the diameter of the chamber or vessel). Another dimensionless parameter that is often used in describing cardiac flows is the Womersley number which is given by $Wo = \frac{\omega L^2}{\nu}$, where ω is the angular frequency of contraction. Note that the Wo describes the transient inertial force over the viscous force and is a measure of the importance of unsteadiness in the fluid. During critical developmental stages such as cardiac looping and the formation of the trabeculae, $Re \approx 1$ and $Wo \approx 1$. In this regime, a number of fluid dynamic transitions can occur, such as the onset of vortical flow and changes in flow direction, that depend upon the morphology, size of the chambers, and effective viscosity of the blood. The flow is also unsteady, and the elastic walls of the heart undergo large deformations.

Since analytical solutions are not readily available for complex geometries at intermediate Re , recent work has used computational fluid dynamics to resolve the flow in the embryonic heart. For example, DeGroff et al. [264] reconstructed the three-dimensional surface of human heart embryo using a sequence of two-dimensional cross-sectional images at stages 10 and 11, when the heart is a mere valveless tube [265]. The cardiac wall was fixed, and steady and pulsatile flows were driven through the chambers. They found streaming flows (particles released on one side of the lumen did not cross over or mix with particles released from the opposite side) without coherent vortex structures. Liu et al. [266] simulated flow through a three-dimensional model of a chick embryonic heart during stage HH21 (after about 3.5 days of incubation) at a maximum Re of about 6.9. They found that vortices formed during the ejection phase near the inner curvature of the outflow tract. More recently, Lee *et al.* [28] performed 2D simulations of the developing zebrafish heart with moving cardiac walls. They found unsteady vortices develop during atrial relaxation at 20-30 hpf and in both the atrium and ventricle at 110-120 hpf. Goenezen *et al.* [267] used subject-specific computational fluid dynamics (CFD) to model flow through a model of the chick embryonic heart outflow tract.

The numerical work described above, in addition to direct *in vivo* measurements of blood flow in the embryonic heart [12, 268], further supports that the presence of vortices is sensitive to changes in Re , morphology, and unsteadiness of the flow. Santhanakrishnan *et al.* [26] used a combination of CFD and flow visualization in dynamically scaled physical models to describe the fluid dynamic transitions that occur as the chambers balloon, the endocardial cushions grow, and the overall scale of the heart increases. They found that the formation of intracardial vortices depended upon

the height of the endocardial cushions, the depth of the chambers, and the Re . Their paper only considers steady flows in an idealized two-dimensional chamber geometry with smooth, stationary walls.

We will study the role of trabeculation on underlying fluid flows in zebrafish hearts using two different models. The two model geometries can be seen in the Figure 5.1. One model will extend the work on Santhanakrishnan *et al.* by considering a trabeculaed ventricular cavity and the other will consider a two-chambered heart with a trabeculated ventricle.

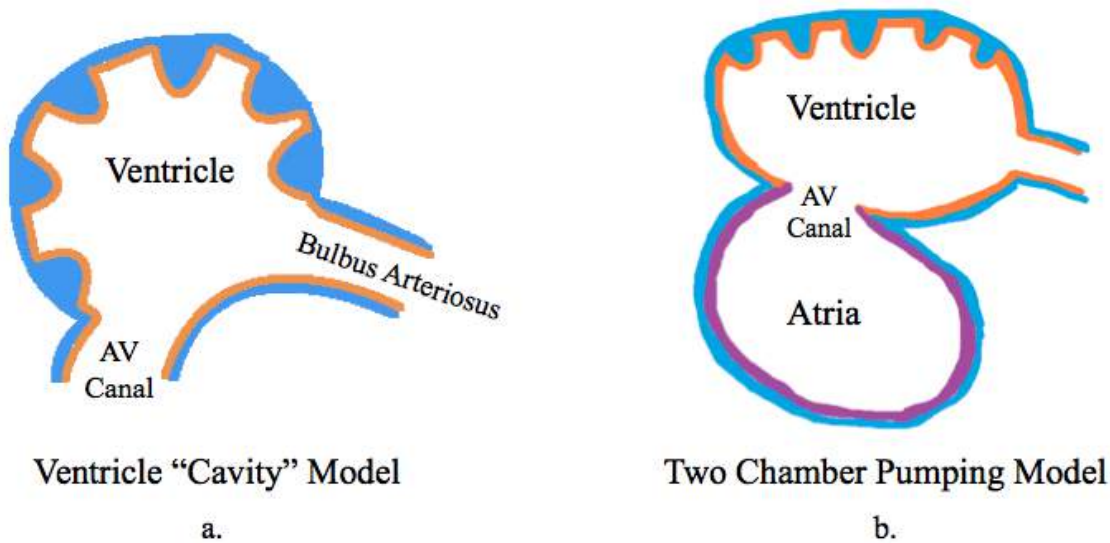


Figure 5.1: Cartoon renditions of the geometries considered for motivation for the computational models in Section 5.2 and Section 5.3. (a) is the trabeculated ventricular cavity model and (b) is the two-chamber model with a trabeculated ventricle.

5.1.1 Goals of cavity model

With the geometry shown in Figure 5.1a, we expand upon the work of Santhanakrishnan *et al.* by considering both pulsatile flows and the addition of trabeculae in a 2D idealized ventricle. We use the immersed boundary method to solve the fluid structure interaction problem of flow through a rigid ventricular cavity. Because the goal of this study is to map out the bifurcations in flow structure that occur as a result of unsteadiness of the flow, trabeculae height, and Re , we restrict the work to this idealized model of the ventricle. Even with these simplifications, we find a variety of interesting bifurcations in flow structures that occur over a biologically relevant morphospace. This data is also presented in [269].

5.1.2 Goals of two-chamber model

Using imaging data from Liu *et al.* [5], we quantify the kinematics of the two-chambered zebrafish heart at 96 *hpf* and use that data to construct both the geometry and prescribed pumping motion of a two-chambered heart computational model, shown in Figure 5.1*b*. We use the immersed boundary method to solve the fluid-structure interaction problem of flow through a two-chambered pumping heart. The goal of this paper is to discern bifurcations in the intracardial and intertrabecular flow structures due to scale (Wo), trabeculae height, and hematocrit. We find a variety of interesting bifurcations in flow structures that occur over a biologically relevant morphospace. The implications of the work are that alterations in bulk flow patterns, and particularly the presence or absence of intracardial and intertrabecular vortices, will augment or reduce mixing in the heart, alter the direction and magnitude of flow near the endothelial surface layer, and potentially change chemical gradients of morphogens which serve as an epigenetic signal. This data is also presented in [270].

5.2 Trabeculated Cavity Model

Both the immersed boundary method and a physical model were used to study the fluid-structure interaction problem of fluid flow moving through an idealized cavity with trabeculae. Trabeculae heights were varied, and simulations were conducted for Reynolds numbers (Re) ranging from 0.01 to 100, while physical model experiments studied $Re \sim 1000$. Using either steady or pulsatile parabolic inflow conditions, both intracardial and intertrabecular vortices formed for biologically relevant parameter values. The bifurcation from smooth streaming flow to vortical flow depends upon the pulsation frequency, trabeculae geometry, and Re . Vorticity can be important in inducing shear stress at the endothelial layer and mixing within the developing chambers, which is believed to aid in chamber morphogenesis, valvulogenesis, and the formation of the trabeculae themselves.

5.2.1 Computational Model

Model Geometry A simplified two dimensional geometry of a 96 hpf zebrafish ventricle, which contains trabeculae, was constructed using Figure 5.2*a*. The ventricle was idealized as a half ellipse, with semi-major axis a_V and semi-minor axis b_V . It is tangentially laid within a channel, which emulates a cavity-flow geometry. The channel models the atrioventricular canal (AV canal), with width w_{AV} , which is modeled as equal to the sinus venosus (SV) width, w_{SV} . Six equally-spaced trabeculae were aligned within the ventricle. The model geometry is illustrated in Figure 5.2*c*.

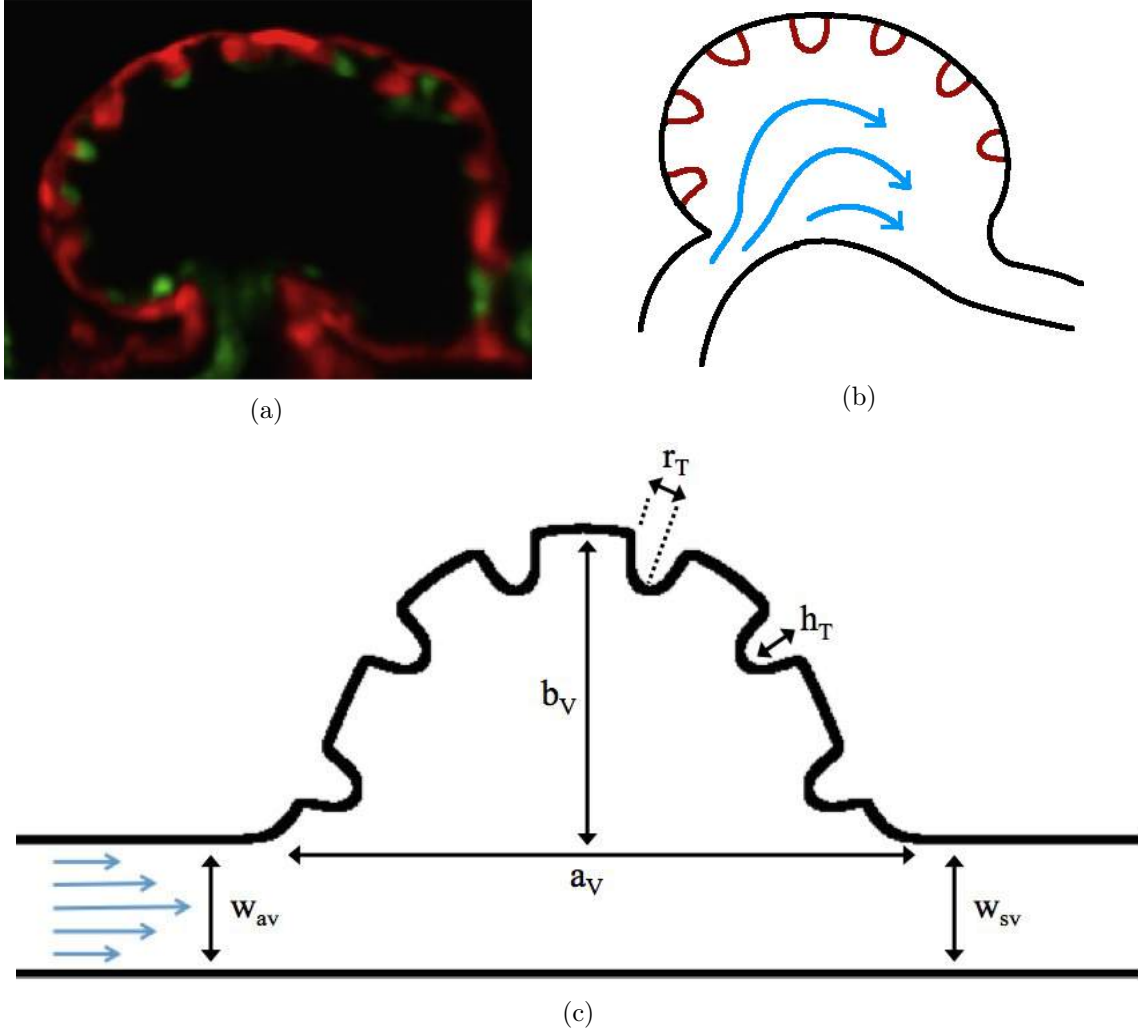


Figure 5.2: 5.2a is a snapshot of an embryonic zebrafish's ventricle at 96 hpf right using spinning disk confocal microscopy. The snapshot was taken right before its systolic phase. The protrusions into the ventricular chamber are trabeculation. Image from Tg(cmlc2:dsRed)s879; Tg(flk1:mcherry)s843 embryos expressing fluorescent proteins that label the myocardium and endocardium, respectively [5]. Figure 5.2b illustrates the idea for our computational model geometry found in Figure 5.2c, that is, blood flows from the atrio-ventricular canal into the ventricle and then proceeds into the bulbus arteriosus. The computational model geometry is a flattened out rendition of 5.2b. The following geometric parameters, a_V and b_V , the semi-major and semi-minor axis of the elliptical chamber, h_T and r_T , the height and radii of the trabeculae, and w_{AV} and w_{SV} , the widths of the AV canal and sinus venosus respectively.

Parameter	Value
a_V	1.0
b_V	0.8
w_{AV}	0.8
w_{SV}	0.8
r_T	0.10
$\frac{h_T}{b_V}$	$\{0, 0.02, 0.04, \dots, 0.16\}$

Table 5.1: Table of non-dimensional geometric parameters used in the numerical model. The height of trabeculae, h_T , were varied for numerical experiments.

The trabeculae geometry was modeled using the following perturbed Gaussian-like function,

$$T(x) = h_T \left(1 - \left(\frac{x}{r_T} \right)^2 \right) e^{-\left(\frac{x}{0.7r_T} \right)^8}, \quad (5.1)$$

where r_T and h_T are the radii and height of each trabecula, respectively. The full geometry can be seen in Figure(5.2). This geometry is used for both the physical and numerical models of the ventricle.

The geometric model parameters are found in Table(5.1), which were scaled from measurements from Figure(5.2a). The parameters describing the ventricle were held constant and are given as the chamber height, b_V , chamber width, a_V , and width of the AV canal and SV, w_{AV} and w_{SV} respectively. Note that the radii of the trabeculae, r_T , was also constant in all numerical simulations, while the height of the trabeculae, h_T , was varied.

Computational Model Implementation The immersed boundary method [162] was used to solve for the flow velocities within the geometric model from Section 5.2.1. The immersed boundary method has been successfully used to study the fluid dynamics of a variety of biological problems in the intermediate Reynolds number range, defined here as $0.01 < Re < 1000$ (see, for example, [238, 271, 272, 145]). The model consists of stiff boundaries that are immersed within an incompressible fluid of dynamic viscosity, μ , and density, ρ .

The fiber models, e.g., force equations are specific to each IB model. In a simple case where a preferred motion or position is enforced, boundary points are tethered to target points via linear springs with zero resting-lengths. The equation describing the force applied to the fluid by the

boundary in Lagrangian coordinates is given by $\mathbf{f}(r, t)$ and is explicitly written as,

$$\mathbf{f}(r, t) = k_{target} (\mathbf{Y}(r, t) - \mathbf{X}(r, t)), \quad (5.2)$$

where k_{target} is the stiffness coefficient, and $\mathbf{Y}(\mathbf{r}, t)$ is the prescribed Lagrangian position of the target structure. In all simulations the immersed structure was held nearly rigid by applying a force proportional to the distance between the location of the actual boundary and the preferred position. The deviation between the actual and preferred positions can be controlled with the variable k_{target} , and chosen to be high as to allow only negligible deformations.

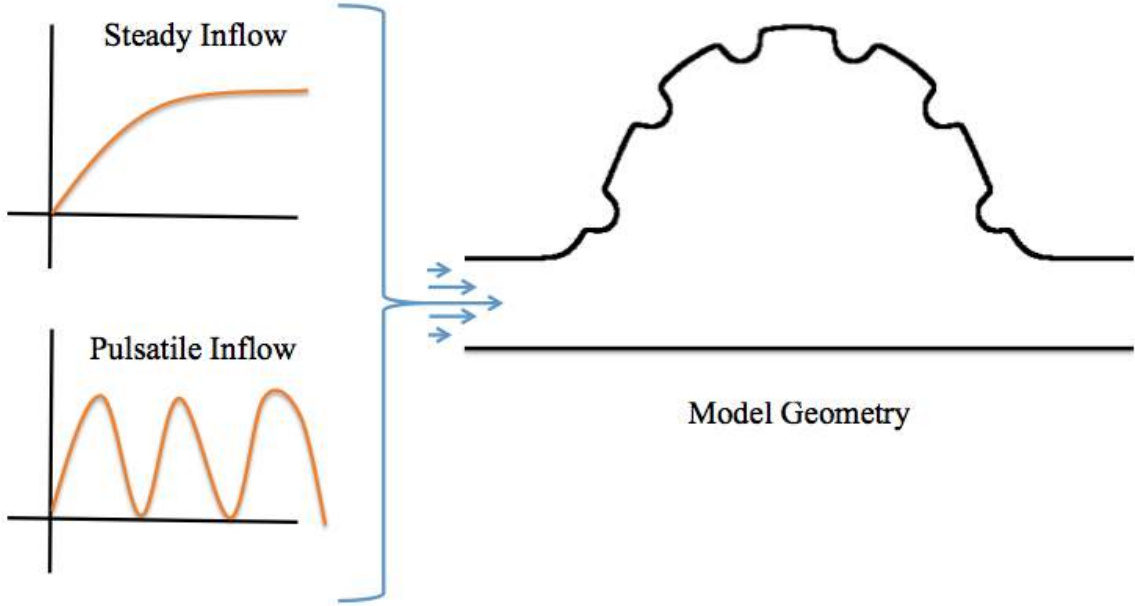


Figure 5.3: A cartoon depiction of the two parabolic inflow conditions within the model geometry.

The fluid flow is driven through the immersed boundary using either pulsatile parabolic inflows or a linear ramp to steady parabolic inflow at the location of the AV canal, as shown in Figure 5.3. The equations describing the specific inflow boundary conditions are given in Table(5.2). A partial Neumann outflow condition is enforced in the direction of flow at the outlet. This outflow condition

Case	Inflow BC
Steady Inflow	$\mathbf{u}_{\text{in}} = \begin{pmatrix} \frac{V_{in}}{d_{AV}^2} \tanh(2t) \left(\frac{1}{4d_{AV}^2} - y^2 \right) \\ 0 \end{pmatrix}$
Pulsatile Inflow	$\mathbf{u}_{\text{in}} = \begin{pmatrix} \frac{V_{in}}{d_{AV}^2} \sin(2\pi ft) \left(\frac{1}{4d_{AV}^2} - y^2 \right) \\ 0 \end{pmatrix}$

Table 5.2: Inflow boundary conditions for both simulations, one pertaining to parabolic steady inflow and the other corresponding to a parabolic pulsatile inflow. The parameters used for the boundary conditions are f , the non-dimensional frequency, which is matched to the zebrafish heart at 96 *hpf*, and V_{in} , the maximum inflow velocity.

is given as

$$\begin{pmatrix} \frac{\partial u}{\partial \hat{n}} \\ v \end{pmatrix} = \begin{pmatrix} 0 \\ 0 \end{pmatrix}. \quad (5.3)$$

where u and v are the x - and y -components of the fluid velocity, respectively, and $\frac{\partial u}{\partial \hat{n}}$ is the directional derivative of the x -component of the velocity taken in the direction normal to the boundary of the fluid domain.

To determine the Re within the ventricle of a 4 *dpf* wild type zebrafish, the characteristic velocity, V_{zf} was taken as the average of the minimum and maximum velocity measured *in vivo*, and the characteristic length, L_{zf} , was taken along a diagonal within the ventricle from Figure(5.2a). The Re was then calculated as

$$Re = \frac{\rho_{zf} L_{zf} V_{zf}}{\mu_{zf}} = 1.07, \quad (5.4)$$

where $V_{zf} = 0.75 \text{ cm/s}$ [12], $\rho_{zf} = 1025 \text{ kg/m}^3$ [15], $\mu_{zf} = 0.0015 \text{ kg/(ms)}$ [242], and $L_{zf} = 208 \text{ }\mu\text{m}$. The characteristic frequency was chosen as $f = 3.95 \text{ beats/s}$ [57]. The dimensionless frequency may then be calculated as

$$\tilde{f} = \frac{L_{zf}}{V_{zf}} f_{zf} = 0.11. \quad (5.5)$$

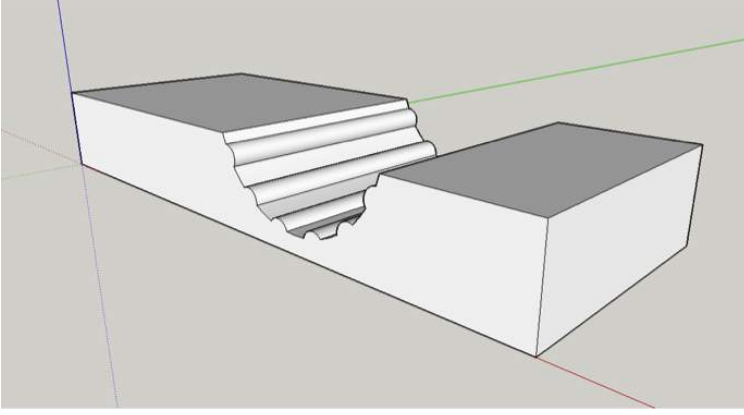
For the mathematical model, the parameters values were chosen to keep the dimensionless frequency fixed at 0.10 for the pulsatile simulations. The Re was varied by changing the kinematic viscosity, $\nu = \mu/\rho$. For the simulations, the Re_{sim} is calculated using a characteristic length of w_{AV} and a characteristic velocity set to V_{in} (steady inflow) or $\frac{1}{2}V_{in}$ (pulsatile inflow). The simulations were performed for $Re_{sim} = 0.01, 0.05, 0.1, 0.5, 1, 5, 10, 20, 30, 40, 50, 100$. The stiffness of the target tethering points were chosen the minimize the deformations of the boundary, i.e, to keep it rigid,

and was directly correlated to Re .

We used an adaptive and parallelized version of the immersed boundary method, IBAMR [138, 128]. IBAMR is a C++ framework that provides discretization and solver infrastructure for partial differential equations on block-structured locally refined Eulerian grids [273, 274] and on Lagrangian (structural) meshes. IBAMR also includes infrastructure for coupling Eulerian and Lagrangian representations.

The Eulerian grid on which the Navier-Stokes equations were solved was locally refined near the immersed boundaries and regions of vorticity with a threshold of $|\omega| > 0.05$. This Cartesian grid was organized as a hierarchy of four nested grid levels, and the finest grid was assigned a spatial step size of $dx = D/1024$, where D is the length of the domain. The ratio of the spatial step size on each grid relative to the next coarsest grid was 1:4. The temporal resolution was varied to ensure stability. Each Lagrangian point of the immersed structure was chosen to be $\frac{D}{2048}$ apart (twice the resolution of the finest fluid grid).

Physical Models: Particle Image Velicometry Particle image velocimetry (PIV) was used to validate the numerical investigation. Physical models, representing static, rigid simplified trabeculated ventricles were designed in SketchUp Make 2013. These models were fabricated using a MakerBot Replicator 2 3D printer in the UNC-CH Kenan Science Library. A lightweight polylactic acid bioplastic material was used as the material, and a schematic image can be seen in Figure 5.4a*a*.



(a)



(b)

Figure 5.4: (a) The PIV physical model geometry, which was 3D printed and placed into a flow tank. (b) the PIV setup, which includes a flow tank, containing the 3D model, with a laser shining orthogonally to the direction of flow, and camera oriented downwards vertically capturing the motion of the neutrally buoyant glass beads.

The physical models are 202 mm long, each with a 60 mm and 24 mm ventricular chamber diameter and depth, respectively. The trabeculae heights were varied from a biologically relevant trabeculae height to chamber depth ratio to twice that ratio (0.08-0.16). Each model ventricle chamber contains six trabeculae protruding radially inward. The model geometry is shown in Figure 5.4a.

Flow velocity measurements were made using 2D planar instantaneous and time-averaged PIV. The laser sheet for the PIV measurements was generated from a 50 mJ double-pulsed Nd:YAG laser (Continuum, Santa Clara, CA, USA), which emitted light at a wavelength of 532 nm with a maximum repetition rate of 15 Hz. The laser beam was converted into a planar sheet approximately 3 mm thick using a set of focusing optics. The laser sheet was located in the x-y plane upstream of the working section. The time interval of separation between two image pairs was varied from 125-150 $\hat{t}_{\frac{1}{4}}$ s. A 14 bit CCD camera (Imager Intense, LaVision, Ypsilanti, MI, USA) with a 1376x1040 pixel array was used to capture images. The spatial resolution was approximately 0.05 mm pixel⁻¹. Uniform seeding was accomplished using 10 μ m hollow glass spheres that were inserted in the flow

tank and mixed to achieve a near-homogeneous distribution prior to each experiment. Volume fractions were such that approximately 40-50 particles were visible within each 64x64 pixel window. In typical experiments there was a maximum particle displacement of 0.8 mm (or 14 pixels) within the correlation window, which corresponds to 25% displacement in a 64x64 pixel window.

The PIV set-up is shown in Figure 5.4b. The flow tank used was first constructed using information from [135] and uses a propeller system to initiate steady flow currents. The long end of the physical model was placed towards the side of incoming flow to minimize edge effects of the model onto the fluid flow. The model was clamped down to minimize any oscillatory effects by the flow and the measurements were taken in the middle of the geometrical model to reduce any boundary or free surface effects.

5.2.2 Experimental Validation of the Numerical Model

In this section we compare simulation results from IBAMR to experimental data for a fluid moving past a trabeculated cavity. The experimental data was obtained using particle image velocimetry (PIV) [195, 275]. The simulations were run on a 1024x1024 grid.

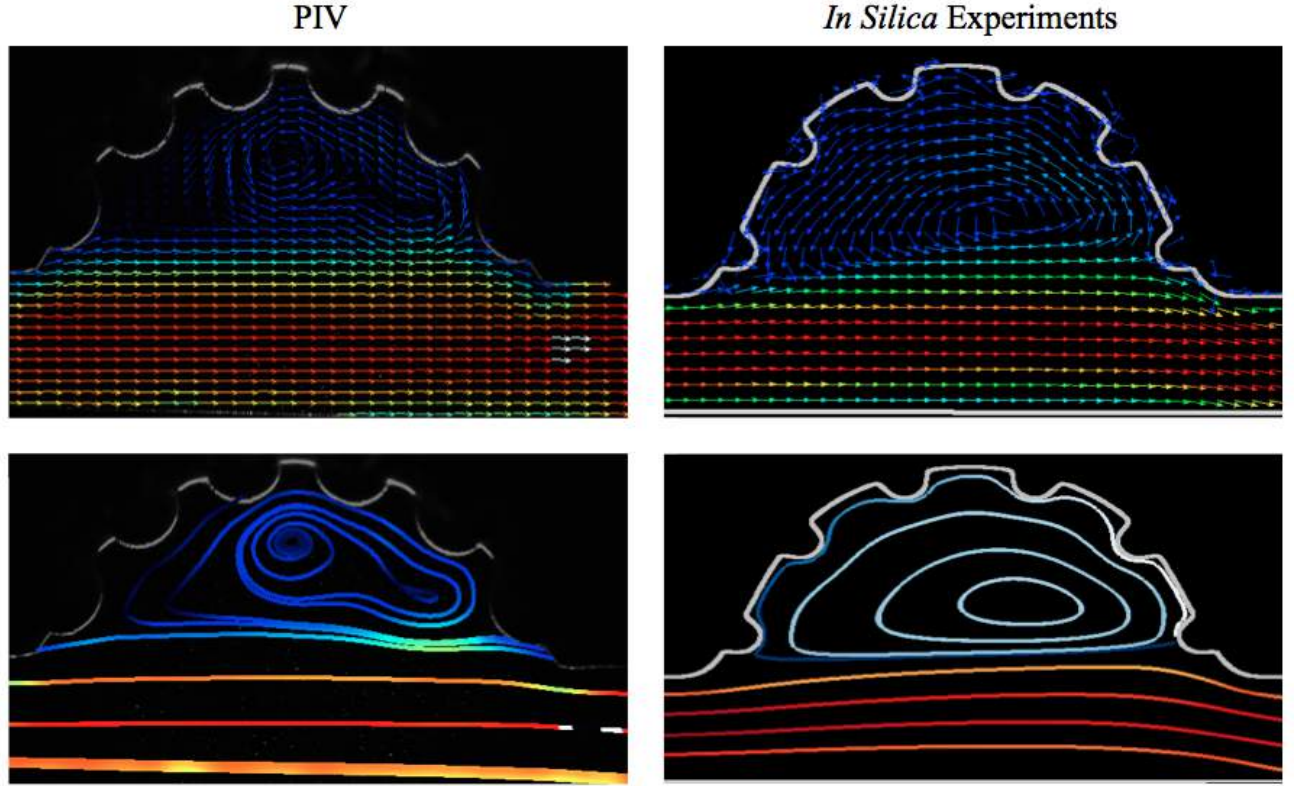


Figure 5.5: Comparison between PIV (left) and simulations (right) of the fluid velocity field (top) and streamlines (bottom). The fluid dynamics qualitatively match in this high Re range.

Figure 5.5 shows a comparison of snapshots taken from IBAMR and the PIV physical model for high Re , $Re \sim 1000$. The basic flow structures are reproduced in all cases. Note that the physical model of trabeculae in Figure 5.5 was 3D printed using the specifications from Figure 5.4a. The trabeculae for the physical and computational models appear to have quite different geometries in Figure 5.5; however, this is an artifact of the PIV setup.

5.2.3 Trabeculated Ventricular Cavity Results

In this section, we present the bulk flow structure over an idealized 2D model of a trabeculated ventricle for the cases of both steady and unsteady flow. The Re is varied from 0.01 to 100, and the trabecular heights are varied from zero to twice the biologically relevant case. Streamlines are used to show the direction of flow. The streamline graphs were generated using VisIt visualization software [192]. When interpreting streamlines, please note that a neutrally buoyant, small particle in the fluid will follow the streamline. The streamlines are drawn by making a contour map of the stream function, since the stream function is constant along the streamline. The stream function,

$\psi(\mathbf{x}, t)$, in 2-D is defined by the following equations:

$$u(\mathbf{x}, t) = \frac{\partial \psi(\mathbf{x}, t)}{\partial y} \quad (5.6)$$

$$v(\mathbf{x}, t) = -\frac{\partial \psi(\mathbf{x}, t)}{\partial x} \quad (5.7)$$

The streamline colors correspond to smooth, streaming flow (blue) and vortical flow (orange).

Steady Flow through Trabeculated Chambers Figure 5.6 shows the flow field streamlines for the case of steady flow through an idealized trabeculated embryonic ventricle. The numerical simulations span five orders of magnitude of Re , varying from 0.01 to 100, while trabeculae heights were set to $0 \leq \frac{h_T}{b_V} \leq 0.16$. Note that the biologically relevant case is $\frac{h_T}{b_V} = 0.08$

In the case of no trabeculae (left column), we find vortex formation only occurs for $Re \geq 15$, in agreement with the findings of [26]. For $Re \leq 10$, the flow bends around the cavity and no flow separation occurs. As Re is increased to 20, flow reversal occurs and a closed vortex is present along the left side of the cavity. The stagnation point is located between the orange and blue streamlines. To the left of this stagnation point, the flow moves along the endocardium from the right to left. To the right of the stagnation point, the flow moves right to left. As Re is further increased, the stagnation point moves to the right, and the intracardial vortex becomes larger until it becomes as large as the cavity itself for $Re = O(100)$.

When half-size biologically relevant trabeculae are introduced into the model ($\frac{h_T}{b_V} = 0.04$), similar flow fields emerge for the case of $Re \leq 10$. Although geometric perturbations now exist along the cavity lining, no flow separation occurs, whether intracardially or intertrabecularly. For $Re = 20$ we see a similar intracardial vortex to the case without trabeculae; however, it is also seen to weave along regions with trabeculae. Furthermore there is an emergence of an independent closed vortex along the right side between two trabeculae. For $Re \geq 50$, we find the presence of one large intracardial vortex wrapping around each trabeculae.

For biologically relevant trabeculae heights, there are closed intertrabecular vortices for Re as low as 0.01, while no intracardial vortices are present at these lower Re . Interestingly, not all intertrabecular regions have closed vortices. As Re is further increased from $Re = 5$ to $Re = 10$, the intertrabecular vortices grow in size. As in previous cases, a larger intracardial vortex forms

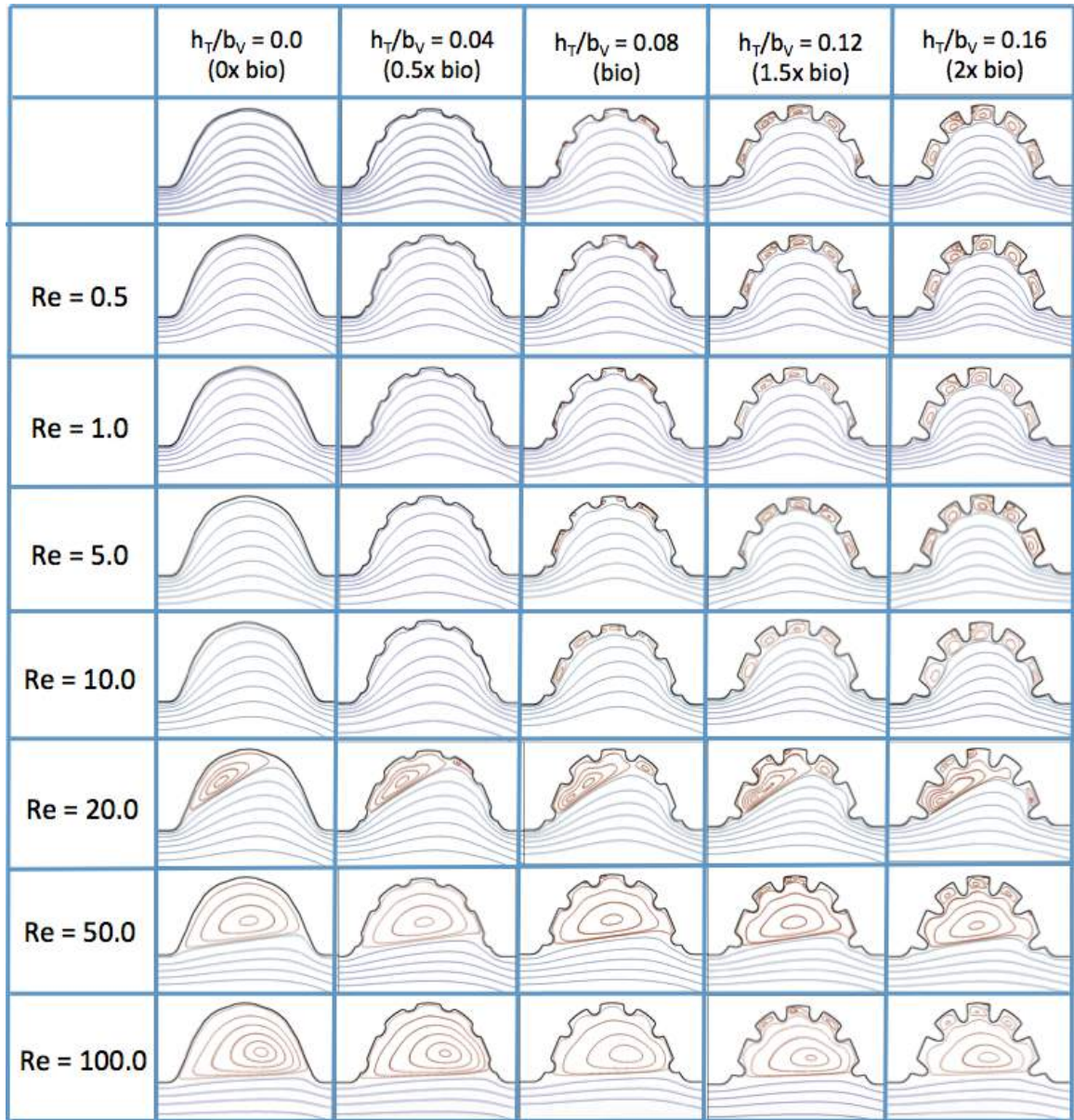


Figure 5.6: Streamline analysis performed for the case of steady flow into the trabeculated ventricle of a zebrafish at 96 hpf for varying Re and trabeculae heights.

at $Re = 20$. On the left hand side of the cavity, there is smooth flow from left to right around the trabeculae. On the right side of the cavity, independent closed vortices form between the trabeculae, and the flow is from right to left. For $Re \geq 50$, a large intracardial vortex forms and no intertrabecular vortices persist.

For trabeculae heights higher than the biologically relevant range, there exist intertrabecular vortices for Re as low as $Re = 0.01$; however, compared to the previous biologically relevant case, there are vortices between every adjacent pair of trabeculae. Moreover, because the trabeculae extend further into the ventricular cavity, these vortices are larger than in previous cases. Intracardial vortices do not develop until $Re \geq 20$, where there is the presence of one large intracardial vortex on the left side of the cavity. When $Re = 20$ and $\frac{h_T}{b_V} = 0.12$, the intracardial vortex only wraps itself around the first four trabeculae with flow moving from left to right. A single intertrabecular vortex forms in the fourth trabecular valley. When $Re = 20$ and $\frac{h_T}{b_V} = 0.16$, the intracardial vortex extends over the left five trabeculae, with an intertrabecular vortex only in last valley between trabeculae on the right side. For $Re \geq 50$, there is the formation of a large intracardial vortex extending throughout the cavity. However, both the trabeculae heights and Re are large enough that this vortex does not wrap around each trabeculae, and intertrabecular vortices are able to form.

Pulsatile Flow through Trabeculated Chambers In the second set of simulations, the flow was pulsed through the idealized chambers at a dimensionless frequency close to that reported for a 96 hpf embryonic zebrafish ($\tilde{f} = 1.0$). The Re was set to 0.1, 1.0, 10 and 100. The dimensionless trabecular heights, $\frac{h_T}{b_V}$ were varied from 0.0 to 0.16. Recall that the biologically relevant Re is about one, and the biologically relevant dimensionless trabecular height is about 0.08. Snapshots of the streamlines showing the flow patterns are given for each simulation for either 9 or 10 time points during the pulse.

Figures 5.7 and 5.8 show streamline plots taken at 9 snapshots in time for lower Re cases, $Re = 0.1, 1.0$, respectively. The streamlines are shown for 5%, 10%, 20%, 40%, 50%, 80%, 90%, 95%, and 100% of the pulse. Finer increments in time are given towards the beginning and end of the pulse to illustrate the rapidly changing dynamics. The $Re = 0.1, 1.0$ cases show similar results. For the majority of the pulse, the flow moves smoothly from left to right within the ventricle. In between the trabeculae, vortices form during most of the pulse if the dimensionless trabecular height

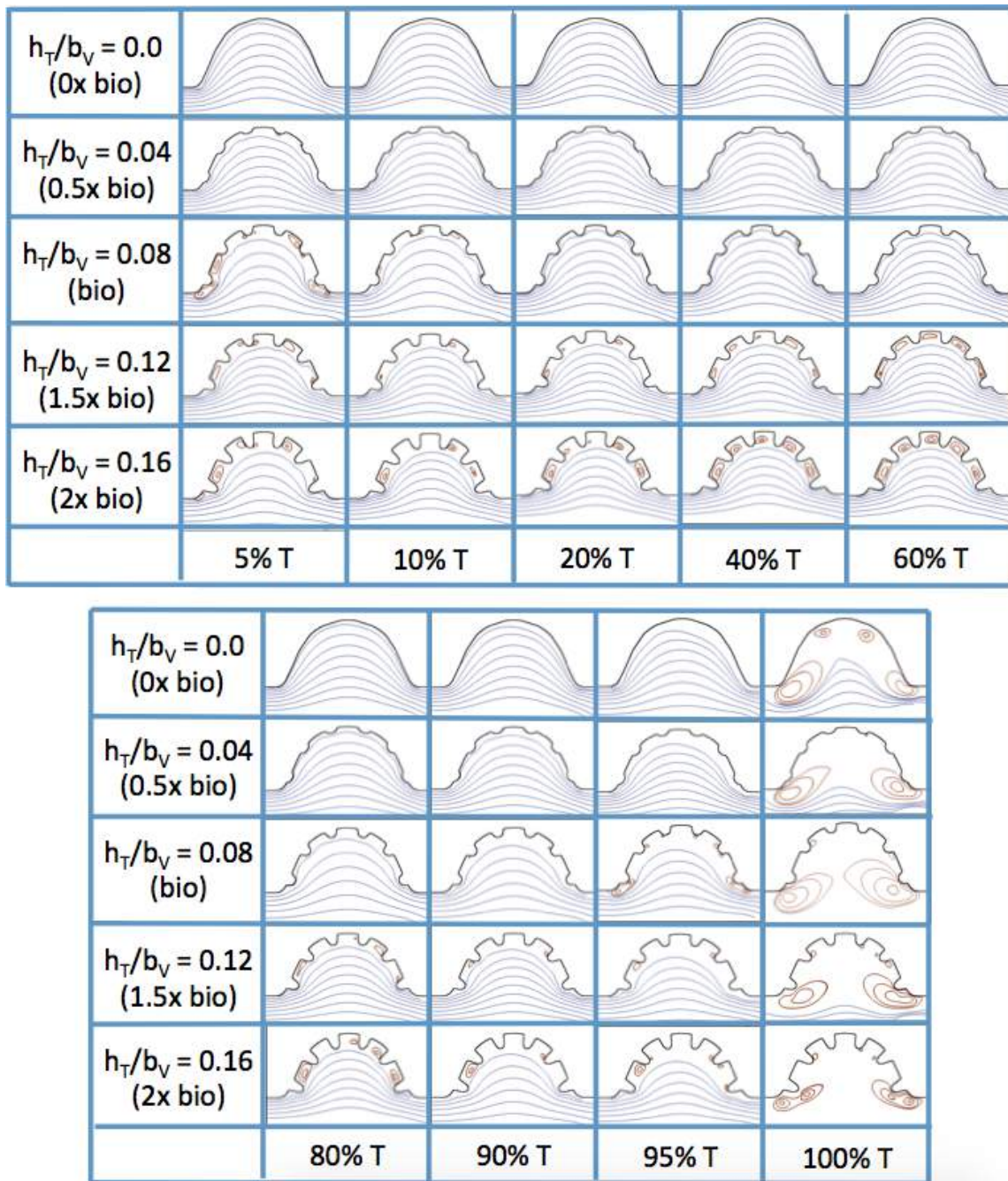


Figure 5.7: Streamline analysis performed for the case of pulsatile flow into the trabeculated ventricle of a zebrafish at 96 hpf for $Re = 0.1$ and varying trabeculae heights.

is at least 0.08. The development of these vortices causes the flow near the endothelial cells to move from right to left between the trabeculae and from left to right on the top of the trabeculae. In most cases, transient vortices form as the flow is decelerated at the end of the pulse. For $Re = 1.0$, intertrabecular vortices form for small trabeculae, $\frac{h_T}{b_V} = 0.04$, as the flow decelerates.

Figure 5.9 shows streamline plots for $Re = 10$ at ten evenly spaced times during a pulse. Intertrabecular vortices form during the first half of the pulse if the dimensionless trabecular height is at least 0.04. For all geometries, intracardial vortices form during the last half of the pulse. The formation of the intracardial vortex annihilates the intertrabecular vortices, at least initially. The intracardial vortices form on the upstream side of the chamber, and grow to fill the entire chamber by the end of the pulse. The intertrabecular vortices form again towards the end of the pulse for $\frac{h_T}{b_V} = 0.12, 0.16$. Note that the presence of the intracardial vortex causes the intertrabecular vortices to change direction so that they spin clockwise (and the intracardial vortices spin counterclockwise).

The results of the inertial dominated case, $Re = 100$, are shown in Figure 5.10. In all cases, a large intracardial vortex that fills the entire chamber is observed at the end of the pulse and beginning of the next pulse. As the flow accelerates, the intracardial vortex is pushed downstream, and another intracardial vortex begins to form ($t = 0.4T - 0.5T$). One or more oppositely spinning vortices form between the trabeculae or between the two counterclockwise spinning intracardial vortices when $t = 0.5T$. The upstream intracardial vortex combines with the original intracardial vortex such that one large intracardial vortex is observed around $t = 0.7T$. When this occurs, the oppositely spinning vortices are annihilated. For $\frac{h_T}{b_V} \geq 0.08$, oppositely spinning intertrabecular vortices reappear at the end of the pulse.

5.2.4 Trabeculated Cavity Conclusions

Two-dimensional immersed boundary simulations were used to solve for the flow fields within an idealized model of a trabeculated ventricle of the zebrafish embryonic heart. Our results show that a large intracardial vortex forms around $Re \approx 20$ when steady flow is pushed through the chamber. When the flow is pulsatile, the intracardial vortex begins to form around $Re \approx 10$. In general, pulsatile flow lowers the Re and trabeculae height needed to generate vortices. For both steady and unsteady flows as the trabeculae grow into the chamber, another bifurcation occurs in which small vortices form between each trabecula. Depending upon the Re and the morphology, the intertrabecular vortices can form without the presence of a large intracardial vortex. In other

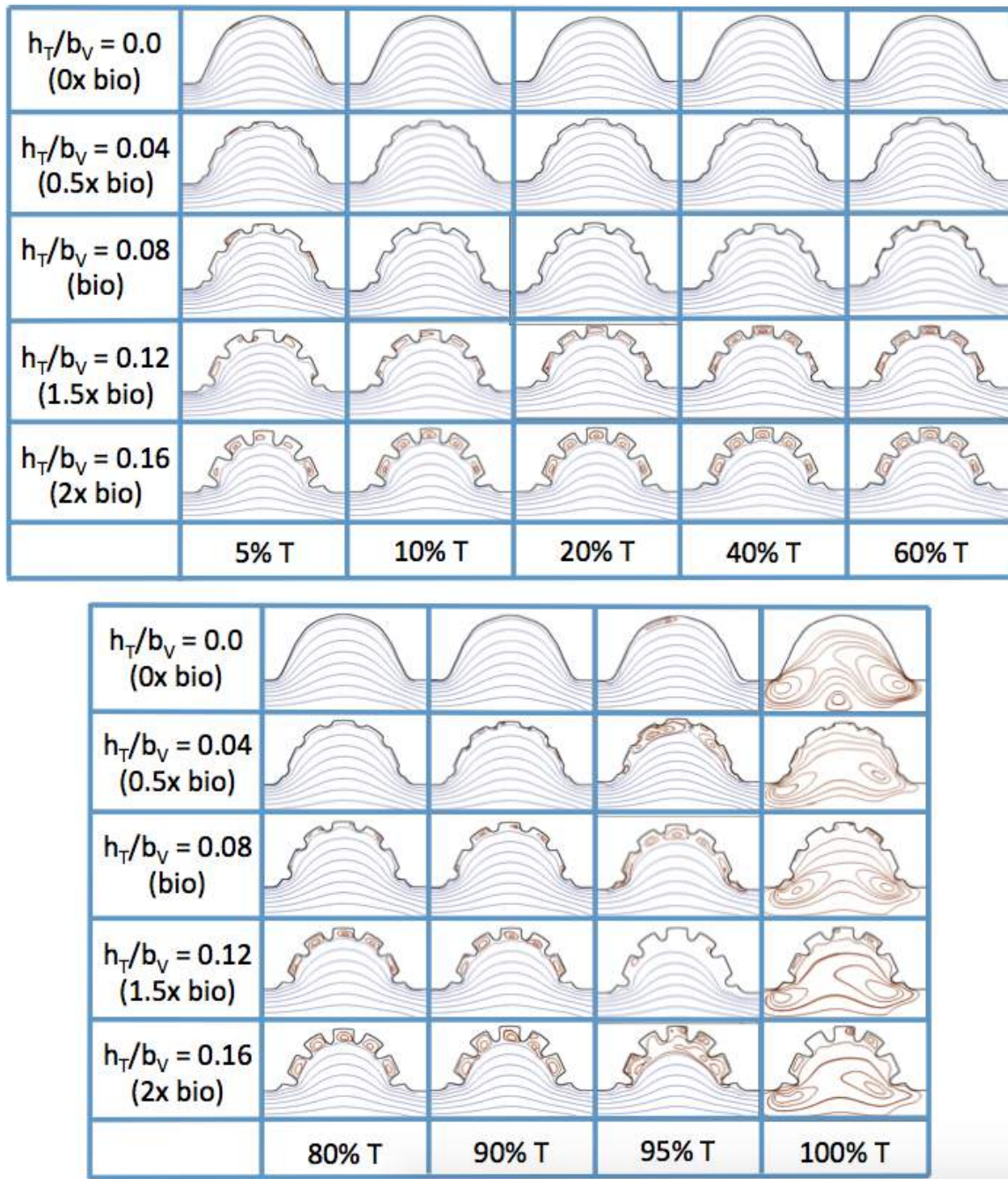


Figure 5.8: Streamline analysis performed for the case of pulsatile flow into the trabeculated ventricle of a zebrafish at 96 hpf for $Re = 1.0$ and varying trabeculae heights.

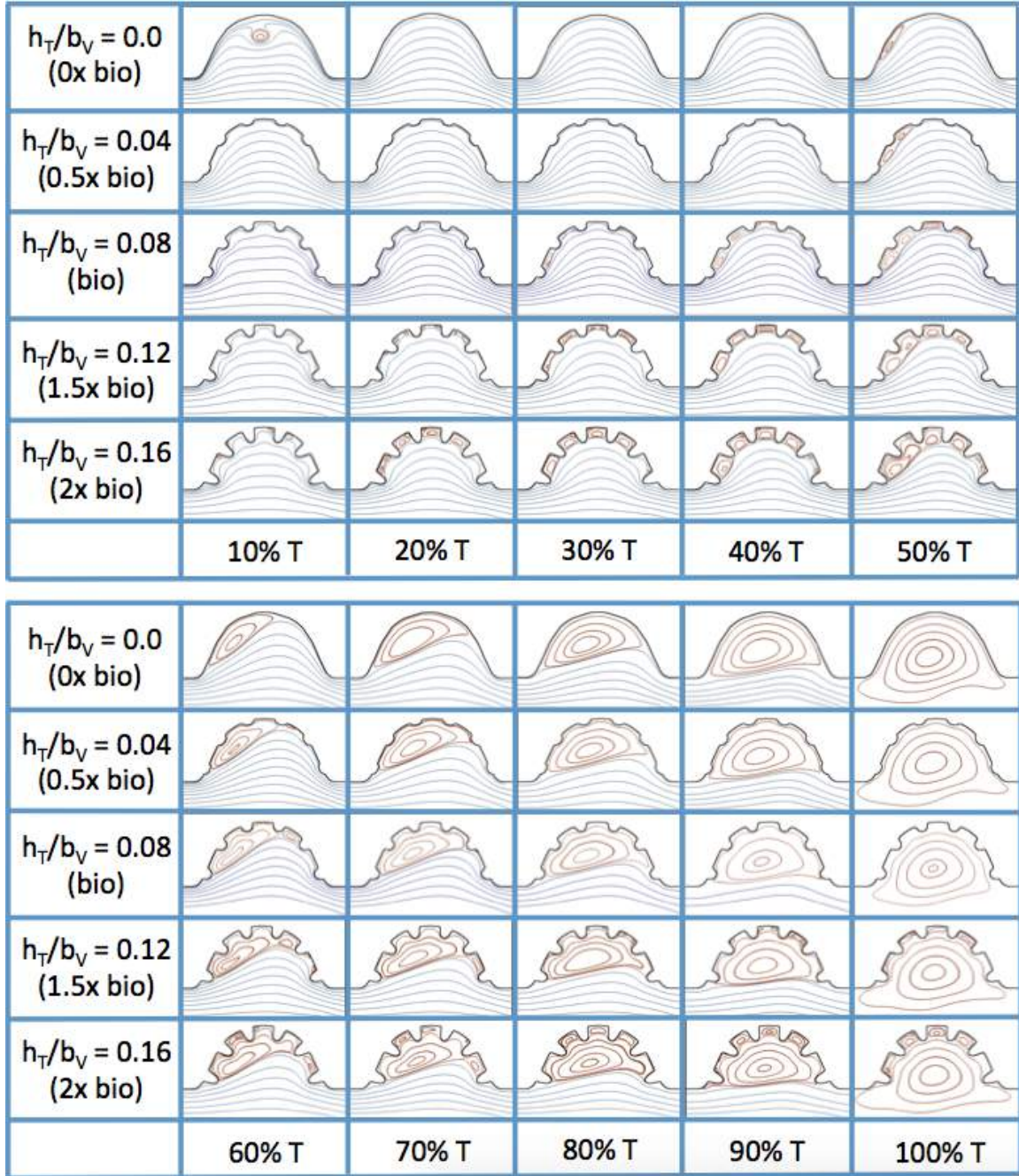


Figure 5.9: Streamline analysis performed for the case of pulsatile flow into the trabeculated ventricle of a zebrafish at 96 hpf for $Re = 10.0$ and varying trabeculae heights.

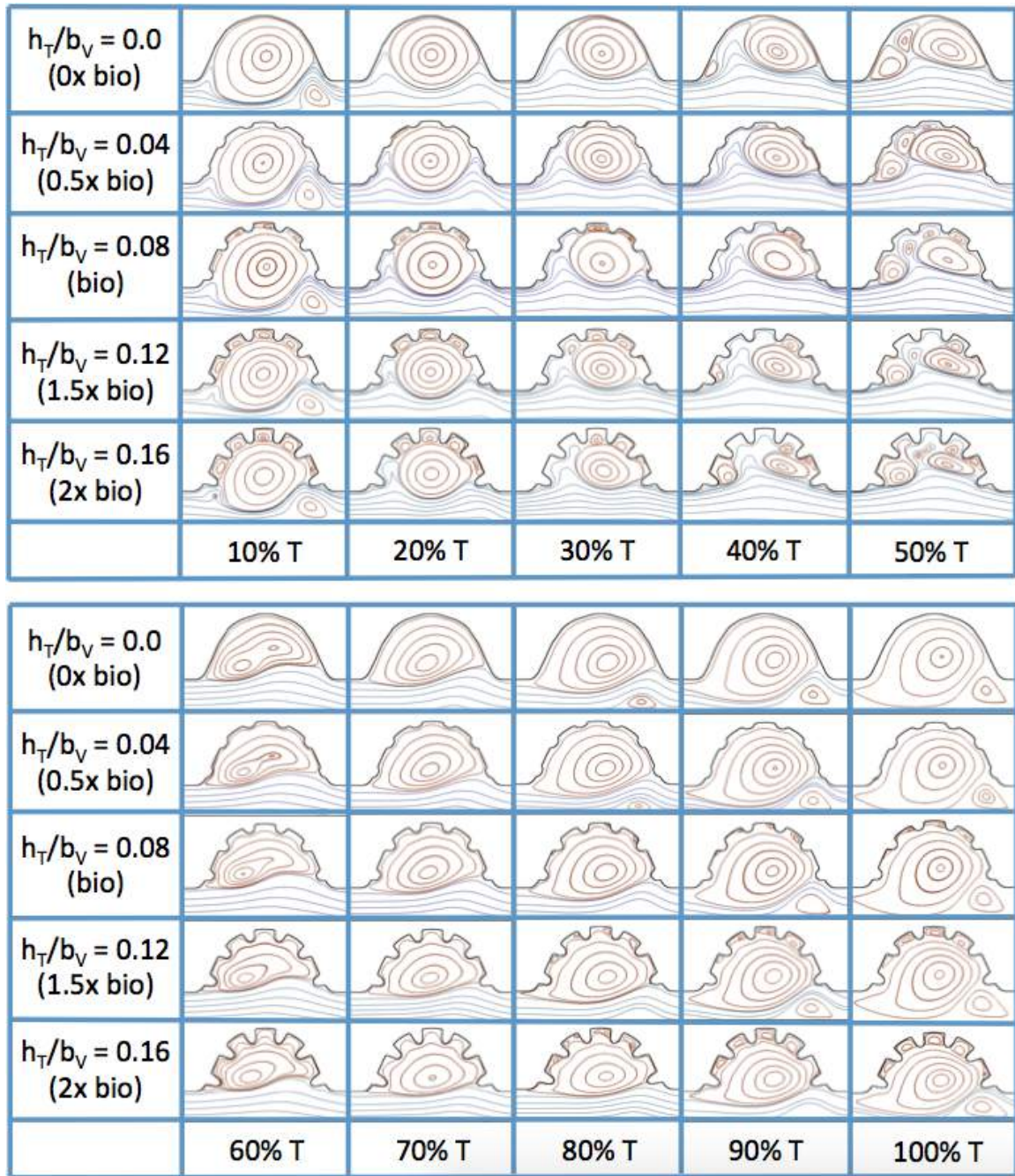


Figure 5.10: Streamline analysis performed for the case of pulsatile flow into the trabeculated ventricle of a zebrafish at 96 hpf for $Re = 100$ and varying trabeculae heights.

cases, typically at higher Re , both the intracardial and intertrabecular vortices form. The presence of intracardial vortices changes the direction of the intertrabecular vortices.

This work focused specifically on the presence or absence of vortices given their significance to both the magnitude and direction of flow as well as the mixing patterns within the ventricle. When an intracardial vortex forms, the direction of the flow changes. When an intracardial vortex forms in unsteady flow, the direction of flow can change during the beat cycle, and the stagnation point moves along the cardiac wall. Since endothelial cells are known to sense and respond to changes in both magnitude and direction of flow, the formation and motion of these vortices could be an important epigenetic signal. The simulations revealed unexpected complexities in vortex dynamics as bulk flow moves from left to right through the chamber. When an intracardial vortex forms in absence of intertrabecular vortices, the flow at the endocardial wall moves from right to left. When the intertrabecular vortices form in absence of an intracardial vortex, the flow again moves from right to left. When both intertrabecular and intracardial vortices form, the flow moves from left to right since the intertrabecular and intracardial vortices spin in opposite directions. We also observe cases where not all intertrabecular spaces have a vortex. In such cases, the flow between different trabeculae will move in different directions.

Importantly, this idealized study demonstrates that small changes in viscosity, scale, morphology, and contraction dynamics can substantially influence bulk flow properties in the embryonic heart. This presents an interesting challenge since each of these parameters is continuously changing during growth. In addition, estimating the effective viscosity of the embryonic blood is nontrivial. Given the sensitivity of the flow to such small perturbations, it is necessary to use well resolved numerical grids that are experimentally validated.

Furthermore, it is evident that there is a strongly coupled relationship between intracardial hemodynamics, genetic regulatory networks, and cardiac conduction. Besides contractions of the myocardial cells, which in turn drive blood flow, hemodynamics are directly involved in proper pacemaker and cardiac conduction tissue formation [94]. Moreover, shear stress is found to govern the conduction velocity distribution of action potentials within the myocardium [14]. It is important to note that changes in the conduction properties of the embryonic heart will also affect the intracardial shear stresses, pressures and patterns of cyclic strains.

The cyclic stresses and strains of the cardiomyocytes can also help shape the overall architecture

of the trabeculated ventricle. The dynamics of these strains depend upon the intracardial fluid dynamics. For example, greater resistant to flow will induce larger cyclic stresses and possibly reduced cyclic strains. It is known that cyclic strains initiate myogenesis in the cellular components of primitive trabeculae. [91] Since trabeculation first occurs near peak stress sites in the ventricle, altering blood flow may directly produce structural and morphological abnormalities in cardiogenesis. Previous work focusing on hemodynamic unloading in an embryonic heart has resulted in disorganized trabeculation and arrested growth of trabeculae [92, 55, 53]. On the other hand, embryos with a hypertrabeculated ventricle also experience impaired cardiac function. [55]

The exact mechanisms of mechanotransduction are not yet clearly understood [245]. Mechanically sensitive biochemical signals are thought to be propagated throughout a pipeline of epigenetic signaling mechanisms, which may lead to regulation of gene expression, cellular differentiation, proliferation, and migration [88]. *In vitro* studies have discovered that endothelial cells can detect shear stresses as low as 1 dyn/cm^2 [12] resulting in up or down regulation of gene expressions. Embryonic zebrafish hearts beyond 36 hpf are known to undergo shear stresses on the order of $\sim 8 - 15 \text{ dyn/cm}^2$, and such magnitudes of shear stress can cause cytoskeletal rearrangement [12]. Mapping out the connection between fluid dynamics, the resulting forces, and the mechanical regulation of developmental regulatory networks will be critical for a global understanding of the process of heart development.

5.3 Two Chamber - Trabeculated Ventricle Model

We studied the fluid-structure interaction problem of fluid flow moving through a two-chambered heart of a zebrafish (*Danio rerio*), with a trabeculated ventricle, at 96 hpf (hours post fertilization). Trabeculae heights and hematocrit were varied, and simulations were conducted for two orders of magnitude of Womersley number, extending beyond the biologically relevant range (0.2 – 12.0). Both intracardial and intertrabecular vortices formed in the ventricle for biologically relevant parameter values. The bifurcation from smooth streaming flow to vortical flow depends upon the trabeculae geometry, hematocrit, and Wo . This work shows the importance of hematocrit and geometry in determining the bulk flow patterns in the heart at this stage of development. Such changes in flow can result in alterations of the shear stress and morphogen distribution along the endothelial lining of the heart, which is believed to aid in chamber morphogenesis, valvulogenesis, and the formation of the trabeculae themselves.

5.3.1 Computational Model

Model Geometry A simplified two dimensional geometry of a 96 hpf zebrafish's two-chambered heart, containing trabeculae, was constructed using Figure 5.11a and 5.11b. The ventricle and atria were idealized as an ellipse, with semi-major axis V_a , and A_a , and semi-minor axis V_b and A_b , respectively. The atrioventricular canal (AV canal) connects the atria and ventricle and is modeled as endocardial cushions, which move to occlude or promote flow through the heart chambers. The sinus venosus (SV) and bulbus arteriosus (BA) are modeled similarly. The width of the AV canal, SV, and BA are given by w_{AV} , w_{SV} , and w_{BA} , respectively. The above parameters are labeled systole and diastole separately, e.g., the ventricular subscripts are given an *exp* label right before systole and are labeled *con* before diastole, while the atrial labels are opposite.

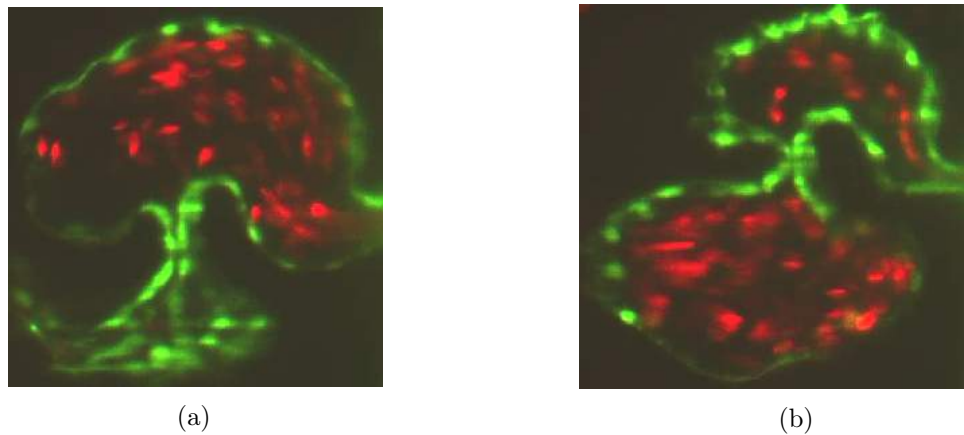


Figure 5.12: 5.12a and 5.12b are snapshots of an embryonic zebrafish's ventricle at 96 hpf right using spinning disk confocal microscopy. The snapshots were taken right before systole and diastole, respectively. The protrusions into the ventricular chamber are trabeculae and blood cells are fluorescing red [5].

Elliptical blood cells of uniform semi-major and semi-minor axis lengths, C_a and C_b , respectively, were included. The volume fraction, or hematocrit, was varied between $[0\%, 25\%]$. Hematocrit increases linearly throughout development [239] from 0% to roughly 32% [276]. The desired volume fraction of blood cells was calculated within the atria, and the blood cells were spaced evenly apart within it. Moreover, as the ejection fraction is 60% [65], 60% of the number of blood cells in the atrium were spaced evenly within the ventricle. *in vivo* images from [5] are shown in Figure 5.12. Note that this placement of blood cells occurred immediately before diastole.

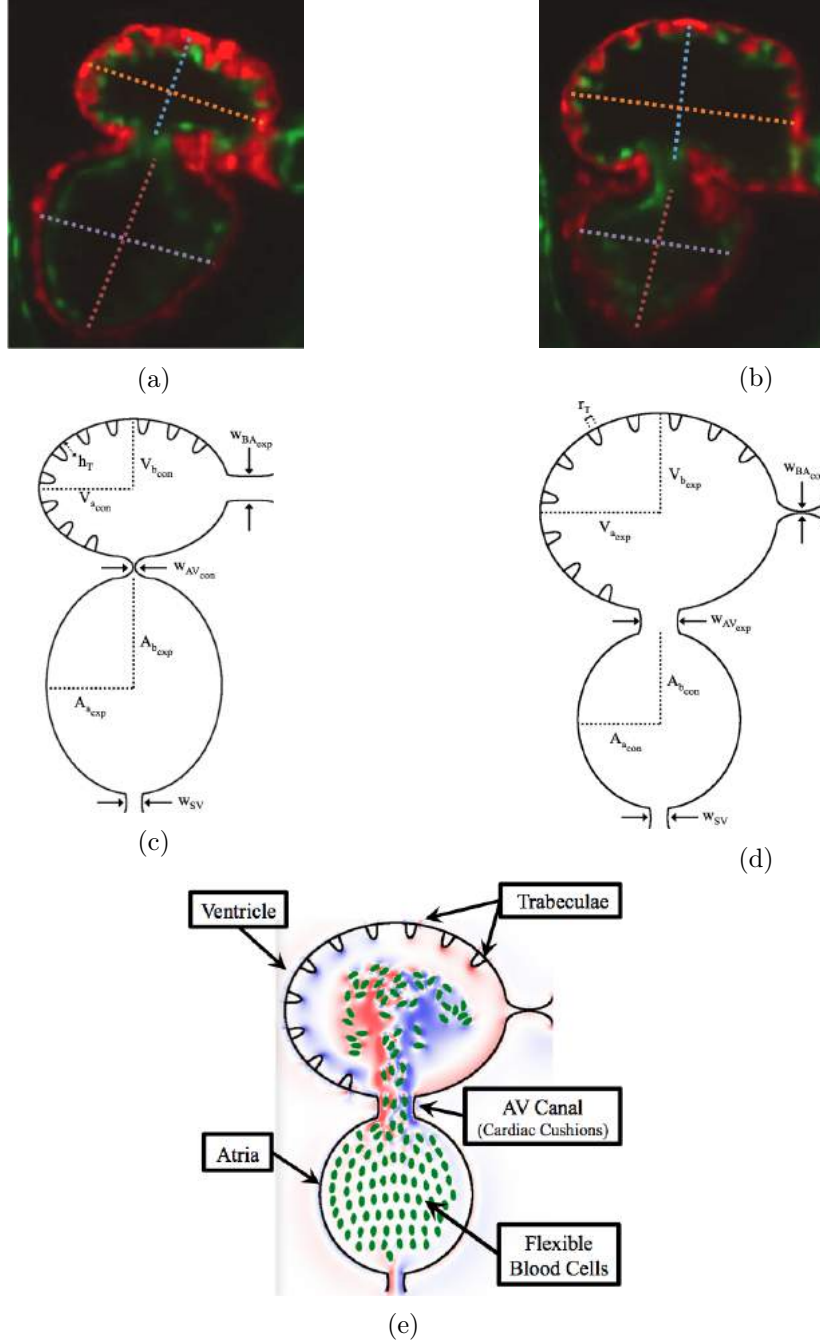


Figure 5.11: 5.11a and 5.11b are snapshots of an embryonic zebrafish's ventricle at 96 hpf right using spinning disk confocal microscopy. The snapshots were taken right before its diastolic and systolic phase, respectively. The protrusions into the ventricular chamber are trabeculae. Dashed lines show the minor and major axes. Images are from $Tg(cmlc2:dsRed)s879$; $Tg(flk1:mcherry)s843$ embryos expressing fluorescent proteins that label the myocardium and endocardium, respectively [5]. 5.11c and 5.11d illustrate the computational geometry right before diastole and systole, respectively. The computational geometry, as shown in 5.11e, includes the two chambers, the atria (bottom chamber) and ventricle (top chamber), the atrioventricular canal connecting the chambers, and the bulbus arteriosus and sinus venosus, which all have endocardial cushions, which can occlude cardiac flow, as well as flexible blood cells.

Parameter	Symbol	Value
Contracted Ventricle Semi-Major Axis	$V_{a_{con}}$	0.80
Contracted Atria Semi-Major Axis	$A_{a_{con}}$	0.68
Contracted Ventricle Semi-Minor Axis	$V_{b_{con}}$	0.64
Contracted Atria Semi-Minor Axis	$A_{b_{con}}$	0.76
Expanded Ventricle Semi-Major Axis	$V_{a_{exp}}$	1.00
Expanded Atria Semi-Major Axis	$A_{a_{exp}}$	0.88
Expanded Ventricle Semi-Minor Axis	$V_{b_{exp}}$	0.84
Expanded Atria Semi-Minor Axis	$A_{b_{exp}}$	1.02
Contracted AV-Canal Width	$w_{AV_{con}}$	0.02
Contracted Bulbus Arteriosus Width	$w_{BA_{con}}$	0.015
Open AV-Canal Width	$w_{AV_{exp}}$	0.34
Open Bulbus Arteriosus Width	$w_{BA_{exp}}$	0.29
Sinus Venosus Width	w_{SV}	0.2
Blood Cell Semi-Major Axis	C_a	0.050
Blood Cell Semi-Minor Axis	C_b	0.025
Trabeculae Radii	r_T	0.06
Trabeculae Height	h_T	$\{0, 0.09, 0.18, 0.27, 0.36\}$

Table 5.3: Table of dimensionless geometric parameters used in the numerical model. The non-dimensionalization was done by dividing by $V_{a_{exp}}$. The height of trabeculae, h_T , were varied for numerical experiments.

The trabeculae geometry was modeled using the following perturbed Gaussian-like function,

$$T(x) = h_T \left(1 - \left(\frac{x}{r_T} \right)^2 \right) e^{-\left(\frac{x}{0.7r_T} \right)^8}, \quad (5.8)$$

where r_T and h_T are the radii and height of each trabecula, respectively. Trabeculae are placed equidistant apart, as estimated from Figures 5.11a and 5.11b. The full geometry can be seen in Figure(5.11).

The blood cells were approximated as ellipses, using Figure 5.12 to estimate their length to width ratios, with respect to the size of the ventricle. The blood cells were held nearly rigid, as described in Section 5.3.1.

The dimensionless geometric model parameters are found in Table(5.3), which were scaled from measurements taken from Figures 5.11a and 5.11b. The radii, r_T , and number of the trabeculae were constant in all numerical simulations, while the height of the trabeculae, h_T , was varied.

Model Geometry Implementation The immersed boundary method [162] was used to solve for the flow velocities within the geometric model from Section 5.3.1. The immersed boundary method

has been successfully used to study the fluid dynamics of a variety of biological problems in the intermediate Reynolds number range, defined here as $0.01 < Re < 1000$ (see, for example, [238, 271, 272, 145]). The model consists of stiff boundaries that are immersed within an incompressible fluid of dynamic viscosity, μ , and density, ρ .

The fiber models, e.g., force equations, are specific to the application. In a simple case where a preferred motion or position is enforced, boundary points are tethered to target points via linear springs with resting-lengths of zero. The equation describing the force applied to the fluid by the boundary in Lagrangian coordinates is given by $\mathbf{f}(r, t)$ and is explicitly written as,

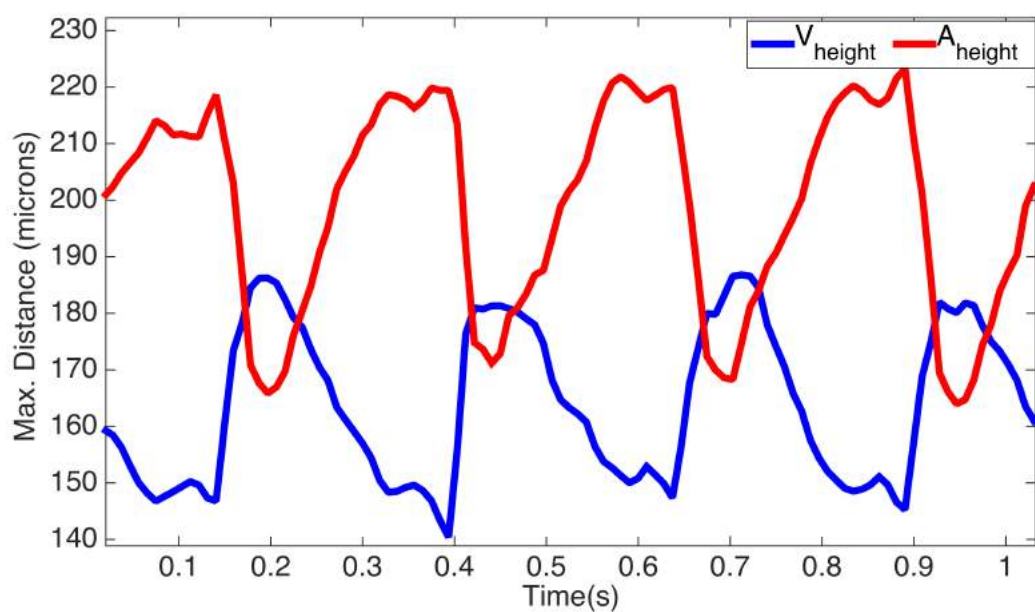
$$\mathbf{f}_{tgt}(r, t) = k_{target} (\mathbf{Y}(r, t) - \mathbf{X}(r, t)), \quad (5.9)$$

where k_{target} is the stiffness coefficient, and $\mathbf{Y}(\mathbf{r}, \mathbf{t})$ is the preferred position Lagrangian position of the target structure. In all simulations the motion of the two-chambered heart (atria, ventricle, AV canal, SV, and BA) was prescribed by applying a force proportional to the distance between location of the actual boundary and the preferred position. The deviation between the actual and preferred positions can be controlled with the variable k_{target} .

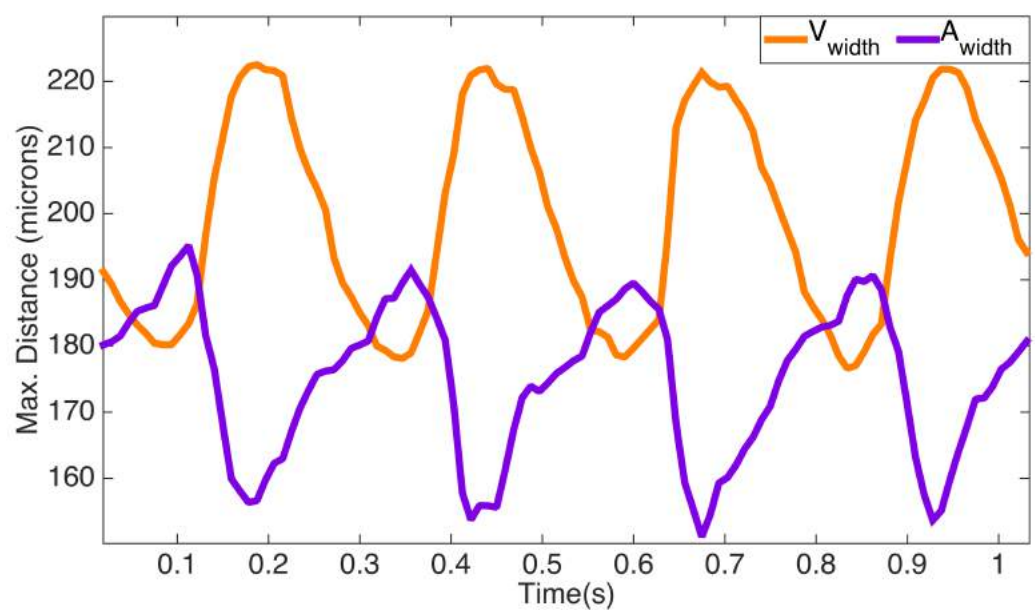
The blood cells' deformations and movement was governed by fully coupled fluid-structure interaction and movement was not prescribed. Linear springs were used to model the flexibility of blood cells; however, the spring stiffnesses were large as only to allow negligible deformations. Springs were attached between both adjacent Lagrangian points as well as the Lagrangian point across from them. The forces applied to the fluid from deformations of the blood cells is given by

$$\mathbf{f}_{spr}(r, t) = k_{spring} \left(1 - \frac{R_L}{\|\mathbf{X}_{SL}(r, t) - \mathbf{X}_M(r, t)\|} \right) \cdot \begin{pmatrix} x_{SL} - x_M \\ y_{SL} - y_M \end{pmatrix}, \quad (5.10)$$

where \mathbf{X}_M and \mathbf{X}_{SL} are the master and slave node, respectively, k_{spring} is the spring stiffness, and R_L is the resting length of the spring. Further details about these fibers models are described in Section 3.3.2.



(a)



(b)

Figure 5.13: 5.13a and 5.13b illustrate the maximum distance for the height and width (in pixels) respectively, in the atria and ventricle of a 4 *dpf* embryonic zebrafish heart from [5].

Ventricular Parameters		Atrial Parameters		Trabecular Parameters	
Parameter	Max. Length (μm)	Parameter	Max. Length (μm)	Parameter	Length(μm)
$\tilde{V}_{a_{con}}$	89.20	$\tilde{A}_{a_{exp}}$	98.11	\tilde{r}_T	7.29
$\tilde{V}_{b_{con}}$	70.84	$\tilde{A}_{b_{exp}}$	113.11	\tilde{h}_T	20.97
$\tilde{V}_{a_{exp}}$	93.78	$\tilde{A}_{a_{con}}$	76.59		
$\tilde{V}_{b_{exp}}$	111.98	$\tilde{A}_{b_{con}}$	84.10		

Table 5.4: The morphological parameters in physical units as computed from the kinematic analysis.

Ventricular Phases			Atrial Phases		
Phase	%ofPeriod	Time (s)	Phase	%ofPeriod	Time (s)
Rest after Contraction	20.7	0.05	Rest after Expansion	20.7	0.05
Expansion	24.0	0.06	Contraction	24.0	0.06
Rest after Expansion	7.9	0.02	Rest after Contraction	2.2	0.01
Contraction	47.4	0.12	Expansion	53.1	0.13

Table 5.5: Average percentage and duration of each phase during the heart cycle obtained from kinematic analysis.

5.3.2 Prescribed Motion of the Two-Chambered Heart

The motion of the two-chambered heart was modeled after a video taken using spinning disk confocal microscopy from [5] of a wildtype zebrafish embryo at 96hpf. The video's images were acquired with a Nikon Te-2000u microscope (Nikon) at a rate of 250 frames per second using a high-speed CMOS camera (MiCam Ultima, SciMedia) [5]. Using the MATLAB software package DLTdv [277], the systolic and diastolic periods were determined by measuring maximum width and height of both the atrial and ventricular chambers. These results are shown in Figure 5.13a and 5.13b. The maximum width of the AV canal was also measured in pixels right before diastole, and found to be 25 pixels. Assuming the width of the AV canal is $42\mu m$ [65], each single pixel corresponds to $1.68\mu m$. The converted height and widths in μm are found in Table 5.4. The average heights and radii of the trabeculae were found to be $20.96\mu m$ and $7.29\mu m$ respectively.

One entire heart cycle was found to take place in approximately 27 frames. Assuming the heart beat frequency is 3.95 beats/s [57], each pumping cycle lasts $\sim 0.25s$. Each heart chamber undergoes four phases during each cycle: a rest period at the end of contraction, a period of expansion, a rest period at the end of expansion, and a period of contraction. The average percentage and duration of each phase are given in Table 5.5.

The prescribed motion of the two-chamber hearts was performed by interpolating between different phases of the heart cycle. This is illustrated in Figure 5.14 which show the beginning of

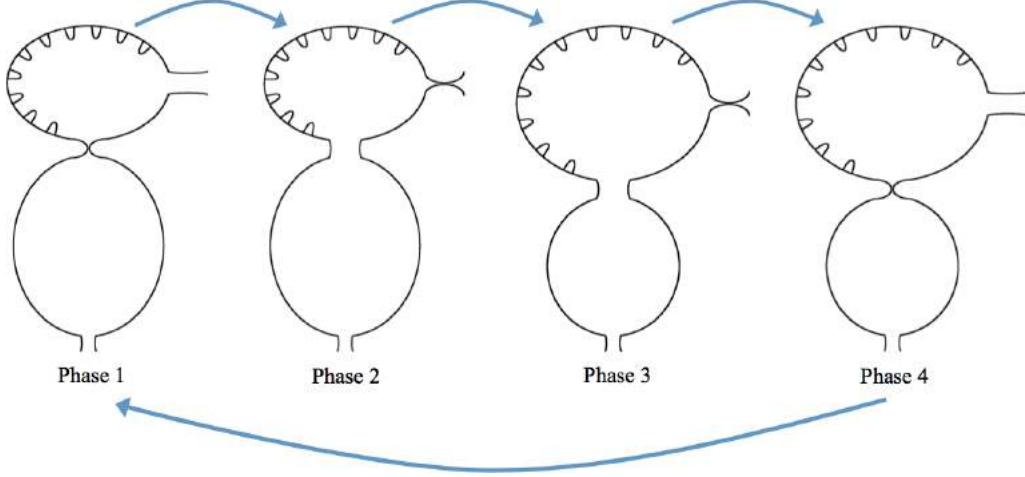


Figure 5.14: We describe four phases of each heart cycle. Note that the position at the beginning of each phase is shown. Phase 1: the ventricle rests after contraction and the atrium rests after expansion. The AV canal goes from fully occluded to 10% occlusion. Phase 2: The diastolic phase when the ventricle expands while the atria contracts. Phase 3: the ventricle rests after expansion and the atrium rests after contraction. The AV canal becomes fully occluded state. Phase 4: The systolic phase, when the ventricle contracts and the atria expands.

each phase. Phase 1: the ventricle rests after contraction and the atrium rests after expansion. The AV canal goes from fully occluded to 10% occlusion. Phase 2: The diastolic phase when the ventricle expands while the atria contracts. Phase 3: the ventricle rests after expansion and the atrium rests after contraction. The AV canal becomes fully occluded state. Phase 4: The systolic phase, when the ventricle contracts and the atria expands. Note we model the time in each phase after the ventricle motion, only.

The actual motion of the heart is driven by changing the preferred position of the target points. Each phase transition used the following interpolation function,

$$\mathbf{X}_{target} = \mathbf{X}_{current} + g_j(t) [\mathbf{X}_{next} - \mathbf{X}_{current}],$$

where

$$g_j(t) = \begin{cases} c_1 \left(\frac{t}{T_{P_j}} \right)^2 & t < t_1 \\ c_3 \left(\frac{t}{T_{P_j}} \right)^3 + c_4 \left(\frac{t}{T_{P_j}} \right)^2 + c_5 \left(\frac{t}{T_{P_j}} \right) + c_6 & t_1 \leq t \leq t_2 \\ -c_2 \left(\frac{t}{T_{P_j}} - 1 \right)^2 + 1 & t > t_2 \end{cases}, \quad (5.11)$$

and T_{P_j} is the total time for Phase j . Eq. (5.11) was chosen to enforce continuous accelerations

Parameter	Value
c_1	2.739726027397260
c_2	2.739726027397260
c_3	-2.029426686960933
c_4	3.044140030441400
c_5	-0.015220700152207
c_6	0.000253678335870

Table 5.6: Table of polynomial coefficients for the interpolating function, $g_j(t)$.

Phase 1		Phase 2	
Parameter	Time	Parameter	Time
T_P	$0.207 \times \text{Period}$	T_P	$0.240 \times \text{Period}$
t_1	$0.05 \times T_{P_1}$	t_1	$0.07 \times T_{P_2}$
t_2	$0.95 \times T_{P_1}$	t_2	$0.93 \times T_{P_2}$
Phase 3		Phase 4	
Parameter	Time	Parameter	Time
T_P	$0.079 \times \text{Period}$	T_P	$0.474 \times \text{Period}$
t_1	$0.05 \times T_{P_3}$	t_1	$0.04 \times T_{P_4}$
t_2	$0.95 \times T_{P_3}$	t_2	$0.96 \times T_{P_4}$

Table 5.7: Table of temporal parameters used in the interpolating function, $g_j(t)$.

between phases. The coefficients $\{c_k\}_{k=1}^6$ are given in Table 5.6 and the durations of each phase are reported in Table 5.7.

To determine the Wo within the heart, we take characteristic values for zebrafish embryonic hearts between 4 and 4.5 dpf and match our dimensionless model parameters accordingly. The characteristic frequency, f_{zf} was measured *in vivo*, and the characteristic length, L_{zf} , was taken as the height of the ventricular right before systole. The Wo was then calculated as

$$Wo = L_{zf} \sqrt{\frac{2\pi \cdot f_{zf} \cdot \rho_{zf}}{\mu_{zf}}} = 0.77, \quad (5.12)$$

where $f_{zf} = 3.95 \text{ s}^{-1}$ [57], $\rho_{zf} = 1025 \text{ kg/m}^3$ [15], $\mu_{zf} = 0.0015 \text{ kg/(m} \cdot \text{s)}$ [242, 243], and $L_{zf} = 0.188 \text{ mm}$ from DLTdv analysis.

The characteristic velocity, V_{zf} , was taken as the average of the minimum and maximum velocity measured *in vivo*. The dimensionless frequency may then be calculated as

$$\tilde{f} = \frac{L_{zf}}{V_{zf}} \cdot f_{zf} = 0.1, \quad (5.13)$$

where $V_{zf} = 0.75 \text{ cm/s}$ [12].

For the mathematical model, the parameters were chosen to keep the dimensionless frequency fixed at $\tilde{f} = 1.0$. The Wo was varied by changing the kinematic viscosity, $\nu = \mu/\rho$. The computational parameters are reported in Table(5.7). For the simulations, the Wo_{sim} is calculated using a characteristic length of V_{bexp} and characteristic velocity is set to the maximum velocity in the AV canal during diastole. Since the pumping motion is prescribed, the maximum velocity in the AV canal remains close to constant, regardless of Wo . The simulations were performed for $Wo_{sim} = \{0.2, 0.5, 1.0, 2.0, 4.0, 8.0, 12.0\}$. The stiffnesses of the target points were chosen to minimize the deviations from the preferred position and varied with Wo_{sim} and the same stiffness was used in all simulations.

We used an adaptive and parallelized version of the immersed boundary method, IBAMR [211, 128]. IBAMR is a C++ framework that provides discretization and solver infrastructure for partial differential equations on block-structured locally refined Eulerian grids [273, 274] and on Lagrangian (structural) meshes. IBAMR also includes infrastructure for coupling Eulerian and Lagrangian representations.

The Eulerian grid on which the Navier-Stokes equations were solved was locally refined near the immersed boundaries and regions of vorticity with a threshold of $|\omega| > 0.05$. This Cartesian grid was organized as a hierarchy of four nested grid levels, and the finest grid was assigned a spatial step size of $dx = D/1024$, where D is the length of the domain. The ratio of the spatial step size on each grid relative to the next coarsest grid was 1:4. The temporal resolution was varied to ensure stability. Each Lagrangian point of the immersed structure was chosen to be $\frac{D}{2048}$ apart (twice the resolution of the finest fluid grid).

5.3.3 Two-Chamber Heart Results

In this section, we describe the bulk flow structure within a two-chambered embryonic heart containing both trabeculae and blood cells. The Wo is varied from 0.2 to 12, and the trabecular heights are varied from half to twice the biologically relevant case. Note that we consider Wo beyond the biologically relevant range for embryonic zebrafish to gain insight into why hearts may change shape and pumping properties as they grow in developmental or evolutionary time. We consider trabeculae heights outside of the biologically relevant range to gain insights into whether or not physical factors constrain the developing heart to this region of the morphospace.

Streamlines and vorticity plots are used to show the direction of flow and mixing within the heart. We are interested in the direction of flow since endothelial cells are known to sense and respond to not only the magnitude of flow but also to its direction [278, 279]. We are also interested in the direction of flow near the cardiac wall since it may alter the advection of morphogens or other signaling agents [280, 281, 282, 283]. The streamline and vorticity graphs were generated using VisIt visualization software [192]. When interpreting streamlines, please note that a neutrally buoyant, small particle in the fluid will follow the streamline. The streamlines are drawn by making a contour map of the stream function, since the stream function is constant along the streamline. The stream function, $\psi(\mathbf{x}, t)$, in 2D is defined by the following equations:

$$u(\mathbf{x}, t) = \frac{\partial \psi(\mathbf{x}, t)}{\partial y} \quad (5.14)$$

$$v(\mathbf{x}, t) = -\frac{\partial \psi(\mathbf{x}, t)}{\partial x} \quad (5.15)$$

The vorticity, ω , is the curl of the velocity field and describes the *local* rotation of the fluid.

$$\omega = \nabla \times \mathbf{u}. \quad (5.16)$$

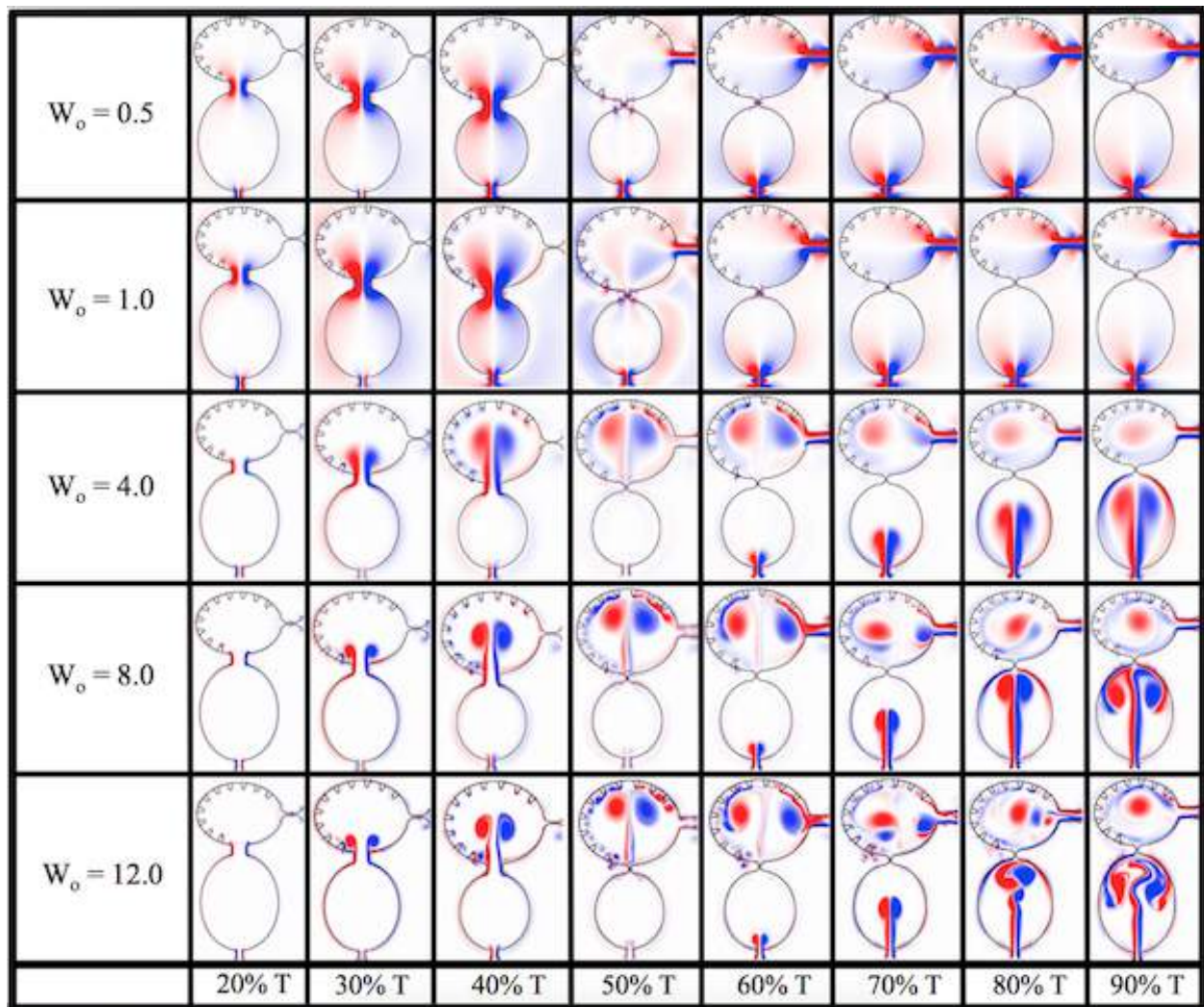
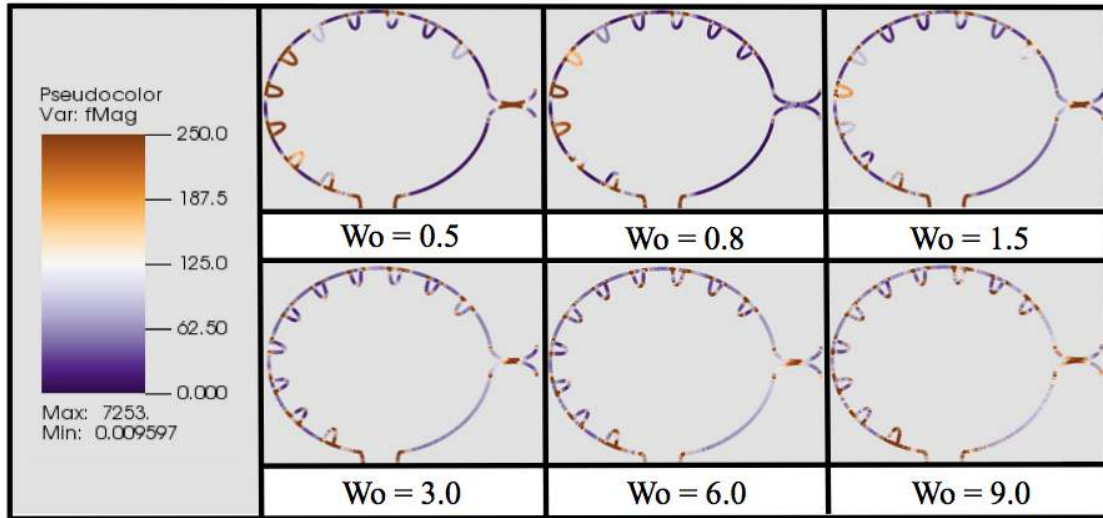
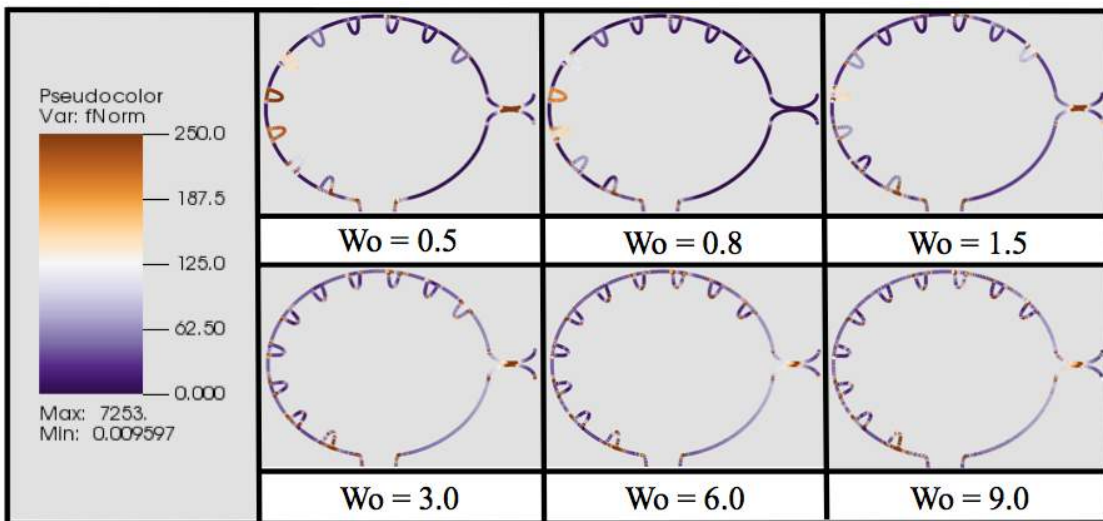


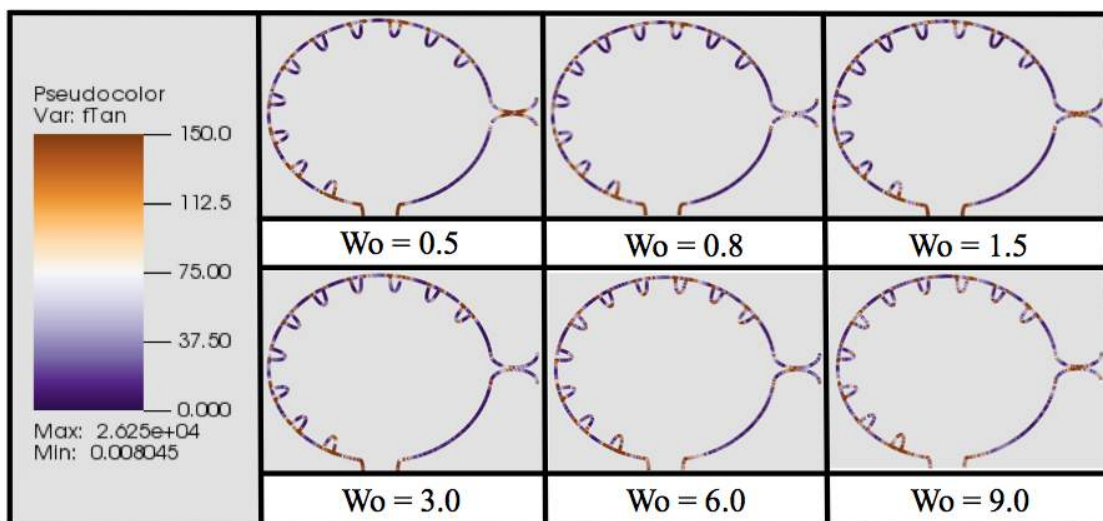
Figure 5.15: Vorticity analysis performed for the case of biologically sized trabeculae and varying Wo at different time points during one heart cycle.



(a)



(b)



(c)

Figure 5.16
223

Figure 5.15 shows the vorticity within the two-chambered heart at different times during one period of the heart cycle, T . The trabeculae heights were fixed at the biological scale and no blood cells were simulated. Five different Wo were considered, $Wo = \{0.5, 1.0, 4.0, 8.0, 12.0\}$. Note that the biologically relevant case is $Wo = 0.77$, which falls between the $Wo = 0.5$ and $Wo = 1.0$ cases. From the vorticity plots, it is clear there is not much difference in vortical flow between these cases, either during diastole or systole. Furthermore, vortices do not form within the atria during atrial filling. As Wo increases to $Wo = 4.0$, two distinct intracardial vortices form, and after systole, a remnant vortex is still present in the ventricle. Two vortices form within the atria during filling. The higher $Wo > 4$ cases, show similar vortex existence; however, the ventricular and atrial vortices that form during diastole and systole, respectively, move within the chamber. Moreover, in the $Wo = 12.0$ case, distinct vortices are observed between trabeculae, and some minor vortex shedding appears as high speed flow moves over the trabeculae. It is clear as Wo increases, intracardial and intertrabecular mixing also increases. The Wo of adult zebrafish and larger vertebrates is above 4 [15], and this suggest that the role of the trabeculae in the adult may be different than it is during development. It is also interesting to note that adult hearts across the animal kingdom operating at $Wo < 4$ typically lack trabeculae.

Figure 5.16 illustrates the total force magnitude (5.16a), the normal force magnitude on the boundary(5.16b), and the tangential force magnitude on the boundary (5.16c) for various Wo between 0.5 and 9.0 immediately after diastole. It appears the main contribution to the total force magnitude comes from the normal component of the force in all cases. Furthermore it appears that as Wo increases, the force felt on the left most trabeculae decreases, and there is an increase in the forces felt by the top surface of each trabeculae as well as between the trabeculae, i.e., both normal and tangential components of the force, see Figures 5.16b and 5.16c.

It is clear from Figure 5.17 that the region experiences the largest forces is on the left side of the ventricle, e.g., the side opposite to the bulbus arteriosus, as diastole finishes. Next we examined the the average magnitude of the force over a trabeculae over one heart cycle for $Wo = 0.8$, see Figure 5.17b. During one heart beat, there appears to be three local extrema in the magnitude of the force for trabeculae #3, #4, #5, two local maxima and one local minimum. To decipher what forces were dominant, we computed the average magnitude of the normal and tangential components of the force on the trabeculae, as illustrated in Figure 5.17c. The analysis shows that the normal

component of the force dominates for trabeculae #3, #4, #5. Moreover, two local maxima and one local minimum are observed for the normal component of the force, averaged over the heartbeat. One local maximum appears for the tangential component of the force for $Wo = 0.8$.

Furthermore, for trabeculae #3, a scaling study was performed for Wo ranging from 0.5 to 12.0. Figure 5.17d depicts the average magnitude of the force over one heartbeat cycle for trabeculae #3. The analysis yielded similar functional behavior, compared with the analogous case in Figure 5.17b, for $Wo \leq 3$. For $Wo > 3$, there is a clear bifurcation where the average force magnitude no longer displays three local extrema, but instead appears to monotonically increase to an asymptotic maximum over one heartcycle.

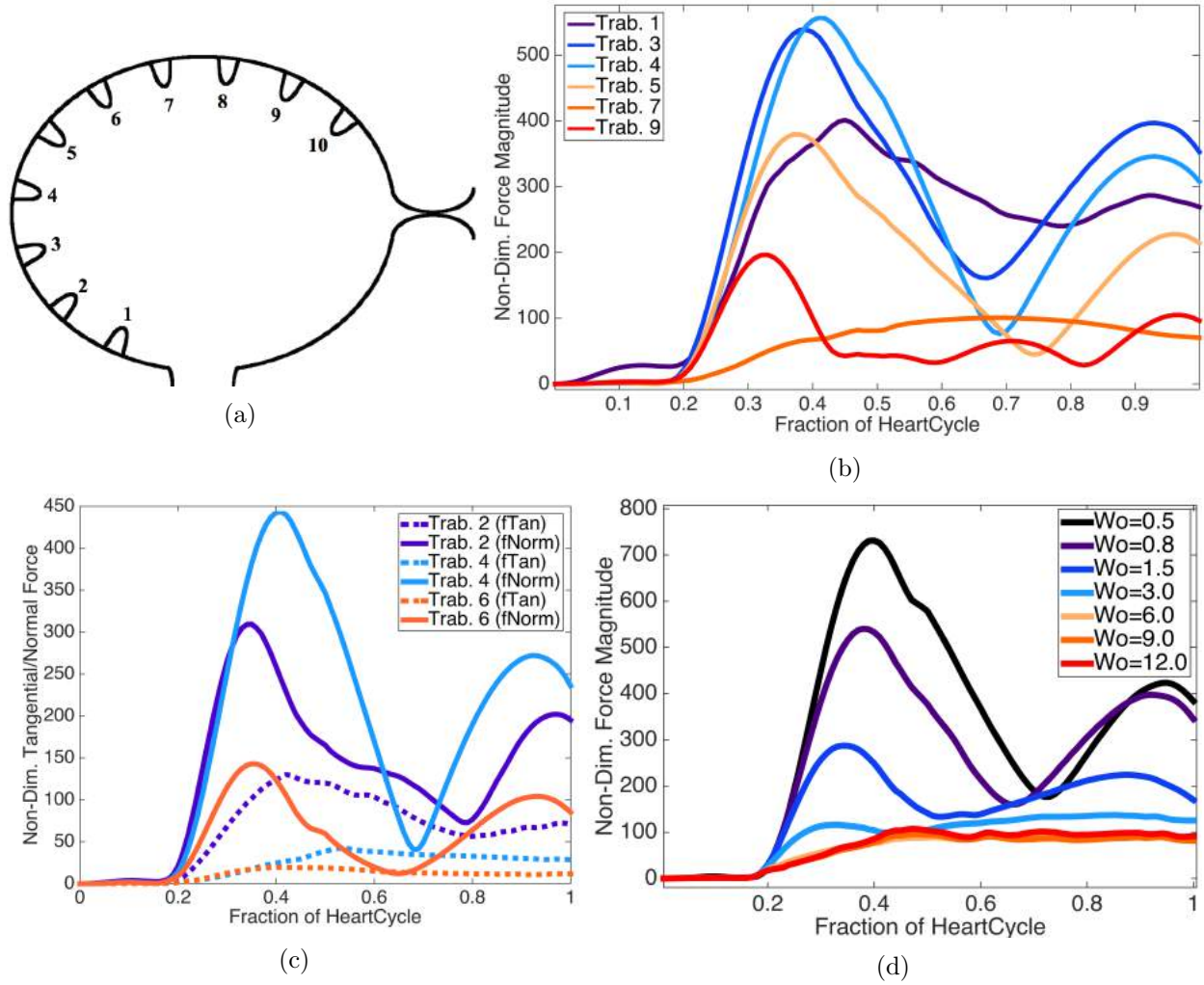


Figure 5.17: (a) Illustrating the indexing of trabeculae (b) Plot illustrating the average magnitude of the force on chosen trabeculae over the course of one heart cycle for $Wo = 0.8$, the biologically relevant case. (c) Plot showing the average magnitude of the tangential and normal forces at each time, for chosen trabeculae, during one heart cycle for $Wo = 0.8$. (d) A plot illustrating the average magnitude of force at each time-step for Wo ranging from 0.5 (half the biologically relevant case) to 12.0.

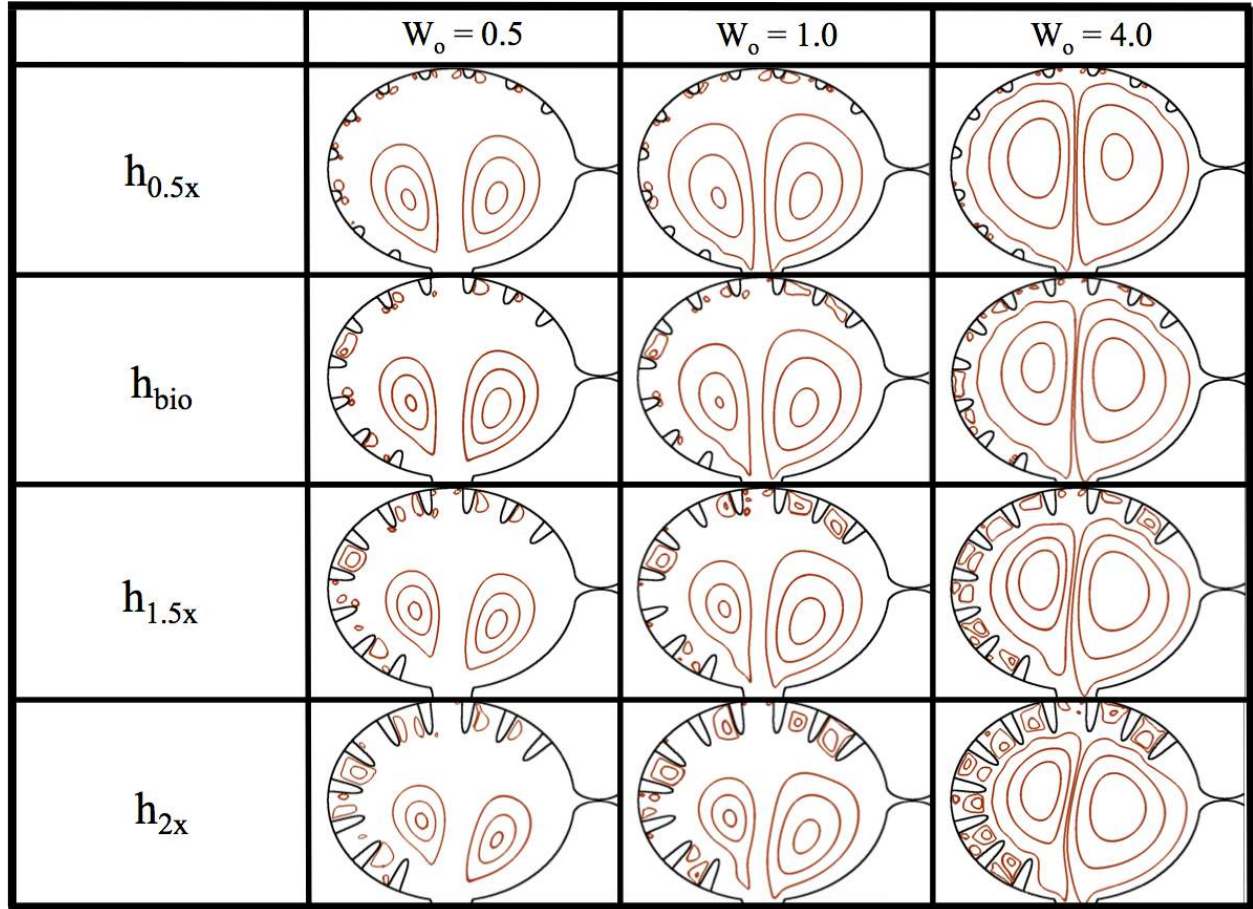


Figure 5.18: Streamline analysis for $W_o = \{0.5, 1.0, 4.0\}$ and trabecular heights from half to twice the biologically relevant size. The analysis was performed within the ventricle immediately after diastole finishes and when the ventricle stops expanding.

Effects of Trabeculae Height Figure 5.18 shows closed streamlines for $W_o = \{0.5, 1.0, 4.0\}$ and trabecular heights ranging from half to twice the biologically relevant size. No blood cells were added to the simulations, and the trabeculae radii and locations were fixed, keeping them equidistant along the ventricular chamber. The analysis was performed within the ventricle immediately after diastole finishes, e.g., the ventricle stops expanding.

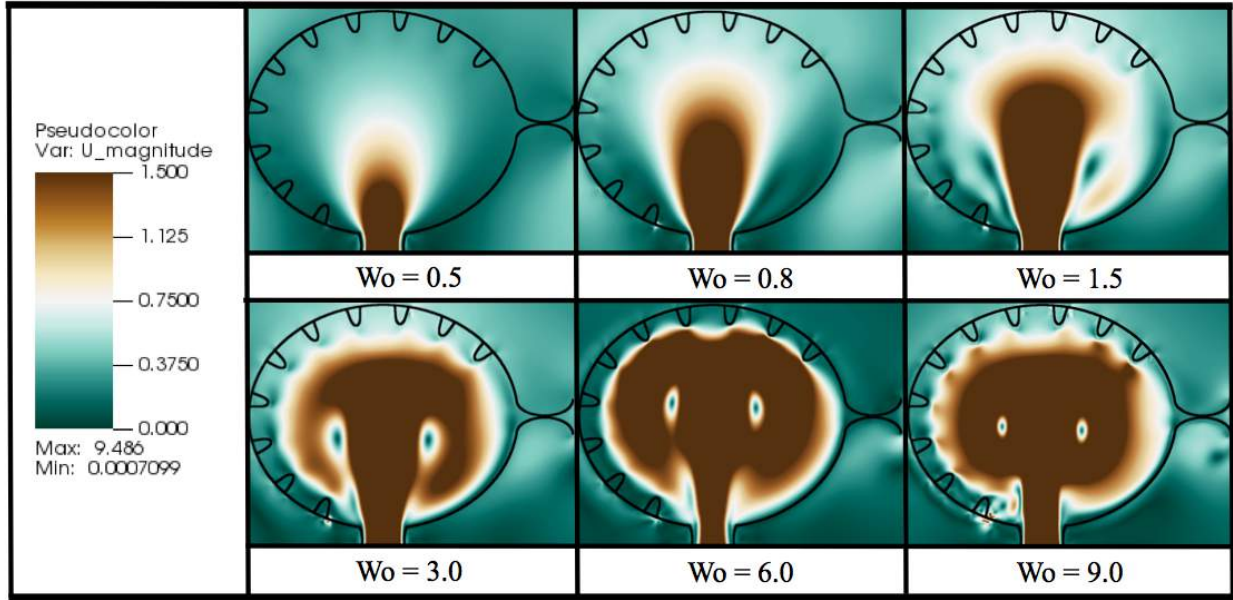


Figure 5.19: Magnitude of velocity colormaps, corresponding to simulations of varying Wo for biologically relevant trabeculae height. The images were taken immediately after diastole, when the ventricle stops expanding.

In the $h_{0.5x}$ case, i.e., half the biologically relevant height, some small vortices appear to form between trabeculae, as seen by the closed streamlines. These closed loops are small relative to the intertrabecular spacing. Note also that the flow velocities between the trabeculae are also quite small, see Figure 5.19, which illustrates the magnitude of velocity for simulations of varying Wo for biologically relevant trabeculae heights. Large intracardial vortices are clearly present in all cases, and the size and strength of these vortices grow as Wo increases.

As the trabeculae height increases, the intertrabecular vortices grow larger. The intracardial vortices remain approximately the same size as height increases. Note also that the intracardial vortex pair becomes more asymmetric as the trabeculae increase in height. Moreover, in the $h_{1.5x}$ and h_{2x} cases, as Wo increases intertrabecular vortices become larger and increase in number (note that these regions still represented relatively slow flow).

The intracardial vortices both spin in opposite directions, e.g., the vortex to the left rotates counter-clockwise while the vortex on the right spins clockwise. Therefore, the intertrabecular vortices on the left side of the ventricle, which form near the head of the trabeculae, spin clockwise, and vice versa on the opposite side of the ventricle. Furthermore, there is a somewhat stagnant region opposite to the AV canal, where the two vortices diverge, and hence no large intertrabecular

vortices form, as compared to different intertrabecular regions in the same simulation. There are small vortices that form in the intertrabecular region opposite to the AV canal in the $h_{0.5x}$ cases; however, as the trabeculae increase in height in the $Wo = 0.5$ and $Wo = 1.0$ cases, this region becomes scarce of vortical flow, while there remains a small amount in the $Wo = 4.0$ case.

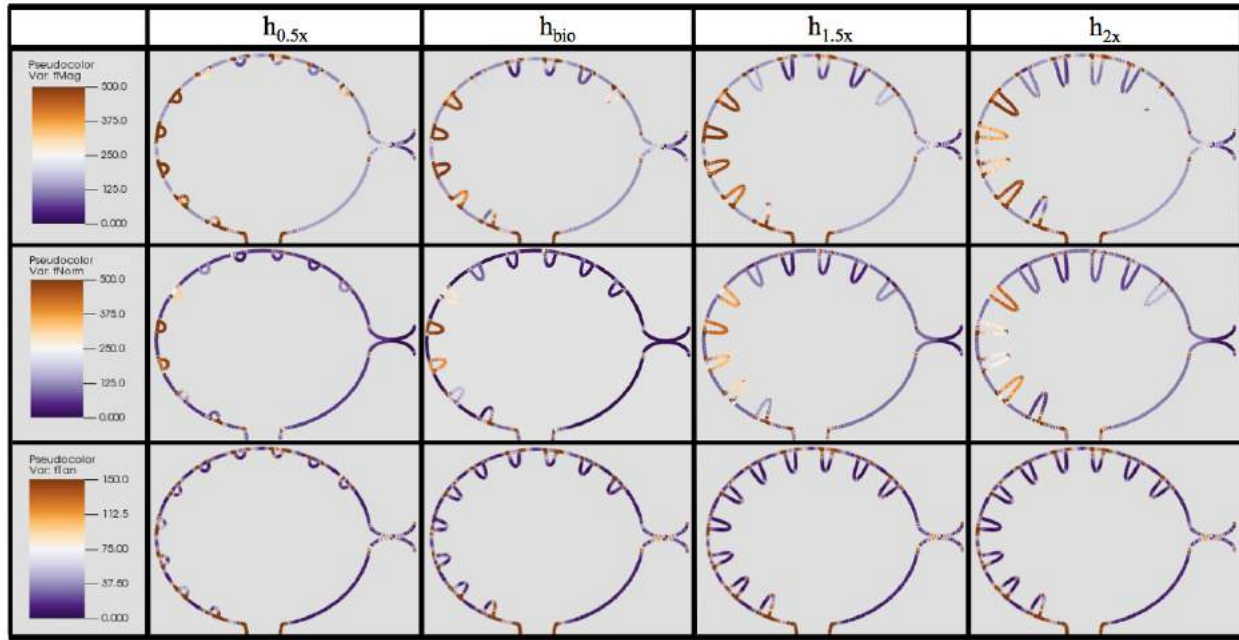


Figure 5.20: The total magnitude of force (top row), magnitude of the normal force to the boundary (middle row), and magnitude of the tangential force to the boundary (bottom) for different trabeculae heights at the biologically relevant Wo , $Wo = 0.8$. It is clear that while the tangential and normal force magnitudes differ, the main contributor to total force on the boundary is the normal component. The largest force are felt by the trabeculae on the left most side of the ventricle. As the trabeculae height increases, the most force is still felt on the same trabeculae, but with reduced magnitude.

For biologically relevant $Wo = 0.8$, in the case of $h_{0.5x}$, the most force is felt by the trabeculae on the left side of the ventricle, see Figure 5.20. This trend continues regardless of height; however, as the height increases the magnitude of that force is decreased. Furthermore, as the height increases, the trabeculae that are exposed to the most force are no longer the left most trabeculae, but the trabeculae next to them. In all cases, the main contribution to the total force magnitude comes from the normal component of the force, rather than the tangential component.

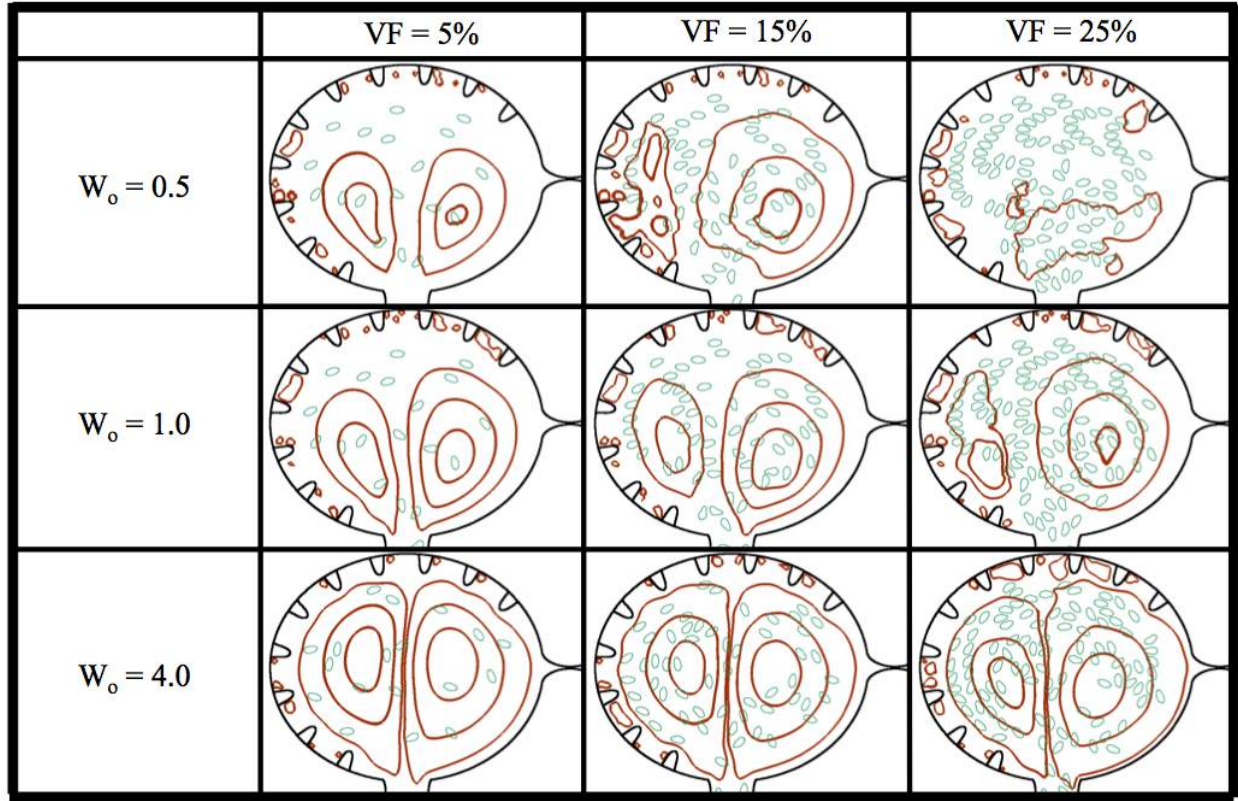


Figure 5.21: Streamline analysis for $W_o = \{0.5, 1.0, 4.0\}$ and hematocrit of $VF = \{5\%, 15\%, 25\%\}$. The analysis was performed within the ventricle immediately after diastole finishes and the ventricle ceases its expansion.

Effects of Hematocrit Figure 5.21 shows the effect that the addition of blood cells has in flow patterns over a range of W_o . In these simulations, trabeculae height, radii, and spacing were fixed. Trabeculae heights were modeled at the biologically relevant size. The analysis was performed within the ventricle immediately at the completion of diastole.

In the case of $W_o = 0.5$, it is clear the addition of blood cells alters the flow pattern within the ventricle. When $VF = 5\%$, the flow resembles that of the analogous case with no hematocrit as seen in Figure 5.18; however, as hematocrit is increased to $VF = 15\%$, the flow patterns are very different. For $VF = 5\%, 15\%$, there are still coherent right or clockwise rotating vortices (shown as the closed streamlines) that form on the right side of the ventricle. The right vortex stretches directly above the AV canal and the left vortex is reduced. For $VF = 25\%$, coherent intracardial vortices are not evident. For larger W_o ($W_o = 1, 4$), the coherent intracardial vortex pair is observed even for higher hematocrit.

In general as Wo increases, the intracardial vortices become more well-defined, e.g., vortical flow is smoother. However, in all cases hematocrit still affects vortical flow patterns intracardially as well as intertrabecularly. Moreover, in these simulations it is clear that after diastole, no blood cells have moved between trabeculae, but rather stay within the middle of the chamber, regardless of volume fraction of Wo . These results suggest that for larger adult vertebrates, when the relative size of the blood cells would also be smaller, the presence of blood cells does not dramatically change the bulk flow. The blood cells do appear to affect the formation of coherent intracardial vortices at this stage of development when $Wo = 0.5 - 1$.

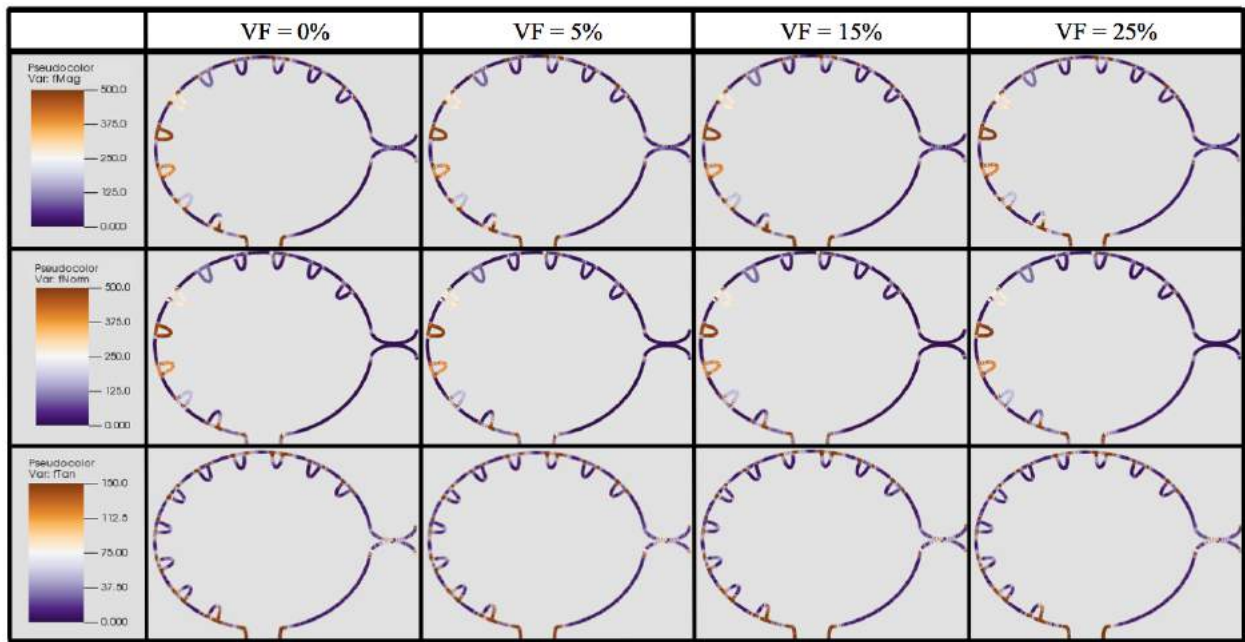


Figure 5.22: The total magnitude of force (top row), magnitude of the normal force to the boundary (middle row), and magnitude of the tangential force to the boundary (bottom) for different volume fractions at the biologically relevant Wo , $Wo = 0.8$. It is clear that while the tangential and normal force magnitudes differ, the main contributor to total force on the boundary is the normal component. Moreover, the blood cells do not appear to affect the magnitude of the force on the boundary in any case.

Although the blood cells do affect intracardial vortices, they do not appear to have significant affect on the magnitude of forces on the boundary for biologically relevant $Wo = 0.8$, see Figure 5.22. It is clear that the main contribution to the total force comes from the normal force component to the boundary, but the net differences between the cases for each volume fraction are minute. This may be the case due to the blood cells having not been thrust close enough to the intertrabecular

regions.

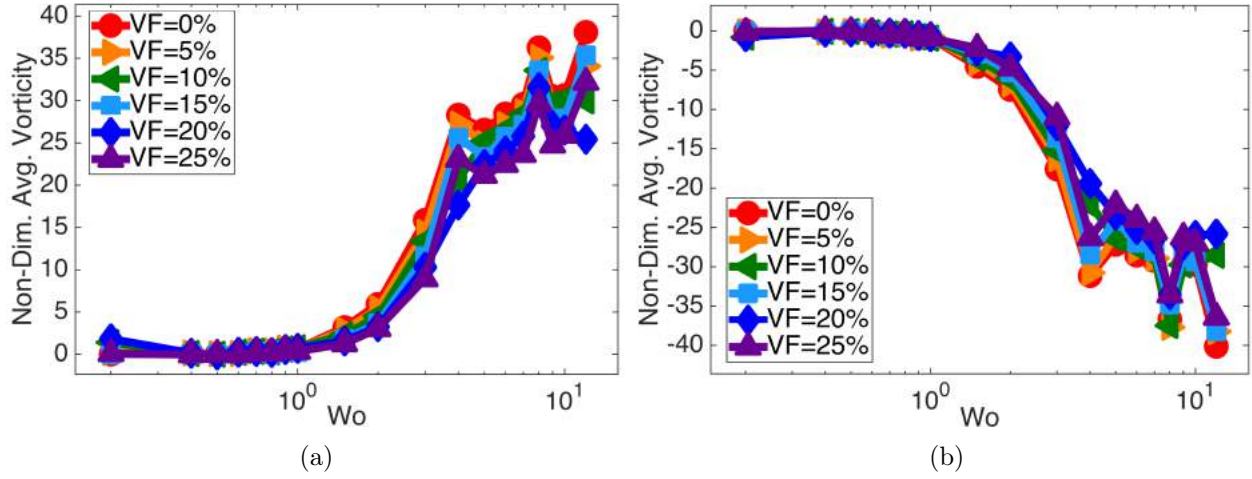


Figure 5.23: 5.23a and 5.23b illustrate the average fluid vorticity on the left and right side of the ventricle, respectively, immediately after diastole, as a function of Wo . It is clear there is a non-linear relationship between the spatially-averaged vorticity and biological scale, given by Wo .

Fluid Mixing As a rough approximation of the rotation and mixing in the fluid, we calculated that spatially-averaged vorticity in the ventricle. Figures 5.23a and 5.23b give the spatially-averaged fluid vorticity on the left and right side of the ventricle, respectively, immediately after diastole, as a function of Wo for $VF = \{0\%, 5\%, \dots, 25\%\}$. It is evident that there is a non-linear relationship between spatially-averaged vorticity and Wo . Furthermore, the overall net sign of the spatially-averaged vorticity is positive in the left side of the ventricle, while it is opposite on the right side. Moreover, the presence of blood cells does not appear to significantly affect the spatially-averaged fluid vorticity for $Wo \leq 1$, although it does affect the generation of a coherent vortex pair.

We report the spatially-averaged vorticity at different times during an entire heartbeat in each side of the ventricle in Figure 5.24. The spatially averaged vorticity was calculated for $Wo = \{0.5, 0.8, 1.5, 8.0\}$ (note the biologically relevant case is $Wo = 0.8$) for hematocrit, $VF = \{0\%, 5\%, 15\%, 25\%\}$. When $Wo \leq 1.5$, there is a clear peak before diastole ends (the vertical dotted line), while for $Wo = 8.0$, the peak occurs the moment when diastole ends. Note also that the width of this peak is larger for $Wo = 8.0$ when inertia dominates.

In general as hematocrit increases, so does the spatially-averaged vorticity. Locally, the presence

of blood cells act to increase vorticity in either direction through their tumbling motion, and this enhancement is not captured in the spatial average.

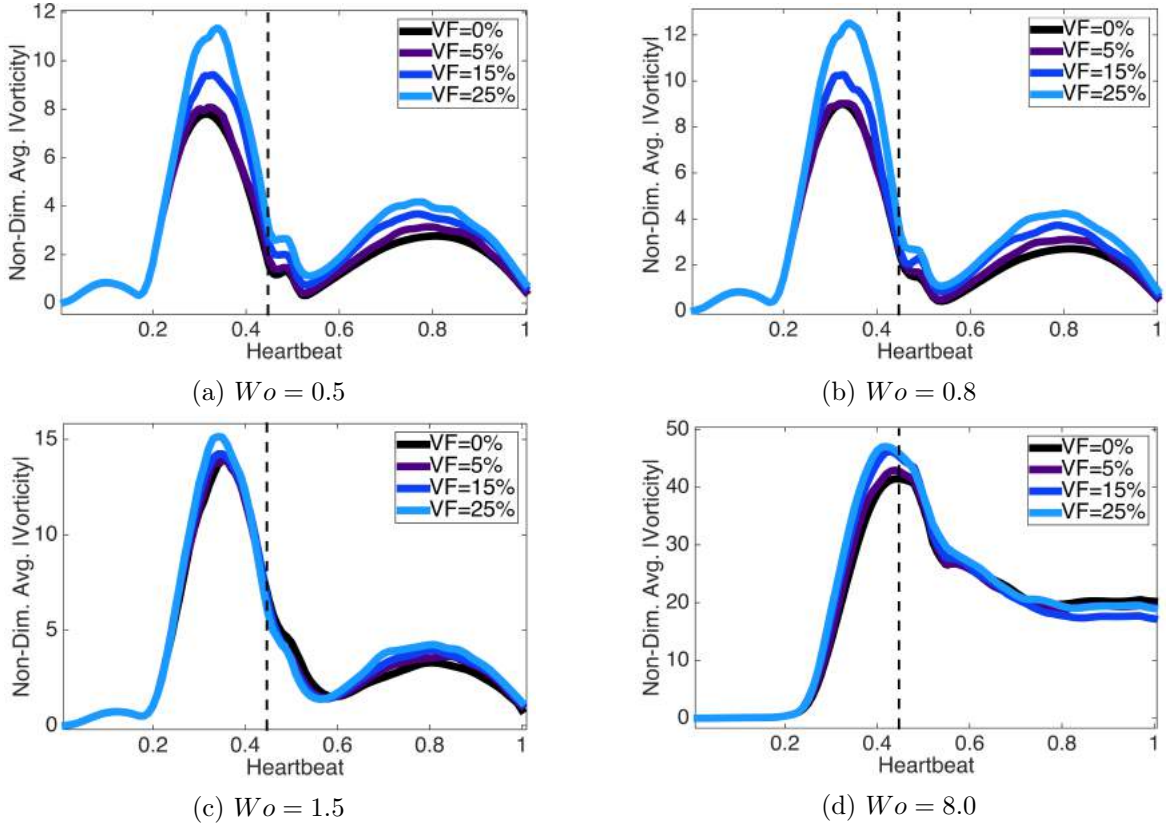


Figure 5.24: Plots of the spatially-averaged magnitude of vorticity for $Wo = \{0.5, 0.8, 1.5, 8.0\}$ for $VF = \{0\%, 5\%, 15\%, 25\%\}$. The vertical dotted line indicates when diastole ends. For every case of Wo , the higher the hematocrit, the more spatially-averaged vorticity magnitude is induced.

5.3.4 Two-Chamber Heart Conclusions

Two-dimensional immersed boundary simulations were used to solve for the fluid motion within an idealized two-chambered pumping heart. The presence of blood cells, trabeculae, and the relative importance of unsteady effects (e.g. the Wo) were considered. The geometry models an idealized embryonic zebrafish heart at 4 *dpf*, and the motion of the chambers was approximated from the kinematic analysis of video taken from a wild type embryonic zebrafish. The main results of the study are as follows: 1) without the presence of blood cells, a large vortex pair forms in the ventricle during filling; 2) with the presence of blood cells at lower Wo , a coherent vortex pair is not formed, 3) for $Wo > 4$, intertrabecular vortices form and vorticity separates from the trabeculae (suggesting

the effect of the trabeculae is different in adult vertebrates than in embryos); 4) the presence of blood cells enhances spatially averaged vorticity in the ventricle, which peaks during diastole; 5) the presence of blood cells does not significantly alter the forces felt by the endocardial cells, and 6) the majority of force is felt by the trabeculae on the outer region of the ventricle.

As mentioned above, an oppositely spinning large intracardial vortex pair forms for all Wo considered, here for $Wo > 0.2$. The vortex on the left spins counterclockwise, while the vortex on the right spins clockwise. This distinction becomes important when considering the formation of vortices between trabeculae. Larger intertrabecular vortices form for simulations with taller trabeculae. Furthermore, when the trabeculae height was $1.5x$ or $2x$ the biologically relevant height in the $Wo = 4$ case, stacked vortices formed between trabeculae; the top vortex spinning opposite to that of the closest intracardial vortex, while the vortex near the base spinning opposite to that. With the addition of blood cells, coherent intracardial vortices do not form when $Wo < 4$ and $VF \leq 15\%$; however, intertrabecular vortical flow patterns were not significantly changed as blood cells were not advected into these regions.

Note that the presence or absence of vortices alter the magnitude and direction of flow near the endocardial wall as well as the mixing patterns within the ventricle. When an intracardial vortex forms, the direction of the flow changes. The presence of two large intracardial vortices forms a stagnation point on the opposite side of the ventricle to the AV canal. Also, the presence of intertrabecular vortices changes the direction of the flow between trabeculae; not all intertrabecular regions have the formation of these vortices. In such cases, the direction of flow between different trabeculae will move in different directions. Since endothelial cells are known to sense and respond to changes in both magnitude and direction of flow [284, 279, 285], the formation and motion of intracardial and intertrabecular vortices may be important epigenetic signals.

For the biologically relevant parameter choices, Wo between 0.5 and 1.0, it is clear that the addition of blood cells significantly affects the formation of coherent vortices. This illustrates the importance of considering hematocrit when conducting fluid dynamics studies at this stage of development. Furthermore, this study demonstrates that small changes in viscosity, scale, morphology, and hematocrit can influence bulk flow properties in the embryonic heart. This presents an interesting challenge since each of these parameters are continuously changing during heart morphogenesis. In addition, estimating the effective viscosity and hematocrit of the embryonic blood is nontrivial.

The results of this paper demonstrate the importance of scale, morphology, and the presence of blood cells in determining the bulk flow patterns through the developing heart. This is important because there is a strongly coupled relationship between intracardial hemodynamics, genetic regulatory networks, and cardiac conduction [59, 12, 53, 75, 54, 15, 91, 52, 286, 88, 89]. Besides contractions of the myocardial cells, which in turn drive blood flow, hemodynamics are directly involved in proper pacemaker and cardiac conduction tissue formation. [94]. Moreover, shear stress is found to regulate spatially dependent conduction velocities within the myocardium. [14]. Myocardial contractions are also required for trabeculation [89]. It is important to note that changes in the conduction properties of the embryonic heart will also affect the intracardial shear stresses and pressures and patterns of cyclic strains.

The cyclic stresses and strains of the cardiomyocytes can also help shape the overall architecture of the trabeculated ventricle. The dynamics of these strains depend upon the intracardial fluid dynamics. For example, greater resistant to flow will induce larger cyclic stresses and possibly reduced cyclic strains. It is known that cyclic strains initiate myogenesis in the cellular components of primitive trabeculae. [91] Since trabeculation first occurs near peak stress sites in the ventricle, altering blood flow may directly produce structural and morphological abnormalities in cardiogenesis. Previous work focusing on hemodynamic unloading in an embryonic heart has resulted in disorganized trabeculation and arrested growth of trabeculae [92, 55, 53]. On the other hand, embryos with a hypertrabeculated ventricle also experience impaired cardiac function. [55]

The exact mechanisms of mechanotransduction are not yet clearly understood [245, 287]. Biochemical signals are thought to be propagated throughout a pipeline of epigenetic signaling mechanisms, which may lead to a regulation of gene expression, cellular differentiation, proliferation, and migration [88]. *In vitro* studies have discovered that endothelial cells can detect shear stresses as low as 0.2 dyn/cm^2 [288] resulting in up or down regulation of gene expressions. Embryonic zebrafish hearts around 36 hpf are believed to undergo shear forces of $\sim 2 \text{ dyn/cm}^2$ and shearing of $\sim 75 \text{ dyn/cm}^2$ by 4.5 dpf [12]. Shear forces in the $\sim 8 - 15 \text{ dyn/cm}^2$ range are known to cause cytoskeletal rearrangement [289, 288, 290]. Mapping out the connection between fluid dynamics, the resulting forces, and the mechanical regulation of developmental regulatory networks will be critical for a global understanding of the process of heart development.

CHAPTER 6

Discussion and Conclusions

*Personally, I liked the university. They gave us money and facilities,
we didn't have to produce anything! You've never been out of college!
You don't know what it's like out there! I've WORKED in the private sector.
They expect *results*. - Dr. Raymond Stantz (Ghostbusters)*

6.1 Quick Review of Thesis Topics

This thesis focused on the effects of morphology on flow during various stages of heart development, namely the linear heart tube stage and during the onset of trabeculation. Various mathematical models were developed and implemented within an immersed boundary framework to study the fully-coupled fluid-structure interaction systems. Furthermore we developed an open source immersed boundary software package, *IB2d*, with full implementations in both MATLAB and Python, that is capable of running a vast range of biomechanics models and is accessible to scientists who have experience in high-level programming environments. We will discuss some of the conclusions below.

6.1.1 *IB2d* Discussion and Conclusion

IB2d is immersed boundary software with full implementations in both MATLAB and Python 3.5. It offers a vast array of fiber model options for constructing the immersed structure and has functionality for advection-diffusion, artificial forcing, muscle mechanics, and electrophysiology. Furthermore, having been written in high-level programming languages, it allows one to implement new fiber models and functionality easily and at an accelerated rate.

High-level programming languages also come with a few drawbacks. Grid sizes should not be implemented beyond a 512×512 resolution due to computational costs. If higher resolution is

required, we suggest moving to IBAMR. Additionally unlike IBAMR, *IB2d* was strictly designed for 2D applications. While full 3D simulations are often desired, some applications may only require fluids with two-dimensions [145, 198, 199, 200, 95]. *IB2d* was written in 2D to make it more readable and to lend itself for easier modification, particularly as a first step in trying to implement a new model.

As of October 2016, *IB2d* has had many users, see Figure B.3, and that number has continued to grow at an accelerated rate since. Furthermore, functionality is constantly being added to the already existing framework and we are open to suggestions for new functionality. It is our hope that for teaching FSI applications, or fast implementations of new fiber models, numerical models and approaches, or varying fluid solvers, *IB2d* will be seen as the ideal environment.

6.1.2 Linear Heart Tube Models Discussion and Conclusions

While studying the linear heart tube stage, three different models were presented. Those models include one in which incorporates blood cells and compares bulk flow properties of prescribed dynamic suction and peristaltic pumping, another which incorporates electrophysiology and traveling action potentials to induce myocardial contraction along the flexible heart tube wall, and one final model which investigates the effect of pumping near the resonant frequencies of the heart tube for dynamic suction pumping. We will discuss the conclusions of each study below.

Heart tube with blood cells discussion and conclusion

Immersed boundary simulations were used to model dynamic suction pumping and peristalsis for a single actuation frequency over a range of Womersley numbers and hematocrits relevant to valveless, tubular hearts. When strong net flow was generated in the tube at higher Wo , blood cells clumped together, and did not flow uniformly throughout the tube. The spatially- and temporally-averaged velocities across a cross-section along the top of the tube showed a non-linear relationship between net flow rates and Wo for DSP. The effect of hematocrit on the net flow rate was significant for $Wo \gtrsim 10$ and was nonlinear. In particular, the varying levels of hematocrit changed the direction of flow for DSP for Wo on the order of 10. The addition of blood cells did not enhance the weak

net flows produced for $Wo < 1$. These results highlight the complex dynamics governing dynamic suction pumping.

For DSP at low Wo and for the range of tube material properties considered here, the fluid is nearly-reversible. This reversibility may explain in part why there is little net flow in the tube for the case of DSP (a reversible motion) at $VF = 0$. This result is in agreement with [20, 21]. Previous studies have shown enhanced fluid transport and animal locomotion in non-Newtonian fluids at low Re and Wo [244]. Since the addition of blood cells in a Newtonian fluid makes the bulk fluid effectively non-Newtonian, it is possible that the addition of blood cells could make the flow in tubular hearts irreversible. For the parameters considered here, any such effect was negligible.

For the case of peristalsis, flow was consistently driven around the racetrack for all Wo and for all hematocrits. Similar to DSP, the addition of hematocrit did not significantly change net flow rates at low Wo . Unlike the case of DSP, the addition of hematocrit also did not significantly alter the velocity waveform or the net flow at higher Wo .

Although the bulk transport of fluid was not significantly changed, the addition of blood cells may affect the shear stresses experienced by the cardiac cells and the amount of mixing within the heart tube. The peristalsis simulations show enhanced mixing as compared to that of DSP at the same Wo and VF . Furthermore for $Wo = 0.2, 2$, peristalsis was able achieve similar levels of blood cell mixing an order of magnitude faster than the DSP simulation at $Wo = 20$. These results are important when considering the role that fluid mixing and shear stress may play in cardiogenesis.

Electro-mechanical model discussion and conclusion

This 2D model coupled the propagation of action potentials, given via the FitzHugh-Nagumo equations, to the force generation and myocardial contraction, given through a non-linear spring-like muscle model, to induce pumping behavior in a flexible tube, where the fully coupled fluid-structure interaction model was solved using the immersed boundary method. This model was first described in [22] and we explored the effect of perturbing a diffusive coefficient in the electrophysiology model to capture different pumping regimes.

It was clear that by varying this diffusive term, \mathbb{D} , the model was able to recreate a spectrum of pumping mechanisms, ranging from one that in which the action potential remained localized

and did not diffusive, i.e., a dynamic suction pumping-esque behavior, and one where the action potential diffused along the heart tube in as a more traveling wave, e.g., peristaltic-like active wave of contraction. Our model showed that when \mathbb{D} was in the more peristaltic-like regime, i.e., $\mathbb{D} \sim 100$, more bulk flow was produced in the racetrack geometry, as compared to more negligible amounts from the dynamic suction pumping-esque regime, $\mathbb{D} \sim 0.1$. This result was consistent for the range of Wo considered.

Moreover, in all cases considered, there was a non-linear relationship between average flow rate, scale (Wo), and diffusivity (pumping behavior). More bulk flow was produced on average (both spatially and temporally), with a maximum around $Wo \sim 0.8$ than for higher Wo , up to $Wo = 30$, in the peristaltic-like regime. However, perturbing the material properties of the tube could potentially affect bulk flow rates across all pumping regimes, given by \mathbb{D} . Our focus was limited to perturbing the stretching and bending stiffnesses of the tube specifically within the dynamic suction pumping-esque regime, $\mathbb{D} \sim [0.1, 1]$. Furthermore, our study only considered increasing the stiffnesses and not decreasing them. For the regime and material properties considered, we found a non-linear relationship between flow rates and stiffness.

Resonant pumping model discussion and conclusion

The preliminary simulations performed here illustrate that exploring the resonance properties of dynamic suction pumping leads to interesting behavior. We first found that over a large regime of viscosities, that the resonance properties of a flexible tube, with material properties given in Table 4.6, show little dependence on viscosity for the first vibrational mode's resonant frequency, while the second mode's resonant frequency depended slightly on viscosity. Using this information allows one to directly compare simulations with the same resonance properties, while varying viscosity (and hence Wo).

Next we showed that while pumping at the first and second mode resonant frequencies that the resulting passive elastic waves from impedance pumping take on that mode's associated vibrational waveform. This remained consistent even in the case of adding mass to the boundaries. Furthermore we saw a non-linear relationship between bulk flow and frequency. Moreover, we witnessed that pumping near resonant frequencies seems to produce more bulk flow, although pumping at the

second mode's resonance frequency did not qualitatively produce more bulk than pumping at a frequency near the first mode's.

Lastly adding mass to the boundary had a significant effect on the resulting passive elastic waveforms from dynamic suction pumping. We saw that the effect of mass looked to decrease the amplitude of oscillation, and hence had an impact on bulk flow rates. For the simulations performed, we qualitatively showed that adding mass to the boundary had a non-linear effect on bulk flow. The added mass has an effect to lower the over-all damping of the system, which seems to significantly contribute to bulk flow rates in dynamic suction pumping.

Although dynamic suction pumping is an easy to prescribe pumping mechanism, the relationships between all parameters of the system (frequency, material properties, viscosity, e.g., scale) and bulk flow rates are very complex in nature. More work can be done in trying to understand the details of these very intricate, non-linear relationships.

6.1.3 Trabeculation Models Discussion and Conclusions

Upon investigating the effects of trabeculae, i.e., complex morphologies along the ventricular endocardium, on intracardial flows, two models were presented. Those models include a steady and pulsatile trabeculated cavity flow model and a two-chamber pumping model with a trabeculated ventricle that includes blood cells. The main results of those models will be discussed below.

Trabeculated cavity model discussion and conclusion

Immersed boundary simulations were used to solve for the flow fields within an idealized model of a trabeculated ventricle of the zebrafish embryonic heart. Our results show that a large intracardial vortex forms around $Re \approx 20$ when steady flow is pushed through the chamber. When the flow is pulsatile, the intracardial vortex begins to form around $Re \approx 10$. In general, pulsatile flow lowers the Re and trabeculae height needed to generate vortices. For both steady and unsteady flows as the trabeculae grow into the chamber, another bifurcation occurs in which small vortices form between each trabecula. Depending upon the Re and the morphology, the intertrabecular vortices can form

without the presence of a large intracardial vortex. In other cases, typically at higher Re , both the intracardial and intertrabecular vortices form. The presence of intracardial vortices changes the direction of the intertrabecular vortices.

Two-chamber model discussion and conclusion

Immersed boundary simulations were used to solve for the fluid motion within an idealized two-chambered pumping heart. The presence of blood cells, trabeculae, and the relative importance of unsteady effects (e.g. the Wo) were considered. The geometry models an idealized embryonic zebrafish heart at 4 dpf , and the motion of the chambers was approximated from the kinematic analysis of video taken from a wild type embryonic zebrafish. The main results of the study are as follows: 1) without the presence of blood cells, a large vortex pair forms in the ventricle during filling; 2) with the presence of blood cells at lower Wo , a coherent vortex pair is not formed, 3) for $Wo > 4$, intertrabecular vortices form and vorticity separates from the trabeculae (suggesting the effect of the trabeculae is different in adult vertebrates than in embryos); 4) the presence of blood cells enhances spatially averaged vorticity in the ventricle, which peaks during diastole; 5) the presence of blood cells does not significantly alter the forces felt by the endocardial cells, and 6) the majority of force is felt by the trabeculae on the outer region of the ventricle.

As mentioned above, an oppositely spinning large intracardial vortex pair forms for all Wo considered, here for $Wo > 0.2$. The vortex on the left spins counterclockwise, while the vortex on the right spins clockwise. This distinction becomes important when considering the formation of vortices between trabeculae. Larger intertrabecular vortices form for simulations with taller trabeculae. Furthermore, when the trabeculae height was $1.5x$ or $2x$ the biologically relevant height in the $Wo = 4$ case, stacked vortices formed between trabeculae; the top vortex spinning opposite to that of the closest intracardial vortex, while the vortex near the base spinning opposite to that. With the addition of blood cells, coherent intracardial vortices do not form when $Wo < 4$ and $VF \leq 15\%$; however, intertrabecular vortical flow patterns were not significantly changed as blood cells were not advected into these regions.

6.1.4 Future Work

To fully understand the intracardial fluid dynamics during heart development, many more studies must be performed. Although, this thesis focused primarily on the linear heart tube stage and the stage during the onset of ventricular trabeculation, many other stages of heart development deserve adequate attention, such as the fluid dynamics of cardiac looping and chamber ballooning, transformation of the endocardial cushions to valve leaflets, ventricular and atrial septation, division of the aortic and pulmonary trunks, as well as further maturation of chamber trabeculation. Moreover, moving from $2D$ to $3D$ simulations are necessary to fully model the intracardial flows and more accurately study the stress distribution along the endocardium of embryonic hearts during heart morphogenesis. Furthermore, more in-depth models that couple hemodynamic forces to cellular signaling mechanisms, e.g., mechanotransductive models, are required to further understand the role of fluid dynamics in cardiogenesis.

APPENDIX A

IMMERSED BOUNDARY DISCRETIZATION APPENDICES

The discretizations used in *IB2d* for solving The Navier-Stokes equations, e.g., (3.72) and (3.73), for computing normal derivatives for porous elements, and for advection-diffusion will be described in this appendix below.

A.1 Discretizing the Navier-Stokes Equations

IB2d uses finite difference approximations to discretize the Navier-Stokes equations on a fixed lattice, e.g., the Eulerian (fluid) grid. It follows the discretization described in [291, 162], and are implicitly defined as follows

$$\rho \left(\frac{\mathbf{u}^{k+1} - \mathbf{u}^k}{\Delta t} + S_{\Delta x}(\mathbf{u}^k) \mathbf{u}^k \right) - \mathbf{D}^0 p^{k+1} = \mu \sum_{\alpha=1}^2 D_{\alpha}^{+} D_{\alpha}^{-} \mathbf{u}^{k+1} + \mathbf{F}^k \quad (\text{A.1})$$

$$\mathbf{D}^0 \cdot \mathbf{u}^{k+1} = 0, \quad (\text{A.2})$$

where Δt and Δx are the time-step and Eulerian meshwidth, respectively, and ρ and μ are the density of the and dynamic viscosity of the fluid, respectively. \mathbf{D}^0 is the central differencing operator, defined as

$$\mathbf{D}^0 = (D_1^0, D_2^0), \quad (\text{A.3})$$

with

$$(D_{\alpha}^0 \phi)(\mathbf{x}) = \frac{\phi(\mathbf{x} + \Delta \mathbf{x} e_{\alpha}) - \phi(\mathbf{x} - \Delta \mathbf{x} e_{\alpha})}{2\Delta x}, \quad (\text{A.4})$$

where (e_1, e_2) is the standard basis in \mathbb{R}^2 . The viscous term, given by $\sum_{\alpha=1}^2 D_{\alpha}^{+} D_{\alpha}^{-} \mathbf{u}^{k+1}$, is a difference approximation to the Laplacian, where the D_{α}^{\pm} operators are the forward and backward approximations to $\frac{\partial}{\partial x_{\alpha}}$. They are defined as

$$(D_{\alpha}^{+}\phi)(\mathbf{x}) = \frac{\phi(\mathbf{x} + \Delta\mathbf{x}e_{\alpha}) - \phi(\mathbf{x})}{\Delta x} \quad (\text{A.5})$$

$$(D_{\alpha}^{-}\phi)(\mathbf{x}) = \frac{\phi(\mathbf{x}) - \phi(\mathbf{x} - \Delta\mathbf{x}e_{\alpha})}{\Delta x}. \quad (\text{A.6})$$

The skew-symmetric difference operator, $S_{\Delta x}$, serves as an approximation to the non-linear advection term, $\mathbf{u} \cdot \nabla \mathbf{u}$, and is defined as follows

$$S_{\Delta x} = \frac{1}{2} [\mathbf{u} \cdot \mathbf{D}_{\Delta x}^0 \phi + \mathbf{D}_{\Delta x}^0 \phi \cdot (\mathbf{u} \phi)]. \quad (\text{A.7})$$

Using the discretizations (A.4), (A.5), (A.6), and (A.7), the equations (A.1) and (A.2) are linear in \mathbf{u}^{k+1} and p^{k+1} . To solve for \mathbf{u}^{k+1} and p^{k+1} from \mathbf{u}^k, p^{k+1} , and F^k , the Fast Fourier Transform (FFT) was implemented [168, 169]. Note that this assumes a periodic domain. Future implementations will include non-square domains and projection methods to incorporate Dirichlet or Neumann Boundary conditions [165, 166].

The Navier-Stokes equations need not be discretized in this manner, and this is where one could implement a fluid solver and discretization of their choice, e.g., finite element or Lattice Boltzmann [148]. However, further consideration must be taken into account on how to spread the Lagrangian forces to the Eulerian grid and move the Lagrangian structure at the local fluid velocity, i.e., Eqns.(3.74) and (3.75), respectively, if implementing in *IB2d*.

If one is interested in solely solving the Navier-Stokes equations there are many methods for doing so, such as projection methods [165, 166], finite volume methods [292], finite element methods [293], Lattice Boltzmann methods [294, 295], panel methods [296], etc. Each method is used for a particular reason, whether it is implementing boundary conditions, accuracy and resolution of specific dynamics, or computational speed. Open source code is available for testing out various methods at [297].

A.2 Discretizing the Fourth Derivatives of the Non-Invariant Beam Model

Recall that the non-invariant beam deformation forces were given by

$$\mathbf{F}_{beam} = k_{NIB} \frac{\partial^4}{\partial s^4} (\mathbf{X}(s, t) - \mathbf{X}_b(s)), \quad (\text{A.8})$$

First we define

$$\begin{aligned} \mathbf{X}(s, t) &= (X_q, Y_q), \\ \mathbf{X}(s+1, t) &= (X_r, Y_r), \\ \mathbf{X}(s-1, t) &= (X_p, Y_p). \end{aligned} \quad (\text{A.9})$$

Recall that by Newton's second law that a force is agiven by an acceleration, hence we only have to discretize (A.8) as a second derivative. Hence we find that the forces are computed as

$$\begin{aligned} F_{beam}(s-1, 1) &= - \begin{pmatrix} k_{NIB}X_r - 2X_q + X_p - C_x \\ k_{NIB}Y_r - 2Y_q + Y_p - C_y \end{pmatrix}, \\ F_{beam}(s, 1) &= 2 \begin{pmatrix} k_{NIB}X_r - 2X_q + X_p - C_x \\ k_{NIB}Y_r - 2Y_q + Y_p - C_y \end{pmatrix}, \\ F_{beam}(s+1, 1) &= - \begin{pmatrix} k_{NIB}X_r - 2X_q + X_p - C_x \\ k_{NIB}Y_r - 2Y_q + Y_p - C_y \end{pmatrix}, \end{aligned} \quad (\text{A.10})$$

where C_x and C_y are the preferred curvatures, given by

$$\mathbf{C} = \begin{pmatrix} C_x \\ C_y \end{pmatrix} = \begin{pmatrix} X_{r_B} - 2X_{q_B} + X_{p_B} \\ Y_{r_B} - 2Y_{q_B} + Y_{p_B} \end{pmatrix}, \quad (\text{A.11})$$

where the B in the subscript denotes the base configuration, or preferred configuration.

A.3 Discretizing the Normal Derivatives on the Boundary

The normal vector to the Lagrangian structure is given by [175, 173],

$$\mathbf{n} = \tau \times e_3, \quad (\text{A.12})$$

where

$$\tau = \frac{\frac{\partial \mathbf{X}}{\partial s}}{\left| \frac{\partial \mathbf{X}}{\partial s} \right|} \quad (\text{A.13})$$

Hence we have that

$$\mathbf{n} = \left(\frac{\partial Y / \partial s}{|\partial \mathbf{X} / \partial s|}, -\frac{\partial X / \partial s}{|\partial \mathbf{X} / \partial s|} \right). \quad (\text{A.14})$$

Unlike [175], who used a 3-*pt* central differencing operator to compute $\frac{\partial \mathbf{X}}{\partial x}$, we compute the partial derivatives using a 5-*pt* differentiation stencil. We do this to both minimize error near end-points of a porous structure and allow functionality for non-closed porous structures. Hence we implement the following five different differentiation operators,

$$\begin{aligned} (D_{\alpha}^{5,-2} \phi)(s) &= \frac{-\frac{25}{12} \phi(s - 2\Delta s e_{\alpha}) + 4\phi(s - \Delta s e_{\alpha}) - 3\phi(s) + \frac{4}{3} \phi(s + \Delta s e_{\alpha}) - \frac{1}{4} \phi(s + 2\Delta s e_{\alpha})}{\Delta s} \\ (D_{\alpha}^{5,-1} \phi)(s) &= \frac{-\frac{1}{4} \phi(s - 2\Delta s e_{\alpha}) - \frac{5}{6} \phi(s - \Delta s e_{\alpha}) + \frac{3}{2} \phi(s) - \frac{1}{2} \phi(s + \Delta s e_{\alpha}) + \frac{1}{12} \phi(s + 2\Delta s e_{\alpha})}{\Delta s} \\ (D_{\alpha}^{5,0} \phi)(s) &= \frac{\frac{1}{12} \phi(s - 2\Delta s e_{\alpha}) - \frac{2}{3} \phi(s - \Delta s e_{\alpha}) + \frac{2}{3} \phi(s + \Delta s e_{\alpha}) - \frac{1}{12} \phi(s + 2\Delta s e_{\alpha})}{\Delta s} \\ (D_{\alpha}^{5,1} \phi)(s) &= \frac{-\frac{1}{12} \phi(s - 2\Delta s e_{\alpha}) + \frac{1}{2} \phi(s - \Delta s e_{\alpha}) - \frac{3}{2} \phi(s) + \frac{5}{6} \phi(s + \Delta s e_{\alpha}) + \frac{1}{4} \phi(s + 2\Delta s e_{\alpha})}{\Delta s} \\ (D_{\alpha}^{5,2} \phi)(s) &= \frac{\frac{1}{4} \phi(s - 2\Delta s e_{\alpha}) - \frac{4}{3} \phi(s - \Delta s e_{\alpha}) + 3\phi(s) - 4\phi(s + \Delta s e_{\alpha}) + \frac{25}{12} \phi(s + 2\Delta s e_{\alpha})}{\Delta s} \end{aligned}$$

A.4 Discretizing the FitzHugh-Nagumo Equations

The spatial grid was discretized on a more coarse mesh than that of the Eulerian grid, call it Δx_f . However, it is scaled to match the geometry of the heart-tube to obtain the desired dynamics of the active wave of contraction. Moreover, the time-step for the FitzHugh-Nagumo equations, Δt_f , was scaled from the *IB* time-step, Δt , i.e.,

$$\Delta t_f = \Delta t \frac{\mathbb{F}}{\mathbb{T}}, \quad (\text{A.15})$$

where \mathbb{F} and \mathbb{T} are a non-dimensional scaling parameter and the desired pumping period, respectively.

The equations themselves are discretized using standard finite difference stencils, with Euler

time-stepping, e.g.,

$$v_j^{n+1} = v_j^n + \Delta t_f \left[\mathbb{D} \frac{v_{j+1}^n - 2v_j^n + v_{j-1}^n}{\Delta x_f^2} - v_j^n (v_a - v_j^n)(v_j^n - 1) + I_j^n - w_j^n \right] \quad (\text{A.16})$$

$$w_j^{n+1} = w_j^n + \Delta t_f \epsilon (v_j^n - \gamma w_j^n). \quad (\text{A.17})$$

A.5 Discretizing the Advection-Diffusion Equation

The concentration is discretized on the same resolution as the Eulerian grid. Each nodal point has a scalar concentration value. One possible choice of discretization for the advection-diffusion equations (3.111) could be as follows,

$$c^{k+1} = c^k + \Delta t \left(D \mathbf{D}^{2,0} c^k - \mathbf{u}^k \cdot \tilde{\mathbf{D}}_0^\pm c^k \right), \quad (\text{A.18})$$

where D is the diffusion coefficient, $\mathbf{D}^{2,0}$ is the central differencing operator for second derivatives, and $\tilde{\mathbf{D}}_0^\pm$ is the upwind differencing operator which depends on the sign of c at that particular point in time. However, we expect better accuracy if we time split the spatial dimensions. Before we discuss *time splitting*, we will explicitly define each of the operators in (A.18). $\mathbf{D}^{2,0}$, is defined as follows,

$$\mathbf{D}^{2,0} = (D_1^{2,0}, D_2^{2,0}) \quad (\text{A.19})$$

with

$$(D_\alpha^{2,0} \phi)(\mathbf{x}) = \frac{\phi(\mathbf{x} + \Delta \mathbf{x} e_\alpha) - 2\phi(\mathbf{x}) + \phi(\mathbf{x} - \Delta \mathbf{x} e_\alpha)}{\Delta x^2}. \quad (\text{A.20})$$

The upwind operator is defined as

$$\tilde{\mathbf{D}}_0^\pm = (\tilde{D}_1^\pm, \tilde{D}_2^\pm) \quad (\text{A.21})$$

with

$$\left(\tilde{D}_\alpha^\pm \phi\right)(\mathbf{x}) = \begin{cases} \frac{\phi(\mathbf{x} + \Delta \mathbf{x} e_\alpha) - \phi(\mathbf{x})}{\Delta x}, & \phi(\mathbf{x}) \leq 0 \\ \frac{\phi(\mathbf{x}) - \phi(\mathbf{x} - \Delta \mathbf{x} e_\alpha)}{\Delta x}, & \phi(\mathbf{x}) > 0. \end{cases} \quad (\text{A.22})$$

We will use the same operators as just described, but not discuss time-splitting for advection. To do this we break the time-step into two parts - the first of which we solve for an auxillary concentration, c^* from c^k , and then update c^* to find c^{k+1} .

First we will advect in x ,

$$c^* = c^k + \Delta t \left(DD_1^{2,0} c^k - u^k \tilde{D}_1^\pm c^k \right), \quad (\text{A.23})$$

where $\mathbf{u}^k = (u^k, v^k)$. Next we advect in y to give the next iteration for c^{k+1} from c^* ,

$$c^{k+1} = c^* + \Delta t \left(DD_2^{2,0} c^* - v^k \tilde{D}_2^\pm c^* \right), \quad (\text{A.24})$$

Splitting recovers some properties of the exact advection by allowing flux from diagonal cells. Computing multi-dimensional flow by time-splitting usually proves a more accurate alternative than multi-dimensional discretization of 3.111.

We show an example of advection-diffusion coupled to a changed velocity field in Section 3.3.4, as well as, an example of advection-diffusion for an arbitrary background velocity field in Appendix A.5.1.

A.5.1 Advection-Diffusion Example

Here we present an example of the advection-diffusion of a background concentration due to a steady background velocity field. Consider a background velocity defined as,

$$\mathbf{u}(\mathbf{x}) = \begin{pmatrix} -\frac{y-0.5}{5} \\ \frac{x-0.5}{5} \end{pmatrix}, \quad (\text{A.25})$$

which is illustrated as the velocity field in Figure A.1 below.

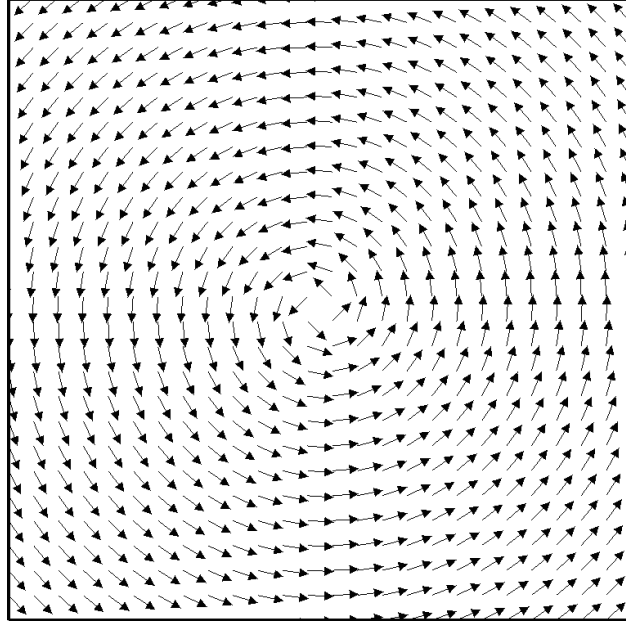


Figure A.1: Steady circular velocity field.

We solved 3.111 on a $[0, 1] \times [0, 1]$ computational domain equally partitioned into a 256×256 grid. Snapshots that illustrate the advection and diffusion of a background concentration in Figure A.2 for various diffusion coefficients, D . It is clear as D is decreased, the initial concentration blob stays better intact for longer throughout the simulation. The circular velocity field pushes the blob around in a circular motion.

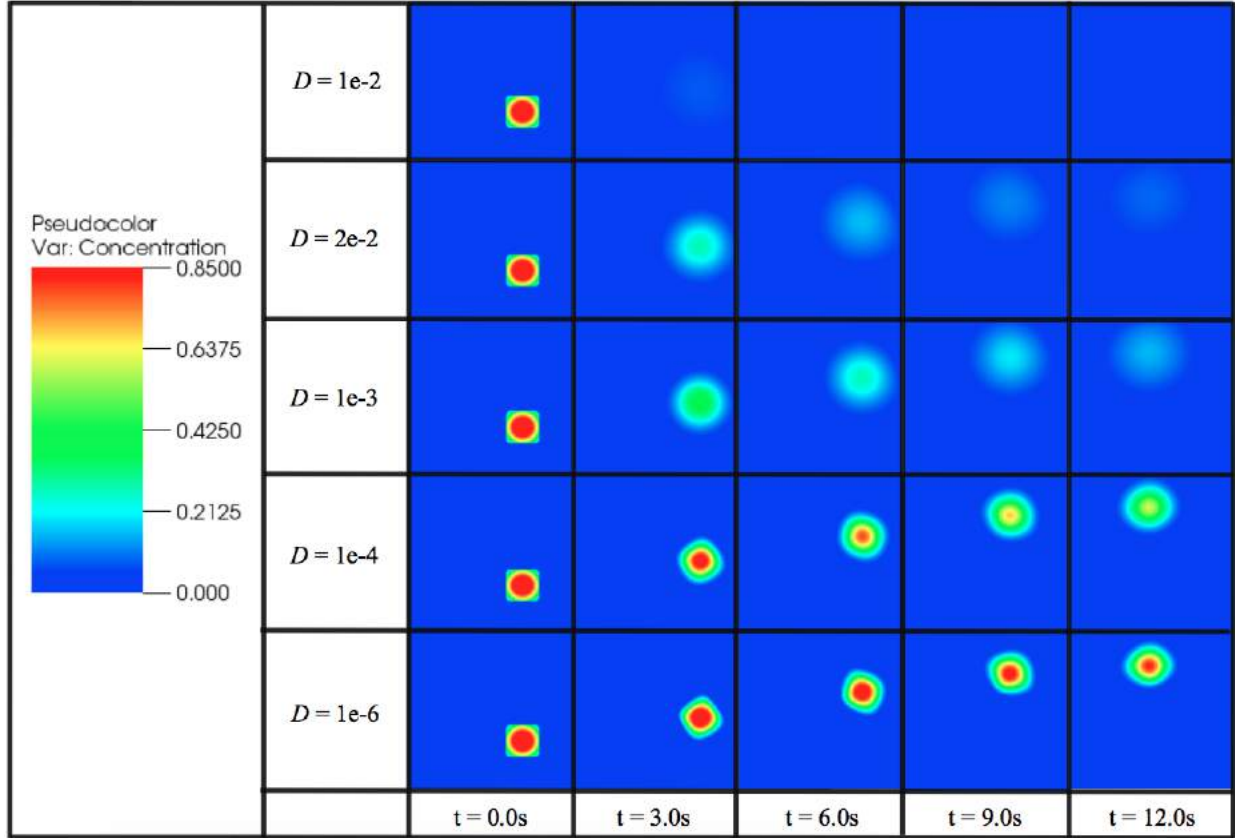


Figure A.2: Illustrated is an initial concentration advecting and diffusing in a circle around the computational domain for various diffusive coefficients, D .

Note that the solutions in Figure A.2 all experience numerical dissipation, as upwind schemes are only 1st-order accurate in both time and space. A blind implementation of a higher order explicit scheme, e.g., the Lax-Wendroff method, may prescribe the sharp interfaces better, as the scheme will be second-order in both time and space; however, other artifacts will arise, namely the presence of high frequency oscillations behind the wave front [194].

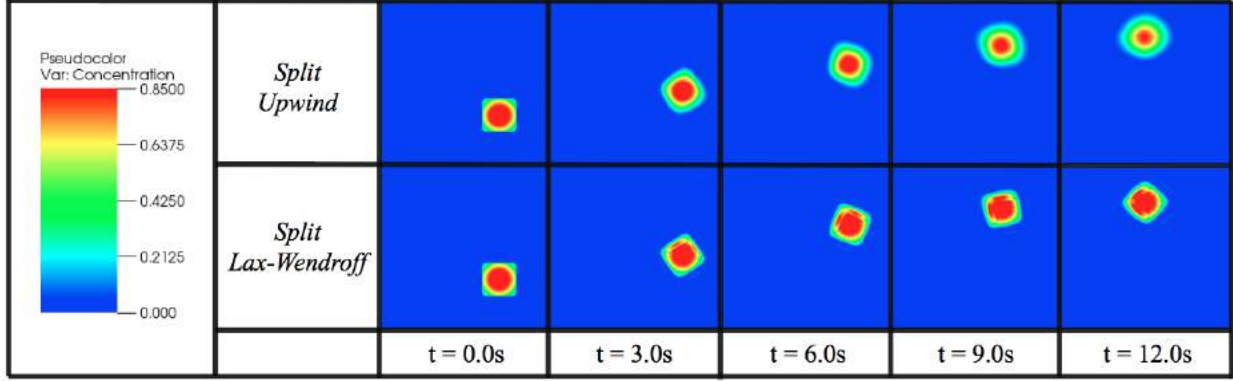


Figure A.3: Illustrated is an initial concentration advecting and diffusing in a circle around the computational domain $D = 1e - 6$ using the split upwind and split Lax-Wendroff method.

We illustrate this phenomena in Figure A.3, where we compare the solutions for the upwind scheme described in Appendix A.5 and the Lax-Wendroff Method with diffusive coefficient $D = 1e - 6$, which will be described below. It is clear that there is more numerical dissipation using the split upwind scheme and that the Lax-Wendroff method better preserves the sharp concentration gradients; however, it is apparent that Lax-Wendroff gives high frequency oscillations behind the wave front. For this reason, we chose the code to has more numerical dissipation artifacts than produce more high frequency oscillations at this time. Future work will include a flux limiting approach to remedy this [194].

Lax-Wendroff uses a central differencing operator to compute the advective terms and an artificial diffusive term to counter instabilities in the advection term. For a simple 1D advection linear equation, i.e.,

$$u_t + au_x = 0, \quad (\text{A.26})$$

where a is the speed of the wave-front, Lax-Wendroff gives the discretization as follows,

$$u_j^{k+1} = u_j^k - a \left(\frac{\Delta t}{\Delta x} \right) \frac{(u_{j+1}^k - u_{j-1}^k)}{2} + a^2 \left(\frac{\Delta t}{\Delta x} \right)^2 \frac{u_{j+1}^k - 2u_j^k + u_{j-1}^k}{2}. \quad (\text{A.27})$$

Using an operator splitting method, we extend (A.27) to 2D analogously,

First we will advect in x ,

$$c_{i,j}^* = c_{i,j}^k + \Delta t \left(D \frac{c_{i+1,j}^k - 2c_{i,j}^k + c_{i-1,j}^k}{\Delta x^2} - u_{i,j}^k \left(\frac{1}{\Delta x} \right) \frac{c_{i+1,j}^k - c_{i-1,j}^k}{2} + \dots \right. \\ \left. \dots + (c_{i,j}^k)^2 \left(\frac{\Delta t}{\Delta x^2} \right) \frac{c_{i+1,j}^k - 2c_{i,j}^k + c_{i-1,j}^k}{2} \right), \quad (\text{A.28})$$

where $\mathbf{u}^k = (u^k, v^k)$. Next we advect in y to give the next iteration for c^{k+1} from c^* ,

$$c_{i,j}^{k+1} = c_{i,j}^* + \Delta t \left(D \frac{c_{i,j+1}^* - 2c_{i,j}^* + c_{i,j-1}^*}{\Delta x^2} - v_{i,j}^k \left(\frac{1}{\Delta x} \right) \frac{c_{i,j+1}^* - c_{i,j-1}^*}{2} + \dots \right. \\ \left. \dots + (c_{i,j}^*)^2 \left(\frac{\Delta t}{\Delta x^2} \right) \frac{c_{i,j+1}^* - 2c_{i,j}^* + c_{i,j-1}^*}{2} \right). \quad (\text{A.29})$$

APPENDIX B

IB2d EXTRAS

Since *IB2d* was first released on github.com/nickabattista/IB2d/, it has been downloaded and used by many people across the United States and the world. An example of weekly statistics about its use are displayed in Figure B.3. We note that these statistics show 50 unique visitors and almost 500 page views on the GitHub page between October 19th, 2016 and November 1st, 2016.

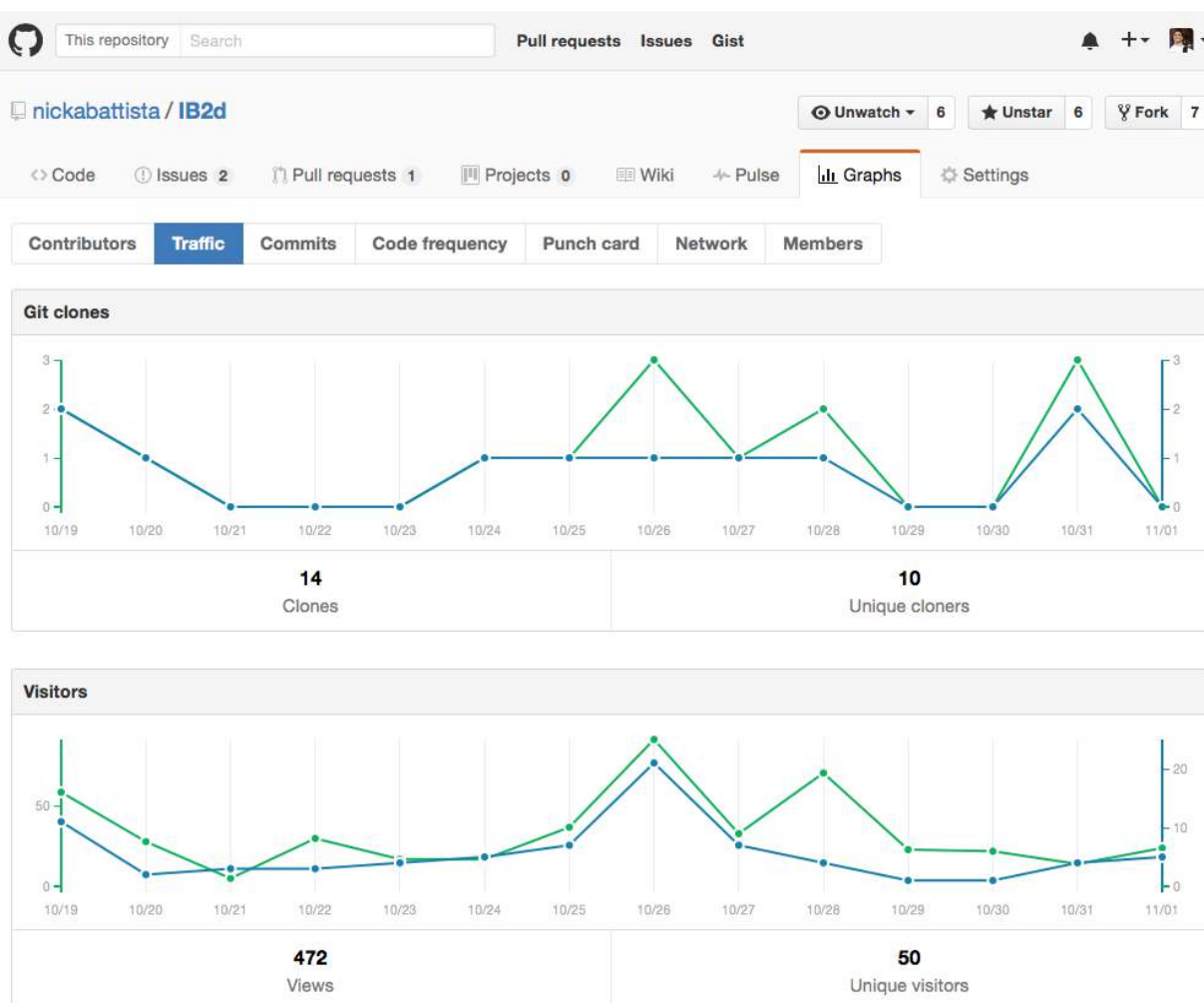


Figure B.1: Example of statistics pertaining to visitors to the GitHub site for *IB2d* from October 19, 2016 to November 1, 2016. We note this was before the release of the *IB2d* paper [37].

Furthermore, for solely entertainment purposes, using GitHub's user-statistics, I can prove that I did, indeed, sleep during my dissertation work. These statistics are shown in Figure B.2. It is my hope this adds a little excitement to this dissertation, similarly like comical papers, such as

[298, 299, 300], or brilliant technical papers, such as [301, 302, 303, 304, 305], have given me during my graduate school tenure.

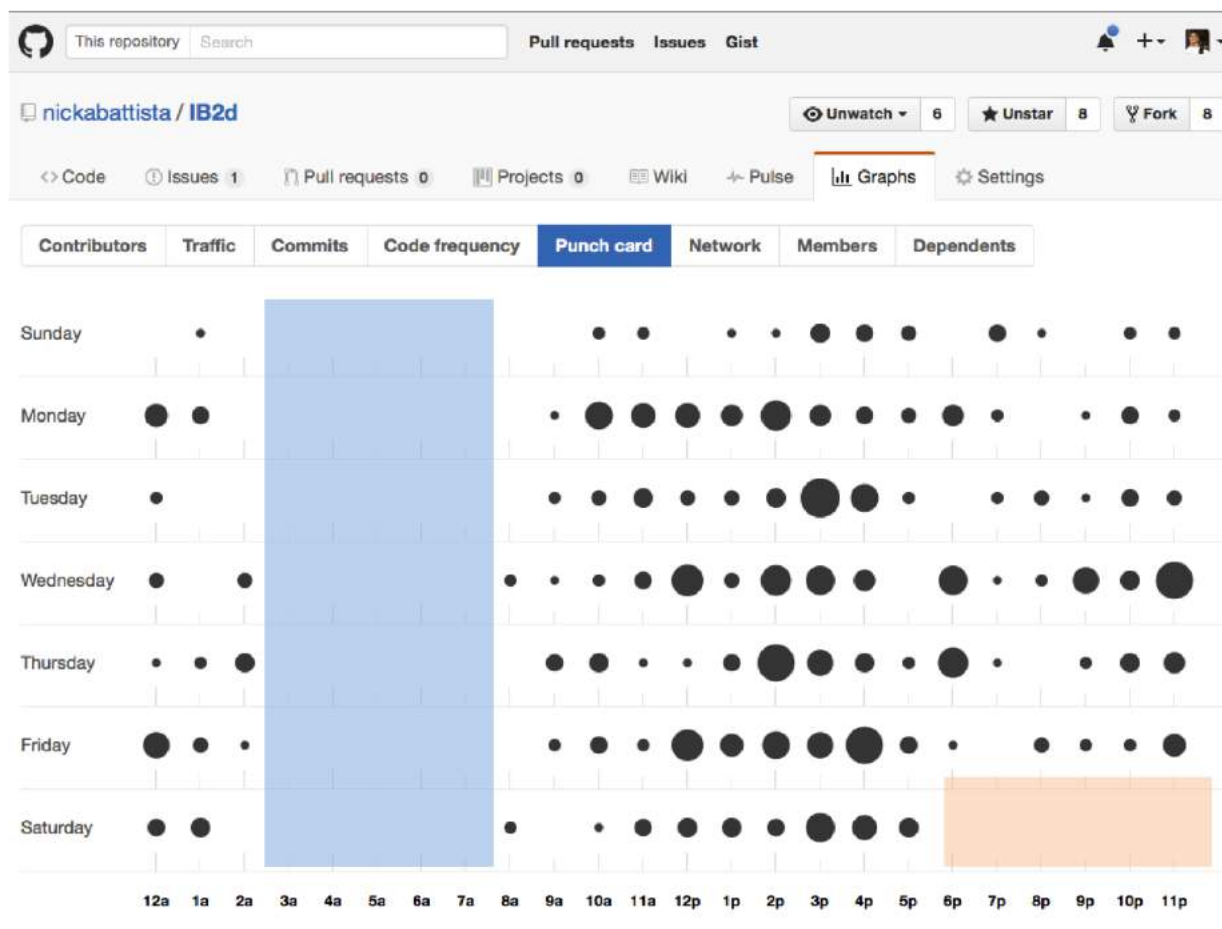


Figure B.2: Punch card from GitHub user-statistics illustrating when I did commits to my GitHub repositories [38]. It is clear that between the hours of 3am and 8am, I tended to sleep, as no code was committed during that time. Moreover, I seemed to reserve Saturday nights for playing music with friends, or at least not committing code.

Lastly, we present a collage of *IB2d* simulation images as shown in Section 3.3. All of the simulations illustrated are but a fraction of the built in examples, all of which are ready to be run immediately upon once having downloaded the software.

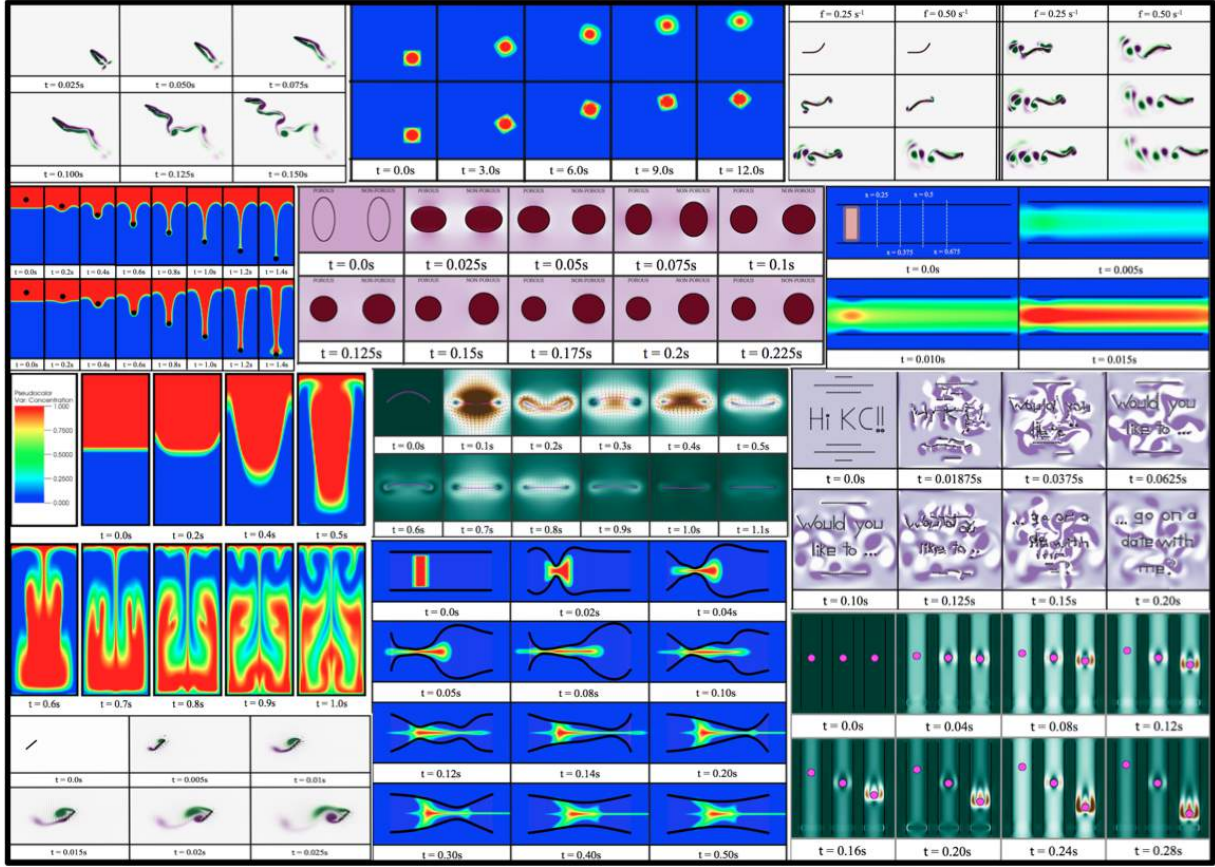


Figure B.3: A collage of a fraction of the simulations that can be run upon immediate download of the open source *IB2d* software.

APPENDIX C

NUMERICAL METHODS FOR COMPUTATIONAL FLUID DYNAMICS (CFD)

In this appendix we will discuss various numerical algorithms for studying fluid dynamics, namely Chorin’s projection method [165, 306, 166], a spectral methods solver based on the Fast Fourier Transform (FFT) [307, 308, 309], and the lattice Boltzmann method [294, 295]. Codes are available to test these methods at [297]. Their corresponding simulation data is saved in the *.vtk* format, as to allow for visualization using open source programs, such as VisIt [192] or ParaView [191].

C.1 Projection Methods

The projection was first introduced by Chorin in 1967 to solve the incompressible, Navier-Stokes equations [165]. The key feature of this method is that it uses operator splitting and Helmholtz-Hodge decomposition to decouple the velocity and the pressure fields, making it possible to explicitly solve the incompressible, Navier-Stokes equations in three steps.

In the first step, an auxillary (intermediate) velocity field is computed by ignoring any dependencies on the pressure. This is essentially an operator split. This velocity field found will not be divergence-free, and hence the necessary incompressible condition will not be satisfied. In discretization terms, this step takes the form of

$$\frac{\mathbf{u}^* - \mathbf{u}^n}{\Delta t} = -(\mathbf{u}^n \cdot \nabla) \mathbf{u}^n + \mu \Delta \mathbf{u}^n, \quad (\text{C.1})$$

where \mathbf{u}^* is the intermediate velocity field, which is not divergence-free. The second step is known as the projection step, where the pressure gets reintroduced to give a final velocity field, \mathbf{u}^{n+1} that satisfied the incompressibility condition. This discretized step takes the following form,

$$\frac{\mathbf{u}^{n+1} - \mathbf{u}^*}{\Delta t} = -\frac{1}{\rho} \nabla p^{n+1}, \quad (\text{C.2})$$

where p^{n+1} is the pressure field at the next time-step. Because it requires an updated pressure term, we must first find such a pressure. To do this we recall Helmholtz-Hodge Decomposition [310, 311], which says any vector field, that is twice continuously differentiable on a bounded domain, say \mathbf{v} , can be decomposed into a solenoidal part (divergence-free) and an irrotational part (curl-free),

i.e.,

$$\mathbf{v} = \mathbf{v}_{sol} + \mathbf{v}_{irr} = \mathbf{v}_{sol} + \nabla\phi, \quad (\text{C.3})$$

where \mathbf{v}_{sol} is the solenoidal part and \mathbf{v}_{irr} is the irrotational part. We note that an irrotational vector field can be written as the gradient of a scalar, e.g., $\mathbf{v}_{irr} = \nabla\phi$, where ϕ is some scalar function.

Note that if we take the divergence of (C.3), we obtain,

$$\nabla \cdot \mathbf{v} = \Delta\phi. \quad (\text{C.4})$$

It is then possible to find the divergence-free part of the vector field \mathbf{v} by solving the above Poisson problem in (C.4). This motivates the form of the second step for a projection method given in (C.2). However, to find the pressure, we take a divergence of (C.2) and note that we require that \mathbf{u}^{n+1} be divergence-free, i.e.,

$$\nabla \cdot \mathbf{u}^{n+1} = 0. \quad (\text{C.5})$$

Taking the divergence of (C.2) and requiring the condition in (C.5), we obtain the following Poisson problem for the pressure, p^{n+1} , in terms of the intermediate velocity field \mathbf{u}^* ,

$$\frac{\Delta t}{\rho} \Delta p^{n+1} = \nabla \cdot \mathbf{u}^* \quad (\text{C.6})$$

Note that this equation can be solved explicitly. Hence once p^{n+1} is found, we can then solve for \mathbf{u}^{n+1} using (C.2).

C.1.1 Projection Methods Example

We illustrate one example using the projection method described above to solve the incompressible, Navier-Stokes equations. Here we model cavity flow within a rectangular cavity. We have no slip boundary conditions, e.g., $\mathbf{u} = 0$ on the right wall, left wall, and bottom wall; however, on the top wall we enforce the following condition

$$\mathbf{u}_{top \text{ wall}} = \begin{pmatrix} v_{Tan} \tanh 0.1t \\ 0 \end{pmatrix}, \quad (\text{C.7})$$

where v_{Tan} is some prescribed velocity. For this example we do not consider any spatially dependent form of v_{Tan} to relax the velocity near the corners, e.g., some parabolic form such that near the corners $v_{Tan}|_{corner} = 0$; however, this is, of course, possible. We are simply illustrating one potential example.

Figure C.1 shows snapshots from the cavity flow problem. Note that as the simulation progresses, a vortex is formed; however, for the specified v_{Tan} it does not create a vortex in the whole cavity. The colormap illustrates the magnitude of velocity and the vector field illustrates the direction of flow. It is clear that the vortex rotates clockwise, i.e., the same direction as the imposed tangential flow condition on the boundary. Note that near the bottom of the cavity, there will be a vortex swirling counter-clockwise due to the shearing of the top vortex; however, its velocity is much lower than near the top wall. This simulation was run on a 256×128 grid.

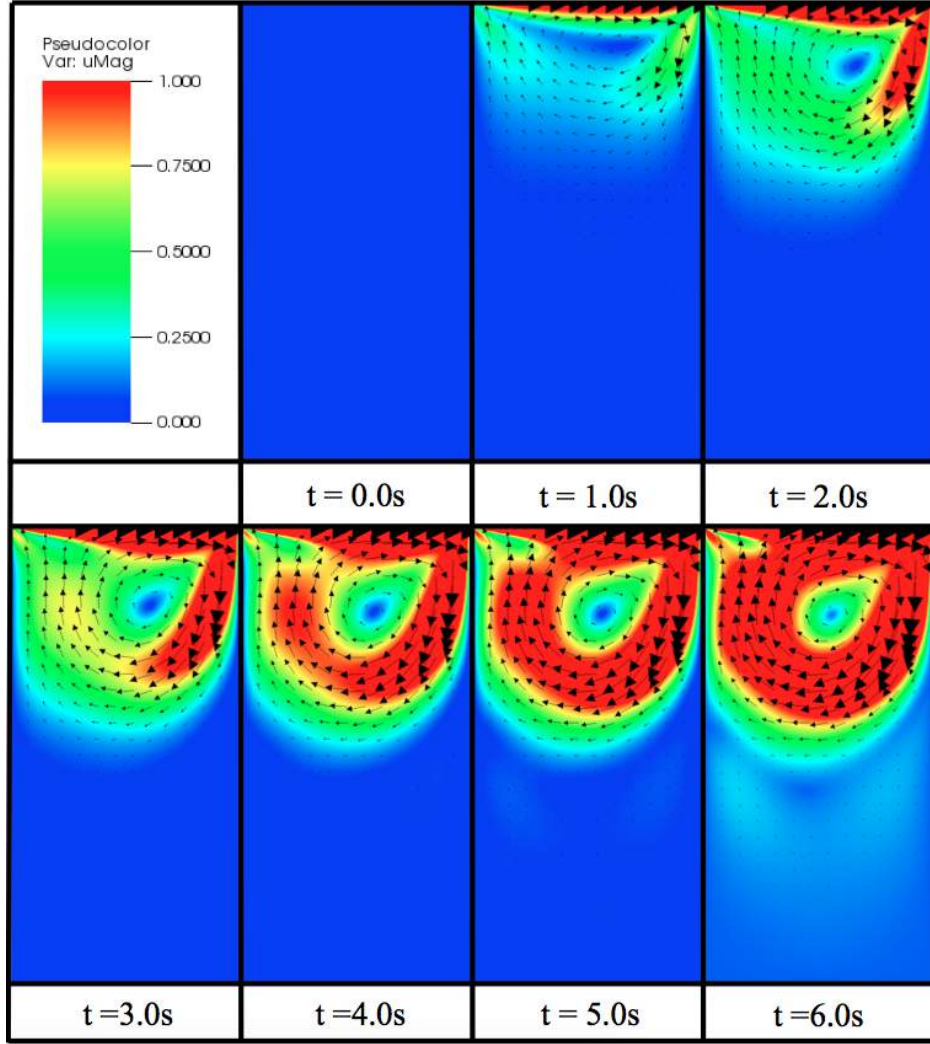


Figure C.1: Snapshots from the simulation using a projection method to model cavity flow. The background colormap is of the magnitude of velocity and the vector field illustrates the fluid's velocity field.

C.2 Spectral Methods via Fast Fourier Transform (FFT)

We first consider the vorticity formulation of the incompressible, Navier-Stokes equations,

$$\frac{\partial \omega}{\partial t} + \nabla \times (\omega \times \mathbf{u}) = \nu \Delta \omega \quad (\text{C.8})$$

$$\nabla \cdot \mathbf{u} = 0 \quad (\text{C.9})$$

Using an identity from vector calculus,

$$\nabla \times (\mathbf{A} \times \mathbf{B}) = (\nabla \cdot \mathbf{B} - \mathbf{B} \cdot \nabla) \mathbf{A} - (\nabla \cdot \mathbf{A} + \mathbf{A} \cdot \nabla) \mathbf{B}, \quad (\text{C.10})$$

we can mathematically massage (C.8) into the following form,

$$\frac{\partial \boldsymbol{\omega}}{\partial t} + \mathbf{u} \cdot \nabla \boldsymbol{\omega} - \boldsymbol{\omega} \cdot \nabla \mathbf{u} = \nu \Delta \boldsymbol{\omega}. \quad (\text{C.11})$$

Note that (C.11) looks like an advection-diffusive-type equation (parabolic PDE), but with the extra term, $\boldsymbol{\omega} \cdot \nabla \mathbf{u}$. Using the incompressibility condition and properties of vorticity in $2D$, this term is identically zero, giving the following form of the momentum equation in terms of vorticity,

$$\frac{\partial \boldsymbol{\omega}}{\partial t} + \mathbf{u} \cdot \nabla \boldsymbol{\omega} = \nu \Delta \boldsymbol{\omega}. \quad (\text{C.12})$$

Next we introduce the streamfunction, ψ , as part of the vector potential for \mathbf{u} ,

$$\mathbf{u} = \nabla \times \psi \hat{k}. \quad (\text{C.13})$$

Hence if we have our streamfunction, $\psi = \psi(x, y)$, it is possible to get the components of the $2D$ fluid velocity, $\mathbf{u} = (u, v)$, e.g.,

$$u = \frac{\partial \psi}{\partial y} \quad \text{and} \quad v = -\frac{\partial \psi}{\partial x}. \quad (\text{C.14})$$

Furthermore, taking the curl of (C.13), we are able to get a Poisson problem for ψ in terms of $\boldsymbol{\omega}$,

$$\Delta \psi = -\boldsymbol{\omega}, \quad (\text{C.15})$$

where we have used the following vector calculus identity,

$$\nabla \times \nabla \times \mathbf{A} = \nabla(\nabla \cdot \mathbf{A}) - \nabla^2 \mathbf{A}, \quad (\text{C.16})$$

and the fact that $\frac{\partial \psi}{\partial z} = 0$ since there is no z -component of the streamfunction. Note that if we

are able to solve for the streamfunction, ψ , from ω , we can then get \mathbf{u} and it will automatically satisfy the incompressibility condition from the form of (C.13).

For this algorithm, we will work as much as possible in the Fourier frequency space, given by the FFT. There are 3 main steps in the algorithm.

1. Solve the Poisson problem for the streamfunction, ψ^n , from the previous time-step's vorticity, ω^n , i.e.,

$$\hat{\psi}_{ij}^n = \frac{\omega_{ij}^n}{k_{X_i}^2 + k_{Y_j}^2}, \quad (\text{C.17})$$

where k_{X_i} and k_{Y_j} are the Fourier wave-numbers.

2. Next we compute the x, y -derivatives of the streamfunction, ψ^n and vorticity, ω^n (in real space), then compute discretized, advection term, and finally transform the advection term into frequency space.

To do this we take derivatives in Frequency space of the streamfunction, ψ , and then use the Inverse Fast Fourier Transverse, to put them back into real space.

$$u_{ij}^n = \mathcal{F}^{-1} \left\{ K_Y \hat{\psi}_{ij}^n \right\} \quad (\text{C.18})$$

$$v_{ij}^n = \mathcal{F}^{-1} \left\{ -K_X \hat{\psi}_{ij}^n \right\} \quad (\text{C.19})$$

$$\omega_{x_{ij}}^n = \mathcal{F}^{-1} \left\{ K_X \hat{\omega}_{ij}^n \right\} \quad (\text{C.20})$$

$$\omega_{y_{ij}}^n = \mathcal{F}^{-1} \left\{ K_Y \hat{\omega}_{ij}^n \right\} \quad (\text{C.21})$$

$$(\text{C.22})$$

Once you have the quantities back in real space, it is possible to compute the advection term, $F_{\text{adv}_{ij}}^n$, from (C.12), i.e.,

$$F_{\text{adv}_{ij}}^n = u_{ij}^n \cdot \omega_{x_{ij}}^n + v_{ij}^n \cdot \omega_{y_{ij}}^n \quad (\text{C.23})$$

and then you can transform (C.23) into frequency space using FFT,

$$\hat{F}_{\text{adv}_{ij}}^n = \mathcal{F} \left\{ F_{\text{adv}_{ij}}^n \right\}. \quad (\text{C.24})$$

3. Finally we use the Crank-Nicholson scheme to update the streamfunction to the next time-step, ψ^{n+1} ,

$$\hat{\psi}_{ij}^{n+1} = \frac{\left[1 + \frac{\nu \Delta t}{2} \left(k_{X_{ij}}^2 + k_{Y_{ij}}^2 \right) \right] \hat{\psi}_{ij}^n - \Delta t \hat{F}_{\text{adv}_{ij}}^n}{1 - \frac{\nu \Delta t}{2} \left(k_{X_{ij}}^2 + k_{Y_{ij}}^2 \right)} \quad (\text{C.25})$$

Note that this method is semi-implicit, explicitly discretizing the advective term, while implicitly discretizing the diffusive viscous term. The Crank-Nicholson scheme is second order accurate in time [312], and is unconditionally stable for an array of parabolic problems of the type $w_t = aw_{xx}$ [313].

C.2.1 Spectral Methods (FFT) Example

We show one example using the FFT spectral method described above to solve the incompressible, vorticity formulation of the Navier-Stokes equations. Here we model regions of high and low vorticity nested within one another, with a random assortment of vorticity values initialized outside of the nested regions. The simulation begins and it is clear that mixing begins. There are no explicit boundary conditions due to the periodicity of the FFT.

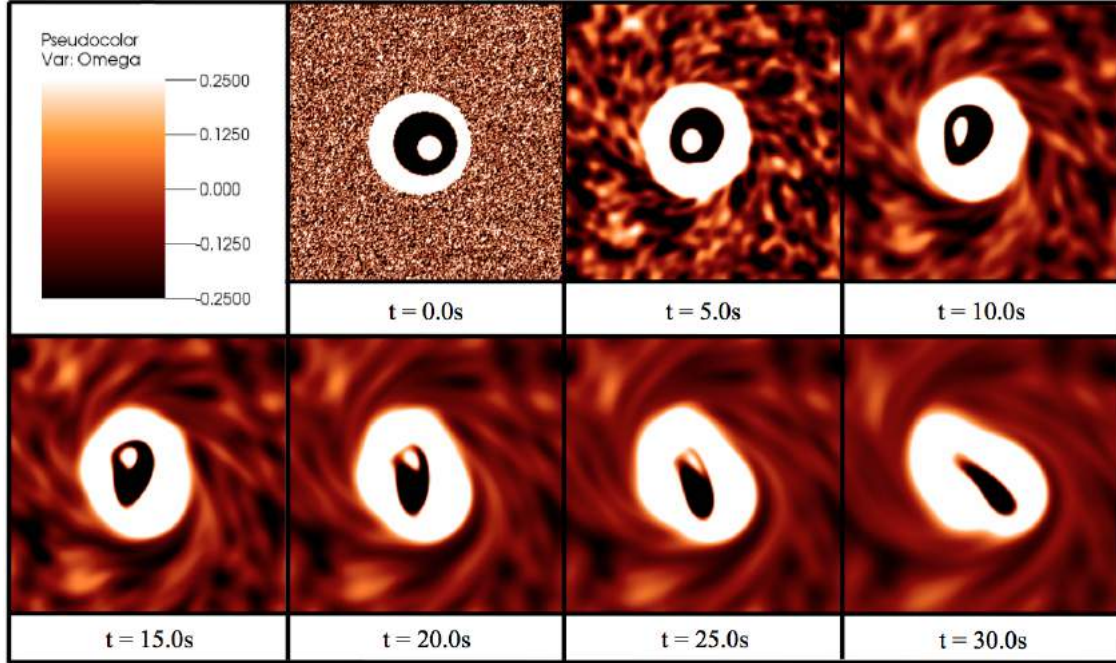


Figure C.2: Snapshots from the simulation using a spectral method (FFT) to solve the incompressible, Navier-Stokes equations in the vorticity formulation. The background colormap is of vorticity.

Figure C.2 shows the dynamics within the simulation. The background colormap illustrates the vorticity. It is evident that the nested vortices eventually begin to mix. Figure C.3 illustrates the resulting velocity field and magnitude of velocity. This simulation was run on a 256×256 grid.

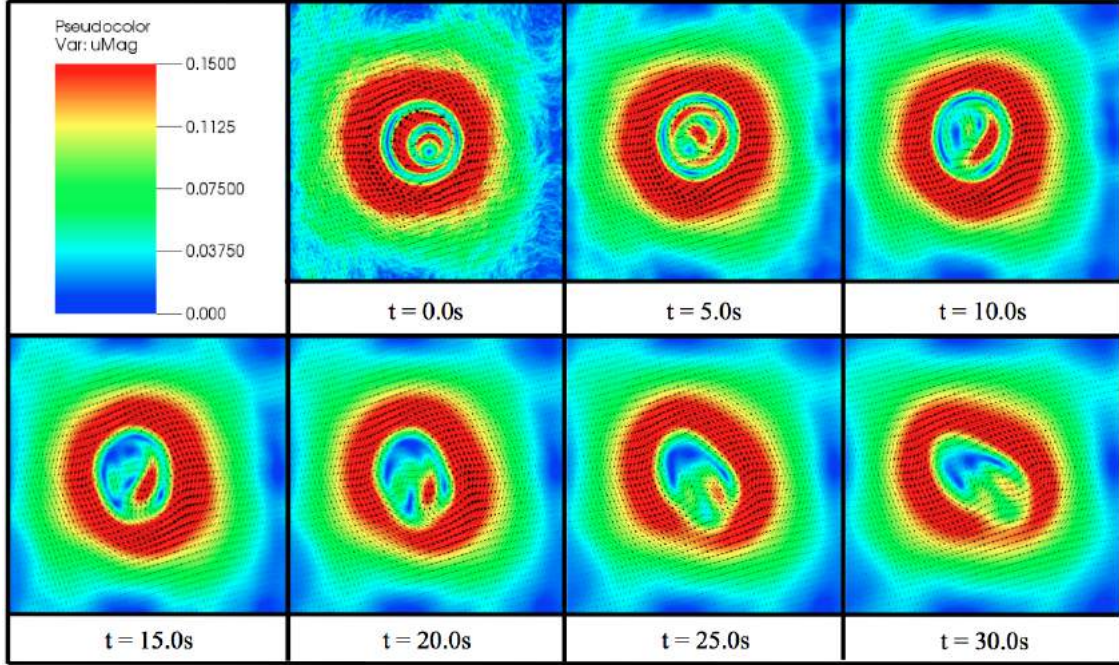


Figure C.3: Snapshots from the same simulation of nested vortices using a spectral method (FFT) to solve the incompressible, Navier-Stokes equations in the vorticity formulation. These images illustrate the magnitude of velocity and the background velocity field.

C.3 Lattice Boltzmann Methods

The Lattice Boltzmann method does not explicitly (or implicitly) solve the incompressible, Navier-Stokes equations, rather it uses discrete Boltzmann equations to model the fluid dynamics. In a nutshell tracks fictitious particles of fluid flow, thinking of the problem more as a transport equation, e.g.,

$$\frac{\partial f}{\partial t} + \mathbf{u} \cdot \nabla f = \Omega, \quad (\text{C.26})$$

where $f(\mathbf{x}, t)$ is the particle distribution function, i.e., a probability density, \mathbf{u} is the fluid particle's velocity, and Ω is what is called the collision operator. However, rather than have these particles moving in a Lagrangian-type frame, the Lattice Boltzmann method simplifies this assumption and restricts the particles to the nodes on a lattice. We will only discuss a two dimensional implementation of this CFD method; however, a three dimensional implementation follows analogously.

From the assumption restricting the fluid particles to reside on a lattice, there are only a possibility of 9 directions that a particle could potential stream, or pass information, along in. These directions are of course in either horizontal or vertical or forward or backward diagonal directions, as well as,

the staying at rest on its current node. These directions are illustrated in Figure C.4, and these streaming velocities, $\{\mathbf{e}_i\}$, are called the *microscopic velocities*. The directions illustrated in Figure C.4 is commonly called the *D2Q9* Lattice Boltzmann Model.

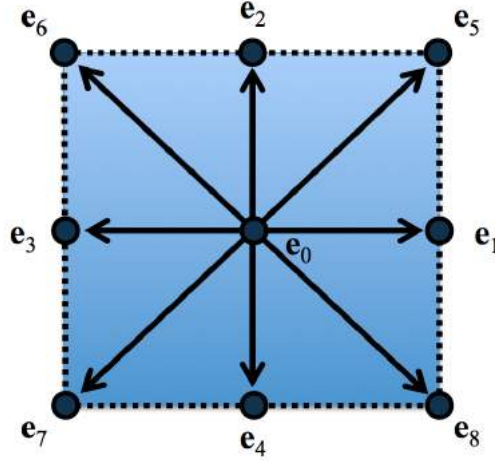


Figure C.4: Figure illustrating the possible streaming directions, $\{\mathbf{e}_i\}$ for the D2Q9 Lattice Boltzmann model.

Now for every point on the lattice, we had a probability function, $f(\mathbf{x}, t)$, associated with it. Discretizing this idea to account for the possibility of moving in the 9 directions described above, we write it as $f_i(\mathbf{x}, t)$, where f_i now gives the probability of streaming in a particular direction \mathbf{e}_i . Using this discretization, we can define the macroscopic fluid density to be the sum of all possible f_i , e.g.,

$$\rho(\mathbf{x}, t) = \sum_{i=0}^8 f_i(\mathbf{x}, t). \quad (\text{C.27})$$

Similarly, we can define the *macroscopic velocity* of the fluid as an average of the microscopic velocities in each direction weighted by their associated particle distribution functions f_i using (C.27),

$$\mathbf{u}(\mathbf{x}, t) = \frac{1}{\rho} \sum_{i=0}^8 c f_i(\mathbf{x}, t) \mathbf{e}_i, \quad (\text{C.28})$$

where $c = \frac{\Delta x}{\Delta t}$ and is referred to as the lattice speed. The key elements that are left to discuss are exactly what it means to *stream* the particle distributions f_i as well as what it meant by the collision, Ω . However, this is essentially what the steps in the Lattice Boltzmann Algorithm are, so we will explicitly define these procedures while describing the algorithmic steps. The steps are below.

1. The first step is to stream the particle densities to propagate in each direction. Explicitly you calculate the following intermediate particle density, f_i^* ,

$$f_i^*(\mathbf{x} + c\mathbf{e}_i\Delta t, t + \Delta t) = f_i^n(\mathbf{x}, t), \quad (\text{C.29})$$

where n is the time-step and where for each direction i , you would in practice compute

$$\begin{aligned} f_1^*(x_i, y_j) &= f_1^n(x_{i-1}, y_j), & f_2^*(x_i, y_j) &= f_2^n(x_i, y_{j-1}), & f_3^*(x_i, y_j) &= f_3^n(x_{i+1}, y_j), \\ f_4^*(x_i, y_j) &= f_4^n(x_i, y_{j+1}), & f_5^*(x_i, y_j) &= f_5^n(x_{i-1}, y_{j-1}), & f_6^*(x_i, y_j) &= f_6^n(x_{i+1}, y_{j-1}) \\ f_7^*(x_i, y_j) &= f_7^n(x_{i+1}, y_{j+1}), & f_8^*(x_i, y_j) &= f_8^n(x_{i-1}, y_{j+1}), & f_9^*(x_i, y_j) &= f_9^n(x_i, y_j) \end{aligned} \quad (\text{C.30})$$

This idea of streaming is show in Figure C.5.

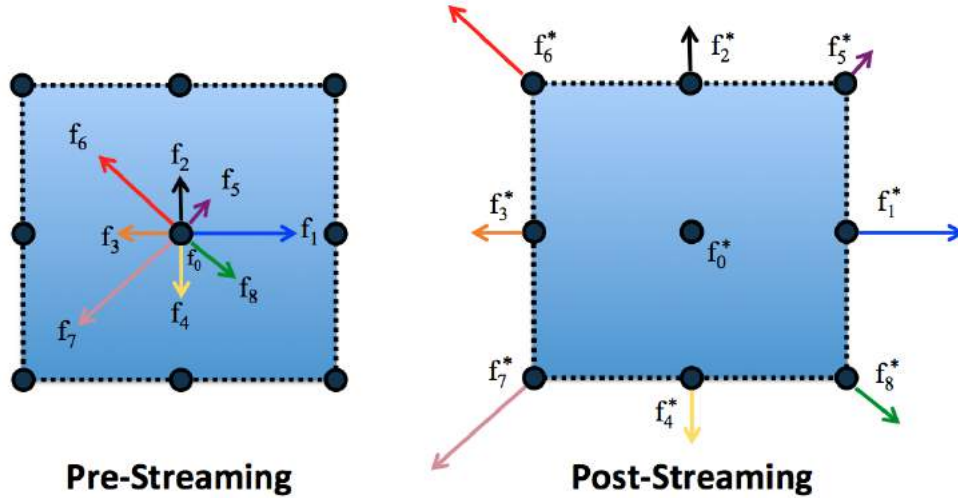


Figure C.5: Figure illustrating the idea of streaming by showing color correlated particle probability functions, f_i , before the streaming process and post-streaming, f_i^* .

2. The second step involves finding what is referred to as the equilibrium distribution. This term is apart of the *collision* step, where you want to relax your particle density distributions towards a local equilibrium. That local equilibrium is denoted $f_i^{eq}(\mathbf{x}, t)$. First we must compute macroscopic the properties (density and velocity) from the intermediate particle distributions f_i^* using (C.27) and (C.28).

Once we have these quantities, we can now define the equilibrium distributions, f_i^{eq} . We note that there are many equilibrium distributions one could use in practice; however, each depends on your model and its assumptions. The Lattice Boltzmann method available at [297] uses what is called the Bhatnagar-Gross-Krook (BGK) collision [314]. The BGK collision model is useful for simulating single phase flows [295] and is most often the classic model to use for solving the incompressible Navier-Stokes equations, although it can also be useful for simulating compressible flows at low Mach numbers [294]. See [294] for a good review of the BGK model. The BGK model's equilibrium distribution can be written as follows

$$f_i^{eq}(\mathbf{x}, t) = w_i \rho + \rho s_i(\mathbf{u}(\mathbf{x}, t)), \quad (\text{C.31})$$

where w_i is a weight and $s_i(\mathbf{u}(\mathbf{x}, t))$ is defined as

$$s_i(\mathbf{u}(\mathbf{x}, t)) = w_i \left[3 \frac{\mathbf{e}_i \cdot \mathbf{u}}{c} + \frac{9}{2} \frac{(\mathbf{e}_i \cdot \mathbf{u})^2}{c^2} - \frac{3}{2} \frac{\mathbf{u} \cdot \mathbf{u}}{c^2} \right]. \quad (\text{C.32})$$

The corresponding weights, w_i are given as

$$w_i = \begin{cases} \frac{4}{9} & i = 0 \\ \frac{1}{9} & i \in \{1, 2, 3, 4\} \\ \frac{1}{36} & i \in \{5, 6, 7, 8\} \end{cases}. \quad (\text{C.33})$$

3. Finally we compute the collision step associated with the BGK model is written as follows

$$f_i^{n+1} = f_i^* - \frac{f_i(\mathbf{x}, t) - f_i^{eq}(\text{bf})}{\tau}, \quad (\text{C.34})$$

where τ is the relaxation parameter and intuitively is related to the viscosity of the fluid, i.e.,

$$\nu = \frac{2\tau - 1}{6} \frac{\Delta x^2}{\Delta t}. \quad (\text{C.35})$$

As of yet we have not mentioned any boundary conditions, but before we discuss that we will discuss the advantages of the Lattice Boltzmann method. One of the tremendous advantages of

Lattice Boltzmann is its implementation lends itself for large scale parallel GPU computing. Because of these parallelization it can be an incredibly fast way of solving fluid problems coupled with equations modeling heat transfer or chemical processes [315]. Moreover, the algorithm also prides itself for the ability to compute flows through complex geometries and porous structures rather easily and efficiently [316]. From the structure of the streaming step, one can easily prescribe boundary conditions and regions in the grid where fluid is not allowed to flow easily. For our considerations here we only will introduce what are referred to as *bounce-back boundary conditions* [316].

The bounce-back boundary conditions are used to enforce no-slip conditions; however, as we will show, they are not only use on the edges of the domain, but can be implemented on the interior to create complex geometries. In a nutshell the incoming streaming directions of the distribution functions are simply reversed when they hit a boundary node. This idea is illustrated in Figure C.6. One can simply mask these boundary points on the domain using boolean logic in practice.

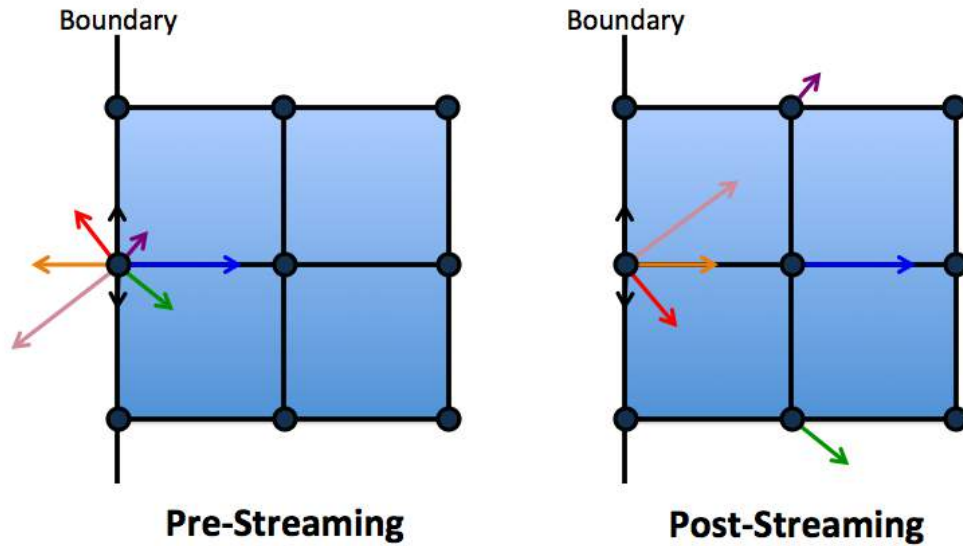


Figure C.6: Illustration of bounce-back boundary conditions. The pre-streaming step there are microscopic velocities set on the boundary and then they are reversed during the streaming step

C.3.1 Lattice Boltzmann Example

Here we present one example of fluid flow using the Lattice Boltzmann method. We model the case of inflow going left to right across the domain with 3 (rigid) cylinders placed in the domain in a triangular configuration. The simulation begins with no inflow and then gradually increases the inflow velocity until a desired velocity is reached.

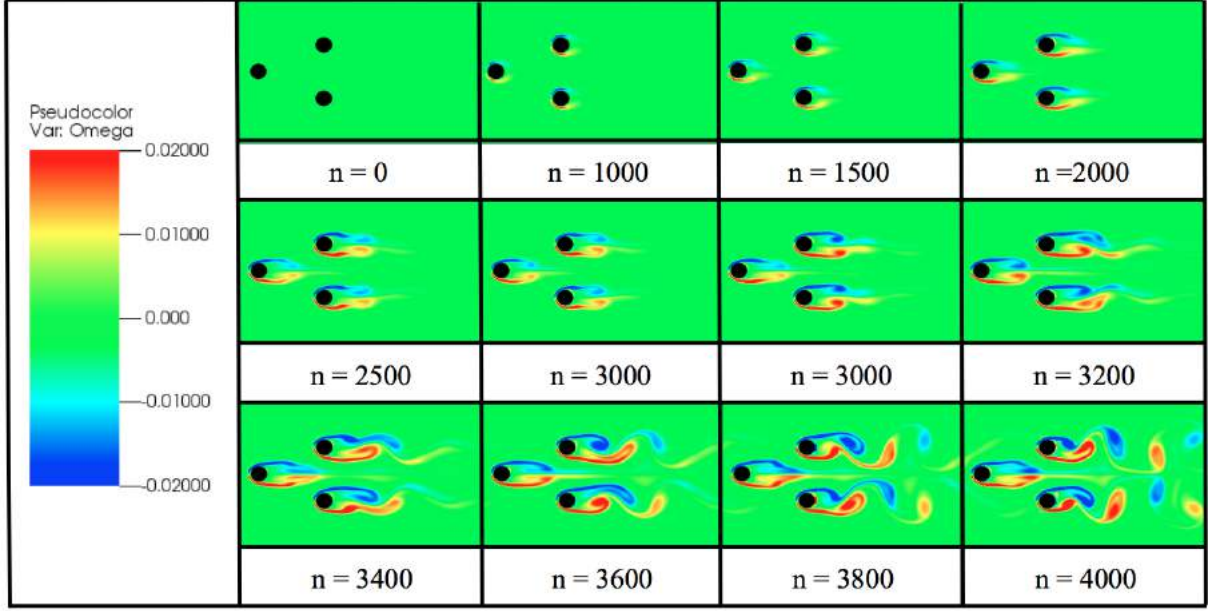


Figure C.7: Snapshots from a Lattice Boltzmann simulation of flow around 3 cylinders. The background colormap is vorticity. It is clear that vortex shedding occurs.

Figure C.7 shows the dynamics within the simulation at varying time-steps, n . The background colormap illustrates the vorticity. It is evident that vortex shedding occurs as the simulation progresses. Furthermore the symmetry in the fluids dynamics is maintained throughout. This simulation was run using 65536 fluid particles (in a 256×256 arrangement).

We note for a comparable grid size, 256×256 , the traditional immersed boundary method with a FFT-based fluid solver will be more computationally expensive, making the Lattice Boltzmann method a better choice for flow through rigid, complex geometries. However, for fully-coupled fluid-structure interaction problems, one still needs an algorithm that relates the motion of an elastic boundary to the fluid motion and vice-versa, such as the one that immersed boundary allows. On that note, the Lattice Boltzmann method can be used in an immersed boundary method as the main fluid solver [148] to help reduce the computational time.

REFERENCES

- [1] A. J. Clark, *Comparative Physiology of the Heart*. Cambridge, UK: Cambridge University Press, 1927.
- [2] T. W. Sadler, *Langman's Medical Embryology (7th Edition)*. Baltimore, USA: Williams and Wilkins, 1995.
- [3] D. Stainier, "Zebrafish genetics and vertebrate heart formation," *Nature Reviews Genetics*, vol. 2, pp. 39–48, 2001.
- [4] D. Stainier, D. Beis, B. Jungblut, and T. Bartman, "Endocardial cushion formation in zebrafish," *Cold Spring Harb. Symp. Quant. Biol.*, vol. 67, pp. 49–56, 2002.
- [5] J. Liu, M. Bressan, D. Hassel, J. Huiskens, D. Staudt, K. Kikuchi, K. Poss, T. Mikawa, and D. Stainier, "A dual role for *erbb2* signaling in cardiac trabeculation," *Development*, vol. 137, pp. 3867–3875, 2010.
- [6] L. A. Samsa, C. E. Ito, D. R. Brown, L. Qian, and J. Liu, "Cardiac contraction activates endocardial notch signaling to modulate chamber maturation in zebrafish," *PLoS ONE*, vol. 11(11), p. e0166734, 2016.
- [7] J. Icardo and A. Fernandez-Teran, "Morphologic study of ventricular trabeculation in the embryonic chick heart," *Acta Anatomica*, vol. 130, pp. 264–274, 1987.
- [8] W. J. Kowalski, K. Pekkan, J. P. Tinney, and B. B. Keller, "Investigating developmental cardiovascular biomechanics and the origins of congenital heart defects," *Front. Physiol.*, vol. 5, p. 408, 2014.
- [9] J. Bakkers, "Zebrafish as a model to study cardiac development and human cardiac disease," *Cardiovasc Res.*, vol. 91, pp. 279–288, 2011.
- [10] M. A. Hill, "Embryology advanced cardiac embryology," 2017.
- [11] S. E. Lindsey, J. T. Butcher, and H. C. Yalcin, "Mechanical regulation of cardiac development," *Front. Physiol.*, vol. 5, p. 318, 2014.
- [12] J. R. Hove, R. W. Koster, A. S. Forouhar, G. Acevedo-Bolton, S. E. Fraser, and M. Gharib, "Intracardiac fluid forces are an essential epigenetic factor for embryonic cardiogenesis," *Nature*, vol. 421, no. 6919, pp. 172–177, 2003.
- [13] N. Nerukar, A. Ramasubramanian, and L. A. Taber, "Morphogenetic adaptation of the looping embryonic heart to altered mechanical loads," *Dev. Dyn.*, vol. 1105, pp. 1822–1829, 2006.
- [14] M. Reckova, C. Rosengarten, A. deAlmeida, C. P. Stanley, A. Wessels, R. G. Gourdie, R. P. Thompson, and D. Sedmera, "Hemodynamics is a key epigenetic factor in development of the cardiac conduction system," *Circ. Res.*, vol. 93, p. 77, 2003.
- [15] A. Santhanakrishnan and L. A. Miller, "Fluid dynamics of heart development," *Cell Biochem. Biophys.*, vol. 61, pp. 1–22, 2011.
- [16] I. Avrahami and M. Gharib, "Computational studies of resonance wave pumping in compliant tubes," *Journal of Fluid Mechanics*, vol. 608, pp. 139–160, 2008.

- [17] A. Hickerson, D. Rinderknecht, and M. Gharib, “Experimental study of the behavior of a valveless impedance pump,” *Experiments in Fluids*, vol. 38, pp. 534–540, 2005.
- [18] A. I. Hickerson, “An experimental analysis of the characteristic behaviors of an impedance pump (ph.d. thesis),” *California Institute of Technology*, vol. 608, pp. 139–160, 2005.
- [19] L. A. Taber, J. Zhang, and R. Perucchio, “Computational model for the transition from peristalsis to pulsatile flow in the embryonic heart tube,” *J. Biomech. Eng.*, vol. 129, no. 3, pp. 441–449, 2007.
- [20] A. J. Baird, T. King, and L. A. Miller, “Numerical study of scaling effects in peristalsis and dynamic suction pumping,” *Biological Fluid Dynamics: Modeling, Computations, and Applications*, vol. 628, pp. 129–148, 2014.
- [21] A. J. Baird, “Modeling valveless pumping mechanisms (ph.d. thesis),” *University of North Carolina at Chapel Hill*, vol. 628, pp. 129–148, 2014.
- [22] A. J. Baird, L. D. Waldrop, and L. A. Miller, “Neuromechanical pumping: boundary flexibility and traveling depolarization waves drive flow within valveless, tubular hearts,” *Japan J. Indust. Appl. Math.*, vol. 32, pp. 829–846, 2015.
- [23] L. D. Waldrop and L. A. Miller, “Large-amplitude, short-wave peristalsis and its implications for transport,” *Biomechanics and Modeling in Mechanobiology*, pp. 1–14, 2015.
- [24] A. Ramasubramanian, N. Nerurkar, K. Achtien, B. Filas, D. Voronov, and L. A. Taber, “On modeling morphogenesis of the looping heart following mechanical perturbations,” *J. Biomed. Eng.*, vol. 130, p. 061018, 2008.
- [25] Y. Shi, J. Yao, J. Young, J. Fee, R. Perucchio, and L. A. Taber, “Bending and twisting the embryonic heart: a computational model for c-looping based on realistic geometry,” *Frontiers in Physiol.: Biophys.*, vol. 5, p. 297, 2014.
- [26] A. Santhanakrishnan, N. Nguyen, J. Cox, and L. A. Miller, “Flow within models of the vertebrate embryonic heart,” *J. Theor. Biol.*, vol. 259, pp. 449–461, 2009.
- [27] L. A. Miller, “Fluid dynamics of ventricular filling in the embryonic heart,” *Cell Biochem. Biophys.*, vol. 61, pp. 33–45, 2011.
- [28] J. Lee, M. E. Moghadam, E. Kung, H. Cao, T. Beebe, Y. Miller, B. L. Roman, C.-L. Lien, N. C. Chi, A. L. Marsden, and T. K. Hsiai, “Moving domain computational fluid dynamics to interface with an embryonic model of cardiac morphogenesis,” *PLoS One*, vol. 8, p. e72924.
- [29] S. Biechler, M. J. Yost, R. L. Goodwin, L. Junor, J. D. Potts, and J. W. Weidner, “Mathematical modeling of flow-generated forces in an in vitro system of cardiac valve development,” *Annals of Biomedical Engineering*, vol. 38, pp. 109–117, 2010.
- [30] P. Buskohl, J. Jenkins, and J. Butcher, “Computational simulation of hemodynamic-driven growth and remodeling of embryonic atrioventricular valves,” *Biomech. Model Mechanobiol.*, vol. 11, pp. 1205–1217, 2012.
- [31] M. Saito, “One-dimensional modeling of pulse wave for a human artery model,” 2010.

- [32] B. E. Griffith, “Simulating the blood-muscle-vale mechanics of the heart by an adaptive and parallel version of the immersed boundary method (ph.d. thesis),” *Courant Institute of Mathematics, New York University*, 2005.
- [33] S. E. Grosskurth, D. Bhattacharya, Q. Wang, and J. J. Lin, “Emergence of xin demarcates a key innovation in heart evolution,” *PLoS One*, vol. 3(8), p. e2857, 2008.
- [34] H. E. Anderson and L. Christiaen, “Ciona as a simple chordate model for heart development and regeneration,” *J. Cardiovasc. Dev. Dis.*, vol. 3, p. 25, 2016.
- [35] F. Maes, B. Chaudhry, P. V. Ransbeeck, and P. Verdonck, “The pumping mechanism of embryonic hearts,” *IFMBE Proceedings*, vol. 37, pp. 470–473, 2011.
- [36] M. W. Konrad, “Blood circulation in the ascidian tunicate corella inflata (corellidae),” *Peer J*, vol. 4, p. e2771, 2016.
- [37] N. A. Battista, W. C. Strickland, and L. A. Miller, “Ib2d: a python and matlab implementation of the immersed boundary method,” *Bioinspir. Biomim.*, vol. 12(3), p. 036003, 2017.
- [38] N. A. Battista, “nickabattista github site,” 2015.
- [39] NIH, “What are congenital heart defects?,” 2011. <https://www.nhlbi.nih.gov/health/health-topics/topics/chd>.
- [40] A. S. Go, D. Mozaffarian, V. L. Roger, E. J. Benjamin, J. D. Berry, W. B. Borden, and et al., “Heart disease and stroke statistics-2013 update: a report from the american heart association,” *Circulation*, vol. 127(1), pp. e6–e245, 2013.
- [41] B. J. Maron, J. A. Towbin, G. Thiene, C. Antzelevitch, D. Corrado, D. Arnett, A. J. Moss, C. E. Seidman, and J. B. Young, “Contemporary definitions and classification of the cardiomyopathies,” *Circulation*, vol. 113(14), pp. 1807–1816, 2006.
- [42] W. Larsen, *Human Embryology (3rd ed.)*. Philadelphia, PA, USA: Elsevier Saunders, 2001.
- [43] J. Gruber and J. Epstein, “Development gone awry-congenital heart disease,” *Circulation Research*, vol. 94, pp. 273–283, 2004.
- [44] N. Sultana, K. Nag, K. Hoshijima, D. W. Laird, A. Kawakami, and S. Hirose, “Zebrafish early cardiac connexin, cx36.7/ecx, regulates myofibril orientation and heart morphogenesis by establishing nkx2.5,” *Proc. Natl. Acad. Sci.*, vol. 12, pp. 4763–3768, 2008.
- [45] A. Spitzer and M. Lev, *The Architecture of Normal and Malformed Hearts*. Springfield, Illinois, USA: Thomas, 1951.
- [46] L. A. Taber, I. E. Lin, and E. B. Clark, “Mechanics of cardiac looping,” *Dev. Dyn.*, vol. 203, pp. 42–50, 1995.
- [47] L. A. Taber, “Biomechanics of growth, remodeling, and morphogenesis,” *Appl. Mech. Rev*, vol. 48(8), pp. 487–545, 1995.
- [48] L. A. Taber, “Biomechanics of cardiovascular development,” *Annu. Rev. Biomed. Eng.*, vol. 3, pp. 1–25, 2001.

- [49] J. M. Tarbell, S. Weinbaum, and R. D. Kamm, "Cellular fluid mechanics and mechanotransduction," *Ann Biomed Eng*, vol. 33, pp. 1719–1723, 2005.
- [50] J. Tarbell and S. Zhong-dong, "Effect of the glycocalyx layer on transmission of interstitial flow shear stress to embedded cells," *Biomech. Model Mechanobiol.*, vol. 12, pp. 111–121, 2013.
- [51] M. M. Collins and D. Y. Stanier, "Organ function as a modulator of organ formation: Lessons from zebrafish," *Essays on Developmental Biology, Part B*, vol. 117, pp. 417–433, 2016.
- [52] J. Granados-Riveron and D. Brook, "The impact of mechanical forces in heart morphogenesis," *Circ. Cardiovasc. Genet.*, vol. 5, pp. 132–142, 2012.
- [53] T. Bartman, E. C. Walsh, K. K. Wen, M. McKane, J. Ren, J. Alexander, P. A. Rubenstein, and D. Y. Stainier, "Early myocardial function affects endocardial cushion development in zebrafish," *PLoS Biol*, vol. 2, p. E129, 2004.
- [54] J. Culver and M. Dickinson, "The effects of hemodynamic force on embryonic development," *Microcirculation*, vol. 17, pp. 164–178, 2010.
- [55] C. Peshkovsky, R. Totong, and D. Yelo, "Dependence of cardiac trabeculation on neuregulin signaling and blood flow in zebrafish," *Developmental Dynamics*, vol. 240, no. 2, pp. 446–456, 2011.
- [56] D. Stainier, R. Lee, and M. Fishman, "Cardiovascular development in the zebrafish," *Development*, vol. 119, pp. 31–40, 1993.
- [57] M. Malone, N. Sciaky, L. Stalheim, H. Klaus, E. Linney, and G. Johnson, "Laser-scanning velocimetry: A confocal microscopy method for quantitative measurement of cardiovascular performance in zebrafish embryos and larvae," *BMC Biotechnology*, vol. 7, p. 40, 2007.
- [58] D. Sedmera and T. McQuinn, "Embryogenesis of heart muscle," *Heart Fail Clin.*, vol. 4, pp. 235–245, 2008.
- [59] N. Hu and E. B. Clark, "Hemodynamics of the stage 12 to stage 29 chick embryo," *Circ. Res.*, vol. 65, pp. 1665–1670, 1989.
- [60] K. L. Poon and T. Brand, "The zebrafish model system in cardiovascular research: A tiny fish with mighty prospects," *Glob. Cardiol. Sci. Pract.*, vol. 1, pp. 9–28, 2013.
- [61] B. Furst, "The heart and circulation: An integrative model," *Springer*, vol. 5, pp. 381–390, 2014.
- [62] V. Hamburger and H. L. Hamilton, "A series of normal stages in the development of the chick embryo," *J. Morphol.*, vol. 88, pp. 49–92, 1951.
- [63] F. Maes, B. Chaudhry, P. V. Ransbeeck, and P. Verdonck, "Visualization and modeling of flow in the embryonic heart," *IFMBE Proceedings*, vol. 22, no. 6919, pp. 1875–1878, 2008.
- [64] A. Moorman, A. Soufan, J. Hagoort, P. De Boer, and V. Christoffels, "Development of the building plan of the heart," *Ann. N.Y. Acad. Sci.*, vol. 1105, pp. 171–181, 2004.
- [65] A. S. Forouhar, M. Liebling, A. Hickerson, A. Nasiraei-Moghaddam, H. J. Tsai, J. R. Hove, S. E. Fraser, M. E. Dickinson, and M. Gharib, "The embryonic vertebrate heart tube is a dynamic suction pump," *Science*, vol. 312, no. 5774, pp. 751–753, 2006.

- [66] D. J. Henderson, S. J. Conway, N. Greene, D. Gerrelli, J. N. Murdoch, R. H. Anderson, and A. J. Copp, "Cardiovascular defects associated with abnormalities in midline development in the loop-tail mouse mutant," *Circulation Research*, vol. 89, pp. 6–12, 2001.
- [67] J. Manner, "On the form problem of embryonic heart loops, its geometrical solutions, and a new biophysical concept of cardiac looping," *Annals of Anatomy*, vol. 195(4), pp. 313–323, 2013.
- [68] J. K. and Butler, "An experimental analysis of cardiac loop formation in the chick (ms thesis)," *University of Texas*, 1952.
- [69] L. A. Taber, "Biophysical mechanisms of cardiac looping," *Int. J. Dev. Biol.*, vol. 50, pp. 323–332, 2006.
- [70] G. Ben-Shachar, R. A. Arcilla, R. V. Lucas, and F. J. Manasek, "Ventricular trabeculations in the chick embryo heart and their contribution to ventricular and muscular septal development," *Circ. Res.*, vol. 57, p. 759, 1985.
- [71] A. F. Moorman and V. M. Christoffels, "Cardiac chamber formation: development, genes, and evolution," *Physiol. Rev.*, vol. 83, p. 1223, 2003.
- [72] A. Moorman, S. Webb, N. Brown, W. Lamers, and R. Anderson, "Development of the heart: Formation of the cardiac chambers and arterial trunks," *Heart*, vol. 89, pp. 806–814, 2003.
- [73] N. Hu, D. Sedmera, H. J. Yost, and E. B. Clark, "Structure and function of the developing zebrafish heart," *Anat. Rec.*, vol. 260, pp. 148–157, 2000.
- [74] D. Sedmera and P. S. Thomas, "Trabeculation in the embryonic heart," *Bioessays*, vol. 18, p. 607, 1996.
- [75] P. Scherz, J. Huisken, P. Sahai-Hernandez, and D. Stainier, "High speed imaging of developing heart valves reveals interplay of morphogenesis and function," *Development*, vol. 135, pp. 1179–1187, 2008.
- [76] F. High and J. Epstein, "The multifaceted role of notch in cardiac development and disease," *Nature Reviews Genetics*, vol. 9, pp. 49–61, 2008.
- [77] R. Thoma, *Untersuchungen uber die Histogenese und Histomechanik des Gefasssystems*. Ferdinand Enke: Stuttgart, 1893.
- [78] W. B. Chapman, "The effect of the heart-beat upon the development of the vascular system in the chick," *Am. J. Anat.*, vol. 23, pp. 175–203, 1918.
- [79] W. W. Burggren, "What is the purpose of the embryonic heart beat? or how facts can ultimately prevail over physiological dogma.," *Physiological and Biochemical Zoology*, vol. 77, pp. 333–345, 2004.
- [80] R. Liao, M. Jain, L. Cui, J. D. an F. Aiello, I. Luptak, S. Ngoy, R. M. Mortensen, and R. Tian, "Cardiac-specific overexpression of glut1 prevents the development of heart failure attributable to pressure overload in mice," *Circ.*, vol. 106(16), pp. 2125–31, 2002.
- [81] Z. Rychter, "Experimental morphology of the aortic arches and the heart loop in chick embryos," *Adv. Morphogen.*, vol. 2, pp. 333–371, 1962.

- [82] O. C. Jaffee, "Hemodynamic factors in the development of the chick embryo heart," *Anat. Rec.*, vol. 151, pp. 69–75, 1965.
- [83] E. B. Clark and G. C. Rosenquist, "Spectrum of cardiovascular anomalies following cardiac loop constriction in the chick embryo," *Birth Defects Orig. Artic. Ser.*, vol. 14(7), pp. 431–442, 1978.
- [84] J. M. Icardo, "Developmental biology of the vertebrate heart," *J. Exp. Zool.*, vol. 275(2-3), pp. 144–161, 1996.
- [85] B. Hogers, M. DeRuiter, A. G. Groot, and R. Poelman, "Unilateral vitelline vein ligation alters intracardiac blood flow patterns and morphogenesis in the chick embryo," *Circ. Res.*, vol. 80(4), pp. 473–481, 1997.
- [86] B. Hogers, M. DeRuiter, A. G. Groot, and R. Poelman, "Extraembryonic venous obstructions lead to cardiovascular malformations and can be embryolethal," *Cardiovasc. Res.*, vol. 41, pp. 87–99, 1999.
- [87] M. Midgett and S. Rugonyi, "Congenital heart malformations induced by hemodynamic altering surgical interventions," *Front. Physiol.*, vol. 5, p. 287, 2014.
- [88] L. Chen, S. Wei, and J. Chiu, "Mechanical regulation of epigenetics in vascular biology and pathobiology," *J. Cell. Mol. Med.*, vol. 11, pp. 437–448, 2014.
- [89] L. A. Samsa, C. Givens, E. Tzima, Y. Didier, R. Stainer, L. Qian, and J. Liu, "Cardiac contraction activates endocardial notch signaling to modulate chamber maturation in zebrafish," *Development*, vol. 142, no. 6919, pp. 4080–4091, 2015.
- [90] S. S. D. Vos, N. Ursem, W. Hop, J. Wladimirioff, A. G. D. Groot, and R. Poelmann, "Acutely altered hemodynamics following venous obstruction in the early chick embryo," *J. Exp. Biol.*, vol. 206, pp. 1051–1057, 2003.
- [91] B. Garita, M. Jenkins, M. Han, C. Zhou, M. VanAuker, A. Rollins, J. Watanabe, J. Fujimoto, and K. Linask, "Blood flow dynamics of one cardiac cycle and relationship to mechanotransduction and trabeculation during heart looping," *Am. J. Physiol. Heart Circ. Physiol.*, vol. 300, pp. H879–H891, 2011.
- [92] B. Sankova, J. Machalek, and D. Sedmera, "Effects of mechanical loading on early conduction system differentiation in the chick," *Am. J. Physiol. Heart Circ. Physiol.*, vol. 298, pp. 1571–1576, 2010.
- [93] L. A. Miller, A. Santhanakrishnan, S. K. Jones, C. Hamlet, K. Mertens, and L. Zhu, "Reconfiguration and the reduction of vortex-induced vibrations in broad leaves," *J. Exp. Biol.*, vol. 215, pp. 2716–2727, 2012.
- [94] D. C. Tucker, C. Snider, and W. T. W. Jr, "Pacemaker development in embryonic rat heart cultured *in oculo*," *Pediatric Research*, vol. 23, pp. 637–642, 1988.
- [95] L. D. Waldrop and L. A. Miller, "The role of the pericardium in the valveless, tubular heart of the tunicate, *Ciona savignyi*," *J. Exp. Biol.*, vol. 218, pp. 2753–2763, 2015.
- [96] D. R. Brown, L. A. Samsa, L. Qian, and J. Liu, "Advances in the study of heart development and disease using zebrafish," *J. Cardiovasc. Dev. Dis.*, vol. 3, no. 2, p. 13, 2016.

- [97] H. Yoshia, F. Manasek, and R. A. Arcilla, "Intracardiac flow patterns in early embryonic life. a reexamination.," *Circ. Res.*, vol. 53(3), pp. 363–371, 1983.
- [98] D. Rodriguez Munoz, M. Markl, J. L. Moya Mur, A. Barker, C. Fernandez-Golfin, P. Lancellotti, and J. L. Zamorano Gomez, "Intracardiac flow visualization: current status and future directions," *Eur. Heart J. Cardiovasc. Imaging*, vol. 14(11), pp. 1029–1038, 2013.
- [99] W. Strychalski and R. D. Guy, "A computational model of bleb formation," *Math. Med. Biol.*, vol. 30, pp. 115–130, 2013.
- [100] W. Strychalski, C. A. Copos, O. L. Lewis, and R. D. Guy, "A poroelastic immersed boundary method with applications to cell biology," *J. Comput. Phys.*, vol. 282, pp. 77–97, 2015.
- [101] W. Strychalski and R. D. Guy, "Intracellular pressure dynamics in blebbing cells," *Biophys. J.*, vol. 110(5), pp. 1168–1179, 2016.
- [102] M. Kapustina, D. Tsygankov, J. Zhao, T. Wessler, X. Yang, A. Chen, N. Roach, T. Elston, Q. Wang, K. Jacobson, and M. Forest, "Modeling the excess cell surface stored in a complex morphology of bleb-like protrusions," *PLoS Comput Biol.*, vol. 12(3), p. e1004841, 2016.
- [103] S. D. Olson, S. S. Suarez, and L. J. Fauci, "Coupling biochemistry and hydrodynamics captures hyperactivated sperm motility in a simple flagellar model," *J. Theor. Biol.*, vol. 283, pp. 203–216, 2011.
- [104] S. D. Olson, "Fluid dynamic model of invertebrate sperm motility with varying calcium inputs," *J. Biomech.*, vol. 46, pp. 329–337, 2013.
- [105] J. Simons, S. D. Olson, R. Cortez, and L. J. Fauci, "The dynamics of sperm detachment from epithelium in a coupled fluid-biochemical model of hyperactivated motility," *J. Theor. Biol.*, vol. 354, pp. 81–94, 2014.
- [106] K. Leiderman and A. L. Fogelson, "Grow with the flow: a spatial-temporal model of platelet deposition and blood coagulation under flow," *Math. Med. Biol.*, vol. 28(1), pp. 47–84, 2011.
- [107] K. Leiderman and A. L. Fogelson, "The influence of hindered transport on the development of platelet thrombi under flow," *Bull. Math. Biol.*, vol. 75(8), pp. 1255–1283, 2013.
- [108] K. Leiderman and A. L. Fogelson, "An overview of mathematical modeling of thrombus formation under flow," *Thrombosis Research*, vol. 133, pp. S12–S14, 2014.
- [109] T. Wessler, A. Chen, S. McKinley, R. Cone, M. G. Forest, and S. Lai, "Using computational modeling to optimize the design of antibodies that trap viruses in mucus," *ACS Infect. Dis.*, vol. 2(1), pp. 92–92, 2016.
- [110] P. A. Vasquez, C. Hult, D. Adalsteinsson, J. Lawrimore, M. G. Forest, and K. Bloom, "Entropy gives rise to topologically associating domains," *Nucleic Acids Research*, vol. 44(12), pp. 5540–5549, 2016.
- [111] D. S. Ross, C. M. Battista, A. Cabal, and K. Mehta, "Dynamics of bone cell signaling and pth treatments of osteoporosis," *Ann. Rev. Fluid Mech.*, vol. 17(6), pp. 2185–2200, 2012.

- [112] K. Yang, C. M. Battista, J. Woodhead, S. Stalh, J. Mettetal, P. Watkins, S. Siler, and B. Howell, "Systems pharmacology modeling of drug-induced hyperbilirubinemia: Differentiating hepatotoxicity and inhibition of enzymes/transporters," *Clin. Pharmacol. Ther.*, vol. 101, pp. 501–509, 2017.
- [113] H. Enderling, A. R. Anderson, M. A. Chaplain, A. J. Munro, and J. S. Vaidya, "Mathematical modelling of radiotherapy strategies for early breast cancer," *J. Theor. Biol.*, vol. 241(1), pp. 158–171, 2006.
- [114] H. Enderling, M. A. Chaplain, A. R. Anderson, and J. S. Vaidya, "A mathematical model of breast cancer development, local treatment and recurrence," *J. Theor. Biol.*, vol. 246(2), pp. 245–259, 2007.
- [115] T. Hillen, H. Enderling, and P. Hahnfeldt, "The tumor growth paradox and immune system-mediated selection for cancer stem cells," *Bull. Math. Biol.*, vol. 75(1), pp. 161–184, 2013.
- [116] F. Markowetz, "All biology is computational biology," *PLOS Biology*, vol. 15(3), p. e2002050, 2017.
- [117] W. Osler, "The evolution of modern medicine," *Kaplan Publishing*, vol. 1105, pp. 1822–1829, 2009.
- [118] W. Harvey, "On the motion of the heart and blood in animals," *London: George Bell and Sons*, vol. 88, pp. 49–92, 1889.
- [119] W. D. Hall, "Stephen hales: theologian, botanist, physiologist, discoverer of hemodynamics," *Clinical Cardiology*, vol. 10, pp. 487–489, 1987.
- [120] S. Suter and R. Skalak, "The history of poiseuille's law," *Annu. Rev. Fluid Mech.*, vol. 25, pp. 1–19, 1993.
- [121] H. Zimmer, "Otto frank and the fascination of high-tech cardiac physiology," *Clin. Cardiol.*, vol. 27, pp. 665–666, 2004.
- [122] J. R. Womersley, "Method for the calculation of velocity, rate of flow and viscous drag in arteries when the pressure gradient is known," *J. Physiol.*, vol. 127, pp. 553–563, 1955.
- [123] C. M. Battista, D. Bia, Y. German, R. Armentano, M. A. Haider, and M. S. Olufsen, "Wave propagation in a 1d fluid dynamics model using pressure-area measurements from ovine arteries," *J. Mech. Med. Biol.*, vol. 16, p. 02, 2016.
- [124] C. Peskin, "Flow patterns around heart valves: A numerical method," *J. Comput. Phys.*, vol. 10(2), pp. 252–271, 1972.
- [125] C. Peskin, "Numerical analysis of blood flow in the heart," *J. Comput. Phys.*, vol. 25, pp. 220–252, 1977.
- [126] D. McQueen and C. S. Peskin, "Shared-memory parallel vector implementation of the immersed boundary method for the computation of blood flow in the beating mammalian heart," *J. Supercomputing*, vol. 11, pp. 213–236, 1997.
- [127] B. E. Griffith and C. S. Peskin, "On the order of accuracy of the immersed boundary method: higher order convergence rates for sufficiently smooth problems," *J. Comput. Phys.*, vol. 208, pp. 75–105, 2005.

- [128] B. E. Griffith, R. Hornung, D. McQueen, and C. S. Peskin, “An adaptive, formally second order accurate version of the immersed boundary method,” *J. Comput. Phys.*, vol. 223, pp. 10–49, 2007.
- [129] D. B. Stein, R. D. Guy, and B. Thomases, “Immersed boundary smooth extension: A high-order method for solving pde on arbitrary smooth domains using fourier spectral methods,” *J. Comp. Phys.*, vol. 304, pp. 252–274, 2016.
- [130] Y. Bao, A. Donev, B. E. Griffith, D. M. McQueen, and C. S. Peskin, “An immersed boundary method with divergence-free velocity interpolation,” *arXiv: <https://arxiv.org/abs/1701.07169>*, 2017.
- [131] B. E. Griffith and X. Luo, “Hybrid finite difference/finite element version of the immersed boundary method,” *Int. J. Numer. Meth. Engng.*, vol. 0, pp. 1–26, 2012.
- [132] T. R. Elliot, “The innervation of the bladder and urethra,” *J. Phys.*, vol. 35, pp. 367–445, 1907.
- [133] D. S. Lee, H. C. Yoon, and J. S. Ko, “Fabrication and characterization of a bidirectional valveless peristaltic micropump and its application to a flow-type immunoanalysis,” *Sensors and Actuators*, vol. 103, pp. 409–415, 2004.
- [134] C. Multiphysics, *version 4.2 (R2015a)*. Burlington, MA, USA: COMSOL Inc., 2015.
- [135] S. Vogel and M. Labarbera, “Simple flow tanks for research and training,” *Bioscience*, vol. 28, pp. 638–643, 1978.
- [136] N. Rott, “Note on the history of the reynolds number,” *Ann. Rev. Fluid Mech.*, vol. 22, pp. 1–11, 1990.
- [137] Wolfram, “Heisenberg, werner,” 2009.
- [138] B. E. Griffith, “An adaptive and distributed-memory parallel implementation of the immersed boundary (ib) method,” 2014.
- [139] K. J. Bathe, “Fluid-structure interactions,” *Mechanical Engineering*, vol. April, pp. 67–68, 2008.
- [140] S. Hieber and P. Koumoutsakos, “An immersed boundary method for smoothed particle hydrodynamics of self-propelled swimmers,” *J. Comput. Phys.*, vol. 227, pp. 8636–8654, 2008.
- [141] A. P. Hoover and L. A. Miller, “A numerical study of the benefits of driving jellyfish bells at their natural frequency,” *J. Theor. Biol.*, vol. 374, pp. 13–25, 2015.
- [142] L. A. Miller and C. S. Peskin, “When vortices stick: an aerodynamic transition in tiny insect flight,” *J. Exp. Biol.*, vol. 207, pp. 3073–3088, 2004.
- [143] L. A. Miller and C. S. Peskin, “A computational fluid dynamics of clap and fling in the smallest insects,” *J. Exp. Biol.*, vol. 208, pp. 3076–3090, 2009.
- [144] S. K. Jones, R. Laurenza, T. L. Hedrick, B. E. Griffith, and L. A. Miller, “Lift- vs. drag-based for vertical force production in the smallest flying insects,” *J. Theor. Biol.*, vol. 384, pp. 105–120, 2015.

- [145] E. Tytell, C. Hsu, T. Williams, A. Cohen, and L. Fauci, “Interactions between internal forces, body stiffness, and fluid environment in a neuromechanical model of lamprey swimming,” *Proc. Natl. Acad. Sci.*, vol. 107, pp. 19832–19837, 2010.
- [146] N. A. Battista, A. J. Baird, and L. A. Miller, “A mathematical model and matlab code for muscle-fluid-structure simulations,” *Integr. Comp. Biol.*, vol. 55(5), pp. 901–911, 2015.
- [147] C. Hamlet, L. J. Fauci, and E. D. Tytell, “The effect of intrinsic muscular nonlinearities on the energetics of locomotion in a computational model of an anguilliform swimmer,” *J. Theor. Biol.*, vol. 385, pp. 119–129, 2015.
- [148] L. Zhu, G. He, S. Wang, L. A. Miller, X. Zhang, Q. You, and S. Fang, “An immersed boundary method by the lattice boltzmann approach in three dimensions,” *Computers and Mathematics with Applications*, vol. 61, pp. 3506–3518, 2011.
- [149] P. R. Kramer, C. S. Peskin, and P. J. Atzberger, “On the foundations of the stochastic immersed boundary method,” *Comp. Meth. in Appl. Mech. and Eng.*, vol. 197, pp. 2232–2249, 2008.
- [150] A. L. Fogelson and R. D. Guy, “Immersed-boundary-type models of intravascular platelet aggregation,” *Comput. Methods Appl. Mech. Engrg.*, vol. 197, pp. 2087–2104, 2008.
- [151] P. Lee, B. E. Griffith, and C. S. Peskin, “The immersed boundary method for advection-electrodifffusion with implicit timestepping and local mesh refinement,” *J. Comp. Phys.*, vol. 229(13), pp. 5208–5227, 2010.
- [152] W. Strychalski and R. D. Guy, “Viscoelastic immersed boundary methods for zero reynolds number flow,” *Comm. in Comp. Phys.*, vol. 12, pp. 462–478, 2012.
- [153] J. Du, R. D. Guy, and A. L. Fogelson, “An immersed boundary method for two-fluid mixtures,” *J. Comp. Phys.*, vol. 262, pp. 231–243, 2014.
- [154] D. J. Eyre and A. L. Fogelson, “Ibis: A software system for immersed boundary and interface simulations,” 1997.
- [155] H. Zhang, “PETSc: Portable, extensible toolkit for scientific computation,” 2009.
- [156] Lawrence Livermore National Laboratory, “SAMRAI: Structured adaptive mesh refinement application infrastructure,” 2007.
- [157] B. S. Kirk, J. W. Peterson, R. H. Stogner, and G. F. Carey, “libMesh: A C++ Library for Parallel Adaptive Mesh Refinement/Coarsening Simulations,” *Engineering with Computers*, vol. 22, no. 3-4, pp. 237–254, 2006. <http://dx.doi.org/10.1007/s00366-006-0049-3>.
- [158] E. Gabriel, G. E. Fagg, G. Bosilca, T. Angskun, J. J. Dongarra, J. M. Squyres, V. Sahay, P. Kambadur, B. Barrett, A. Lumsdaine, R. H. Castain, D. J. Daniel, R. L. Graham, and T. S. Woodall, “Open MPI: Goals, concept, and design of a next generation MPI implementation,” in *Proceedings, 11th European PVM/MPI Users’ Group Meeting*, (Budapest, Hungary), pp. 97–104, September 2004.
- [159] B. D. Froese and J. Wiens, “Matib: A simple immersed boundary method solver in matlab,” 2013.
- [160] O. Mesnard, “pyibm: An immersed boundary method python code,” 2014.

- [161] C. S. Peskin, “The immersed boundary method,” 2008.
- [162] C. S. Peskin, “The immersed boundary method,” *Acta Numerica*, vol. 11, pp. 479–517, 2002.
- [163] MATLAB, *version 8.5.0 (R2015a)*. Natick, Massachusetts, USA: The MathWorks Inc., 2015.
- [164] G. Van Rossum, *Python*. <https://www.python.org>: version 3.5, 2015.
- [165] A. J. Chorin, “The numerical solution of the navier-stokes equations for an incompressible fluid,” *Bull. Am. Math. Soc.*, vol. 73, pp. 928–931, 1967.
- [166] D. L. Brown, R. Cortez, and M. L. Minion, “Accurate projection methods for the incompressible navier-stokes equations,” *J. Comp. Phys.*, vol. 168, pp. 464–499, 2001.
- [167] Y. Liu and Y. Mori, “Properties of discrete delta functions and local convergence of the immersed boundary method,” *SIAM J. of Numerical Analysis*, vol. 50, pp. 2986–3015, 2012.
- [168] J. W. Cooley and J. W. Tukey, “An algorithm for the machine calculation of complex fourier series,” *Math. Comput.*, vol. 19, pp. 297–301, 1965.
- [169] W. H. Press, B. P. Flannery, S. A. Teukolsky, and W. T. Vetterling, “Fast fourier transform,” *Ch. 12 in Numerical Recipes in FORTRAN: The Art of Scientific Computing*, vol. 2, pp. 490–529, 1992.
- [170] B. E. Griffith, “An accurate and efficient method for the incompressible navier-stokes equations using the projection method as a preconditioner,” *J. Comput. Phys.*, vol. 228, pp. 7565–7595, 2009.
- [171] A. Bhalla, B. E. Griffith, and N. Patankar, “A unified mathematical frame-work and an adaptive numerical method for fluid-structure interaction with rigid, deforming, and elastic bodies,” *J. Comput. Phys.*, vol. 250, pp. 446–476, 2013.
- [172] C. Hamlet and L. A. Miller, “Feeding currents of the upside-down jellyfish in the presence of background flow,” *Bull. Math. Bio.*, vol. 74(11), pp. 2547–2569, 2012.
- [173] J. M. Stockie, “Modelling and simulation of porous immersed boundaries,” *Computers and Structures*, vol. 87, pp. 701–709, 2009.
- [174] C. S. Peskin and B. F. Printz, “Improved volume conservation in the computation of flows with immersed elastic boundaries,” *J. Comput. Phys.*, vol. 105, pp. 33–46, 1993.
- [175] Y. Kim and C. S. Peskin, “2d parachute simulation by the immersed boundary method,” *SIAM J. Sci. Comput.*, vol. 28, pp. 2294–2312, 2006.
- [176] A. V. Hill, “The heat of shortening and the dynamic constants of muscle,” *Proc. R. Soc. Lond.*, vol. 126, pp. 136–195, 1938.
- [177] Y. C. Fung, *Biomechanics: mechanical properties of living tissues*. New York, USA: Springer-Verlag, 1993.
- [178] H. Hatze, “A comprehensive model for human motion simulation and its application to the take-off phase of the long jump,” *J. Biomech.*, vol. 14, pp. 135–142, 1981.

- [179] J. H. Challis and D. G. Kerwin, “Determining individual muscle forces during maximal activity: Model development, parameter determination, and validation,” *Hum. Movement Sci.*, vol. 13, pp. 29–61, 1994.
- [180] J. Boussinesq, *Theorie de l’ecoulement tourbillonnant et tumultueux des liquides dans les lits rectilignes a grande section (Vol. 1)*. Paris, France: Gauthier-Villars, 1897.
- [181] D. J. Tritton, *Physical fluid dynamics*. New York, NY, USA: Van Nostrand Reinhold Co., 1977.
- [182] E. P. Newren, A. L. Fogelson, R. D. Guy, and R. M. Kirby, “Unconditionally stable discretizations of the immersed boundary equations,” *J. Comput. Phys.*, vol. 222, pp. 702–719, 2007.
- [183] J. M. Teran and C. S. Peskin, “Tether force constraints in stokes flow by the immersed boundary method on a periodic domain,” *SIAM J. Sci. Comput.*, vol. 31(5), pp. 3404–3416, 2009.
- [184] J. M. Teran, L. Fauci, and M. Shelley, “Viscoelastic fluid response can increase the speed and efficiency of a free swimmer,” *Phys. Rev. Lett.*, vol. 104(3), p. 038101, 2010.
- [185] B. E. Griffith and C. S. Peskin, “Electrophysiology,” *Comm. Pure Appl. Math.*, vol. 66, pp. 1837–1913, 2013.
- [186] T. L. Williams, G. Bowtell, and N. A. Curtin, “Predicting force generation by lamprey muscle during applied sinusoidal movement using a simple dynamic model,” *J Exp Biol.*, vol. 201, pp. 869–875, 1998.
- [187] T. McMillen, T. Williams, and P. Holmes, “Nonlinear muscles, passive viscoelasticity and body taper conspire to create neuromechanical phase lags in anguilliform swimmers,” *PLoS Comp. Bio.*, vol. 4(8), p. e1000157, 2008.
- [188] S. Ghosh and J. Stockie, “Numerical simulations of particle sedimentation using the immersed boundary method,” *Commun. Comput. Phys.*, vol. 18(2), pp. 380–416, 2015.
- [189] A. Frisani, “Direct forcing immersed boundary methods: Finite element versus finite volume approach (ph.d. thesis),” *Nuclear Engineering ,Texas A&M University*, 2012.
- [190] W. Schroeder, K. Martin, and B. Lorensen, *The Visualization Toolkit (4th edition)*. Carrboro, USA: Kitware, 1993.
- [191] J. Ahrens, B. Gervaci, and C. Law, *ParaView: An End-User Tool for Large Data Visualizations*. Atlanta, USA: Elsevier, 2005.
- [192] H. Childs, E. Brugger, B. Whitlock, J. Meredith, S. Ahern, D. Pugmire, K. Biagas, M. Miller, C. Harrison, G. H. Weber, H. Krishnan, T. Fogal, A. Sanderson, C. Garth, E. W. Bethel, D. Camp, O. Rübel, M. Durant, J. M. Favre, and P. Navrátil, “VisIt: An End-User Tool For Visualizing and Analyzing Very Large Data,” in *High Performance Visualization—Enabling Extreme-Scale Scientific Insight*, pp. 357–372, Oct 2012.
- [193] A. Chertock and A. Kurganov, “On Splitting-Based Numerical Methods for Convection-Diffusion Equations,” 2012. <http://www4.ncsu.edu/~acherto/papers/Chertock-Kurganov.pdf>.

- [194] R. J. LeVeque, *Finite Volume Methods for Hyperbolic Problems*. Cambridge, UK: Cambridge University Press, 2002.
- [195] K. Kiger, J. Westerweel, and C. Poelma, “Introduction to Particle Image Velocimetry,” 2016. <http://www2.cscamm.umd.edu/programs/trb10/presentations/PIV.pdf>.
- [196] M. H. D. K and Gotz, “Unsteady aerodynamic performance of model wings at low reynolds numbers,” *J. Exp. Biol.*, vol. 174, pp. 45–64, 1993.
- [197] J. Birch, W. Dickson, and M. H. Dickinson, “Force production and flow structure of the leading edge vortex at high and low reynolds numbers,” *J. Exp. Biol.*, vol. 207, pp. 1063–1072, 2004.
- [198] L. M. Crowl and A. L. Fogelson, “Analysis of mechanisms for platelet near-wall excess under arterial blood flow conditions,” *J. Fluid Mech.*, vol. 676, pp. 348–375, 2011.
- [199] C. Zhang, R. D. Guy, B. Mulloney, Q. Zhang, and T. J. Lewis, “The neural mechanism of optimal limb coordination in crustacean swimming,” *PNAS*, vol. 111, pp. 13840–13845, 2014.
- [200] O. L. Lewis, S. Zhang, R. D. Guy, and J. del Alamo, “Coordination of contractility, adhesion and flow in migrating physarum amoebae,” *J. R. Soc. Interface*, vol. 12(106), 2015.
- [201] O. Foundation, “Official openfoam repository,” 2014.
- [202] C. ANSYS Fluent, CFD, *version 17.0*. Cecil Township, Pennsylvania, USA: ANSYS Inc., 2016.
- [203] L. Lee and R. J. Leveque, “An immersed interface method for incompressible navier-stokes equations,” *SIAM J. SCI. COMPUT.*, vol. 25(3), pp. 832–856, 2000.
- [204] Z. Li, “An overview of the immersed interface method and its applications,” *Taiwanese J. Math.*, vol. 7(1), pp. 1–49, 2003.
- [205] O. Ubbink and R. I. Issa, “Method for capturing sharp fluid interfaces on arbitrary meshes,” *J. Comp. Phys.*, vol. 153, pp. 26–50, 1999.
- [206] H. Udaykumar, R. Mittal, P. Rampunggoon, and A. Khanna, “A sharp interface cartesian grid method for simulating flows with complex moving boundaries,” *J. Comp. Phys.*, vol. 20, pp. 345–380, 2001.
- [207] R. Cortez and M. Minion, “The blob projection method for immersed boundary problems,” *J. Comp. Phys.*, vol. 161, pp. 428–453, 2000.
- [208] J. A. Sethian, *Level Set Methods and Fast Marching Methods : Evolving Interfaces in Computational Geometry, Fluid Mechanics, Computer Vision, and Materials Science*. Cambridge, UK: Cambridge University Press, 1999.
- [209] S. J. Osher and R. Fedkiw, *Level Set Methods and Dynamic Implicit Surfaces*. New York, NY, USA: Springer-Verlag, 2002.
- [210] R. Mittal and C. Iaccarino, “Immersed boundary methods,” *Annu. Rev. Fluid Mech.*, vol. 37, pp. 239–261, 2005.
- [211] B. E. Griffith, “Ibmr: an adaptive and distributed-memory parallel implementation of the immersed boundary method,” 2014.

- [212] A. M. Roma, “A multilevel self adaptive version of the immersed boundary method (ph.d. thesis),” *Courant Institute of Mathematical Sciences, NYU*, 1996.
- [213] A. M. Roma, C. S. Peskin, and M. J. Berger, “An adaptive version of the immersed boundary method,” *J. Comp. Phys.*, vol. 153, pp. 509–534, 1999.
- [214] S. Alters, *Biology: Understanding Life*. Boston, USA: Jones and Bartlett Publishers, 2000.
- [215] J. Xavier-Neto, R. Castro, A. Sampaio, A. Azambuja, H. Castillo, R. Cravo, and M. Simoes-Costa, “Parallel avenues in the evolution of hearts and pumping organs,” *Cell. Mol. Life Sci.*, vol. 64, pp. 719–734, 2007.
- [216] C. J. Vivien, J. E. Hudson, and E. R. Porrello, “Evolution, comparative biology and ontogeny of vertebrate heart regeneration,” *Regen. Med.*, vol. 1, p. 16012, 2016.
- [217] R. L. Calabrese and C. S. Cozzens, “Heart (invertebrate) from *Access Science*,” 2016. <https://doi.org/10.1036/1097-8542.309800>.
- [218] N. D. Holland, T. V. Ventatesh, L. Z. Holland, D. K. Jacob, and R. Bodmer, “Amphink2-tin, an amphioxus homeobox gene expressed in myocardial progenitors: insights into evolution of the vertebrate heart,” *Dev. Biol.*, vol. 255(1), pp. 128–137, 2003.
- [219] N. D. Holland and J. Y. Chen, “Origin and evolution of the vertebrates: new insights from advances in molecular biology,” *BioEssays*, vol. 23, pp. 142–151, 2001.
- [220] J. J. Smith and M. C. Keinath, “The sea lamprey meiotic map improves resolution of ancient vertebrate genome duplications,” *Genome Res.*, vol. 25(8), pp. 1081–90, 2015.
- [221] L. Percy and I. C. Potter, “Description of the heart and associated blood vessels in larval lampreys,” *J. Zoology*, vol. 208(4), pp. 479–492, 1986.
- [222] S. A. Green and M. E. Bronnera, “The lamprey: A jawless vertebrate model system for examining origin of the neural crest and other vertebrate traits,” *Differentiation*, vol. 87(1), pp. 44–51, 2015.
- [223] M. E. Kriebel, “Conduction velocity and intracellular action potentials of the tunicate heart,” *The Journal of General Physiology*, vol. 50, pp. 2097–2107, 1967.
- [224] D. J. Randall and P. S. Davie, “The hearts of urochordates and cephalochordates,” *Comparative Anatomy and Development*, vol. 1, pp. 41–59, 1980.
- [225] M. Morad and L. Cleemann, “Tunicate heart as a possible model for the vertebrate heart,” *Fed Proc.*, vol. 39(14), pp. 3188–3194, 1980.
- [226] T. Kenner, M. Moser, I. Tanev, and K. Ono, “The liebau-effect or on the optimal use of energy for the circulation of blood,” *Scripta Medica*, vol. 73, pp. 9–14, 2000.
- [227] J. Manner, A. Wessel, and T. M. Yelbuz, “How does the tubular embryonic heart work? looking for the physical mechanism generating unidirectional blood flow in the valveless embryonic heart tube,” *Developmental Dynamics*, vol. 239, pp. 1035–1046, 2010.
- [228] J. Meier, “A novel experimental study of a valveless impedance pump for applications at lab-on-chip, microfluidic, and biomedical device size scales (ph.d. thesis),” *California Institute of Technology.*, pp. 8636–8654.

- [229] H. T. Chang, C. Y. Lee, and C. Y. Wen, “Design and modeling of electromagnetic actuator in mems-based valveless impedance pump,” *Microsystems Technologies / Micro-and Nanosystems-Information Storage and Processing Systems*, vol. 13, pp. 1615–1622, 2007.
- [230] C. Y. Lee, H. T. Chang, and C. Y. Wen, “A mems-based valveless impedance pump utilizing electromagnetic actuation,” *Journal of Micromechanics and Microengineering*, vol. 18, pp. 225–228, 2008.
- [231] T. Bringley, S. Childress, N. Vandenberghe, and J. Zhang, “An experimental investigation and a simple model of a valveless pump,” *Physics of Fluids*, vol. 20, p. 033602, 2008.
- [232] J. Ottesen, “Valveless pumping in a fluid-filled closed elastic tube-system: one-dimensional theory with experimental validation,” *Journal of Mathematical Biology*, vol. 46, pp. 309–332, 2003.
- [233] D. Auerbach, W. Moehring, and M. Moser, “An analytic approach to the liebau problem of valveless pumping,” *Cardiovascular Engineering: An International Journal*, vol. 4, pp. 201–207, 2004.
- [234] C. G. Manopoulos, D. S. Mathioulakis, and S. G. Tsangaris, “One-dimensional model of valveless pumping in a closed loop and a numerical solution,” *Physics of Fluids*, vol. 18, pp. 201–207, 2006.
- [235] O. Samson, “A review of valveless pumping: History, applications, and recent developments,” 2007.
- [236] C. Babbs, “Behavior of a viscoelastic valveless pump: a simple theory with experimental validation,” *BioMedical Engineering Online*, vol. 9:42, pp. 19832–19837, 2010.
- [237] E. Jung, “Two-dimensional simulations of valveless pumping using the immersed boundary method (ph.d. thesis),” *Courant Institute of Mathematics, New York University*, vol. 608, pp. 139–160, 1999.
- [238] E. Jung and C. Peskin, “2-d simulations of valveless pumping using immersed boundary methods,” *SIAM Journal on Scientific Computing*, vol. 23, pp. 19–45, 2001.
- [239] S. Al-Roubaie, E. D. Jahnsen, M. Mohammed, C. Henderson-Toth, and E. A. Jones, “Rheology of embryonic avian blood,” *Am. J. Physiol. Heart Circ. Physiol.*, vol. 301, no. 6919, pp. 2473–2481, 2011.
- [240] N. A. Battista, A. N. Lane, and L. A. Miller, “On the dynamic suction pumping of blood cells in tubular hearts,” *in press Association for Women in Mathematics Series: Research Collaborations in Mathematical Biology*, 2017.
- [241] L. M. Crowl and A. L. Fogelson, “Computational model of whole blood exhibiting lateral platelet motion induced by red blood cells,” *Int. J. Numer. Meth. Biomed. Engng.*, vol. 26, pp. 471–487, 2009.
- [242] M. Mohammed, S. Roubaie, E. Jahnsen, and E. Jones, “Drawing first blood: Measuring avian embryonic blood viscosity,” *SURE Poster Presentation*, vol. 61, pp. 33–45, 2011.
- [243] S. Al-Roubaie, E. D. Jahnsen, M. Mohammed, C. Henderson-Toth, and E. A. Jones, “Rheology of embryonic avian blood,” *Am. J. Physiol. Heart Circ. Physiol.*, vol. 301(6), pp. 2473–2481, 2011.

- [244] E. Lauga, “Propulsion in a viscoelastic fluid,” *Phys.Fluids*, vol. 19, p. 083104, 2007.
- [245] S. Weinbaum, X. Zhang, Y. Han, H. Vink, and S. Cowin, “Mechanotransduction and flow across the endothelial glycoalyx,” *PNAS*, vol. 100, pp. 7988–7995, 2003.
- [246] M. Kalk, “The organization of a tunicate heart,” *Tissue Cell*, vol. 2, pp. 99–118, 1970.
- [247] M. Anderson, “Electrophysiological studies on initiation and reversal of the heart beat in *ciona intestinalis*,” *J. Exp. Biol.*, vol. 49, pp. 363–385, 1968.
- [248] E. M. Jucker and M. Martin-Smith, *Comparative Physiology of the Heart: Current Trends*. Hanover, New Hampshire, USA: Springer, 1968.
- [249] R. FitzHugh, “Impulses and physiological states in theoretical models of nerve membrane,” *Biophys. J.*, vol. 1(6), pp. 445–466, 1961.
- [250] A. L. Hodgkin and A. F. Huxley, “Propagation of electrical signals along giant nerve fibres,” *Proc. Roy. Soc. Lond. B, Biol. Sci.*, vol. 140, pp. 177–183, 1952.
- [251] A. S. French, “Mechanotransduction,” *Annu. Rev. Physiol.*, vol. 54, pp. 135–152, 1992.
- [252] M. Weckstrom and P. Tavi, *Cardiac Mechanotransduction*. New York, USA: Springer Science and Business, 2007.
- [253] J. B. Gurdon and P. Y. Bourillot, “Morphogen gradient interpretation,” *Nature*, vol. 413, pp. 797–803, 2001.
- [254] J. L. Christian, “Morphogen gradients in development: from form to function,” *Wiley Interdiscip Rev. Dev. Biol.*, vol. 1(1), pp. 3–15, 2012.
- [255] C. Patterson, “Even flow: Shear cues vascular development,” *Arteriosclerosis, Thrombosis, and Vascular Biology*, vol. 25, pp. 1761–1762, 2005.
- [256] P. F. Davies, “Hemodynamic shear stress and the endothelium in cardiovascular pathophysiology,” *Nat. Clin. Pract. Cardiovasc. Med.*, vol. 6(1), pp. 16–26, 2009.
- [257] A. D. Taylor, S. Neelamegham, J. D. Hellums, C. W. Smith, and S. I. Simon, “Molecular dynamics of the transition from l-selectin- to beta 2-integrin-dependent neutrophil adhesion under defined hydrodynamic shear,” *Biophys. J.*, vol. 71(6), pp. 3488–3500, 1996.
- [258] J. H. Cartwright, O. Piro, and I. Tuval, “Fluid dynamics in developmental biology: moving fluids that shape ontogeny,” *HFSP J.*, vol. 3, pp. 77–93, 2009.
- [259] J. B. Freund, J. G. Goetz, K. L. Hill, and J. Vermot, “Fluid flows and forces in development: functions, features and biophysical principles,” *Development*, vol. 139, pp. 1229–1245, 2012.
- [260] B. J. Martinsen, “Reference guide to the stages of chick heart embryology,” *Developmental Dynamics*, vol. 233, no. 4, pp. 1217–1237, 2005.
- [261] N. C. Chi, R. M. Shaw, B. Jungblut, J. Huiskens, T. Ferrar, and R. Arnaout et al., “Genetic and physiologic dissection of the vertebrate cardiac conduction system,” *PLoS Biology*, vol. 6(5), p. e109, 2008.

- [262] D. W. Staudt, J. Liu, K. S. Thorn, N. Stuurman, M. Liebling, and D. Y. Stainier, “High-resolution imaging of cardiomyocyte behavior reveals two distinct steps in ventricular trabeculation,” *Development*, vol. 141(3), pp. 585–593, 2014.
- [263] D. W. Staudt and D. Y. Stainier, “Uncovering the molecular and cellular mechanisms of heart development using the zebrafish,” *Annual Review of Genetics*, vol. 46, pp. 397–418, 2012.
- [264] C. G. DeGroff, B. L. Thornburg, J. O. Pentecost, K. L. Thornburg, M. Gharib, and D. J. S. *et al.*, “Flow in the early embryonic human heart,” *Pediatric Cardiology*, vol. 24, pp. 375–380, 2003.
- [265] M. A. Hill, “Embryology cardiovascular system development,” 2017.
- [266] A. Liu, S. Rugonyi, J. Pentecost, and K. Thornburg, “Finite element modeling of blood flow-induced mechanical forces in the outflow tract of chick embryonic hearts,” *Computers and Structures*, vol. 85, pp. 727–738, 2007.
- [267] S. Goenezen, V. K. Chivukula, M. Midgett, L. Phan, and S. Rugonyi, “4d subject-specific inverse modeling of the chick embryonic heart outflow tract hemodynamics,” *Biomech Model Mechanobiol*, 2015.
- [268] P. Vennemann, K. T. Kiger, R. Lindken, B. C. W. Groenendijk, S. S. de Vos, and T. L. M. ten Hagen *et al.*, “In vivo micro particle image velocimetry measurements of blood-plasma in the embryonic avian heart,” *Journal of Biomechanics*, vol. 39, pp. 1191–1200, 2006.
- [269] N. A. Battista, A. N. Lane, L. A. Samsa, J. Liu, and L. A. Miller, “Vortex dynamics in an idealized embryonic ventricle with trabeculae,” *arXiv: <https://arxiv.org/abs/1601.07917>*, 2015.
- [270] N. A. Battista, A. N. Lane, J. Liu, and L. A. Miller, “Fluid dynamics of heart development: Effects of trabeculae and hematocrit,” *arXiv: <https://arxiv.org/abs/1610.07510>*, 2016.
- [271] G. Hershlag and L. A. Miller, “Reynolds number limits for jet propulsion: a numerical study of simplified jellyfish,” *J. Theor. Biol.*, vol. 285, pp. 84–95, 2011.
- [272] A. Bhalla, B. E. Griffith, and N. Patankar, “A forced damped oscillation framework for undulatory swimming provides new insights into how propulsion arises in active and passive swimming,” *PLOS Comput. Biol.*, vol. 9, p. e1003097, 2013.
- [273] M. J. Berger and J. Oliger, “Adaptive mesh refinement for hyperbolic partial-differential equations,” *J. Comput. Phys.*, vol. 53, no. 3, pp. 484–512, 1984.
- [274] M. J. Berger and P. Colella, “Local adaptive mesh refinement for shock hydrodynamics,” *J. Comput. Phys.*, vol. 82, no. 1, pp. 64–84, 1989.
- [275] Dantec, “Measurement Principles of PIV,” 2016. <http://www.dantecdynamics.com/measurement-principles-of-piv>.
- [276] S. C. Eames, L. H. Philipson, V. E. Prince, and M. D. Kinkel, “Blood sugar measurement in zebrafish reveals dynamics of glucose homeostasis,” *Zebrafish*, vol. 7(2), pp. 205–213, 2010.
- [277] T. L. Hedrick, “Software techniques for two- and three-dimensional kinematic measurements of biological and biomimetic systems,” *Bioinspiration and Biomimetics*, vol. 3, no. 3, pp. 1–6, 2008.

- [278] C. Wang, B. M. Baker, C. S. Chen, and M. A. Schwartz, "Endothelial cell sensing of flow direction," *Arterioscler Thromb Vasc Biol.*, vol. 33(9), pp. 2130–2136, 2013.
- [279] J. Heuslein, J. Meisner, and R. Price, "Reversal of flow direction enhances endothelial cell arteriogenic signaling," *FASEB J*, vol. 28, p. 670.9, 2014.
- [280] A. M. Turing, "The chemical basis of morphogenesis," *Proc. R. Soc. Lond. B Biol. Sci.*, vol. 237, pp. 37–72, 1952.
- [281] D. Dan, C. Mueller, K. Chen, and J. A. Glazier, "Solving the advection-diffusion equations in biological contexts using the cellular potts model," *Phs. Rev. E*, vol. 72, p. 041909, 2005.
- [282] O. Wartlick, A. Kicheva, and M. González-Gaitán, "Morphogen gradient formation," *Cold Spring Harbor Perspectives in Biology*, vol. 1, p. a001255, 2009.
- [283] J. Howard, S. W. Grill, and J. S. Bois, "Turing's next steps: the mechanochemical basis of morphogenesis," *Nature Reviews Molecular Cell Biology*, vol. 12, pp. 392–398, 2011.
- [284] G. P. Sorescu, M. Sykes, D. Weiss, M. O. Platt, A. Saha, and J. Hwang et al, "Bone morphogenic protein 4 produced in endothelial cells by oscillatory shear stress simulates an inflammatory response," *J. Biological Chemistry*, vol. 278(33), pp. 31128–31135, 2008.
- [285] M. A. Ostrowski, N. F. Huang, T. W. Walker, T. Verwijlen, C. Poplawski, and A. S. Khoo et al., "Microvascular endothelial cells migrate upstream and align against the shear stress field created by impinging flow," *Biophysical Journal*, vol. 106(2), pp. 366–374, 2014.
- [286] R. Jamison, C. Samarage, R. Bryson-Richardson, and A. Fouras, "In vivo wall shear measurements within the developing zebrafish heart," *PLoS ONE*, vol. 8(10), p. e75722, 2013.
- [287] E. K. Paluch, C. M. Nelson, N. Biais, B. Fabry, J. Moeller, B. L. Pruitt, C. Wollnik, G. Kudryashova, F. Rehfeldt, and W. Federle, "Mechanotransduction: use the force(s)," *BMC Biology*, vol. 13, p. 47, 2015.
- [288] S. P. Olesen, D. E. Clapham, and P. F. Davies, "Hemodynamic shear-stress activates a K^+ current in vascular endothelial cells," *Nature*, vol. 331, pp. 168–170, 1988.
- [289] P. F. Davies, A. Remuzzi, E. J. Gordon, C. F. Dewey, and M. A. Gimbrone, "Turbulent fluid shear-stress induces vascular endothelial-cell turnover in vitro," *Proc. Natl Acad. Sci.*, vol. 83, pp. 2114–2117, 1986.
- [290] A. M. Malek and S. Izumo, "Mechanism of endothelial cell shape change and cytoskeletal remodeling in response to fluid shear stress," *J. Cell Science*, vol. 137(22), pp. 3867–3875, 1996.
- [291] C. S. Peskin and D. M. McQueen, "Fluid dynamics of the heart and its valves," in *Case Studies in Mathematical Modeling: Ecology, Physiology, and Cell Biology* (F. R. Adler, M. A. Lewis, and J. C. Dalton, eds.), ch. 14, pp. 309–338, New Jersey: Prentice-Hall, 1996.
- [292] S. Patankar, *Numerical Heat Transfer and Fluid Flow. Hemisphere Series on Computational Methods in Mechanics and Thermal Science*. New York, USA: Taylor and Francis, 1980.
- [293] K. H. Huebner, E. A. Thornton, and T. D. Byron, *The Finite Element Method for Engineers (Third ed.)*. New York, USA: Wiley Interscience, 1995.

- [294] S. Chen and G. D. Doolen, “Lattice boltzmann method for fluid flows,” *Annual Review of Fluid Mechanics*, vol. 30, pp. 329–364, 1998.
- [295] S. Succi, *The Lattice Boltzmann Equation for Fluid Dynamics and Beyond*. Oxford, UK: Oxford University Press, 2001.
- [296] J. L. Hess and A. M. Smith, “Calculation of potential flow about arbitrary bodies,” *Progress in Aerospace Sciences*, vol. 8, pp. 1–138, 1967.
- [297] N. A. Battista, “The holy grail: an array of fluid solver codes, including projection, pseudo-spectral (fft), lattice boltzmann, and the panel method,” 2015.
- [298] G. C. Smith and J. P. Pell, “Parachute use to prevent death and major trauma related to gravitational challenge: systematic review of randomised controlled trials,” *BMJ*, vol. 327, p. 1459, 2003.
- [299] A. F. Goldberg and C. J. Chemjobber, “A comprehensive overview of chemical-free consumer products,” *Nature: Chemistry*, vol. 50(2), pp. 145–146, 2014.
- [300] SMACK: Study of Maternal and Child Kissing (SMACK) Working Group, “Maternal kisses are not effective in alleviating minor childhood injuries (boo-boos): a randomized, controlled and blinded study,” *Journal of Evaluation in Clinical Practice*, vol. 21, pp. 1244–1246, 2015.
- [301] R. J. Booth and S. E. Lofland, “Modelling of microwave magnetoabsorption in magnetic microwires,” *J. Phys. D: Appl. Phys.*, vol. 42(9), p. 095004, 2009.
- [302] R. J. Booth, “Energy estimates on asymptotically flat surfaces of revolution (m.s. thesis),” *Dept. of Mathematics, University of North Carolina at Chapel Hill*, 2011.
- [303] K. M. Carroll, “Markov diagrams for some non-markovian systems (masters project),” *Dept. of Mathematics, University of North Carolina at Chapel Hill*, 2014.
- [304] K. M. Carroll and K. Petersen, “Markov diagrams for some non-markovian systems,” *Contemporary Mathematics*, vol. 678, pp. 73–101, 2016.
- [305] W. Qu, N. Brandon, D. Chen, J. Huang, and T. Kress, “A numerical framework for integrating deferred correction methods to solve high order collocation formulations of odes,” *J. Sci. Comp.*, vol. 68(2), pp. 484–520, 2016.
- [306] A. J. Chorin, “Numerical solution of the navier-stokes equations,” *Math. Comp.*, vol. 22, pp. 745–762, 1968.
- [307] B. Costa, “Spectral methods for partial differential equations,” *CUBO: A Mathematical Journal*, vol. 6(4), pp. 1–32, 2004.
- [308] H. Uecker, “A short ad hoc introduction to spectral methods for parabolic pde and the navier-stokes equations,” 2009.
- [309] M. Suzuki, “Fourier-spectral methods for navier stokes equations in 2d,” 2014.
- [310] H. Helmholtz, “Über integrale der hydrodynamischen gleichungen, welcher der wirbelbewegungen entsprechen,” *J. für die reine und angewandte Mathematik*, vol. 55, pp. 25–50, 1858.

- [311] J. Boussinesq, *On Helmholtz's Theorem in Finite Regions*. Madison, Wisconsin: Midwestern Universities Research Association, 1958.
- [312] J. Crank and P. Nicholson, "A practical method for numerical evaluation of solutions of partial differential equations of the heat conduction type," *Proc. Camb. Phil. Soc.*, vol. 43(1), pp. 50–67, 1947.
- [313] J. W. Thomas, *Numerical Partial Differential Equations: Finite Difference Methods*. New York, USA: Springer-Verlag, 1995.
- [314] P. L. Bhatnagar, E. P. Gross, and M. Krook, "A model for collision processes in gases. i. small amplitude processes in charged and neutral one-component systems," *Phys. Rev.*, vol. 94(3), pp. 511–525, 1954.
- [315] P. Asinari, "Multi-scale analysis of heat and mass transfer in mini/micro structures (ph.d. thesis)," *Energy Engineering*, Politecnico di Torino, 2005.
- [316] Y. B. Bao and J. Meskas, "Lattice boltzmann method for fluid simulations," 2011.